Development of Novel Alternative Chemistry Processes for Dielectric Etch Applications

by

Simon Martin Karecki

B.S. Electrical Engineering
Yale University, 1994

S.M. Electrical Engineering and Computer Science
Massachusetts Institute of Technology, 1997

Submitted to the Department of Electrical Engineering and Computer Science in Partial Fulfillment of the Requirements for the Degree of

Doctor of Philosophy
in
Electrical Engineering and Computer Science

at the
MASSACHUSETTS INSTITUTE OF TECHNOLOGY
June, 2000

© Massachusetts Institute of Technology, 2000. All Rights Reserved.

Signature of Author

Department of Electrical Engineering and Computer Science
May 19, 2000

Certified by

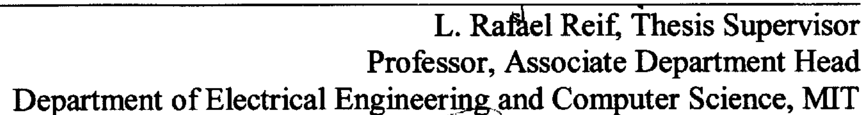

L. Rafael Reif, Thesis Supervisor
Professor, Associate Department Head
Department of Electrical Engineering and Computer Science, MIT

Accepted by

A. C. Smith
Chairman, Department Committee on Graduate Students

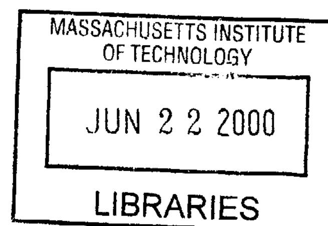

MASSACHUSETTS INSTITUTE OF TECHNOLOGY
JUN 2 2 2000
LIBRARIES
ENG

Development of Novel Alternative Chemistry Processes for Dielectric Etch Applications

by

Simon Martin Karecki

Submitted to the Department of Electrical Engineering and Computer Science in Partial Fulfillment of the Requirements for the Degree of

Doctor of Philosophy
in
Electrical Engineering and Computer Science

at the
MASSACHUSETTS INSTITUTE OF TECHNOLOGY
June, 2000

Abstract

The removal of dielectric films in semiconductor processing relies almost exclusively on the use of perfluorocompounds (PFCs), which are suspected global warming agents. The two applications in semiconductor manufacture that account for the largest use and emissions of PFCs are the patterning of dielectric films and the cleaning of dielectric film plasma enhanced chemical vapor deposition (PECVD) chambers. The work discussed in the author's Ph.D. thesis was conducted as part of a project whose goal is to identify and develop novel replacement etchants for these applications. The focus of the author's Ph.D. thesis is the patterning application. The research discussed in this document constitutes a follow up to the author's M.S. thesis, which discussed the initial stages of this project. These stages consisted primarily of preliminary screening tests involving a class of chemistries which was expected to be promising from a process standpoint at an early point in the project. The work carried out subsequently covered a far greater scope of activities and included additional preliminary screening tests with chemistries that were not covered by the author's M.S. thesis as well as extensive concept-and-feasibility tests and subsequent process development efforts using several of the more promising chemistries in a dielectric wafer patterning application. Much of this experimental work had been carried out in collaboration with industrial partners belonging to the semiconductor manufacturer, equipment supplier, and gas supplier communities. These tests were carried out on process tools housed both within MTL's Integrated Circuits Laboratory and at an industrial location, namely Motorola Inc.'s Advanced Products Research and Development Laboratory (APRDL). The project to identify and develop alternative chemistries for dielectric film removal applications is continuing after the completion of the author's thesis, with subsequent studies that will build on the results of the work done to date.

The research presented in this document involved the evaluation of fluorinated compounds belonging to three principal families of modified fluorocarbon molecules: hydrofluorocarbons (HFCs), iodofluorocarbons (IFCs), and unsaturated fluorocarbons (UFCs). In addition, other chemistries, namely trifluoroacetic anhydride (TFAA), oxalyl fluoride, and octafluorotetrahydrofuran, were also examined. The focus of much of the work was on the etching of patterned silicon oxide films in back-end-of-the-line (BEOL) applications such as via etch. In its mature phases, the work conducted relied on a two-pronged approach toward evaluating new etchants: characterization of their process performance and characterization of their process emissions prior to release into the atmosphere. Cross-sectional scanning electron microscopy (SEM) was the principal means of process performance characterization, whereas Fourier transform infrared (FTIR) spectroscopy was the principal technique employed for effluent characterization. At appropriate times, other diagnostic techniques, namely x-ray photoelectron spectroscopy (XPS), time-of-flight secondary ion mass spectrometry (TOF-SIMS), Auger electron spectroscopy (AES), and quadrupole mass spectrometry (QMS) were also used for film or effluent characterization.

Within the HFC family, candidates were identified that exhibited generally good process results with emissions reductions ranging from ~40% into the 70% range relative to a PFC based reference. More comprehensive tests with IFC compounds demonstrated that emissions reductions in the 80% range are attainable for working processes. Good performance was obtained with respect to some, but not all, key process metrics, demonstrating the potential utility of IFCs in certain dielectric etch applications, but also indicating that there were significant limitations to their use, stemming mostly from selectivity problems. In tests with UFC compounds, emissions reductions on the order of 85%, combined with good process performance, were obtained. This family of compounds showed the greatest promise from both an emissions standpoint and a process standpoint. In particular, compounds in this family showed very good mask layer and stop layer selectivity, in addition to good etch rates and good profile control. It is particularly encouraging that the use of some of these compounds, in addition to offering emissions reductions, may, in fact, offer a process advantage over conventional chemistries in applications requiring high selectivity. At the time of this writing, unsaturated fluorocarbons are viewed as a major avenue for further exploration within the ongoing PFC alternatives project.

Thesis Supervisor: L. Rafael Reif
Professor, Associate Department Head
Department of Electrical Engineering and Computer Science, MIT

Acknowledgments

Thanks go out, first of all, to Prof. Rafael Reif for all his guidance and support during the course of this project, and for being a mentor to me through all this time. I will always remain indebted to him for the innumerable lessons I learned as his student and for the indelible impact he has made on my growth as a researcher and scientist. I also would like to thank my colleagues and partners on this project, Laura Pruette and Ritwik Chatterjee, for all their hard work, for long days and nights spent in fabs and subfabs, and for numerous frequent flyer miles earned together. It is an understatement to say that they played an instrumental role in the work presented in this document. Thanks also to the members of my thesis committee for their inputs: Prof. Duane Boning from MIT's Dept. of Electrical Engineering and Computer Science – who holds the (perhaps dubious) distinction of having served on every academic committee (Oral Qualifying Exam Committee, Area Exam Committee, and Thesis Committee) involved in my career at MIT; Prof. Karen Gleason from MIT's Dept. of Chemical Engineering; and Laurie Beu from Motorola's APRDL (Advanced Products Research and Development Laboratory).

Much of the work in this document would have quite simply never occurred if not for the contribution of three people at Motorola APRDL, where this project lived a parallel life to the one it had at MIT.* Many thanks go out to: Laurie Beu (once more), in her capacity as Manager of APRDL's Environmental Department, for making it possible for me to conduct my research at APRDL in the first place; Terry Sparks, for teaching me everything I know about dielectric etch and showing me why it *is* rocket science; and Victor Vartanian, for endless hours spent in the APRDL subfab on *n*th shift, for his patience in editing almost every draft I wrote in the last three years, and for his tireless support of our work, regardless of which shift it happened to fall on. APRDL's contribution to this work cannot be emphasized enough, given that it is represented by every activity discussed in Chapters 5 and 6 of this document. My gratitude also goes out to numerous individuals within that organization, and Motorola's Ed Bluestein facility in general, who played at times essential roles in supporting this project: Dan Babbitt, Jeff Rose, Ralph Garza, J. Davidson, Lloyd Gonzalez, and the entire APRDL Etch Maintenance Team, along with Chuck Miller, J. J. Lee, Mike Lindell, Tra Baumeister, Ai Koh, Kitty Corbett, Rode Mora, Benny Perez, James Dixon, Laura Mendicino, Paul Thomas Brown, Paul Thomas Leigh, and Deborah Friedman.

In the course of some of the PACE activities as well as the several PECVD chamber clean projects at MIT, we have also benefited from interacting with a number of individuals representing a cross section of semiconductor companies, equipment suppliers, and materials vendors: John Langan, Steve Rogers, Ralph Ciotti, Brian Felker, and Bill Entley from Air Products and Chemicals, Inc.; Lew Tousignant, Larry Zazzera, and John Owens from the 3M Company; Ken Aitchison and Viral Hazari from Novellus

* Like all good Motorola activities, it had an acronym to go with it: PACE, which stood for "Project on Alternative Chemistries for Etch" or "PFC Alternative Chemistries Evaluation," depending on whom one asked.

Systems, Inc.; Bernie Pogge and Cynthia Hines from IBM Microelectronics; Mike Mocella and Charles Allgood from DuPont Fluoroproducts; and Matthew Luly from AlliedSignal, Inc.

Much of the FTIR work presented in this document was carried out with gas standards prepared by Jimmy Hebert of HP Gas Products / Accurate Gases / Tex-La Gases. A thank you goes out to Jimmy for always going the extra mile for us.

Within MIT's Microsystems Technology Labs, thanks go out to Vicky Diadiuk and the entire MTL staff, past and present, for all their assistance – in particular, Joe Walsh, Wayne Price, Kurt Broderick, and Barry Farnsworth; to Debb Hodges-Pabon, for making everything turn out right for me so many times when things were in a crunch; to Pat Varley in MTL and Ishara Smith in EECS for their help and support; and, also in EECS, to Marilyn Pierce and Monica Bell, for their patience with me (and this document).

On a personal note, I will always be indebted to those closest to me – Anna and Richard, my parents, for their sacrifices and for their unfailing belief in me; Yumi Oshima, for her support and understanding and, most importantly, for always being there for me during the ups and downs of the last few years; Matt Reagan, for helping me maintain my sanity by constantly reminding me that Jay Peak at –20 °F is more fun than my office at 70 °F any day; as well as all my friends in Boston: Brian Chen, Matthew Dyer, Paul Huibers, Yoshi Uchida, Karen Willcox, and everyone else who has been there to help me remember that occasionally there is more to life than straight sidewalls and good resist selectivity...

A thank you also goes out to Ginny Poe at the Semiconductor Research Corporation for always looking out for me during the time I spent as an SRC Fellow. Finally, thanks to Walter Worth and SEMATECH for the initial funding of this project and to the NSF/SRC Engineering Research Center for Environmentally Benign Semiconductor Manufacturing for its continuing funding of this work (SRC contract ID 425.001) and, in particular, Prof. Farhang Shadman at the University of Arizona for his tireless efforts as the Center's Director.

Table of Contents

Abstract 3
Acknowledgments 5
Table of Contents 7

1. Introduction 11
   1.1 Perfluorocompounds in the Semiconductor Industry and Their Environmental Concerns 12
      1.1.1 Approaches to Treating PFC Emissions 13
      1.1.2 Atmospheric Properties of Perfluorocompounds 15
      1.1.3 Policy Issues 17
   1.2 Project Overview 21
      1.2.1 Project Strategy 22
         1.2.1.1 Initial Strategy 22
         1.2.1.2 Modifications to the Initial Strategy 26
      1.2.2 Review of Related Work 32
         1.2.2.1 Early Hydrofluorocarbon Studies 32
         1.2.2.2 PECVD Chamber Clean Studies 33

2 Selection of Candidate Chemistries 37
   2.1 Selection Criteria 37
   2.2 Families of Compounds 39
      2.2.1 Hydrofluorocarbons 39
      2.2.2 Iodofluorocarbons 40
      2.2.3 Unsaturated Fluorocarbons 42
      2.2.4 Other Compounds 43

3 Basic Mechanisms and Tool Concepts in Plasma Etching 52
   3.1 Plasma Fundamentals 52
      3.1.1 Gas Phase Collision Processes 53
      3.1.2 Elastic and Inelastic Collisions 54
      3.1.3 Glow Discharges 57
      3.1.4 Surface Potentials, Sheath Formation 59
   3.2 High vs. Low Density Plasma Sources 61
      3.2.1 The Parallel Plate Diode 61
      3.2.2 Medium Density Plasma Tool Designs 64
      3.2.3 Low Pressure, High Density Sources 64
         3.2.3.1 Non-Resonant ICP (Inductively Coupled Plasma) Sources 67
         3.2.3.2 Helical Resonator Sources 68
         3.2.3.3 ECR (Electron Cyclotron Resonance) Sources 68
         3.2.3.4 Helicon Sources 69
         3.2.3.5 Other High Density Source Designs 70
   3.3 Fluorocarbon Plasmas in Dielectric Etch Processes 71
      3.3.1 Etching of Si vs. Etching of Dielectrics 72

3.3.2 Polymer Formation 72
3.3.3 Oxygen Effects 73
3.3.4 Hydrogen Effects 75
3.3.5 F:C Ratio Model and Polymerization 78
3.4 Process Tools Used 79
3.4.1 Applied Materials Precision 5000 80
3.4.2 Applied Materials Centura 5200/5300 HDP/IPS 83

4 Screening Stage Studies 88
4.1 Initial Iodofluorocarbon Study and Trifluoroacetic Anhydride Study 88
4.1.1 Experimental Setup 90
4.1.1.1 Octafluoropropane and TFAA Experiments 90
4.1.1.2 Iodofluorocarbon Experiments 91
4.1.2 Results and Discussion 92
4.1.2.1 Octafluoropropane and TFAA Experiments 92
4.1.2.2 Iodofluorocarbon Experiments 95
4.1.3 Conclusions 100
4.2 Follow-up Study with Additional Iodofluorocarbon Species 101
4.2.1 Experimental Setup 102
4.2.2 Results and Discussion 103
4.2.3 Conclusions 107

5 Wafer Patterning Studies: Hydrofluorocarbons and Iodofluorocarbons 109
5.1 2H-heptafluoropropane and Iodofluorocarbon Concept-and-Feasibility Study 111
5.1.1 Experimental Setup 112
5.1.2 Results and Discussion 117
5.1.2.1 2H-heptafluoropropane 119
5.1.2.2 Iodotrifluoromethane 121
5.1.2.3 2-iodoheptafluoropropane 122
5.1.2.4 1-iodoheptafluoropropane 125
5.1.3 Conclusions 127
5.2 2H-heptafluoropropane Via Etch Process Development Study 130
5.2.1 Experimental Setup 130
5.2.2 Results and Discussion 132
5.2.3 Conclusions 137
5.3 Pentafluoroethane/1,1-difluoroethane Concept-and-Feasibility Study 139
5.3.1 Experimental Setup 140
5.3.2 Results and Discussion 146
5.3.2.1 Basic Mechanisms 146
5.3.2.2 Process Results 152
5.3.2.3 Emissions Results 185
5.3.3 Conclusions 196
5.4 1- and 2-iodoheptafluoropropane Via Etch Process Development Study 201
5.4.1 Process Characterization 201
5.4.1.1 Experimental Setup 202

5.4.1.2 Results and Discussion – Neural Network Experiments 207
5.4.1.3 Results and Discussion – Effects of Wall and Chiller Temperature 231
5.4.1.4 Results and Discussion – Cross-sectional SEM Analysis 232
5.4.1.5 Results and Discussion – Comparison between 1- and 2-iodoheptafluoropropane 238
5.4.1.6 Results and Discussion – Stop Layer Selectivity Experiments 239
5.4.1.7 Conclusions 241
5.4.2 Deposited Film Characterization 243
5.4.2.1 Experimental Setup 244
5.4.2.2 Results and Discussion – XPS Surface Scans 245
5.4.2.3 Results and Discussion – XPS Depth Profiles 247
5.4.2.4 Results and Discussion – XPS F:C Ratios and C 1*s* Spectrum Analysis 260
5.4.2.5 Results and Discussion – TOF-SIMS Analysis (Depth Profiles) 263
5.4.2.6 Conclusions 266
5.4.3 Effluent Characterization 267
5.4.3.1 Experimental Setup 268
5.4.3.2 Results and Discussion 273
5.4.3.3 Conclusions 291

6 Wafer Patterning Studies: Unsaturated Fluorocarbons and Other Compounds 295
6.1 Oxalyl Fluoride Concept-and-Feasibility Study 296
6.1.1 Experimental Setup 297
6.1.2 Results and Discussion 301
6.1.3 Conclusions 319
6.2 Unsaturated Fluorocarbon Concept-and-Feasibility Study 321
6.2.1 Experimental Setup 322
6.2.2 Results and Discussion 326
6.2.2.1 Comparison of all Gases at Same Process Condition 326
6.2.2.2 Comparison of C_4F_8 Isomers 330
6.2.2.3 Comparison of C_4F_6 Isomers 336
6.2.2.4 c-C_5F_8, C_3F_6, and c-C_4F_8O Processes 341
6.2.2.5 Extended Etch Time Experiments 344
6.2.3 Conclusions 345

7 Summary and Recommendations for Future Studies 348
7.1 Summary of Results 349
7.2 Conclusions Regarding Fluorocarbon Plasmas and Global Warming Emissions 352
7.3 Future Directions for New Dielectric Etchants 355

Appendix A - FTIR Methodology 358
A.1 FTIR Instrument 358

A.2 Calibration 360
A.3 Beer's Law and Pressure / Temperature Scaling 364
A.4 Analysis Methods 366

Appendix B - FTIR Spectra and Calibration Data 369

1. Introduction

The aim of the research discussed in this document has been the evaluation of new fluorinated compounds for potential use in dielectric plasma etch processes in wafer patterning applications. The motivation for this work has been the fact that, presently, dielectric etching is almost exclusively dependent on a class of substances known as perfluorocompounds (PFCs). These compounds, while generally possessing desirable handling properties, are believed to have an unfavorable long-term impact on climate change. PFCs have come under increased scrutiny over the course of the mid- to late 1990s because of their alarmingly potent global warming properties, prompting the emergence of activities focused on PFC emissions reduction among semiconductor manufacturers, within their equipment and materials supplier communities, as well as within academia.

This document will describe work undertaken under a project whose goal is to address this issue through the replacement of PFCs with novel fluorinated compounds that lead to processes with reduced global warming emissions. The introductory material in Chapter 1 will review key background points regarding the PFC issue within the semiconductor industry (Section 1.1). It will also supply an overview of the scope and direction of the PFC alternatives project as a whole to provide the reader with a context for each of the individual studies (Section 1.2.1) as well as review other work carried out as part of the project that was either early work incorporated into the author's M.S. thesis [1] or that falls outside the main scope of the present document (Section 1.2.2).

Chapter 2 will focus on the properties of the novel compounds selected for the various activities described herein. Chapter 3 will attempt to provide a brief overview of plasma etching in general and fluorocarbon plasma etching of dielectric films in high density plasma (HDP) tools – which is at the heart of this work – in particular. Chapter 4 will discuss the early screening efforts that, together with the hydrofluorocarbon (HFC) work discussed in Section 1.2.2.1, provided the initial direction for the project. This work, which was introductory in nature and limited in its scope, was conducted on a medium

density magnetically enhanced plasma etch tool housed in MIT's Integrated Circuits Laboratory. Subsequent studies shifted their focus to HDP tools. Chapters 5 and 6 will discuss a series of studies that were used to evaluate and characterize a number of novel chemistries in actual dielectric etch processes on a high density inductively coupled plasma tool, all within the context of a far-reaching collaboration with Motorola Inc.'s Advanced Products Research and Development Laboratory (APRDL). All of the work discussed in Chapters 5 and 6 was carried out at APRDL. Chapter 7 will be devoted to conclusions regarding plasma chemistry vis a vis global warming emissions and process capability that were drawn from these studies.

Finally, the Appendices will provide the reader with supplementary material that falls outside the main flow of the document. Appendix A, in particular, will be devoted to a discussion of practical details of Fourier transform infrared (FTIR) spectroscopy as implemented within the context of this project. Gas phase extractive FTIR spectroscopy was a key diagnostics technique used to characterize the effluent streams emitted by the various processes studied. The methodology developed for this purpose was of central importance to these studies. As of this writing, FTIR has gained prominence as, arguably, the technique of choice for complex effluent analysis. Many of the practical details that are essential to its successful deployment have been the product of in-house expertise by a small number of research groups, including the author and his collaborators. Appendix A will be an attempt to provide a reader who has an interest in implementing FTIR for process effluent characterization with some practical notes on the hardware setup and procedures used by the author and his coworkers. Appendix B contains a library of FTIR reference spectra for compounds of interest in the studies discussed in this document.

1.1 Perfluorocompounds in the Semiconductor Industry and Their Environmental Concerns

In the past decade, perfluorocompounds, which are used by the microelectronics industry for the etching of thin film dielectrics and *in-situ* cleaning of plasma enhanced chemical

vapor deposition (PECVD) chambers, have come under increased scrutiny because of their suspected global warming nature. These gases include CF_4, C_2F_6, C_3F_8, c-C_4F_8, NF_3, and SF_6. Their global warming potentials (GWPs) range from thousands to tens of thousands times that of CO_2 [2-5], the most heavily emitted global warming gas today. In addition, their atmospheric lifetimes range from hundreds to tens of thousands of years. [2-5] To address this environmental issue, the semiconductor industry and its partners in academia and in its supplier communities have proposed and are investigating a range of options that include process optimization, abatement, capture/recovery, and alternative chemistries.

1.1.1 Approaches to Treating PFC Emissions

Process optimization is widely regarded as a necessary first step toward lowering the semiconductor industry's PFC emissions. Until the PFC issue gained prominence in the late 1990s, very little consideration was given in plasma tool and process design toward process effluent quantity and composition, particularly with regard to global warming impact. Because of this, many processes were designed to operate in regimes that are now understood to be inefficient with respect to emissions – regimes characterized by high process gas flows and low utilization. In many cases, equivalent process performance can be achieved under more efficient, lower flow operating conditions that result in lower global warming emissions and often have the additional benefit of lower feed gas consumption, with the associated cost savings. Optimization, however, will generally result in only incremental improvements, necessitating the need for other approaches.

Capture/recovery systems have been constructed and tested by virtually all of the major semiconductor gas suppliers in the US. They typically treat the exhaust emitted by a number of process tools within a wafer fab (on the order of tens) and require a correspondingly large footprint. A number of these systems, which rely on technologies such as membrane separation, cryogenic collection, or pressure swing absorption [6], have demonstrated good performance in terms of PFC recovery (quantified by percentage

of influent material captured) and concentration (quantified by percentage of recovered material this is the desired product, rather than ballast nitrogen). Among the principal drawbacks to their widespread deployment, however, are their size and, more importantly, cost to build and operate. At the present time, there is a growing sentiment among semiconductor manufacturers that capture/recovery schemes may not prove to be a cost effective solution, especially if repurification and reuse are more costly than the purchase of new gas. [7]

Abatement technologies were among the earliest proposed solutions to the PFC issue. Early systems operated by thermally destroying PFC molecules "post-pump", *i.e.,* after the process effluent had been mixed with pump ballast nitrogen and introduced into the exhaust stream. These systems were essentially thermal "burn boxes" adapted for operation at higher temperatures required to destroy PFCs. Initial designs were troubled by high levels of NO_x generation and poor destruction efficiencies for CF_4, a particularly stable and, unfortunately, particularly common PFC. These issues were eventually resolved; nevertheless, thermal systems have other drawbacks, namely high usage of cooling water and, again, cost effectiveness. More promising approaches have been pursued in the areas of catalytic decomposition and plasma abatement. In the former case, a single system is typically scaled to handle the output of several process chambers and uses a catalyst heated to a high temperature (~700 °C) to break down the PFC molecules. [8, 9] The limitations on the number of chambers that can be handled by a single unit are posed chiefly by the pump ballast requirements for individual process tools. Typical process pump nitrogen use is on the order of 50 slm (standard liters per minute) per process chamber. While "post-pump" systems operate at atmospheric pressures, plasma abatement devices are designed to operate at lower pressure (millitorr to torr range) before the process rough pump, hence before the effluent stream is diluted with ballast nitrogen. A single unit is dedicated to treat each process chamber. Presently, catalytic systems and plasma abatement systems are regarded as having the greatest potential among abatement devices for successful deployment. The reader is referred to Refs. [10] and [11] for more detailed descriptions of promising examples of plasma abatement systems.

The approach investigated by the author and his collaborators has been the replacement of PFCs with other fluorinated compounds. This approach is regarded as a long-term solution that aims to address the issue at the source, rather than at "end-of-pipe". Because process qualification in manufacturing environments is generally a time- and cost-intensive task, the idea of "drop-in" replacements for existing processes has only limited applicability. Specifically, out of the two principal PFC-using and emitting applications, dielectric PECVD chamber clean and dielectric etch, the former has been found to be more suitable for drop-in replacement into existing tools, due to its lower process complexity and less stringent process requirements. In the case of etch processes, new chemistries are more likely to be introduced concurrently with new process tools. Hence one of the major focal points of the strategy adopted within this work has been the desire to address leading edge current generation and future generation process tools; to that end, much of the work carried out in the mature phases of the project emphasized a focus on high density plasma tools.

1.1.2 Atmospheric Properties of Perfluorocompounds

Generally speaking, the compounds classified as PFCs are non-corrosive, non-flammable, and (with the exception of NF_3) for all practical purposes non-toxic, all of which makes this class of compounds highly desirable from a handling standpoint. However, the low reactivity of these molecules manifests itself not only in their handling properties but also in their atmospheric longevity. PFCs are thought to be potent global warmers because of a confluence of two properties: high stability (and therefore atmospheric longevity) and excellent infrared absorbency [2-4]. This combination results in long-lived species that are very efficient at trapping and re-emitting longwave radiation emitted by the Earth's surface.

Global warming compounds are often compared using a metric known as the global warming potential (GWP). This index is defined as the time-integrated warming effect resulting from an instantaneous release of a unit mass (1 kg) of a given compound in

today's atmosphere, relative to that from 1 kg of carbon dioxide [12], which is nominally assigned a GWP of 1. This is formally quantified in the following equation [13]:

$$GWP_T = \frac{\int_0^T a_i c_i dt}{\int_0^T a_{CO_2} c_{CO_2} dt}, \qquad (1.1)$$

where a_i is a coefficient quantifying the instantaneous radiative forcing that results from a unit increase in the atmospheric concentration of a given gas i, c_i is the concentration of that gas in the atmosphere as a function of time, and T is the integration time, *i.e.,* the time after the release through which the calculation is being performed. Typically GWPs are listed for 20, 100, and 500 year time horizons, with the 100 year value (GWP_{100}) being used most commonly. Hence, since GWP is a function of both the atmospheric longevity and the infrared absorbency of a compound, it is not surprising that perfluorocompounds possess very high GWPs (see Table 1.1).† Table 1.1 also lists some toxicological properties of these compounds. Cardiac sensitization levels are given in addition to acute toxicity indicators because heart arrhythmia is often the first acute adverse physiological effect seen after exposure to halocarbons. [14] As the table indicates, PFCs (with the exception of NF_3) are largely non-toxic. NF_3, in addition to having moderate toxicity concerns, is also a potent oxidizer. Despite this reactivity, however, it possesses considerable atmospheric stability.

Currently, CF_4, C_2F_6, SF_6, NF_3, and, more recently, C_3F_8 and c-C_4F_8 are the principal PFCs used in integrated circuit (IC) fabrication. See Table 1.2. CHF_3, though not strictly a perfluorinated compound, is also a heavily used etchant that shares the same environmental concerns as the PFCs, and is therefore treated as one for practical purposes (see Table 1.1).

PFCs can be used to etch a variety of materials: polysilicon, dielectrics (*i.e.,* silicon dioxide and silicon nitride), as well as refractory metals (*i.e.,* tungsten). Silicon dioxide

---

† GWP_{100} values: In the experimental work presented in Chapters 5 and 6, GWP_{100} values are employed to calculate the global warming impact of a given process. Sections 5.1, 5.2, 5.3, and 6.1 employ 1995 values, obtained from Ref. [3]; Sections 5.4 and 6.2, for which the data analysis was carried out later, employ 1998 values obtained from Ref. [4].

(and, to a lesser extent, nitride) chamber cleaning and patterning, however, account for the largest share of PFC usage and emission in semiconductor manufacturing. Moreover, as Table 1.2 shows, these films are exclusively dependent on PFCs, while tungsten and polysilicon etch processes are not. Present day estimates place the breakdown of PECVD clean versus etch emissions at 60/40 for older (150 mm wafer size and below) fabs and 70/30 to 90/10 for 200 mm facilities. [7] Despite the lower share of the emissions being accounted for by etch, the etch application is still a major focus for this project and for other activities seeking to address PFC emissions because: 1) as reductions in PECVD chamber clean applications (which are inherently easier to address) are implemented, the volume of PFC emissions from etch applications will grow in relative terms (it is, of course, also projected to grow in absolute terms, due to the increase in production levels); and 2) as will be discussed shortly, very large reductions will still be needed in both PECVD clean and etch applications to meet the industry's targets.

1.1.3 Policy Issues

While no regulatory driver – domestic or international – presently exists to mandate specific reductions in PFC emissions, the emergence of regulatory protocols regarding PFCs is a possibility. Most present anthropogenic greenhouse gas emissions are in the form of gases such as CO_2, N_2O, and CH_4. [2-4] Consequently, the focus of international attention at fora such as the 1992 United Nations Conference on Environment and Development and its subsequent Conferences of the Parties (COPs), has been on addressing CO_2 emissions. PFCs, however, have come under increased scrutiny because of their alarming potency and the relative permanence of their effects. For instance, the 1993 U.S. Climate Change Action Plan, which had become a policy blueprint on this issue for the US Environmental Protection Agency (EPA), specifically calls for reductions in the emissions of halogenated compounds, including PFCs. [15] More recently, the Kyoto Protocol, established in December, 1997 at the third COP in Kyoto, included PFCs as part of the basket of gases that are subject to voluntary emissions reductions on the part of the signatories by 2008-2012. [7] Even prior to this development, the global semiconductor industry, first in the U.S., then in Asia and

Europe, had made the determination that proactive programs to implement PFC emissions reductions are preferable to external regulatory pressures. Initially, the US had been the locus of most semiconductor industry activity on the PFC issue. In recent years, however, Asian and European integrated circuit manufacturers have also become active in exploring solutions in this area.

A key development in the U.S. was the voluntary Memorandum of Understanding (MOU) program established in 1996. Under its auspices, semiconductor companies within the U.S. industry have entered into voluntary agreements with the U.S. EPA, whereby the signatories committed to reporting their PFC emissions (on a company-blind basis) as well as to pursuing technological solutions to the PFC issue through research and development activities. [21] European and Japanese semiconductor industry organizations have since also implemented similar programs. As of this writing an extension of the U.S. MOU program is being negotiated, with the Semiconductor Industry Association (SIA) assuming collective responsibility for its member companies.

Table 1.1: Properties of global warming compounds used in semiconductor applications.

Name	Formula	FC Number	1995 Values		1998 Values		Acute Toxicity (LC_{Lo}, LC_{50}, or ALC, ppm)	Cardiac Sensitization (LOAEL, ppm)
			Lifetime (years)	Global Warming Potential (100 Yr. Integrated Time Horizon)	Lifetime (years)	Global Warming Potential (100 Yr. Integrated Time Horizon)		
Tetrafluoromethane	CF_4	14	50,000	6,500	50,000	5,700	895,000 (a)	
Hexafluoroethane	C_2F_6	116	10,000	9,200	10,000	11,400	>200,000 (b)	
Octafluoropropane	C_3F_8	218	2,600	7,000	2,600	8,600	>800,000 (c)	400,000 (d)
Octafluorocyclobutane	c-C_4F_8	C318	3,200	8,700	3,200	11,200		
n-Decafluorobutane	n-C_4F_{10}	3-1-10	2,600	7,000	2,600	8,600		
Sulfur hexafluoride	SF_6		3,200	23,900	3,200	22,200		
Nitrogen trifluoride	NF_3		740	8,100	740	10,800	6,700 (e) 10,000 (f)	
Trifluoromethane	CHF_3	23	264	11,700	243	14,800		~700,000 (g)
*Carbon dioxide**	CO_2		*50-200*	*1*		*1*		

1995 GWP_{100} and lifetime values from Ref [3], except NF_3, Ref. [5], 1998 values from Ref. [4].
*CO_2 given as reference.
(a) LC_{Lo} (lowest observed lethal concentration), rat, source [16].
(b) ALC (approximate lethal concentration), rat, 2-hr. exposure, source [17].
(c) ALC, source [14].
(d) LOAEL (lowest observed adverse effect level), dog, source [14].
(e) LC_{50}, rat 1 hr exposure, source .[18]
(f) LC_{50}, monkey, source [18]
(g) Effects observed at this conc., cat, source [19]

Table 1.2: Applications of perfluorocompounds. [20]

Use	Gases
Silicon patterning	C_2F_6, SF_6, NF_3, CF_4, BCl_3, HBr, Cl_2, HCl
SiO_2 patterning	C_2F_6, SF_6, CF_4, CHF_3, C_3F_8, c-C_4F_8
Si_3N_4 patterning	CF_4, C_2F_6, SF_6, CHF_3
W patterning	SF_6, NF_3, Cl_2
SiO_2, SiN_x, and W PECVD chamber cleaning	C_2F_6, NF_3, CF_4, C_3F_8

A significant development in early 1999 was an agreement reached by the member organizations of the World Semiconductor Council (WSC) to reduce semiconductor industry emissions by 10% relative to baseline levels by the year 2010 [7]. For the US semiconductor industry, represented by the SIA, the baseline year was established as 1995. Baseline years for other WSC member organizations are: 1995 for EECA (European Electronic Component Manufacturers Association), and EIAJ (Electronic Industries Association of Japan) and 1997 for KSIA (Korea Semiconductor Industry Association), and TSIA (Taiwan Semiconductor Industry Association). The proposed 10% reduction, while numerically modest, in actuality represents a commitment of considerable scale, given the fact that this figure is intended to be an absolute reduction versus 1995/1997 levels, not a reduction normalized for projected increases in production levels. Under the WSC's assumptions, it is estimated that PECVD chamber clean emissions must be reduced by 95% from the 1995 process of record, whereas etch emissions must be reduced by 90% on a per-process basis in order for the overall target to be met. [7]

1.2 Project Overview

The author's Ph.D. thesis will present the results of the intermediate stage of a long-term project on alternative chemistries as PFC replacements. This work consisted of a series of experimental studies conducted between 1996 and the present in which a number of novel compounds were evaluated as etch chemistries in wafer etch and chamber clean applications. The goal of the initial studies was simply to test the feasibility of using alternative compounds as etchants. As the project evolved, diagnostic techniques such as Fourier transform infrared spectroscopy and x-ray photoelectron spectroscopy were applied with the intent of generating insight into mechanisms affecting process and emissions behavior. The focus of this document will be restricted to the wafer patterning application, although the results of the chamber cleaning studies that were also conducted within the same project framework will also be presented in summary form (Section 1.2.2.2).

This work was funded in large part by the NSF/SRC Engineering Research Center for Environmentally Benign Semiconductor Manufacturing (SRC contract ID 425.001), with additional funding from SEMATECH as well as significant contributions of resources from Motorola, Inc. and Novellus, Inc., who were heavily involved in collaborations with the MIT project. Other industrial collaborators included IBM Microelectronics, Applied Materials, Inc., Schumacher, Air Products and Chemicals, Inc., the 3M Company, DuPont Fluoroproducts, and AlliedSignal, Inc.

1.2.1 Project Strategy

This section will discuss the strategy which guided the progress of the experimental work over the course of the project from 1995 to the present time. Despite the fact that it has undergone significant changes over the last few years, the strategy still provides a blueprint for all of the project's activities discussed here. This strategy originally anticipated a significant amount of MIT-based activity to be followed by interaction with industrial partners at a more mature stage of the project. In actuality, that strategy has evolved considerably over the last few years. The two subsections following will discuss the initial strategy as well as how it came to be modified in the course of executing the experimental work.

1.2.1.1 Initial Strategy

After an initial paper study, carried out in 1994, which assessed the industry's needs and set out the long-term objectives of the project, it was assumed that all work to be undertaken as part of the alternative chemistries project would be organized into three stages: an "etch viability" or "screening" stage, to be followed by two "process viability" stages that would address the two applications of interest – dielectric wafer etch and dielectric PECVD chamber clean. All three stages were intended to be carried out at MIT using process tools available within the Microsystems Technology laboratories (MTL), not necessarily sequentially, as it was envisioned that new chemistries could be added to

the initial list of those to be examined. If a given solution or set of solutions was to be successful, an industry site beta test would then be planned. See Figure 1.1.

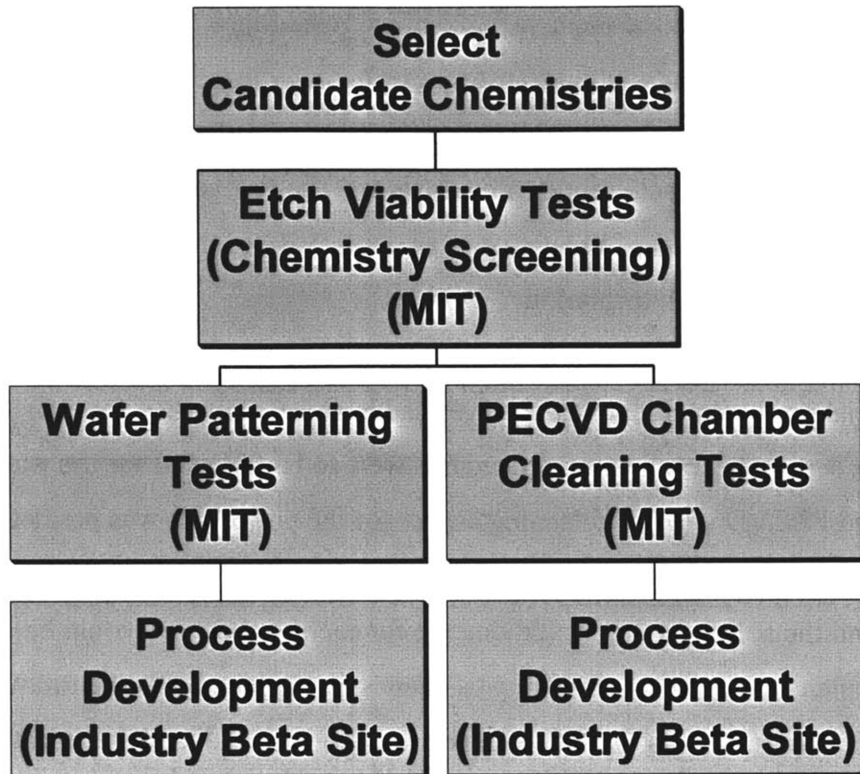

Figure 1.1: Schematic representation of initial project strategy.

Screening Stage. In the "etch viability" stage, a large number of potential replacement chemistries were to be tested for etch performance relative to established (PFC) etchants. The experiments to be carried out during this stage were intended to be simple enough to be generic to both intended applications and to serve as a method of screening the candidate chemistries. Subsequent stages would then address the wafer patterning and the chamber cleaning applications separately. These stages would use a smaller subset of the chemistries initially examined, which were to be selected largely on the basis of results from the initial stage.

The primary focus of this first stage was to determine under what conditions, if any, a given candidate chemistry would etch two principal dielectric films of interest - silicon

dioxide and silicon nitride. It was intended to focus primarily on the etching of blanket oxide and nitride wafers in a medium density dielectric etch tool (an Applied Materials Precision 5000 with Mark II etch chambers) housed in the Integrated Circuits Laboratory (ICL) with film etch rate as the main variable of interest. Since, from its inception, the end goal of the project was eventual transfer of technology to semiconductor equipment vendors, it was decided that it would be preferable for the work to be carried out in commercial, rather than experimental, process tools. The Precision 5000 is a once widely used commercial tool that was in many ways representative of the then current level of commercially available etch technology.

Once the initial pool of candidate alternatives had been benchmarked for etch performance, separate experimental procedures were to be followed for the wafer patterning and PECVD chamber cleaning aspects of the project. It was predicted that, because process requirements in the two applications are quite different, the subset of gases used and the solutions that would emerge for each application would be different. The original plan called for the screening of chemistries belonging to the following three families: hydrofluorocarbons (HFCs), iodofluorocarbons (IFCs), and unsaturated fluorocarbons (UFCs). Trifluoroacetic anhydride (TFAA) was also added to this list. The properties of compounds belonging to the above classes of fluorinated molecules will be discussed in greater detail in Chapter 2.

Wafer Patterning Process Viability Stage. The criteria for evaluating the performance of a wafer patterning process are numerous, but four primary parameters that were identified as being of fundamental importance in this application were etch rate, uniformity, selectivity, and anisotropy. Since the project strategy was originally formulated, a number of other considerations have also become significant and have been incorporated into the testing methodology. These will be discussed below.

During this stage, blanket and patterned oxide and nitride wafers were to be etched in the Precision 5000 in ICL. The etch processes were to be characterized with respect to key parameters, such as those listed above. Additionally, surface analysis techniques were to

be used when appropriate to study the surfaces of the etched wafers. The goal of this stage was planned to be the development of effective alternative chemistry etching processes for silicon dioxide and nitride, as defined by the above criteria. As a test of the viability of a given etch process, devices and possibly circuits such as ring oscillators were to be fabricated using alternative processes. These were then to be compared against the performance of similar devices and circuits made using a standard PFC-based etch chemistry.

One of the most important diagnostics in this stage was to be effluent characterization using quadrupole mass spectroscopy (QMS) and/or Fourier transform infrared (FTIR) spectroscopy. Even when gases which themselves pose no short- or long-term environmental hazards are used, undesirable products may be formed in the plasma. A concern particular to carbon/fluorine chemistries is the possibility of perfluorocarbon formation through the recombination of F atoms and CF_x radicals through both surface and gas phase processes. For instance, it is well established that, in processes which utilize larger perfluorocarbon species, *e.g.*, C_2F_6 and C_3F_8, a substantial fraction of the effluent is in the form of CF_4. A process recipe which produces significant amounts of perfluorocarbons is clearly undesirable.

Chamber Cleaning Process Viability Stage. Again, in this stage of the project, a smaller subset of the chemistries evaluated in the initial stage would be used to develop an effective process for cleaning dielectric PECVD chambers. This subset would not necessarily be the same as that to be used in the wafer patterning experiments. The reason for this is that the process requirements for chamber cleaning are different and, in general, simpler than those for patterning. In chamber cleaning, the principal parameter of interest is cleaning time, *i.e.*, etch rate. Secondary considerations, such as selectivity and anisotropy, are, generally speaking, not important.

The initial plan anticipated the installation of a PECVD chamber on the Precision 5000 (the Precision 5000 cluster tool will be described in greater detail in Section 3.4). Chamber cleaning simulations using blanket wafers with PECVD oxide and nitride films,

as well as actual chamber cleans, were to be performed. In the actual chamber cleans, a deposition process would be performed in the chamber, then a cleaning process would be run. The effectiveness of the cleaning recipe would be measured by the time necessary for the chamber to be cleaned. Finally, effluent characterization would be performed.

1.2.1.2 Modifications to the Initial Strategy

Perhaps, the most significant departure from the original approach set out in 1994-1995 was the high degree of industrial collaboration that would become part of almost all aspects of the project. It was largely opportunities for interacting with industrial partners rather early in the course of the project that had provided the impetus for significant departures from the initial plan. Whereas the original plan anticipated significant involvement of industrial partners only as beta sites after initial development work had been carried out at MIT, in actuality, numerous opportunities for collaboration with industry presented themselves during the course of the project and, after the initial screening stage was completed for the first set of chemistries to be examined, all etch and clean process development activity was conducted through interactions with industry partners, both at MIT and at industry sites. Thus, whereas the original strategy called for a beta test stage for successful solutions, in effect, some of the interactions that occurred over the course of the last few years filled the role of the industry beta test, which, in those cases, became rolled up into the process development activity. Other specific departures from the initial plan are discussed below.

Screening Stage. As the project progressed, it became clear that use in a "screening stage" was not necessarily required or, at times, even appropriate for a decision to be made on the evaluation of a given chemistry in an etch or clean application. Initially, the notion of a screening stage had been useful because of the expectation that the methodologies that would be necessary to evaluate a compound in the actual application would be resource intensive. Hence, there was a need for obtaining initial information on a new compound's behavior in a plasma environment in an efficient manner. To a large extent, this information did become available upon the completion of the screening stage with an initial pool of chemistries that consisted of members of the hydrofluorocarbon

and iodofluorocarbon families as well as the compound TFAA. The unsaturated fluorocarbon family was not examined at the time because members of the HFC and IFC families appeared to be sufficiently promising and possessed lower health and safety tradeoffs than those of the unsaturated fluorocarbons. As had been planned earlier, the studies in the screening stage had been limited to obtaining only etch rate information as a function of various process parameters. In some cases, these results were supplemented by surface analysis data obtained by Auger electron spectroscopy (AES). As will be discussed in Chapter 4, the experiments performed provided a large amount of information about the effects of various process parameters on etch behavior; additionally, they provided much needed information about basic process trends within each of two families of similar compounds – HFCs and IFCs.

However, it also became apparent from the screening stage results, as well as from subsequent data, that screening compounds on the basis of etch rate data alone was insufficient to provide information on how they would behave in other process tools and that effluent composition data should be provided for new compounds as early as possible. This latter judgment stemmed from the observation that the question which the screening stage was intended to answer ("Does it etch?") could almost always be answered "yes" and that the truly critical question to be answered through experimental means should become "What are the emissions?" Presently, after several years of experimental effort, one can make the following general statements: 1). under appropriate conditions, almost any fluorinated compound can be made to interact with silicon oxide or nitride in a plasma environment in a manner that causes net removal of the silicon-based film; 2). the composition of the global warming emissions from a given process is often not dominated by the atmospheric properties of the source etchant itself, but by the plasma byproducts that it produces. Hence, the rationale for carrying out a screening stage for new compounds based on film etch rate alone became supplanted by the need for more detailed information up front. It should be pointed out, however, that, while such conclusions can be made now, the above statements were by no means apparent at the time the project was initiated, at which time answering the "Does it etch?" question appeared to be most critical. Additionally, as interactions with industry partners

increased, other new potential candidate compounds emerged without passing through the screening stage, having been pre-selected by the industrial partners. Table 1.3 lists all of the compounds that have been examined in the course of the work discussed in this document.

Wafer Patterning Process Viability Stage. In contrast to the intent of the initial plan, all of the wafer patterning work over the course of the project so far has been carried out at an industrial partner site – Motorola's Advanced Products Research and Development Laboratory in Austin, TX. This arrangement has provided numerous advantages over an attempt to carry out the same work at MIT with the resources available at the time. Foremost among these was the availability of a leading edge process tool – an Applied Materials Centura 5300 platform equipped with HDP dielectric etch chambers. While the HDP chamber itself has recently been supplanted by its second generation variant, the IPS chamber, the Centura 5300 HDP is a process tool that is representative of a generation of etchers that has only recently begun to play a role in volume semiconductor production. Moreover, the plasma environment in a high density plasma etch chamber such as the Applied Materials HDP product differs significantly from what is available in older low and medium density tools. In addition to the opportunity to work on leading edge process equipment, the availability of patterned substrates with 0.35 μm features, maintenance support for the process tool, and the support of a dedicated physical analysis facility added a degree of efficiency to effort that would have been difficult to achieve at MIT at the time. The activities carried out at APRDL spanned several stages in themselves, beginning with a concept-and-feasibility study in which leading candidates from the HFC and IFC families were tested in the HDP tool. These candidates were selected on the basis of results obtained in the earlier screening stage. Blanket oxide, nitride, and photoresist wafers, as well as patterned oxide wafers, were used. Emissions data were taken as well.

This phase was then followed by two process development activities which built on the earlier results. In the first, a process for an oxide etch application was developed using an HFC chemistry (2H-heptafluoropropane); in the second, an attempt was made to do the

same with a IFC chemistries (1- and 2-iodoheptafluoropropane). Emissions data were taken during these phases of the work as well. In addition to this work, concept-and-feasibility studies were also carried on compounds donated by two gas supplier companies: oxalyl fluoride, donated by AlliedSignal, Inc., and an additional HFC combination, pentafluoroethane/1,1-difluoroethane, donated by DuPont Fluoroproducts. Both process and emissions data were taken during these activities. Arguably the most successful of the Motorola/MIT studies to be discussed within this document, however, was the unsaturated fluorocarbon concept-and-feasibility study, the last of the activities conducted within the scope of this thesis. In this study, a number of UFC compounds, along with an additional (fully fluorinated) compound – octafluorotetrahydrofuran, were evaluated in tests similar to those conducted earlier. As will be discussed in subsequent chapters, the UFC family emerged as having the greatest potential for successfully combining high emissions reductions with good process performance. The high density plasma studies are given detailed consideration in Chapters 5 and 6, with the former devoted to the HFC and IFC efforts and the latter to the oxalyl fluoride and UFC studies.

Table 1.3: Overview of compounds examined as potential PFC replacements.

Name	Formula	Family	AMAT Precision 5000 Mk II	AMAT Centura 5300 HDP	Novellus Concept One 200	Commercialization Stage	Section in Document
1H-heptafluoropropane	$CF_2H\text{-}CF_2\text{-}CF_3$	HFC	X				1.2.2.1
2H-heptafluoropropane	$CF_3\text{-}CFH\text{-}CF_3$	HFC	X	X			1.2.2.1 5.1, 5.2
Pentafluoroethane	$CF_3\text{-}CF_2H$	HFC	X	X			1.2.2.1 5.3
1,1,1,2-tetrafluoroethane	$CF_3\text{-}CFH_2$	HFC	X				1.2.2.1
Trifluoroethylene	$CF_2{=}CFH$	HFC	X				1.2.2.1
Difluoromethane	CF_2H_2	HFC	X				1.2.2.1
1,1-difluoroethane	$CF_2H\text{-}CH_3$	HFC		X			5.3
Iodotrifluoromethane	CF_3I	IFC	X	X			4.1 5.1
Iodopentafluoroethane	$CF_3\text{-}CF_2I$	IFC	X				4.1
1-iodoheptafluoropropane	$CF_2I\text{-}CF_2\text{-}CF_3$	IFC	X	X			4.1 5.1, 5.4
2-iodoheptafluoropropane	$CF_3\text{-}CFI\text{-}CF_3$	IFC	X	X			4.1 5.1, 5.4
Iodotrifluoroethylene	$CF_2{=}CFI$	IFC	X				4.1
Hexafluoropropene	$CF_3\text{-}CF{=}CF_2$	UFC		X			6.2
Hexafluoro-1,3-butadiene	$CF_2{=}CF\text{-}CF{=}CF_2$	UFC		X			6.2
Hexafluoro-2-butyne	$CF_3\text{-}C{\equiv}C\text{-}CF_3$	UFC		X			6.2
Hexafluorocyclobutene	$c\text{-}C_4F_6$	UFC		X			6.2
Octafluoro-2-butene	$CF_3\text{-}CF{=}CF\text{-}CF_3$	UFC		X			6.2
Octafluorocyclopentene	$c\text{-}C_5F_8$	UFC		X			6.2
Trifluoroacetic anhydride	$C_4F_6O_3$		X		X		1.2.2.2 4.2
Oxalyl fluoride	$C_2F_2O_2$			X			6.1
Dilute NF_3/Helium	NF_3/He				X	X	1.2.2.2
Octafluorotetrahydrofuran	$c\text{-}C_4F_8O$			X	X		1.2.2.2 6.2

As will again be discussed in detail in subsequent chapters, one of the motivations for evaluating UFC compounds after the HFC and IFC studies was a desire to address the phenomenon of perfluorocarbon re-formation within the plasma. The strategy employed in this case was based on the hypothesis that, by starting with molecules which lacked fully fluorinated CF_x moieties, the reactions that are believed to lead to the formation of compounds such as CF_4, CHF_3, and C_2F_6 could be suppressed. An alternative approach toward addressing PFC re-formation that was taken up in tandem with the UFC activity was the total decoupling of F and C in the feed gas chemistry, implemented through the use of an inorganic fluoride (NF_3) and hydrocarbon additives. Whereas NF_3 is itself still a global warming compound, it tends to be utilized very efficiently in both high and low density plasmas, under the appropriate conditions. Discussion of this work is beyond the scope of the present document; the reader is referred to Ref. [22] for a discussion of the preliminary work in this area.

Chamber Cleaning Process Viability Stage. After the screening stage (Chapter 4) was completed, most chamber clean development activity took place at MIT as planned. However, the work was done on a Novellus Concept One 200 PECVD tool, rather than on a PECVD chamber that was to be installed on the existing Precision 5000 platform. The Concept One was donated to MTL by Novellus, Inc., partially in support of this project, and is housed in ICL. Moreover, as was the case with the effort on the wafer patterning side, not all chemistries that were tested as part of this activity had been earlier subjected to the set of experiments that defined the screening stage. See Table 1.3. All of the chamber clean work involved the collection of both process (chamber clean time) data, as well as emissions, with FTIR spectroscopy being the principal diagnostic used for effluent analysis. Three activities were carried out; in these studies, trifluoroacetic anhydride, dilute NF_3/He, and octafluorotetrahydrofuran were evaluated, respectively. One of the more successful activities that was undertaken during this stage of the project was the NF_3/He study, a collaboration involving Novellus, IBM, and Air Products, which led to further development work by Novellus and the eventual release of a commercial process based on the same chemistry.

1.2.2 Review of Related Work

This section will present, in summary form, the results of the first portions of the screening stage, which was conducted using a number of hydrofluorocarbon etchants. This work has been described in detail in the author's M.S. thesis [1], as well as in other publications [23, 24]. Whereas the focus of the present document is on fluorocarbon based wafer patterning processes, a significant amount of related work was also carried out to address the PECVD chamber clean application. The results of those studies are also presented below, again, in summary form. The reader is referred to Refs. [25-28] for more detailed discussions.

1.2.2.1 Early Hydrofluorocarbon Studies

In these early experiments, six hydrofluorocarbon gases (1H- and 2H-heptafluoropropane, pentafluoroethane, difluoromethane, 1,1,1,2-tetrafluoroethane, and trifluoroethylene) were examined for their ability to etch silicon dioxide and silicon nitride films in an Applied Materials Precision 5000 etch tool. Octafluoropropane, a perfluorinated gas, was used as a reference. To the author's knowledge, 1H- and 2H-heptafluoropropane and trifluoroethylene had not previously been examined in a dielectric etch application. All seven gases were found to be capable of etching both types of substrates under the appropriate set of conditions. The first three gases, along with octafluoropropane, were evaluated in a designed experiment matrix study. Neural network software was utilized in the analysis of the data. The etch behavior of these four gases varied noticeably from gas to gas, but over large regions of the parameter space, the two heptafluoropropane isomers and pentafluoroethane were capable of etching both substrates at rates comparable to those of octafluoropropane. Generally speaking, octafluoropropane yielded the fastest etch rates for most process conditions in the matrix parameter space. However, the fact that the other three gases offered comparable performance over a wide range of conditions, at least in terms of etch rate, was taken as encouraging. Moreover, no significant memory effects (*i.e.,* process drifts) due to a change in chamber condition were noted with these gases, indicating that these chemistries did not polymerize heavily enough to leave enough polymeric residue in the chamber to alter the performance of subsequent processes.

The remaining three chemistries, difluoromethane, 1,1,1,2-tetrafluoroethane, and trifluoroethylene, on the other hand, were found to polymerize heavily at pressures and etch gas flow rates at which the other gases etched readily. Etching of oxide and nitride with these gases was achieved at lower pressures and flows. All seven gases were evaluated in non-matrix experiments in this low pressure/low etch gas flow regime. Oxide and nitride etch rate as a function of oxygen flow was studied. Additional, more limited tests were also carried out with all seven gases to establish the effects of pressure and etch gas flow rate on the process. In addition to this, a number of tests were carried out with trifluoroethylene in particular, in which the effects of various process variables on polymerization behavior were studied, along with the effect of chamber condition on the etch process. In general, oxide and nitride etch rates observed for difluoromethane, 1,1,1,2-tetrafluoroethane, and trifluoroethylene were considerably lower than those of the other gases. Thus, while these compounds may have some limited application in wafer patterning processes where polymerizing behavior is desirable for selectivity or anisotropy considerations, their use in chamber cleaning processes, which take place at high pressures and flow rates, relative to those typical of patterning processes, was determined to be unlikely. On the other hand, 1H- and 2H-heptafluoropropane and pentafluoroethane once again were found to have oxide and nitride etch behavior similar to that of octafluoropropane. These gases were found to exhibit the same trends as octafluoropropane, as well as comparable etch rates under the conditions studied. These results suggested then that these gases may indeed be promising as viable etchants of dielectrics and that further work was warranted to test the feasibility of their use in wafer patterning and, possibly, chamber cleaning applications. 2H-heptafluoropropane would later become one of the gases used in the Motorola APRDL studies. Pentafluoroethane would also be evaluated at APRDL in collaboration with DuPont Fluoroproducts.

1.2.2.2 PECVD Chamber Clean Studies

In all three of the chamber clean studies that were carried out in the Novellus Concept One at MIT (the TFAA study [25], the NF_3/He study [26], and the octafluorotetrahydrofuran study [27, 28]), the compound being tested was found to offer

a significant reduction in emissions (greater than 90%), relative to a standard C_2F_6-based process of record, while providing equivalent or faster chamber clean time. Despite very encouraging experimental data, TFAA did not capture significant interest on the part of semiconductor manufacturers or equipment vendors because it became apparent that there would be handling and delivery issues with this compound. The fact that it could liberate corrosive trifluoroacetic acid when exposed to moisture, along with its low vapor pressure, which made delivery of high flows through unheated ¼" lines difficult, both weighed against a continuation of development activity at a significant level. The TFAA chamber cleaning tests at MIT were carried out in collaboration with Schumacher and Air Products and Chemicals, Inc. Octafluorotetrahydrofuran also offered greater than 90% emissions savings with a comparable clean time. Despite the fact that this compound is itself stable atmospherically and highly global warming, it was found to decompose very efficiently in the plasma, with relatively high destruction efficiencies and relatively low levels of PFC re-formation. Further work may yet be done with this compound at industrial sites. However, the most successful activity in the chamber clean area was the testing of dilute NF_3 (NF_3 in helium) on the Concept One. The best process tested at MIT offered approximately a 90% reduction in emissions over the C_2F_6 process of record, together with a 30% reduction in chamber clean time. The results have been transferred to Novellus, Inc., where further work was undertaken. A commercially available process based on this chemistry has recently been released with further optimization work still underway as of this writing.

References[‡]

1. S. Karecki, *Alternative Chemistries for Etching of Silicon Dioxide and Silicon Nitride*, M. S. Thesis in *Electrical Engineering and Computer Science*, Massachusetts Institute of Technology, Cambridge, MA, 167 p. (1996).
2. *Radiative Forcing of Climate Change: The 1994 Working Report of the Scientific Assessment Working Group of IPCC,* Intergovernmental Panel on Climate Change (IPCC) (1994).

[‡] A note on placement of references and numbering of figure/table captions: In place of a single section at the end of the document, a References section has been provided at the end of each chapter. The exceptions to this scheme are the longer chapters, 5 and 6, where each top-level section receives its own References section. Figures, tables, and equations are numbered within each chapter.

3. *Radiative Forcing of Climate Change: The 1995 Working Report of the Scientific Assessment Working Group of IPCC,* Intergovernmental Panel on Climate Change (IPCC) (1995).
4. *Scientific Assessment of Ozone Depletion: 1998, Volume 2,* World Meteorological Organization, Global Ozone Research and Monitoring Project, Report No. 44 (1998).
5. L. T. Molina, P. J. Wooldridge, and M. J. Molina, Geophy. Res. Lett., **22**, p. 1873 (1995).
6. M. Mocella, *PFC Recovery: Issues, Technologies, and Considerations for Post-Recovery Processing*, in Proceedings of *U.S. EPA Global Semiconductor Industry Conference on Perfluorocompound Emissions Control*, Monterey, CA (1998).
7. L. Beu and P. T. Brown, *An Analysis of Fluorinated Compound Emissions Reduction Technologies and Emission Reduction Goals*, in Proceedings of *Environmental Issues in the Electronics and Semiconductor Industries (Second International Symposium)*, Seattle, WA, L. Mendicino, Editor, The Electrochemical Society Proceedings Series, **PV 99-8**, p. 1-9, Electrochemical Society, Pennington, NJ (1999).
8. K. Aitchison, *Novellus Systems Catalytic Oxidation Technology*, in Proceedings of *U.S. EPA Global Semiconductor Industry Conference on Perfluorocompound Emissions Control*, Monterey, CA, Section 8 (1998).
9. S. Tamata, *Catalytic Destruction of PFCs*, in Proceedings of *U.S. EPA Global Semiconductor Industry Conference on Perfluorocompound Emissions Control*, Monterey, CA, Section 8 (1998).
10. E. Tonnis, V. Vartanian, L. Beu, T. Lii, R. Jewett, J. Daniels, and D. Graves, *Evaluation of a Litmas "Blue" Plasma Abatement Device for Perfluorocompound (PFC) Destruction,* SEMATECH, Report No. 98123605A-ENG (1998).
11. V. Vartanian, L. Beu, T. Lii, B. Wofford, C. Hartz, and J. Bevan, *Evaluation of Rf Environmental Systems/Texas A&M University Surface Wave Plasma Device for Abatement of Perfluorocompound (PFC) Emissions,* SEMATECH, Report No. 98083551A-ENG (1998).
12. *Climate Change: The IPCC Scientific Assessment,* Intergovernmental Panel on Climate Change (IPCC) (1990).
13. L. Marinilli and W. Worth, *Global Warming: A White Paper on the Science, Policies, and Control Techniques That Impact the U. S. Semiconductor Industry,* SEMATECH, Report No. 93112074A-TR (1994).
14. S. R. Skaggs, T. A. Moore, and R. E. Tapscott, *Chapter 10*, in *Halon Replacements: Technology and Science*, A. W. Miziolek and W. Tsang, Editors, American Chemical Society, Washington, DC, p. 99 (1995).
15. *U. S. Climate Change Action Plan* (1993).
16. *SilverPlatter Database,* Registry of Toxic Effects of Chemical Substances (RTECS) (1996).
17. J. W. Clayton, *The Toxicity of Fluorocarbons with Special Reference to Chemical Constitution*, J. Occup. Med., **4**, p. 262-273 (1962).
18. Material Safety Data Sheet Information from Air Products and Chemicals, Inc., Allentown, PA.

19. C. A. Branch, J. R. Ewings, S. C. Fagan, D. A. Goldberg, and K. M. Welch, *Acute toxicity of a nuclear magnetic resonance cerebral blood flow indicator in cats*, Stroke, **21**(8), p. 1172-1177 (1990).
20. Personal communication, various semiconductor manufacturers and equipment vendors, 1994-1998.
21. *Memorandum of Understanding: PFC Emissions Reduction Partnership for the Semiconductor Industry,* U. S. Environmental Protection Agency (1996).
22. L. Pruette, S. Karecki, R. Chatterjee, R. Reif, T. Sparks, and V. Vartanian, *High Density Plasma Oxide Etching Using Nitrogen Trifluoride and Acetylene*, J. Vac. Sci. Technol. A, submitted (2000).
23. B. A. Tao, S. M. Karecki, and L. R. Reif, *Alternative Chemistries to Perfluorocompounds for Dielectric Plasma Etching*, in Proceedings of *11th International Symposium on Plasma Processing*, Los Angeles, CA, G. S. Mathad and M. Meyyappan, Editors, The Electrochemical Society Proceedings Series, **PV 96-12**, p. 424-434, Electrochemical Society, Pennington, NJ (1996).
24. S. M. Karecki, B. A. Tao, and L. R. Reif, *Etching of Silicon Dioxide and Silicon Nitride Films with Non-Perfluorocompound Gases*, in Proceedings of *SRC TECHCON 1996 Conference*, Phoenix, AZ, Semiconductor Research Corporation, Research Triangle Park, NC (1996).
25. L. C. Pruette, S. M. Karecki, R. Reif, J. G. Langan, S. A. Rogers, R. J. Ciotti, and B. S. Felker, *Evaluation of trifluoroacetic anhydride as an alternative plasma enhanced chemical vapor deposition chamber clean chemistry*, J. Vac. Sci. Technol. A, **16**(3), p. 1577-1581 (1998).
26. L. Pruette, S. Karecki, R. Reif, W. Entley, J. Langan, V. Hazari, and C. Hines, *Evaluation of a Dilute Nitrogen Trifluoride Plasma Clean in a Dielectric PECVD Reactor*, Electrochem. Solid-State Lett., **2**(11), p. 592-594 (1999).
27. L. Pruette, S. Karecki, R. Reif, L. Tousignant, W. Reagan, S. Kesari, and L. Zazzera, *Evaluation of C_4F_8O as an Alternative Plasma Enhanced Chemical Vapor Deposition Chamber Clean Chemistry*, in Proceedings of *Environmental Issues in the Electronics and Semiconductor Industries (Second International Symposium)*, Seattle, WA, L. Mendicino, Editor, The Electrochemical Society Proceedings Series, **PV 99-8**, p. 20-29, Electrochemical Society, Pennington, NJ (1999).
28. L. Pruette, S. Karecki, R. Reif, L. Tousignant, W. Reagan, S. Kesari, and L. Zazzera, *Evaluation of C_4F_8O as an Alternative Plasma Enhanced Chemical Vapor Deposition Chamber Clean Chemistry*, J. Electrochem. Soc., **147**(3), p. 1149-1153 (2000).

2. Selection of Candidate Chemistries

This chapter will discuss the process by which potential replacement chemistries were selected for testing. Section 2.1 will discuss criteria which were considered in the selection process. Section 2.2 will turn to specifics, providing an overview of the properties of the compounds belonging to each of the three main families of fluorocarbons that were evaluated in the etch studies: hydrofluorocarbons (HFCs), iodofluorocarbons (IFCs), and unsaturated fluorocarbons (UFCs). It will also briefly discuss the properties of the other molecules that were used, namely, trifluoroacetic anhydride (TFAA), oxalyl fluoride, and octafluorotetrahydrofuran.

2.1 Selection Criteria

It is widely accepted that an effective etchant for use in either PECVD chamber clean or etch applications must be a fluorinated compound because other halogens are ineffective at etching dielectric films. In contrast to PECVD chamber clean processes, where the perfluorinated etch gas serves principally as a source of atomic fluorine, wafer patterning processes have numerous additional constraints which must be considered in the selection and evaluation of potential replacements.

Foremost among these is the need for a polymerization mechanism in the plasma, since it is acknowledged that polymer formation is critical for achieving selectivity to materials such as photoresist and stop layers. [1-5] The need for both carbon and fluorine to be present in the etch chemistry places constraints on the options available for potential replacement compounds. Moreover, the actual selection of potential replacement compounds involves a number of tradeoffs. A principal consideration is the long-term atmospheric properties of the alternative etchant itself. A candidate replacement chemistry should ideally be atmospherically unstable and possess low/zero GWP. That property, however, should be balanced by acceptable handling characteristics. Fluorinated compounds that are very stable and pose little risk from a health and safety standpoint, *e.g.*, PFCs, also tend to have high atmospheric stability. More reactive

fluorinated species tend to have no long-term environmental concerns associated with them because their atmospheric lifetimes tend to be short; however they tend to possess potentially unacceptable health and safety risks. In addition to the health, safety, and long-term environmental standpoint, *e.g.*, PFCs, also tend to have high atmospheric stability. More reactive fluorinated species tend to have no long-term environmental concerns associated with them because their atmospheric lifetimes tend to be short; however they tend to possess potentially unacceptable health and safety risks. In addition to the health, safety, and long-term environmental characteristics of the candidate chemistry itself, an important consideration is the identity of its plasma decomposition products, which can be global warming gases, and whose identity can also depend on the presence of other materials on the wafer, most significantly, photoresist.

Furthermore, a manufacturable process must not only offer performance comparable to that of existing processes, as measured by etch rate, anisotropy, selectivity, uniformity, etc., but also cannot have an adverse long-term impact on the process tool. Also, it should not necessitate costly or cumbersome maintenance procedures, such as frequent wet cleans of the process chamber. Moreover, the use of a new etch process should pose no additional hazards, such as the presence of toxic byproducts, when the chamber is opened for maintenance. An evaluation of a new etch chemistry for a wafer patterning application must therefore rely necessarily on a combination of metrics that reflect not only process performance and the environmental impact of the new process, but manufacturability as well. Finally, the use of new etchants must be cost effective in manufacturing; however, the cost of potential new alternatives is, of course, strongly dependent on present and potential future suppliers of these chemicals and, as such, is an issue that is beyond the scope of these studies. Whereas it is unlikely that a non-global warming PFC replacement can be identified which fulfills all of the above criteria to the same extent that existing etchants used in manufacturing do, the author believes that it is possible to develop alternative etch processes which meet performance and manufacturability requirements, offer substantial reductions in the overall global warming impact of the process, and possess acceptable health and safety tradeoffs.

2.2 Families of Compounds

Prior to their actual use, the compounds used in the studies described in this document had been subjected to an evaluation of their health, safety, and environmental characteristics. Tables 2.1 through 2.4 summarize a number of key properties for the compounds used in these studies. In the case of a number of the compounds studied, information from sources in literature, material safety data sheet (MSDS) information, and various databases was supplemented by a compilation of Structure Activity Team studies carried out by the Environmental Protection Agency. [6] It should be pointed out, however, that, because of the novel nature of many of these compounds, complete data on the atmospheric, toxicological, or even physical properties of many of them are unavailable.

2.2.1 Hydrofluorocarbons

Hydrofluorocarbons were deemed to be, in a sense, the next logical step in an attempt to move away from perfluorinated species. As can be seen from Tables 1.1 and 2.1, comparison of HFC lifetimes and GWPs with those of their fully fluorinated counterparts, indicates that modification of the fluorocarbon molecule by replacing fluorine with hydrogen leads to lower atmospheric stability. HFC atmospheric lifetimes, for instance, tend to be significantly lower than those of the analogous fully fluorinated molecules. However, it should be noted that, although HFC GWP values are in general lower than those reported for perfluorocompounds (except in the case of trifluoromethane, CHF_3, an HFC, but nearly as stable as perfluorinated compounds), these values are still significant. On the other hand, an attractive property of HFCs is the fact that they are relatively easy to handle. Most have slight or negligible toxic effects. None are corrosive. Most are also non-flammable. (As the number of hydrogens relative to the number of fluorines in the molecule increases, the properties of these molecules begin to resemble those of their hydrocarbon analogues: atmospheric lifetimes and GWPs generally decrease, while flammability increases.)

Certain HFCs have been used as etchants for some time, most notably CHF_3, which, like fully fluorinated alkanes, has a significant GWP (14,800, as calculated over a 100 year time horizon, relative to CO_2 [7]). In addition, at the time the initial selection of candidate chemistries was made, several other HFCs had also already been used for dielectric etching, namely CF_2H_2, C_2F_5H, and $C_2F_4H_2$ [8-10]. It had been found that, for patterning applications, these HFCs could be an attractive alternative for some processes because they can provide high selectivity to mask and stop layer materials. Since the MIT project was initiated, other workers have also conducted etch studies with HFCs in etch applications, including CH_3F, CH_2F_2, C_2F_5H, CHF_2-CHF_2, CH_2F-CF_3, and CH_3-CF_3 [11, 12]. Because the presence of hydrogen in the source chemistry tends to lead to enhanced polymer formation, HFCs were not expected to perform well in chamber cleaning applications and none have been tested in that role. Table 2.1 lists the properties of the HFCs used in the studies discussed in later chapters. As indicators of toxicity, Table 2.1 shows lethal concentrations, as well as lowest observed cardiac sensitization levels; the latter is a relevant metric because heart arrhythmia is often the first acute adverse physiological effect seen after exposure to halocarbons. [13] For comparison, Table 1.1 provides the analogous toxicological information for a number of common PFC species. Due to its potent global warming properties, CHF_3 has been included in Table 1.1 rather than Table 2.1, being viewed as one of the compounds to be replaced, rather than as a potential alternative.

2.2.2 Iodofluorocarbons

A second family of fluorocarbons that was selected to be investigated was the iodofluorocarbon family. It has been reported that the relatively weak C-I bond in these compounds causes IFCs to photolyze readily once released into the atmosphere, resulting in negligible atmospheric lifetimes. The strength of the C-I bond in CF_3I has been given as 53 kcal/mol (2.30 eV per bond), versus 130 kcal/mol (5.65 eV) for the C-F bond. [14] The lifetime calculated for CF_3I has been reported as 0.0026 to 0.005 years (approximately one to two days) [7, 15] whereas the GWP_{100} value for CF_3I has been estimated to be less than 1, relative to CO_2 [7]. Other IFCs are expected to have similarly

short atmospheric lifetimes by analogy to CF_3I. Though IFCs are not as chemically inert as their fully fluorinated counterparts, they are still quite stable from a handling standpoint. As a family, IFCs are also non-flammable; in fact, some have been considered for fire-fighting applications. [13, 16] While toxicity concerns tend to be higher than those associated with HFCs (IFC material safety data sheets also describe them as irritant to eyes, mucous membranes, and the respiratory tract), IFCs are still relatively benign compared to other atmospherically short-lived fluorinated species. The exception among the IFCs evaluated is iodotrifluoroethylene, which is more reactive, hence more toxic, because of the presence of the C=C bond (see Table 2.2). In terms of chronic effects, iodotrifluoromethane has been reported to score positively on the Ames mutagenicity assay for 4 out of 5 strains in one study, as well as in the mouse micronucleus test; however it scored negatively on the mouse lymphoma test. [16] Table 2.2 shows lethal concentrations and lowest observed cardiac sensitization levels for the IFCs used in this study, along with atmospheric and physical properties.

One possible difficulty that was foreseen in using these heavy, iodine-containing compounds, however, was their high boiling points and low vapor pressures (see Table 2.2). This problem is particularly pronounced in the longer-chain species. 1- and 2-iodoheptafluoropropane, for instance, are liquids at room temperature, with boiling points of 40 and 38 °C, respectively [17]. Although heated lines were not employed in any of the experiments that have been carried out, it was anticipated that they might be needed to avoid condensation if the cylinders were staged remotely from the process tool. Another possible drawback that was recognized in using IFCs stems from the fact that iodine is likely to be easily liberated in the plasma, which was anticipated to have potentially adverse hardware implications. This was not borne out, however, in the etch studies conducted. On the other hand, as will be discussed in subsequent chapters, the presence of iodine in the plasma did turn out to have process implications. The etch viability of these chemicals was less certain than that of the HFCs at the time they were selected for testing: only one of the chemicals in this family appeared to have been used for etching, namely, CF_3I for silicon trenches [18]. In general, until this project, relatively little research effort appears to have been expended on the investigation of

IFCs in plasma applications. However, lack of serious handling concerns combined with the low atmospheric stability of these compounds made them attractive candidates for study. Since the MIT project was initiated, other workers have also conducted etch studies with IFCs [14, 19-22].

2.2.3 Unsaturated Fluorocarbons

The third principal family of fluorinated compounds that was initially chosen for evaluation was the unsaturated fluorocarbon family. These compounds contain double or triple carbon-to-carbon bonds. As of this writing, atmospheric lifetime and GWP_{100} values have been made available only for octafluorocyclopentene (c-C_5F_8). See Table 2.3. Other UFCs are expected to be similarly short-lived, with lifetimes and GWPs lower or comparable to those given for octafluorocyclopentene Table 2.3 provides some *estimated* values for GWP_{100} for these compounds. These figures, which should not be treated as authoritative, are based on estimated radiative forcing factors based on the number of C-F bonds in each molecule* and on estimated atmospheric lifetimes based on hydroxyl radical reaction rates [23].

A tradeoff to the atmospheric instability of these molecules, however, is much greater reactivity. The compounds in Table 2.3 are more toxic and/or otherwise reactive than those in the previously discussed categories. In terms of etch viability, these species were expected to perform well in wafer patterning applications because of their ability to polymerize and thus provide selectivity mechanisms. C_2F_4 and C_3F_6 were among the earliest UFCs used in etch studies, having been employed for etching of SiO_2 in high density ECR (electron cyclotron resonance) and inductively coupled plasmas. In keeping with predictions based on their low F/C ratio, they have been found to polymerize heavily, and thus etch oxide with good selectivity (about 50:1) to silicon in these studies [24, 25]. More recently, c-C_5F_8 has generated considerable interest as an etchant, particularly within the Japanese semiconductor community, with a number of c-C_5F_8 etch studies being conducted [20, 26-29].

---

* Formulae courtesy of John Owens, 3M Company.

2.2.4 Other Compounds

In addition to the species discussed above, three other gases were evaluated in various etch studies: trifluoroacetic anhydride (TFAA), oxalyl fluoride, and octafluorotetrahydrofuran. Their properties are given in Table 2.4. Some properties of TFAA had already been discussed in the context of the TFAA chamber clean study (Section 1.2.2.2). Since it is an acid anhydride, this compound is hygroscopic and hence corrosive in the presence of moisture. Its atmospheric persistence is expected to be negligible, however, precisely because of this property. [30] Some studies using TFAA in dielectric chamber clean applications had been carried out prior to the MIT study discussed in Chapter 4 [30]. To the author's knowledge, however, TFAA had not previously been tested in a dielectric film etch application in a wafer patterning tool.

Oxalyl fluoride is also a hygroscopic gas; its atmospheric stability is therefore expected to be low. The global warming impact of unutilized oxalyl fluoride in process emissions has been predicted to be negligible. The study discussed in Chapter 6 is believed to be the first attempt to use oxalyl fluoride in a dielectric patterning application. The primary motivation for the evaluation of oxalyl fluoride as an etchant was the absence of CF_x groups in its molecular structure, which was expected to minimize the formation of CF_x-based plasma by-products. The role of CF_x moieties in the structure of the molecule will be discussed in greater detail in subsequent chapters.

Octafluorotetrahydrofuran, on the other hand, is quite stable atmospherically; hence its GWP and lifetime values are estimated to be quite high (see Table 2.4). Not surprisingly, it is also quite inert and non-toxic from a handling standpoint. In the chamber clean study discussed in Section 1.2.2.2, it was found to have very high utilization efficiency in the Novellus Concept One tool. This, combined with relatively low amounts of PFC re-formation, resulted in the significant emissions reductions relative to the baseline process that were obtained. Despite its high GWP value, it was considered for evaluation in an etch application on the basis of these encouraging initial results. The results discussed in Chapter 6 are believed to represent the first use of this compound in a dielectric patterning application.

Table 2.1: Properties of HFCs evaluated.

Name	Formula	Line Formula	FC Number	Flamm.	GWP_{100}	Lifetime (yrs.)	Used Prev-iously as Etchant ?	Vapor Pressure	Boiling Point (°C)	Acute Toxicity (LC_{50}, LC_{Lo}, or ALC, ppm)	Cardiac Sensitiz-ation (LOAEL, ppm)	Corrosive-ness	TSCA Listing
Fluoromethane	CH_3F		41	Y	140	3.7	Y	2858 mmHg @ 21 °C	-78			none	Y
Difluoromethane	CF_2H_2		32	Y	650	5.6	Y	185 psia @ 20 °C	-51.6 -51.7	760,000 (a)	350,000 (b)	none	
Pentafluoroethane	C_2F_5H	CF_3-CF_2H	125	N	3800	32.6	Y	190 psia @ 25 °C	-48.5	709,000 (c)	100,000 (d)	none	Y
1,1,1,2-tetrafluoroethane	$C_2F_4H_2$	CF_3-CFH_2	134a	N (e)	1600	13.6	Y	96 psia @ 25 °C	-26.5	567,000 (c)	75,000 (d)	none	Y
1,1-difluoroethane	$C_2F_2H_4$	CF_2H-CH_3	152a	Y	190	1.5		87 psia @ 25 °C	-25	383,000 (c)	150,000 (f)	none	
1H-heptafluoropropane	C_3F_7H	CF_2H-CF_2-CF_3	227ca	N	*~5000 (g)*	132 (h)		*8890 mmHg (i)*	-16.3 (j)				
2H-heptafluoropropane	C_3F_7H	CF_3-CFH-CF_3	227ea	N	3800	36.5		3120 mmHg (j)	-16.3 -15.2	800,000 (l)	105,000 (m) 119,000 (k)	none	
Trifluoroethylene	C_2F_3H	CF_2=CFH	1123	Y	N/A	N/A		325 psia @ 20 °C	-51			none	Y

1998 values used for GWP and lifetime data; from Ref[7], exc. 1H-heptafluoropropane (see below).

Physical properties, TSCA (Toxic Substances Control Act) listings from [31], unless otherwise specified

(a) ALC (approximate lethal concentration) rat, 4 hr exposure, source [32]

(b) Effects observed at this level, dog, source [32]

(c) ALC rat, 4 hr exposure, source [33]

(d) LOAEL (lowest observed adverse effect level) dog, source [33]

(e) At ambient temperature and atmospheric pressure, source [33]

(f) Effects observed at this level, dog, source [33]

(g) Estimated, source [34]

(h) Source [35]

(i) Estimated, source [36]

(j) Source [37]

(k) Effects observed at this level, dog, source [38]

(l) LC_{50} (lethal concentration for 50% of the population) rat, 4 hr exposure, source [13]

(m) LOAEL dog, source [13]

Table 2.2: Properties of IFCs evaluated.

Name	Formula	Line Formula	FC Number	Flamm.	GWP_{100}	Lifetime (yrs.)	Used Previously as Etchant ?	Vapor Pressure	Boiling Point (°C)	Acute Toxicity (LC_{50}, LC_{Lo}, or ALC, ppm)	Cardiac Sensitization (LOAEL, ppm)	Corrosiveness	TSCA Listing
Iodotrifluoromethane	CF_3I		13I1	N	<1 (a)	0.005 (a) 0.0026 (b)	Y	85 psia @ 20 °C	-22.5	274,000 (c)	4,000 (d)	none	Y
Iodopentafluoroethane	C_2F_5I	CF_3-CF_2I		N	N/A	N/A		35 psia @ 20 °C 738.9 mmHg @ 10 °C	12 13	40,000 (e)	500 (f)	none	Y
1-iodoheptafluoropropane	C_3F_7I	CF_2I-CF_2-CF_3		N	N/A	N/A		*443 mmHg (g)*	40	~49,000 – 62,000 (h) 404 g/m^3 (i)	~1,000 (j)	none	Y
2-iodoheptafluoropropane	C_3F_7I	CF_3-CFI-CF_3		N	N/A	N/A		7.12 psia @ 20 °C 23.29 psia @ 55 °C	38 40	~49,000 – 62,000 (h) ~890 (k)	~1,000 (j)	none	Y
Iodotrifluoroethylene	C_2F_3I	CF_2=CFI		N	N/A	N/A		*64 mmHg (l)*	30	91 (m)		none	

Physical properties, TSCA (Toxic Substances Control Act) listings from Ref [31], unless otherwise specified

(a) Source [7]

(b) Source [15]

(c) LC_{50} (lethal concentration for 50% of the population) rat, 15 min exposure, source [13]

(d) LOAEL (lowest observed adverse effect level) dog, source [13]

(e) Transient signs of neurotoxicity noted, source [39]

(f) Effects observed at this level, dog, source [40]

(g) Estimated, source [36]

(h) LC_{50} rat, 15 min exposure, source [16]

(i) LC_{50} mouse, 2 hr exposure, source [41]

(j) LOAEL dog, source [16]

(k) LC_{50} rat, 4 hr exposure, source [42]

(l) Estimated, source [36]

(m) ALC (approximate lethal concentration) rat, 4 hr exposure, source [43]

Table 2.3: Properties of UFCs evaluated.

Name	Formula	Line Formula	FC Number	Flamm.	GWP_{100}	Lifetime (yrs.)	Used Previously as Etchant ?	Vapor Pressure	Boiling Point (°C)	Acute Toxicity (LC_{50}, LC_{Lo}, or ALC, ppm)	Corrosiveness	TSCA Listing
Hexafluoropropylene	C_3F_6	CF_3-CF=CF_2	1216	N (a)	*<5 (f)*	*0.05 (e)*	Y	100 psia @ 25 °C	-29 -28	750 (b) 20,000 mg/m^3 (c) 2800-3000 (d) 11,200 mg/m^3 (d)	none	Y
Hexafluoro-2-butyne	C_4F_6	CF_3-C≡C-CF_3		Y	*<5 (f)*	*0.0015 (e)*		105 psia @ 20 °C	-24.6 -25	55 (g)	none	
Hexafluoro-1,3-butadiene	C_4F_6	CF_2=CF-CF=CF_2		Y	*~100 (f)*	*1.32 (e)*		*1460 mmHg (h)*	6 7		none	
Hexafluorocyclobutene	c-C_4F_6	CF_2-CF_2-CF=CF-	c-1316		*<5 (f)*	*0.014 (e)*		35 psia @ 20 °C	1 5	50 (i) 520 (j)	none	
Octafluoro-2-butene	C_4F_8	CF_3-CF=CF-CF_3	1318my	N	*<5 (f)*	*0.014 (e)*		30 psia @ 21 °C	-1.2 1.2	81 (k)	none	Y
Octafluorocyclopentene	c-C_5F_8	CF=CF-CF_2-CF_2-CF_2-	c-1418		90 (l)	0.98 (m)	Y	614 mmHg @ 21 °C (n) 256 mmHg @ 0 °C (n)	27		none	

Physical properties, TSCA (Toxic Substances Control Act) listings from [31], unless otherwise noted

(a) at ambient temperature and atmospheric pressure, source [17]

(b) LC_{50} (lethal concentration for 50% of the population) mouse, 4 hr exposure, source [17, 44]

(c) LC_{50} rat, 2 hr exposure, source [17]

(d) LC_{50} rat, 4 hr exposure, source [17, 44]

(e) Estimates based on hydroxyl radical reaction rates, source [23]

(f) Estimates derived from (e); formulae courtesy of J. Owens, 3M

(g) ALC (approximate lethal concentration) rat, 4 hr exposure, source [45]

(h) Estimated, source [36]

(i) LC_{50} unknown, source [17]

(j) ALC unknown, 2.5 min exposure [46]

(k) LC_{50} rat, 4 hr exposure, source [47]

(l) Source [20, 27, 29]

(m) Source [20]

(n) Source [29]

Table 2.4: Properties of other compounds evaluated.

Name	$C_xF_yH_z$	Line Formula	FC Number	Flamm.	GWP_{100}	Lifetime (yrs.)	Used Previously as Etchant?	Vapor Pressure	Boiling Point (°C)	Acute Toxicity (LC_{50}, LC_{Lo}, or ALC, ppm)	Corrosiveness	TSCA Listing
Trifluoroacetic anhydride	$C_4F_6O_3$	$(CF_3\text{-}C{=}O)_2O$		N	N/A	N/A	Y	325 mmHg @ 20 °C	39		severe irritant (a)	Y
Oxalyl fluoride	$C_2F_2O_2$	$(CF{=}O)_2$		N	N/A	N/A		2000 mmHg @ 20 °C	-3	4500 mg/m^3 (b)	corrosive (b)	Y
Octafluorotetrahydrofuran	c-C_4F_8O	$CF_2\text{-}CF_2\text{-}CF_2\text{-}CF_2\text{-}O\text{-}$		N	11,200 (c)	3,200 (c)		30 – 40.6 psia @ 20 °C	0		none	

Physical properties, TSCA (Toxic Substances Control Act) listings from [48], unless otherwise noted

(a) Skin (750 μg) and eye (5 mg) irritation studies, rabbit, 24 hr exposure, source [41]

(b) LC_{Lo} (lowest observed lethal concentration) mouse, 10 min exposure, source [49]

(c) Estimates based on analogy to c-C_4F_8

References

1. J. W. Coburn and H. F. Winters, *Plasma etching - A discussion of mechanisms*, J. Vac. Sci. Technol., **16**(2), p. 391-403 (1979).
2. J. W. Coburn, *Plasma-Assisted Etching*, Plasma Chemistry and Plasma Processing, **2**(1), p. 1-41 (1982).
3. G. Turban, *Basic Phenomena in Reactive Low Pressure Plasmas Used for Deposition and Etching - Current Status*, Pure & Appl. Chem., **56**(2), p. 215-230 (1984).
4. J. A. Mucha, The Gases of Plasma Etching: Silicon-Based Technology, in Solid State Technology, 1985, p. 123-127.
5. D. L. Flamm and J. A. Mucha, *Plasma Etching*, in *Chemistry of the Semiconductor industry*, S. J. Moss and A. Ledwith, Editors, Chapman and Hall, New York, NY, p. 343-390 (1987).
6. J. L. Tunkel, D. Aronson, H. Printup, and P. H. Howard, *Draft Report, EPA Contract 68-D2-0182,* U. S. Environmental Protection Agency (1996).
7. *Scientific Assessment of Ozone Depletion: 1998, Volume 2,* World Meteorological Organization, Global Ozone Research and Monitoring Project, Report No. 44 (1998).
8. M. C. Olewine, *Alternative Etch Chemistries and Optimization Studies for Dielectric Reactor Cleaning*, in Proceedings of *Global Warming Symposium*, SEMATECH (1994).
9. V. Mohindra, H. H. Sawin, M. T. Mocella, J. M. Cook, J. Flanner, and O. Turmel, *Alternatives to Perfluorocompounds as Plasma Processing Gases: SiO_2 Etching Using C_2F_5H and $C_2F_4H_2$*, in Proceedings of *10th Symposium on Plasma Processing*, San Francisco, CA, G. S. Mathad, D. W. Hess, and M. Engelhardt, Editors, The Electrochemical Society Proceedings Series, **PV 94-20**, p. 300-310, Electrochemical Society, Pennington, NJ (1994).
10. J. E. Nulty and P. S. Trammel, *Self-Aligned (SAC) Dry Etch Process for 0.5 μm SRAM Technology*, in Proceedings of *41st National Symposium*, American Vacuum Society (1994).
11. C. J. Choi, C. Parko, O. S. Kwon, Y. C. Kim, Y. S. Deol, and I. H. Choi, *Reduction of PFC Emission Using HFC Gases in Oxide Etch Processes*, in Proceedings of *6th Annual International Semiconductor Environmental, Safety, and Health Conference*, Williamsburg, VA (1999).
12. F. Illuzzi, R. d'Agostino, C. Cascarano, V. Colaprico, and F. Fracassi, *Alternative Compounds for SiO_2 Etching*, in Proceedings of *6th Annual International Semiconductor Environmental, Safety, and Health Conference*, Williamsburg, VA (1999).
13. S. R. Skaggs, T. A. Moore, and R. E. Tapscott, *Chapter 10*, in *Halon Replacements: Technology and Science*, A. W. Miziolek and W. Tsang, Editors, American Chemical Society, Washington, DC, p. 99 (1995).
14. F. Fracassi, R. d'Agostino, M. Stenardo, L. R. Atzei, and F. Illuzzi, *Environmental Impact of Fluorocarbon and Iodofluorocarbon Containing Glow Discharges for*

SiO_2 Etching, in Proceedings of *4th International ESH Conference*, Milan, Italy, **1** (1997).
15. S. Solomon, J. B. Burkholder, A. R. Ravishankara, and R. R. Garcia, *Ozone depletion and global warming potentials of CF_3I*, Journal of Geophysical Research, **99**(D10), p. 20929-20935 (1994).
16. R. E. Tapscott, S. R. Skaggs, and D. Dierdorf, *Chapter 14*, in *Halon Replacements: Technology and Science*, A. W. Miziolek and W. Tsang, Editors, American Chemical Society, Washington, DC, p. 151 (1995).
17. Material Safety Data Sheet Information from PCR, Inc., Gainesville, FL.
18. V. N. Bliznetsov, O. P. Gutshin, and V. V. Yachmenev, *Reactive ion etching of deep trenches in silicon*, in Proceedings of *SPIE International Conference of Microelectronics*, **1783**, p. 584-589 (1992).
19. F. Fracassi and R. d'Agostino, *Evaluation of trifluoroiodomethane as SiO_2 etchant for global warming reduction*, J. Vac. Sci. Technol. B, **16**(4), p. 1867-1872 (1998).
20. Y. Matsushita, *EIAJ Presentation*, in Proceedings of *6th Annual International Semiconductor Environmental, Safety, and Health Conference*, Williamsburg, VA (1999).
21. S. Samukawa and K.-i. Tsuda, *New Radical-Control Method for SiO_2 Etching with Non-Perfluorocompound Gas Chemistries*, Jpn. J. Appl. Phys., **37, Part 2**(10A), p. L1095-L1097 (1998).
22. S. Samukawa, T. Mukai, and K.-i. Tsuda, *New radical control method for high-performance dielectric etching with nonperfluorocompound gas chemistries in ultrahigh-frequency plasma*, J. Vac. Sci. Technol. A, **17**(5), p. 2551-2556 (1999).
23. J. L. Tunkel, D. Aronson, H. Printup, and P. H. Howard, *Draft Report, EPA Contract 68-D2-0182, Vol. 1,* U. S. Environmental Protection Agency, p. 35 (1996).
24. O. Joubert, G. S. Oehrlein, and Y. Zhang, *Fluorocarbon high-density plasmas. V. Influence of aspect ratio on the etch rate of silicon dioxide in an electron cyclotron resonance plasma*, J. Vac. Sci Technol. A, **12**(3), p. 658 (1994).
25. F. H. Bell, O. Joubert, G. S. Oehrlein, Y. Zhang, and D. Vender, *Investigation of selective SiO_2-to-Si etching in an inductively coupled high-density plasma using fluorocarbon gases*, J. Vac. Sci. Technol. A, **12**(6), p. 3095 (1994).
26. S. Samukawa and T. Mukai, *Differences in radical generation due to chemical bonding of gas molecules in a high-density fluorocarbon plasma: Effects of the C=C bond in fluorocarbon gases*, J. Vac. Sci. Technol. A, **17**(5), p. 2463-2466 (1999).
27. S. Ibuka, *PFC Reduction Approach for Oxide Etchers*, in Proceedings of *U.S. EPA Global Semiconductor Industry Conference on Perfluorocompound Emissions Control*, Monterey, CA, Section 3 (1998).
28. Y. Yoshida, *Japan's Research on Alternative Etching Gases*, in Proceedings of *U.S. EPA Global Semiconductor Industry Conference on Perfluorocompound Emissions Control*, Monterey, CA, Section 7 (1998).
29. S. Jimbo, M. Muto, K. Ito, and K. Goto, *C_5F_8 evaluation as an alternative gas to CF_4 using Chemical Dry Etch*, in Proceedings of *6th Annual International*

Semiconductor Environmental, Safety, and Health Conference, Williamsburg, VA (1999).
30. S. Soggs, B. Bryant, B. A. Boeck, S. Rogers, R. Vrtis, and L. Mendicino, *Trifluoroacetic Anhydride as an Alternative Plasma Clean Chemistry*, in Proceedings of *SEMICON Southwest 1996: A Partnership for Emissions Reduction*, Austin, TX, Proceedings of the SEMI Technical Program, p. 71-80, SEMI (1996).
31. Material Safety Data Sheet information from: Aldrich Chemical Co., Inc., Milwaukee, WI; DuPont Fluoroproducts, Wilmington, DE; Matheson Gas Products, Secaucus, NJ; Oakwood Products, Inc., W. Columbia, SC; and PCR, Inc./Lancaster Synthesis, Gainesville, FL.
32. PAFT, *Programme for Alternative Fluorocarbon Toxicity Testing: Toxicology Summary* (1995).
33. Material Safety Data Sheet Information from DuPont Fluoroproducts, Wilmington, DE.
34. J. L. Tunkel, D. Aronson, H. Printup, and P. H. Howard, *Draft Report, EPA Contract 68-D2-0182, Vol. 1,* U. S. Environmental Protection Agency, p. 34 (1996).
35. R. Atkinson, *Gas-Phase Tropospheric Chemistry of Organic Compounds*, J. Phys. Chem. Ref. Data, Monograph No. 2 (1994).
36. J. L. Tunkel, D. Aronson, H. Printup, and P. H. Howard, *Draft Report, EPA Contract 68-D2-0182, Vol. 1,* U. S. Environmental Protection Agency, p. 22 (1996).
37. A. L. Beyerlein, D. D. Marteau, S. Hwang, N. Smith, and P. Joyner, *Physical Property Data on Fluorinated Propanes and Butanes as CFC and HCFC Alternatives,* Clemson University, Report No. EPA/600/A 93/062 PB93-173102 (1993).
38. (Sanitized), *Toxic Substances Control Act 8E Submission,* U. S. EPA, Report No. Microfiche No. OTS0538269, Document No. 88-930000004S (1992).
39. E. I. Dupont de Nemours & Co., *Toxic Substances Control Act 8E Submission,* U. S. EPA, Report No. Microfiche No. OTS0556370, Document No. 88-950000046 (1994).
40. Dupont Chemicals, *Toxic Substances Control Act 8ECP Submission,* U. S. EPA, Report No. Microfiche No. OTS0571176, Document No. 88-920009519 (1973).
41. *SilverPlatter Database,* Registry of Toxic Effects of Chemical Substances (RTECS) (1996).
42. Hoechst Celanese Corp., *Toxic Substances Control Act 8E Submission,* U. S. EPA, Report No. Microfiche No. OTS0537909, Document No. 88-930000207 (1993).
43. Dupont Chemicals, *Toxic Substances Control Act 8ECP Submission,* U. S. EPA, Report No. Microfiche No. OTS0570972, Document No. 88-920009222 (1984).
44. Material Safety Data Sheet Information from Aldrich Chemical Co., Inc., Milwaukee, WI.
45. E. I. Dupont de Nemours & Co., *Toxic Substances Control Act FYI Submission,* U. S. EPA, Report No. Microfiche No. OTS0000725-1, Document No. FYI-OTS-0390-0725 (1990).

46. *Structure Team Activity Report on Perfluorocyclobutene,* U. S. EPA (1995).
47. Dupont Chemicals, *Toxic Substances Control Act 8ECP Submission,* U. S. EPA, Report No. Microfiche No. OTS0571518, Document No. 88-920009866 (1966).
48. Material Safety Data Sheet information from: Schumacher, Carlsbad, CA; AlliedSignal, Inc., Morristown, NJ; and 3M Company, St. Paul, MN.
49. Material Safety Data Sheet information from AlliedSignal, Inc., Morristown, NJ.

3. Basic Mechanisms and Tool Concepts in Plasma Etching

The present chapter will provide the reader with a brief review of key physical and chemical phenomena that play a role in plasma etch processes. This review is not intended to be exhaustive, but merely to supply a background for subsequent discussions. The reader is referred to Ref. [1] for a detailed discussion of early plasma tools and basic concepts in plasma processing. For a more up to date treatment which includes a systematic discussion of modern high density plasma sources, the reader will find Ref. [2] to be of considerable utility. Section 3.1 will provide some basic concepts, primarily as they relate to early, capacitively coupled plasma tools. Since reactor designs today differ vastly from early plasma tools, Section 3.2 will discuss the key differences, focusing specifically on the non-resonant inductively coupled design, which is represented in the Applied Materials Centura 5300 HDP platform used extensively in this work (Chapters 5 and 6). Section 3.3 will change the focus of the discussion from tool concepts to plasma chemistry, as it pertains to fluorocarbon based dielectric (principally silicon dioxide) etching. There exists an extensive body of work in the early literature in which basic plasma chemistry mechanisms, such as fluorocarbon formation and the role of oxygen and hydrogen in fluorocarbon plasmas, are treated in detail. Refs. [3-10], among others, are representative of this material. Section 3.3 will attempt to provide a summary intended to serve as a lead-in to the more detailed discussions in Chapters 5 and 6. Finally, The specific process tools used in this work – the Applied Materials Precision 5000 Mark II (Chapter 4) and the Applied Materials Centura 5300 HDP (Chapters 5 and 6) – will be presented in Section 3.4.

3.1 Plasma Fundamentals

The framework of the discussion of basic mechanisms in this section is drawn, in large part, from Ref. [1] and a condensed treatment of the topic in Ref. [11].

3.1.1 Gas Phase Collision Processes

Energy Transfer. Collision processes can be broadly divided into elastic and inelastic collisions, depending on whether the internal energies of the colliding bodies are maintained. *Particles* are usually described as possessing *kinetic* energy due to their motion (and equal to $mv^2/2$ for translational motion), and *internal* or potential energy which may be in the form of electronic excitation, ionization, etc. An elastic collision is one in which there is an interchange of kinetic energy only. In an inelastic collision, the internal energies change as well.

An energy transfer function which gives the maximum energy transferable in an elastic **binary** collision can be given by

$$\frac{E_t}{E_i} = \frac{4m_i m_t}{(m_i + m_t)^2}, \qquad (3.1)$$

where *t* refers to the target particle and *i* refers to the incident particle. For example, the fraction of energy transferred from an electron to a nitrogen molecule in an elastic binary collision is $\sim 10^{-4}$. However, if one allows the collision to be inelastic so that the molecule struck gains internal energy ΔU, then the fraction of the kinetic energy of the first particle that can be transferred to the internal energy of the second has a maximum value of

$$\Delta U_{max} = \frac{1}{2} \frac{m_t m_i}{m_t + m_i} v_i^2 \cos^2 \Theta . \qquad (3.2)$$

In a head-on collision (*i.e.*, Θ=0), the maximum inelastic energy transfer from an electron to a molecule may be more than 99.9% since in this case $m_t >> m_i$.

Main collision process. The gas phase environment of a glow discharge contains electrons, ions, neutral atoms and molecules, and photons. Collisions involving electrons are dominant in determining the macroscopic behavior of the glow discharge. If an electron is accelerated between two points of potential difference X volts, then it loses eX joules of potential energy and gains eX joules of kinetic energy (e is the electron charge

of 1.602 x 10 $^{-19}$ Coulombs). This eX joules of energy are also referred to as X electron volts or X eV, so that

$$1 \text{ eV} = 1.602 \times 10^{-19} \text{ joules} = 1.602 \times 10^{-12} \text{ ergs}$$

The electron volt as an energy unit is also applied to neutral as well as to other charged particles. Additionally, in the plasma processing field, it is customary to express bond strengths within molecules in eV (per bond) rather than in kcal/mol or J/mol.

3.1.2 Elastic and Inelastic Collisions

Elastic collisions. Kinetic energy is conserved. Because the electron and any given atom have very different masses, the transfer of energy is negligible and the electron changes direction after the collision without significantly changing speed. When the electron is moving in an electric field, elastic collisions restrict the electron velocity in the direction of the field.

Electron impact ionization. Here the primary electron removes an electron from an atom, molecule, or molecular fragment, producing a positive ion and two electrons, *e.g.*,

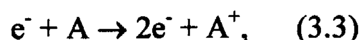

$$e^- + A \rightarrow 2e^- + A^+, \qquad (3.3)$$

where A represents a generalized particle such as an atom, molecule, or molecular fragment. The two electrons produced by the ionizing collision can then be accelerated by an electric field until they too can produce ionizations. This multiplication process is what maintains a glow discharge. The **ionization potential** is the energy required to remove the most weakly bound electron from the particle and is the minimum energy required for this ionization process to occur.

Table 3.1: Ionization potentials for selected atoms, source [12].

Neutral Atom	Ionization Energy (eV)
Hydrogen	13.5984
Helium	24.5874
Carbon	11.2603
Nitrogen	14.5341
Oxygen	13.6181
Fluorine	17.4228
Neon	21.5646
Chlorine	12.9676
Argon	15.7596
Bromine	11.8138
Krypton	13.9996
Iodine	10.4513
Xenon	12.1298

Electron impact excitation. In ionization, a bound electron in a particle is ejected from that particle. In excitation, the transfer of energy to the bound electron enables the electron to jump to a higher energy level within the particle with a corresponding quantum absorption of energy. This process is represented as:

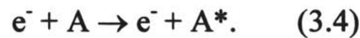

$$e^- + A \rightarrow e^- + A^*. \qquad (3.4)$$

As with ionization, there is a minimum energy required for excitation to occur. This **excitation potential** is somewhat lower than the ionization potential, since excitation raises an electron to a higher shell, while ionization completely removes the electron from the particle.

Dissociation. Another key process that occurs in a plasma is the breakup of a species via impact from an energetic electron:

$$e^- + AB \rightarrow e^- + A + B. \qquad (3.5)$$

The two resultant species need not necessarily be neutrals. The collision may, for instance, result in the formation of positive or, in certain plasma environments, negative ions, *e.g.*,

$$e^- + AB \rightarrow 2e^- + A^+ + B, \quad (3.6a)$$

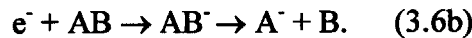

$$e^- + AB \rightarrow AB^- \rightarrow A^- + B. \quad (3.6b)$$

Such events are often called **dissociative ionization** and **dissociative attachment,** respectively. Respective examples include

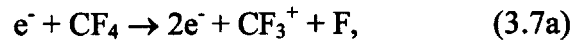

$$e^- + CF_4 \rightarrow 2e^- + CF_3^+ + F, \quad (3.7a)$$

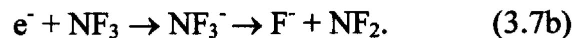

$$e^- + NF_3 \rightarrow NF_3^- \rightarrow F^- + NF_2. \quad (3.7b)$$

It should be pointed out that dissociative attachment is more likely to occur when the incident electron is less energetic and/or the target species has a larger number of degrees of freedom.

Relaxation. The de-excitation of electronically excited atoms and molecules is essentially the inverse of excitation. The excited states are unstable and the electron configuration quickly returns to its original (ground) state with lifetimes varying from nanoseconds to seconds. Each transition is accompanied by the emission of a photon of energy equal to the difference ΔE in the energy between the relevant quantum levels. (This is what makes the plasma glow.) Human eyes are sensitive to wavelengths between about 4100 Å (violet) and 7200 Å (red), which correspond to electron transitions of 3.0 and 1.7 eV, respectively.

Recombination. This is the inverse of ionization: here an electron coalesces with a positive ion to form a neutral atom. It can be demonstrated that a two body coalescence is not possible, because in such a collision both energy and momentum cannot be conserved. Recombination in a three body collision, in which the third body is either a wall or another gas atom, however, is possible.

Penning mechanisms and charge exchange collisions. These types of collisions are also of importance. They involve a collision between two gas phase species that results in a transfer of exited state or of charge, respectively:

$$A^* + B \rightarrow A + B^*, \quad (3.8a)$$

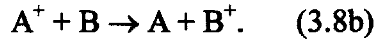

$$A^+ + B \rightarrow A + B^+. \quad (3.8b)$$

3.1.3 Glow Discharges

A plasma, generally speaking, is a partially ionized gas in which the charged species have sufficient concentrations to interact through Coulombic collisions. One can broadly differentiate between two types of plasmas. The first is an equilibrium plasma, where the temperatures of the ions and the electrons are equal – broadly speaking, examples (spanning a vast range of pressure and temperature conditions) include the sun and arc welder discharges. What is known as a "plasma" in semiconductor processing usage is actually the second type, sometimes more accurately described as a glow discharge, or a type of non-equilibrium plasma. In such a discharge, for reasons to be discussed below, the electron temperature is higher than the ion temperature.

Electron and ion densities. A simple model for a plasma consists of positive ions and negative electrons in a sea of neutral species. Ion-electron pairs are continuously created by ionization and destroyed by recombination. Because these processes are always pair-wise, the total space occupied remains charge neutral. Electron impact excitation and the subsequent relaxation of the atom leading to photon emission is another common feature of the plasma. In the type of plasmas used in microelectronics, the degree of ionization can vary widely. Collectively, older "low density" systems have been characterized by having plasma (*i.e.,* electron and ion) densities on the order of 10^9 - 10^{11} cm^{-3} and ionization fractions on the order of 10^{-6} - 10^{-3} [13]. This is in contrast to more recent "high density" systems, which use different power coupling configurations to achieve plasma densities of 10^{11} cm^{-3} or higher and attain ionization fractions of 10^{-4} to 10^{-1}, *i.e.,* as high as 10% [13].

Electronegative plasmas. Not all discharges, however, fit the simple model presented above. Whereas there exists a broad class of discharges where nearly all ions are positive and nearly all negative charge in the discharge is carried by electrons, there also exist discharges where the electron population is quite small relative to the size of the *negative ion* population. The former type of discharge is termed **electropositive**, while the latter is called **electronegative**. Under conditions of interest in semiconductor processing, argon, for example, will form an electropositive discharge, while other gases, such as nitrogen trifluoride, will tend to form electronegative discharges. These differences in plasma behavior stem largely from differences in cross sections for electron attachment. Molecules with high electron attachment cross sections will naturally tend to be more likely to form negative ions. One of the consequences of the large difference in mobility between negative ions and electrons in a discharge is the fact that electronegative plasmas tend to be more unstable. Consequently, gases which are known to form electronegative discharges are often used in conjunction with diluents such as He or Ar, which are known to form electropositive plasmas.

Electron and ion temperatures. For simplicity, consider a plasma where the charged particles are singly charged positive ions and electrons. To maintain a steady state of electron and ion densities, the recombination process must be balanced by an ionization process, *i.e.*, an external energy source is required. This energy source is provided by electromagnetic fields which act directly on the charged particles only. Let m_e and m_i be the masses of the electron and the ion, respectively. For simplicity, consider an electric field **E** acting on an initially stationary ion. The work done by the electric field, and hence the energy transferred to the ion, is given by (ignoring collisions):

$$E_{transferred} = \frac{(e\mathrm{E}t)^2}{2m_i}, \qquad (3.9)$$

where t is the time over which the field acts on the particle, e is the electron charge, and **E** is the magnitude of the electric field. A similar relationship holds for the electrons. Since $m_i >> m_e$, the action of the field is primarily to give energy to the electrons. Moreover, electrons collide with neutral atoms and ions, but lose very little energy to these heavy particles. In contrast, the neutral species and ions share their energy

efficiently in collision processes. The net result is that electrons can have a high average kinetic energy, typically 2-8 eV. The ions, which can absorb somewhat more energy than neutral species, gain energy above the ambient primarily by collisions with ions and remain essentially at room temperature; *i.e.*, ~1/40 eV (compare this with 2-8 eV).

Because $\frac{1}{2}m\bar{c}^2 = \frac{3}{2}kT$, where $\bar{c}$ is the average speed of a given population of particles and k is Boltzmann's constant (1.381×10^{-23} J/K = 8.620×10^{-5} eV/K), one can associate an effective temperature T_e with the electron motion. For electron energies ~2 eV, this yields an electron temperature of 23,200 K, which makes a plasma a highly non-equilibrium environment.

3.1.4 Surface Potentials, Sheath Formation

Plasma potential, floating potential. If a small electrically isolated substrate is suspended into the plasma, initially it will be struck by electrons and ions with charge fluxes given by following:

$$j_e = \frac{en_e\bar{c}_e}{4} \text{ and} \qquad (3.10a)$$

$$j_i = \frac{en_i\bar{c}_i}{4}, \qquad (3.10b)$$

where j is the current density due to the arrival of charge at the surface, and $\bar{c}$ is the mean speed of the charged species *while still in the plasma.* (These speeds are not the classical mean square speeds, given by $1/2\ mc^2 = 3/2\ kT$, but the mean speeds of the electron and ion populations of the plasma, which – to first order – are the mean speeds of a Maxwellian distribution, given by: $\bar{c} = (8kT/\pi m)^{1/2}$.) The electron density, n_e, and ion density, n_i, are equal; these are often referred to as the *plasma density.* (This density is much lower than that of neutrals.) But since $\bar{c}_e >> \bar{c}_i$ (due to both the higher temperature and lower mass of the electrons), $j_e >> j_i$ and the substrate immediately starts to build a negative charge, and hence negative potential, with respect to the plasma. As a

result, the electron flux decreases, but the substrate continues to charge negatively until the electron flux is reduced enough by repulsion to balance the ion flux. We can associate a **floating potential**, V_f, with the isolated substrate, and a **plasma potential**, V_p, with the plasma. Since V_f is such as to repel electrons, $V_f < V_p$.

Sheath formation. Because electrons are repelled by the potential difference $V_p - V_f$, it follows that the isolated substrate will acquire a net positive charge around it. This is known as a **space charge** and, in the context of glow discharge plasmas, it forms a **sheath**. The net positive charge in the sheath also means that the electron density decreases in the sheath. But the plasma glow is due to the relaxation of atoms excited by electron impact. The glow intensity depends on the number density and energy of the exciting electrons. Since the electron density is lower in the sheath, this is an area of lower luminosity than the glow itself, *i.e.*, the substrate is surrounded by a **dark space**.

Fluxes and energies. The fluxes j_i, j_e are limited by the arrival rate of each species at the interface with the sheath. In light of the argument made above, the ion flux cannot increase beyond Φ_I, its value at the interface. The ions merely arrive at the surface with greater velocity, but at the same rate. The electron flux, however, is lower at the surface than at the interface, because only those fast enough to overcome the potential barrier of the sheath arrive at the surface. Thus, the number of electrons hitting the surface is reduced:

$$\Phi_{e,surface} = \Phi_e \exp(-\frac{e(V_p - V_f)}{kT_e}) = \Phi_i \quad , \qquad (3.11)$$

where e is the electronic charge, k is Boltzmann's constant, and T_e is the electron temperature. In the steady state, the electron and ion fluxes at the surface must balance. Thus V_f will become fixed at a value appropriate to this condition. Put another way, the voltage drop across the sheath at a floating surface can be related to the mean speeds of the ion and electron populations in the plasma, and this relation is:

$$V_p - V_f = \frac{kT_e}{e} \ln \frac{\bar{c}_e}{\bar{c}_i} \quad . \qquad (3.12)$$

For a floating surface, typical values for electron and ion masses and temperatures in conventional parallel plate diode systems give a value V_p - V_f ≈ 15 V, which is roughly consistent with measured values.

Besides repelling electrons, the voltage across the sheath attracts positive ions and influences the energy with which the ions strike the substrate. The ion enters the sheath with very low energy. It is then accelerated by the sheath voltage and, in the absence of collisions in the sheath, strikes the substrate with a kinetic energy equivalent to the sheath voltage.

3.2 High vs. Low Density Plasma Sources

The focus of this section will be on high density plasma tools and, to some extent, so-called medium density tools. A cursory description of the earliest – and most basic – type of reactor employed for plasma etching applications, the parallel plate diode, is provided for contrast with the medium and high density systems that were used in this work. For a more detailed discussion of the parallel plate diode, in both its dc and rf configurations, the reader is referred to Refs. [1, 2].

3.2.1 The Parallel Plate Diode

The earliest type of plasma equipment configuration was the capacitively coupled diode reactor. In this configuration, power, whether dc or rf, is typically supplied to the discharge via a pair of parallel plate electrodes. In a very simple model of such a discharge, since power is dissipated in the bulk of the plasma, the bulk may be modeled as a resistive component. Since the formation of the sheaths at each surface wet by the discharge stems from the buildup of charge on those surfaces, the sheaths may be modeled as capacitive components. Hence this configuration is said to be **capacitively coupled**. For the purposes of subsequent discussion, capacitively coupled diode reactors will be frequently referred to as **low density plasma** systems, in contradistinction to high density plasma systems, to be discussed shortly. The first order voltage distribution in a

parallel plate diode reactor (of the dc variety) is shown graphically in Figure 3.1. In typical early parallel plate diode systems used for wafer patterning applications, the wafer would be placed on the cathode. In some applications, *e.g.*, resist ashing in oxygen discharges, where ion bombardment was not needed for anisotropy considerations – or not desired, the wafer would be placed on the grounded anode of the system. Note that the plasma bulk is treated as quasi-neutral and that the largest voltage drop in the system is at the cathode sheath. The same general picture is applicable to rf systems, with the qualification that, in rf systems, in addition to the existence of an (rf) sheath voltage at all surfaces being wet by the plasma, there exists an additional dc component at all surfaces that are not at dc ground known as the **dc offset** or the **self-bias**. This voltage, along with the rf sheath voltage which modulates it, determines the energy of the bombarding ions striking those surfaces.

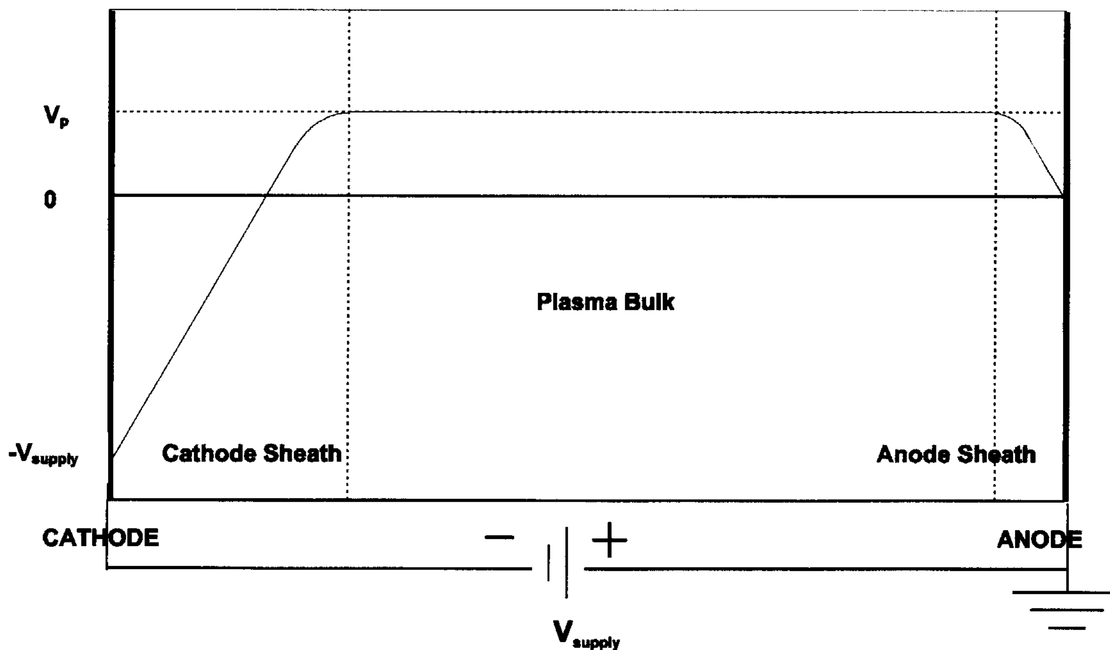

Figure 3.1: First order voltage distribution in a capacitively coupled (dc) parallel plate diode system.

The bulk of the discussion in Section 3.1 is generally applicable to most types of past and present reactor configurations employed in plasma etching. Where treatment of the subject begins to diverge is when plasma heating mechanisms begin to enter the

discussion. The dominant plasma excitation mechanisms are, generally speaking, considerably different in capacitively coupled parallel plate systems than in high density systems. In the former case, a principal heating mechanism is the emission of energetic electrons from the cathode. The cathode, being the powered electrode, typically sustains a large voltage drop across its sheath, which leads to significant ion bombardment of its surface. This, in turn, leads to the emission of significant quantities of secondary electrons from the surface, which are then accelerated across the cathode sheath and injected into the quasi-neutral plasma bulk with considerable energy, where they act to sustain the discharge through ionizing collisions. As will be seen shortly, one of the principal differences between high density systems and the diode design lies, in fact, in the plasma heating mechanism; additionally, the roles played by various static and time-varying electromagnetic fields in maintaining the discharge also differ considerably.

One shortcoming of the simple diode design has been the fact that the voltage across the sheath at the cathode is inherently dependent on the level of power supplied to maintain the discharge and one cannot be controlled independently from the other. In other words, increasing plasma power to increase the degree to which the feed gas is dissociated (*i.e.,* to increase ion and neutral fluxes to the wafer surface) can only be done by increasing the dc or rf voltage applied to the powered electrode, which inherently results in an increase in the accelerating voltage seen by ions bombarding the wafer surface. Put another way, the *ion energy* and the *ion flux* (along with related neutral fluxes) cannot be decoupled.

Increasing ion energy at the cathode is not necessarily desirable. Energetic bombardment of the wafer surface can lead to substrate damage or loss of linewidth (critical dimension) control. Additionally, feed gas utilization is often low in capacitively coupled low density plasma systems; conversion efficiencies for gases such as CF_4 or C_2F_6 on the order of 20% are not uncommon.

3.2.2 Medium Density Plasma Tool Designs

Ref. [14]. The need to attain independent control of ion flux and ion energy initially led to the development of a number enhancements to the capacitively coupled diode configuration. In the 1980's, so called *medium density plasma* systems began to become common. These tools utilized additional energy inputs that were independent of the power supplied to the cathode. One configuration, the **rf triode**, exemplified by the Lam Research 384T etch system, placed the wafer on a second electrode which was biased independently of the cathode of the system. (The grounded chamber walls formed the anode.) Another approach, utilized by Applied Materials in the Precision 5000 etch chamber, involved the use of a dc magnetic field in a direction transverse to the chamber axis. The chamber is equipped with four magnet coils, arranged around the walls of the chamber. Two coils facing each other form a set; the two sets are 90 degrees out of phase. A rotating magnetic field whose lines of flux are parallel to the surface of the wafer may thus be generated. This configuration is often referred to as MERIE (magnetically enhanced reactive ion etcher). Magnetic flux densities in the range of 0-100 gauss were nominally available in this model. The magnetically enhanced rf diode design evolved into other etch chamber variants made by Applied Materials, namely the MxP, MxP+, eMxP+, and, more recently, the Super *e*. This design will be discussed again in Section 3.4.

3.2.3 Low Pressure, High Density Sources

These approaches, though they succeeded in elevating the plasma density at a given level of bombardment, still did not allow for true independent control of ion energy and the ion and neutral fluxes. The limitations of these approaches led to the development of what are today collectively termed **high density plasma (HDP)** sources. All the designs mentioned below share several key features:

1. Separation of plasma source power from wafer bias.
2. Higher plasma density than available in capacitively coupled diode systems.
3. Low pressure regime of operation.

4. Coupling of power to the plasma across a dielectric (or, in some cases, semiconducting) window, rather than by direct contact of an electrode with the plasma.

This last feature is, in fact, what makes achieving low voltages at all plasma surfaces attainable [15]. Table 3.2 summarizes some typical values for operating parameters seen in low density rf-driven systems versus those seen in HDP systems (after Ref. [13]). Schematic representations of four of the more commonly encountered types of HDP sources can be seen in Figure 3.2. The source design employed in the Centura 5300 HDP tool for a number of the experiments to be discussed in later chapters is of the non-resonant ICP ("inductively coupled plasma") variety. Broadly speaking, among the most commonly encountered types of source configurations, one can differentiate between inductively coupled sources and wave heated sources. The former include the non-resonant ICP as well as its resonant variant, known as the helical resonator, whereas the latter include the ECR (electron cyclotron resonance) source and the helicon source.

Table 3.2: Comparison between typical low and high density plasma systems.

Parameter	Capacitively coupled rf diode	High density plasma source
Pressure (mTorr)	10-5000	0.5-200
Plasma density (cm^{-3})	10^{9}-10^{11}	10^{11}-10^{13}
Substrate sheath voltage (V)	200-1000	20-500
Ionization fraction	10^{-6}-10^{3}	10^{-4}-10^{-1}

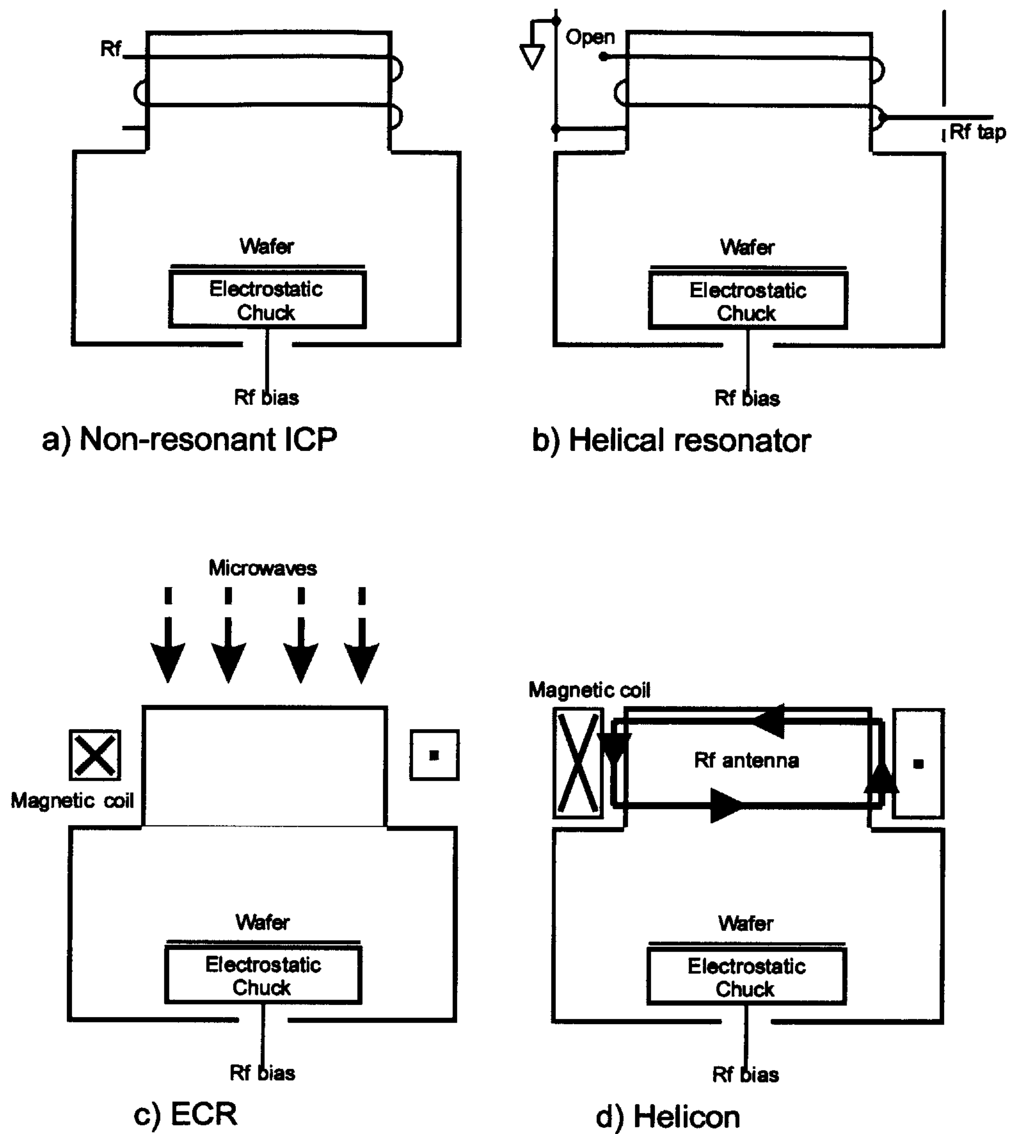

Figure 3.2: Examples of several high density plasma source configurations: inductively coupled sources: a) non-resonant ICP, b) helical resonator, wave heated sources: c) ECR, d) helicon, after Ref. [15].

3.2.3.1 Non-Resonant ICP (Inductively Coupled Plasma) Sources

Two types of inductively driven source configurations are often discussed: the non-resonant inductive coil design and the resonant coil design. While the term **inductively coupled plasma** is, strictly speaking, applicable to both, in practical usage, which will be followed in this discussion, it is associated with the non-resonant variety. The two basic variations of the non-resonant ICP design are the planar coil and the cylindrical antenna (shown in Figure 3.2). In the latter configuration, an rf-driven coil is wound around a dielectric window. In the former case, a planar rf-driven coil is located above the substrate in the process chamber with the dielectric window between the two. In both designs, the coil element is located outside the process chamber with the dielectric material (typically quartz or aluminum oxide) forming part of the process chamber wall.

The cylindrical antenna is seen in systems like the Applied Materials HDP etch chamber and the Novellus Speed PECVD tool. The planar coil design is perhaps most commonly encountered in Lam Research 9100, 9400, and 9600 series etch tools, for dielectric, polysilicon, and metal etch, respectively. In these tools in particular, the planar coil configuration is often referred to as the TCP (transformer coupled plasma) design.

Inductive coils are typically driven at rf frequencies, *e.g.,* the standard frequency 13.56 MHz or lower. (The Applied Materials HDP chamber, for instance uses frequencies in the 1.8 – 2.0 MHz range for both bias and source rf power.) In ICP systems, the plasma acts as one half of a transformer, with the other half being the multi-turn cylindrical antenna or planar coil. Thus power is coupled inductively, as in a transformer.

The non-resonant ICP configuration has become, by the late 1990s, the most commonly used HDP source design in semiconductor applications. Among the reasons for this is its inherent simplicity. It requires no magnetic fields or microwave power, which are features seen in wave heated sources.

3.2.3.2 Helical Resonator Sources

The **helical resonator** is a variation on the inductively coupled design where the rf energy supplied to the inductive coil is coupled in a resonant mode. Besides the inductive coupling, key features that it has in common with the non-resonant ICP design are use of rf rather than microwave power and no requirement for additional electromagnetic field sources, such as dc magnets. The helical resonator, however, is a more complicated system than the non-resonant ICP and, as such, it is still not fully understood in all aspects.

The essential feature of this design utilizes the notion that helical structures can be used to propagate slow-moving electromagnetic waves (*i.e.,* waves with phase velocity much lower than the speed of light). Its construction consists of a helical coil around a cylindrical dielectric window, surrounded by a ground shield (whose role is to reduce the amount of capacitive coupling between the helix structure and the plasma). One end of the coil is grounded, one end is open, while, at an appropriate point along the helix, an rf tap is made, connecting the coil to the rf supply. This structure becomes resonant when an integral multiple of quarter-wavelengths of the rf field are made to fit between the two ends of the structure. At this condition, electromagnetic fields within the helix can sustain a low pressure, high density discharge with little loss. [16]

3.2.3.3 ECR (Electron Cyclotron Resonance) Sources

Another important HDP source design is the ECR (**electron cyclotron resonance**) source. The ECR source is an example of a *wave heated* source, where power is coupled to the discharge through electromagnetic waves generated near a plasma surface. These waves may propagate either into the plasma body or along its surface, being absorbed, and thus heating electrons in the discharge. In the ECR configuration, electromagnetic waves are injected into a chamber through a dielectric window. A microwave frequency, typically 2.45 GHz, is often used. One or more magnetic coils are used to set up a magnetic field within the chamber; the strength of this field is chosen to achieve a *localized* resonance condition, defined by $\omega \approx \omega_{ce}$, where ω is the frequency of the

applied microwave energy and $\omega_{ce} = eB/m$ is the electron cyclotron frequency at a given magnetic flux density B. Numerically, the electron cyclotron frequency (in MHz) is given by $f_{ce} = \omega_{ce}/2\pi \approx 2.8B_{res}$, with B given in gauss. Thus for $f_{ce} = f = 2.45$ GHz, one obtains $B_{res} = 875$ G. It is significant that the polarization of the applied electromagnetic wave is not arbitrary. Only right hand polarized (RHP) waves, *i.e.*, waves in which the electric field vector rotates in a right hand sense around the direction of propagation, can result in net heating of the discharge. This is because an electron in a magnetic field B will also gyrate in a right hand sense around the lines of magnetic flux, which, in the ECR configuration, are aligned with the direction of propagation of the applied microwaves. As a consequence, when $\omega = \omega_{ce}$, an electron is continuously accelerated along its circular orbit, resulting in significant energy gain while the electron is within the resonance zone. In contrast, a left hand polarized wave, results in zero average energy gain. [17].

There are a number of ECR based commercially available plasma tools. One of the disadvantages of ECR systems, particularly for large area substrates, however, stems from the fact that the electromagnetic fields propagating through the chamber typically reach the wafer with radially nonuniform power profiles. This inherent lack of radial uniformity in the discharge tends to translate into process nonuniformity on the substrate. Various modifications to the ECR design have been implemented in order to address this problem; nevertheless, as substrate areas increase, it becomes apparent that it may be considerably less challenging to achieve radially uniform discharges using other source designs, notably ICP.

3.2.3.4 Helicon Sources

The helicon design is another example of a wave excited discharge. The modes of coupling are more difficult to analyze than those seen in ECR discharges. In the helicon, an rf antenna around a dielectric cylinder is used in conjunction with a dc magnetic field to generate slow moving electromagnetic waves that propagate down the length of the cylinder. The design relies on coupling of the antenna to transverse electric and/or

magnetic fields to achieve energy gain; the energy is then deposited into the plasma as the wave moves down the length of the chamber and its electromagnetic fields excite electrons in the discharge.

Among potential advantages that the helicon design has over ECR is the fact that it is rf, rather than microwave, driven (typically at 13.56 MHz). Additionally, while ECR requires fairly high dc magnetic fields (typically 875 G) to operate, fields on the order of 20 to 200 G are typical in helicon sources. Both these features have the potential for lower manufacturing cost relative to ECR. Moreover, helicon sources are capable of exciting plasmas of higher density than many other sources of comparable power and dimensions, with plasma densities as high as 10^{14} cm^{-3} being reported. This may eventually lead to a larger share of HDP process tools utilizing helicon designs if still higher plasma density becomes a requirement. [18]

3.2.3.5 Other High Density Source Designs

The above discussion is by no means intended to be an exhaustive review of all types of existing schemes for generating high density discharges for silicon processing. There exist a number of other designs that may in the future prove commercially viable. Two other sources worth mentioning presently are **surface wave** discharges and so-called **ultrahigh frequency (UHF)** discharges. The surface wave source, as the name implies, is another example of a wave heated design. In this configuration, an electromagnetic wave is set up to propagate along the surface of the discharge chamber, coupling power to the discharge by exciting electrons in the plasma near the surface of the vessel. In the UHF design, a spokewise antenna is used to transmit power at a frequency on the order of 500 MHz through a dielectric window into the plasma. One advantage of the UHF design over rf-driven ICP reactors is that the significantly higher frequency of operation results in a shift of the peak of the electron energy distribution function (eedf) toward lower energies, without necessarily lowering of plasma density. This translates to even lower sheath voltages than those attainable in ICP discharges [19].

3.3 Fluorocarbon Plasmas in Dielectric Etch Processes

The earlier discussion on plasma systems attempted to provide some insight into discharge physics, reactor design, as well as power coupling schemes. This section will apply these concepts to the important class of processes collectively termed "plasma etching," specifically focusing on fluorocarbon plasmas. In the early days of the discipline, the term "plasma etching" has often referred to an etch reactor configuration where the wafer was placed on a grounded electrode; hence, in the absence of significant bombardment, the etch was largely chemical in nature. A distinction was often made between these processes and "reactive ion etching," where the wafer was placed on a powered electrode. "Reactive ion etching," however, has since come to be regarded as a misnomer. The term refers to etch processes which have a significant physical (ion-induced sputtering) component, in addition to the chemical one. It was coined in the belief that ion chemistry played a dominant role in the removal of the film being etched. It had since been found that, especially in low density systems, neutrals, rather than ions, dominate the *chemistry* of the process, which is not surprising, given that neutral populations are several orders of magnitude larger than ion populations in typical plasmas. (Ironically, even though the term "reactive ion etching" has for some time been regarded as physically inaccurate, more recent studies suggest that, under appropriate conditions in *high* density systems, even though ions continue to be in the minority in the plasma bulk by up to a few orders of magnitude, ion *fluxes* may actually be on the same order of magnitude as neutral fluxes [20], suggesting that, if "reactive ion etching" occurs anywhere, it is in high density systems rather than in the low density systems for which the term was originally coined.) In this text, the term "plasma etching" is used generically to refer to any process that involves the removal of films from a substrate using a plasma environment, regardless of reactor configuration.

The subsections that follow offer a discussion of several key mechanisms known to play a key role in fluorocarbon etch plasmas, namely, polymer formation, oxygen and hydrogen effects, and the F:C ratio model. This discussion is based on sources in the early literature of the discipline and does not yet taken into account insights gained from subsequent work with low pressure, high density plasma tools. Nevertheless, the

fundamental concepts presented here still form the basis for much of today's understanding of fluorocarbon plasmas. Section 5.3 will revisit the discussion that is about to follow, incorporating results obtained from studies carried out in high density tools.

3.3.1 Etching of Si vs. Etching of Dielectrics

When silicon is etched in a fluorine-bearing plasma, the etch reaction has a tendency to proceed isotropically [9]. This is consistent with the observation that F atoms will etch Si readily without the presence of any ion bombardment; silicon dioxide [4, 6, 21] and silicon nitride, on the other hand, are not readily etched by F atoms under such conditions. When subjected to ion bombardment, however, oxide and nitride etch readily in fluorine plasmas and with high anisotropy [21], which is consistent with the fact that the spontaneous or isotropic etch rates of these materials are low. When fluorocarbon plasmas are used, all three materials etch readily, with Si exhibiting considerably greater tendencies toward isotropic behavior [9]. A key phenomenon present in these discharges is the tendency for a fluoropolymer layer to form on the surfaces being etched. This phenomenon is perhaps the salient feature of fluorocarbon discharges. Manipulation of the polymerization mechanism through adjustment of process parameters, most notably through altering the chemistry of the discharge itself, is critical to obtaining etch rate enhancement as well as selectivity among these materials. CF_4 has often been used as the vehicle through which these effects were studied, particularly in the early work in this area, but the discussion which follows may be extended to fluorocarbon discharges in general.

3.3.2 Polymer Formation

References [3, 4, 6, 7, 9, 21]. It has been established that a CF_x-film forms on Si and Si-compound surfaces by the adsorption of certain C_xF_y species. CF_x fragments, which are generated by dissociation of the parent fluorocarbon molecule into CF_x and atomic fluorine, as well as unsaturated C_xF_y species (*e.g.*, C_2F_4) that may be formed in the discharge have been identified as the building blocks for this mechanism. These layers

serve as an inhibitor to etching. In the steady state, the formation of this layer and its removal are competing processes and a finite thickness of this film is believed to be present on the surfaces being etched as the etch reaction proceeds. It is possible, however, to drive the conditions in the discharge to a regime where net deposition of the polymer occurs and all etching ceases.

It should be noted that the presence of an inhibiting layer in the steady state during the etch process is believed to be one of the mechanisms that assist anisotropic etching in fluorocarbon plasmas. Other mechanisms believed to play a major role in achieving anisotropy are ion sputtering of adsorbed reaction products and/or damage-induced etch-rate enhancement on surfaces exposed to bombardment [6, 7]. Sidewall passivation by fluoropolymer films is believed to inhibit lateral etching, while vertical etching is allowed to proceed because this film is actively removed, or its formation is suppressed, on surfaces exposed to ion flux. Which mechanism dominates in a given system is believed to be reactor and process dependent (and is often a subject of debate).

3.3.3 Oxygen Effects

References [3, 4, 6, 7, 9, 21]. It has been well established that the addition of O_2 to fluorocarbon plasmas can have the effect of dramatically boosting the etch rates of silicon and its compounds. Oxygen is thought to play several roles when added to a fluorocarbon discharge and its effects are intimately connected with the presence of the fluoropolymer layer on the substrate surface. Oxygen is believed to attack this layer. (This mechanism is probably analogous to the random scission of hydrocarbon polymer chains, which is the process believed to occur in the etching of organic resists by oxygen discharges [5, 9, 21].) This attack has essentially three consequences: 1). the removal of the inhibitor film, which facilitates attack of the underlying Si-based layer by fluorine, 2). the freeing up of gas-phase fluorine that would otherwise be consumed in attacking the polymer, and 3). the direct release of fluorine from the polymer film, which makes more etchant available to attack the Si-based film. Evidence of this has been established through the tracking of increases in optical emission signatures of F and CO, which

correlate well with increasing Si etch rate, as oxygen content in a CF_4 discharge is varied [3]. In SiO_2 etching, oxygen present in the film itself is also believed to make a contribution, in that the oxygen liberated from the etched film plays a role in the reactions described above.

Some of the early literature on the subject also mentions possible roles that oxygen may play in the gas phase through oxidation of fluorocarbon fragments to produce CO or COF_2 [3, 4]. Flamm and coworkers [6, 7, 21] discuss a more elaborate mechanism, whereby high F and F_2 levels suppress the concentrations of unsaturated fluorocarbon species in a CF_4 discharge, both in the gas phase and through third-body recombination on surfaces, *e.g.*:

$$F + CF_2 (+ M) \rightarrow CF_3 \qquad (3.13a)$$

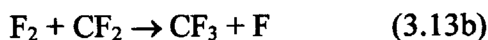

$$F_2 + CF_2 \rightarrow CF_3 + F \qquad (3.13b)$$

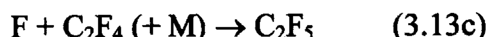

$$F + C_2F_4 (+ M) \rightarrow C_2F_5 \qquad (3.13c)$$

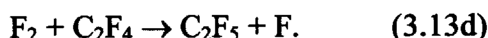

$$F_2 + C_2F_4 \rightarrow C_2F_5 + F. \qquad (3.13d)$$

Oxygen competes with fluorine in this process, through reactions like:

$$O + CF_2 + M \rightarrow COF_2 \qquad (3.14a)$$

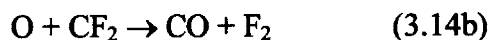

$$O + CF_2 \rightarrow CO + F_2 \qquad (3.14b)$$

$$O_2 + CF_2 + M \rightarrow CO_2 + F_2 \qquad (3.14c)$$

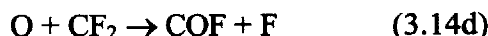

$$O + CF_2 \rightarrow COF + F \qquad (3.14d)$$

where unsaturate levels are suppressed and fluorine atom density is increased. More recent views, however, tend to discount the importance of gas-phase chemistry in favor of a dominant role being played by surface reactions. It is also true that, in the mTorr pressure regime seen in today's HDP etch tools, gas phase reactions play a much weaker role than they would in tools operating in the Torr pressure regime, such as the early etch reactors.

When oxygen is added to the discharge in amounts larger than some optimum value, a reduction in etch rate occurs. Some authors [9, 21] cite oxygen reactions with the film being etched as inhibiting etching under these conditions. This may occur through

competition with fluorine for active sites on the etched layer. While this mechanism may be plausible, simple dilution of the fluorine concentration in the discharge by the presence of large concentrations of another gas is perhaps the more straightforward explanation.

One important caveat regarding the addition of oxygen to fluorocarbon plasmas is that one must remember that oxygen is a very effective etchant for organic materials, namely photoresist. It is typically the case then that addition of oxygen carries the penalty of reducing selectivity to photoresist. Both in older generation etch equipment and in modern tools, one frequently encounters processes that avoid oxygen altogether, largely for this reason.

Finally, it should be pointed out that the effects achieved by adding O_2 to a discharge such as a CF_4 plasma can also be attained by incorporating oxygen into the molecular structure of the fluorocarbon feed gas, *e.g.*, COF_2, CF_3OOCF_3, CF_3OCF_3, etc. [3]. This will also be true in the discussion of the role of hydrogen in fluorocarbon plasmas that is about to follow.

3.3.4 Hydrogen Effects

References [3, 4, 6, 7, 9, 21]. Whereas the presence of oxygen in fluorocarbon plasmas generally tends to enhance fluorine concentrations and improve etch rates, the addition of hydrogen tends to accomplish the opposite. In the gas phase or, as will be discussed in later chapters, at the surface, hydrogen is thought to "scavenge" free fluorine through the reactions [6, 7, 21]:

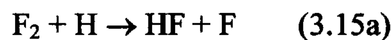

$$F_2 + H \rightarrow HF + F \qquad (3.15a)$$

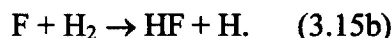

$$F + H_2 \rightarrow HF + H. \qquad (3.15b)$$

Moreover, in addition to reducing fluorine levels directly, hydrogen has also been posited by Flamm to abstract fluorine from fluorocarbon species, producing film-forming precursors, *e.g.*:

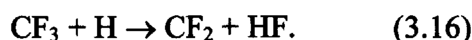

$$CF_3 + H \rightarrow CF_2 + HF. \qquad (3.16)$$

Thus the addition of H_2 to a CF_4 plasma promotes the formation of unsaturates (which are believed to play a role in fluorocarbon deposition) and reduces fluorine concentrations, which in turn may further augment the concentrations of unsaturates if one accepts that fluorine in the gas phase suppresses them.

H_2 addition has been linked to enhanced rates of polymer formation on the etched surfaces by studies in which a silicon surface was subjected to etching in a CF_4/H_2 discharge [4]. It was found that, as H_2 content was increased, etching stopped sooner (at lower H_2 percentages) in the case where the substrate was not subjected to energetic ion bombardment as opposed to the case where it was. This finding suggests the addition of H_2 promotes polymer formation. Where the polymer is removed by bombardment, etching continues to proceed. Without bombardment, at sufficiently high H_2 percentages, the polymer layer is allowed to build up at a rate that outcompetes the etch mechanism and etching ceases. This mechanism is consistent with the "scavenging" and unsaturate promotion effects discussed above.

Why one would wish to intentionally induce greater polymerization in a discharge becomes clear from the observation that the suppression of etching is more pronounced with some materials (Si) than with others (SiO_2, Si_3N_4) [9]. A partial explanation for this phenomenon has been offered for the oxide case by Coburn and coworkers [3, 4], who posit that the polymer layer forms preferentially on Si as opposed to SiO_2. The argument is rooted in two observations: 1). experiments have shown that the carbon-containing layer does indeed accumulate more slowly on Si than on SiO_2 and 2). when SiO_2 is etched in a pure CF_4 discharge, the presence of CO, CO_2, and COF_2 is detected in the effluent. The conclusion is that the difference is caused by the liberation of oxygen from the silicon dioxide, which reacts with carbon in the fluorocarbon layer, a mechanism mentioned earlier in this discussion. By this argument, as conditions are pushed toward increasing polymerization, Si surfaces are subjected to increasing rates of fluoropolymer deposition, while SiO_2 surfaces "offset" the buildup of polymer, staving off the onset of net deposition. Indeed, experiments have shown that, as H_2 content in a CF_4 plasma is

increased, the SiO_2 etch rate drops off, but the Si etch rate does so even more precipitously, leading to a high SiO_2-Si selectivity window [3].

It has been observed that SiO_2-to-Si selectivity can be enhanced through mechanisms other than H_2 addition, namely through the use of other fluorocarbon precursors which are more likely to promote polymerization (C_3F_8, C_2F_4), the addition of other sources of hydrogen (CH_4, C_2H_4), or the addition of other "unsaturated" species (C_2H_4, C_2F_4) [3, 9]. Coburn's argument above is readily extended to these plasmas, as it is not dependent on the presence of hydrogen itself, but merely on the existence of conditions which enhance polymer formation. It should be pointed out that conspicuously absent from the above discussion is an explanation which is applicable to silicon nitride films, which have also been observed to etch faster than Si in polymerizing plasmas.

In any case, the concept which has emerged is the notion of "fluorine deficient" plasmas. Whereas the fluorine "scavenging" explanation involving hydrogen appears adequate for H_2 containing plasmas or gases like CHF_3, a more general model is necessary to explain why certain fluorocarbon chemistries are more apt to polymerize than others. This model, though simplistic and lacking additional physical insight beyond what was already discussed in this section, has gained a great deal of currency. It is the "relative stoichiometry" concept or fluorine/carbon ratio model.

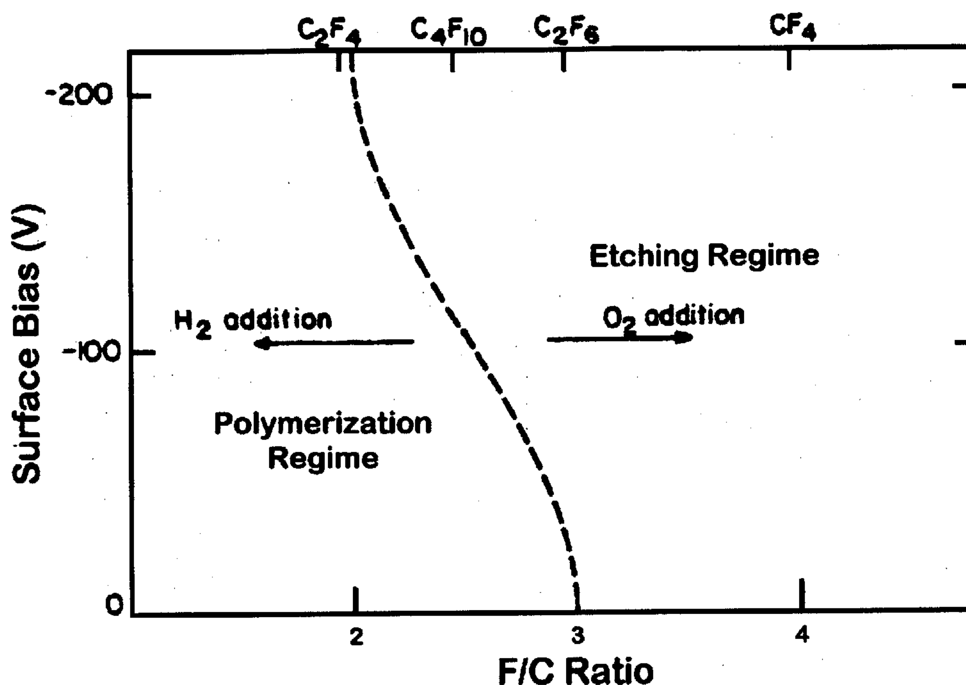

Figure 3.3: Fluorine/carbon ratios for several fluorocarbon gases in a parallel plate system, after [3].

3.3.5 F:C Ratio Model and Polymerization

References [3, 4, 9]. The essential message of the F:C ratio model is conveyed in Figure 3.3. The F:C ratio model ties together the phenomena discussed earlier by stating, quite simply, that lower fluorine concentrations relative to carbon concentrations tend to promote polymerizing behavior. What is the F:C ratio a ratio of? One might suggest that the region in the plasma where this ratio is appropriate to take is the region near the substrate. Calculating the F:C ratio in the fluxes arriving at the wafer surface is, in practice, a difficult exercise. Instead, F:C ratios are frequently calculated for fluorocarbon films deposited on the substrate as well as (trivially) for the feed gas composition itself. In essence, the model states that "fluorine deficient" plasmas tend to contain lower concentrations of etchant species and higher concentrations of polymer-forming precursors. The issue of what constitutes "etch" versus "deposition" precursors has itself been the subject of considerable discussion. Much of the early work in the field was conducted under the, often implicit, assumption that atomic fluorine was the

principal etchant species in the system and that CF_x species were predominantly deposition precursors. Current understanding acknowledges that fact that the dividing line between the two is far from sharp. Much of the focus in mechanistic explanations being discussed today, including many of the ones in this document, is on surface, rather than gas phase processes, with the understanding that much of the bond breakage that occurs in order to liberate the F that eventually reacts with the film being etched occurs on the wafer surface, in the presence of ion bombardment. The force of this statement becomes more apparent when one considers the fact that today's plasma processes typically operate in lower pressure regimes than those of their 1980s predecessors (the pressure regime explored in the high density plasma experiments discussed in Chapters 5 and 6, for instance, was roughly 5-25 mTorr). From this standpoint, CF_x species arriving on the wafer surface can be viewed as both etch and deposition precursors. More up to date theories of fluorocarbon etching in high density systems are considered in Sections 5.3 and 5.4; the present treatment of the F:C ratio model – and, in fact, Section 3.3 in general – is intended to provide a context for this discussion.

Before leaving the subject, one ought to point out that the border line between etching and polymerization regimes is by no means well defined and will differ from system to system. However, the shift of this boundary toward lower F:C ratios with higher ion bombardment (see Figure 3.3) is well-established and provides a consistent representation of the fact that etching may be sustained in the presence of large populations of film precursors if a means for the suppression of film formation (*e.g.*, bombardment of the surface) is present. The concept is particularly useful when discussing oxide/nitride to silicon selectivity, which is believed to be maximized when operating close to the onset of net polymer deposition.

3.4 Process Tools Used

This section will provide brief descriptions of the two plasma etch tools that were employed in the course of the work presented in this document: the Applied Materials Precision 5000 platform equipped with Mark II etch chambers and the Applied Materials

Centura 5300 platform equipped with HDP chambers. The former is an example of the "medium" density etch tools that emerged during the 1980s, while the latter is a more modern inductively coupled high density tool which made its appearance in the mid 1990s. Both platforms are examples of the "cluster" concept, whereby a standardized mainframe is used for wafer transfer operations, with multiple chambers (often of different types) attached to the mainframe.

3.4.1 Applied Materials Precision 5000

The Applied Materials Precision 5000 platform is capable of supporting etch as well as chemical vapor deposition (CVD) chambers. The Precision 5000 cluster is pictured in Figure 3.4. This platform was the first of a family of *cluster* tool platforms made by Applied Materials for CVD, etch, PVD, RTP (rapid thermal processing), silicon epitaxy, and other applications. The Precision 5000 can be configured with up to four etch or deposition chambers. The unit used for the work discussed in this document (housed in MIT's Integrated Circuits Laboratory) is configured with two 100 mm etch chambers. The platform design used in the Precision 5000 is an early variant of a configuration that has become increasingly common in today's tools. The system consists of a mainframe with a loadlock/transfer chamber connected to one or more (up to four in the case of the Precision 5000) independent process chambers.

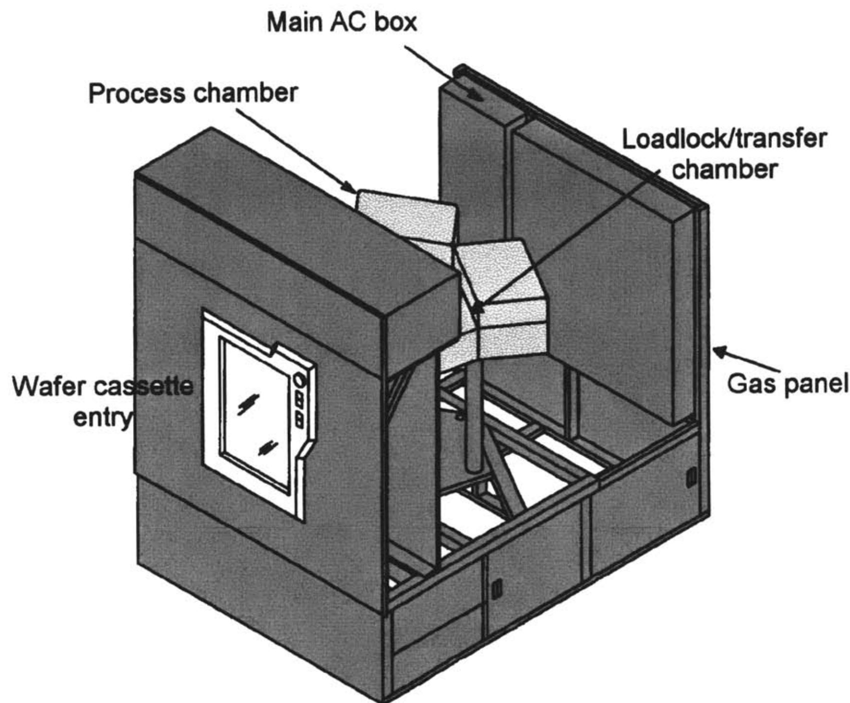

Figure 3.4: The Precision 5000 mainframe, after [22].

More advanced variants of this, reflected in the Applied Materials Centura (etch, CVD, RTP) and Endura (PVD) platforms, separate the functions of the central transfer chamber from those of the loadlocks. Whereas in the Precision 5000, the wafer cassette(s) reside at atmosphere and the entire transfer chamber is vented and pumped down during wafer transfer, in the more modern systems, a separate loadlock chamber is dedicated to each wafer cassette. These are pumped down to vacuum when the wafers are first loaded; consequently, all wafer transfers take place under vacuum, resulting in improvements in both throughput and contamination control. A defining characteristic shared by all cluster tools is the fact that all chambers are of the single wafer type.

The original Precision 5000 etch chamber, along with its later variants (Mark II, MxP, MxP+, eMxP+, and, most recently, the Super *e*), was the chamber design that became synonymous with the term **magnetically enhanced reactive ion etching (MERIE)**.

MERIE was one of the so-called "medium density plasma" solutions developed to address the need for decoupling control over ion flux and ion energy. This design has proven to be quite robust over time and has been enhanced with each succeeding generation, continuing to play a major role among commercial plasma etch tools, alongside emerging high density plasma solutions.

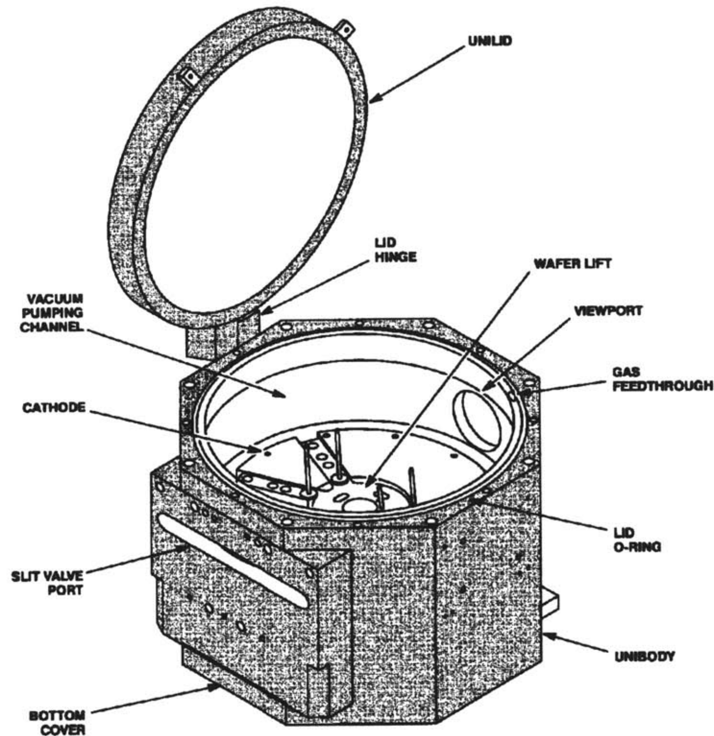

Figure 3.5: An MxP etch chamber – a more modern variant of the Mark II etch chambers, after [22].

In the MERIE configuration, the wafer is placed on the cathode of a capacitively coupled rf diode system. The plasma density is significantly enhanced, however, by the presence of a rotating magnetic field, whose magnetic flux density is nominally controllable from 0 to 100 gauss (in the original Precision 5000 chamber). A typical frequency of rotation is 0.5 Hz. The rotation of the field aids in alleviating azimuthal nonuniformities in the

plasma. Typical process parameters in this chamber may be: pressure ranging from ~30 mTorr to several hundred mTorr (maintained by a throttle valve, with the chamber being exhausted by a turbomolecular pump, backed by a mechanical pump), several tens of sccm gas flow rate (typically CF_4 and/or CHF_3 for dielectric etch, HBr/Cl_2 for polysilicon etch), several hundred watts of rf power, and several tens of gauss of B-field. Other etch gases have also been used with these systems, including NF_3 and SF_6. Even with magnetic enhancement, typical conversion efficiencies for the feed gas in these systems are not very large, with values well under 50% not uncommon. MERIE etchers were first introduced in the mid 1980s starting with the 100 mm wafer generation and have been adapted to each succeeding wafer size since.

3.4.2 Applied Materials Centura 5200/5300 HDP/IPS

The Centura cluster tool has been a mainstay Applied Materials product in the 1990s, with variants in use that support chambers for applications as diverse as PECVD, etch, epitaxial growth, and RTP (rapid thermal processing). In the etch area, the Centura 5200 model presently supports medium density chambers like the MxP and its more recent variants, as well as high density chambers for dielectric etch, like the HDP[1] model and its successor, the IPS, among others. The 5300 model of the cluster normally supports only the HDP and IPS chambers.

[1] The acronym "HDP", in this section, refers to a specific *model* of inductively coupled high density plasma etch chamber manufactured by Applied Materials. In general usage, the term refers to a broad class of systems; inductively coupled etch tools, like the Applied Materials "HDP" etch chamber, are just one subset of high density plasma (HDP) systems.

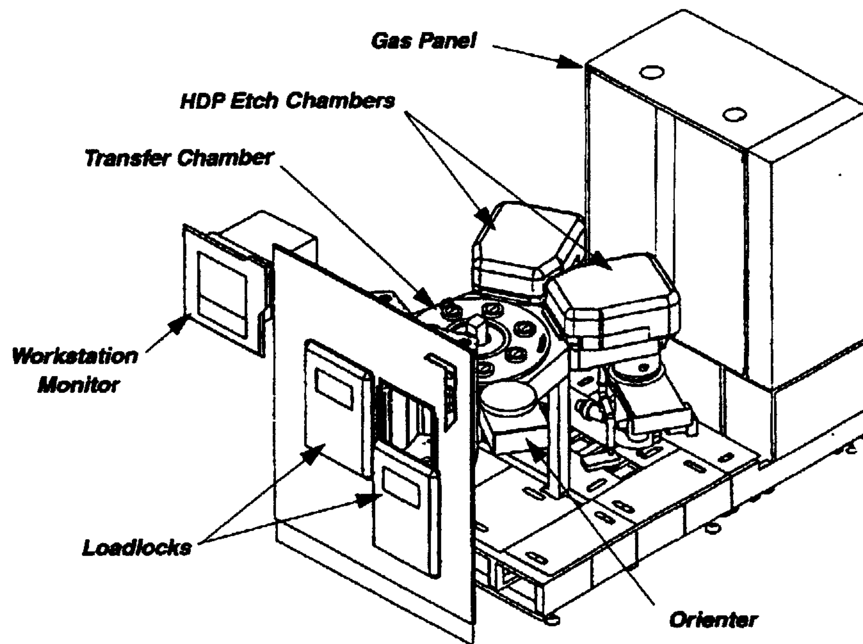

Figure 3.6: The Centura 5300 mainframe, after [22].

The Centura mainframe is equipped with two loadlock chambers, a transfer chamber with a wafer handling robot, and up to two wafer orienters. The HDP and IPS chambers are both examples of the non-resonant ICP (inductively coupled plasma) high density plasma source design. The power coupling modes in the two chambers differ somewhat, however. The earlier HDP uses a multi-turn antenna coil that couples to the discharge through the upper part of the chamber wall, which is made of quartz. The roof of the chamber is a grounded silicon slab that serves as both a ground point and as a sink for atomic fluorine during the process. The IPS chamber is similar in many respects; in fact processes developed on the HDP are, in practice, often transferable to the IPS with relatively minor development work. One major difference, however, is that, in the IPS, the upper part of the chamber and the roof slab are a single component, both made of silicon. The antenna is now split into two independent coils, an inner one and an outer one, which are located above the silicon roof and which couple to the plasma through a semiconducting material (*i.e.*, the silicon), rather than a dielectric window, as is typically

the case in ICP systems. (Put another way, in the IPS chamber, the Si roof serves both as a ground point and as a "dielectric" window for the antenna.)

In both chambers, the roof and the walls are heated using resistive heaters. In the HDP, typical temperatures range from 200 to 300 °C. As is the case in many etch systems, the wafer is kept cool using a combination of a recirculating chiller and helium backside cooling. In the IPS and in later variants of the HDP, the wafer is clamped using an electrostatic chuck (ESC) assembly. (Earlier models of the HDP employed a mechanical chuck instead). At various times, the HDP chamber was available with 125 mm, 150 mm, and 200 mm chuck assemblies. The more recent IPS chamber, as of this writing, is available with a 200 mm chuck assembly. Typical operating pressures range from several mTorr to tens of mTorr. Chamber pressure is maintained using a throttle valve. The chamber is exhausted using a turbomolecular pump, backed by a mechanical pump.

Since the HDP/IPS is intended for dielectric etch, the etch chemistries used are fluorocarbons, with flows in the tens of sccm range being typical. Noble gas dilution, however, is essential for maintaining discharge stability. Whereas in systems such as the Precision 5000, the plasma is lit with the process gas already flowing, in these chambers, the plasma is lit using a noble gas such as argon; only once a stable discharge exists is the etch gas introduced. High density etch tools such as the HDP/IPS exhibit much higher conversion efficiencies than their low/medium density counterparts. Conversion efficiencies of 80% and higher for the fluorocarbon feed gas are typical.

In the HDP chamber, rf source power up to 3000 W may be applied to the antenna coil. An independent rf bias is also applied to the chuck holding the wafer (up to 2000 W in the HDP). Both the HDP and the IPS use relatively low rf frequencies: ~2.0 MHz and ~1.8 MHz for the source and bias inputs, respectively. In the HDP, a matching network is used on both the source and bias power inputs. The IPS, on the other hand, relies principally on frequency tuning by the source and bias generators themselves. Variable frequency generators are becoming increasingly common in modern plasma tools; one

significant advantage of using frequency tuning is that it all but eliminates the need for an independent matching network (thereby removing the power losses associated with it).

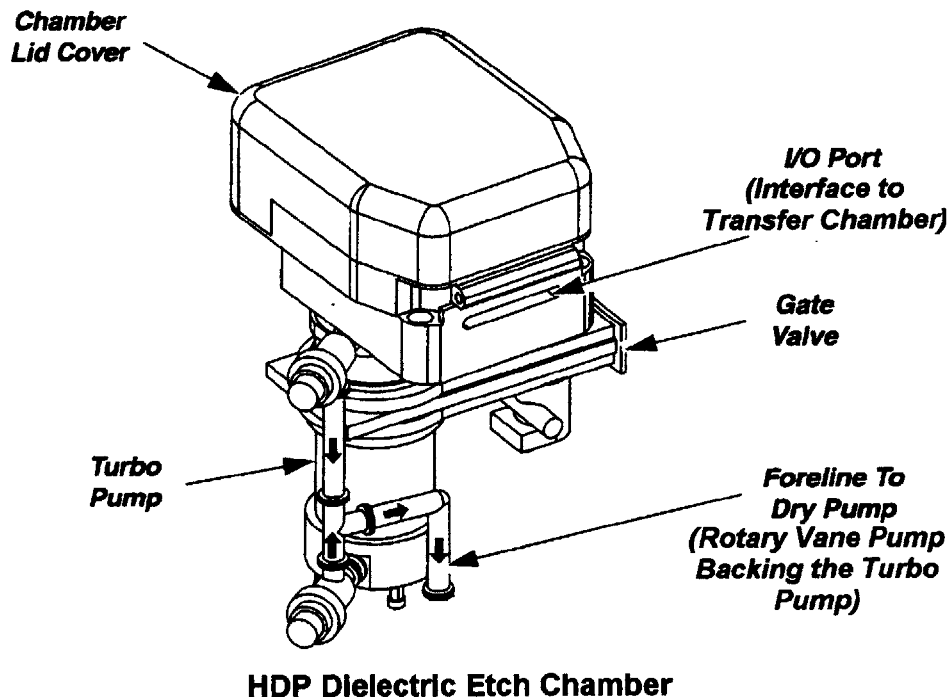

Figure 3.7: An HDP etch chamber; all of the work discussed in Chapters 5 and 6 has been performed in chambers of this type. After [22].

References

1. B. Chapman, *Glow Discharge Processes - Sputtering and Plasma Etching*. New York, NY: John Wiley & Sons, Inc. (1980).
2. M. A. Lieberman and A. J. Lichtenberg, *Principles of Plasma Discharges and Materials Processing*. New York, NY: John Wiley & Sons, Inc. (1994).
3. J. W. Coburn and H. F. Winters, *Plasma etching - A discussion of mechanisms*, J. Vac. Sci. Technol., **16**(2), p. 391-403 (1979).
4. J. W. Coburn, *Plasma-Assisted Etching*, Plasma Chemistry and Plasma Processing, **2**(1), p. 1-41 (1982).
5. D. L. Flamm and V. M. Donnelly, *The Design of Plasma Etchants*, Plasma Chemistry and Plasma Processing, **1**(4), p. 317-363 (1981).
6. D. L. Flamm, V. M. Donnelly, and D. E. Ibbotson, Basic Chemistry And Mechanisms of Plasma Etching, in Semiconductor International, 1983, p. 136-143.

7. D. L. Flamm, V. M. Donnelly, and D. E. Ibbotson, *Basic chemistry and mechanisms of plasma etching*, J. Vac. Sci. Technol. B, **1**(1), p. 23-30 (1983).
8. C. J. Mogab, A. C. Adams, and D. L. Flamm, *Plasma etching of Si and SiO_2 - The effect of oxygen additions to CF_4 plasmas*, J. Appl. Phys., **49**(7), p. 3796-3803 (1978).
9. J. A. Mucha, The Gases of Plasma Etching: Silicon-Based Technology, in Solid State Technology, 1985, p. 123-127.
10. G. Turban, *Basic Phenomena in Reactive Low Pressure Plasmas Used for Deposition and Etching - Current Status*, Pure & Appl. Chem., **56**(2), p. 215-230 (1984).
11. R. Reif, Multilevel Interconnect Process Technologies for Microelectronic Fabrication, 6.74s Class Notes, 1999, Massachusetts Institute of Technology, Cambridge, MA.
12. National Institute of Standards and Technology, http://physics.nist.gov/PhysRefData/IonEnergy/tblNew.html (2000).
13. M. A. Lieberman and A. J. Lichtenberg, *op. cit.* p. 16
14. M. A. Lieberman and A. J. Lichtenberg, *op. cit.* p. 19
15. M. A. Lieberman and A. J. Lichtenberg, *op. cit.* p. 20
16. M. A. Lieberman and A. J. Lichtenberg, *op. cit.* p. 404
17. M. A. Lieberman and A. J. Lichtenberg, *op. cit.* p. 413, 419
18. M. A. Lieberman and A. J. Lichtenberg, *op. cit.* p. 434-435
19. T. Nakano and S. Samukawa, *Radical distributions of ion velocity, temperature, and density in ultrahigh-frequency, inductively coupled, and electron cyclotron resonance plasmas*, J. Vac. Sci. Technol. A, **16**(4), p. 2065-2072 (1998).
20. H.-J. Lee, J. K. Kim, J. H. Kim, K.-W. Whang, J. H. Kim, and J. H. Joo, *Selective SiO_2/Si_3N_4 etching in magnetized inductively coupled C_4F_8 plasma*, J. Vac. Sci. Technol. B, **16**(2), p. 500-506 (1998).
21. D. L. Flamm and J. A. Mucha, *Plasma Etching*, in *Chemistry of the Semiconductor industry*, S. J. Moss and A. Ledwith, Editors, Chapman and Hall, New York, NY, p. 343-390 (1987).
22. Documentation courtesy of Applied Materials, Inc.

4. Screening Stage Studies

Chapter 4 begins the discussion of the experimental work that had been carried out for the author's thesis research. The work described herein was conducted in the Applied Materials Precision 5000 Mark II etch tool housed in MIT's Integrated Circuits Laboratory (ICL). It was carried out after the completion of the screening stage for the hydrofluorocarbon family of chemistries in the same tool (Section 1.2.2.1, [1]). The compounds evaluated belonged to the iodofluorocarbon family. In addition to these, the compound trifluoroacetic anhydride (TFAA) was also evaluated. The tests performed were limited in scope, involving blanket silicon dioxide and silicon nitride films with film etch rate being the only parameter of interest. The work was carried out in two phases. Section 4.1 will discuss the first phase, in which iodotrifluoromethane (CF_3I), iodopentafluoroethane (C_2F_5I),and 2-iodoheptafluoropropane (CF_3-CFI-CF_3) were evaluated in a limited series of experiments. Along with these, TFAA was also examined. A designed experiment scheme was employed for the TFAA tests with the same matrix of experiments also run with C_3F_8, which served the role of the PFC reference gas against which etch performance was benchmarked in the study. As a follow up to the initial iodofluorocarbon experiments, a second phase was also carried out, with the compounds 1-iodoheptafluoropropane and iodotrifluoroethylene being evaluated, again in a limited series of tests involving blanket oxide and nitride wafers. The results of this second phase are discussed in Section 4.2 The properties of the compounds used in these studies have been discussed in Chapter 2. The material in this chapter is based on work published by the author and his coworkers in Refs. [2, 3].

4.1 Initial Iodofluorocarbon Study and Trifluoroacetic Anhydride Study

This section will present the results of etch rate comparisons between TFAA and octafluoropropane, a perfluorinated dielectric etchant. Designed experiment (DOE) methodology, combined with neural network analysis, was used to study a broad parameter space of reactor conditions in the case of TFAA and C_3F_8. The effects of

pressure, magnetic field, and gas flow rates were studied. Additionally, more limited tests were carried out with the three iodofluorocarbon gases. Etch rate data, as well as Auger electron spectroscopy data from substrates exposed to IFC plasmas will be presented. All gases were evaluated using both silicon dioxide as well as silicon nitride substrates. The results obtained indicated that these compounds may be potentially viable in plasma etching applications. Two of the three iodofluorocarbons examined in this phase of the work, would later be employed in the high density plasma etch studies discussed in Chapter 5.

At the time this work was carried out, octafluoropropane (C_3F_8) was beginning to find application as a more efficient alternative to hexafluoroethane as a cleaning gas for dielectric PECVD chambers [4]. At this time, it was believed that the overall environmental impact of octafluoropropane, as compared to hexafluoroethane (C_2F_6) in analogous processes, was expected to be significantly lower (due to a combination of greater process efficiency as well as somewhat lower global warming potential and atmospheric lifetime). This did, in fact, prove to be true in a number of PECVD chamber clean processes. Later work, discussed in subsequent chapters of this document, however, showed that C_3F_8 and C_2F_6 processes had comparable global warming impact in the high density plasma etch tool in which they were run. Nevertheless, during the earlier hydrofluorocarbon screening stage study, C_3F_8 was chosen as the PFC reference compound because it was known to be a fast and efficient etchant of dielectric films.

TFAA, on the other hand, was, at the time, a recently proposed alternative to hexafluoroethane for dielectric PECVD chamber clean. Because it is known to hydrolyze readily, its atmospheric persistence is negligible [5]. Prior to this study, which, to the author's knowledge, represented the first use of TFAA in a dielectric etch application, other studies using TFAA had been carried out for dielectric chamber clean applications [5].

Iodofluorocarbon species were seen as attractive potential alternatives to PFCs from an environmental standpoint because they too are known to be very short-lived in the

atmosphere, largely due to the weakness of their C-I bond, which causes them to be readily photolyzed in the atmosphere. See Chapter 2. Of the three IFCs investigated in the present study, CF_3I was the only one which had seen use in etch application before, having been investigated for Si trench etch in combination with SF_6 in an experimental application [6]. To the author's knowledge, C_2F_5I and CF_3-CFI-CF_3 had not been previously tested in etch processes.

4.1.1 Experimental Setup

The etch performance of TFAA, as well as three iodofluorocarbon gases was evaluated using unpatterned blanket films of thermal SiO_2 and LPCVD (low pressure chemical vapor deposited) Si_3N_4, both grown on 100 mm p-type (6-12 Ω-cm resistivity) (100) silicon substrates. The oxide films were at least 6900 Å thick, whereas the nitride films were at least 5000 Å thick. The process tool used was an Applied Materials Precision 5000 magnetically enhanced reactive ion etch tool. All gases used were 99+% pure, with the exception of C_2F_5I, which was assayed at 98+%. TFAA was provided by Schumacher, Carlsbad, CA; C_3F_8 was provided by 3M Specialty Chemicals, St. Paul, MN; CF_3I and C_2F_5I were supplied by Oakwood Products, Inc., West Columbia, SC; 2-iodoheptafluoropropane was supplied by PCR, Inc., Gainesville, FL.

4.1.1.1 Octafluoropropane and TFAA Experiments

TFAA was evaluated using a 39-experiment, four variable central composite design (CCD) matrix which was used in conjunction with NNAPER, neural network-based data analysis software developed by E. I. du Pont Nemours and Company. The parameter space of the matrix was defined by: 35-150 mTorr chamber pressure, 0-100 Gauss magnetic field, 10-40 sccm etch gas flow, and 0-40 sccm oxygen flow. Rf power (13.56 MHz) was fixed at 600 W. The experimental matrix was run twice, once for SiO_2 substrates, once for Si_3N_4 substrates. In order to permit a direct comparison of TFAA with a perfluorinated compound in use as a dielectric etchant, octafluoropropane was used as a reference gas. The same matrix was used with octafluoropropane, again twice - with both oxide and nitride substrates. Optical emission interferometry (OEI), a technique which uses a charge coupled device camera overlooking the wafer in the etch

chamber to measure film etch rates *in-situ*, was employed to measure the oxide or nitride etch rates on each run. The technique is described in detail elsewhere [7]. All etch rate models generated by NNAPER were based on average etch rates calculated from OEI data.

4.1.1.2 Iodofluorocarbon Experiments

Preliminary tests were also carried out with the three iodofluorocarbon gases on silicon dioxide and silicon nitride substrates. For each gas, two oxide substrates, two nitride substrates, and one bare Si wafer were etched. The following sequence of experimental runs was used: 1). 15 min. oxygen plasma chamber clean*, 2). 180 s oxide substrate etch, 3). 180 s nitride substrate etch, 4). 300 s bare Si substrate etch, 5). 180 s nitride substrate etch, and 6). 180 s oxide substrate etch. The etch recipe used for all runs was: 50 Gauss magnetic field, 93 mTorr pressure, 600 W rf power, 0 sccm oxygen flow, and 25 sccm IFC etch gas flow. Thus, for each gas, the chamber was subjected to an IFC plasma for a total of 17 min. After each experimental sequence, the chamber was opened and examined for residue. It was then subjected to a wet methanol clean, followed by a plasma clean†, and again opened and examined for residue. During each run, etch rate was again measured *in-situ* using optical emission interferometry (OEI). In the case of those data points where no OEI etch rate data were available, etch rates were determined by Nanospec® measurement. Finally, each of the three bare Si wafers used during these experimental sequences was analyzed using Auger electron spectroscopy (AES). A Physical Electronics Model 660 scanning Auger spectrometer was used. All samples were analyzed in an area mode (100 × 100 μm) at 10 nA of electron beam current, using an electron beam voltage of 10 kV. All AES measurements were taken near the primary flat location of the wafer.

---

* Oxygen clean: t=15 min. at 0 Gauss, 200 mTorr, 750 W, 60 sccm O_2, 5 sccm CF_4.

† Clean sequence consisted of: 15 min H_2 plasma (50 Gauss, 93 mTorr, 600 W, 20 sccm H_2) followed by a 15 min O_2 clean (0 Gauss, 200 mTorr, 750 W, 60 sccm O_2, 5 sccm CF_4).

4.1.2 Results and Discussion

The experiments carried out as part of this study were cursory in nature in comparison to the studies discussed in Chapters 5 and 6. At the time, however, they were valuable in aiding the author in selecting compounds to be employed in some of those studies. What was established in this phase of the screening studies was that compounds that were considerably different than established etchants could potentially be employed in dielectric etching.

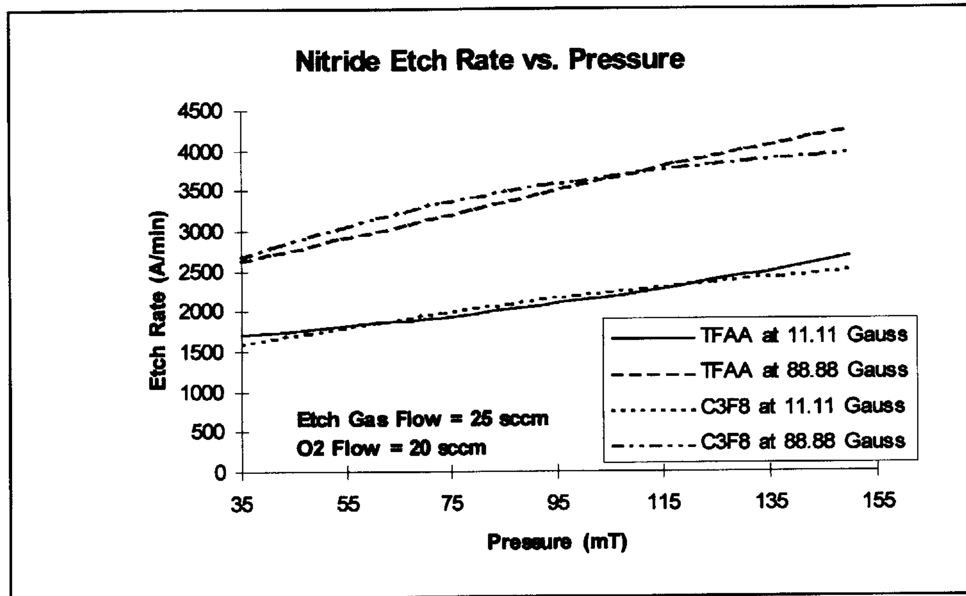

Figure 4.1: Modeled nitride etch rates of TFAA and C_3F_8 versus pressure at low and high magnetic fields.

4.1.2.1 Octafluoropropane and TFAA Experiments

Generally speaking, TFAA was found to exhibit trends which were very similar to those seen in octafluoropropane with both oxide and nitride substrates. In the case of silicon nitride, not only the trends, but also the etch rates of the two gases were remarkably similar in nearly all regions of the parameter space explored. Figure 4.1 shows a typical cross-section of the four-dimensional model generated by the NNAPER software. Other cross-sections convey the same pattern: the modeled etch rates of the two gases are nearly the same at virtually all process conditions. One significant exception to this pattern

occurs at low etch gas flows and high oxygen flows, where TFAA nitride etch rates are significantly lower than C_3F_8 nitride etch rates (see Figure 2). For instance, at the 93 mTorr, 50 Gauss, 10 sccm etch gas flow, and 40 sccm O_2 flow condition, the modeled C_3F_8 etch rate is 2760 Å/min, while the TFAA etch rate is only 1360 Å/min.

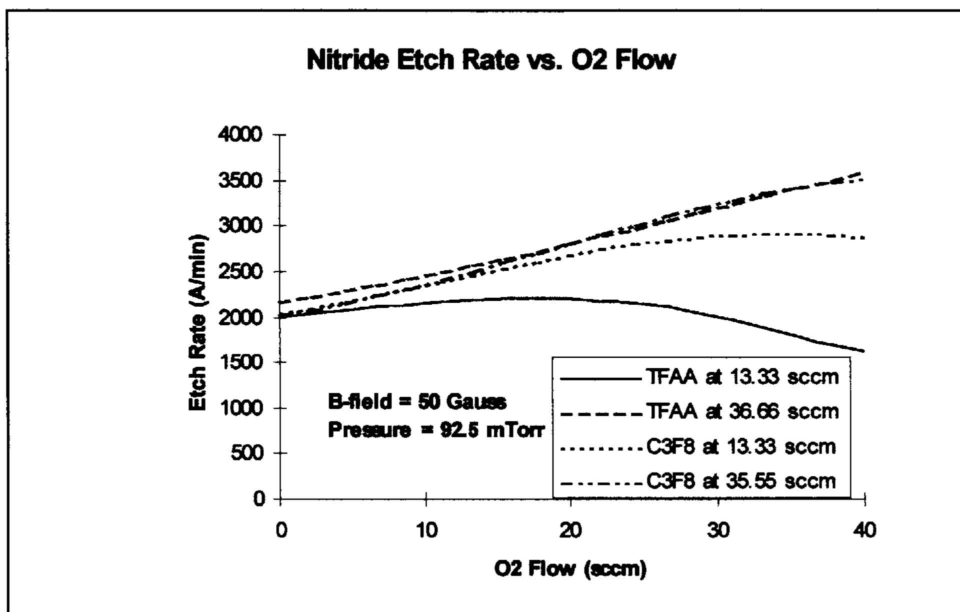

Figure 4.2: Modeled nitride etch rates of TFAA and C_3F_8 versus O_2 flow at low and high etch gas flow rates.

In general, nitride etch rate in both gases increases monotonically with increasing pressure and increasing magnetic field under all conditions. Increasing oxygen flow has the effect of improving TFAA nitride etch rate at all conditions, except at low etch gas flows (see Figure 4.2), where the addition of oxygen beyond a certain point causes a decrease in etch rate. This fold-over point occurs at approximately 15 sccm at 10 sccm TFAA flow (at 93 mTorr, 50 Gauss) and appears to move to higher values of oxygen flow as TFAA flow increases. Increasing oxygen flow in a C_3F_8 plasma also generally tends to increase nitride etch rate, except in low pressure regimes, where the etch rate appears to be relatively insensitive, and again in low C_3F_8 flow regimes (Figure 4.2), where the etch rate increases with oxygen addition at low oxygen flows, but decreases at higher oxygen flows. At 10 sccm C_3F_8 flow (at 93 mTorr, 50 Gauss), the model predicts

the fold-over point to occur around 35 sccm of oxygen flow. Increasing etch gas flow rate also has a generally positive effect on nitride etch rate in both gases. However, at high pressures as well as at high magnetic fields, the etch rate in C_3F_8 becomes insensitive to etch gas flow. At low oxygen flows, the nitride etch rate in both gases also appears to be insensitive to etch gas flow rate.

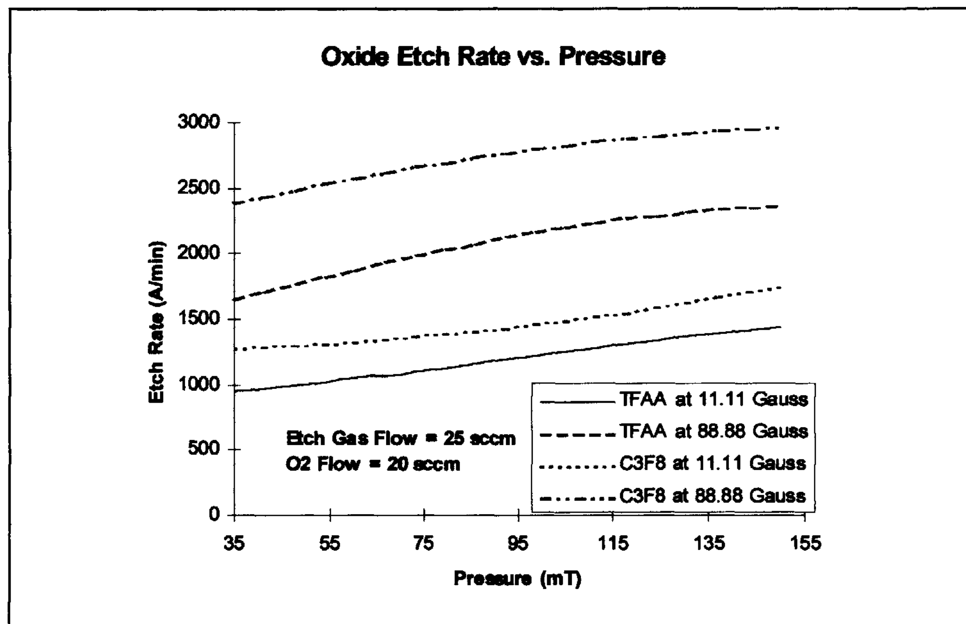

Figure 4.3: Modeled oxide etch rates of TFAA and C_3F_8 versus pressure at low and high magnetic fields.

In the silicon dioxide case, the two gases still exhibited very similar trends, but throughout the parameter space studied, oxide etch rates in TFAA were lower than those in C_3F_8, typically by a few hundred Å/min. Figures 4.3 and 4.4 show typical cross-sections of the modeled responses for both gases. As in the nitride case, increasing pressure, as well as magnetic field has a positive effect on etch rate for both gases in this parameter space. Increasing etch gas flow also increases oxide etch rate in both gases. The dependence on oxygen flow, however, is quite different than that in the nitride case. With C_3F_8 as the etch gas, the addition of oxygen appears to have no beneficial effect on oxide etching: oxide etch rate has a negative dependence on oxygen flow rate throughout the parameter space explored. With TFAA, this is still the general trend, although this

dependence tends to be less pronounced than with C_3F_8; moreover, there exist regimes (at high pressures, and also at high TFAA flows) where the TFAA oxide etch rate appears to become insensitive to oxygen flow (see Figure 4.4).

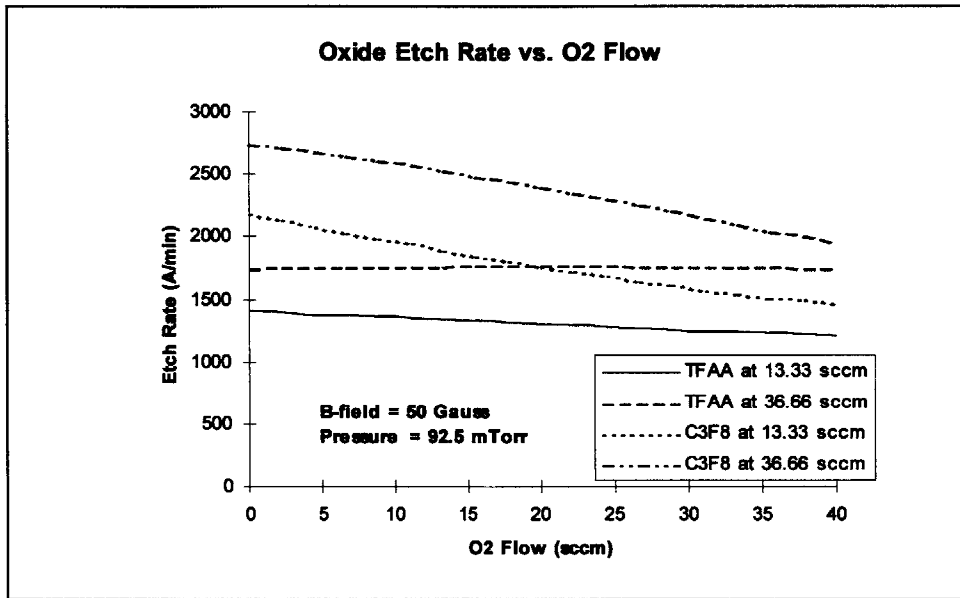

Figure 4.4: Modeled oxide etch rates of TFAA and C_3F_8 versus O_2 flow at low and high etch gas flow rates.

4.1.2.2 Iodofluorocarbon Experiments

Oxide and nitride etch behavior in iodofluorocarbon plasmas differed significantly as a function of the identity of the etch gas. All three IFCs were found to etch oxide readily under the process parameters used in these tests. As Figure 4.5 shows, the oxide etch rate was found to increase as one moved from iodotrifluoromethane to pentafluoroethane to 2-iodoheptafluoropropane. For iodotrifluoromethane, average etch rate was found to be 1162 Å/min on the first wafer in the experimental sequence and 1216 Å/min on the second wafer in the experimental sequence. In the case of iodopentafluoroethane, the etch rates were 1690 Å/min and 1710 Å/min, respectively; in the case of 2-iodoheptafluoropropane the rates were 1772 Å/min and 1806 Å/min, respectively. A chamber "seasoning" effect seemed to be present. That is, the second oxide wafer in

each sequence consistently exhibited higher etch rates than the first. For comparison, Figure 4.5 also shows TFAA and C_3F_8 oxide etch rates at the same process conditions.

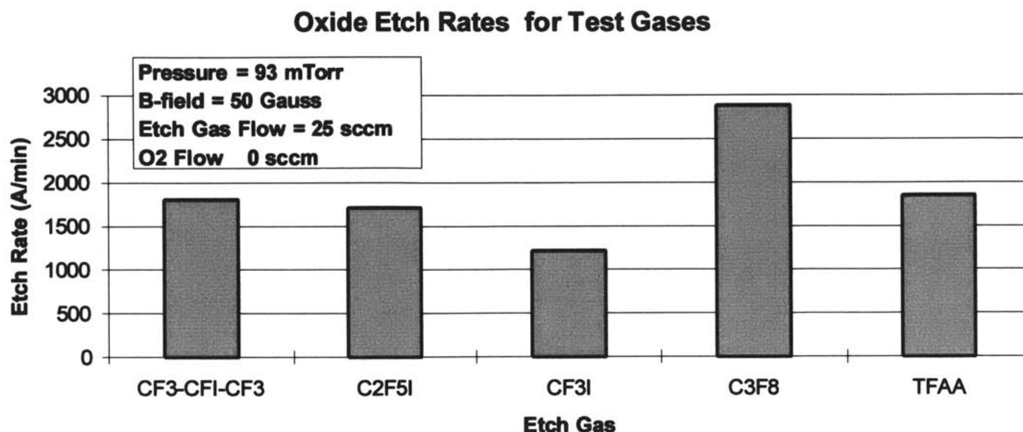

Figure 4.5: Oxide etch rates for all gases at 93 mTorr, 50 Gauss, 25 sccm etch gas flow, and 0 sccm etch gas flow. All IFC etch rates shown are wafer averages taken from the second oxide wafer etched with each of those gases.

The nitride substrates, on the other hand, were found to exhibit entirely opposite trends as a function of etch gas identity. In the CF_3I case, the nitride films etched faster than oxide films - average etch rates of 1876 Å/min on the first wafer and 1868 Å/min on the second wafer were seen. As one moved toward longer-chain compounds, however, the nitride etch rate decreased. In the case of iodopentafluoroethane, the etch process exhibited a high degree of radial nonuniformity: etch rates measured at locations near the primary flat were 1315 Å/min on the first wafer and 1454 Å/min on the second wafer, while rates measured in the center of the wafer were only 263 Å/min and 412 Å/min, respectively. OEI data indicate that, at locations near the edge of the wafer, etching proceeded at a roughly constant rate throughout the 180 s during which the substrate was exposed to the C_2F_5I plasma. However, in the center of the wafer, all of the etching appeared to occur in an initial 30-60 s period; after this phase, etching appeared to be suppressed, presumably by a competing process of film formation. No average etch rates for these wafers were calculated because no OEI data were available for the slow etch rate region in the center of the wafers. Finally, when nitride substrates were exposed to a 2-

iodoheptafluoropropane plasma, virtually no etching was found to occur. The nitride films were found to etch at a noticeable rate only in a narrow (~2 mm) ring at the very edge of the wafer. The etch rates measured at locations near the primary flat were 31 Å/min and 63 Å/min (first and second wafer, respectively); in the center locations of the two wafers, net deposition of film was detected. Figure 4.6 compares the nitride etch performance of the three IFCs with C_3F_8 and TFAA.

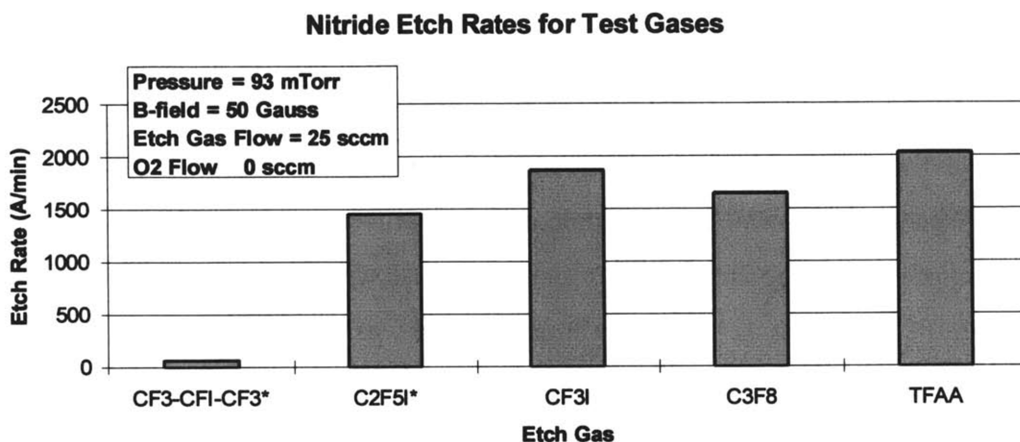

Figure 4.6: Nitride etch rates for all gases at 93 mTorr, 50 Gauss, 25 sccm etch gas flow, and 0 sccm etch gas flow. The CF_3I etch rate shown is a wafer average taken from the second nitride wafer etched in CF_3I; the C_2F_5I and CF_3-CFI-CF_3 rates were taken at the primary flat location on the second nitride wafers etched with each of those gases.

The trends in oxide and nitride etch rate as a function of chain length are consistent with known mechanisms regarding differences in polymerizing behavior for different substrates exposed to fluorocarbon plasmas (see Section 3.3). Oxide:nitride selectivity mechanisms are generally discussed in terms of the role oxygen in the oxide film plays in removing deposited carbon from the surface as CO and, to a lesser extent, CO_2 and COF_2. Whereas CN formation in fluorocarbon etching of nitride films is also a well known phenomenon, the removal of the carbon as CO_x is regarded as a more efficient mechanism. Thus, under polymerizing conditions, one often observes continuing etching of oxide accompanied by no etching – or significantly retarded etching – of nitride. Increasing the length of the carbon chain increases the supply of both fluorine and

carbon, on a molar basis, for the same gas flow rate. However, since the F:C ratio of the molecule changes from 3:1 in the case of CF_3I to 2.5:1 for C_2F_5I to 2.33:1 for 2-iodoheptafluoropropane, one expects a shift toward more polymerizing conditions with increasing chain length. On nitride surfaces, this results in a transition into the net deposition regime. On oxide surfaces, the carbon appears to be removed efficiently enough by interaction with oxygen in the film so that the net effect observed is that of increased availability of fluorine through higher F and/or CF_x fluxes to the surface and hence higher etch rate.

The three gases were also found to exhibit very different behavior in terms of residue deposition in the chamber. After the sequence of experiments for each gas (a total of 17 min. of IFC plasma rf on time) was completed, the chamber was opened and examined. The amount of residue deposition was found to increase with the length of the carbon chain in the IFC molecule. 2-iodoheptafluoropropane was found to produce significant amounts of residue in the chamber; pentafluoroethane was also observed to generate some residue, though noticeably less than the three-carbon compound; no visible deposits, on the other hand, were found in the chamber after the iodotrifluoromethane runs. The runs in which bare Si wafers were exposed to an IFC plasma for 300 s confirmed these trends. A thick deposit visible to the naked eye was found on the wafer exposed to 2-iodoheptafluoropropane; a thin film was found on that exposed to iodopentafluoroethane; however, almost no film was found on the wafer exposed to iodotrifluoromethane. Not surprisingly, AES data taken from the surface layers of all three of these bare Si substrates indicated the presence of carbon and fluorine, suggesting that IFC chemistries deposit a fluoropolymer layer similar to those deposited by more standard fluorocarbon chemistries. As a reference, a thermal SiO_2 wafer that had been exposed to a CF_4 plasma was also examined using AES. A fluorocarbon layer containing carbon and fluorine in an approximate ratio of 5.2:1 was found on the surface of this wafer. By comparison, the approximate C:F ratios of the films found on the substrates exposed to IFC plasmas were: 10.1:1 for CF_3I, 6.0:1 for C_2F_5I, and 4.2:1 for CF_3-CFI-CF_3. Whereas these numbers are to be taken only as estimates based on instrumental sensitivity factors, one can make the observation that shorter-chain IFCs had a tendency

to deposit more carbon-rich films at the process conditions which were used. The H_2/O_2 plasma clean employed after each sequence was found to be effective in removing residue from the chamber.

In addition to the presence of carbon and fluorine in the deposited films, some iodine was also detected in the films from C_2F_5I and CF_3-CFI-CF_3 runs. Figure 7 shows AES data indicating the presence of the dominant MNN iodine peak in the film from the wafer exposed to the C_2F_5I plasma. AES spectra for the film from the CF_3-CFI-CF_3 run are similar.

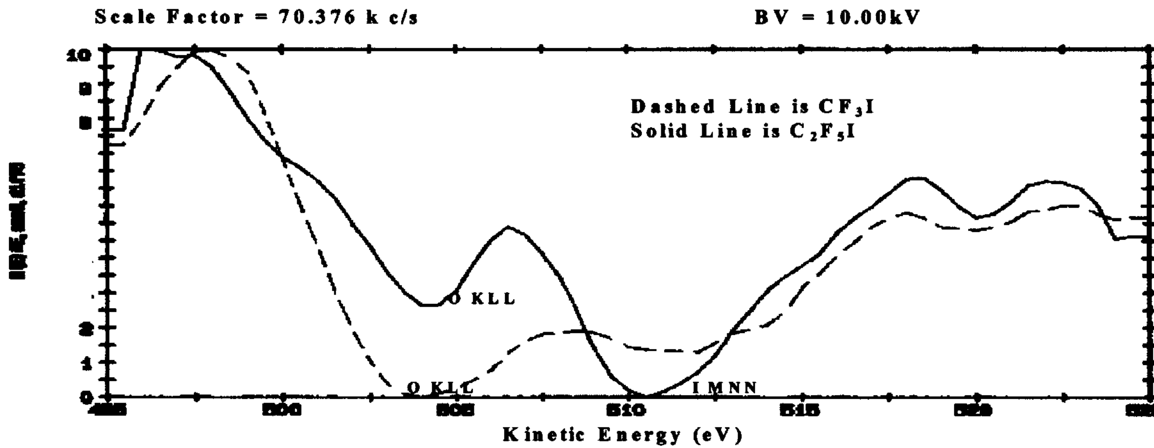

Figure 4.7: Smoothed and differentiated Auger signal: bare silicon wafers exposed to C_2F_5I and CF_3I plasmas.

Quantification of the amount of iodine present in the films was difficult because the dominant iodine peak (a double peak at energies of approximately 511 and 520 eV) partially overlaps with the dominant KLL oxygen peak centered around approximately 505 eV.‡ (The origin of the oxygen peak is believed to be a thin native oxide layer present on the wafers.) An estimate was made, however, which placed the iodine content in the fluoropolymer films deposited by C_2F_5I and CF_3-CFI-CF_3 at approximately 5-7 at. %. In contrast to these results, the presence of iodine in the film left by the CF_3I plasma could not be confirmed by AES. However, the possibility that iodine was in fact present

on this wafer as well cannot be excluded entirely because of the possibility that its peak was masked by the nearby oxygen signature. On the other hand, since the net amount of film deposition by CF_3I at the conditions tested was very low (the film thickness was below the detection limits of a Nanospec® instrument), if iodine was present in the film, its quantities would have been very small. A comparison of the CF_3I AES spectrum (Figure 4.7) with data taken from the wafer exposed to CF_4 only and no iodine-containing species (see Figure 4.8) indicates that the level of iodine in the film deposited by CF_3I was below the detection limit of the instrument.

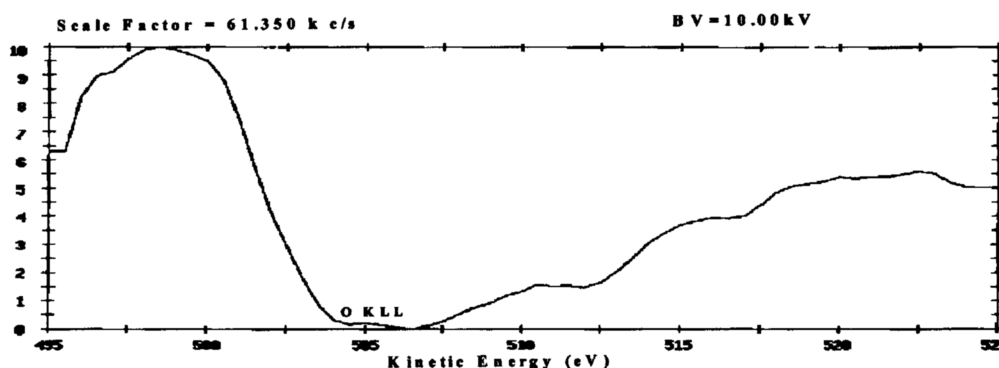

Figure 4.8: Smoothed and differentiated Auger signal: oxide wafer exposed to CF_4 plasma.

4.1.3 Conclusions

Four non-perfluorinated etchants - TFAA, CF_3I, C_2F_5I, and CF_3-CFI-CF_3 - were evaluated in an Applied Materials Precision 5000 etch tool using thermal silicon dioxide and LPCVD nitride substrates. Designed experiment (DOE) methods were used to evaluate TFAA and baseline it against C_3F_8. TFAA was found to exhibit generally the same trends as the octafluoropropane within the parameter space tested. Whereas its etch

---

[‡] In subsequent studies (Section 5.4.2), surface analysis of films deposited by iodofluorocarbon plasmas would be carried out using x-ray photoelectron spectroscopy (XPS), avoiding this limitation.

rates on silicon dioxide substrates were noticeably lower than those of octafluoropropane under all conditions, TFAA silicon nitride etch rates were remarkably similar to those of octafluoropropane in nearly all regions of the parameter space explored. More limited tests were carried out with three iodofluorocarbon chemistries - CF_3I, C_2F_5I, and CF_3-CFI-CF_3. CF_3I was found to etch both silicon dioxide and silicon nitride quite readily at the conditions tested. Moreover, it appeared to leave no chamber or wafer residues beyond the thin carbon/fluorine films that are normally expected with the use fluorocarbon chemistries like CF_4. As one moved toward longer chain IFCs, the oxide etch rate improved at the conditions tested, whereas the nitride etch rate decreased significantly. Under the conditions tested, some (highly non-uniform) etching of nitride was found to occur with C_2F_5I, whereas CF_3-CFI-CF_3 was found to be almost completely selective to nitride (while it etched oxide at a reasonably rapid rate). More chamber and wafer residue was also observed as one moved from CF_3I to C_2F_5I and still more was seen with CF_3-CFI-CF_3. The films deposited by these latter two gases contained mostly carbon and fluorine, with small amounts of iodine. All films deposited by IFCs were readily removed by a simple plasma clean. These preliminary tests suggested that, at least under conditions similar to the ones used in this work, short chain IFCs may be less likely to leave polymer deposits on chamber and wafer surfaces, whereas longer chain IFCs may be potentially useful in etch applications where high oxide:nitride selectivity is desired.

4.2 Follow-up Study with Additional Iodofluorocarbon Species

After the initial study with iodotrifluoromethane, iodopentafluoroethane, and 2-iodoheptafluoropropane was completed, two other novel etch chemistries belonging to the iodofluorocarbon family, iodotrifluoroethylene (C_2F_3I), and 1-iodoheptafluoropropane (CF_2I-CF_2-CF_3), were examined in similar screening experiments. Etch rate data, as well as Auger electron spectroscopy data from substrates exposed to the two IFC chemistries is presented below. Both gases were again evaluated using both silicon dioxide as well as silicon nitride substrates. Under the conditions tested, the two iodofluorocarbons discussed in this section had both been found to etch

silicon dioxide films readily. 1-iodoheptafluoropropane had also been found to be capable of etching silicon nitride films under the same conditions. The same Applied Materials Precision 5000 etch tool that had been used for the work discussed in Section 4.1 was employed here.

4.2.1 Experimental Setup

As was the case for the earlier IFC experiments and the C_3F_8 baseline experiments, all films were grown on 100 mm p-type (100) silicon substrates (6-12 Ω-cm resistivity). The oxide films were at least 6900 Å thick, whereas the nitride films were at least 5000 Å thick. The iodotrifluoroethylene was assayed at 98.8% pure, while the 1-iodoheptafluoropropane was assayed at 99%. Both gases were supplied by PCR, Inc., Gainesville, FL.

In the case of 1-iodoheptafluoropropane, the following experimental sequence, involving two silicon dioxide substrates, two silicon nitride substrates, and one bare silicon wafer, was used: 1). 15 min. oxygen plasma chamber clean (t=15 min. at 0 Gauss, 200 mTorr, 750 W, 60 sccm O_2, 5 sccm CF_4.), 2). 180 s oxide substrate etch, 3). 180 s nitride substrate etch, 4). 300 s bare Si substrate etch, 5). 180 s nitride substrate etch, and 6). 180 s oxide substrate etch. The etch recipe used for all runs was the following: 50 Gauss magnetic field, 93 mTorr pressure, 600 W rf power, and 25 sccm IFC etch gas flow. These conditions were the same as those under which the earlier experiments involving CF_3I, C_2F_5I, and 2-iodoheptafluoropropane were carried out. In the case of iodotrifluoroethylene, the same sequence but with only one substrate of each kind was used.

As in the earlier experiments, optical emission interferometry (OEI) was employed for *in-situ* etch rate measurement. When no OEI etch rate data were available, etch rates were determined by Nanospec® measurement. The results of these experiments are summarized in the figures below, along with earlier IFC and C_3F_8 data. All data shown below were taken from the second oxide/nitride wafer in the sequence, with the exception

of iodotrifluoroethylene data, where only one substrate of each type was used. OEI etch rates are wafer averages. Nanospec® etch rate data was taken at the primary flat location of the wafer.

Additionally, Auger electron spectroscopy (AES) was used to analyze the composition of the residues deposited on the surfaces of the bare Si wafers used in the experiments. The same procedure had been followed earlier for the bare Si wafers used in the CF_3I, C_2F_5I, and 2-iodoheptafluoropropane experiments. The instrument used was a Physical Electronics Model 660 scanning Auger spectrometer. All samples were analyzed in an area mode (100×100 μm) at 10 nA of electron beam current and an electron beam voltage of 10 kV; the measurements were all taken near the primary flat location of the wafer.

4.2.2 Results and Discussion

It was found that both 1-iodoheptafluoropropane and iodotrifluoroethylene are capable of etching silicon dioxide films, though, at this particular experimental condition, at rates slower than that of the perfluorinated reference gas, octafluoropropane. The oxide etch rates on the first wafer etched with 1-iodoheptafluoropropane, as measured by OEI, were 1837.76 and 1881.46 Å/min at the primary flat and center locations, respectively; on the second wafer, the corresponding rates were 1937.35 and 2005.05 Å/min. The respective average etch rates for the two wafers were 1870.6 Å/min. and 1996.9 Å/min. This increase in etch rate from the first wafer to the second (a "seasoning" effect) was also reported for the three IFC compounds tested earlier under the same conditions. The oxide etch rate of C_2F_3I, as measured by Nanospec®, was 1380 Å/min at the primary flat location and 1383 Å/min at the center location. A comparison of the present data with the results of the earlier experiments (see Figure 4.9), shows that the fastest IFC oxide etch rate under the conditions used was that of 1-iodoheptafluoropropane, which etched somewhat faster than its isomer, 2-iodoheptafluoropropane.

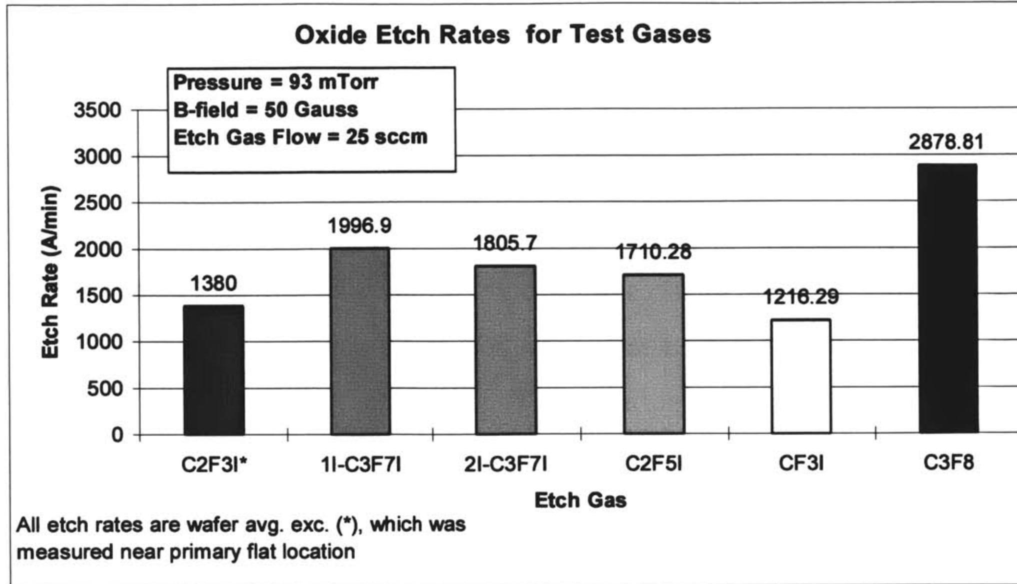

Figure 4.9: Oxide etch rates for C_3F_8 and all IFC gases at 93 mTorr, 50 Gauss, and 25 sccm etch gas flow. All IFC etch rates shown were taken from the second oxide wafer etched with each of those gases, except for C_2F_3I, where only a single oxide wafer was etched. (CF_3I, C_2F_5I, CF_3-CFI-CF_3 and C_3F_8 data is taken from Section 4.1).

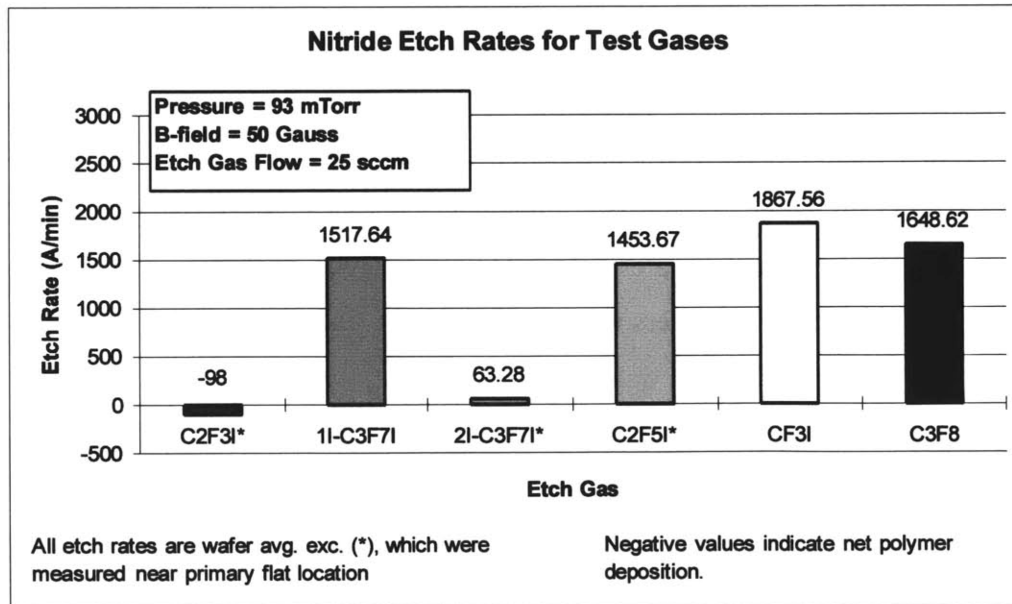

Figure 4.10: Nitride etch rates for C_3F_8 and all IFC gases at 93 mTorr, 50 Gauss, and 25 sccm etch gas flow. All IFC etch rates shown were taken from the second nitride wafer etched with each of those gases, except for C_2F_3I, where only a single nitride wafer was etched. (CF_3I, C_2F_5I, CF_3-CFI-CF_3, and C_3F_8 data is taken from Section 4.1).

The behaviors of 1-iodoheptafluoropropane and iodotrifluoroethylene differed markedly, however, when these gases were used with silicon nitride wafers. Iodotrifluoroethylene was found to deposit a polymeric film on the surface of the nitride wafer. No net etching was observed at any location on the wafer. Estimated deposition rates (as measured by Nanospec®, using the refractive index of thermal oxide as a rough estimate for the refractive index of the film) were 98 Å/min and 409 Å/min at the primary flat and center locations, respectively. 1-iodoheptafluoropropane, on the other hand, removed nitride at 1852.89 Å/min at the primary flat location and 1417.91 Å/min at the center location on the first wafer, and 1668.12 Å/min at the primary flat location and 1282.6 Å/min at the center location on the second wafer. The average etch rates were 1658.55 and 1517.64 Å/min for the two wafers, respectively. (Thus, in contrast to the oxide case, a decrease, rather than an increase, in etch rate was observed from the first to the second wafer.) All 1-iodoheptafluoropropane nitride etch rates reported were measured by OEI.

Hence, while C_2F_3I appeared to be quite selective to silicon nitride at the conditions used, 1-iodoheptafluoropropane etched nitride quite readily (at a rate comparable to that of the C_3F_8 reference – see Figure 4.10). It is interesting to point out that the nitride etch behavior of 1-iodoheptafluoropropane was entirely different from that of 2-iodoheptafluoropropane, which was highly selective to nitride. This somewhat unexpected result suggests that the 2-iodo isomer has a greater tendency to fragment into deposition precursors than its cousin under the conditions used. However, a more detailed explanation of the mechanism responsible for the striking difference in the behaviors of the two species will require further investigation.

When a bare Si wafer was exposed to the 1-iodoheptafluoropropane plasma for 300 s, very little deposition was seen on the surface of the wafer. The thickness of this light deposit was estimated to be ~100 Å by Nanospec® measurement. The iodotrifluoroethylene bare Si wafer, on the other hand, was found to be coated with a deposit estimated to be on the order of 3800 Å thick from OEI data, where the refractive index of thermal oxide was again used as an estimate of the index of the polymeric film. In the earlier IFC experiments with bare Si substrates, almost no deposit was found on the

wafer exposed to CF_3I, a light deposit was found on the C_2F_5I wafer, and a heavy deposit (though not one as thick as the one produced in the C_2F_3I plasma) was found on the 2-iodoheptafluoropropane wafer. The present results are consistent with the trend reported earlier that greater amounts of polymer deposited on the bare Si wafer correlate well with a decrease in silicon nitride etch rate in the IFC etch processes studied.

Table 4.1: Relative carbon, fluorine, and iodine content of films deposited by IFC plasmas on bare Si substrate. All data taken at the primary flat location of the wafer.

Compound	Carbon at. %	Fluorine at. %	Iodine at. %	C:F Ratio
CF_3I	90.98	9.02	negligible	10.1:1
C_2F_5I	79.47	13.34	7.20	6.0:1
CF_3-CFI-CF_3	76.62	18.39	4.99	4.2:1
CF_2I-CF_2-CF_3	81.18	14.40	4.42	5.6:1
C_2F_3I	76.93	12.33	10.74	7.2:1

AES data taken from the surface layers of the bare Si substrates exposed to iodotrifluoroethylene and 1-iodoheptafluoropropane indicated the presence of carbon, fluorine, and iodine. The relative percentages of these three elements in the films found on the wafer surface were estimated on the basis of instrumental sensitivity factors and are given in Table 4.1, along with the corresponding numbers for the three IFC compounds discussed earlier. The 1-iodoheptafluoropropane data are consistent with the trend extracted from the earlier data, which suggests that the film C:F ratio among the iodine-containing fluoroalkanes decreases as one moves from shorter to longer molecules. Beyond this observation, however, it is difficult to draw trends. A comparison between 1-iodoheptafluoropropane and 2-iodoheptafluoropropane films indicates that the iodine content of the films is similar, but the 1-iodoheptafluoropropane film appears to be somewhat more carbon rich. Moreover, there does not appear to be a correlation between either the C:F ratio of the film deposited on silicon or its iodine content and the tendency of the etch gas to polymerize (the chemistries which deposited the least polymer on silicon were iodotrifluoromethane and 1-iodoheptafluoropropane,

whereas those that deposited the most polymer on silicon were 2-iodoheptafluoropropane and iodotrifluoroethylene). Further study will be required to identify the specific mechanisms responsible for polymerization in iodofluorocarbon plasmas, as well as to determine why the polymerization behavior of the two isomers of iodoheptafluoropropane is so dissimilar.

4.2.3 Conclusions

Two iodofluorocarbon (IFC) chemistries were evaluated as etchants of silicon dioxide and silicon nitride films in an Applied Materials Precision 5000 etch tool. Under the conditions used, 1-iodoheptafluoropropane was found to etch both silicon dioxide and silicon nitride quite readily, whereas iodotrifluoroethylene etched oxide but deposited a thick iodine containing fluoropolymer film on the nitride substrate. Both compounds were determined to be potentially useful as dielectric etchants. 1-iodoheptafluoropropane was identified as an etchant potentially useful for the removal of both silicon dioxide and silicon nitride films, whereas iodotrifluoroethylene appeared to be a potential oxide etchant that exhibited high selectivity to silicon nitride, at least on blanket films.

References

1. S. Karecki, *Alternative Chemistries for Etching of Silicon Dioxide and Silicon Nitride*, M. S. Thesis in *Electrical Engineering and Computer Science*, Massachusetts Institute of Technology, Cambridge, MA, 167 p. (1996).
2. S. M. Karecki, L. C. Pruette, and L. R. Reif, *Plasma Etching of Silicon Dioxide and Silicon Nitride with Non-Perfluorocompound Chemistries: Trifluoroacetic Anhydride and Iodofluorocarbons*, in Proceedings of *Environmental, Safety, and Health Issues in IC Production*, Boston, MA, R. Reif, *et al.*, Editors, Proceedings of the Materials Research Society, **447**, p. 67-74, Materials Research Society, Pittsburgh, PA (1997).
3. S. M. Karecki, L. C. Pruette, and R. Reif, *Plasma etching of dielectric films with novel iodofluorocarbon chemistries: Iodotrifluoroethylene and 1-iodoheptafluoropropane*, J. Vac. Sci. Technol. A, **16**(2), p. 755-758 (1998).
4. L. Zazzera, B. Reagen, and P. Mahal, *Process Emissions Monitoring During C_3F_8 CVD Chamber Cleaning Using FTIR*, in Proceedings of *SEMICON Southwest 1996: A Partnership for Emissions Reduction*, Austin, TX, Proceedings of the SEMI Technical Program, p. 81-85, SEMI (1996).

5. S. Soggs, B. Bryant, B. A. Boeck, S. Rogers, R. Vrtis, and L. Mendicino, *Trifluoroacetic Anhydride as an Alternative Plasma Clean Chemistry*, in Proceedings of *SEMICON Southwest 1996: A Partnership for Emissions Reduction*, Austin, TX, Proceedings of the SEMI Technical Program, p. 71-80, SEMI (1996).
6. V. N. Bliznetsov, O. P. Gutshin, and V. V. Yachmenev, *Reactive ion etching of deep trenches in silicon*, in Proceedings of *SPIE International Conference of Microelectronics*, **1783**, p. 584-589 (1992).
7. 1000-IS Full Wafer Imaging Interferometer - Manual, 1995, Low Entropy Systems, Inc., Boston, MA.

5. Wafer Patterning Studies: Hydrofluorocarbons and Iodofluorocarbons

Chapter 5 is the first of two chapters that discuss a series of studies carried out in a commercial inductively coupled high density plasma etch tool with a number of novel fluorocarbon chemistries All the work in this chapter, as well as the following one, was performed on an Applied Materials Centura 5300 HDP tool, in collaboration with Motorola, Inc.'s Advanced Products Research and Development Laboratory (APRDL). The present chapter deals with hydrofluorocarbon and iodofluorocarbon etch chemistries, whereas Chapter 6 will discuss work carried out with unsaturated fluorocarbons (and octafluorotetrahydrofuran) as well as oxalyl fluoride. In contrast to the simple experiments described in the previous chapter, all of the studies discussed from this point forward involved effluent characterization employing extractive gas phase Fourier transform infrared (FTIR) spectroscopy and use of patterned substrates with sub-half-micron features. The same dielectric patterning application – a high aspect ratio (HAR) oxide via etch – was used as the test vehicle in all six of the studies discussed in Chapters 5 and 6.

The present chapter is structured as follows: Section 5.1 will discuss the first of several concept-and feasibility (C&F) studies carried out on the Centura 5300 HDP tool. This study evaluated one of the hydrofluorocarbon species (2H-heptafluoropropane) that was identified as promising in the HFC screening studies carried out at MIT (Section 1.2.2.1, [1-3]), along with three iodofluorocarbon species (iodotrifluoromethane, and 1- and 2-iodoheptafluoropropane) that were selected on the basis of the results presented in the previous chapter. Two follow-up projects emerged out of the work discussed in Section 5.1: a brief process development activity carried out with 2H-heptafluoropropane and a more in-depth process development activity carried out with the iodoheptafluoropropanes. Whereas the goal of the HFC/IFC C&F study was to establish the viability of these etchants in an actual dielectric patterning application, the objectives of the process development activities were to demonstrate a working process that met a set of performance criteria and to characterize its effluents. The following section, 5.2, will

discuss the first of these efforts, which was carried out with 2H-heptafluoropropane. Section 5.3 will discuss a second C&F study that was carried out with HFC chemistries: a collaboration with DuPont Fluoroproducts involving pentafluoroethane (C_2F_5H, FC-125) and 1,1-difluoroethane (CF_2H-CH_3, FC-152a). Finally, Section 5.4 will present the results of the iodofluorocarbon process development study that was carried out with the iodoheptafluoropropanes.

Over the course of time, additional characterization techniques and progressively more in-depth forms of analysis were applied to the processes discussed in this chapter. The study discussed in Section 5.1 employed blanket film and patterned wafers experiments, with cross-sectional SEM used for process characterization and FTIR spectroscopy used for effluent characterization. The process development study in Section 5.2 added the use of test wafers with silicon nitride and Cu stop layers. The extensive characterization of the FC-125/FC-152a chemistry in Section 5.3 provided the data for a systematic discussion of mechanisms and process and emissions trends. Additionally, for the first time in the course of the author's work, an attempt was made to identify and quantify all species present in the effluent above the detection limits of the FTIR instrument. A detailed breakdown of the effluent composition, along with a systematic discussion of trends in major effluent species with respect to key process variables was also included. Finally, the work described in Section 5.4, in addition to all of the above, also made an effort to study the composition of the fluorocarbon films deposited by IFC processes using x-ray photoelectron spectroscopy (XPS) and time-of-flight secondary ion mass spectrometry (TOF-SIMS) and to correlate this information with the process and emissions data.

In Sections 5.1, 5.2, and 5.3, all carbon equivalent calculations are carried out using 1995 GWP_{100} values taken from Ref. [4]. In Section 5.4, all carbon equivalent calculations are carried out using 1998 GWP_{100} values taken from Ref. [5].

5.1 2H-heptafluoropropane and Iodofluorocarbon Concept-and-Feasibility Study

This section presents the results of an effort to test several novel chemistries for use as replacements for perfluorocompounds in dielectric etch processes. Chemistries belonging to the hydrofluorocarbon and iodofluorocarbon families, namely 2H-heptafluoropropane (CF_3-CFH-CF_3), iodotrifluoromethane (CF_3I), 1-iodoheptafluoropropane (CF_2I-CF_2-CF_3), and 2-iodoheptafluoropropane (CF_3-CFI-CF_3), were tested in an Applied Materials Centura 5300 HDP etch tool, using a high aspect ratio silicon dioxide via etch application as the test vehicle. Effluent was analyzed using Fourier transform infrared spectroscopy and, on a limited basis, quadrupole mass spectrometry. The performance of the alternative etchants in a high aspect ratio via etch process was compared to that of a standard C_3F_8 based process on the Centura 5300 etch tool. Significant reductions in global warming emissions, relative to a perfluorinated baseline process, were found to be attainable with the alternative chemistries.

Relevant properties of 2H-heptafluoropropane and the three IFC compounds employed in this study are summarized in Tables 2.1 and 2.2. At the outset of the study, larger emissions reductions were believed to be possible with the use of the IFCs than with 2H-heptafluoropropane, as was indeed borne out by the data obtained. Nevertheless, 2H-heptafluoropropane was selected for this study alongside the IFC compounds because, based on the data obtained in earlier studies [1-3], it was expected to offer process behavior that was similar to that of C_3F_8, in contrast to the IFCs, whose etch viability was less certain. The evaluation of 2H-heptafluoropropane thus offered the possibility of an interim solution that would require a shorter development period than the more novel IFC compounds.

To the author's knowledge, prior to this work, 2H-heptafluoropropane had not been investigated for dielectric applications by groups other than the author's. CF_3I had been employed in a silicon trench etch prior to the inception of the MIT project. [6]. Subsequent to the study discussed in Section 4.1, investigations of CF_3I as an etchant for dielectric films were carried out by another group using a different type of process tool in

approximately the same timeframe as the study discussed in this section. [7, 8] To the author's knowledge, prior to this work, no other studies had been made involving the use of iodoheptafluoropropane for etch applications other than those discussed in the previous chapter.

The discussion of this study is organized as follows: Section 5.1.1 discusses the experimental setup used. Section 5.1.2 provides a discussion of the experimental data. Finally Section 5.1.3 offers conclusions regarding this study. The material in Section 5.1 is based on work published by the author and his coworkers in Refs. [9, 10].

5.1.1 Experimental Setup

A via etch application was chosen as the test vehicle for evaluation of the etch performance of 2H-heptafluoropropane, iodotrifluoromethane, 1-iodoheptafluoropropane, and 2-iodoheptafluoropropane on patterned substrates. An etch process based on C_3F_8, a standard etch gas on the tool used for the study, was used as a reference process against which both emissions and process data were compared. The tool used was an Applied Materials Centura 5300 platform with an HDP dielectric etch chamber, an inductively coupled, high density plasma chamber, described in detail in Section 3.4.2.

With the exception of iodotrifluoromethane, each test gas, as well as C_3F_8, was used in at least four sets of experiments, where a multivariable matrix of conditions was run on the following types of 200 mm substrates: blanket TEOS (tetraethoxysilane)-deposited oxide wafers (~ 16,000 Å thick), blanket PECVD nitride wafers (~ 7,000 Å thick), blanket photoresist (JSR 061 I-line resist) wafers (~ 10,000 Å thick), and patterned TEOS oxide wafers (~32,000 Å thick) masked with APEX deep UV resist (~10,000 Å), which is compositionally highly similar to the I-line resist used on the blanket wafers. For reasons discussed below, only an oxide and a photoresist lot were run with iodotrifluoromethane. Effluent data were gathered on the blanket TEOS oxide, blanket nitride, and blanket resist lots. The structures etched on the patterned wafers were via holes with nominal printed dimensions of 0.6, 0.45, and 0.35 μm. The discussion in this section will be limited to the

results of the patterned wafer experiments, along with the corresponding effluent data, which were typically gathered from the blanket photoresist lot for the same gas. The photoresist lot was run under the same matrix of conditions as the patterned wafer lot. It was possible to gather effluent data from blanket resist wafers rather than from patterned wafers because the patterned substrates had only approximately 0.5% open area and the two resists used were compositionally very similar. Hence, for all practical purposes, the material on the wafer surface exposed to the plasma, and consequently the emissions, were identical.

The first gas to be characterized was the reference gas, octafluoropropane. A three-variable matrix of experiments was run, where source power, chamber roof temperature, and etch gas flow rate were varied. This matrix was run with all four types of substrates. The procedure was then repeated for 2H-heptafluoropropane, iodotrifluoromethane, and 2-iodoheptafluoroprane, with only the oxide and photoresist lots being run for iodotrifluoromethane. The ranges explored were 1850 to 2900 W for the source power, 240 °C to 280 °C for the roof temperature, and 10 to 40 standard cubic centimeters per minute (sccm) for the etch gas flow. Based largely on the outcome of the 2-iodoheptafluoropropane experiments, for 1-iodoheptafluoropropane, a somewhat different parameter space was chosen: 1900 to 2600 W for the source power, 20 to 34 sccm for the etch gas flow, with the roof temperature fixed at 260 °C. Instead of varying roof temperature in the matrix experiments, bias power (1700 to 1995 W) was varied. (In previous experiments with the other gases, bias power was fixed at 1500 W.) The remaining process parameters in these experiments were: 50 sccm of Ar flow, 12 mTorr chamber pressure, 200 °C wall temperature, 10 °C chiller temperature, and 15 Torr backside He cooling pressure.

In the case of 1-iodoheptafluoropropane, additional tests, involving only patterned substrates, were carried out beyond the initial set of matrix experiments with four types of substrates. Additional parameters, namely pressure, chiller temperature setpoint, and argon flow rate, were also varied. In the matrix experiments with all five gases, effluent

had been characterized for the oxide, nitride, and resist lots. In the case of the additional 1-iodoheptafluoropropane tests, effluent measurements were taken on patterned wafers.

All of the processes discussed in this work were timed runs lasting 120 s. Cross-sectional scanning electron microscopy (SEM) was used to characterize process performance with respect to etch rate, mask layer (photoresist) selectivity, and via profile. At the time of this study, selectivity to stop layers (*e.g.*, silicon nitride, silicon, titanium nitride, and metal layers) had not yet been evaluated with the four experimental gases.

Quantitative effluent measurements were taken using FTIR spectroscopy. A Nicolet Magna 550 optical bench with a 1.3 cm absorption cell with zinc selenide windows was used. The instrument was set up to sample the process effluent downstream of both the chamber turbopump and its backing dry mechanical pump. The pump purge flow rate was measured daily by flowing a fixed amount of CF_4 using a mass flow controller on the process tool and calculating the amount of dilution due to nitrogen ballast in the dry mechanical pump; this calculation was repeatedly verified by performing the same measurement with other process gases on the tool. The pump purge flow rate was typically about 39 standard liters per minute (slm), whereas the flow rate through the sampling loop itself was set to be roughly 3 to 3.5 slm. The FTIR cell and a 25 ft. sampling line leading to it were heated to a target temperature of 185 °C. The target sampling pressure in the cell was 600 Torr.

The compounds quantified in this study were CF_4, C_2F_6, C_3F_8, CHF_3, HF, SiF_4, as well as 2H-heptafluoropropane, 1- and 2-iodoheptafluoropropane, and iodotrifluoromethane, where appropriate. Reference spectra for all species quantified by FTIR, with the exception of CHF_3, for which a library file was used, were generated on the same instrument at the same pressure and temperature conditions as those used for actual sampling. In the case of CF_4, C_2F_6, C_3F_8, HF, and SiF_4, reference FTIR spectra were generated through a multipoint calibration procedure which utilized a certified gas mixture of each gas (nominally 1% in nitrogen) diluted with ultrapure nitrogen in varying ratios. In the case of 2H-heptafluoropropane, iodotrifluoromethane, and 1- and 2-

iodoheptafluoropropane, no such standards were available at the time, therefore FTIR references were generated on the process tool itself. A multipoint calibration procedure was used in these cases as well to ensure linearity of response for the FTIR instrument. A file from a software library of FTIR spectra was used to quantify CHF_3. Both the cell pressure as well as the cell/sampling line temperature were controlled during data acquisition. Minor deviations from target settings (typically ~2% or less) were corrected for by appropriate scaling. The sampling lines themselves were stainless steel and Teflon.*

The global warming impact of each process was characterized by calculating the mass of carbon equivalent emitted by the process, using the kgCE (kilograms of carbon equivalent) metric, which has been defined as

$$kgCE = \sum_i Q_i \times \frac{12}{44} \times GWP_{100i} \qquad (5.1)$$

where GWP_{100i} is the global warming potential of each component (integrated over a 100-year time horizon) of the calculation and Q_i is the total mass of that species (in kg) released during the process. This metric is derived directly from the MMTCE (million metric tons of carbon equivalent) metric, the *de facto* emissions reporting standard used by the US semiconductor industry and the US Environmental Protection Agency. The kgCE metric is numerically equivalent to MMTCE multiplied by a factor of 10^9; it is employed in the studies discussed in this document instead of MMTCE because the magnitude of the units involved in the MMTCE calculation (used to report emissions by entire industries on an annual basis) is the grossly inappropriate to the quantities emitted in a 120 s etch process (tens to hundreds of grams). In the case of C_3F_8, the species found in the effluent that were included in the calculation were: C_3F_8, C_2F_6, CF_4, and CHF_3. In the case of 2H-heptafluoropropane, the following species were included: 2H-heptafluoropropane, C_2F_6, CF_4, and CHF_3. For CF_3I, the only global warming species determined to be present in the effluent stream above the detection limits of the instrument

---

* In subsequent studies, starting with the work discussed in Section 5.3, a different FTIR instrument and a somewhat different FTIR sampling procedure (see Appendix A) than the one described above would be used, resulting in a number of improvements in the quality of the data. One of the drawbacks of the methodology employed for the work in this section was the length of the sample cell (1.3 cm), which was determined to be inadequate for the concentrations of gas that were present.

were CF_4 and CHF_3, whereas, for the two isomers of iodoheptafluoropropane, C_2F_6, CF_4, and CHF_3 were included in the calculation.† Additionally, FTIR was used to quantify the concentrations of SiF_4, HF, and, where appropriate, CF_3I, and 1- or 2-iodoheptafluoropropane. No absorbance features corresponding to either C_2F_5H or C_2F_5I were seen in any of the spectra.

An MKS PPT series quadrupole mass spectrometer (QMS) was also used and was installed between the chamber turbopump and the chamber itself. In this configuration, its principal utility lay in providing semi-quantitative information about species leaving the chamber, which was used to complement the FTIR data. Specifically, the principal species of interest which the QMS was used to monitor for was molecular iodine (mass 254). Molecular iodine, a homonuclear diatomic, does not absorb in the infrared region accessible by FTIR spectroscopy, and hence is not detectable using that technique. The sampling configuration used for the QMS and FTIR instruments is shown in Figure 5.1.

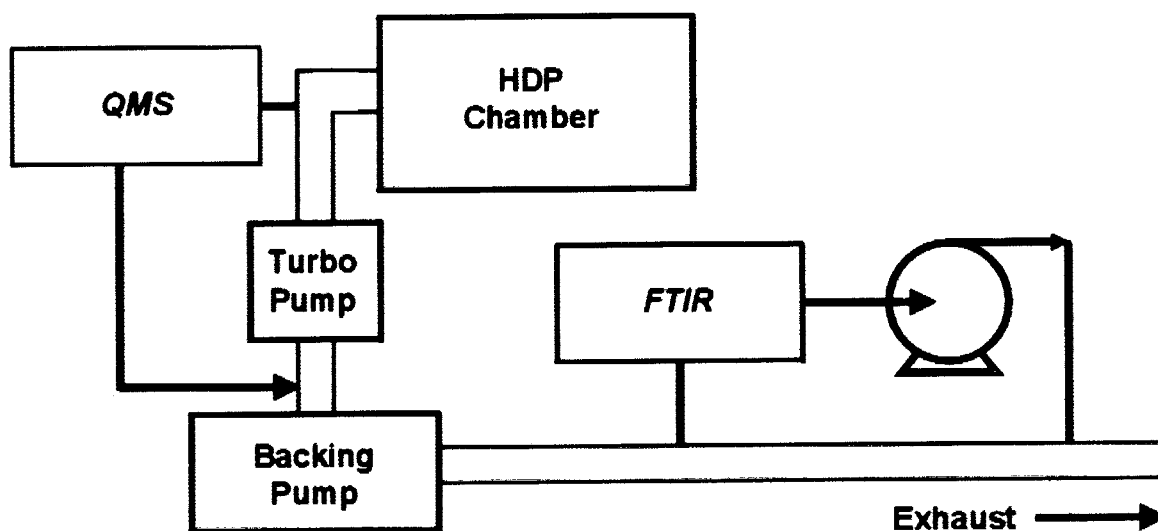

Figure 5.1: Diagnostic setup.

† In subsequent studies, where a more sensitive (10 cm cell) FTIR configuration was employed, C_3F_8 would also be identified in the effluent from IFC processes, albeit in small quantities.

As part of the experimental procedure used for each set of runs, seasoning runs using bare silicon wafers, along with oxygen plasma clean steps, were used between matrix test points in each lot that was run. The seasoning recipe was typically the matrix center point recipe for each set of experiments. After the completion of the experiments for each gas (except C_3F_8), the chamber was opened and a standard isopropyl alcohol / deionized water wet clean was performed on the process kit. No special safety precautions beyond those normally used were employed during the first wet clean (following 2H-heptafluoropropane). However, full Class B personal protective gear, including supplied air, was worn by the maintenance team performing the wet cleans following iodotrifluoromethane and 2-iodoheptafluoropropane. Air sampling instruments were used during the clean following the 2-iodoheptafluoropropane experiments to monitor for the presence of fluorocarbons, as well as iodine, hydrogen iodide, and hydrogen fluoride while the chamber was open. The results of the air sampling tests showed, however, that these additional safety precautions are not necessary in the case of 2-iodoheptafluoropropane. On the basis of this data, the 1-iodoheptafluoropropane wet clean was performed without additional safety precautions beyond those required by standard procedures.

All of the alternative etch gases were supplied by PCR Inc., Gainesville, FL. The purity of the 2-iodoheptafluoropropane and the iodotrifluoromethane was assayed at 99.6%. The 2H-heptafluoropropane was assayed at 99.7%, whereas the 1-iodoheptafluoropropane purity specification was 99%.

5.1.2 Results and Discussion

Tables 5.1 and 5.2 summarize emissions and process data, respectively, for selected experimental runs. A typical C_3F_8 HDP oxide etch recipe was selected as the baseline for this experimental evaluation and served as the reference point against which all other process and effluent data were compared. Except for iodotrifluoromethane, all other gases in Tables 5.1 and 5.2 have a "best emissions" point and a "best process" point. The former represents the experimental recipe which offered the largest percent reduction in

global warming emissions relative to the C_3F_8 reference, as measured by kgCE. This excluded runs where the etch gas flow rate was 10 sccm, where overall fluorocarbon emissions approached the detection limits of the FTIR instrument and therefore could not be reliably quantified. The latter represents the recipe resulting in the best overall etch profile, which in all cases corresponded to either the process with the fastest via etch rates or one whose etch rates were within 5% of the fastest process, as determined by the 0.6 μm via etch rate at the center location on the wafer. In the case of 1-iodoheptafluoropropane, the same recipe gave both the best via profile and best emissions, as determined by the above criteria. Also note that, in the case of 2H-heptafluoropropane and 2-iodoheptafluoropropane, the net kgCE reduction relative to the C3F8 reference for the "best process" recipe was within 5% of the highest value achieved with that gas, *i.e.*, the "best emissions" recipe (see Table 5.1). Thus, an encouraging general observation is that, for the set of gases used in this study, in the parameter spaces that were explored, competing trends between low emissions and good etch performance were not observed, suggesting that it may be possible to simultaneously optimize etch processes based on these compounds for emissions as well as process performance.

Table 5.1: Emissions data from selected experimental points.

Etch Gas	Exp. Point Description	Etch Gas Flow (sccm)	kgCE	% kgCE Reduction vs. C_3F_8 Reference	Milligrams of Global Warming Gas Emitted					Utilization Efficiency (%)	Fluorocarbon Species in Effluent**
					C_3F_8	C_2F_6	CF_4	CHF_3	2H-C_3F_7H		
C_3F_8	Reference	20	0.3152	0.0%	80.8	32.5	23.1	12.1		78.9%	*C_3F_8, CF_4, C_2F_6, CHF_3*
2H-C_3F_7H	BP	20	0.1340	57.5%		8.5	12.0	19.4	37.3	90.3%	*2H-C_3F_7H, CF_4, C_2F_6, CHF_3*
2H-C_3F_7H	BE	20	0.1251	60.3%		5.8	10.4	19.5	37.6	89.7%	*2H-C_3F_7H, CF_4, C_2F_6, CHF_3*
2I-C_3F_7I	BP	30	0.0564	82.1%		6.0	7.9	8.6		96.8%	2I-C_3F_7I, CF_3I, *CF_4, C_2F_6, CHF_3*
2I-C_3F_7I	BE	20	0.0422	86.6%		5.3	5.1	6.2		99.5%	2I-C_3F_7I, CF_3I, *CF_4, C_2F_6, CHF_3*
1I-C_3F_7I	BP/BE	20	0.0174	94.5%		1.8	6.7	0.4		89.9%	1I-C_3F_7I, CF_3I, *CF_4, C_2F_6, CHF_3*
CF_3I	BE*	20	0.0134	95.8%			1.6	3.3		93.7%	CF_3I, *CF_4, CHF_3*

BE = best emissions point, BP = best process point,
* = no process data was taken for CF_3I,
** = italicized species included in kgCE calculation, etch time = 120 s.

Table 5.2: Process data from selected experimental points.

Etch Gas	Exp. Point Description	0.6 µm Via Depth (µm)	0.6 µm Via Patterned TEOS Oxide ER (Å/min)	0.45 µm Via Depth (µm)	0.45 µm Via Patterned TEOS Oxide ER (Å/min)	0.35 µm Via Depth (µm)	0.35 µm Via Patterned TEOS Oxide ER (Å/min)
C_3F_8	Reference	1.62	8079	1.43	7165	1.13	5640
2H-C_3F_7H	BP	1.24	6200	1.10	5500	0.94	4700
2H-C_3F_7H	BE	1.17	5833	1.02	5119	0.88	4405
2I-C_3F_7I	BP	1.76	8816	1.63	8158	1.34	6711
2I-C_3F_7I	BE	1.50	7500	1.39	6974	1.21	6053
1I-C_3F_7I	BP/BE	2.05	10250	1.91	9550	1.64	8200

ER = etch rate,
BE = best emissions point, BP = best process point,
etch time = 120 s.

5.1.2.1 2H-heptafluoropropane

As Table 5.1 indicates, kgCE savings on the order of 60% relative to the C_3F_8 reference appear to be attainable when 2H-heptafluoropropane is used as the etchant. In both the C_3F_8 processes and the 2H-heptafluoropropane processes, the fluorinated species identified in the effluent by FTIR were the following: HF, SiF_4, CF_4, C_2F_6, CHF_3, as well as unreacted 2H-heptafluoropropane in the case of the 2H-heptafluoropropane runs and unreacted C_3F_8 in the case of the C_3F_8 runs. The most abundant fluorinated species detected in the effluent were SiF_4 and HF.[‡] (The HDP chamber contains quartz and silicon surfaces that are exposed to the process plasma, which account for the bulk of SiF_4 emissions from etch processes in the HDP chamber.) A comparison to effluent data from blanket oxide and nitride films etched with 2H-heptafluoropropane, as well as to that from resist films etched with the other chemistries, shows that CHF_3 was formed in a 2H-heptafluoropropane plasma as a decomposition product of the source gas itself, regardless of the type of film being etched. Additionally, for all five gases evaluated, it was formed whenever resist was exposed to the process plasma, regardless of the fluorocarbon etch

---

[‡] In subsequent studies, it would be determined that CO was also among the most abundant species present in fluorocarbon etch plasmas in this tool. Additional species that would later be identified were C_2F_4, CO_2, and COF_2.

gas used. The utilization efficiencies measured for the 2H-heptafluoropropane processes reported here also tended to be higher than that of the C_3F_8 reference process (see Table 5.1), suggesting more efficient breakup of the source gas in the plasma. It was found that, in the parameter space explored, both C_3F_8 and 2H-heptafluoropropane exhibited an increase in global warming emissions as measured by kgCE with increasing etch gas flow rate. No clear trend in kgCE could be determined as a function of source power with either gas. Finally, C_3F_8 exhibited an increase in kgCE with increasing roof temperature; a similar but less pronounced trend was also seen with 2H-heptafluoropropane.

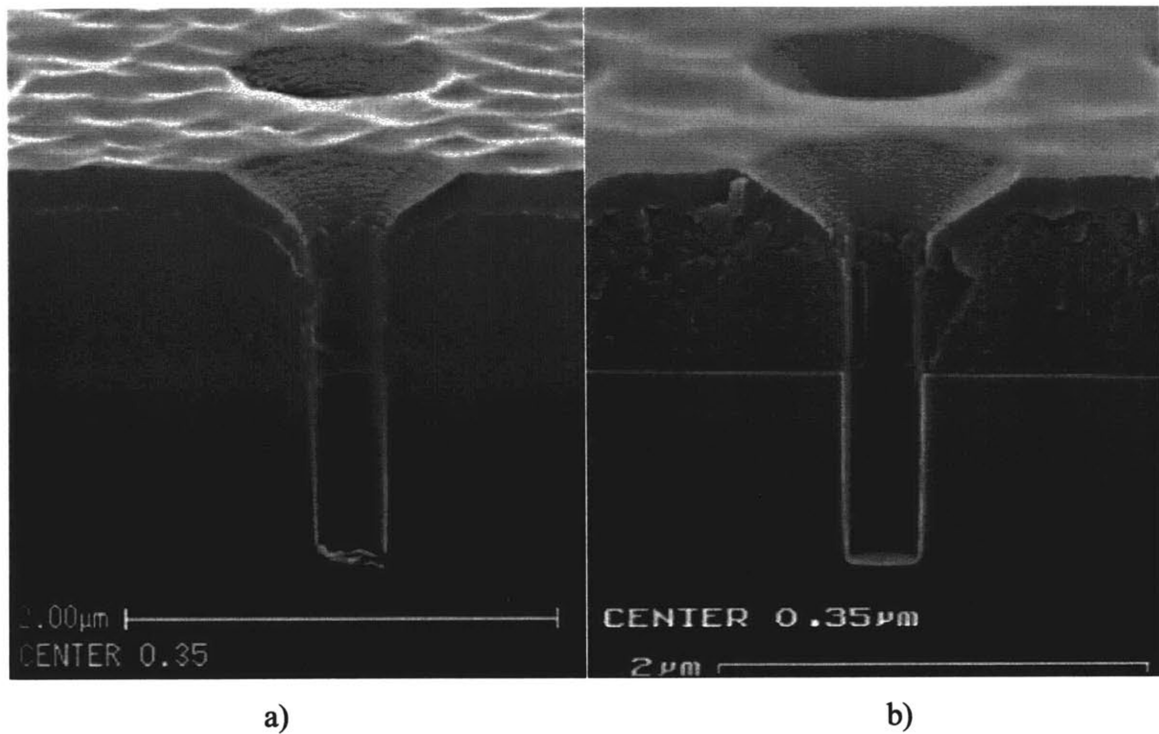

a) b)

Figure 5.2: 0.35 µm vias etched by a a) C_3F_8 process, b) 2H-heptafluoropropane process.

For the best 2H-heptafluoropropane process point, the patterned TEOS oxide etch rates ranged from 77% of the corresponding C_3F_8 etch rates for the 0.6 and 0.45 µm features in the center of the wafer to 83% for the 0.35 µm features. Table 5.2 lists etch rate data for the experimental gases tested. As can be seen from a comparison of Figures 5.2a and 5.2b, 2H-heptafluoropropane is capable of achieving highly directional etch profiles comparable to those attained with the reference process. The amount of resist erosion is also comparable to what is seen in the reference process. However, further data is needed

to assess the selectivity of 2H-heptafluoropropane to stop layers such as silicon nitride or silicon. It should be pointed out that, beyond the initial matrix of experiments, no attempt at fine tuning the process for either etch performance or emissions has yet been made with this chemistry, hence the results presented here should be considered as starting points, rather than optimized recipes.

When the chamber was opened for a wet clean after the completion of the 2H-heptafluoropropane experiments, no abnormal adverse effects due to the new chemistry were noted.

5.1.2.2 Iodotrifluoromethane

As can be seen from Table 5.1, iodotrifluoromethane appeared to offer the possibility for very significant emissions savings relative to the C_3F_8 reference process – up to approximately 96%. The utilization efficiency for this gas was also quite high (in the mid-90% range for the best emissions point, see Table 5.1). The fluorinated species present in the largest concentrations in the effluent were once again SiF_4 and HF. The fluorocarbons identified were CF_3I itself, and, in smaller quantities, CHF_3 and CF_4. With this gas, no clear trend in kgCE was seen as a function of roof temperature. As was expected, an increase in process kgCE was seen with increasing etch gas flow. Additionally, a slight decrease in global warming emissions was seen with increasing source power.

In these experiments, however, CF_3I proved highly non-selective to photoresist in the matrix space explored. Additionally, the interaction of CF_3I with the resist was found to create significant particle problems which made it impossible to continue running experiments with this chemistry. Only the oxide lot and a partial resist lot were run for this gas.

When the chamber was opened for the wet clean, brown residues (suspected to be iodine-containing fluoropolymer or an iodine-containing silicon-based film) were found on the roof and other surfaces. Some of the residues proved difficult to remove, but the chamber

was recovered. Some evidence of formation of I_2 deposits was also seen, as indicated by evolution of vapor when chamber surfaces were wet with deionized water and isopropyl alcohol. During the CF_3I process runs, data from the QMS instrument sampling the exhaust stream close to the chamber indicated the presence of a signal at mass 254, which can be uniquely assigned to I_2 in these processes. Unfortunately, air monitoring equipment was unavailable for this wet clean, so no air composition data was taken.

No etch profile data is available for this chemistry since the patterned wafer lot was not run. Generally speaking, at least in the parameter space used for this work, CF_3I appeared to be a very problematic gas to work with. It appeared to be a fairly non-selective to photoresist and generated unacceptable amounts of particles in the chamber when photoresist was present. It may be possible to successfully employ CF_3I as a dielectric etchant if it could be made to operate in a regime where interaction with the photoresist is minimized. At the time, however, it was deemed to be the least viable of the four alternative chemistries explored in this work and, in fact, the only one which did not yield promising results from a process standpoint.

5.1.2.3 2-iodoheptafluoropropane

2-iodoheptafluoropropane compared very favorably to the reference process in terms of kgCE. For the best emissions point, the kgCE reduction that was achieved was approximately 87%, whereas, for the best process point, a kgCE reduction of approximately 82% was attained, despite the fact that this run used 50% higher gas flow (30 sccm) than that of the C_3F_8 reference point (20 sccm). See Table 5.1. Once again, the major fluorinated species detected in the effluent were SiF_4 and HF. Among the fluorocarbon species, the compound present in the largest quantities was CF_3I, with CHF_3, CF_4, C_2F_6, and 2-iodoheptafluoropropane itself also detected. Note that the most abundant fluorocarbon species in the effluent from these processes was a shorter chain IFC, CF_3I, rather than a perfluorocarbon. The reasons for this behavior are presently still not well understood, especially in light of the relative weakness of the C-I bond in IFCs. As was the case with iodotrifluoromethane, 2-iodoheptafluoropropane also exhibited a

high utilization efficiency in the processes reported here (see Table 5.1). With 2-iodoheptafluoropropane, no clear trend in kgCE was seen as a function of source power or roof temperature. However, the expected increase in kgCE with etch gas flow was observed.

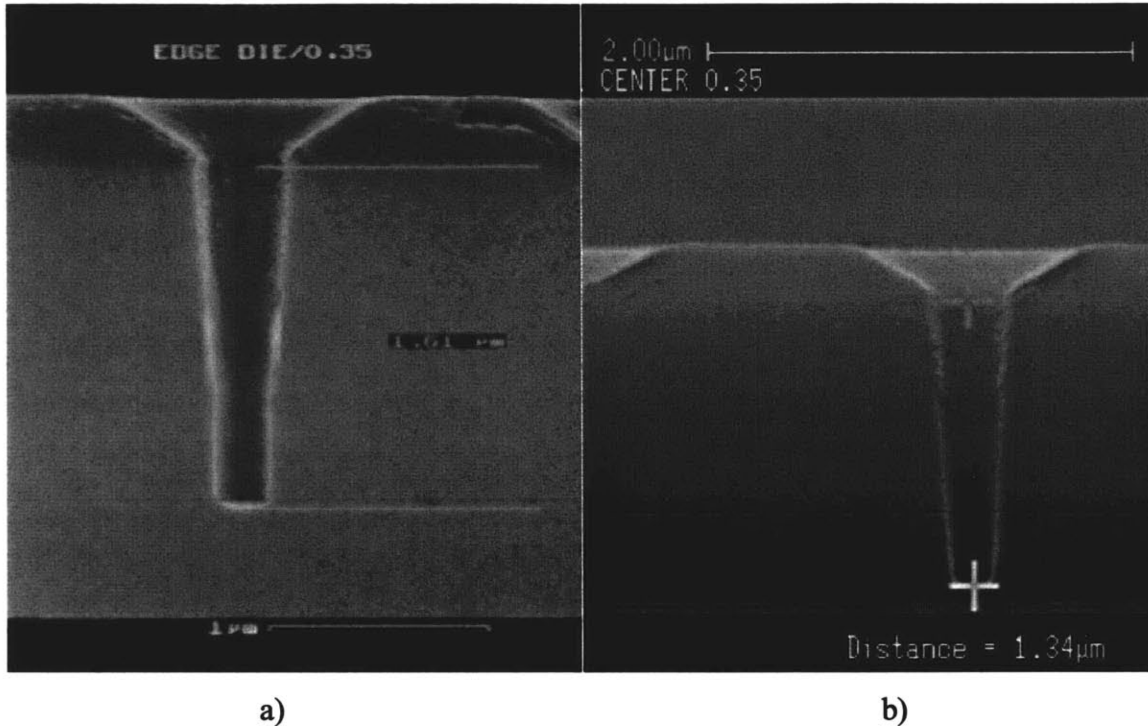

a) b)

Figure 5.3: 0.35 µm vias etched by a a) 1-iodoheptafluoropropane process, b) 2-iodoheptafluoropropane process.

At the best emissions point, the etch rates attained with 2-iodoheptafluoropropane were comparable to those of the C_3F_8 reference process, ranging from 93% of the corresponding C_3F_8 rate (0.6 µm via, center die) to 107% (0.35 µm via, center die). At the best process point, however, they were generally higher, ranging from 109% (0.6 µm via, center die) to 119% (0.35 µm via, center die). See Table 5.2. Where the 2-iodoheptafluoropropane process was found to need improvement was its selectivity to the mask layer. A comparison of Figure 5.3b with Figure 5.2 shows that there is considerable resist erosion present in the 2-iodoheptafluoropropane processes evaluated so far. It appears to be the case that, in the HDP chamber, within the process window tested, IFC etch chemistries are inherently less selective to photoresist than 2H-heptafluoropropane

and C_3F_8. It is not necessarily surprising that this compound exhibits lower selectivity than its H-substituted analog. The presence of hydrogen in the etchant molecule is known to provide an enhancement in polymerization. Well established explanations for this phenomenon invoke the mechanism of scavenging of atomic fluorine by hydrogen atoms (see Section 3.3). The role which iodine plays in polymerization processes remained to be established at the time of this study. As Figure 5.3b shows, a noticeable via taper is also present in features etched with 2-iodoheptafluoropropane. It was determined that via taper and bulk photoresist selectivity were among the most critical issues which need to be addressed in later studies. It was also determined that selectivity to stop layers such as silicon and silicon nitride needed to be examined as well.

The opening of the chamber for the wet clean after this chemistry showed it to be in much better condition than after the iodotrifluoromethane experiments. A flaky, reddish-brown deposit that peeled when exposed to air was found in the chamber, principally on the silicon roof of the chamber. The deposit was localized in a central region of the roof, as well as in an annular region on the roof above the clamp ring, with little or no deposit between these two areas. The centrally located deposit was thicker and more difficult to remove mechanically. Some deposit was also seen on the tapered edge of the quartz wafer clamp ring. No evidence of I_2 formation was seen, *i.e.*, no visual signs of the presence of iodine were observed when the chamber was opened (no evolution of vapor from chamber surfaces); nor was evolution of vapor or formation of reddish-brown liquid seen when chamber surfaces were wet with deionized water / isopropyl alcohol. All this suggested that the primary deposit on chamber surfaces was an inert film, rather than molecular iodine. Film from the chamber taken via a wipe sample was analyzed using x-ray fluorescence and x-ray diffraction. The results indicated that the residue was completely amorphous, containing mostly oxygen and silicon in approximately a 2.1:1 ratio by at. %, with an approximate iodine content of 1.1 at. % (6.4 wt. %), suggesting that the residue may have been an iodine-doped silica film, rather than an iodine-containing fluoropolymer as initially expected.

Interestingly, while QMS data taken during 2-iodoheptafluoropropane runs still indicated the presence of a signal at mass 254 (I_2), the magnitude of this signal was lower than what was seen earlier with CF_3I, suggesting that less iodine was produced by the 2-iodoheptafluoropropane processes, an observation consistent with the difference in chamber condition seen between the two gases. As an aside, in contrast to what is generally observed with perfluoroalkanes, with 2-iodoheptafluoropropane, it was possible to see the parent compound (at mass 296) with the QMS.

During the chamber wet clean following the 2-iodoheptafluoropropane experiments, samples of the air were taken with personal air samplers, some of which were placed in the immediate area around the chamber and some of which were worn by a member of the maintenance team, who was wearing full Class B personal protective gear. The air samples taken were analyzed for the presence of 2-iodoheptafluoropropane itself, iodine, hydrogen iodide, and hydrogen fluoride. 2-iodoheptafluoropropane was collected and analyzed according to NIOSH (National Institute for Occupational Safety and Health) 1003 method (halogenated hydrocarbons). Iodine and HI were analyzed according to OSHA (Occupational Safety and Health Administration) method ID-212, whereas HF was analyzed according to NIOSH method 7903. Iodine, hydrogen iodide, and 2-iodoheptafluoropropane were not detected in the air samples. Very low airborne levels of HF were detected; however, these levels were significantly below the OSHA PEL (permissible exposure limit) and were similar to those detected in the field blank samples. Generally speaking, sampling results indicate that maintenance activities did not produce significant levels of airborne chemicals and that the safety precautions which had been used up to this point for wet cleans following IFC processes would no longer be necessary for 2-iodoheptafluoropropane.

5.1.2.4 1-iodoheptafluoropropane

The final experimental etch gas examined was the other isomer of iodoheptafluoropropane. For this gas, after an initial experimental matrix was run with blanket oxide, nitride, and resist wafers, followed by patterned wafers, additional tests

were run with patterned wafers only, in an attempt to improve process characteristics. FTIR data were also taken during this stage of the experiments. With this gas, the best emissions point and the best process point happened to coincide. The highest measured kgCE savings value relative to the C_3F_8 reference process was approximately 95% (see Table 5.1). As was expected, the effluent composition was similar to that of the 2-iodoheptafluoropropane processes. Again, the most abundant fluorinated species were SiF_4 and HF. CF_3I was once more the most abundant among the fluorocarbon species present. The other fluorocarbon species that were detected and quantified were CHF_3, CF_4, C_2F_6 and unreacted 1-iodoheptafluoropropane. Again, the utilization efficiency seen with this IFC gas was higher than that of the C_3F_8 reference process (see Table 5.1). The dependence of kgCE on roof temperature was not studied with this gas. As was the case with the other isomer, the expected increase in kgCE with etch gas flow was observed, while no clear trend in kgCE was seen as a function of source power.

As Figure 5.3a shows, the etch profiles seen with this gas exhibit the same problems as those seen with the other isomer, namely noticeable resist erosion and via taper. It was again determined that, in future studies with iodoheptafluoropropane etch processes, these issues would need to be among the first to be addressed, along with an examination of the selectivity to stop layers such as silicon and silicon nitride. On the other hand, etch rates considerably higher than those of the reference process or even those seen with 2-iodoheptafluoropropane were attained, ranging from 127% (0.6 μm via, center die) to 145% (0.35 μm via, center die) of the corresponding C_3F_8 etch rate (see Table 5.2). In fact, for the 0.6 μm features, via etch rates of over 10,000 Å/min were achieved readily with this gas under a range of conditions. Moreover, with 1-iodoheptafluoropropane, the best process point was realized at an etch gas flow rate of 20 – as opposed to 30 – sccm.

On the basis of the data obtained from the air samples taken during the 2-iodoheptafluoropropane wet clean, a standard wet clean procedure was used when the chamber was opened for inspection and cleaning after this last set of experiments. No personal protective gear was worn, nor was the process area evacuated. Again, no evidence of molecular iodine deposits in the chamber was seen. This time, the chamber

residue was a very thin, very flaky, yellowish-white film, covering all of the roof and also present in a powdery form on the inner edge of the silicon ring surrounding the perimeter of the chuck. No iodine odor was detected around the chamber. A sample of this film was taken from the roof and analyzed. Preliminary results indicated a high silicon content in the film, with some fluorine present.

In contrast to what was seen during the CF_3I and 2-iodoheptafluoropropane runs, only trace levels of I_2 (mass 254) were detected by QMS during 1-iodoheptafluoropropane runs. Whereas the mass spectrum of 2-iodoheptafluoropropane did contain the parent compound at mass 296, no signal at this mass was observed for the other isomer.

5.1.3 Conclusions

Four novel fluorocarbon gases were evaluated in a dielectric etch application in a high density plasma etch tool. A high aspect ratio TEOS oxide via etch served as the test process. The process tool used was an Applied Materials Centura 5300 HDP etch system. Via holes of varying critical dimension were etched, ranging from 0.6 μm (nominal printed CD) down to 0.35 μm. Blanket TEOS oxide, plasma deposited nitride, and photoresist films were also used in the evaluation. Process performance was evaluated principally on the basis of cross-sectional SEM. Effluent composition was quantified using FTIR spectroscopy; supplementary information about the presence of iodine in the effluent stream was provided by QMS. Three of the four experimental gases tested yielded promising results that were determined to warrant further evaluation. 2H-heptafluoropropane was found to be capable of process performance that was roughly equivalent to that of the C_3F_8 reference process, while yielding a reduction in global warming gas emissions of on the order of 60%. Despite the fact that it appeared to emit very low quantities of global warming gases, iodotrifluoromethane was found to be the least viable of the four compounds tested, as it generated unacceptable levels of macroscopic particles and deposited in the chamber what appeared to be iodine-containing residues that proved to be difficult to remove. However, the remaining IFC chemistries did not exhibit these problems and both showed promising process characteristics.

Representative emissions reductions relative to the reference process were measured to be on the order of 80-90%. A kgCE reduction on the order of 95% vs. the reference process was also recorded with 1-iodoheptafluoropropane. It is encouraging that, in the case of 1-iodoheptafluoropropane, it was possible to simultaneously improve both emissions and process performance. Both isomers of iodoheptafluoropropane were found to be capable of etch rates faster than those measured with the reference process. In the case of 1-iodoheptafluoropropane, especially high TEOS oxide etch rates (in excess of 10000 Å/min for 0.6 μm features) were seen.

While the most promising process as well as emissions results for IFCs used in this study came from 1-iodoheptafluoropropane experiments, it should be pointed out that this was the result of additional fine tuning work done with this compound. Such work was not carried out with 2-iodoheptafluoropropane; hence it was determined that further efforts with 2-iodoheptafluoropropane may yield results equivalent to those seen with the other isomer.

In summary, three out of the four gases tested showed considerable promise as replacements for C_3F_8 in a TEOS oxide via etch application on an Applied Materials Centura 5300 HDP etch tool. The results generated by this work would later be leveraged by further efforts in this area, with follow-up process development studies being undertaken with both 2H-heptafluoropropane (Section 5.2) and the iodoheptafluoropropanes (Section 5.4).

References

1. S. Karecki, *Alternative Chemistries for Etching of Silicon Dioxide and Silicon Nitride*, M. S. Thesis in *Electrical Engineering and Computer Science*, Massachusetts Institute of Technology, Cambridge, MA, 167 p. (1996).
2. B. A. Tao, S. M. Karecki, and L. R. Reif, *Alternative Chemistries to Perfluorocompounds for Dielectric Plasma Etching*, in Proceedings of *11th International Symposium on Plasma Processing*, Los Angeles, CA, G. S. Mathad and M. Meyyappan, Editors, The Electrochemical Society Proceedings Series, **PV 96-12**, p. 424-434, Electrochemical Society, Pennington, NJ (1996).

3. S. M. Karecki, B. A. Tao, and L. R. Reif, *Etching of Silicon Dioxide and Silicon Nitride Films with Non-Perfluorocompound Gases*, in Proceedings of *SRC TECHCON 1996 Conference*, Phoenix, AZ, Semiconductor Research Corporation, Research Triangle Park, NC (1996).
4. *Radiative Forcing of Climate Change: The 1995 Working Report of the Scientific Assessment Working Group of IPCC,* Intergovernmental Panel on Climate Change (IPCC) (1995).
5. *Scientific Assessment of Ozone Depletion: 1998, Volume 2,* World Meteorological Organization, Global Ozone Research and Monitoring Project, Report No. 44 (1998).
6. V. N. Bliznetsov, O. P. Gutshin, and V. V. Yachmenev, *Reactive ion etching of deep trenches in silicon*, in Proceedings of *SPIE International Conference of Microelectronics*, **1783**, p. 584-589 (1992).
7. F. Fracassi, R. d'Agostino, M. Stenardo, L. R. Atzei, and F. Illuzzi, *Environmental Impact of Fluorocarbon and Iodofluorocarbon Containing Glow Discharges for SiO_2 Etching*, in Proceedings of *4th International ESH Conference*, Milan, Italy, **1** (1997).
8. F. Fracassi and R. d'Agostino, *Evaluation of trifluoroiodomethane as SiO_2 etchant for global warming reduction*, J. Vac. Sci. Technol. B, **16**(4), p. 1867-1872 (1998).
9. S. Karecki, L. Pruette, R. Reif, L. Beu, T. Sparks, and V. Vartanian, *Use of 2H-heptafluoropropane, 1-iodoheptafluoropropane, and 2-iodoheptafluoropropane for a high aspect ratio via etch in a high density plasma etch tool*, J. Vac. Sci. Technol. A, **16**(4), p. 2722-2724 (1998).
10. S. Karecki, L. Pruette, R. Reif, T. Sparks, L. Beu, and V. Vartanian, *Use of Novel Hydrofluorocarbon and Iodofluorocarbon Chemistries for a High Aspect Ratio Via Etch in a High Density Plasma Etch Tool*, J. Electrochem. Soc., **145**(12), p. 4305-4312 (1998).

5.2 2H-heptafluoropropane Via Etch Process Development Study

This section will present emissions as well as process performance data from the first alternative chemistry process development study carried out in the Centura 5300 HDP. This study was performed as a follow-up activity to the work described in Section 5.1. The goal of the work presented here was to develop a manufacturable high density plasma etch process using 2H-heptafluoropropane as a source gas that demonstrated equivalent or better process performance than C_3F_8 in conjunction with reduced emission of global warming gases in the process effluent. A high aspect ratio (HAR) via etch application was chosen as the testbed. Cross-sectional scanning electron microscopy (SEM) was used for process characterization, while Fourier transform infrared (FTIR) spectroscopy was used to characterize the process effluent in this study. Both process performance and emissions were compared to a C_3F_8 based reference process. The process recipe itself* was somewhat different than the initial reference recipe that was used in Section 5.1; the etch and emissions performance of this reference process, however, were similar to those of the earlier recipe. The material in Section 5.2 is based on work published by the author and his coworkers in Ref. [1].

5.2.1 Experimental Setup

The first stage of the process development work was to develop a silicon dioxide via etch process with 2H-heptafluoropropane that performed comparably to a typical C_3F_8 via etch process. The equipment used was an Applied Materials Centura 5300 platform with inductively coupled HDP chambers, described in detail in Section 3.4.2. The 200 mm test wafers consisted of patterned TEOS oxide (~32,000 Å) masked with APEX deep UV resist (10,000 Å). The vias etched had nominal printed dimensions of 0.6, 0.45, and 0.35

μm. Several multi-variable designed experiments were performed to examine the effect of change in etch gas flow rate (17 to 27 sccm), source power (1800 to 2200 W), bias power (600 to 1000 W), and silicon roof temperature (200 to 220 °C) on the process and on the global warming emissions. Criteria evaluated for the process performance included anisotropy, resist selectivity, critical dimension control, etch rate, and etch rate lag for smaller dimensions. Cross-sectional scanning electron microscopy (SEM) was used to evaluate the etch process performance, while FTIR spectroscopy was used to quantify the global warming emissions from the process using the kgCE (kilograms of carbon equivalent) metric, defined in Section 5.1. After examining the data from the designed experiments to identify a 2H-heptafluoropropane process demonstrating acceptable via etch performance with reduced emissions, further work was done to ensure that the process would continue to perform well in actual semiconductor manufacturing etch applications. The selectivity to a thin PECVD nitride layer was tested. Additionally, a number of experimental runs testing the ability of 2H-heptafluoropropane to stop on Cu lines were performed.

A Nicolet Magna 550 optical bench with a 9.6 cm absorption cell and KBr windows was used for Fourier Transform Infrared (FTIR) spectroscopy. The instrument sampled the process effluent downstream of both the chamber turbopump and its backing dry mechanical pump. Calibrations for gases quantified in the effluent (2H-heptafluoropropane, C_3F_8, C_2F_6, CF_4, CHF_3, HF, SiF_4) were performed on the FTIR spectrometer, and all showed linear responses in the concentration regime in which they were expected to appear in the process effluent. The kgCE calculation included each global warming species appearing in the effluent, and was integrated over the entire 120 s etch.

---

[*] All C_3F_8 based reference processes used in the studies discussed in Sections 5.1, 5.2, 5.4, and 6.2 of this document were proprietary recipes developed by Motorola APRDL. Hence, recipe details for these processes are not disclosed in this document. All had very similar emissions performance, however (~0.3 kgCE for a 120 s etch) and a target etch depth of 1 μm; hence the specific choice of the reference recipe was never critical for comparison against alternative chemistry processes.

5.2.2 Results and Discussion

Earlier work (see Section 5.1) had indicated that the process window for achieving reduction of global warming emissions with 2H-heptafluoropropane was potentially a large one; therefore, after confirming this observation by measuring the emissions at several test points spread over the new parameter space, it was decided that FTIR data would be collected only after the etch process performance was optimized.

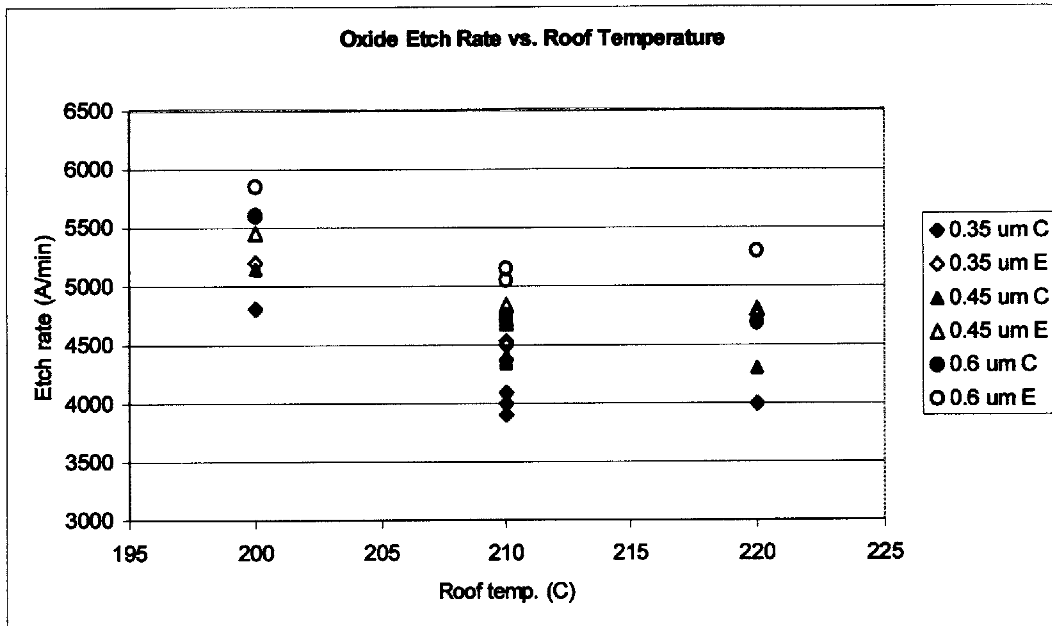

Figure 5.4: Etch rate as a function of roof temperature for 2H- heptafluoropropane.

The oxide etch rate, photoresist selectivity, and critical dimension were measured for the 2H-heptafluoropropane experimental runs while source power, bias power, etch gas flow rate, and roof temperature were varied. The etch rate was found to increase linearly with both increased bias power and increased etch gas flow rate. Since the goal of the project was to minimize the emissions of global warming gases, increasing the etch gas flow rate was the least acceptable choice for improving the etch rate. While the bias power had an observable effect on the etch rate, the source power did not. The etch rate appeared to be relatively insensitive to source power in the regime tested. Interestingly, the temperature

had a more complex effect on the etch rate (see Figure 5.4). The etch rate maxima occur at both high temperature and low temperature within the range tested. Since one of the objects of the process development study was to identify a 2H-heptafluoropropane process that is manufacturable, it was considered desirable to operate the chamber with the roof at a lower temperature, since the lifetime of the process kit on in the chamber is thought to be adversely affected by high surface temperatures due to higher rates of consumption by fluorine in the plasma. On the other hand, reducing the roof temperature much below 200 °C was thought not to be practical because heating caused by the plasma makes the temperature of the chamber to difficult to control below this value. The approach used for maximizing the etch rate without significantly increasing the global warming emissions of the process was adjusting the bias power and roof temperature.

Other factors considered in the evaluation of potential 2H-heptafluoropropane etch processes were selectivity to photoresist and the proximity to the nominal printed dimension measurement for the via. Increasing the 2H-heptafluoropropane flow rate had a positive effect on photoresist selectivity, whereas increasing source power and bias power had a noticeable negative effect on this parameter. Interestingly, the roof temperature dependence appeared to follow a trend similar to that seen for etch rate, with the lowest selectivity seen at the 210 °C condition. The bias power result highlighted a major tradeoff for the development of this etch process: increasing the bias power improves the etch rate, but decreasing the bias power improves the photoresist selectivity. No trend could be established for the effect of any of the parameters on the critical dimension.

A process was identified that provided optimal etch rate, photoresist selectivity, and adherence to the nominal printed dimension while demonstrating comparable process performance to C_3F_8. Figure 5.5 shows a comparison of performance between the C_3F_8 process and the 2H-heptafluoropropane process.

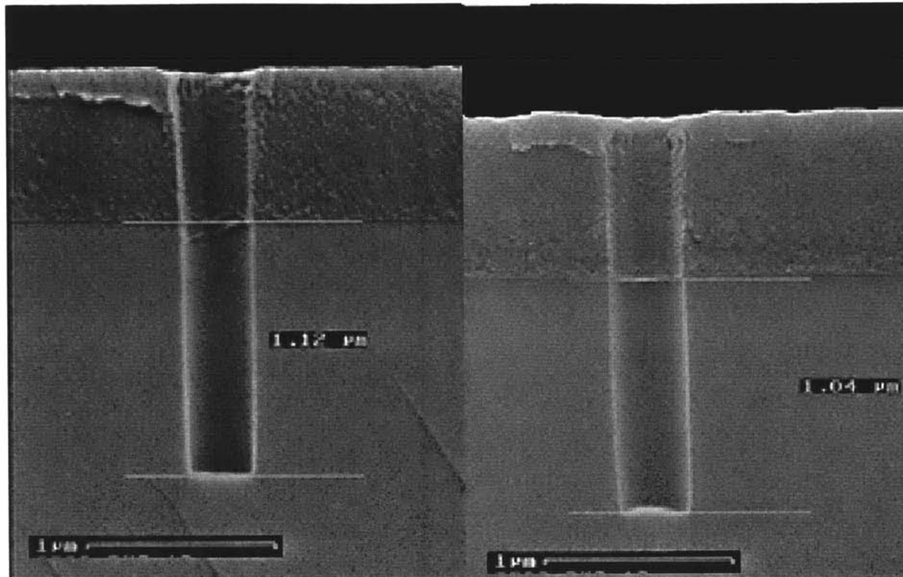

Figure 5.5: 0.35 μm vias etched with C_3F_8 (left) and 2H-heptafluoropropane (right) processes.

The TEOS etch rate for the 2H-heptafluoropropane process was found to be slightly slower than that of the C_3F_8 reference process (see Table 5.3). Apart from the etch rate, however, the two processes exhibit virtually identical etch process performance. In fact, the photoresist selectivity for the 2H-heptafluoropropane process is higher than that of the C_3F_8 process. Table 5.4 gives specific process performance comparisons for resist selectivity and other parameters.

After the process was developed with 2H-heptafluoropropane to etch a patterned TEOS oxide film, it was tested with stop layers commonly encountered in back-end-of-line oxide etching. Figure 5.6 shows an SEM taken from a wafer used to test the selectivity of 2H-heptafluoropropane to plasma deposited nitride. Based on the amount of nitride remaining on the wafer from this series of tests and the oxide etch rate calculated for the process at the 0.45 μm center point, the oxide:nitride selectivitity is approximately 1.4:1. Additional test wafers were run to determine 2H-heptafluoropropane's ability to stop on metal lines. A representative result of those experiments is displayed in Figure 5.7. In each case, the 2H-heptafluoropropane demonstrated infinite selectivity to the metal.

Table 5.3: TEOS oxide etch rate performance of 2H-heptafluoropropane.

Location and Nominal Printed Dimension	C_3F_8 TEOS Oxide Etch Rate (A/min)	2H TEOS Oxide Etch Rate (A/min)	Percent Difference (2H vs. C_3F_8)
Center: 0.6 μm	6250	5600	-10.4%
Center: 0.45 μm	5950	5150	-13.4%
Center: 0.35 μm	5450	4810	-11.7%
Edge: 0.6 μm	6450	5850	-9.3%
Edge: 0.45 μm	6450	5450	-15.5%
Edge: 0.35 μm	5600	5200	-7.1%

Table 5.4. Resist selectivity, uniformity, and lag performance of 2H-heptafluoropropane.

Etch Gas and Nominal Printed Dimension	Minimum Measured Resist Selectivity	Center to Edge Etch Rate Uniformity	Etch Rate Lag (0.6μm to 0.35μm)
2H: 0.6 μm	4.96	+4.5% C→E	Center: -14% decrease 0.6μm→0.35μm Edge: -11% decrease 0.6μm→0.35μm
2H: 0.45 μm	4.74	+5.8% C→E	
2H: 0.35 μm	4.52	+8% C→E	
C_3F_8: 0.6 μm	3.73	+3.2% C→E	Center: -12.8% decrease 0.6μm→0.35μm Edge: -13.1% decrease 0.6μm→0.35μm
C_3F_8: 0.45 μm	3.73	+8.4% C→E	
C_3F_8: 0.35 μm	3.23	+2.7% C→E	

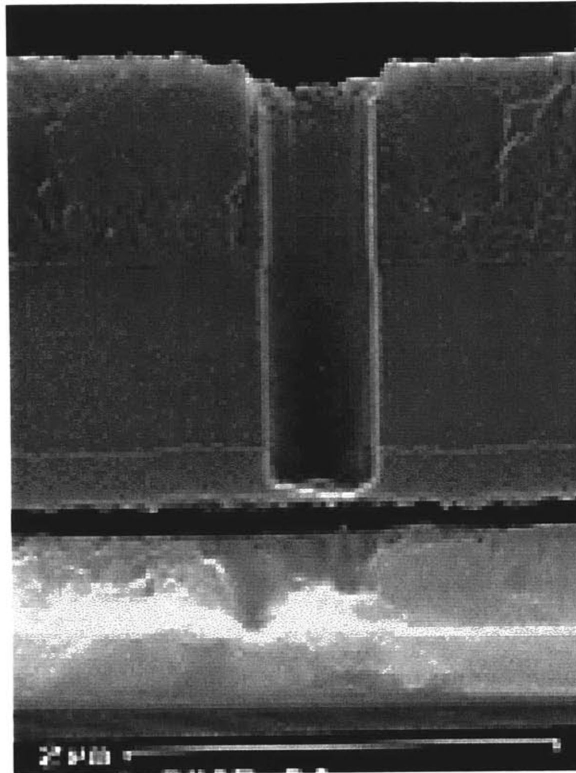

Figure 5.6: Selectivity of 2H-heptafluoropropane process to plasma-enhanced nitride. Films on the wafer are (top down): photoresist, TEOS oxide, nitride, and Cu metal. Oxide to nitride selectivity is approximately 1.4:1.

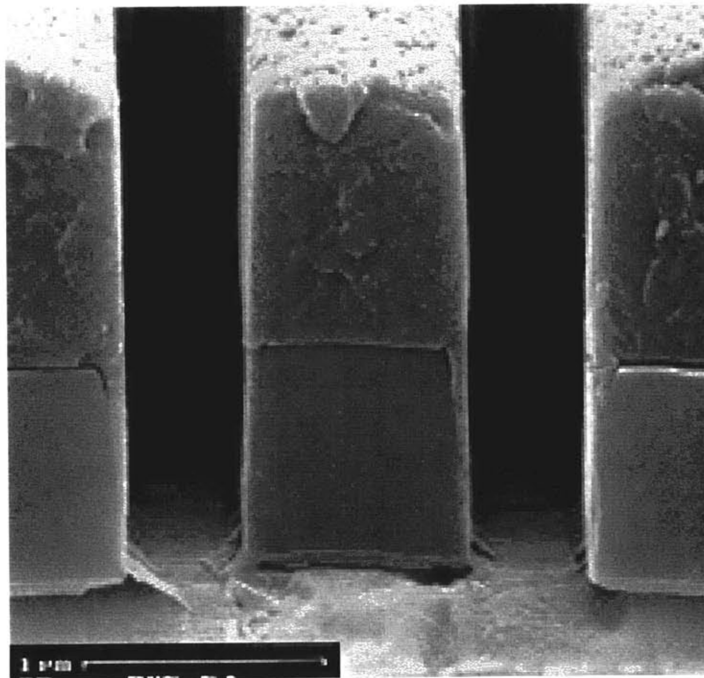

Figure 5.7: 2H-heptafluoropropane process stopping on Cu line.

Emissions measurements were performed for both the C_3F_8 process and the 2H-heptafluoropropane process using FTIR spectroscopy. All potential global warming gases in the effluent (C_3F_8, C_2F_6, CF_4, C_3F_7H, and CHF_3) were used in the kgCE calculation for each process. The decrease in the overall global warming emissions from the C_3F_8 process to the 2H-heptafluoropropane process was determined to be 42%. However, the emissions of CF_4, the longest-lived global warming gas in the atmosphere, were reduced by over 60% in the 2H-heptafluoropropane process.

The emission of hazardous air pollutants (HAPs) is also an issue to be considered with etch processes. Dramatically reducing the global warming emissions of a process while increasing the emission of HAPs trades one environmental problem for another. FTIR spectroscopy was used to quantify the emission of SiF_4 and HF from both the 2H-heptafluoropropane process and the C_3F_8 process. There was a decrease of 38 percent in the amount of SiF_4 produced in the 2H-heptafluoropropane process, relative to the equivalent C_3F_8 process. The HF emissions increased somewhat (20 percent) with the 2H-heptafluoropropane process. The emission of molecular fluorine could not be quantified because FTIR spectroscopy cannot detect homonuclear diatomics.

5.2.3 Conclusions

An oxide via etch process has been developed using 2H-heptafluoropropane that offers equivalent (or better, in some aspects) etch process performance to a typical C_3F_8 process with lower emissions of global warming gases. Etch rate, photoresist selectivity, anisotropy, critical dimension, and etch rate lag were all factors in evaluating the process performance of 2H-heptafluoropropane as parameters such as source power, bias power, etch gas flow rate, and temperature were varied.

The process developed operates in a standard regime for the Applied Materials Centura 5300 HDP chamber and can be considered as a drop-in replacement for C_3F_8 in this oxide via etch application. However, one hurdle presently blocking the implementation of 2H-

heptafluoropropane as an etch gas in manufacturing is its absence from the Toxic Substances Control Act (TSCA) list. Without TSCA listing, most manufacturing facilities will not approve the use of 2H-heptafluoropropane for etch processing. Although the etch process developed is both tool and chamber specific, it is likely that processes that demonstrate similarly good performance in combination with reduced emission of global warming gases can be developed using 2H-heptafluoropropane for oxide etch applications in a variety of high density plasma tools.

References

1. L. C. Pruette, S. M. Karecki, R. Reif, T. Sparks, L. Beu, and V. Vartanian, *High Density Plasma (HDP) Oxide Etching with Reduced Global Warming Emissions Using 2H-Heptafluoropropane*, in Proceedings of *Environmental Issues in the Electronics/Semiconductor Industries and Electrochemical/Photochemical Methods for Pollution Abatement*, San Diego, CA, C. R. Simpson, *et al.*, Editors, The Electrochemical Society Proceedings Series, **PV 98-5**, p. 58-62, Electrochemical Society, Pennington, NJ (1998).

5.3 Pentafluoroethane/1,1-difluoroethane Concept-and-Feasibility Study

In the work presented in this section, a combination of two hydrofluorocarbon compounds, pentafluoroethane (FC-125, C_2HF_5) and 1,1-difluoroethane (FC-152a, CF_2H-CH_3), was evaluated as a potential replacement for perfluorocompounds in dielectric etch applications. A high aspect ratio oxide via etch was used as the test vehicle for this study, which was conducted in a commercial inductively coupled high density plasma etch tool, an Applied Materials Centura 5300 HDP, described in detail in Section 3.4.2. Both process and emissions data were collected and compared to those provided by a process utilizing a standard perfluorinated etch chemistry (C_2F_6). Global warming (CF_4, C_2F_6, CHF_3) and hygroscopic gas (HF, SiF_4) emissions were characterized using Fourier transform infrared (FTIR) spectroscopy. FC-125/FC-152a was found to produce significant reductions in global warming emissions, on the order of 68 to 76% relative to the reference process. Although etch stopping, caused by a high degree of polymer deposition inside the etched features, was observed, process data otherwise appeared promising for an initial study, with good resist selectivity and etch rates being achieved.

Members of the hydrofluorocarbon family of compounds have seen use as etchants for some time. Trifluoromethane (FC-23, CHF_3), for instance, has been in widespread use in dielectric film applications for a number of years. Like various fully fluorinated gases, however, it has a significant GWP (14800). [1] Two carbon and higher HFCs, however, tend to have lower GWPs. A number of these compounds had been investigated in dielectric etch processes by both the author and his coworkers and by other researchers, including 1,1,1,2-tetrafluoroethane (FC-134a, CF_3-CH_2F) [2], 1,1,2,2-tetrafluoroethane (FC-134, CHF_2-CHF_2) [3], 1H- and 2H-heptafluoropropane (FC-227ea, CHF_2-CF_2-CF_3 and FC-227ca, CF_3-CHF-CF_3), and pentafluoroethane (FC-125, CF_3-CHF_2) [2]. These five compounds have GWP_{100} values of 1600, 1200, ~5000, 3800, and 3800, respectively. While these GWP values are still significant, HFCs such as these have much lower atmospheric lifetimes than their fully fluorinated analogues: the corresponding lifetimes for these compounds are 13.6, 10.6, 132, 36.5, and 32.6 years, respectively. [1, 4] The

GWP_{100} value and the atmospheric lifetime for 1,1-difluoroethane (FC-152a, CHF_2-CH_3) are 190 and 1.5 years, respectively. [1] The addition of FC-152a to an FC-125 etch process was suggested by preliminary work carried out in an ICP etch tool of a planar coil design. The work conducted in that study indicated that good oxide etch rate and good resist selectivity could be obtained using the FC-125/FC-152a combination at FC-152a content ranging from 0 to 20% of the etch gas flow. [5] The work discussed in Section 5.3 had been carried out in collaboration with DuPont Fluoroproducts as a follow-up study to the preliminary tests that had been presented in Ref. [5].

The discussion of this study is organized as follows: Section 5.3.1 discusses the experimental setup used. Section 5.3.2 provides a discussion of the experimental data. Within this section, Section 5.3.2.1 provides a discussion of known mechanisms in fluorocarbon etching in high density plasmas. This discussion is intended to serve as a follow up to the more general comments regarding basic mechanisms that was offered in Section 3.3. Sections 5.3.2.2 and 5.3.2.3 present a discussion of the process and emissions results from this study, respectively. Finally Section 5.3.3 offers conclusions regarding this study. The material in Section 5.3 is based on work published by the author and his coworkers in Ref. [6].

5.3.1 Experimental Setup

The Applied Materials Centura 5300 HDP etch tool used in the present study is described in detail in Section 3.4.2. In this study process and emissions data were collected. Two sets of experiments were carried out. The first was a screening experiment with patterned wafers, in which a pattern containing via arrays of 0.6, 0.45, and 0.35 μm nominal printed critical dimension (CD) was etched in TEOS (tetraethoxysilane)-deposited silicon oxide masked with a deep UV photoresist (~7580 Å thick, on average). The second set of experiments involved a 3-variable, 5-level central composite design (CCD) matrix (α = 2) in which wafers of a similar type as those used for the first matrix - TEOS oxide with deep UV photoresist (~1 μm thick, on average) - were etched. The second set of experiments also included some additional non-matrix experiments in which process

variables not included in the CCD matrix were varied. Cross-sectional scanning electron microscopy (SEM) was used to characterize the features etched in the first experiment. Cross-sectional SEM was also used to characterize the features etched in the second experiment; additionally, Fourier transform infrared (FTIR) spectroscopy was used in the second experiment to collect and quantify effluent data (for the CCD matrix portion only). As a reference point for both process and emissions data, a standard C_2F_6-based via etch recipe was also run.

The starting point for both sets of FC-125/FC-152a experiments was based on the reference C_2F_6 recipe, with an equivalent total flow of FC-125/FC-152a substituted for C_2F_6. The conditions for this reference recipe were as follows: 1600 W source power, 1400 W bias power, 25 sccm total etch gas flow, 100 sccm He, throttle valve at 50%, 240 °C roof temperature, 220 °C wall temperature, -10 °C chiller temperature, and 15 Torr backside He pressure. The 50% throttle valve setting corresponded to pressures of approximately 7 mTorr for these and all other FC-125/FC-152a processes. "Source power" refers to the inductively coupled power applied to the source antenna in the chamber, whereas "bias power" refers to the capacitively coupled power applied independently to the electrostatic chuck. "Roof temperature" refers to the temperature of the silicon slab which forms the top portion of the etch chamber. In the screening experiments (Stage I), two parameters were varied: total etch gas flow rate and amount of additive gas as fraction of total etch gas flow rate. With total etch gas flow held constant at 25 sccm, the fraction of FC-152a in the etch gas mix was set at 0, 10%, and 20%. Additionally, with the FC-152a fraction of the total etch gas flow held constant at 10%, total etch gas flow rate was set at 22, 25, and 28 sccm.

In the CCD matrix experiments (Stage II), the C_2F_6 recipe formed the basis for the center point of the matrix. The fraction of FC-152a at the center point of the CCD matrix was 5% (23.75 sccm FC-125, 1.25 sccm FC-152a). In these experiments, total etch gas flow (21, 23, 25, 27, 29 sccm), fraction of FC-152a (0, 2.5, 5, 7.5, 10 %), and source power (1400, 1500, 1600, 1700, 1800 W) were varied, with all other parameters held constant at the same values as those in the reference C_2F_6 recipe. The fraction of FC-152a in the etch gas mix was reduced from 0-20% to 0-10% on the basis of results obtained in the first set

of experiments, which indicated that 20% FC-152a at 25 sccm total etch gas flow did not offer additional improvement in photoresist selectivity while it led to excessive etch stopping (see below). The experimental points in the matrix were run in a randomized order. The center point in the matrix was run only once due to wafer availability constraints.

Table 5.5: Process conditions used in first stage of experiments. Bias power 1400 W, throttle valve setting 50%, roof temp. 240 °C, wall temp. 220 °C, chiller temp. –10 °C, He flow 100 sccm, backside He pressure 15 Torr, etch time 120 s.

Exp point #	Point type	Total flow (sccm)	% 152a	125 flow (sccm)	152a flow (sccm)	Source power (W)
1	25 sccm, 10%	25	10.0%	22.5	2.5	1600
2	25 sccm, 0%	25	0%	25	0	1600
3	25 sccm, 20%	25	20.0%	20	5	1600
4	28 sccm, 10%	28	10.0%	25.2	2.8	1600
5	22 sccm, 10%	22	10.0%	19.8	2.2	1600

Table 5.6a: Process conditions used in second stage of experiments (CCD matrix). Bias power 1400 W, throttle valve setting 50%, roof temp. 240 °C, wall temp. 220 °C, chiller temp. –10 °C, He flow 100 sccm, backside He pressure 15 Torr, etch time 120 s.

Exp point #	Point type	Total flow (sccm)	% 152a	125 flow (sccm)	152a flow (sccm)	Source power (W)
1	A (-2 0 0)	21	5.0%	19.95	1.05	1600
2	F (-1 -1 -1)	23	2.5%	22.425	0.575	1500
3	F (-1 -1 +1)	23	2.5%	22.425	0.575	1700
4	F (-1 +1 -1)	23	7.5%	21.275	1.725	1500
5	F (-1 +1 +1)	23	7.5%	21.275	1.725	1700
6	A (0 -2 0)	25	0.0%	25	0	1600
7	A (0 0 -2)	25	5.0%	23.75	1.25	1400
8	C (0 0 0)	25	5.0%	23.75	1.25	1600
9	A (0 0 +2)	25	5.0%	23.75	1.25	1800
10	A (0 +2 0)	25	10.0%	22.5	2.5	1600
11	F (+1 -1 -1)	27	2.5%	26.325	0.675	1500
12	F (+1 -1 +1)	27	2.5%	26.325	0.675	1700
13	F (+1 +1 -1)	27	7.5%	24.975	2.025	1500
14	F (+1 +1 +1)	27	7.5%	24.975	2.025	1700
15	A (+2 0 0)	29	5.0%	27.55	1.45	1600

Table 5.6b: Process conditions used in second stage of experiments (non-matrix experiments). Total flow 25 sccm, 5% 152a (23.75 sccm FC-125 flow, 1.25 sccm FC-152a flow), source power 1600 W, throttle valve setting 50%, chiller temp. –10 °C, He flow 100 sccm, backside He pressure 15 Torr, etch time 120 s.

Exp point #	Point type	Bias power (W)	Roof temp. (°C)	Wall temp. (°C)
16	1200 W bias	1200	240	220
17	1000 W bias	1000	240	220
18	Roof/Wall 220/210 °C	1400	220	210
19	Roof/Wall 200/200 °C	1400	200	200

Four additional wafers were also run as part of the second experimental set. Two were run at center point conditions for all parameters other than bias power, which was lowered from 1400 W to 1200 W and 1000 W, respectively. Two more wafers were run at center point conditions for all parameters other than the roof and wall temperatures, which were lowered from 240 °C roof / 220 °C wall to 220 °C roof / 210 °C wall and 200 °C roof / 200 °C wall, respectively. No FTIR data were collected on these wafers because global warming emissions were expected to exhibit the largest variation with etch gas flow rate, etch gas composition, and source power. In both stages of experiments, all processes used had an etch time of 120 s. All runs were preceded by an Ar/O_2 preprocess which was used to restore the chamber to a polymer free condition for the run to follow. The process conditions used for the two sets of experiments are listed in Tables 5.5 and 5.6a, b.

Quantitative emissions data were collected using an FTIR optical bench equipped with a heated 10 cm stainless steel absorption cell with zinc selenide windows and a mercury cadmium telluride (MCT) detector. The instrument was set up to sample the process effluent downstream of the dry mechanical pump backing the chamber turbopump. The pump purge flow rate was controlled at 45.0 standard liters per minute (slm) using a mass flow controller, whereas the flow rate through the sampling loop itself was set to be roughly 3.5 slm. The FTIR cell and a 25 ft. Teflon sampling line leading to it were heated to a target temperature of 121 °C. The target sampling pressure in the cell was 600 Torr. The compounds quantified in this study were CF_4, C_2F_6, CO, CO_2, COF_2,

CHF_3, HF, SiF_4, as well as FC-125 and FC-152a. C_2F_4 was also identified in the FTIR spectra, but was not quantified. Reference spectra for all species quantified by FTIR were generated on the same instrument at the same pressure and temperature conditions as those used for actual sampling. All data and reference spectra used in the analysis were collected at a resolution of 0.5 cm^{-1}. Multipoint calibrations, utilizing a certified gas mixture of each gas (nominally 1% in nitrogen) diluted with ultrapure nitrogen in varying ratios, were performed to ensure that the concentrations being sampled were within a linear range for that analyte. The global warming impact of each process was characterized by calculating the mass of carbon equivalent emitted by the process, using the kgCE (kilograms of carbon equivalent) metric defined in Section 5.1. For convenience, in the discussion which follows, emissions have been expressed in grams of carbon equivalent, rather than kilograms. The analysis of the FTIR data was carried out using commercially available software supplied by the manufacturer of the instrument. The software utilizes a classical least squares algorithm to interpret the spectral information collected by the FTIR spectrograph. This technique is acknowledged to perform very well in the case of compounds with overlapping spectral signatures. Figure 5.8 shows the FTIR spectra for FC-125 and FC-152a. The FC-125 and FC-152a material used in this study was supplied by DuPont Fluoroproducts, Wilmington, DE.

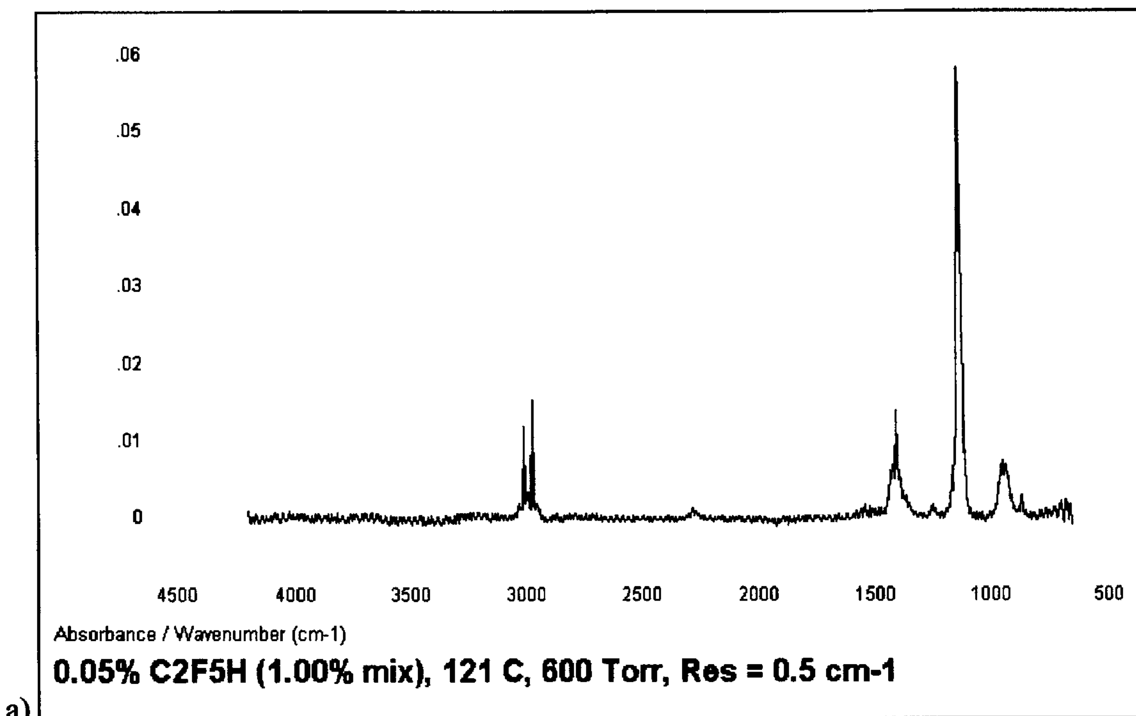

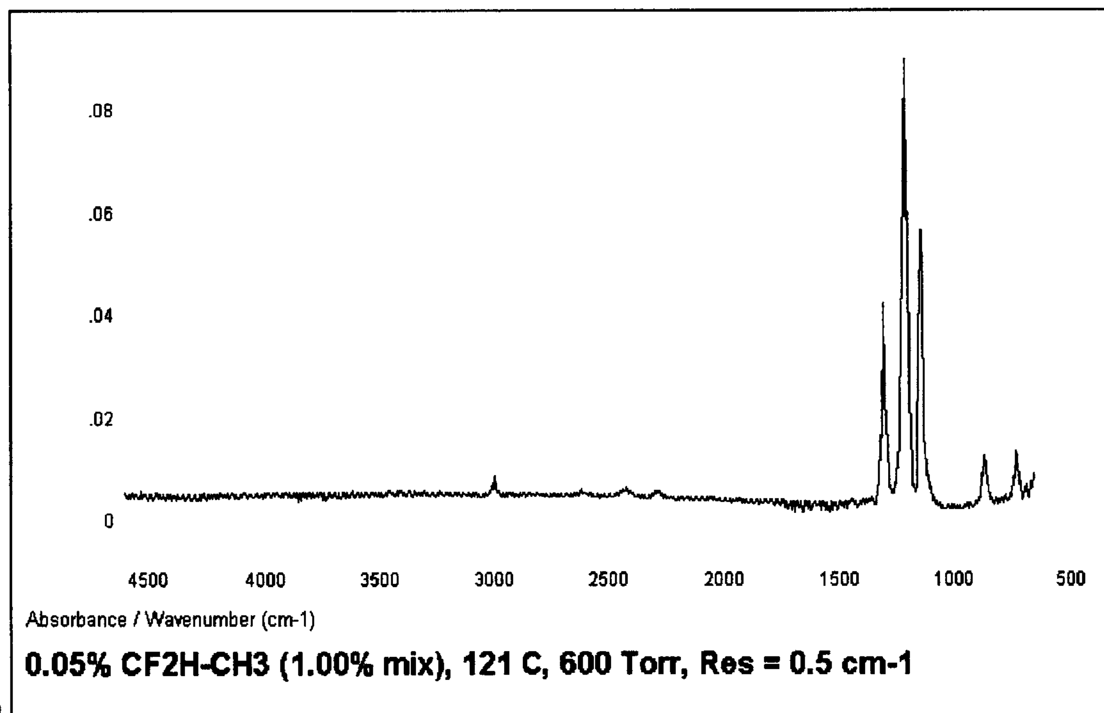

Figure 5.8: FTIR spectra of (a) FC-125, (b) FC-152a; spectra collected at 500 ppm using 10 cm cell (50 ppm-m nominal optical depth).

5.3.2 Results and Discussion

At this point in the discussion, it is useful to review some key aspects of fluorocarbon etching processes, in particular, those of critical importance in the discharges considered here.

5.3.2.1 Basic Mechanisms

Polymer formation. Well accepted models [7-9] state that the boundary between net etching and net deposition is a function of the F:C ratio present in the discharge, with higher F:C ratios favoring etching versus deposition. In practice, whether in fluorocarbon SiO_2 etch specifically or in fluorocarbon etch in general, it is known that discharges rich in atomic fluorine, on one end of the spectrum, tend to push the process away from deposition and into a net etch regime, while discharges rich in fluorine-deficient fluorocarbon fragments will favor the buildup of film. Some authors have pointed to gas-phase polymerization of C_xF_y chains as a potentially significant mechanism for polymer formation in fluorocarbon plasmas, even at low pressures. [10] Most workers, however, emphasize surface reactions involving CF_x species as having central importance in film building processes. In this framework, it is, in fact, often facile to view the products of fluorocarbon dissociation as either species that contribute primarily to net etching, *e.g.*, F, or species that contribute primarily to net deposition, *e.g.*, CF_x radicals in general [11] and CF [11] and CF_2, [11-14] in particular. The discussion is somewhat complicated by consideration of ionic versus neutral species. In low pressure, high density discharges, the ion flux can be a significant fraction of the neutral flux. [15] Some workers [12-14] point to the role played by the CF_3^+ ion in oxide etching, while others [11] draw attention to CF^+ and CF_2^+ ions as serving a role in decreasing the F:C ratio of the overall flux reaching the surface, hence playing an implicit role in promoting film formation. Alternatively, other authors [16, 17] cite evidence for CF_3^+ *and* CF_2^+ ions as contributing primarily to the etching of SiO_2 with CF^+ ions being characterized as serving the role of deposition precursors. While it is generally accepted that lower F:C ratio in the radical *and* ion fluxes reaching the wafer tends to promote polymer formation rather than net

etching, there is still considerable discussion regarding the roles of specific species, especially since those roles may themselves be chamber-dependent.

This picture, however, is incomplete without the understanding that the CF_x layer is significantly different under net deposition conditions than under net etch conditions. Under net deposition conditions, it has been observed that the film is predominantly CF_x and polymerlike. [18] However, on silicon-based surfaces in a net etch regime, the layer is seen to have more Si-F and Si-C groups and is significantly thinner [18], indicating that the etch occurs *through* a carbonaceous fluorosilyl reaction layer at the surface. The thickness of this layer has been described as being on the order of nanometers for Si surfaces and tenths of nanometers for SiO_2 surfaces. [19-21] The mechanisms by which this film is believed to impact the etch rates of various materials are complex, but a few general trends are readily discernable. Namely, it has been observed that, under net deposition conditions, the fluorocarbon film is fluorine deficient, while, under etch conditions, it is fluorine rich, [22] which is consistent with the F:C ratio model, as well as with observations by other workers that fluorine content tends to vary inversely with film thickness. [20] Film fluorine content and thickness are thus thought to be two of the key factors in the mechanisms considered here. (Under *net etch* conditions for resist, a similar reaction layer is believed to form on resist surfaces as well, incorporating carbon-based fragments of the resist surface rather than silicon.) Numerous process variables affect the properties of the fluorocarbon surface layer, often in complex ways. A key role, however, is played by ion bombardment, which, in the net etch regime, is instrumental in allowing for reactive mixing of arriving species with the top monolayers of the film being etched. [22]

A variant of this model [19-21] actually considers two surface layers: a fluorocarbon overlayer and, in the case of Si-based materials, an Si-F "silicon damage" or reactive mixing underlayer, which forms upon transition from net deposition to net etching. Moreover, interaction with the underlying film being etched can lead to considerable variation in the steady state thickness of the fluorocarbon layer. For instance, formation of CO or CN by abstraction of C from the film by oxygen in oxide films or nitrogen in

nitride films, respectively, can reduce the steady state thickness of the film. Such phenomena, in fact, are believed to serve a critical role in selectivity mechanisms between various films. A well known example is the role that oxygen released from SiO_x plays in forming volatile CO, CO_2, and COF_2 as it interacts with the CF_x layer, [8] thereby reducing the thickness of the fluorocarbon layer that forms on oxide surfaces while thicker layers are seen to form on Si or resist.

In sum, CF_x radicals formed in fluorocarbon plasmas are not necessarily cleanly divisible into "etching" versus "deposition" species. Species such as CF, CF_2, and CF_3, in this context, are thus not readily characterized as simply either etch or deposition precursors. Rather, in a deposition regime, they are generally all thought to contribute to the formation of the fluorocarbon layer in varying degrees; in a net etch regime, they contribute to both forming the film and supplying fluorine for the etch process.

Role of hydrogen. The presence of H in fluorocarbon plasmas can have important effects on the film formation mechanisms discussed above. It is a well established phenomenon that a principal role played by hydrogen in fluorocarbon plasmas is that of scavenging free fluorine through the formation of HF. [7, 22] Both gas phase and, more recently, surface [22] mechanisms for this reaction have been cited by various authors. (The reader is referred to Ref. [22] for a bibliography of the extensive early literature on the subject of hydrogen in fluorocarbon plasmas.) An important consequence of the scavenging mechanism is that increasing hydrogen content in the plasma is seen either to lower the F:C ratio of the deposited fluoropolymer, whether through gas phase or surface mechanisms, [22-24] or to defluorinate the CF_x film through HF formation within the film itself, [20] all of which are consistent with the observation that hydrogen addition drives the process toward conditions favoring net deposition versus net etching in fluorocarbon plasmas.

In hydrofluorocarbon plasmas, the fundamental mechanisms described above are believed to hold as well. There is evidence that the principal role of H in HFC plasmas is essentially similar. The amount of hydrogen incorporated into films deposited from HFC

or fluorocarbon/H_2 plasmas, as well as its effects on the film's F:C ratio can vary. [18, 20, 23, 25] However, it does appear that the fluorine scavenging mechanism, whether in the gas-phase, on the surface, or within the film itself, is of primary importance; consequently, films deposited from HFC or fluorocarbon/H_2 plasmas tend to posses predominantly CF_x, rather than CF_xH_y, stoichiometry and hydrogen incorporation is generally believed to be low relative to the stoichiometry of the feed gas.

Source power. It is generally expected that increasing power input in a plasma system increases the plasma density and hence the degree of dissociation in the feed gas. A greater degree of breakup of the feed gas is thus, to first order, expected to result in the production of more etchant species rather than deposition promoters. However, as had been noted earlier, radicals formed in fluorocarbon plasmas are not necessarily cleanly divisible into "etching" versus "deposition" precursors.

Additionally, source power input also has an effect on the ion bombardment energy seen by the wafer. In low density plasma systems – capacitively coupled parallel plate systems, in particular – the power applied to the plasma also increases the bias voltage across the plasma sheath at the wafer surface because of the capacitive nature of the coupling. In inductively coupled high density tools, while the bias voltage is controlled primarily by the bias power supplied to the wafer pedestal, the source power applied to the plasma also interacts with the bias voltage seen by the wafer, though in a more complex way. In general, increasing source power increases the ion generation rate in the plasma, resulting in a greater ion arrival rate at the edge of the sheath above the wafer. This, in turn, produces a higher ion current to the wafer. It has been shown that, with bias power fixed at a given level, an increase in ion current must result in a decrease in ion voltage at the wafer surface, [26] *i.e.*, an effect essentially opposite to that seen in capacitively coupled tools.

Other workers studying Si and SiO_2 etching using fluorocarbon and hydrofluorocarbon plasmas in an inductively coupled plasma (ICP) tool have also confirmed that a significant effect of increasing source power in an ICP tool is an increase in ion current

density. They also note that, despite higher atomic fluorine concentrations seen in the plasma, increasing source power leads to greater defluorination of the fluorocarbon film being deposited, *i.e.,* a lowering of its F:C ratio. [19-21] This, in turn, is observed to correspond to thicker polymer deposits. These mechanisms are consistent with observations by other authors [15] who note that, because the ionization potential for F (~17 eV) is higher than those for CF and CF_2, the F:C ratio of the ion flux is lower than that of the neutral flux. They give the ionization thresholds of CF and CF_2 as ~14 and ~12.7 eV, respectively. (Other workers have published lower CF_x ionization threshold values: 9.4, 11.5, and 8.9 eV for CF, CF_2, and CF_3, respectively [27, 28].) If the ion flux represents a significant fraction of the overall flux reaching the wafer, as is believed to be possible in high density systems, then conditions which generate high ion/neutral flux ratios will favor the formation of carbon rich CF_x layers.

Bias power. The bias voltage, *i.e.,* the voltage present across the plasma sheath at the wafer surface, directly affects the energy with which positive ions impinge on the surface of the wafer. Increasing bias power in an ICP tool such as the one used here, however, increases not only the bias voltage but also the ion current density at the wafer. The former relates directly to the intensity of the physical sputtering component of the etch, as well as to the amount of energy supplied to the film surface per arriving ion, while the latter directly affects the ionic fraction of the total flux arriving at the wafer.

As had been discussed earlier, higher ion flux fraction is believed to result in a lower F:C ratio in the total flux arriving at the wafer and hence contributes to the formation of thicker, defluorinated CF_x films. Increasing bias voltage has the principal effect of reducing the thickness of the CF_x layer. It has also been shown, however, that increasing bias voltage *also* results in defluorination of the film, [19] believed to be due to enhancement of the rate of formation of volatile F-containing products as ion energy increases. However, this effect, which in earlier discussion had been associated with regimes in which CF_x layer thickness *increases* and the process moves away from etching toward deposition, appears to be secondary. The dominant effect is that of net decrease in CF_x film thickness. [19]

In sum, increase in bias power in etch tools like the one considered in this work causes several competing effects: on one hand, the resulting increase in ion current density causes a decrease in the F:C ratio of the arriving flux, a mechanism associated with polymer formation enhancement. On the other hand, the increase in ion voltage which also occurs is *also* seen to cause defluorination of the CF_x film. However, whereas the former mechanism is consistent with net *increase* in CF_x film thickness, because of an increase in carbon content of the arriving species, the latter is consistent with a net *decrease* in film thickness, because it is based on an increase in the removal rate of fluorine from the film, *i.e.,* an increase in CF_x etch rate. Since the removal of F from the CF_x layer is believed to take place primarily through the formation of species such as CF_4, it is readily apparent that an increase in CF_x etch rate results in the removal of more fluorine than carbon. The effect which generally dominates is, in fact, this last mechanism – CF_x etch rate enhancement and hence a reduction in the CF_x film thickness – which occurs as a result of an increase in the supply of energy available to form volatile CF_4 and related etch products and/or an increase in the physical sputtering component of the etch.

Temperature of chamber surfaces. Higher temperature on chamber surfaces leads to lower sticking probabilities for adsorbing species in general, and polymer forming precursors in particular. Since the *production* of these polymerization precursors is believed to be dependent primarily on plasma, rather than surface, conditions, comparable quantities are believed to be generated from the feed gas at all surface temperatures. However, since elevated temperature at chamber surfaces tends to keep them less heavily coated, the polymer precursors that do not deposit on the surfaces of the chamber must either be exhausted or coalesce on another surface. In the ICP system used for this work, since the chuck is maintained at a temperature that is significantly lower than that of the roof/walls, it is believed that, at higher roof/wall temperature, polymer precursors are available in greater quantity to deposit on the wafer surface, rather than elsewhere in the chamber.

There is evidence in literature that the above described process is precisely what is observed in ICP systems. See Ref. [29] and references therein. Deposition of CF_x polymer on chamber surfaces is found to decrease as the temperature of those surfaces is increased. In fact, at high enough temperatures, net polymer removal is observed. Optical and mass spectrometric results indicate that this lowering of condensation rates on chamber surfaces has the expected effect of increasing the availability of CF_x species in the plasma. In conjunction with this, a decrease in F concentration in the plasma is observed, as more fluorine is consumed by reaction with Si-based reactor surfaces, now protected by thinner polymer deposits. This is, moreover, consistent with the observation that the lifetime of the Si/quartz process kit used in ICP systems of the type used in this work can be extended by operation at lower roof/wall temperature.

5.3.2.2 Process Results

Table 5.7 shows selected highlights from the process results from both the first and second stage of experiments. Figures 5.9 and 5.10 show 0.35 μm (nominal printed CD) vias etched using FC-125/FC-152a processes. Figure 5.9 shows the best experimental point in the initial set of experiments (Stage I, Run I-2), whereas Figure 5.10 shows the best experimental point in the CCD matrix (Stage II, Run II-3). As Figure 5.10 indicates, FC-125/FC-152a is capable of achieving very good selectivity to photoresist (for many runs, several times higher than that of the reference process) as well as good etch rate (the target depth for this 120 s process was 1 μm). Moreover, good anisotropy is also attainable. However, as can be seen in the center location micrograph in Figure 5.9, etch stopping (buildup of polymer at the bottom of the via resulting from a transition from net etching to net deposition with increasing aspect ratio) has been found to occur under a number of the conditions tested. Figure 5.11 shows 0.35 μm (nominal printed CD) vias etched by the C_2F_6 reference process for comparison.

Table 5.7: Process results from selected runs. Bias power 1400 W, throttle valve setting 50%, roof temp. 240 °C, wall temp. 220 °C, chiller temp. –10 °C, He flow 100 sccm, backside He pressure 15 Torr, etch time 120 s. C = wafer center, E = wafer edge.

Exp point #	Point type	Total flow (sccm)	% 152a	125/C_2F_6 flow (sccm)	152a flow (sccm)	Source power (W)	0.35 μm etch rate (C) (Å/min)	0.35 μm etch rate (E) (Å/min)	0.35 μm PR sel. (C)	0.35 μm PR sel. (E)
Stage I, 2	25 sccm, 0%	25	0%	25	0	1600	5800	6350	9.9	4.5
Stage II, 3	F (-1 -1 +1)	23	2.5%	22.425	0.575	1700	5290	5300	14.9	3.2
Stage II, 8	C (0 0 0)	25	5.0%	23.75	1.25	1600	3923	5700	13.4	7.8
*	C_2F_6 Ref.	25	-	25	-	1600	6150	7650	3.6	3.1

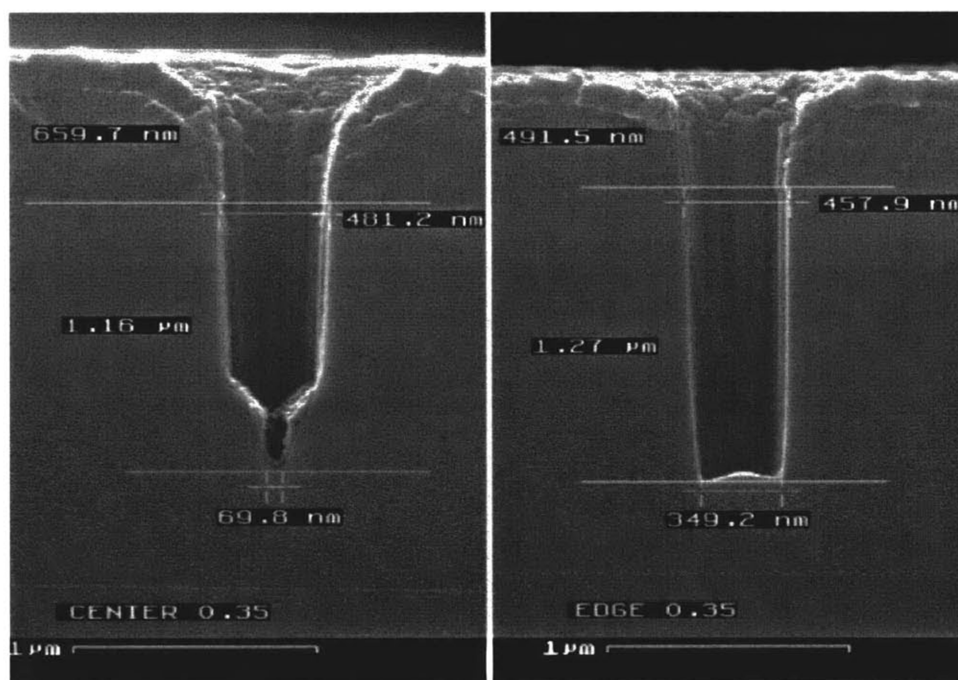

Figure 5.9: Best process point from initial matrix (Stage I Run I-2, 25 sccm, 0% 152a), 0.35 μm nominal printed CD.

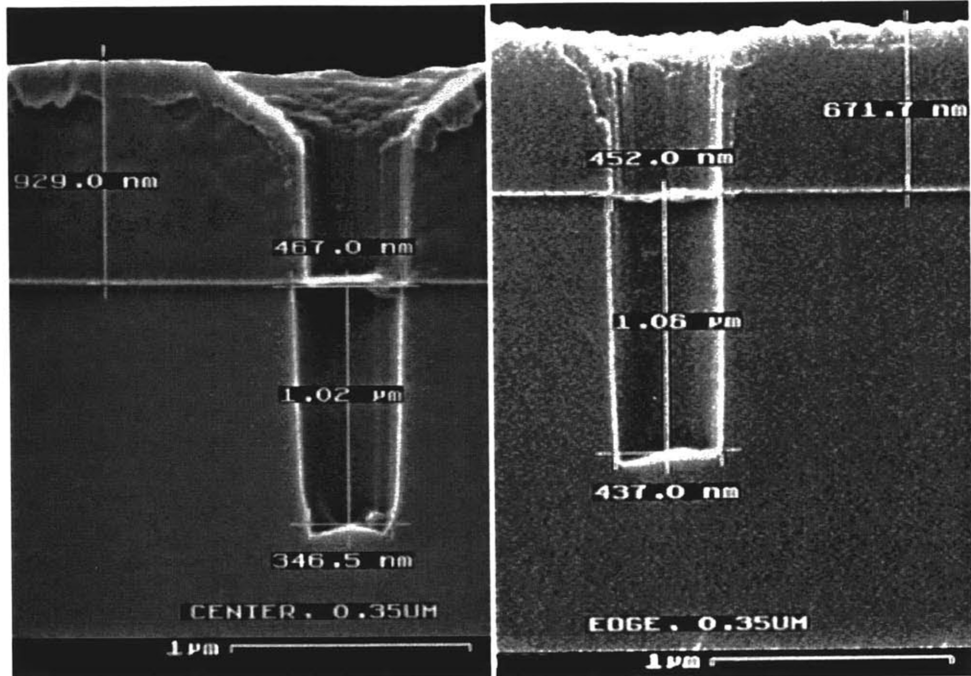

Figure 5.10: Best process point from CCD matrix (Stage II Run II-3, 23 sccm, 2.5% 152a, 1700 W), 0.35 µm nominal printed CD.

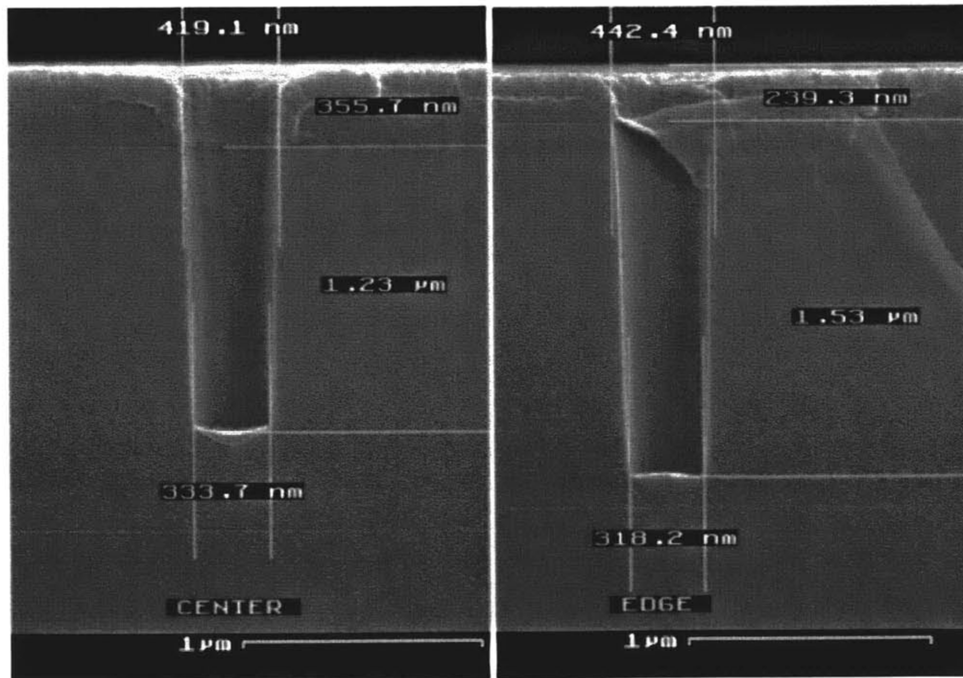

Figure 5.11: C_2F_6 reference process, 0.35 µm nominal printed CD.

Process Trends, Stage I. Figures 5.12a-c and 5.14a-c show the trends seen in the Stage I experiments, plotting TEOS oxide etch rate, thickness of photoresist eroded, and photoresist selectivity as a function of total flow and % 152a, respectively. Resist eroded has been defined as T_i - T_f, where T_i is the initial (pre-process) thickness of resist measured at a center or edge die location by reflectometry and T_f is the final (post-process) resist thickness measured near a given feature by cross-sectional SEM. Photoresist selectivity has been defined as the ratio of oxide etch depth in a given feature to the thickness of resist eroded near that feature.

Figure 5.12a shows the TEOS oxide etch rate as a function of increasing total etch gas flow rate. The etch rate is generally seen to increase as total etch gas flow rate increases from 22 to 28 sccm, suggesting that the process is occurring in a regime limited by supply of etchant species. The significant exception to this trend is the center of wafer point at 0.35 μm, for which the etch rate is seen to drop substantially at 28 sccm of flow. As the SEM data indicated, this etch rate dropoff is indicative of the onset of etch stopping and a transition into a deposition regime within the feature. Supporting evidence for this is seen at 0.45 μm for 28 sccm, where the center etch rate is also lower than the edge etch rate. At all other data points, center and edge etch rates are very close. Thus, increasing total etch gas flow generally increases the TEOS oxide etch rate, but it also appears to increase the rate of polymer formation, which is evident in the center of the wafer, as etch stopping begins to occur in smaller (0.35 μm) features while the etch rate continues to increase in larger (0.6 μm) features, with the 0.45 μm vias exhibiting intermediate behavior. The observations made here are consistent with those made by other workers who have studied the etch stop phenomenon in an ICP tool of the same type as the one used in this work [30] and who also observe a higher propensity toward etch stopping in features with higher aspect ratio, *i.e.,* smaller CD. They explain the effect as being caused by a power density loss – a decrease in both ion density and ion energy – at the bottom of the features being etched as the etch proceeds. This loss, which is believed to result from sidewall charging effects, causes a shift from net etching toward net deposition at the bottom of the feature. This power density loss, moreover, causes significant changes in the F:C ratio of the film being deposited at the feature bottom, with

feature bottom, with greater defluorination occurring under conditions of greater ion bombardment. [30] At the edge of the wafer, the transition into a deposition regime is not as pronounced, suggesting that polymer deposition rate is higher in the center than at the edge. As will be discussed below, this hypothesis is supported by measurements of thickness of photoresist eroded.

Figure 5.12b shows the thickness of photoresist eroded near a feature of each size at both the center and edge locations as a function of total flow. Since the amount of resist eroded is expected to be independent of feature size near the measurement location, any discrepancies between values given for different feature sizes at the same location are thus likely to stem from local variations and/or measurement error. It appears that the amount of resist eroded reaches a minimum around 25 sccm. Such behavior may stem from the interaction of two competing effects: increase in availability of etchant species with increasing flow rate and increase in polymer formation with increasing flow rate. The effect of the former would be to increase the etch rate of all materials being etched on the wafer (namely, not only oxide but photoresist as well), whereas the effect of the latter would be to decrease the resist etch rate by suppression of etching through deposition of polymer on the wafer surface. The data seen in Figure 5.12b suggest then that, as one moves from 22 to 25 sccm total etch gas flow, the latter effect (enhancement of polymerization) dominates, but also that this trend reverses itself, with the former effect (increase in etchant availability) dominating as one continues to increase the etch gas flow past 25 sccm.

It should be noted that the effects seen in Figures 5.12a and 5.12b are not attributed to residence time effects in this regime, because, with the total flow (etch gas and diluent) dominated by 100 sccm of He and with the pressure ~7 mTorr for all conditions, the residence time was nearly constant in all experiments (calculated to be ~89 ms).

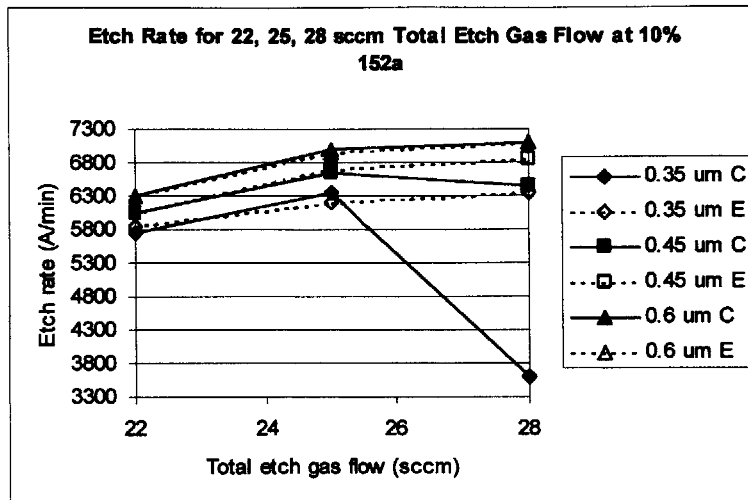

a)

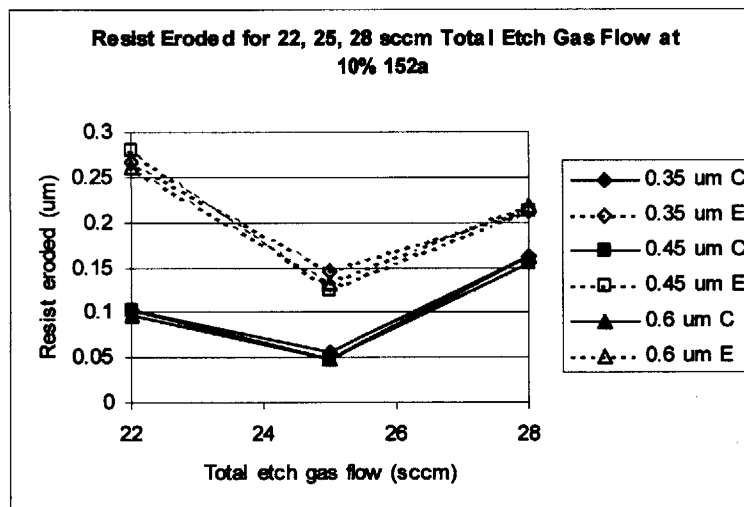

b)

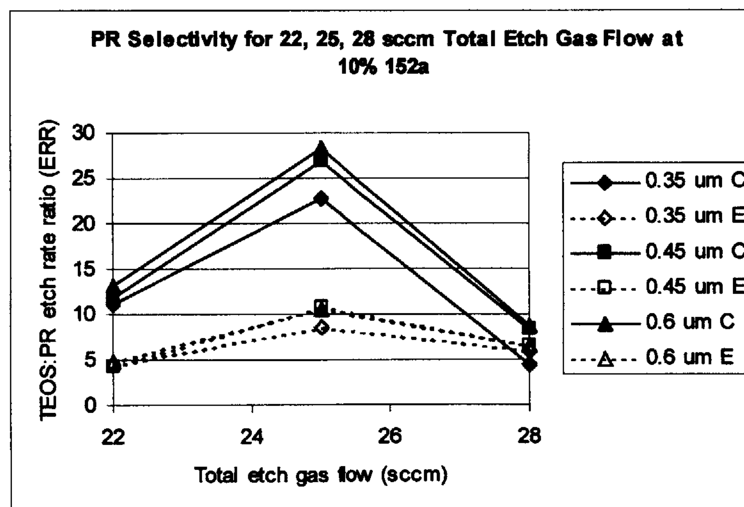

c)

Figure 5.12: Stage I results – a) oxide etch rate, b) resist eroded, and c) oxide:resist selectivity vs. total etch gas flow at 10% 152a, 1600 W source power.

One also notes that the amount of resist removed at the edge of the wafer is higher than the amount removed in the center for all conditions and feature sizes. This again suggests that polymer deposition rate may be higher in the center of the wafer than at the edge. This is consistent with the earlier observation that, at 28 sccm, etch stopping begins to occur in small features in the center of the wafer, but not at the edge.

Figure 5.12c plots the TEOS oxide:photoresist selectivity as a function of total etch gas flow rate, which is defined as the ratio of TEOS oxide etch rate within the feature to bulk photoresist etch rate near that feature. Figure 5.12c therefore captures the combination of the effects seen in Figures 5.12a and 5.12b. Not surprisingly, the selectivity is highest at the 25 sccm condition. Moreover, selectivity is significantly higher in the center of the wafer than at the edge for all three feature sizes, which follows directly from the earlier observation that thickness of photoresist eroded at the edge is consistently higher than in the center.

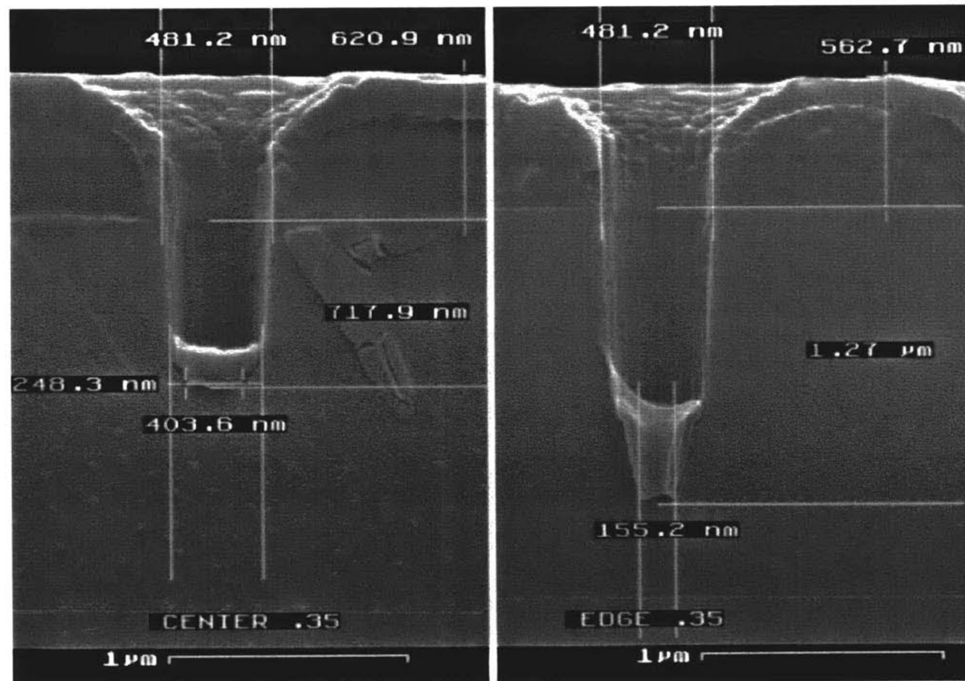

Figure 5.13: Stage I Run I-4, 28 sccm, 10% 152a, 0.35 μm nominal printed CD.

Finally, a significant amount of polymer deposition was observed inside most of the features. At 0.35 μm, only at the edge location in Run I-5 (22 sccm) is an acceptable profile obtained, indicating that, at higher flows, excessive polymerization leads to etch stopping; even at 22 sccm, etch stopping is still seen to occur in the center of the wafer. It should be pointed out that only the 22 sccm, 10% 152a condition (Run I-5) and the 25 sccm, 0% 152a condition (Run I-2) offer an acceptable profile at 0.35 μm and even here only at the edge location, suggesting that increasing total flow or increasing % 152a leads to excessive polymer formation inside small features. Note the convex profile of the bottom of the feature for Run I-2 (edge). This profile is indicative of the etch proceeding without the onset of etch stopping. Once polymer deposition begins to dominate etching at the bottom of the via, the profile becomes increasingly more concave, after which the feature begins to fill with polymer (see, for instance, center location of Run I-4, Figure 5.13) or a highly tapered profile develops (see, for instance, edge location of Run I-4, Figure 5.13). While larger features also exhibit polymer deposits, the issue is most pronounced at 0.35 μm, as one would expect. These observations are, again, consistent with the power density loss mechanism outlined earlier.

Figure 5.14a shows the TEOS oxide etch rate as a function of % 152a at a constant total etch gas flow rate of 25 sccm. For most features, from 0 to 10%, there appears to be little effect on etch rate, with perhaps a slight drop seen at some feature sizes/locations; above 10%, however, the etch rate is seen to decrease more visibly. This dropoff is, in all likelihood, due to an increase in polymer formation with higher FC-152a content in the input gas mix. It had earlier been noted that the addition of hydrogen to feed gas chemistry in fluorocarbon plasmas results in the scavenging of free fluorine through HF formation, typically resulting in enhanced fluorocarbon film deposition rates. Since the hydrogen content of FC-152a is higher than that of FC-125 and the fluorine content lower, it is not surprising that higher % 152a results would result in more polymerization and the associated suppression of etching. As can also be seen from SEM micrographs for 0, 10, and 20% 152a, respectively, higher % 152a indeed appears to result in more polymer deposition inside the vias, bringing the process closer to the onset of early etch stopping. The data point which appears to be an exception to the above trend is the 0.35

μm center point, where the etch rate is seen to be lower at 0% 152a than at 10%, in contrast with the other data series in Figure 5.14a. However, the presence of significant amounts of deposit inside all the 0.35 μm features in the center location makes accurate via depth measurement difficult in some cases and is probably responsible for the discrepancy seen here.

Figure 5.14b shows the thickness of photoresist eroded near a feature of each size at both the center and edge locations as a function of % 152a. (Again, since the amount of resist eroded is expected to be independent of feature size near the measurement location, any discrepancies between values given for different feature sizes at the same location are thus likely to stem from local variations and/or measurement error.) From 0% to 10% 152a, the amount of resist eroded decreases significantly, as would be expected with higher polymer deposition due to the presence of more hydrogen-containing species. In this regime, HF scavenging is believed to result in a fluorine-deficient and thicker CF_x layer on the resist surface, in accordance with the mechanisms discussed earlier. Again, one sees more resist erosion at the edge of the wafer than in the center, suggesting that more polymer deposition occurs in the center than at the edge, which is consistent with observations made above.

What is interesting, however, is that at 20% 152a, the amount of resist removed is higher than at 10%. As was observed above, as % 152a increases, polymer deposition inside the feature increases as well, but it appears that this increase does *not* correlate with an increase in polymer formation on the *bulk* of the resist film, which is believed to be the primary mechanism responsible for slowing the erosion of the bulk resist. As would be later confirmed in Stage II (see Figure 5.16), it appears that high percentages of FC-152a lead to more etch stopping, but also, surprisingly, more resist erosion.

a) 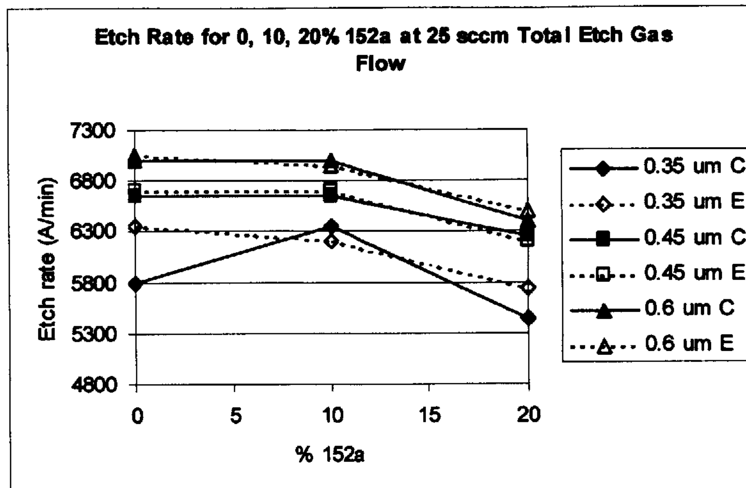

b) 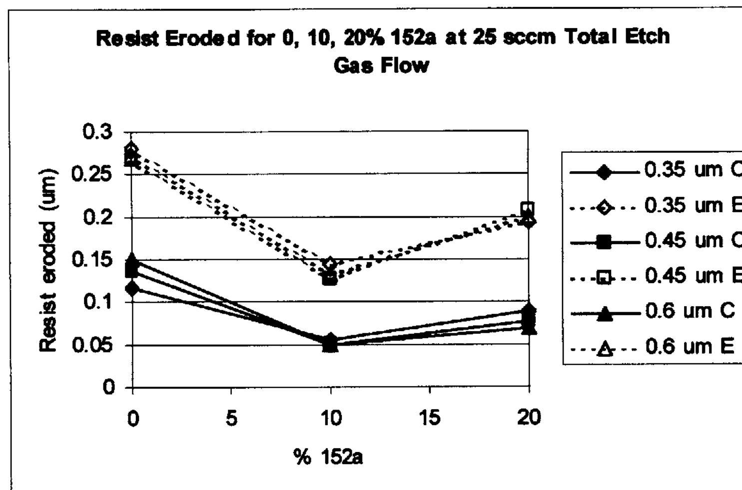

c) 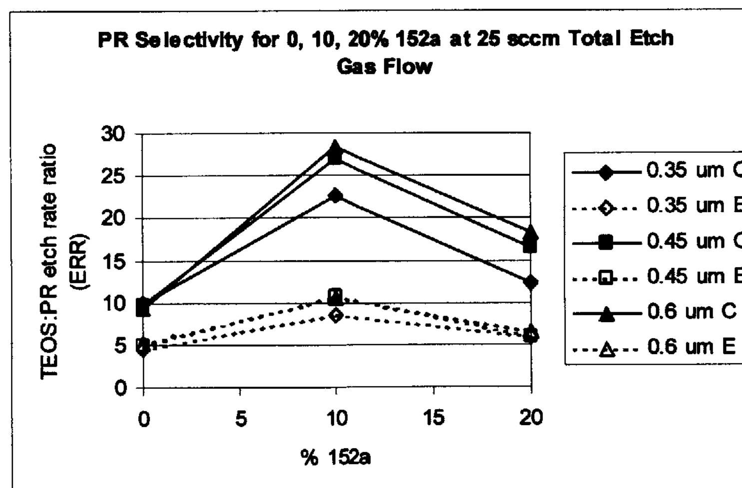

Figure 5.14: Stage I results – a) oxide etch rate, b) resist eroded, and c) oxide:resist selectivity vs. % 152a at 25 sccm, 1600 W source power.

Prima facie, this result appears to be somewhat unexpected, given the well known effect hydrogen typically has on polymer formation rate. However, the assumption that lowering the F:H ratio in the feed gas chemistry, while keeping the C input constant, monotonically increases film formation rate may need to be examined more carefully. The data suggest that, in this regime, the presence of excess hydrogen contributes negatively to film formation. This hypothesis stems from the observation that the higher flow rate of FC-152a in Run I-3 does not appear to compensate for the lower flow of FC-125 in terms of bulk polymer formation rate. (For this experimental point, the FC-125 flow is only 20 sccm.) There is, in fact, evidence in the literature that indicates that the amount of CF_2 adsorption and the rate of polymer deposition from a fluorocarbon precursor is *lower* in an Ar/H_2 plasma than in an Ar plasma. [31] The authors interpret their finding in terms of a reduction in the sticking probability of CF_2 radicals on a fluorocarbon film where a significant portion of the surface sites is becoming passivated by H, resulting in a decrease of adsorptive sites available to the CF_2 radicals. Since the thickness of the fluorocarbon layer is considered to be a primary determinant in the etch rate of the material beneath it [19-21], one is led to believe that, in this regime, the excess hydrogen leads to a retardation in film deposition rate on photoresist, resulting in a lower steady state thickness as well, and that this effect now offsets the positive effect on film formation that F scavenging by H is typically observed to have. It is also reasonable to suggest that, for the above reasons, FC-125 may be a more effective polymer forming gas than FC-152a in hydrogen rich regimes, and that, under such conditions, as FC-152a content is increased, one observes an effect associated with the reduction of the flow of the principal source of polymer precursors.

Inside the feature, on the other hand, polymer formation continues to be enhanced as % 152a is increased, as initially expected. This therefore suggests that significantly different conditions exist in the plasma at the surface and inside the features, namely, that power density is significantly lower at the bottom of the features versus the surface, favoring deposition rather than net etch.

Figure 5.14c plots the TEOS oxide:photoresist selectivity as a function of % 152a. Again, since Figure 5.14c captures the combination of the effects seen in Figures 5.14a and 5.14b, the selectivity is highest at the 10% 152a condition. And again, selectivity is significantly higher in the center of the wafer than at the edge for all three feature sizes, which follows directly from the earlier observation that thickness of photoresist eroded at the edge is consistently higher than in the center.

Finally, as had been pointed out in the earlier discussion, the only experimental condition out of the three being discussed presently that had an acceptable via profile at 0.35 μm was the 0% 152a condition (Run I-2). Higher % 152a appears to result in more polymerization inside the vias, leading to etch stopping and profile degradation for the smaller features (0.35 and 0.45 μm). Even at the 0% 152a condition, however, the process is still highly polymerizing in the center of the wafer. Consequently, the 0.35 μm center feature experiences pronounced etch stop, as can be seen in Figure 5.9.

Process Trends, Stage II. Figures 5.15a-c, 5.16a-c, 5.17a-c, 5.18a-c, and 5.19a-c below show the trends seen in the Stage II experiments, respectively plotting TEOS oxide etch rate, thickness of photoresist eroded, and photoresist selectivity as a function of total flow, % 152a, source power, bias power, and temperature. For the wafers used in Stage II, a T_i of 1 μm was used for all resist erosion data. Here, photoresist selectivity has been defined as the ratio of oxide etch depth in a given feature to the thickness of resist eroded at that location on the wafer *averaged* over the three measurements made (one near a feature of each size). The error bars in the plots of resist eroded versus a process parameter (b graphs) are defined as the standard deviation of the three measurements of resist eroded (one near a feature of each size) at each of the two locations on the wafer. The error bars in the plots of photoresist selectivity versus a process parameter (c graphs) are defined as the standard deviation of three selectivity values for each feature size at each location, each calculated using one of the three measurements of resist eroded per location. One can clearly see that very high values of selectivity (several tens to one) tend to have a correspondingly large error associated with them, which stems from the

error associated with measurements of very small amounts of resist erosion. For clarity, error bars in the selectivity graphs are shown for only the 0.35 μm and 0.6 μm series.

A comparison of Figures 5.15 and 5.16 (effects of total etch gas flow rate and % 152a in Stage II) with Figures 5.12 and 5.14 (effects of total etch gas flow rate and % 152a in Stage I) shows essentially the same behavior in the case of oxide etch rate, though somewhat different trends for resist eroded and oxide:resist selectivity. Figure 5.15 shows the effect of varying total etch gas flow rate from 21 to 29 sccm at 5% 152a, while Figure 5.12 shows the effect of varying the flow rate from 22 to 28 sccm at 10% 152a, with all other parameters the same (1600 W source power, 1400 W bias power, 240°C/220°C roof/wall temperature). Thus, other than the somewhat expanded range for total etch gas flow rate covered in Stage II, the principal difference between the two regimes is the 152a fraction. It was observed earlier that increasing total etch gas flow generally increased etch rate as well as polymerization rate, until the latter effect began to dominate inside the features, resulting in etch stopping – see Figure 5.12a. It was also noted that this transition tended to occur earlier (*i.e.,* at lower total flow) for smaller features. Additionally, because polymer formation was observed to proceed more rapidly in the center, rather than at the edge, of the wafer, this transition was seen to occur earlier in the center. As Figure 5.15a indicates, all these trends are borne out in the Stage II data as well. (It appears, moreover, that at lower % 152a the process is more sensitive to the effect of total flow rate. Whereas, in Stage I, the onset of etch stopping was seen to occur strongly only at the 0.35 μm center of wafer location at the high flow condition, in Stage II, it is seen much earlier.) Thus, for 0.6 μm edge features, oxide etch rate continues to increase from 25 to 29 sccm total etch gas flow, the onset of etch stopping not yet having been reached. On the other hand, at 0.35 μm center, oxide etch rate is already dropping off as total etch gas flow is increased from 21 to 25 sccm. 0.35 μm edge, 0.45 μm, and 0.6 μm center features exhibit intermediate behavior, as is expected.

In Figure 5.15b, the amount of resist eroded generally tends to decrease as total etch gas flow increases. The values shown are averages of measurements taken near 0.35, 0.45, and 0.6 μm features. Earlier, it was suggested that increasing total etch gas flow rate is

likely to have two competing effects: increase in availability of etchant species and increase in polymer formation, with the effect of the former being to increase the etch rate of all materials being etched on the wafer (including photoresist) and the effect of the latter being to decrease the resist etch rate by suppression of etching through deposition of polymer on the wafer surface. In keeping with the mechanisms proposed earlier, it appears therefore that the latter effect is dominant at the 5% 152a condition, in contrast to the mixed trend seen at a 10% 152a condition in the Stage I data (see Figure 5.12b).

Figure 5.15c shows the photoresist selectivity as a function of total etch gas flow. The average resist eroded values used in Figure 5.15b were also used here. One sees that, generally speaking, selectivity increases monotonically with total flow rate from 21 to 25 sccm. Above 25 sccm, selectivity continues to increase for features at the center location; at the edge, it continues to increase for large features and decreases for small features. Since Figure 5.15c reflects a composite of the trends seen in Figures 5.15a and 5.15b, it can be assumed that, in this regime, where the selectivity is seem to increase with total etch gas flow, the dominant effects are those of suppression of resist erosion due to enhanced polymerization and/or increase in oxide etch rate due to a greater supply of etch species; on the other hand, where a dropoff in selectivity is seen, these effects must be insufficient to compensate for earlier etch stopping at higher flows. It should be noted that, because the amount of resist erosion is, in general, very small in this regime and selectivity is expressed as a ratio of oxide and resist etch rates, small errors in measurement of resist remaining will translate to large errors in the numerical value of the selectivity metric. What is most important to note here is perhaps the fact that high selectivity values are readily attainable throughout the parameter space explored. It should also be pointed out that "infinite" photoresist selectivity is not necessarily desirable if it is accompanied by the poor profile control and lowered etch rate and/or etch stopping.

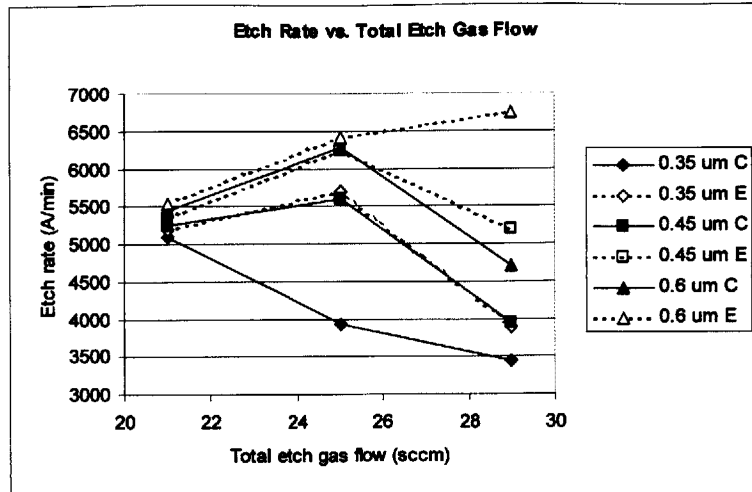

a)

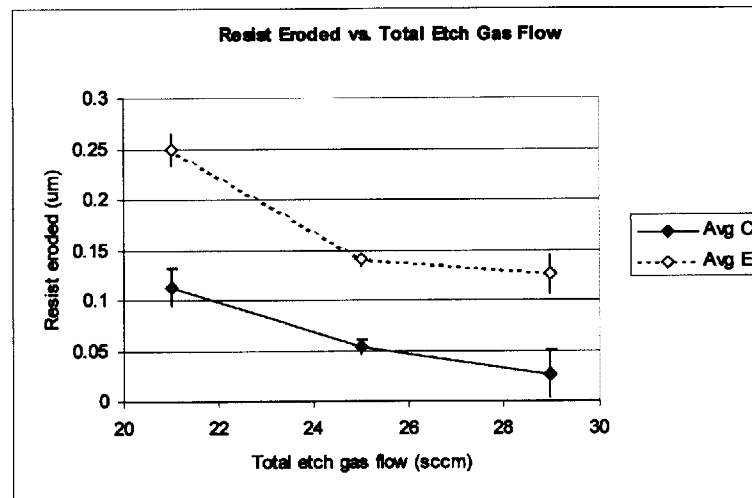

b)

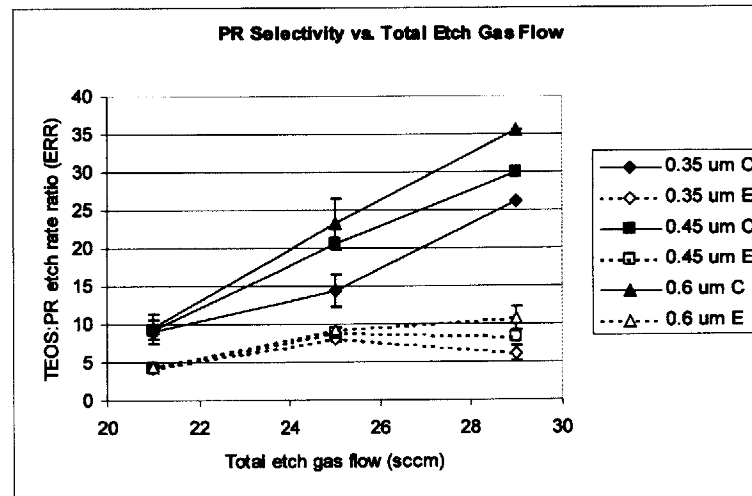

c)

Figure 5.15: Stage II results – a) oxide etch rate, b) resist eroded, and c) oxide:resist selectivity vs. total etch gas flow at 5% 152a, 1600 W source power.

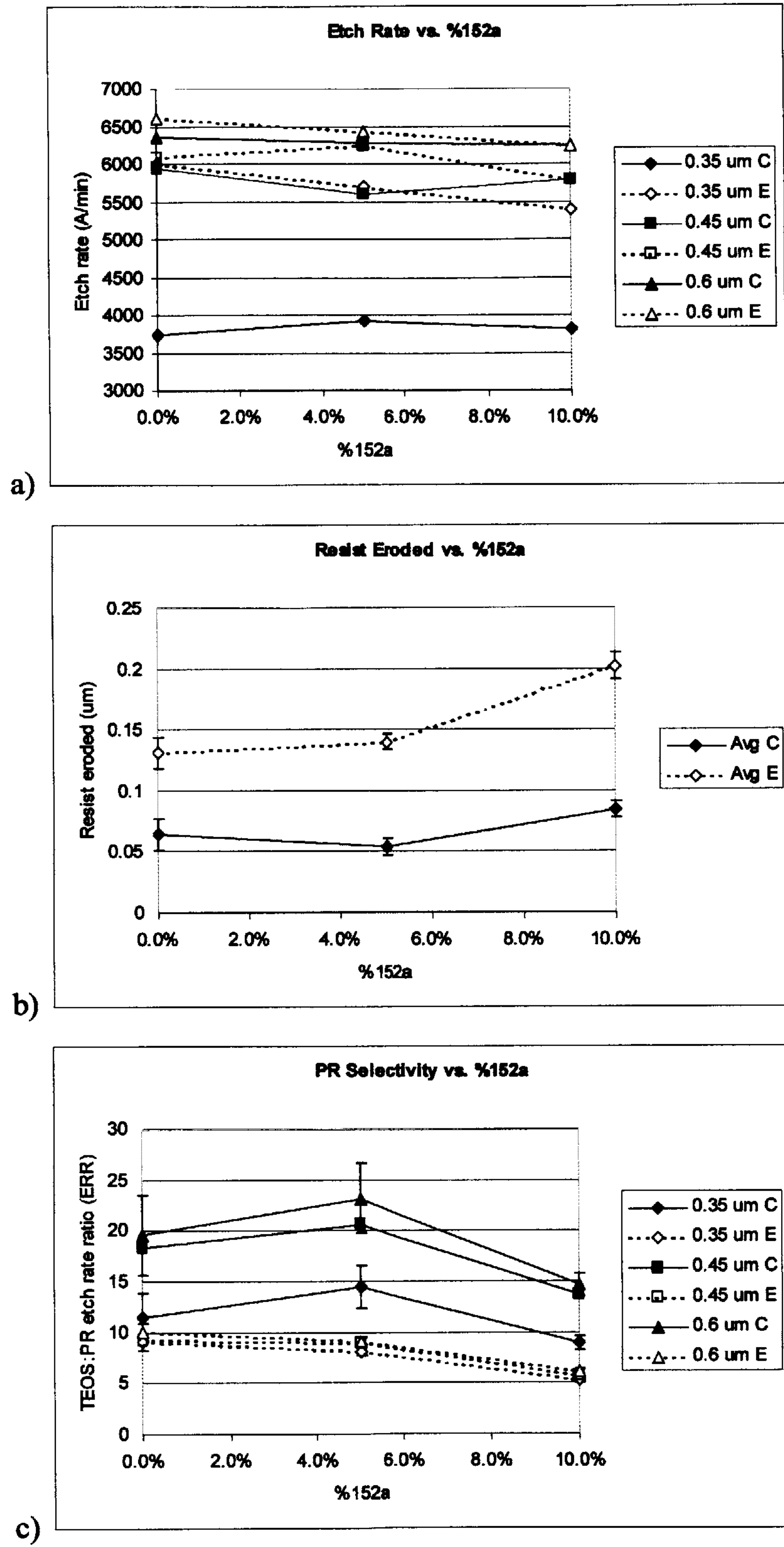

Figure 5.16: Stage II results – a) oxide etch rate, b) resist eroded, and c) oxide:resist selectivity vs. % 152a at 25 sccm, 1600 W source power.

Finally, there is a general tendency toward greater etch stopping, and thus poorer profile, with increasing flow rate. At 21 sccm (Run II-10), a good etch profile at 0.35 μm is seen at the edge of the wafer, while in the center of the wafer, past a certain depth, the etch proceeds only in the very center of the feature, with polymer buildup suppressing etching near the walls of the feature. As one moves to 25 sccm (Run II-8), the center location profile of the 21 sccm condition is now seen at the edge of the wafer, while in the center, the etch has stopped everywhere in the bottom of the feature. At 29 sccm (Run II-15), one sees this profile at both the center and edge locations, reflecting complete etch stop everywhere on the wafer. At this condition, the measured 0.35 μm etch depth at the center location is lower than that at the edge, which is lower still than the depth at the center location at 25 sccm. These findings are thus entirely consistent with the mechanisms proposed earlier, with greater polymer deposition on the surface correlated closely with the etch stop phenomenon inside the vias and with both effects most pronounced in the center location of the wafer and the latter most evident at smaller geometries.

Figure 5.16 shows the effect of varying % 152a from 0 to 10% at 25 sccm total etch gas flow, while Figure 5.14 shows the effect of varying % 152a from 0 to 20% at 25 sccm total etch gas flow, with all other parameters the same (1600 W source power, 1400 W bias power, 240°C/220°C roof/wall temperature). Thus, the data shown in Figure 5.16 essentially covers half the range covered by the data in Figure 5.14. It was observed earlier that increasing % 152a over the range 0% to 10% increased polymerization rate, though not etch rate, leading to greater resist selectivity but also to earlier etch stopping. Above 10% 152a, the amount of resist eroded, however, appeared to *increase*, despite the fact that more polymer deposition inside the vias was observed.

Figure 5.16a shows the TEOS oxide etch rate as a function of % 152a at a constant total etch gas flow rate of 25 sccm. For some data series (0.35 μm center, 0.45 μm center, 0.45 μm edge), the trend is mixed; for the others, however, there is a dropoff in etch rate as % 152a increases. This decrease is not surprising, since increasing % 152a is believed to reduce the amount of atomic fluorine available (both through reduction of FC-125 flow

and HF scavenging) and increase the amount of polymer deposition inside the vias, as was noted earlier. In all cases, however, the effect is not very pronounced. It should be noted that Run 6 in Stage II and Run 2 in Stage I, which were run at the same conditions (25 sccm total etch gas flow, 0% 152a), do not yield the same process results, with a greater degree of polymer formation (as evidenced by earlier etch stopping and less bulk resist erosion) seen in the Stage II result. The same is true for Run 10 in Stage II and Run 1 in Stage I, which were also run at the same conditions (25 sccm total etch gas flow, 10% 152a). One difference between these experiments was that a number of FC-125/FC-152a wafers were run in the chamber between the two Stage I wafers and the two Stage II wafers being discussed presently. During these experiments, the chamber was operated in a "clean" mode, with O_2/Ar preprocess steps being run between wafers (the intent of which was to restore the chamber to a clean condition between every wafer). The apparent process drift seen between Stage I and Stage II, however, may be evidence that the clean which was employed was inadequate to sufficiently clean the chamber with this highly polymerizing chemistry. It may be the case then that further use of this chemistry in a process tool such as the one used in the study will require a more effective cleaning process, possibly a longer one.

Figure 5.16b shows the amount of resist eroded as a function of % 152a at 25 sccm total etch gas flow. It was earlier noted that, in the Stage I data, one was able to discern an initial decrease in the amount of resist eroded (as % 152a increased from 0% to 10%), followed by an increase in resist eroded (as % 152a increased from 10% to 20%). See Figure 5.14b. The results plotted in Figure 5.16b do not follow the same initial trend, with little effect seen at the edge location and with an apparent slight increase in the amount of resist eroded in the center. There is, however, a marked increase in resist loss above 5% 152a, just as there was one in the Stage I data above 10%, *i.e.*, one common trend evident in both sets of data is that, after a point, increasing the percentage of FC-152a in the feed gas results in a *greater* degree of resist erosion. (As was noted above, the results from the 0% 152a and 10% 152a conditions are not the same in Stage I and Stage II.)

The reason for the difference in process behavior at low FC-152a percentages between the two sets of experiments is not immediately apparent. Figure 5.14b, however, suggests that, as % 152a increases, there is a transition from a regime where the increase initially results in lower resist erosion (attributed to a thicker and less fluorinated steady state fluorocarbon layer on the resist surface) to one where the increase causes greater resist erosion (attributed to H passivation of surface sites otherwise available for CF_x polymer building). In Figure 5.16b, if it is assumed that the same mechanisms are at work, one sees that the inflection in the trend has already been reached below 5% 152a and that the behavior seen between 10% and 20% 152a in Stage I is now seen between 5% and 10% in Stage II. Similarly, the earlier comparison of the 0% and 10% data points in Stage I and Stage II also indicated that a shift in the process window had occurred between the two sets of experiments – a shift that could essentially be interpreted as process behavior which was seen at higher FC-152a percentages now being seen at lower FC-152a percentages. This shift was probably caused by a change of chamber condition (*i.e.,* the presence of polymer in the chamber). Thus, it seems reasonable to suggest that the likely presence of additional polymer in the chamber in Stage II had resulted in elevated concentrations of species which would otherwise be present at higher % 152a, namely H or H-containing species. Additional work is likely to be required before this effect is fully understood.

Figure 5.16c shows the photoresist selectivity as a function of % 152a at 25 sccm total etch gas flow. Below 5% 152a, selectivity at the edge location appears to decrease somewhat, while selectivity in the center of the wafer appears to increase. Again, these apparent trends are simply the cumulative effect of the trends seen in Figures 5.16a and 5.16b. However, it should be pointed out that the center of wafer resist eroded trend below 5% 152a was not judged to be defინititive. (Note error bars in Figures 5.16b and 5.16c.) Above 5% 152a, selectivity decreases for both center and edge locations, largely because of the increase in resist erosion in that regime – an effect that was also observed in Stage I above 10% 152a.

All the features in this series (Run II-6 at 0% 152a, Run II-8 at 5%, and Run II-10 at 10%) suffer from etch stopping, with more etch stopping taking place at the center rather than edge of the wafer. Moreover, the 0.45 μm and 0.6 μm SEMs indicate that the etch stop phenomenon becomes significantly less pronounced as feature size increases, as is expected. The SEMs of the 0.45 μm edge and the 0.6 μm features at the 10% 152a condition, for instance, do not show any indications of etch stopping, in keeping with the observed trend with respect to feature size and location. On the other hand, the 0.35 μm center and edge and 0.45 μm center features all show evidence of etch stopping, with more polymer buildup seen at the bottom of the via at 5% and 10% 152a than at 0%.

Figure 5.17 shows the effects of varying source power from 1400 W to 1800 W at 25 sccm total etch gas flow, 5% 152a, 1400 W bias power, and 240°C/220°C roof/wall temperature. In the discussion that follows, the effects of source power on oxide and resist etch rate will be treated in terms of the interplay between the effects of increasing source power outlined earlier: increased ion flux and its consequences, increased feed gas dissociation and fluorine generation, and decreased bias voltage at the wafer.

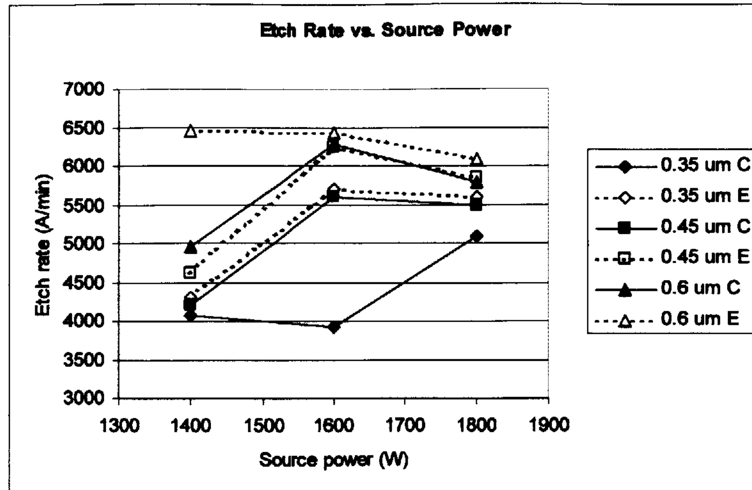

a)

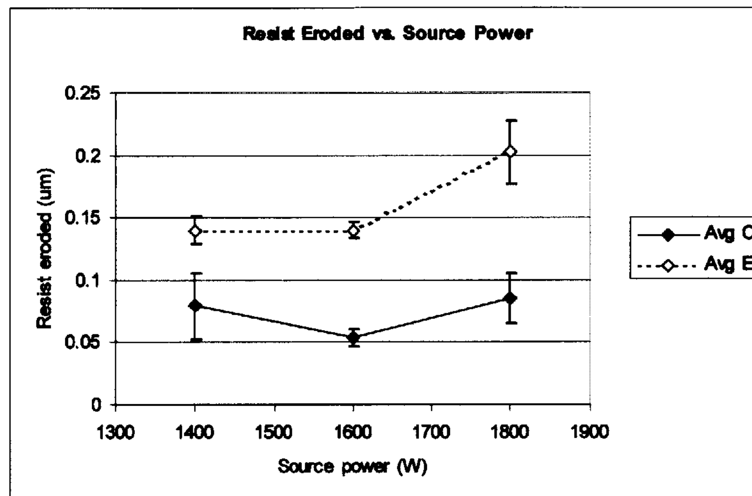

b)

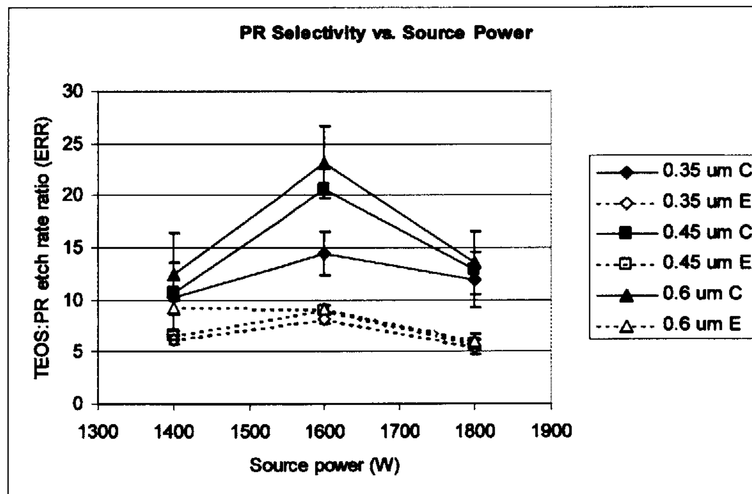

c)

Figure 5.17: Stage II results – a) oxide etch rate, b) resist eroded, and c) oxide:resist selectivity vs. source power at 25 sccm, 5% 152a.

A comparison of Figure 5.17a with Figure 5.16a (effect of total etch gas flow) shows roughly the opposite trend with respect to an increase in control variable. At this point in the analysis, it has become well established that the vias etched in these experiments span a continuum of susceptibility to early onset of etch stop, ranging from 0.35 μm center as the most prone to etch stop to 0.6 μm edge as the least prone. Figure 5.17a suggests that features that are most prone to etch stop do not experience an increase in oxide etch rate until relatively high source power is applied. As one moves across the continuum of feature size/location from 0.35 μm center to 0.6 μm edge, the increase in etch rate occurs earlier, *i.e.,* at lower source power (0.35 μm edge, 0.45 μm center). Further along this continuum, one notices an inflection in etch rate, with an initial increase, followed by a decrease at higher source power (0.45 μm edge, 0.6 μm center). Finally, at 0.6 μm edge, one sees that etch rate starts out high at low source power and drops off at high source power. This suggests that the transition point seen around 1600 W for the 0.35 μm edge and 0.45 μm center data series may be present at powers greater than 1800 W for features more susceptible to etch stop and at powers less than 1400 W for features less susceptible to etch stop.

Figure 5.17b shows the amount of resist eroded as a function of source power in the same regime. At the edge location, the amount of resist eroded is roughly constant from 1400 W of source power (Run II-7) to 1600 W (Run II-8), whereas it actually appears to decrease in the same regime in the center location. This decrease may be an artifact of the measurement error, however. (Note that the spread in resist eroded as measured near three different features at the center location is relatively large at 1400 W.) On the other hand, between 1600 W and 1800 W (Run II-9), the amount of resist loss increases significantly at both wafer center and wafer edge.

It appears that, under the conditions in these experiments, the dominant mechanism is the greater degree of dissociation in the feed gas and the increased availability of fluorine as an etchant for both the oxide and the resist, rather than the increase in ion flux with its accompanying decrease in ion energy and shift toward lower overall flux F:C ratio. This conclusion is reached because the trends seen in Figures 5.17a and 5.17b are consistent

with a general shift further into the etch regime for both oxide and resist and a move away from the deposition regime, resulting in an increase in etch rate for both the oxide and the resist layer. This is consistent with the observation that the SEM micrographs show progressively less etch stopping as one moves from 1400 W to 1800 W. Increased fluorine availability with higher source power is also likely in light of a consideration of the ordering of bond strengths in the hydrofluorocarbon molecules introduced in the feed gas. The strength of the H-C_2F_5 bond in FC-125 is given as 429.7 kJ/mol (4.45 eV per bond); the strength of the H-CF_2CH_3 bond in FC-152a is 416.3 kJ/mol (4.32 eV); estimates of the C-C and C-F bonds in these molecules can be obtained from the CF_3-CF_3 and F-C_2F_5 bonds in C_2F_6, which are 413.0 kJ/mol (4.28 eV) and 530.5 kJ/mol (5.50 eV), respectively. [32] Thus C-F bonds require more energy to break than C-C or C-H bonds, which has also been pointed out by other workers. [13, 14, 33] Although average electron temperature does not necessarily increase strongly with source power in ICP reactors, electron density does. [34] Consequently, the population of electrons energetic enough to break the C-F bond is expected to be larger at higher source power, providing a mechanism for more atomic fluorine generation from the same feed gas composition.

As the figures indicate, however, actual process behavior is somewhat more complex here than what can be explained simply by an increase in fluorine concentration with higher source power. The dependence on feature size/location (*i.e.,* correlation with etch stop susceptibility) again supports the suggestion that the power deposition characteristics (and hence the F:C ratios in the film) inside the features may be significantly different from those seen by the wafer surface. Features that are more susceptible to etch stop (*e.g.,* 0.35 μm center) appear to require more source power to shift the balance further away from deposition toward etch, which is consistent with the idea that local conditions inside those features are, to begin with, more favorable to deposition than the conditions that exist, for instance, inside 0.6 μm edge vias.

A possible reason for the dropoff in etch rate at high power for features that are less susceptible to etch stop, on the other hand, may be the decrease in ion bombardment energy that results from the drop in bias voltage with higher source power discussed

earlier. For these features, it is likely that the etch process is less heavily influenced by feature-scale effects like sidewall charging phenomena and the resulting lowering of both local ion density and ion energy; instead, larger features are likely to be more influenced by more macroscopic effects, such as the lowering of ion energy while ion density over the entire wafer increases with source power. Further work is required before the details of this phenomenon are fully understood, however.

An important phenomenon that has received only partial treatment in earlier discussion is the center-to-edge effect seen in all experimental runs with all feed gas compositions. It has been pointed out that the amount of polymer formation is higher in the center than at the edge. More generally, oxide etch rate as well as resist erosion rate are, as a rule, higher at the wafer edge than in the center as well, an observation consistent with ones made by other workers using the same type of etch tool [30]. These effects are believed to stem from the fact that the wafer edge has greater proximity to the source antenna coil in the dome of the chamber. This geometry effect results in higher local plasma density at the wafer edge. This, in keeping with the mechanisms discussed above, results in a greater degree of dissociation of the feed gas, favoring the generation of atomic fluorine, in all likelihood at the expense of CF_x and related deposition species. Additionally, work done by other authors in a different ICP system at pressures similar to the ones seen here (6 mTorr) suggests that polymer deposition in the center of the wafer is more likely because the center is farther away from the heated walls of the chamber. Thus species that leave the chamber wall are more likely to reach the edge of the wafer than the center without undergoing gas phase collisions. [29] (The mean free path at ~7 mTorr, the approximate chamber pressure in the FC-125/FC-152a experiments, is on the order of 1-2 cm, depending on assumptions made about the average molecular diameter of the species in the plasma and the neutral temperature in the discharge, which is, in any event, less than the distance from the chamber wall to the center of a 200 mm wafer.)

Figure 5.17c plots oxide:resist selectivity as a function of source power. Below 1600 W, the selectivity, being a combination of the effects seen in Figures 5.17a and 5.17b, generally improves, except for the 0.6 μm edge data series, since, in most cases, the etch

rate generally improves. The increase in selectivity is more pronounced in the center. Above 1600 W, regardless of the trend in oxide etch rate, the dominant effect appears to be the increase in resist erosion, presumably due to larger fluxes of atomic fluorine assumed to be present with higher source power, resulting in a net decrease in selectivity.

There appears to be a general improvement in profile with increasing source power. This improvement can probably be attributed to suppression of polymer deposition inside the feature as conditions shift away from favoring deposition to favoring net etching with increasing abundance of atomic F and with higher power density. This is supported by analysis of the SEMs, which indicates that, once again, vertical profiles are attainable under conditions where etch stop polymerization and excessive sidewall coverage can be suppressed, which appears to be easier to achieve under higher source power.

Figure 5.18 shows the effects of varying bias power from 1000 W to 1400 W at 25 sccm total etch gas flow, 5% 152a, 1600 W source power, and 240°C/220°C roof/wall temperature. Figure 5.18a plots the dependence of the oxide etch rate against bias power. It can be seen that reducing bias power from 1400 W to 1000 W decreases the oxide etch rate in a nearly linear manner for all features, which, to first order, can be readily attributed to decreases in both ion voltage (hence ion energy) and ion current that are known to occur with decreasing bias power. Lower ion energy, in particular, can unambiguously be linked to a reduction in the physical sputtering component of the etch. A comparison of SEM micrographs for Runs II-17 (1000 W), II-16 (1200 W), and II-8 (1400 W) also suggests that another reason for the increase in etch rate with bias power is suppression of polymer formation inside the feature, a mechanism consistent with the earlier discussion of bias power effects. At the 1400 W condition, the 0.35 μm edge feature exhibits continued etching in the center of the via and polymer buildup near the sidewalls. This pattern, also noted earlier in a number of the other features in this study, has been observed earlier to be an intermediate stage between a progressing etch and total etch stop.

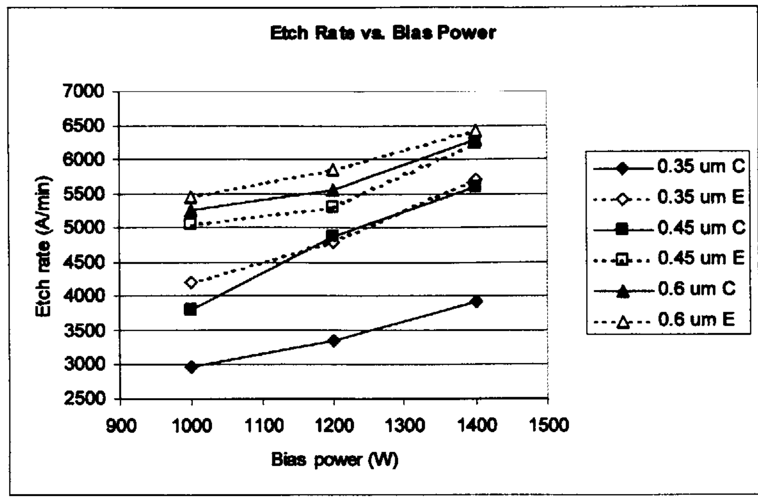

a)

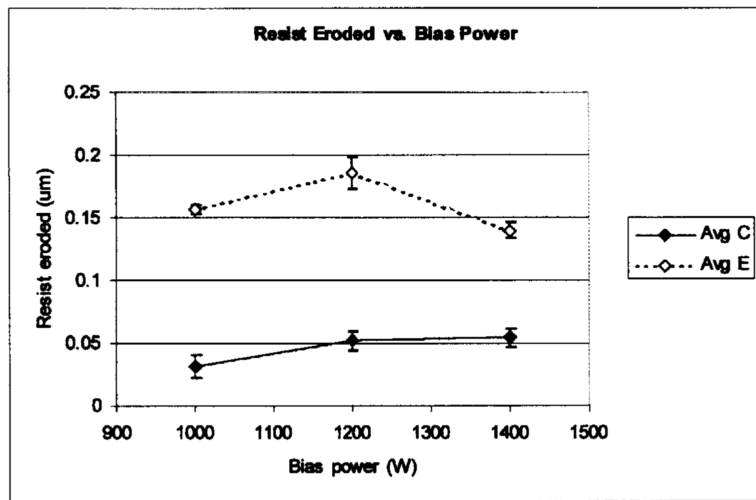

b)

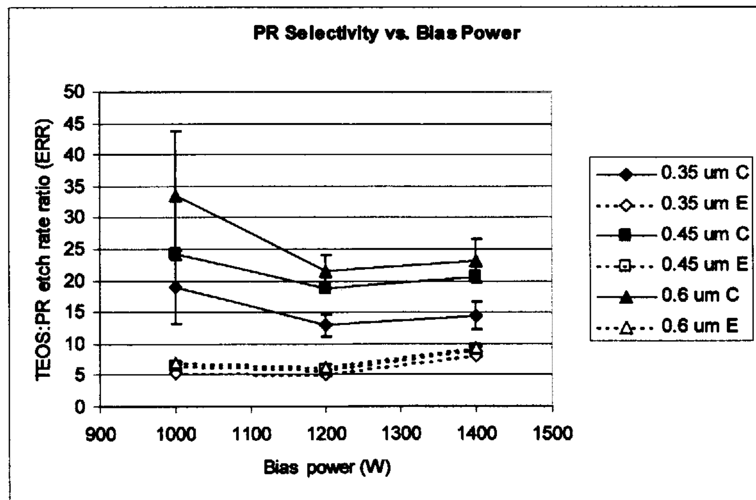

c)

Figure 5.18: Stage II results – a) oxide etch rate, b) resist eroded, and c) oxide:resist selectivity vs. bias power at 25 sccm, 5% 152a, 1600 W source, and 240/220 °C roof/wall temperature.

Figure 5.18b plots the amount of resist eroded versus bias power. If the dominant effect is the increase of CF_x film etch rate, leading to a thinner CF_x layer on all surfaces, the expected trend would be a monotonic increase in resist eroded as a function of bias power. This is observed below 1200 W and, to a lesser extent, between 1200 W and 1400 W at the center location, but not between 1200 W and 1400 W at the edge. The reason for this departure from expected behavior is perhaps due to the fact that the increase in ion flux that also results from bias power increase itself promotes the formation of C-rich polymer, due to a lowering of the F:C ratio in the arriving flux (see earlier discussion). It is reasonable to suggest then, that between 1200 and 1400 W bias, this effect becomes more pronounced and partially (in the center) or totally (at the edge) offsets the CF_x etch rate enhancement caused by the increase in ion bombardment energy.

Figure 5.18c plots the oxide:resist selectivity as a function of bias power. This parameter can either increase or decrease with bias, depending on whether the increase in oxide etch rate or the increase in resist etch rate is more pronounced. Neglecting the ion flux effect discussed above, one expects that, at *high* bias settings, a larger component of the etch will be physical and, since physical sputtering rates of different materials on the wafer are likely to be similar, one consequently expects a net decrease in selectivity at high bias. Here, however, one sees a trend toward *increasing* selectivity above 1200 W. Since the slopes of the oxide etch rate curves (Figure 5.18a) are similar between the 1000 W – 1200 W range and the 1200 W – 1400 W range, the reversal in the selectivity trend may largely reflect the increased importance of ion flux increase in this regime and its effects on resist etch rate.

Finally, as is expected, increasing bias power appears to result in slightly more vertical profiles, which is consistent with the increase in the physical sputtering component which is, of course, highly, directional.

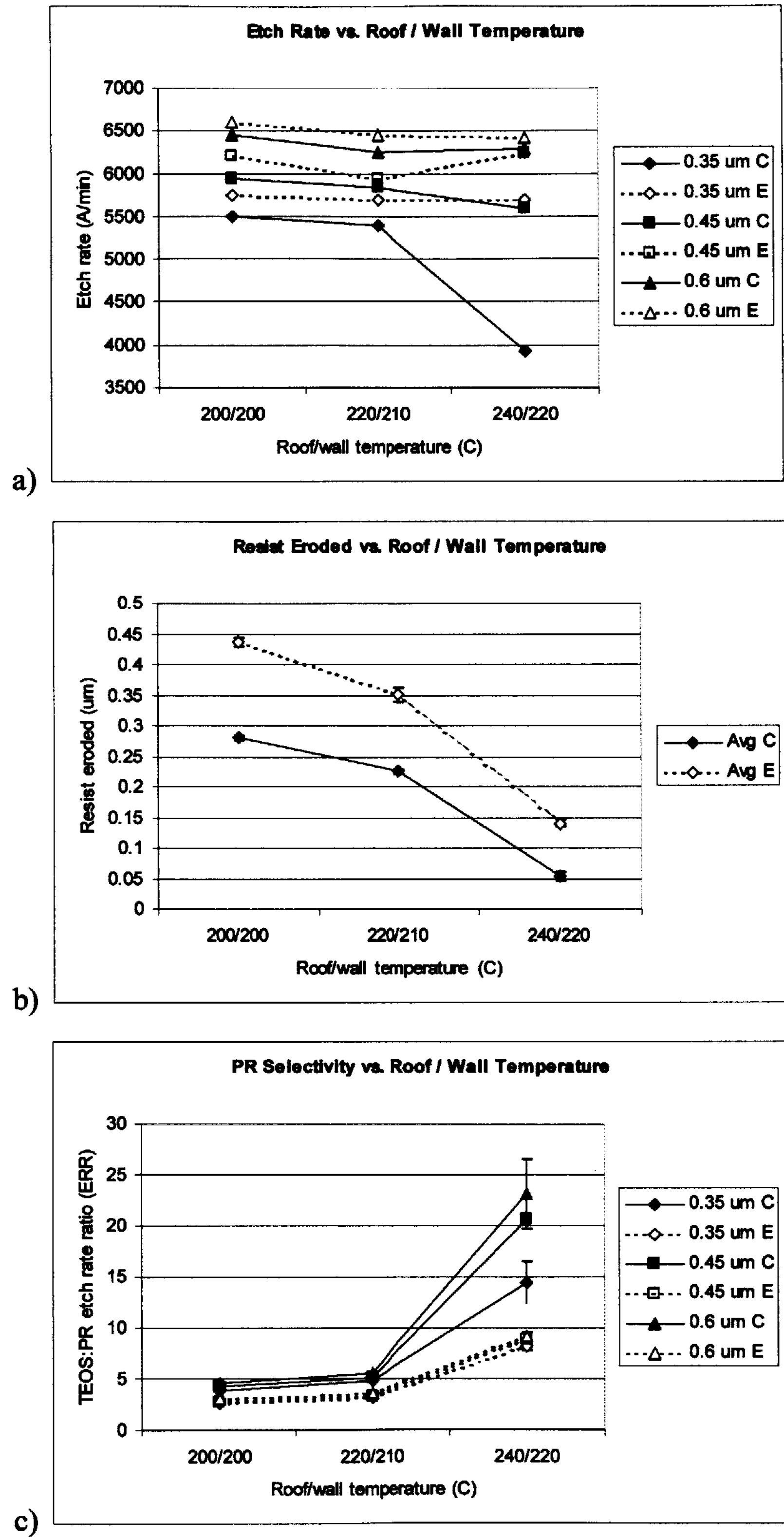

Figure 5.19: Stage II results – a) oxide etch rate, b) resist eroded, and c) oxide:resist selectivity vs. roof/wall temperature at 25 sccm, 5% 152a, 1600 W source, and 1400 W bias.

Figure 5.19 plots process data against chamber roof and wall temperature. Roof and wall temperature were varied in tandem, using 20°C increments for the former, 10°C increments for the latter. Three experiments were carried out: at 200°C/200°C, 220°C/210°C, and 240°C/220°C roof/wall temperature. The other process parameters were fixed at 25 sccm total etch gas flow, 5% 152a, 1600 W source power, and 1400 W bias power. Figure 5.19a shows the dependence of oxide etch rate on chamber temperature. In general, etch rate does not appear to be significantly affected, except at 0.35 μm center, where a significant dropoff is seen at the high temperature condition. A comparison of the SEM data for Run II-19 (200°C/200°C), Run II-18 (220°C/210°C), and Run II-8 (240°C/220°C) shows that complete etch stop occurred in the 0.35 μm center feature at high temperature, while only partial etch stop was seen at lower temperatures. Similarly, whereas partial etch stop was seen in the 0.35 μm edge feature at high temperature, the etch continued to progress at lower temperatures.

Figure 5.19b shows the effect of varying roof/wall temperature on the amount of resist eroded. A very pronounced increase is seen as temperature is decreased. As was discussed above, this is not accompanied by a pronounced increase in oxide etch rate (except at 0.35 μm center), suggesting that the principal cause is not related to a change in abundance of etchant species. Rather, it was seen that at high temperature small features have a greater propensity to experience etch stopping, an effect consistent with the mechanisms posited earlier, according to which, lowering the temperature of chamber surfaces results in a decrease in polymer deposition on the wafer. Such a decrease would account for both the etch stop and resist erosion effects. (In the experiments, the chiller temperature, *i.e.*, the temperature of the coolant flowing through the chuck assembly, was -10°C; the actual temperature of the wafer is believed to be up to several tens of degrees higher, [30, 35] but still substantially lower than the temperature of the chamber surfaces.)

Figure 5.19c plots the oxide:resist selectivity against roof/wall temperature. Since the dominant effect of increasing chamber temperature has been shown to be a pronounced

decrease in resist erosion, the selectivity is seen to increase markedly as roof/wall temperature increases.

Finally, for large features, where etch stopping is not observed, temperature has little effect on sidewall slope. For smaller features that are more susceptible to etch stopping, higher temperature leads to more polymer buildup at the bottom, which is reflected in the degradation of the profile. This effect is consistent with the observed trend in resist erosion and is believed to be the result of more polymer deposition on the wafer at higher chamber temperature.

Neural Network Analysis. The trends discussed above are also evident from the neural network models that were generated from the CCD matrix data in Stage II. The validity of the use of neural network methodology versus more traditional response surface methodology (RSM), as well as the greater robustness of neural networks for datasets of this type had been established elsewhere. [36] Hence only neural network analysis was carried out with the present dataset. The 0.35 μm center location data was chosen for analysis via neural network model. Figures 5.20, 5.21, and 5.22 show NNAPER [37] neural network models for 0.35 μm center oxide etch rate as a function of the three matrix variables: total etch gas flow, % 152a, and source power over the ranges 21 to 29 sccm , 0% to 10%, and 1400 to 1800 W, respectively. Experimental points 1-15 in Stage II were used to generate the model.* A model with two hidden nodes was found to give the best fit. Due, in all likelihood, to the sparse nature of the data, good neural network fits were not obtained for the remaining process outputs (resist eroded, and selectivity), which were taken out of the final form of the neural network model, which did, however, include grams of carbon equivalent as another output – to be discussed below. The R^2 value obtained for the oxide etch rate model was 0.9606. Because no center point replicates were available, no F-factor has been computed.

---

* With the exception of Run II-5, which was not used in any analyses because it was found (through review of post-process wafer history data collected by the etch tool software) that the mass flow controller used for FC-125 on that run may have delivered an actual flow deviating from the requested setpoint. However, a second model generated with the same data, but *including Run II-5*, yielded nearly identical results,

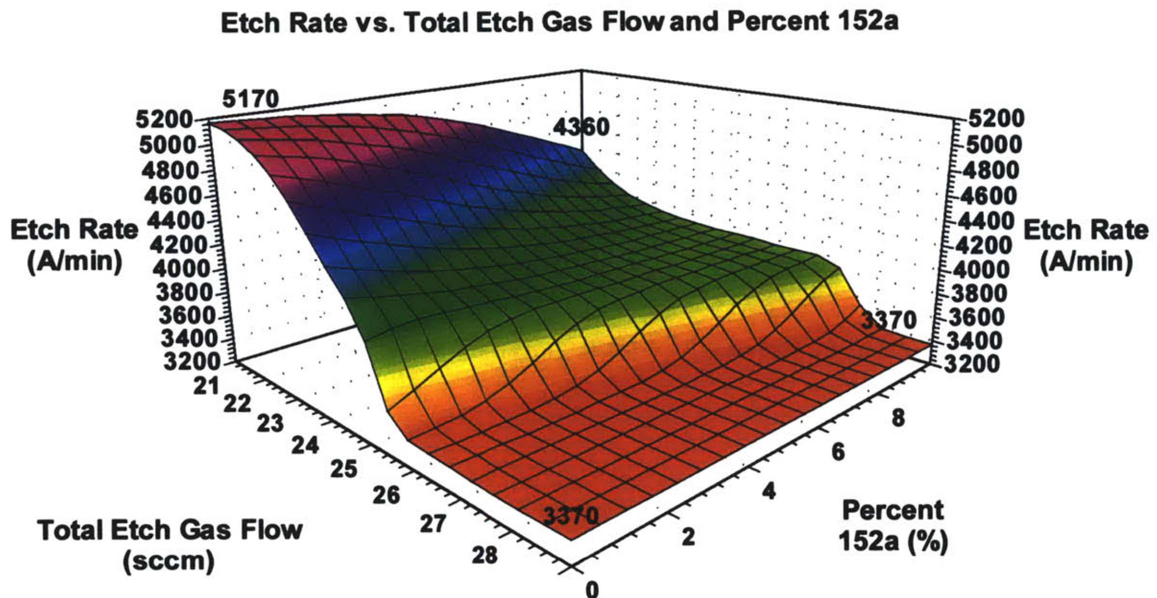

Figure 5.20: Stage II results – neural network model of 0.35 μm center TEOS oxide etch rate as a function of total etch gas flow and % 152a at 1600 W source power.

It is important to point out that, because the data set used to generate the model was quite sparse, few conclusions can be drawn from the exact *form* of the surfaces seen in Figures 5.20 through 5.22. One can, however, discuss *trends*. As Figures 5.20 through 5.22 show, in the regime explored, 0.35 μm center oxide etch rate is predicted to decrease with total etch gas flow and increase with source power above a threshold roughly in the middle of the power range, in agreement with the 0.35 μm center trends seen in Figures 5.15a and 5.17a. In Figure 5.22, % 152a is seen to have generally little effect on the etch rate at 0.35 μm center, which is again in agreement with the trend seen in Figure 5.16a. In Figure 5.20, this is the case at the 25 sccm, 1600 W condition, which is also in agreement with Figure 5.16a, whose data was taken at 25 sccm, 1600 W source.

---

suggesting that the overall effect of the apparent MFC malfunction on this run may not have been significant or that the error was not as large as indicated by wafer history data.

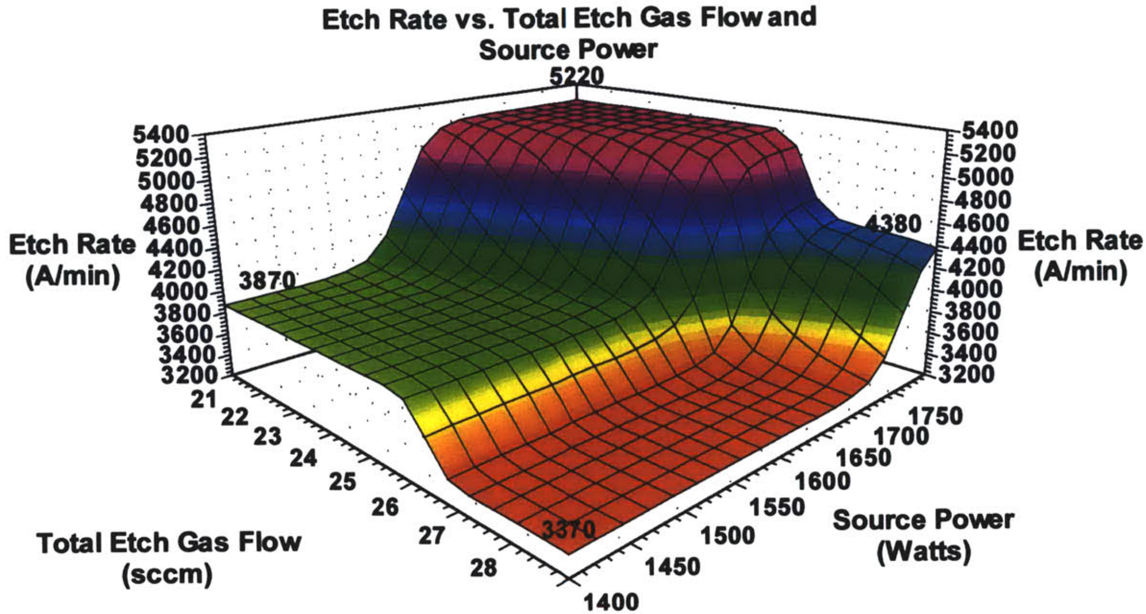

Figure 5.21: Stage II results – neural network model of 0.35 μm center TEOS oxide etch rate as a function of total etch gas flow and source power at 5% 152a.

One subtlety present in the neural network model that cannot be seen from the axial point trends is that, at low total etch gas flow, the model predicts a decrease in etch rate with increasing % 152a (see Figure 5.20). However, a comparison of the SEMs for Run II-2 (23 sccm, 2.5% 152a, 1500 W source) and Run II-4 (23 sccm, 7.5% 152a, 1500 W source) shows that center location etch rate actually *increases* as % 152a increases from 2.5% to 7.5%. Additionally, a comparison between the SEMs for Run II-3 (23 sccm, 2.5% 152a, 1700 W source) and Run II-5 (23 sccm, 7.5% 152a, 1700 W source) shows that etch rate again *increases* as % 152a increases from 2.5% to 7.5%. Hence, it appears that the trend with respect to % 152a suggested by the model may be more likely to be an artifact of the model, than an actual effect. This is perhaps not surprising given the fact that % 152a had the least pronounced and most ambiguous effects in the axial point analysis.

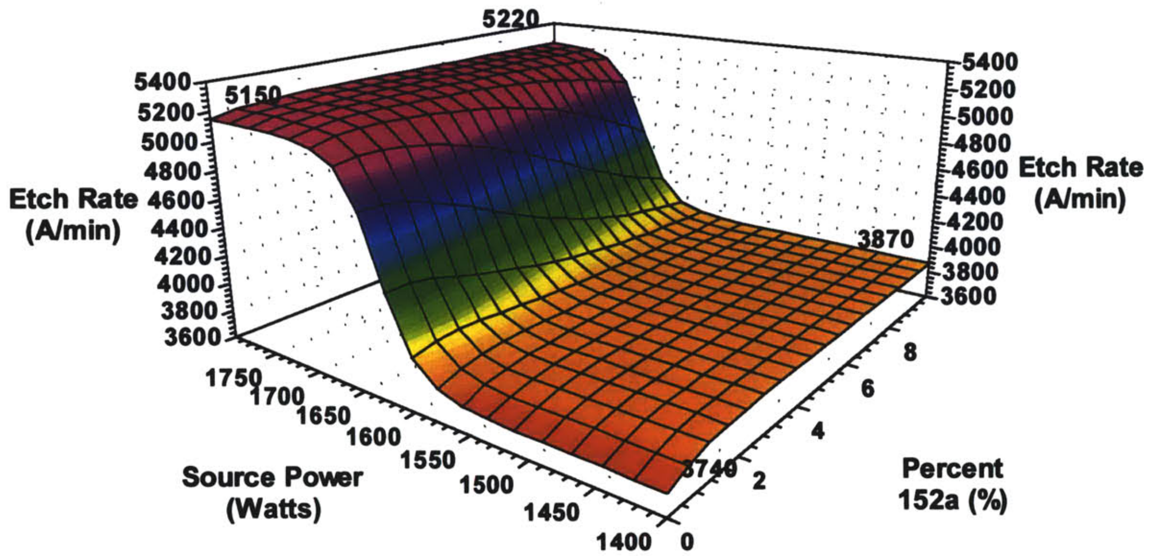

Figure 5.22: Stage II results – neural network model of 0.35 μm center TEOS oxide etch rate as a function of % 152a and source power at 25 sccm total etch gas flow.

Process Comparison with C_2F_6 Reference. Comparing results obtained with the C_2F_6 reference process to the FC-125/152a results, one sees that the C_2F_6 process has generally higher etch rate but lower mask layer selectivity than the FC-125/152a processes. The features obtained with the C_2F_6 process, moreover, show no evidence of etch stop (see Figure 5.11). The top CDs are larger than nominal for all processes in this study, including the C_2F_6 reference. The 0.35 μm center etch rate, selectivity, and top CD for the C_2F_6 reference process are 6150 Å/min, 3.6:1, and 0.42 μm, respectively. At the 0.35 μm edge location, the corresponding numbers are 7650 Å/min, 3.1:1, and 0.44 μm. The overall best Stage I FC-125/152a process (Run I-2) yielded: 5800 Å/min, 9.9:1, and 0.47 μm (center); and 6350 Å/min, 4.5:1, and 0.46 μm (edge), respectively. The overall best Stage II process (Run II-3) yielded: 5290 Å/min, 14.9:1, and 0.47 μm (center); and 5300 Å/min, 3.2:1, and 0.45 μm (edge), respectively.

5.3.2.3 Emissions Results

Figures 5.23-5.25 show NNAPER neural network models for carbon equivalent (CE) generated from the FTIR data collected in the CCD matrix experiments. The R^2 value for the carbon equivalent model fit was 0.7557. The general trends in global warming emissions as a function of total etch gas flow, fraction of FC-152a, and source power are also shown in Figure 5.26, where the CE values calculated from the FTIR data are plotted for the axial points of the matrix. The emissions for the FC-125/FC-152a processes used ranged from about 70.3 to about 94.0 grams of carbon equivalent (CE). The utilization efficiency (averaged over the duration of the etch process) for FC-125 in these experiments was calculated to be ~100% in all runs.

Emissions Comparison with C_2F_6 Reference. The CE value measured for the C_2F_6 reference process was 289.0 grams; hence the values obtained for FC-125/FC-152a represent emissions savings ranging from 67.5 to 75.7% relative to the reference process. The average utilization efficiency obtained for the C_2F_6 process was 78.3%. The breakdown of the global warming effluent composition in the C_2F_6 reference process was: 48.24 x 10^{-5} moles of C_2F_6, 26.96 x 10^{-5} moles of CHF_3, 34.53 x 10^{-5} moles of CF_4, and 2.19 x 10^{-5} moles of C_3F_8. Adjusted by the GWP_{100} value of each gas, the relative contributions to the carbon equivalent value of this process were: 57.8%C_2F_6, 20.8%CHF_3, 18.7%CF_4, and 2.7%C_3F_8. Thus a large factor accounting for the significant emissions reductions seen for the FC-125/FC-152a processes is the higher feed gas utilization efficiency, as unreacted C_2F_6 is a significant contributor to the overall emissions from the C_2F_6 process. The HF and SiF_4 emissions were 135.12 x 10^{-5} moles and 69.62 x 10^{-5} moles, respectively. The HF and CHF_3 emissions in the C_2F_6 process result from an interaction with the H in the resist as it is etched.

A representative FC-125/FC-152a process, the Stage II centerpoint process (Run II-8), had an overall CE value of 74.7 grams (74.1% reduction versus C_2F_6). The principal global warming components were determined to be: CHF_3 (26.02 x 10^{-5} moles, 77.8% of the CE value), CF_4 (7.45 x 10^{-5} moles, 15.6% of the CE value), and C_2F_6 (1.30 x 10^{-5} moles, 6.0% of the CE value). A comparison with the C_2F_6 process indicates that, while

CHF_3 levels are comparable, C_2F_6 as well as CF_4 levels are significantly lower. C_3F_8 was determined not to be present in the effluent of the FC-125/FC-152a processes. The HF and SiF_4 emissions for the centerpoint process were 351.09 x 10^{-5} moles and 44.92 x 10^{-5} moles, respectively. The increase in HF generation relative to the C_2F_6 process is attributed primarily to the increase in H content in the plasma, whereas the decrease in SiF_4 generation is attributed mainly to reduced etching of the process kit resulting from more polymer formation.

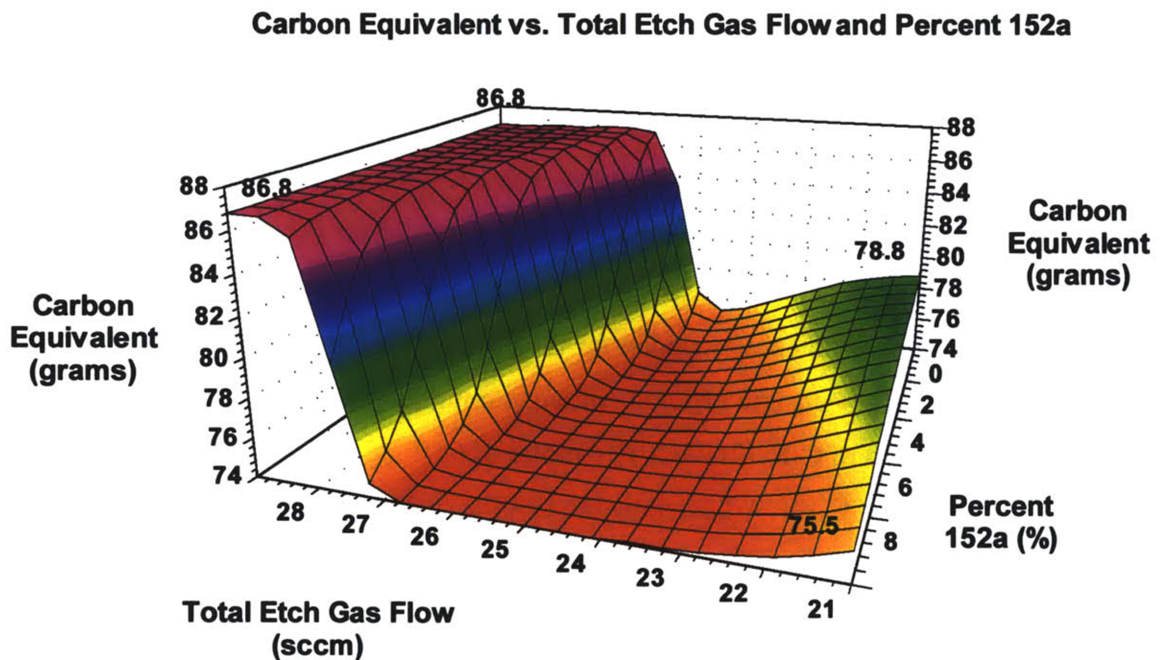

Figure 5.23: Stage II results – neural network model of FC-125/FC-152a emissions in grams of carbon equivalent as a function of total etch gas flow and % 152a at 1600 W source power.

Emissions Trends. Within the FC-125/FC-152a data, emissions generally appear to increase with total etch gas flow at fixed fraction of FC-152a and fixed source power (see Figures 5.23, 5.24, and 5.26a), which is not surprising. Additionally, emissions also appear to increase with source power at fixed total etch gas flow and fixed fraction of FC-152a (see Figures 5.24, 5.25, and 5.26b). This, combined with the fact that FTIR data indicates complete (or nearly complete) destruction of FC-125 during the stable part of the etch process for all data points, suggests that increasing source power tends to

promote the formation of global warming plasma byproducts. Finally, increasing the fraction of FC-152a in the etch gas mix appears to have the effect of decreasing total CE (see Figures 5.23, 5.25, and 5.26c), although this effect is less pronounced. This suggests that the breakdown products of FC-152a are species that are less likely to serve as building blocks in the formation of global warming products. It may be the case that the reason for the decrease in CE with increasing FC-152a fraction could be the presence of fewer trifluoromethyl (CF_3) radicals, all of which are likely to be contributed by FC-125, and which are known to play a role in the formation of CHF_3, CF_4, and C_2F_6 as plasma byproducts (see below). A comparison of Figures 5.26a-c, which are plotted on the same scale, shows that, over the ranges explored, global warming emissions are most sensitive to changes in source power and least sensitive to changes in % 152a. It should also be pointed out that the curvature seen in the neural network surfaces is believed to be an artifact of the model; as Figures 5.26a-c indicate, the actual trend for all three variables is likely to have a more uniform slope.

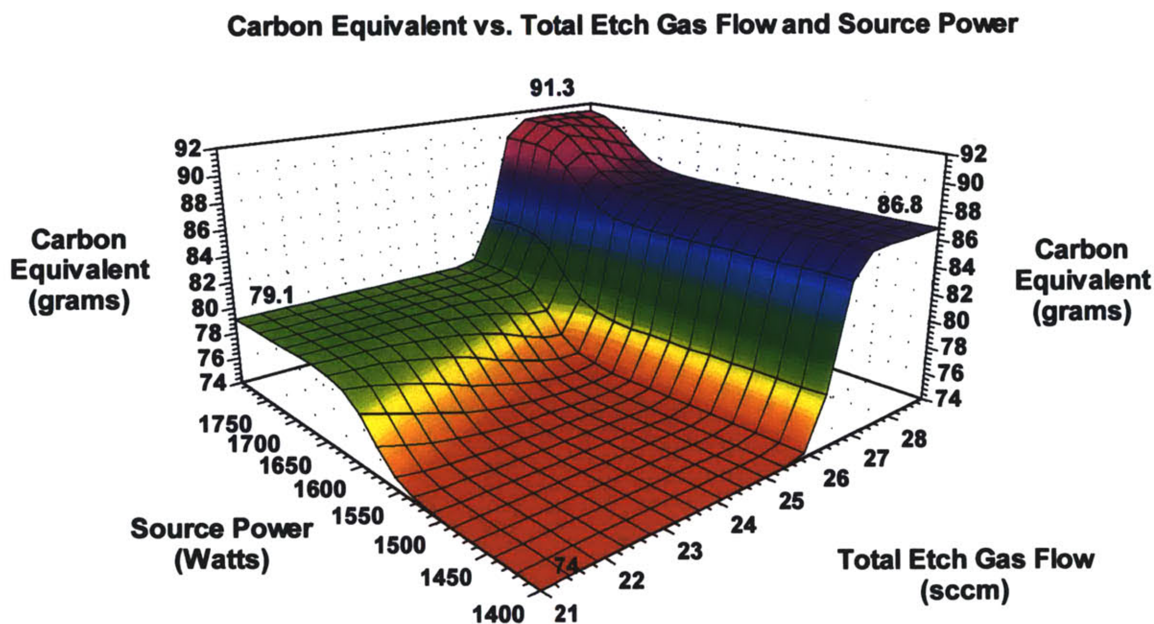

Figure 5.24: Stage II results – neural network model of FC-125/FC-152a emissions in grams of carbon equivalent as a function of total etch gas flow and source power at 5% 152a.

FC-125/FC-152a FTIR data indicate that the most abundant global warming species produced by the process is CHF_3, which was calculated to account for 70.9-84.1% of the total CE value under the experimental conditions tested. The bulk of the balance of the CE value is contributed by CF_4 (10.8-20.6%) and C_2F_6 (3.4-8.1%). Together, CHF_3, CF_4, and C_2F_6 were calculated to account for 98.9 or more percent of the CE contribution in all runs, with the remainder being assigned to small amounts of unreacted FC-125 and FC-152a. The presence of CF_4 and CHF_3 can be readily confirmed through manual analysis of FTIR spectra taken during these experiments, which show prominent features that can be uniquely assigned to CF_4 (at ~1283 cm^{-1}) and CHF_3 (at ~ 1152 cm^{-1}). The identification of C_2F_6 from the FTIR spectra was more difficult because its primary feature (at ~1248 cm^{-1}) has a rounded, symmetric shape that makes it difficult to identify when surrounded by other larger features; however, because its primary peak did not significantly overlap with peaks of other analytes, a large degree of confidence may be placed in its quantification by the software.

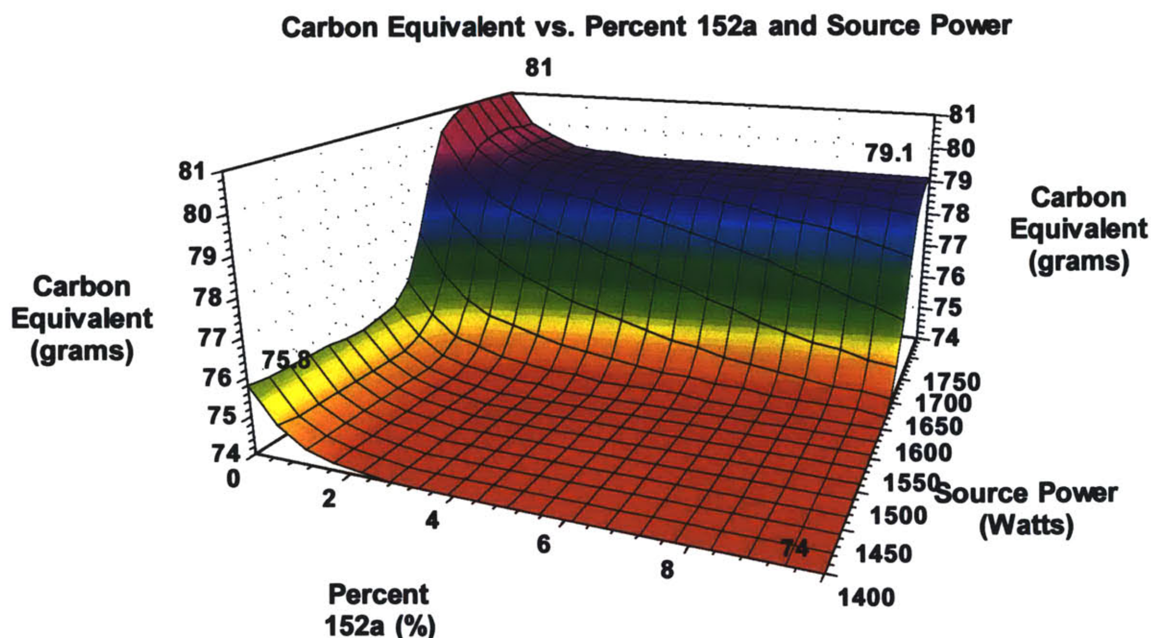

Figure 5.25: Stage II results – neural network model of FC-125/FC-152a emissions in grams of carbon equivalent as a function of % 152a and source power at 25 sccm total etch gas flow.

In all FC-125/FC-152a runs in this set of experiments, the species present in the effluent in the highest concentrations were HF and CO, respectively, with typical concentrations of 700-1000 ppm and 200-300 ppm, respectively. The next most abundant species seen in the effluent was SiF_4, with typical concentrations on the order of 100 ppm. (The process chamber contains quartz and silicon surfaces that are exposed to the process plasma and these account for the SiF_4 emissions from etch processes in the chamber even when no silicon-based materials on the wafer are exposed to the plasma.) The concentrations of all other species measured by FTIR were generally below 100 ppm. Other gases observed in the effluent were CHF_3, COF_2, CF_4, and smaller quantities of CO_2 and C_2F_6. C_2F_4 was also identified in the FTIR spectra, but was not quantified.

A problematic compound was FC-152a. In all runs, concentrations higher than those corresponding to unreacted input flows were detected, suggesting net production of FC-152a in the plasma, which is highly unlikely. (Given the complete utilization of FC-125, a high, if not 100%, utilization efficiency would also be expected for this gas.) Several efforts to revise the FTIR analysis method to correct for this artifact were made, without success. The most probable cause that can be assigned for this is considerable overlap of two major FC-152a features with two CHF_3 features whose centroids fall at nearly the same wavenumbers (~1208 cm^{-1} and ~1146 cm^{-1}). Moreover, FC-152a also partially interferes with the primary FC-125 feature at ~1140 cm^{-1}. Fortunately, the CE calculation indicated that, in all cases, the calculated flow of FC-152a accounted for less than 1% of the total CE value.

When an alternate FTIR analysis method, which was identical to the first except that it excluded FC-152a as an analyte, was run on three of the 15 points, the CHF_3 concentrations measured increased somewhat, C_2F_6 concentrations decreased, and traces of FC-125 appeared, bringing the measured FC-125 utilization efficiencies down to ~99%. Fortunately, on balance, the measured CE values did not differ significantly between the two analysis methods (the discrepancy ranges from -2.1% to +4.2%), with the apparent decrease in C_2F_6 compensating for the increase in FC-125 and CHF_3 in the effluent stream (the elimination of FC-152a itself has a negligible effect on overall CE,

because of the small global warming potential of this compound relative to other fluorocarbon species found in the effluent). Thus the emissions data presented in Figures 23-26 are unlikely to contain gross inaccuracies and the overall CE reductions relative to the C_2F_6 process are likely to be close to the values reported above.

Figures 5.27a-c show the emissions of the principal global warming products on a molar basis as a function of each variable by individual component, in this case CHF_3, CF_4, and C_2F_6. Additionally, the plots also indicate the emissions of the hygroscopic gases SiF_4 and HF. It is posited that the primary formation mechanisms for CF_4, CHF_3, and C_2F_6 are:

$$CF_3 + F \rightarrow CF_4, \qquad (5.2)$$

$$CF_3 + H \rightarrow CHF_3, \qquad (5.3)$$

$$CF_3 + CF_3 \rightarrow C_2F_6, \qquad (5.4)$$

respectively.

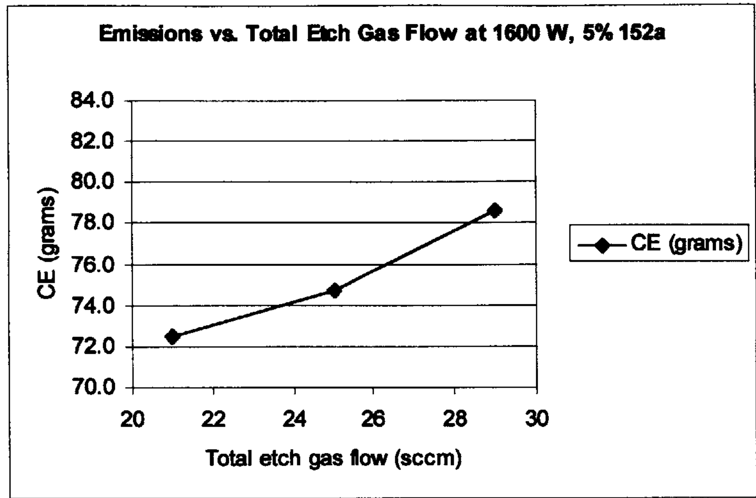

a)

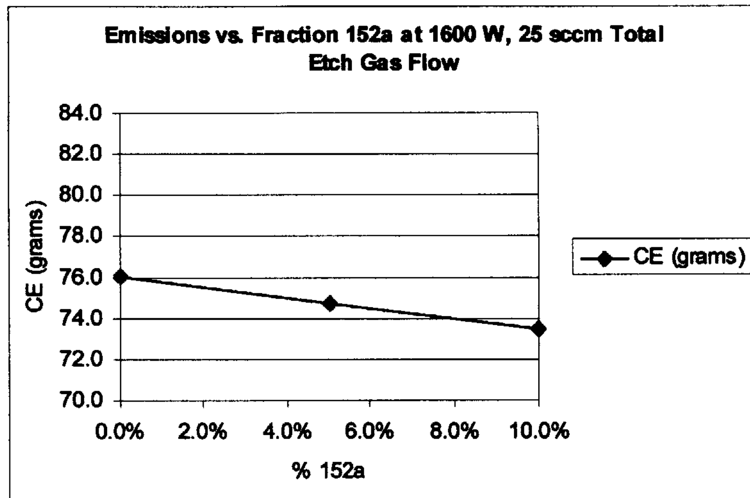

b)

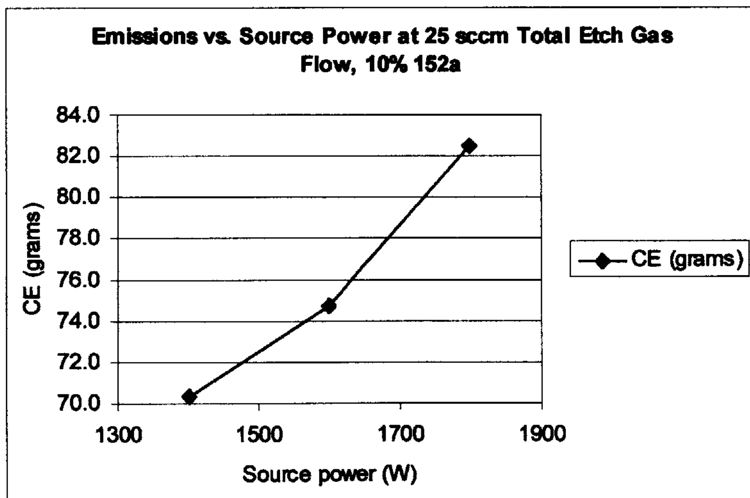

c)

Figure 5.26: Stage II results – emissions (in carbon equivalent) vs. a) total etch gas flow at 1600 W source power, 5% 152a, b) fraction of 152a at 1600 W source power, 25 sccm total etch gas flow, c) source power at 25 sccm total etch gas flow, 5% 152a.

As Figure 5.27a indicates, CF_4 emissions increase as a function of total etch gas flow with constant gas composition (5% 152a) but CHF_3 and C_2F_6 emissions remain nearly the same. It had earlier been established that both FC-125 and FC-152a were likely to be almost completely utilized at all process conditions in this study. Thus, to first order, one would expect that plasma composition would remain similar at low versus high flows and that the levels of CF_x, CF_xH_y, H, and F produced would increase but remain in roughly the same proportions. Instead, as etch gas flow increases, one only observes a significant absolute increase in CF_4 formation, suggesting perhaps a *relative* abundance of F at high flow conditions, the reasons for which are not well understood from this data alone, but which are consistent with the increase in oxide etch rate generally observed in the same regime. The relative (and absolute) increase in CF_4 emissions is also reflected in the individual component breakdown of the overall global warming emissions, as measured by CE. Hence, in this calculation, the contribution of each gas reflects its GWP_{100} value. The relative contribution of CF_4 to overall CE increases with increasing total etch gas flow (from 12.5% at 21 sccm to 17.0% at 29 sccm). At the same time, the C_2F_6 fraction remains relatively unchanged (5.5% at 21 sccm, 6.0% at 25 sccm, 5.4% at 29 sccm), while the CHF_3 fraction decreases (from 89.5% at 21 sccm to 76.6% at 29 sccm). As Figure 5.27a indicates, HF production also increases with total etch gas flow. The absolute and relative increases for the four gases at 29 sccm versus 21 sccm are: HF, 67.29×10^{-5} moles (+21.4%); CHF_3, 0.51×10^{-5} moles (+1.9%); CF_4, 2.79×10^{-5} moles (+48.2%); C_2F_6, 0.09×10^{-5} moles (+7.6%).

The increase in HF levels, together with Figure 5.27a, suggests that, as more F becomes generated at higher flows, its preferential sinks are CF_4 and HF formation, with the latter mechanism competing with CHF_3 formation for the available H:

$$H + F \rightarrow HF. \qquad (5.5)$$

If one assumes that there exists a relative abundance of F at high flow conditions, this mechanism may account for why, despite the likely generation of additional H at higher flows, a significant absolute increase in CHF_3 formation is not seen (which corresponds to a relative decrease in CHF_3 fraction of CE as CF_4 formation increases).

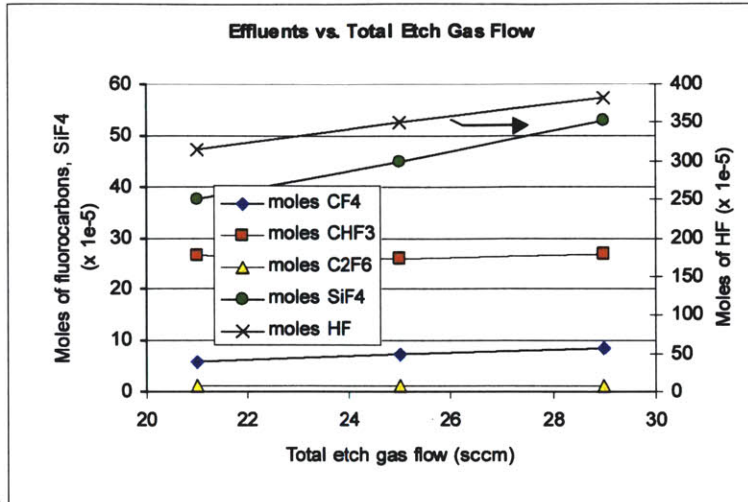

a)

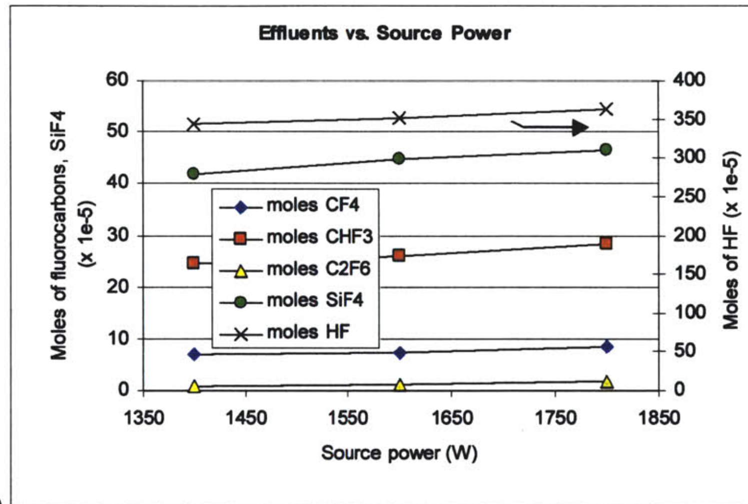

b)

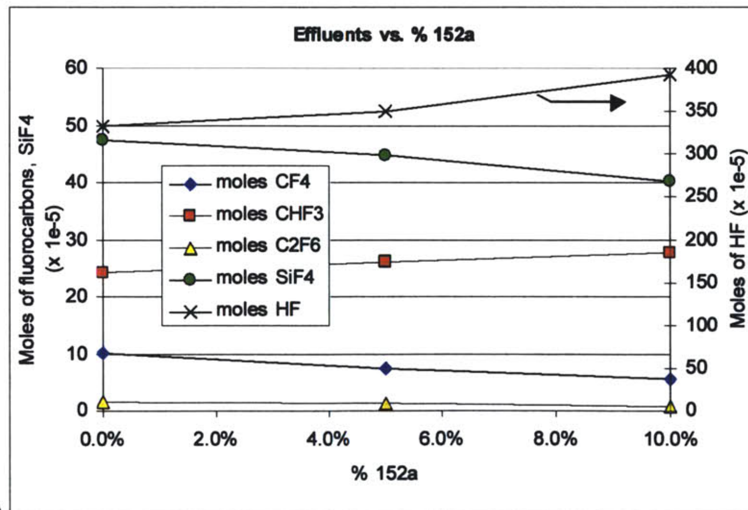

c)

Figure 5.27: Stage II results – moles of effluent vs. a) total etch gas flow at 5% 152a, 1600 W source power, b) source power at 5% 152a, 25 sccm total etch gas flow, c) % 152a at 1600 W source power, 25 sccm total etch gas flow.

Figure 5.27b indicates that the emissions of all three global warming species increase with increasing source power. The increase, however, is not proportional for the three species: as power changes from 1400 W to 1800 W, the amount of C_2F_6 formed increases by 0.69 x 10^{-5} moles (+70.3%), versus 1.33 x 10^{-5} moles (+18.8%) for CF_4 and 3.61 x 10^{-5} moles (+14.6%) for CHF_3. Thus while the absolute increase, on a molar basis, is largest for CHF_3, the largest relative increase is seen for C_2F_6 and vice versa. Correspondingly, the CE breakdown calculation shows a slight decrease in the relative contribution due to CHF_3 (78.4% at 1400 W versus 76.6% at 1800 W), along with a slight increase in the relative contribution due to C_2F_6 (4.8% at 1400 W versus 7.0% at 1800 W). The CF_4 contribution remains essentially unchanged: 15.7% at 1400 W, 15.6% at 1600 W, and 15.9% at 1800 W. The fact that the production of all three species increases with source power in absolute terms, in light of complete or nearly complete conversion of the source gases, suggests that increased source power leads to more complete dissociation of the initial dissociation products of those molecules. The bond strengths for C-C and C-H bonds in the parent hydrofluorocarbon molecules have been shown to be lower than that of the C-F bond (~4.3-4.5 eV versus 5.5 eV). Since the order of bond energy in fluorocarbon molecules is C-F > C-C ~ C-H, initial electron impact is likely to lead to the breaking of a C-C or C-H bond, rather than a C-F bond. For FC-125, initial electron impact may thus be likely to yield (neglecting ionizing impacts for simplicity):

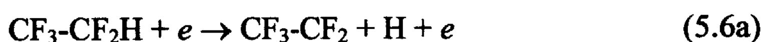

$$CF_3\text{-}CF_2H + e \rightarrow CF_3\text{-}CF_2 + H + e \qquad (5.6a)$$

$$\text{or } CF_3\text{-}CF_2H + e \rightarrow CF_3 + CF_2H + e. \qquad (5.6b)$$

Similarly, for FC-152a, the event may be likely to yield:

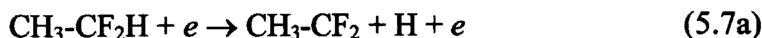

$$CH_3\text{-}CF_2H + e \rightarrow CH_3\text{-}CF_2 + H + e \qquad (5.7a)$$

$$\text{or } CH_3\text{-}CF_2H + e \rightarrow CH_2\text{-}CF_2H + H + e \qquad (5.7b)$$

$$\text{or } CH_3\text{-}CF_2H + e \rightarrow CH_3 + CF_2H + e. \qquad (5.7c)$$

Subsequent electron collisions would then further dissociate these fragments to yield CF_x, CF_xH_y, F, and more H. This, along with the HF trend shown in Figure 5.27b, suggests a possible mechanism which accounts for the decrease in the CHF_3 contribution to CE and the increase in the C_2F_6 contribution. Figure 5.27b indicates that HF formation increases as a function of source power. Since HF is formed according to the simple stoichiometry:

$H + F \rightarrow HF$, the increase in HF seen in Figure 5.27b suggests that, at higher source power, there is more F, H, or both available for HF formation. The ordering of the bond strengths, in turn, suggests that more C-H and C-C bonds are likely to be broken by initial electron impact than C-F bonds. At higher source power, the number of C-F bonds broken is likely to increase as plasma density increases, resulting in more F production. Since HF formation is observed to increase with source power, it may therefore be the case that more of the H produced at high power is used up in HF formation by reaction with F, which is likely to be more abundant in both relative and absolute terms at high power. Thus, even though more H is available at high power in absolute terms (accounting for the absolute increase in CHF_3 production), less of that H is now available to form CHF_3 by reaction with CF_3 radicals versus HF by reaction with atomic F. This, in turn, may leave more CF_3 available for reaction with itself to form C_2F_6, accounting for both the absolute and the relative increase in C_2F_6 production. The net trend in CF_4 fraction of CE with source power appears to be flat, suggesting perhaps that the increase in CF_3 and F concentrations that is postulated to arise from higher source power is partially offset by the scavenging of the F population to form HF. It should be pointed out that, while the increase in HF from 1400 W to 1800 W is small on a percentage basis (5.8% of 1400 W levels), it is large on a molar basis compared to the increases seen in the fluorocarbon gases: 19.87×10^{-5} moles.

Figure 5.27c plots changes in effluent composition as a function of % 152a in the source gas. It can be seen that the amounts of CHF_3 and HF produced increase with % 152a, while the amounts of CF_4 and C_2F_6 decrease. As the fraction of FC-152a changes from 0% to 10%, the amount of HF formed increases by 62.05×10^{-5} moles (+18.7%) while the amount of CHF_3 formed increases by 3.52×10^{-5} moles (+14.6%). CF_4 and C_2F_6 decrease by 4.53×10^{-5} moles (-45.1%) and 0.97×10^{-5} moles (-57.2%), respectively. The overall effect is a net decrease in global warming emissions. These trends are not surprising in light of the mechanisms of formation for CF_4, CHF_3, C_2F_6, and HF given above. Given the dissociation mechanisms postulated above, a larger fraction of FC-152a in the feed gas will lead to lower concentrations of atomic fluorine and, perhaps more significantly, CF_3 radicals, resulting in decreased production of CF_4 and C_2F_6. In the case

of CHF_3 and HF, the decrease in CF_3 and F concentrations is apparently more than offset by the increase in the H population which results from higher % 152a. These trends are reflected in the emissions breakdown calculation, which indicates that a larger percentage of the carbon equivalent value comes from CHF_3 at the expense of CF_4 and C_2F_6 as % 152a increases: the CHF_3 contribution increases from 70.9% at 0% 152a to 84.1% at 10% 152a, while the CF_4 fraction decreases from 20.6% to 11.7% and the C_2F_6 fraction decreases from 7.7% to 3.4%.

Finally, Figure 5.27 also provides the trend in SiF_4 formation with respect to the three process variables under consideration. As total etch gas flow changes from 21 to 29 sccm, SiF_4 is seen to increase by 15.25 x 10^{-5} moles (+40.6%). Similarly, as source power changes from 1400 W to 1800 W, SiF_4 is seen to increase by 4.63 x 10^{-5} moles (+11.0%). As had been pointed out earlier, in both cases, the F population in the plasma is likely to increase with the control variable, resulting in more etching of Si-based process kit surfaces, which accounts for most of the SiF_4 signal. In contrast, as % 152a is increased from 0% to 10%, the plasma becomes increasingly fluorine poor, due to the fact that FC-125 is a more efficient source of F than FC-152a. This corresponds to a decrease in SiF_4 production of 7.36 x 10^{-5} moles (-15.5%).

5.3.3 Conclusions

A systematic study of the behavior of FC-125/FC-152a in a high aspect ratio oxide via etch application has been carried out. Process performance, as characterized by oxide etch rate, resist erosion, and oxide:resist selectivity was evaluated as a function of several key process parameters, namely total etch gas flow, etch gas composition, source power, bias power, and roof/wall temperature. It was found that, in the parameter space explored, this chemistry tended to be highly polymerizing, resulting in very good bulk resist selectivity, but also in significant etch stopping at most conditions. Good etch rates, however, were achieved, along with anisotropic profiles (up to the point of etch stopping). In certain regions of the parameter space, good overall profiles, free from etch stop problems, were obtained, demonstrating that, given an appropriate level of process

optimization, FC-125/152a has the potential to be used successfully in a via etch application. It was found that lower FC-152a content, lower total etch gas flow, higher source power, higher bias power, and lower roof/wall temperature were generally beneficial with regard to reducing etch stopping, although the observed process trends were often complex.

Global warming and hygroscopic gas (HF, SiF_4) emissions as a function of total etch gas flow, etch gas composition, and source power, were also collected and quantified. Global warming emissions, measured using the carbon equivalent metric, were found to increase with total etch gas flow as well as source power and decrease with FC-152a content. The increase with total etch gas flow was, of course, expected, since higher feed gas flow typically results in higher levels of all effluents. The increase in emissions with higher source power was attributed to more complete breakup of the feed gas (nearly 100% utilized at all experimental conditions) and the accompanying generation of larger amounts of CF_3, F, and H, believed to be the primary precursors in the formation of the principal global warming species seen in these processes: CF_4, CHF_3, and C_2F_6. The decrease in carbon equivalent as a function of higher FC-152a content was attributed principally to decreases in F and CF_3 radical production believed to result from a lowering of the FC-125:FC-152a ratio. A comparison of the emissions from FC-125/FC-152a processes and a reference C_2F_6 based process showed that emissions reductions of 68 to 76% were attainable, in large part due to much higher feed gas conversion efficiency (estimated at close to 100% for FC-125/FC-152a) versus 78% for C_2F_6.

Further process optimization, along with characterization with respect to other key process parameters (notably stop layer selectivity), is likely to be required for the successful use of FC-125/FC-152a in a via etch application in an ICP tool such as the one used for this study. However, the present data also indicate that good process performance with this chemistry is possible and that its use can result in significant global warming emissions reductions relative to perfluorinated processes – on the order of 70-75%.

References

1. *Scientific Assessment of Ozone Depletion: 1998, Volume 2,* World Meteorological Organization, Global Ozone Research and Monitoring Project, Report No. 44 (1998).
2. V. Mohindra, H. H. Sawin, M. T. Mocella, J. M. Cook, J. Flanner, and O. Turmel, *Alternatives to Perfluorocompounds as Plasma Processing Gases: SiO_2 Etching Using C_2F_5H and $C_2F_4H_2$*, in Proceedings of *10th Symposium on Plasma Processing*, San Francisco, CA, G. S. Mathad, D. W. Hess, and M. Engelhardt, Editors, The Electrochemical Society Proceedings Series, **PV 94-20**, p. 300-310, Electrochemical Society, Pennington, NJ (1994).
3. F. Illuzzi, R. d'Agostino, C. Cascarano, V. Colaprico, and F. Fracassi, *Alternative Compounds for SiO_2 Etching*, in Proceedings of *6th Annual International Semiconductor Environmental, Safety, and Health Conference*, Williamsburg, VA (1999).
4. J. L. Tunkel, D. Aronson, H. Printup, and P. H. Howard, *Draft Report, EPA Contract 68-D2-0182, Vol. 1,* U. S. Environmental Protection Agency, p. 34 (1996).
5. M. Mocella, C. Allgood, H. Sawin, and H. Chae, *Poster paper #7*, in Proceedings of *SEMICON Southwest 1998: A Partnership for PFC Emissions Reductions*, Austin, TX, SEMI (1998).
6. S. Karecki, R. Chatterjee, L. Pruette, R. Reif, T. Sparks, L. Beu, and V. Vartanian, *Evaluation of Pentafluoroethane and 1,1-Difluoroethane for a Dielectric Etch Application in an Inductively Coupled Plasma Etch Tool*, Jpn. J. Appl. Phys., **39**(7B) (2000).
7. J. W. Coburn and H. F. Winters, *Plasma etching - A discussion of mechanisms*, J. Vac. Sci. Technol., **16**(2), p. 391-403 (1979).
8. J. W. Coburn, *Plasma-Assisted Etching*, Plasma Chemistry and Plasma Processing, **2**(1), p. 1-41 (1982).
9. J. A. Mucha, The Gases of Plasma Etching: Silicon-Based Technology, in Solid State Technology, 1985, p. 123-127.
10. W. W. Stoffels, E. Stoffels, and K. Tachibana, *Polymerization of fluorocarbons in reactive etching plasmas*, J. Vac. Sci. Technol. A, **16**(1), p. 87-95 (1998).
11. B.-O. Cho, S.-W. Hwang, I.-W. Kim, and S. H. Moon, *Expression of the Si Etch Rate in a CF_4 Plasma with Four Internal Process Variables*, J. Electrochem. Soc., **146**(1), p. 350-358 (1999).
12. S. Samukawa and K.-i. Tsuda, *New Radical-Control Method for SiO_2 Etching with Non-Perfluorocompound Gas Chemistries*, Jpn. J. Appl. Phys., **37, Part 2**(10A), p. L1095-L1097 (1998).
13. S. Samukawa and T. Mukai, *Differences in radical generation due to chemical bonding of gas molecules in a high-density fluorocarbon plasma: Effects of the C=C bond in fluorocarbon gases*, J. Vac. Sci. Technol. A, **17**(5), p. 2463-2466 (1999).
14. S. Samukawa, T. Mukai, and K.-i. Tsuda, *New radical control method for high-performance dielectric etching with nonperfluorocompound gas chemistries in ultrahigh-frequency plasma*, J. Vac. Sci. Technol. A, **17**(5), p. 2551-2556 (1999).

15. H.-J. Lee, J. K. Kim, J. H. Kim, K.-W. Whang, J. H. Kim, and J. H. Joo, *Selective SiO_2/Si_3N_4 etching in magnetized inductively coupled C_4F_8 plasma*, J. Vac. Sci. Technol. B, **16**(2), p. 500-506 (1998).
16. Y. Chinzei, M. Ogata, H. Shindo, T. Ichiki, and Y. Horiike, *Flow rate rule for high aspect ratio SiO_2 hole etching*, J. Vac. Sci. Technol. A, **16**(3), p. 1519-1524 (1998).
17. Y. Chinzei, T. Ichiki, N. Ikegami, Y. Feurprier, H. Shindo, and Y. Horiike, *Residence time effects on SiO_2/Si selective etching employing high density fluorocarbon plasma*, J. Vac. Sci. Technol. B, **16**(3), p. 1043-1050 (1998).
18. G. M. W. Kroesen, H.-J. Lee, H. Moriguchi, H. Motomura, T. Shirafuji, and K. Tachibana, *Investigations of the surface chemistry of silicon substrates etched in a rf-biased inductively coupled fluorocarbon plasma using Fourier-transform infrared ellipsometry*, J. Vac. Sci. Technol. A, **16**(1), p. 225-232 (1998).
19. N. R. Rueger, J. J. Beulens, M. Schaepkens, M. F. Doemling, J. M. Mirza, T. E. F. M. Standaert, and G. S. Oehrlein, *Role of steady state fluorocarbon films in the etching of silicon dioxide using CHF_3 in an inductively coupled plasma reactor*, J. Vac. Sci. Technol. A, **15**(4), p. 1881 (1997).
20. T. E. F. M. Standaert, M. Schaepkens, N. R. Rueger, P. G. M. Sebel, and G. S. Oehrlein, *High density fluorocarbon etching of silicon in an inductively coupled plasma: Mechanism of etching through a thick steady state fluorocarbon layer*, J. Vac. Sci. Technol. A, **16**(1), p. 239 (1998).
21. N. R. Rueger, M. F. Doemling, M. Schaepkens, J. J. Beulens, T. E. F. M. Standaert, and G. S. Oehrlein, *Selective etching of SiO_2 over polycrystalline silicon using CHF_3 in an inductively coupled plasma reactor*, J. Vac. Sci. Technol. A, **17**(5), p. 2492-2502 (1999).
22. D. C. Marra and E. S. Aydil, *Effect of H_2 addition on surface reactions during CF_4/H_2 plasma etching of silicon and silicon dioxide films*, J. Vac. Sci. Technol. A, **15**(5), p. 2508-2517 (1997).
23. C. B. Labelle and K. K. Gleason, *Pulsed plasma-enhanced chemical vapor deposition from CH_2F_2, $C_2H_2F_4$, and $CHClF_2$*, J. Vac. Sci. Technol. A, **17**(2), p. 445-452 (1999).
24. S. Den, T. Kuno, M. Ito, M. Hori, T. Goto, P. O'Keeffe, Y. Hayashi, and Y. Sakamoto, *Influence on selective SiO_2/Si etching of carbon atoms produced by CH_4 addition to a C_4F_8 permanent magnet electron cyclotron resonance etching plasma*, J. Vac. Sci. Technol. A, **15**(6), p. 2880-2884 (1997).
25. K. K. S. Lau and K. Gleason, *Solid-State Nuclear Magnetic Resonance Spectroscopy of Low Dielectric Constant Films from Pulsed Hydrofluorocarbon Plasmas*, J. Electrochem. Soc., **146**(7), p. 2652-2658 (1999).
26. S. K. Baldwin, R. Patrick, and N. Williams, *RF Peak Voltage Control at the Bias Electrode of Inductively Coupled Plasma Etchers for Improved Process Stability*, in Proceedings of *Plasma Etching Processes for Sub-Quarter Micron Devices*, Honolulu, HI, G. S. Mathad, Editor, Electrochemical Society Meeting Abstracts, **PV 99-30**, p. 55-63, Electrochemical Society, Pennington, NJ (1999).
27. V. Tarnovsky and K. Becker, J. Chem. Phys., **98**, p. 7868 (1993).

28. S. G. Lias, J. E. Bartmess, J. F. Liebman, J. L. Holmes, R. D. Levine, and W. G. Mallard, J. Phys. Chem. Ref. Data, **17**(Suppl 1) (1988).
29. M. Schaepkens, R. C. M. Bosch, T. E. F. M. Standaert, G. S. Oehrlein, and J. M. Cook, *Influence of reactor wall conditions on etch processes in inductively coupled fluorocarbon plasmas*, J. Vac. Sci. Technol. A, **16**(4), p. 2099-2107 (1998).
30. O. Joubert, P. Czuprynski, F. H. Bell, P. Berruyer, and R. Blanc, *Analyses of the chemical topography of silicon dioxide contact holes etched in a high density plasma source*, J. Vac. Sci. Technol. B, **15**(3), p. 629-639 (1997).
31. M. Inayoshi, M. Ito, M. Hori, and T. Goto, *Surface reaction of CF_2 radicals for fluorocarbon film formation in SiO_2/Si selective etching process*, J. Vac. Sci. Technol. A, **16**(1), p. 233-238 (1998).
32. D. F. McMillen and D. M. Golden, Ann. Rev. Phys. Chem., **33**, p. 493 (1982).
33. H.-S. Kim, W.-J. Lee, G.-Y. Yeom, J.-H. Kim, and K.-W. Whang, *Etch-Induced Physical Damage and Contamination during Highly Selective Oxide Etching Using C_4F_8/H_2 Helicon Wave Plasmas*, J. Electrochem. Soc., **146**(4), p. 1517-1522 (1999).
34. T. Hori, M. D. Bowden, K. Uchino, K. Muraoka, and M. Maeda, *Measurements of electron temperature, electron density, and neutral density in a radio-frequency inductively coupled plasma*, J. Vac. Sci. Technol. A, **14**(1), p. 144-151 (1996).
35. E. Yeh, , in Proceedings of *Northern California Chapter American Vacuum Society Plasma Etch Users Group Meeting*, Santa Clara, CA, NCCAVS (1999).
36. L. Pruette, S. Karecki, R. Reif, L. Tousignant, W. Reagan, S. Kesari, and L. Zazzera, *Evaluation of C_4F_8O as an Alternative Plasma Enhanced Chemical Vapor Deposition Chamber Clean Chemistry*, J. Electrochem. Soc., **147**(3), p. 1149-1153 (2000).
37. Neural Network Analyzer of Process Evaluation Responses, developed by E. I. du Pont Nemours and Company.

5.4 1- and 2-iodoheptafluoropropane Via Etch Process Development Study

The work presented in Section 5.4 represents a follow-on activity to the work described in Section 5.1. The intent of the present study was to generate understanding of the iodoheptafluoropropane etch process with regard to three areas: on wafer process performance, properties of films deposited by the process, and global warming emissions. Section 5.4.1 treats the first of these areas, discussing trends in process behavior, as characterized by oxide etch rate, photoresist erosion, feature profile, and stop layer selectivity behavior as a function of various process variables, comparing the iodoheptafluoropropane processes to a PFC-based (C_3F_8/CH_3F) reference. Section 5.4.2 provides an analysis of films deposited by 1-iodoheptafluoropropane using x-ray photoelectron spectroscopy (XPS) and time-of-flight secondary ion mass spectrometry (TOF-SIMS). The discussion in Section 5.4.2 provides detail for an attempt to understand one of the critical phenomena that appears to be present in IFC etching, namely energetic iodine bombardment. Finally, Section 5.4.3 presents process effluent data collected by Fourier transform infrared (FTIR) spectroscopy under a subset of the same conditions used in the experiments in Part I and engages in a discussion of phenomena in the plasma that affect effluent composition and process behavior.

5.4.1 Process Characterization

1-iodoheptafluoropropane (CF_2I-CF_2-CF_3) was characterized as a potential etch chemistry for dielectric etch applications in a high density plasma tool. An extensive array of experiments was run with this chemistry. In these experiments, etch process data were collected from patterned silicon dioxide wafers using cross-sectional scanning electron microscopy (SEM). Certain experiments were repeated with the other isomer of this molecule, 2-iodoheptafluoropropane, as the etch gas. Finally, selectivities to key stop layers were evaluated in an additional series experiments using both isomers. Additional work was also carried out to characterize films deposited by 1-iodoheptafluoropropane and process emissions from 1-iodoheptafluoropropane processes

(see Sections 5.4.2 and 5.4.3). Section 5.4.1.1 presents the experimental setup used. Section 5.4.1.2 covers the discussion of those experiments in the study that were analyzed for process trends using neural network methodology. Section 5.4.1.3 covers additional experiments (concerning the effects of wall and chiller temperature) that were carried out outside the neural network framework. Section 5.4.1.4 presents cross-sectional SEM data representative of the processes characterized in this study. Section 5.4.1.5 compares the process performance of 1-iodoheptafluoropropane with that of its 2-iodo isomer. Completing the discussion of experimental data is Section 5.4.1.6, which presents the results of stop layer selectivity experiments carried out with both isomers. Finally, Section 5.4.1.7 offers conclusions.

5.4.1.1 Experimental Setup

The process tool used for this study was the same Centura 5300 HDP etch tool used for the experiments discussed elsewhere in Chapter 5. The HDP chamber is described in detail in Section 3.4.2 of this document. All of the experiments discussed in Section 5.4.1 were conducted on patterned oxide wafers. Except for those used for the stop layer selectivity tests, the features used were via hole arrays of 0.35, 0.45, and 0.6 μm nominal printed critical dimension (CD). The discussion that follows, however, will limit itself to results obtained from the 0.35 μm CD data. The film stack consisted of TEOS (tetraethoxysilane)-deposited silicon oxide masked with a deep UV photoresist. In most of the experiments, the resist was APEX type resist. In the case of a few wafers, K2G type resist, which is compositionally very similar to APEX, was employed, with the principal difference being the initial resist thickness prior to the etch experiments. Whereas the APEX resist was nominally 1 μm thick, the K2G resist was measured to be 0.698 to 0.734 μm thick. In order to provide a basis for comparison where the amount of resist remaining was used as a process metric, the initial resist thickness in the K2G wafer runs was adjusted to match that of the APEX wafers.

In the discussion that follows, three process variables were generally used as figures of merit: 0.35 μm CD in-feature oxide etch rate, calculated as the measured etch depth

inside the 0.35 μm via divided by the etch time; thickness of resist remaining; and sidewall slope. The latter was calculated as:

$$Slope = 90° - \arctan\left(\frac{(TopCD - BotCD)/2}{EtchDepth}\right). \qquad (5.8)$$

For all experiments discussed in Section 5.4, the backside He pressure under the wafer was maintained at 15 Torr while the He flow which made up the bulk of the process gas was maintained at 75 sccm. Except as noted, the electrostatic chuck chiller loop temperature was set at 34 °C.

A. Neural Network Experiments

In all, nearly 200 individual experiments were run in the course of this work. Two neural network models were created to interpret the data from the experimental runs generated with 1-iodoheptafluoropropane as the etch gas. One incorporated a large set of data points run at a wall temperature (*WT*) of 200 °C, while the other, much smaller, was comprised of a more limited set of data points run at a wall temperature of 230 °C. This was done because, in contrast to most of the other process parameters used in this study, which each took on a number of values distributed throughout the experimental space, only two settings were used for wall temperature in most of the experiments: 200 °C and 230 °C, with only 1 run at an intermediate wall temperature setting. Hence wall temperature was deemed unsuitable as a continuous variable to be included as a neural network input.

The first (200 °C *WT*) neural network model consisted of 146 patterned wafer data points and had six inputs (source power, *SP*; bias power, *BP*; etch gas flow, *EF*; CH_3F flow, *CF*; roof temperature, *RT*; and pressure, *PR*). "Source power" refers to the inductively coupled power applied to the source antenna in the dome of the chamber. "Bias power" refers to the capacitively coupled power applied independently to the electrostatic chuck. "Roof temperature" refers to the temperature of the silicon slab which forms the top portion of the etch chamber, in contrast to the "wall temperature," which refers to the

temperature setting of the quartz dome that houses the antenna coil and forms the upper part of the chamber wall. The etch gas in these experiments was 1-iodoheptafluoropropane. In a number of the experiments, CH_3F was also introduced as a polymer forming additive with the aim of improving oxide:resist selectivity.

Three output variables were analyzed using data collected from 0.35 μm via hole features at the center of wafer location: patterned TEOS oxide etch rate, thickness of resist remaining, and sidewall slope. The variable ranges covered were: 1450 – 2400 W *SP*, 600 – 1400 W *BP*, 12.5 – 28 sccm *EF*, 0 – 21 sccm *CF*, 200 – 260 °C *RT*, and 6 – 24 mTorr *PR*. See Table 5.8. There were three replicates of a "center point" process. A separate neural network model was constructed for each of the outputs. The etch rate and resist remaining models used 146 data points, whereas the sidewall slope model used a subset of 140. For all three models, a network with two hidden nodes was found to be optimal. Good fits to the data were obtained for the etch rate and resist remaining cases, with an overall R^2 value of 0.8794 and an F-ratio of 7.3877 for the etch rate model and an overall R^2 value of 0.9223 and an F-ratio of 11.9394 for the resist remaining model. The sidewall slope model had a somewhat poorer fit, with an overall R^2 value of 0.8107 and an F-ratio of 4.4020, which was attributed to the fact that, under the etch stop conditions encountered in a number of the experiments (see discussion below), accurate measurement of feature bottom CD was difficult, which introduced greater uncertainty in the sidewall slope calculation.

Table 5.8: Parameter space covered by the 200 °C wall temp. neural network.

Parameter	Units	-1 value (min)	-0.5 value	0 value (center)	+0.5 value	+1 value (max)
Source Power (SP)	watts	1450	1687.5	1925	2162.5	2400
Bias Power (BP)	watts	600	800	1000	1200	1400
Etch Gas Flow (EF)	sccm	12.5	16.375	20.25	24.125	28
CH_3F Flow (CF)	sccm	0	5.25	10.5	15.75	21
Roof Temp (RT)	°C	200	215	230	245	260
Pressure (PR)	mTorr	6	10.5	15	19.5	24

The second (230 °C *WT*) neural network model was much more limited. It consisted of only 9 data points and no center point replicates. It had two inputs (source power, *SP* and pressure, *PR*). Patterned TEOS oxide etch rate and thickness of resist remaining were once again analyzed using data collected from 0.35 µm via hole features at the center of wafer location. The variable ranges covered were: 1500 – 1700 W *SP* and 20 – 30 mTorr *PR*. A single model was constructed for the two outputs. A network with one hidden node was found to be optimal. Good data fits were obtained, with an overall R^2 value of 0.8875 and an F-ratio of 7.2919. A neural network model was not constructed for sidewall slope because all calculated 0.35 µm center sidewall slope values in this parameter space were nearly the same with no trend seen with respect to either variable (see discussion below).

B. Effects of Wall and Chiller Temperature

In addition to the two neural network matrices described above, additional experiments were run to determine the process behavior as a function of wall temperature and chiller temperature. In the former case, wall temperature was varied from 200 to 215 to 230 °C with the remaining parameters at: 2000 W *SP*, 800 W *BP*, 16 sccm *EF*, 15 sccm *CF*, 230 °C *RT*, 6 mTorr *PR*, and 34 °C chiller temperature. In the latter set of experiments, chiller temperature was varied from 34 to 15 to 0 to –15 °C with the remaining parameters at: 2400 W *SP*, 600 W *BP*, 20 sccm *EF*, 12 sccm *CF*, 230 °C *RT*, 6 mTorr *PR*, and 200 °C *WT*.

C. Cross-sectional SEM Analysis

A C_3F_8/CH_3F-based etch recipe was used as a reference process against which the performance of the 1- and 2-iodoheptafluoropropane processes was compared. Cross sectional SEM was employed as the means of characterization for all of the wafers that were analyzed as part of the work presented in Section 5.4.1. For brevity, only cross-sectional micrographs of the reference process as well as several 1-iodoheptafluoropropane processes representing important stages of process development in this study will be presented.

D. Comparison with 2-iodoheptafluoropropane

After the 1-iodoheptafluoropropane experiments were concluded, a set of runs was chosen to be repeated with the other isomer of the compound, 2-iodoheptafluoropropane. The experiments carried out with both isomers spanned the following variable range: 1620 – 2020 W *SP*, 700 – 1100 W *BP*, and 6 – 18 mTorr *PR*, at 16 sccm *EF*, 0 sccm *CF*, 255 °C *RT*, 200 °C *WT*, and 34 °C chiller temperature.

E. Stop Layer Selectivity Experiments

Finally, experiments were run with both 1- and 2-iodoheptafluoropropane using patterned wafers to determine the selectivity of the process to several stop layers. Wafers patterned with the same mask as those used for the earlier experiments were employed to evaluate plasma enhanced nitride (PEN) and TiN selectivity. The film stack for the PEN wafers consisted of 10,000 Å of APEX resist, 10,000 Å of TEOS oxide, a 500 Å PEN etch stop layer (ESL), on top of 250 Å of TiN, 1000 Å of Ti and 4000 Å of TEOS oxide. The stack for the TiN wafers was the same except for the absence of the 500 Å PEN layer. In these experiments, the overetch period was varied from 25% (150 s etch) to 50% (180 s etch). The process used for both isomers was: 1580 W *SP*, 800 W *BP*, 14 sccm *EF*, 0 sccm *CF*, 230 °C *RT*, and 12 mTorr *PR*, at 200 °C *WT*, and 34 °C chiller temperature.

Additionally, wafers patterned with a different mask were also used to determine stop on PEN and stop on Cu performance. Via 1 features were etched within already formed trenches at the Metal 2 level, stopping on Cu Metal 1 lines covered by a 500 Å PEN ESL. A standard O_2-based *in-situ* post etch treatment (PET) was run on these wafers to remove remaining resist and polymer deposits so that the micrographs would reveal the feature as it would appear prior to the next processing step. A 150 s etch (30 s overetch) was used. The C_3F_8/CH_3F reference process was also run on the PEN, TiN, and Cu substrates for comparison.

5.4.1.2 Results and Discussion – Neural Network Experiments

1st Neural Network: Patterned TEOS Oxide Etch Rate

Source Power (*SP*). The principal effect of increasing source power is generally seen to be an increase in TEOS oxide etch rate. See Figures 5.28a-c for examples. This effect is readily explained by well known phenomena associated with increasing source power, namely an increase in plasma density and the accompanying increase in the degree of dissociation in the feed gas. A first order effect believed to arise from this process is the production of larger amounts of etchant species at the expense of deposition precursors. While it is often difficult to cleanly characterize fragments and radicals produced from fluorocarbon etch gases as either "etching" or "deposition" precursors (see Section 5.3.2.1 and references therein for a more extensive discussion), it is generally fair to state that a lower degree of gas dissociation results in the formation of fluorine deficient CF_x species whose presence tends to drive the process toward net deposition rather than net etching. To first order, therefore, a higher degree of gas breakup leads to conditions favoring net etching.

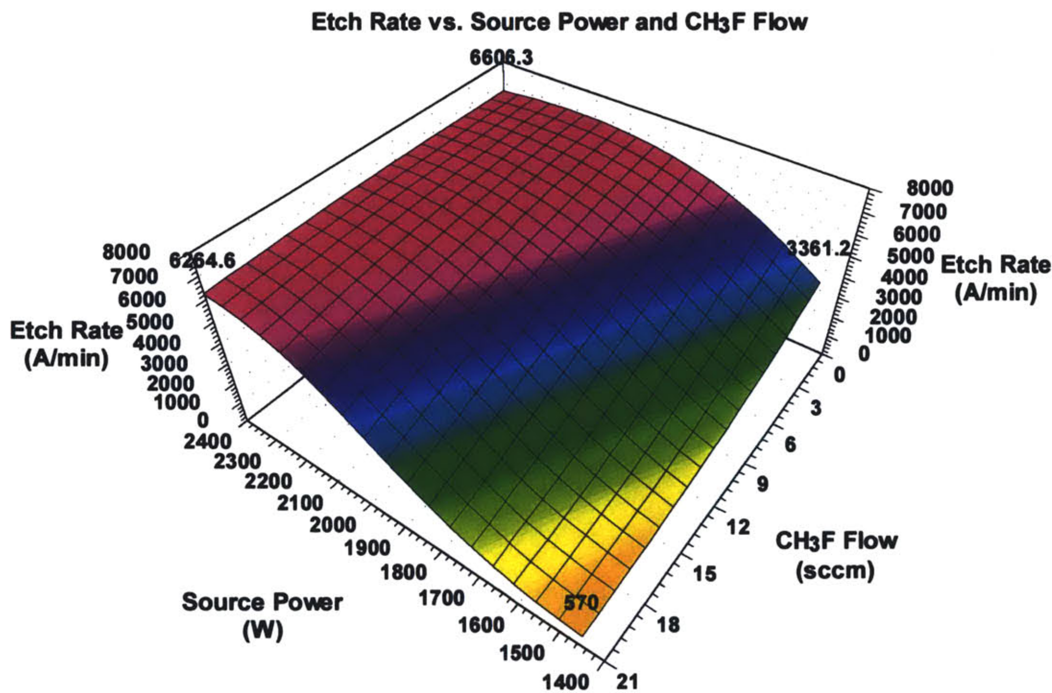

Figure 5.28a: First neural network data - TEOS oxide etch rate vs. source power and CH_3F flow. 1000 W bias power, 20.25 sccm etch gas flow, 230 °C roof temp, 15 mTorr pressure.

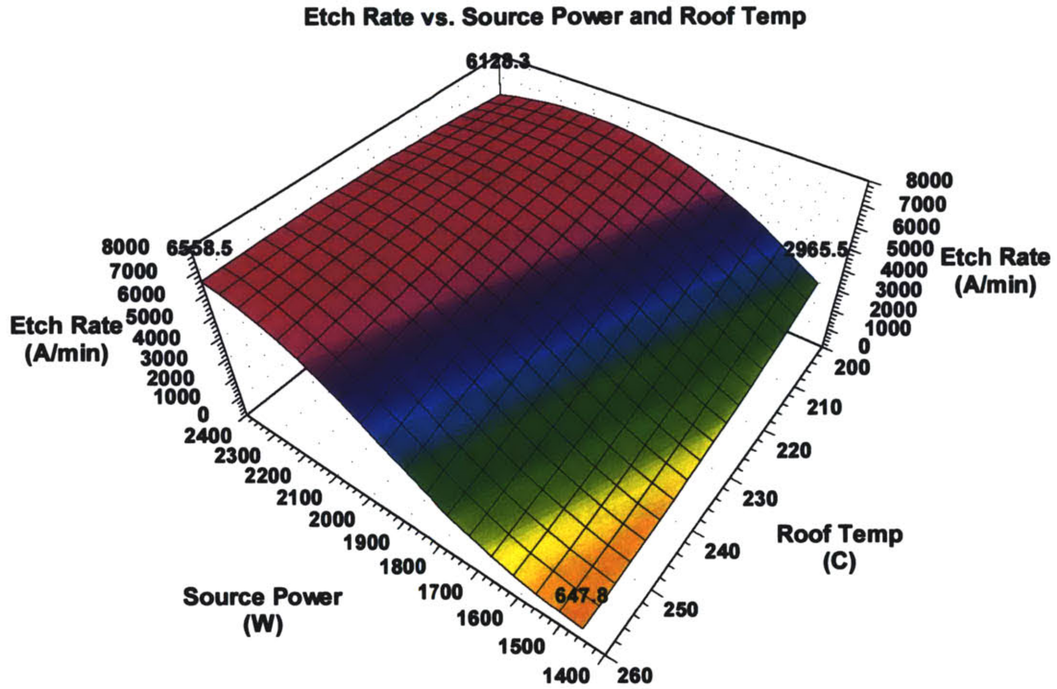

Figure 5.28b: First neural network data - TEOS oxide etch rate vs. source power and roof temperature. 1000 W bias power, 20.25 sccm etch gas flow, 10.5 sccm CH_3F flow, 15 mTorr pressure.

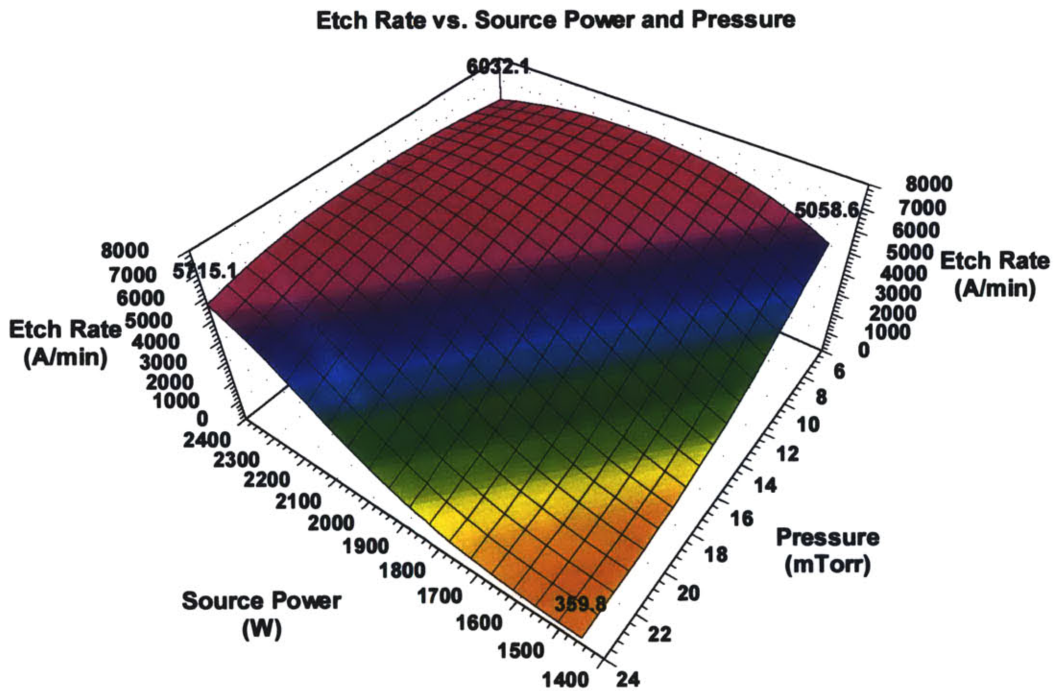

Figure 5.28c: First neural network data - TEOS oxide etch rate vs. source power and pressure. 1000 W bias power, 20.25 sccm etch gas flow, 10.5 sccm CH_3F flow, 230 °C roof temp.

What is observed in the analysis of the 200 °C wall temperature neural network model, however, is that, in certain regions of the parameter space explored, there appears to be an inversion in the basic trend discussed above (contrast Figures 5.29a-c with Figures 5.28a-c, respectively). Specifically, in regions of low etch gas flow, low CH_3F flow, low roof temperature, and/or low pressure, TEOS oxide etch rate is seen to *decrease* with increasing source power. The effect of the remaining variable, bias power, on source power trends has been found to be ambiguous. An analysis of the data used to create the matrix shows that regions in which the inversion is seen are the following: high *SP* / low *EF*, high *SP* / low *CF*, high *SP* / low *RT*, and high *SP* / low *PR*.

As will be evident from the subsequent discussion, low *EF*, low *CF*, low *RT*, and low *PR* all tend to result in conditions where polymer formation is reduced. Hence, it appears that, in a parameter space where polymer formation is significant, increasing source power continues to increase etch rate, most probably due to a combination of two effects: 1) higher degree of breakup of the etchant and 2) higher power density at the surface of the wafer. The latter effect is discussed in some detail in Refs. [1, 2] for etch tools of the same type as the one used in this study. There, the authors propose that etch stopping is seen in submicron contact features like the ones used here in large part due to a reduction in power density at the bottom of the feature as aspect ratio increases with increasing etch depth. The power density loss is described as a localized reduction in both ion energy and ion density resulting from charging of the feature sidewalls and shadowing effects. While ion energy has been noted by other workers to actually *decrease* with increasing source power under appropriate conditions (see below), a primary effect of increasing source power is an increase in plasma density and hence ion density in the flux arriving at the surface. Since a dominant effect of increasing source power in the present experiments is observed to be the suppression of polymer formation inside etched features, one concludes that net power density increase occurs at the bottom of the features.

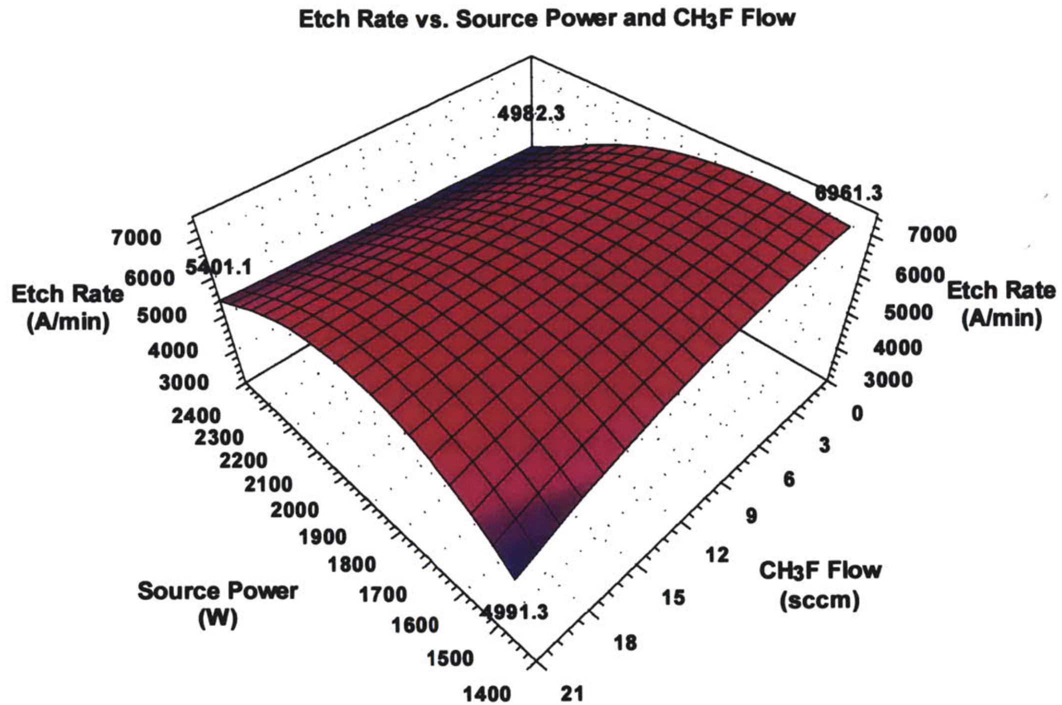

Figure 5.29a: First neural network data - TEOS oxide etch rate vs. source power and CH_3F flow. 1150 W bias power, 16 sccm etch gas flow, 205 °C roof temp, 12 mTorr pressure.

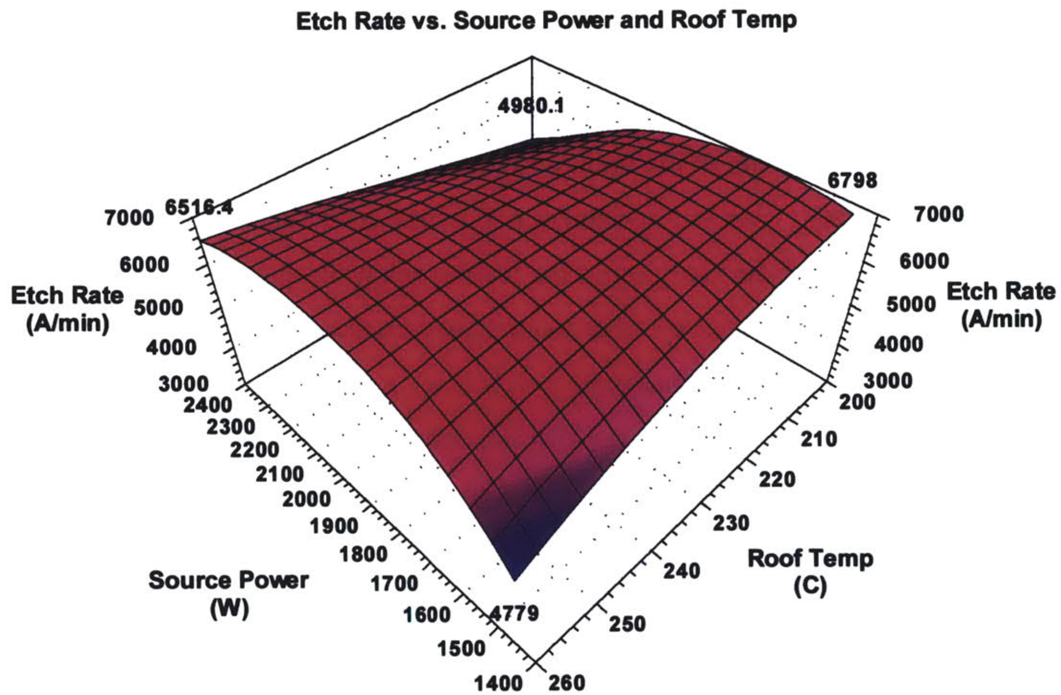

Figure 5.29b: First neural network data - TEOS oxide etch rate vs. source power and roof temperature. 1150 W bias power, 16 sccm etch gas flow, 6 sccm CH_3F flow, 12 mTorr pressure.

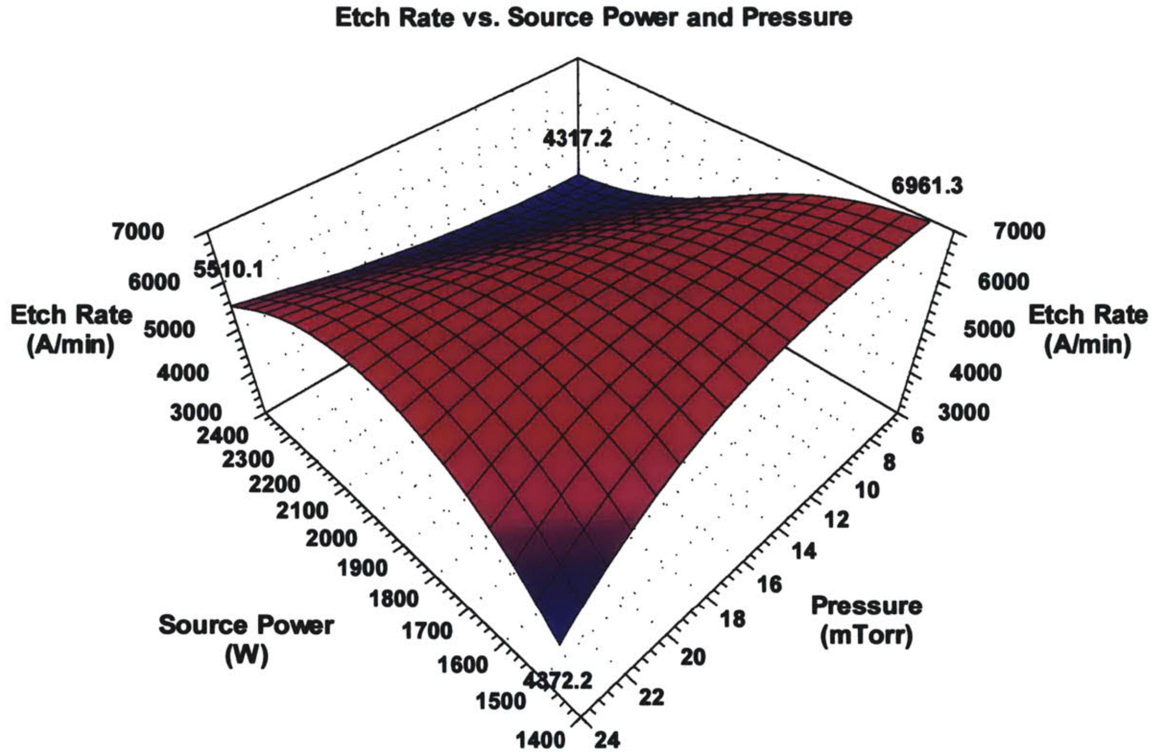

Figure 5.29c: First neural network data - TEOS oxide etch rate vs. source power and pressure. 1150 W bias power, 14 sccm etch gas flow, 6 sccm CH_3F flow, 205 °C roof temp.

In low polymerization regimes, however, it appears that the importance of the above effects is diminished, at least inside the via hole features, where the oxide etch rate was measured. This is likely due to the fact that polymer formation is already low, hence increasing source power does not necessarily further suppress polymer formation. Secondly, the reduction in etch rate at higher source power in these regimes is consistent with observations made by other workers that increasing source power at a fixed bias power can actually *decrease* the energy of the ions impinging on the substrate. In general, increasing source power increases the ion generation rate in the plasma; this results in ions arriving at the edge of the sheath above the wafer at a greater rate, which implies that the ion current to the wafer must increase. It has been shown that, for a fixed bias power, this increase in ion current must result in a decrease in ion voltage at the wafer surface. [3] The data in the present study therefore suggest that, while power density at the wafer surface is generally understood to increase with higher source power, there are regimes (which appear to correspond to low polymerization conditions) where

the reduction in ion energy that accompanies the increase in ion current at fixed bias power appears to play a significant role.

As had been pointed out in Section 5.3.2.1, it has been reported that, despite higher atomic fluorine concentrations seen in the plasma at higher source power in an inductively coupled tool, increasing source power leads to greater defluorination of the fluorocarbon film being deposited, *i.e.,* a lowering of its F:C ratio, which, in turn, is observed to correspond to thicker polymer deposits. If the ion flux (which has been reported to be more fluorine deficient than the neutral flux due to the lower ionization potentials of CF_x species versus F [4]) represents a significant fraction of the overall flux reaching the wafer, as is believed to be possible in high density systems, then conditions which generate high ion/neutral flux ratios may favor the formation of carbon rich CF_x layers, an effect consistent with an overall lowering of the SiO_2 etch rate. As will be evident from the discussion of sidewall slope trends below, however, it appears unlikely that this mechanism plays a significant role in the system presently being considered. Even though, under some conditions, in-feature oxide etch rate is clearly seen to decrease with increasing source power, there is no evidence that this is accompanied by a greater degree of polymer formation inside the features (higher source power leads to less, not more, polymer deposition inside the features under all conditions examined). It is clear, however, that such a regime exists and that, since it is a low polymerization regime to begin with, polymer suppression with higher source power is no longer the dominant mechanism. Moreover, in an iodofluorocarbon plasma, higher ion/neutral flux ratios are likely to lead to conditions where the physical sputtering component of the etch dominates, due to the presence of a large population of massive iodine ions. This effect is discussed in greater detail below and in Section 5.4.2.

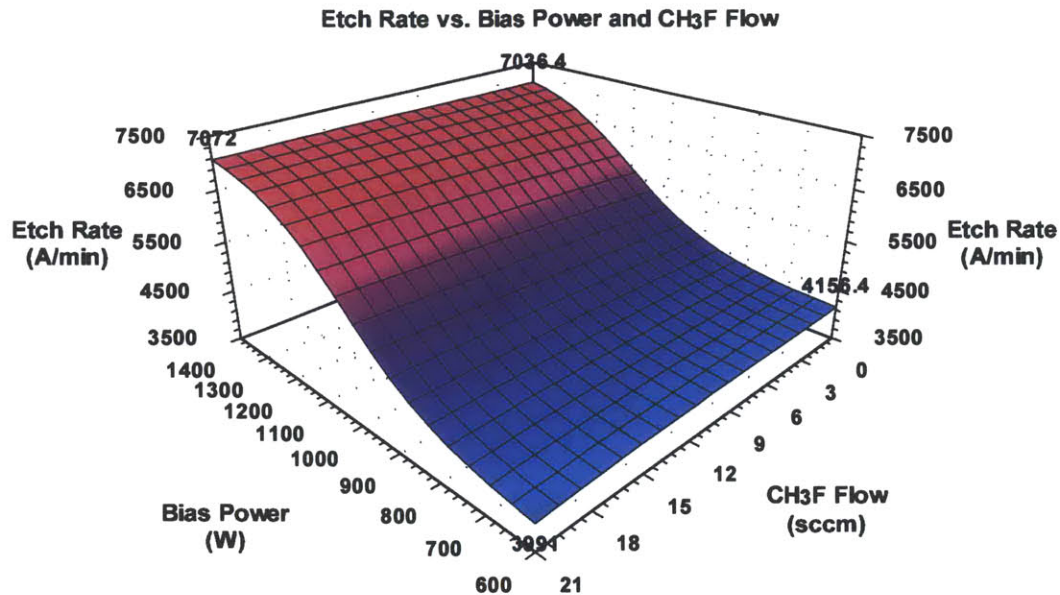

Figure 5.30a: First neural network data - TEOS oxide etch rate vs. bias power and CH_3F flow. 2150 W source power, 16 sccm etch gas flow, 205 °C roof temp, 12 mTorr pressure.

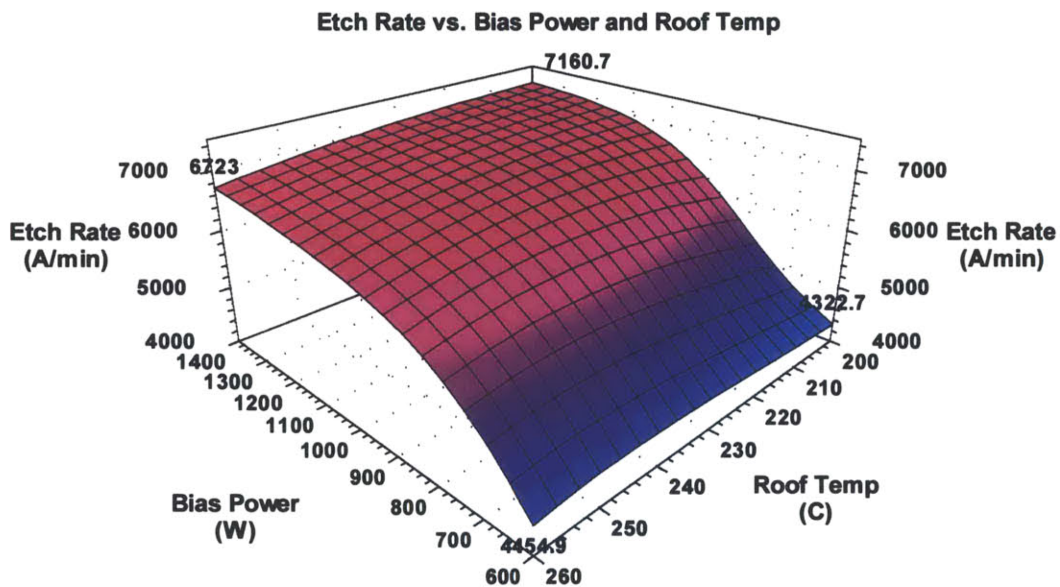

Figure 5.30b: First neural network data - TEOS oxide etch rate vs. bias power and roof temperature. 2000 W source power, 19 sccm etch gas flow, 8 sccm CH_3F flow, 12 mTorr pressure.

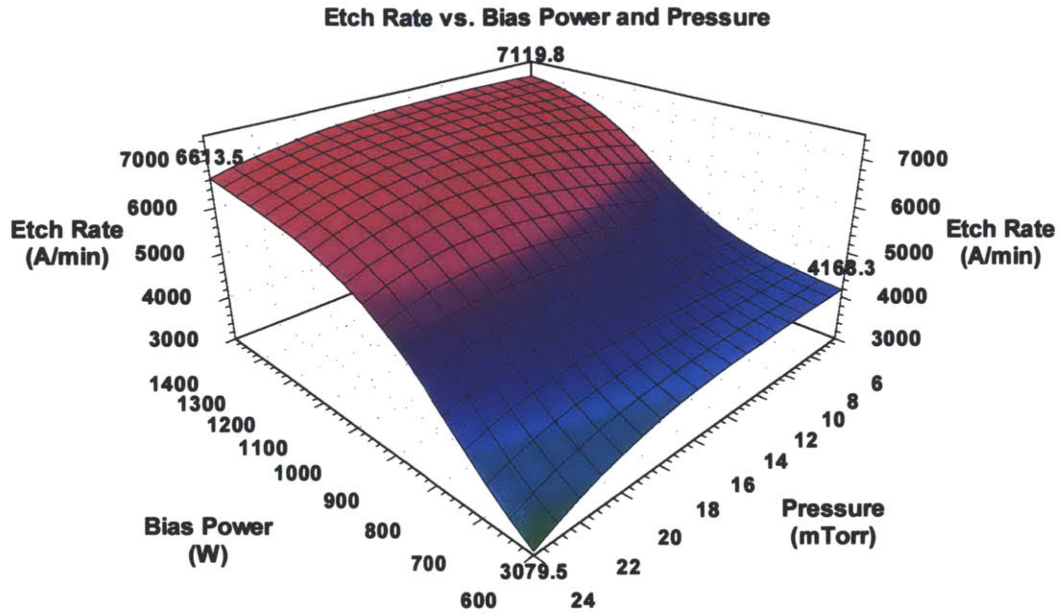

Figure 5.30c: First neural network data - TEOS oxide etch rate vs. bias power and pressure. 2000 W source power, 16 sccm etch gas flow, 8 sccm CH_3F flow, 215 °C roof temp.

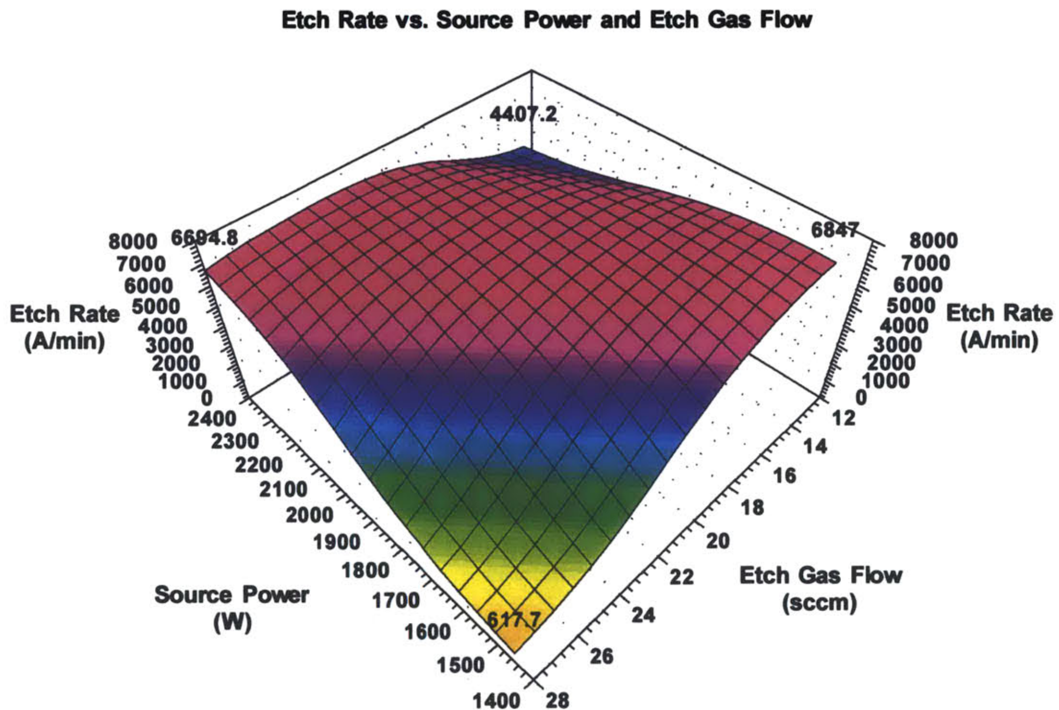

Figure 5.31: First neural network data - TEOS oxide etch rate vs. source power and etch gas flow. 1150 W bias power, 8 sccm CH_3F flow, 215 °C roof temp, 12 mTorr pressure.

Bias Power (*BP*). The effect of increasing bias power on TEOS oxide etch rate is that of a monotonic increase in etch rate in all regions of the parameter space. See, for instance, Figures 5.30a-c. As bias power is increased, both bias voltage and bias current are observed to rise, contributing to a net increase in the power density at the wafer surface. Specifically, the increase in bias voltage will generally act to increase the etch rates of all materials on the wafer, this increase resulting directly from the higher energy with which ions impinge on the wafer surface. As will be discussed in detail in Section 5.4.2, this mechanism appears to play an especially significant role in these experiments, given the abundance of massive iodine ions in the plasma.

Etch Gas Flow Rate (*EF*). The effect of etch gas flow on oxide etch rate is typical of what is observed in fluorocarbon etch plasmas: in a low polymerization regime, increasing flow rate tends to supply more etchant species and hence results in an etch rate increase; in a high polymerization regime, on the other hand, increasing etch gas flow tends to promote even more net polymer formation. As etch gas flow increases beyond a critical point for a given set of process conditions, the supply of additional feed gas results in fluorocarbon fluxes to the surface that now accumulate faster than they can be removed by competing processes. Since, in most regimes, the first order effect of increasing source power is to shift the process away from polymerization and into net etching, one would expect that, at low source power, increasing etch gas flow would result in lower oxide etch rate due to more polymer formation, whereas, at high source power, increasing etch gas flow would result in higher etch rate, since the plasma can dissociate the additional feed gas more efficiently at higher power. This effect is indeed seen in the present data, as Figure 5.31 shows. Similarly, since higher *CF*, *RT*, and *PR* are known to generally result in more polymer formation (see discussion below), one expects that at low *CF*, *RT*, or *PR*, an increase in oxide etch rate with increasing etch gas flow would be observed, whereas, as the process moves toward higher *CF*, *RT*, and/or *PR*, the balance shifts from etching to polymerization and a decrease in oxide etch rate with etch gas flow is observed. This can indeed be seen in Figures 5.32a-c. Finally, the effect of bias power on the etch gas flow trend appears to be weak. No trend is readily discernable in the interaction between bias power and etch gas flow.

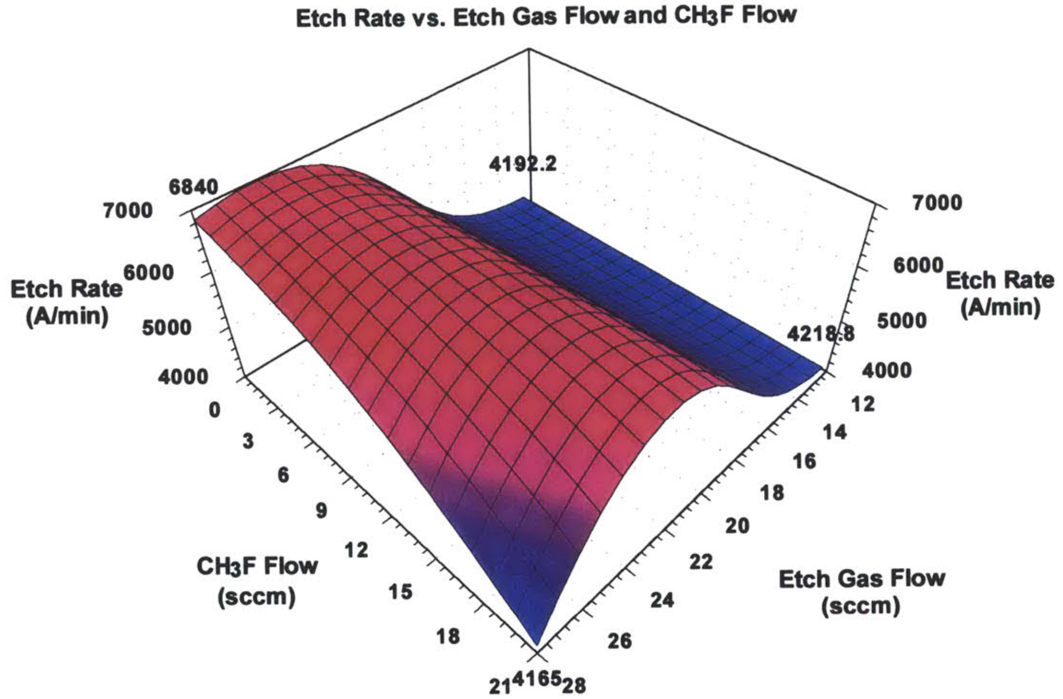

Figure 5.32a: First neural network data - TEOS oxide etch rate vs. etch gas flow and CH_3F flow. 2150 W source power, 900 W bias power, 215 °C roof temp, 7.5 mTorr pressure.

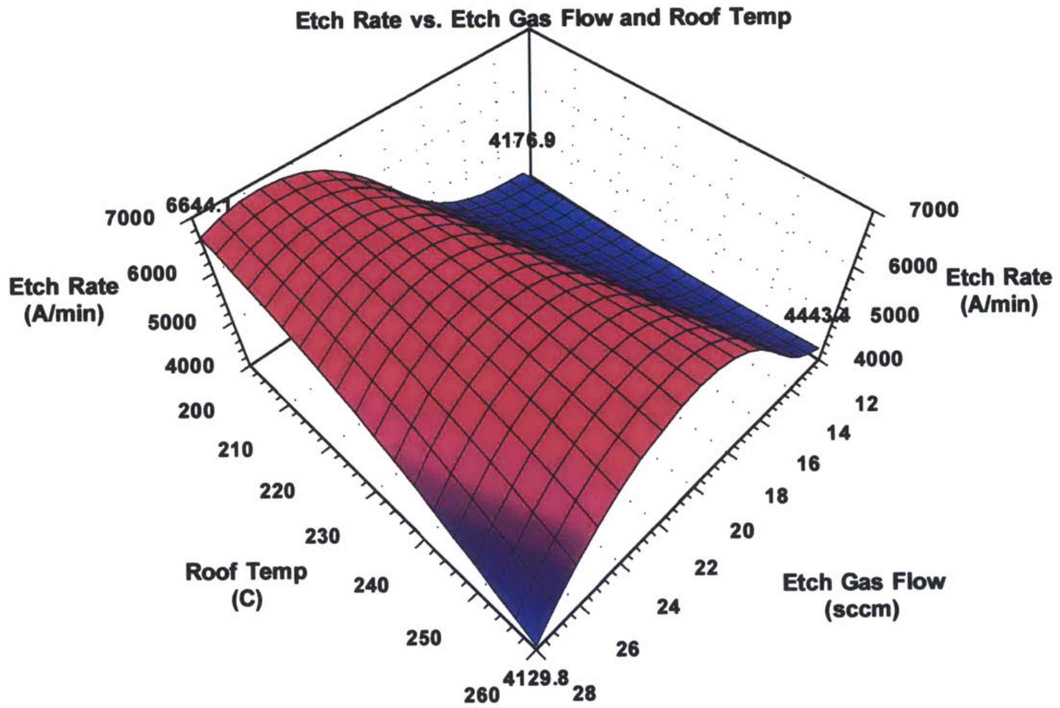

Figure 5.32b: First neural network data - TEOS oxide etch rate vs. etch gas flow and roof temperature. 2150 W source power, 900 W bias power, 8 sccm CH_3F flow, 7.5 mTorr pressure

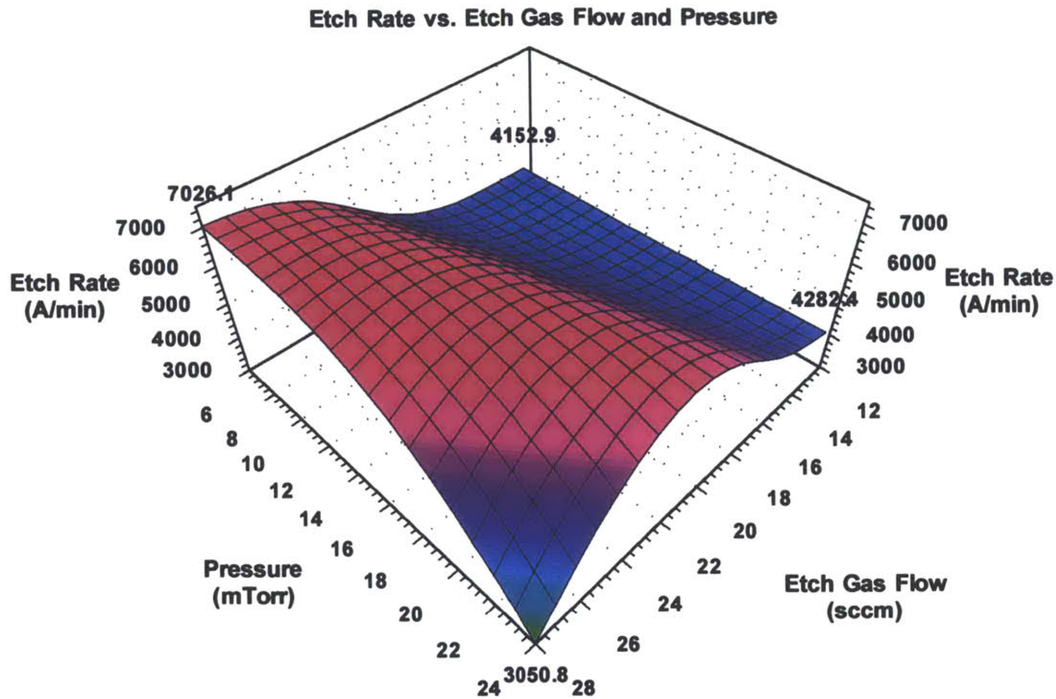

Figure 5.32c: First neural network data - TEOS oxide etch rate vs. etch gas flow and pressure. 2300 W source power, 900 W bias power, 2 sccm CH_3F flow, 205 °C roof temp.

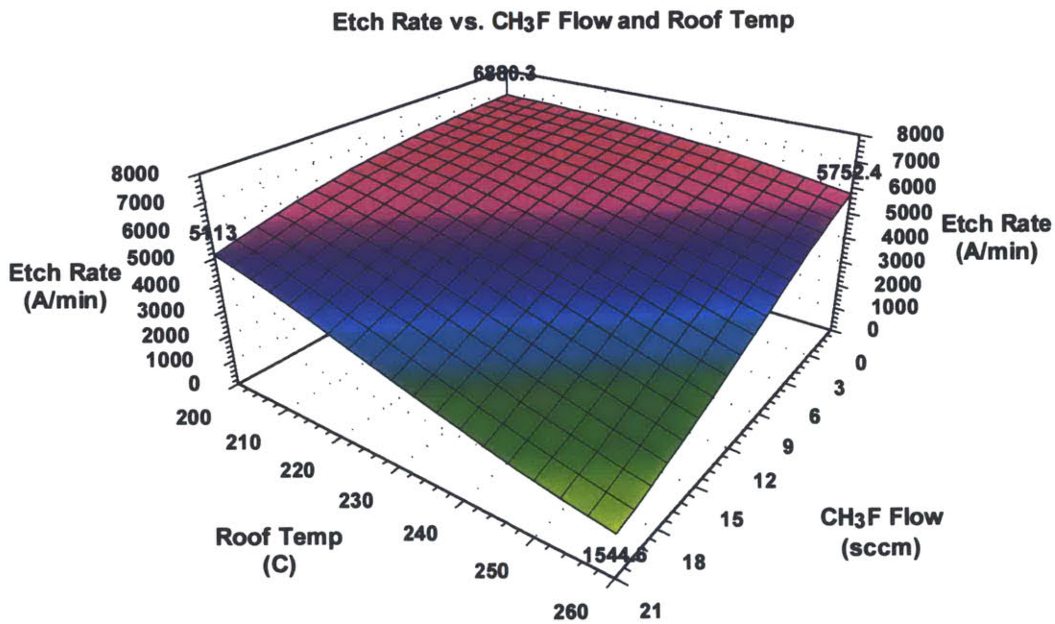

Figure 5.33a: First neural network data - TEOS oxide etch rate vs. CH_3F flow and roof temperature. 1925 W source power, 1000 W bias power, 20.25 sccm etch gas flow, 15 mTorr pressure.

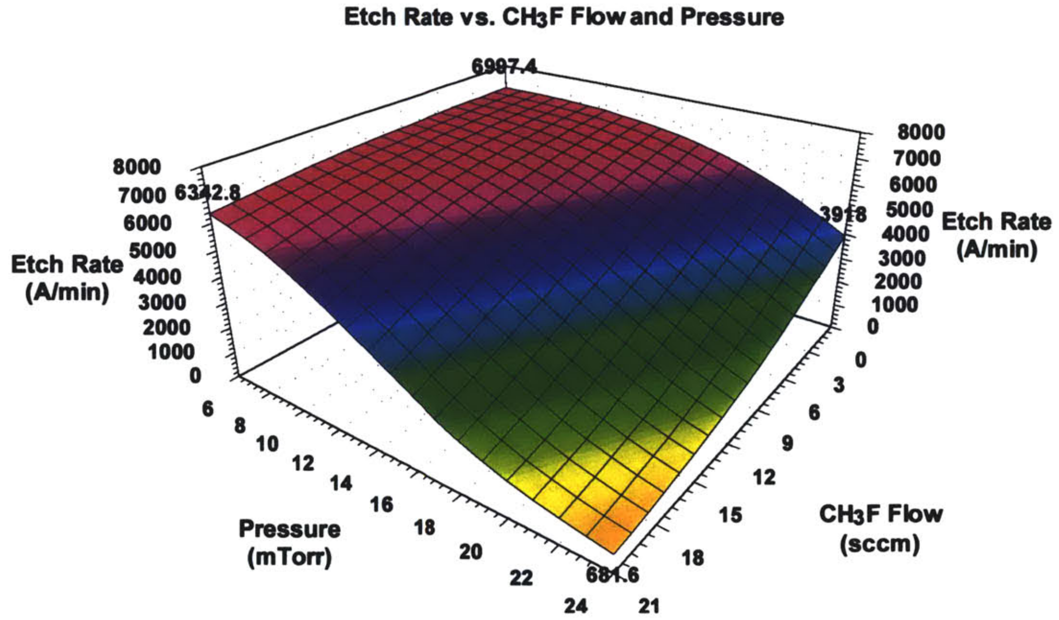

Figure 5.33b: First neural network data - TEOS oxide etch rate vs. CH_3F flow and pressure. 1925 W source power, 1000 W bias power, 20.25 sccm etch gas flow, 230 °C roof temp.

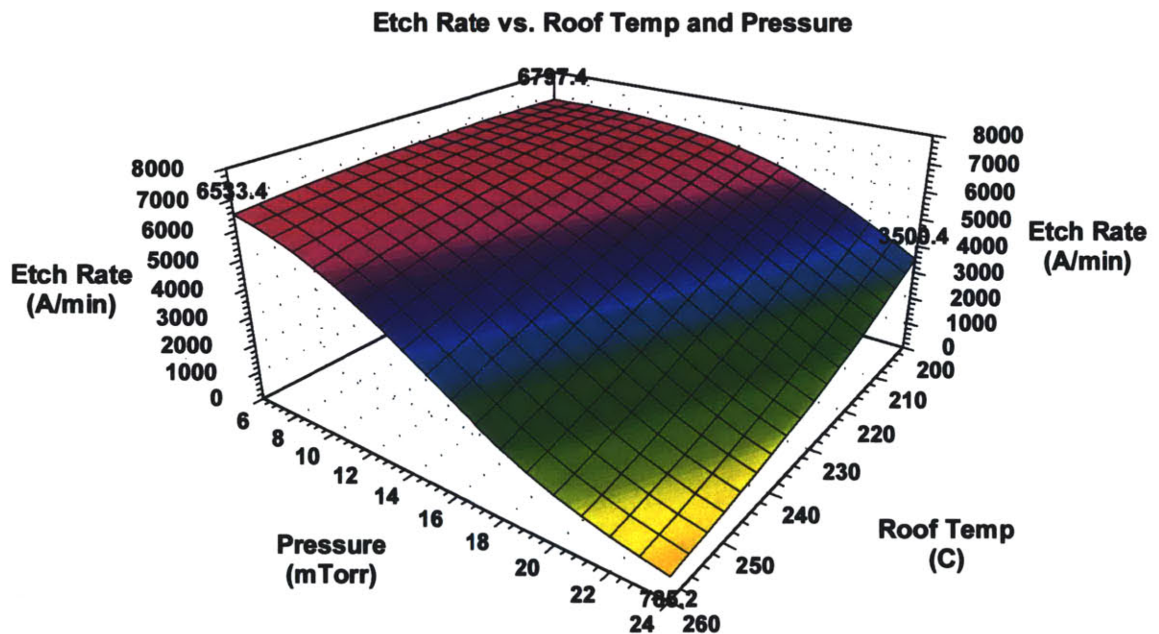

Figure 5.33c: First neural network data - TEOS oxide etch rate vs. roof temperature and pressure. 1925 W source power, 1000 W bias power, 20.25 sccm etch gas flow, 10.5 sccm CH_3F flow.

CH_3F Flow Rate (*CF*), Roof Temperature (*RT*), and Pressure (*PR*). Increasing each of these variables independently has the primary effect of enhancing polymerization mechanisms. Together, they reinforce each other in a roughly linear fashion. Their net effects are quite similar and hence will be dealt with collectively. Generally speaking, oxide etch rate decreases as *CF*, *RT*, and *PR* are increased. See Figures 5.33a-c.

The mechanisms by which this occurs are fairly well established. The presence of H in a fluorocarbon plasma is well known to generally promote polymer formation through the scavenging of F by hydrogen via both gas phase and surface phenomena. These mechanisms tend to either lower the F:C ratio of the deposited fluoropolymer, whether through gas phase or surface mechanisms, [5-7] or to defluorinate the CF_x film through HF formation within the film itself, [8] shifting the process toward conditions favoring net deposition versus net etching.

In the case of roof temperature, higher chamber surface temperature tends to result in lower condensation rates of polymer building species generated in the plasma. This makes more polymerization precursors available to coalesce on other surfaces in the chamber that are maintained at lower temperatures, [9] namely the electrostatic chuck, which, in these processes, was maintained at a temperature roughly 200 °C below that of the chamber roof. This again shifts the process toward conditions favoring polymerization rather than etching.

Finally, in the case of pressure, the number density of polymerization precursors in the plasma is known to increase with increasing pressure, along with the number of gas phase collisions, as well as the total fluorocarbon flux to the substrate. Less dissociation takes place, due to the sharing of energy among a larger number of parent species. [10] As has been discussed earlier, the same CF_x species can play the role of etch or deposition precursors, depending on whether the removal rate of the carbonaceous film on the substrate surface is sufficient to balance the ionic and neutral CF_x fluxes arriving at the substrate. If the process regime is such that polymerization phenomena already play a

significant role, increasing CF_x fluxes to the substrate is likely to have the effect of overwhelming CF_x film removal processes, resulting in a thicker CF_x film inside features, which impedes SiO_2 etching, or in the net buildup of film inside features, *i.e.,* etch stop. This argument applies not only to the effect of increasing pressure but to the effect of increasing roof temperature as well. (In general, it is also the case that increasing pressure results in a larger number of collisions in the sheath, which has the effect of reducing the energy with which ions arrive at the surface – again contributing to the shift from etching to polymerization. In the low pressure regime in this study, however, that effect is unlikely to play a dominant role.) One key difference, however, between the polymer forming mechanisms associated with increasing CH_3F flow and pressure and those associated with increasing chamber surface temperature is that, whereas the former increase the rate of polymer buildup on the wafer as well as on chamber surfaces, the latter increases polymer formation on the wafer at the expense of polymer buildup on the heated surfaces of the chamber.

There are regimes, however, where etch rate is seen to become insensitive with respect to CH_3F flow, roof temperature, and pressure (see Figures 5.32a-c or 5.30a-c) – or even to increase with increases in these variables (see Figures 5.34a-c). These regimes tend to be low polymerization regimes, characterized by higher source power, lower etch gas flow, lower CH_3F flow, lower roof temperature, and lower pressure. Varying bias power has no discernable effect on these trends, suggesting little interaction between bias power and these three variables. The earlier discussion suggested that a general effect of increasing CH_3F flow, roof temperature, and pressure is to increase the total CF_x fluxes to the wafer. In low polymerization regimes, however, as long as the fluorocarbon film removal rate is sufficient, an increase in CF_x fluxes may have a positive effect on oxide etch rate. It is therefore reasonable to suggest that, under low polymerization conditions, this mechanism appears simply to provide more F-containing species available to react with the TEOS oxide inside the features.

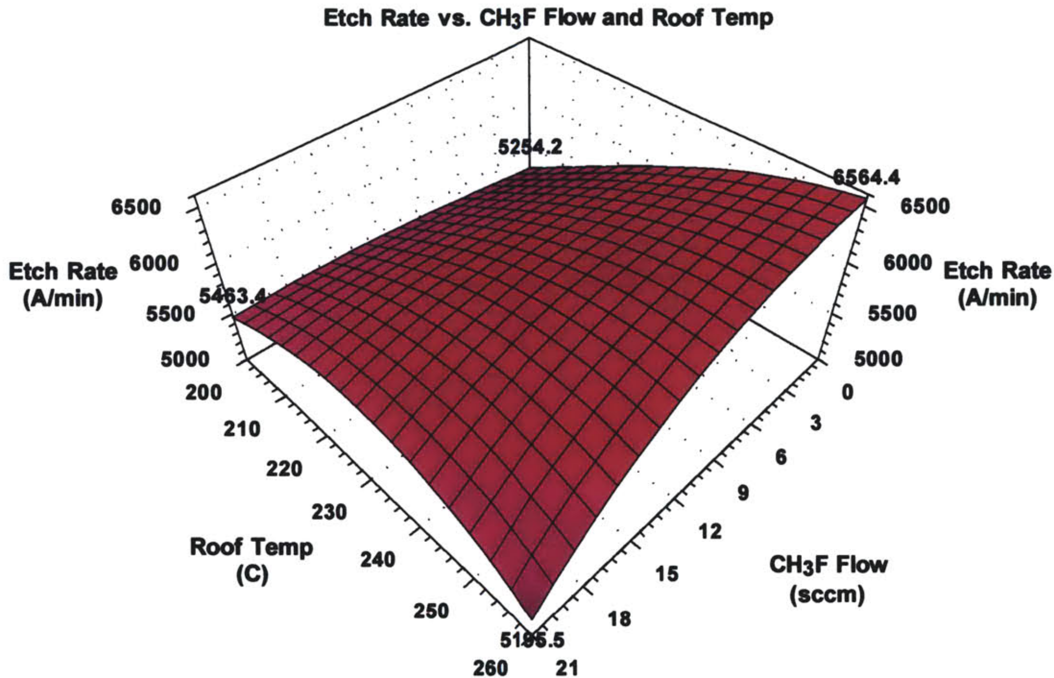

Figure 5.34a: First neural network data – TEOS oxide etch rate vs. CH_3F flow and roof temperature. 2100 W source power, 900 W bias power, 18 sccm etch gas flow, 12 mTorr pressure.

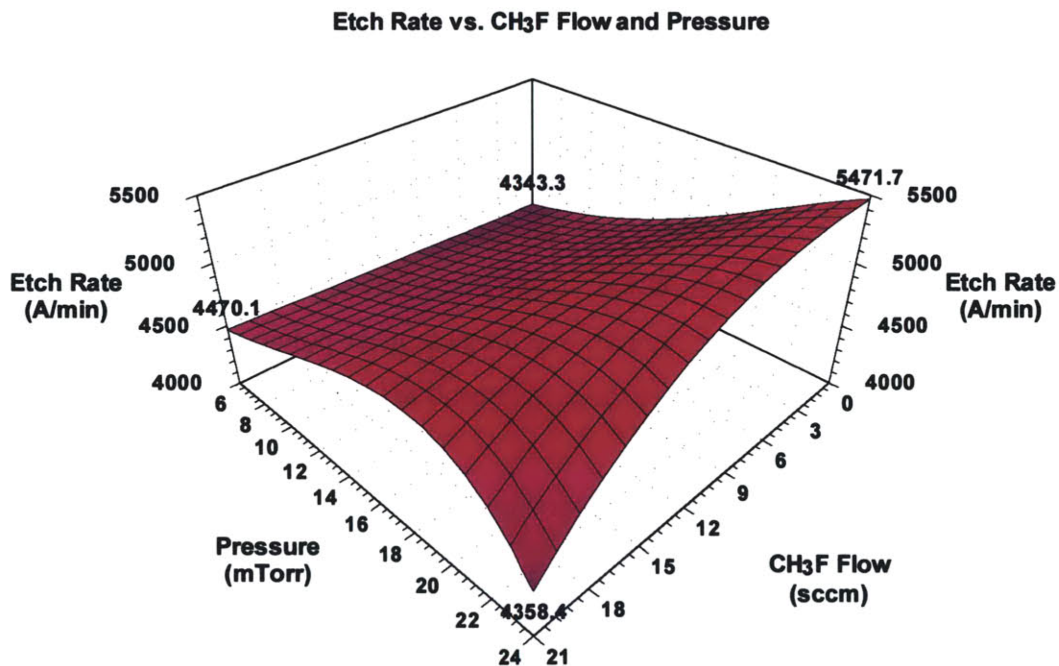

Figure 5.34b: First neural network data – TEOS oxide etch rate vs. CH_3F flow and pressure. 2150 W source power, 900 W bias power, 16 sccm etch gas flow, 205 °C roof temp.

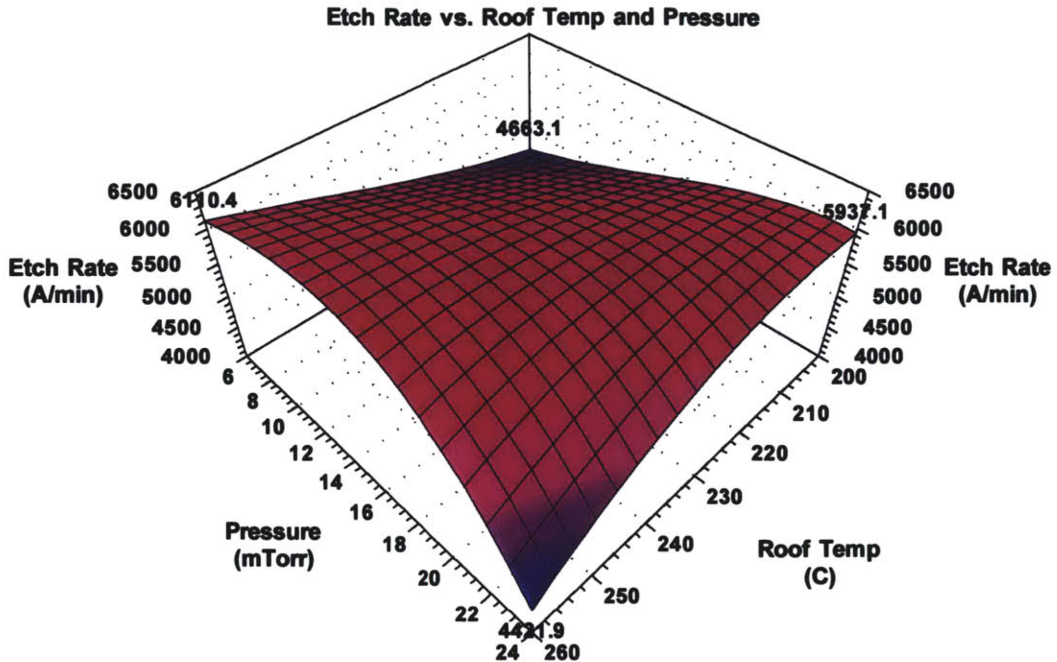

Figure 5.34c: First neural network data - TEOS oxide etch rate vs. roof temperature and pressure. 2150 W source power, 900 W bias power, 18 sccm etch gas flow, 4 sccm CH_3F flow.

1st Neural Network: Resist Remaining and Sidewall Slope

The analysis of the trends in the amount of resist remaining on the wafer is considerably more straightforward. As Figures 5.35, 5.36, and 5.37 show, the amount of resist remaining on the wafer increases with decreasing source power, decreasing bias power, increasing etch gas flow, increasing CH_3F flow, increasing roof temperature, and increasing pressure. Generally speaking, as will be evident from the discussion below, these trends indicate that process regimes that promote more polymer formation (low *SP* or *BP* or high *EF, CF, RT,* or *PR*) are those that result in lower amounts of resist erosion.

The neural network model did, however, produce some inversions in these trends. The apparent inversions, however, were all found to lie in regions of the parameter space defined by a combination of three of the following parameters: low *BP*, low *CF*, high *SP*, high *EF*, high, *RT*, and high *PR* (*e.g.*, low *CF* / high *RT* / high *PR*, but not high *CF* / high *RT* / high *PR*), where "low" is defined as a value less than the –0.5 value for that parameter and "high" is defined as a value greater than the +0.5 value for that parameter

(see Table 5.8). Subsequent analysis showed that only 4 out of 146 points used to create the matrix were located in these regions of the parameter space, suggesting that these regions were underrepresented in the model and that care should be taken in interpreting the apparent inversions. Therefore, for the purposes of this discussion, these inversions in the main trends will be treated as artifacts of the model and the trend analysis will be focused on the main trends shown in Figures 5.35, 5.36, and 5.37.

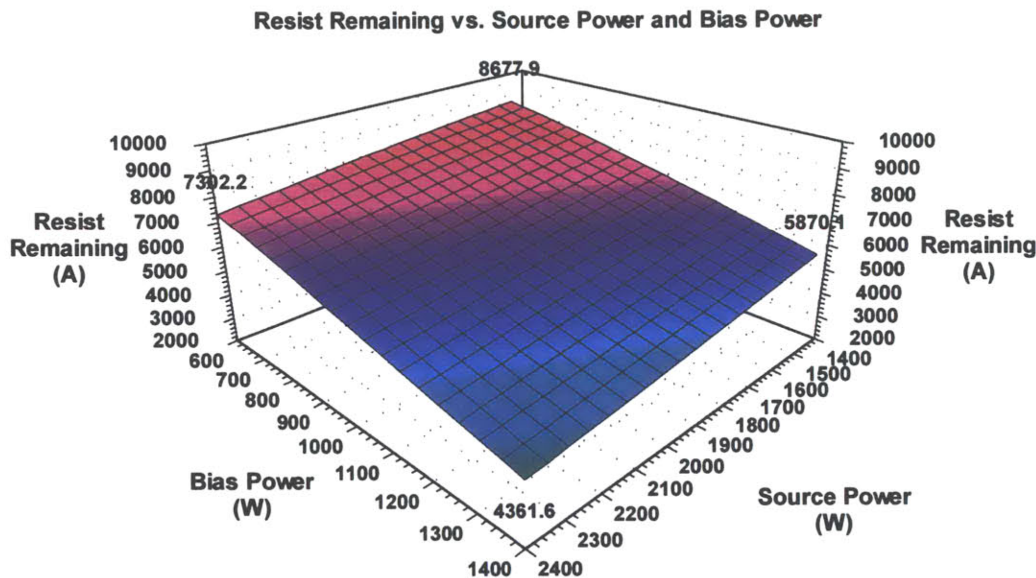

Figure 5.35: First neural network data – resist remaining vs. source power and bias power. 20.25 sccm etch gas flow, 10.5 sccm CH_3F flow, 230 °C roof temp, 15 mTorr pressure.

The trends in the 0.35 μm center location sidewall slope are consistent with those observed for the thickness of resist remaining, in that process regimes which yield lower amounts of resist erosion also correspond to more polymer formation inside the features. As Figures 5.38, 5.39, and 5.40 show, the sidewall slope in degrees decreases (becomes less vertical) with decreasing source power, decreasing bias power, increasing etch gas flow, increasing CH_3F flow, increasing roof temperature, and increasing pressure, *i.e.*, feature profile deteriorates under the same conditions which were identified above as promoting more polymerization on the wafer surface. These trends are monotonic throughout the entire parameter space explored. In general, sidewall slope is found to be most sensitive to any given variable in regimes associated with increased rates of

polymer formation; *i.e.,* changing any variable in a direction that moves the process away from polymerization (increasing *SP* or *BP* or decreasing *EF, CF, RT,* or *PR* in regimes characterized by low *SP* or *BP* or high *EF, CF, RT,* or *PR*) is observed to produce a marked improvement in feature profile. In low polymerization regimes (characterized by high *SP* or *BP* or low *EF, CF, RT,* or *PR*), on the other hand, the response surfaces level out asymptotically around 88°, which is readily understood, since, once near vertical profiles are achieved, additional polymer suppression produces little incremental benefit.

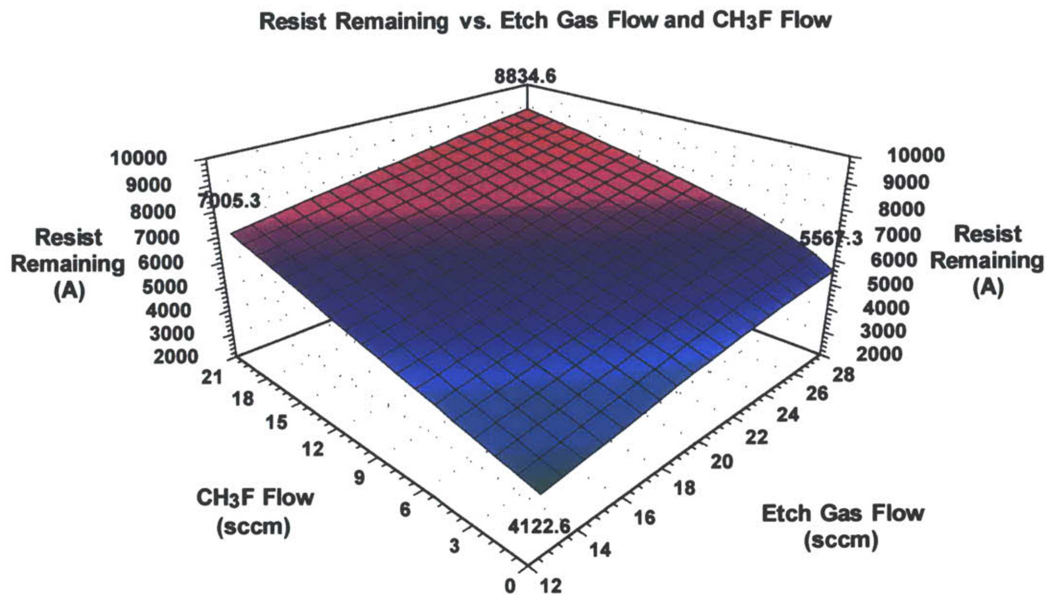

Figure 5.36: First neural network data – resist remaining vs. etch gas flow and CH_3F. 1925 W source power, 1000 W bias power, 230 °C roof temp, 15 mTorr pressure.

Source Power (*SP*). Increasing source power generally results in more complete breakup of the feed gas molecule, hence is expected to produce conditions less favorable to polymer formation on the wafer surface, which is the principal mechanism that competes with the etching of the resist. "More complete breakup" is not necessarily intended to be synonymous with "higher utilization efficiency," that is to say, at very high source gas utilization across all conditions (values of ~95% will be reported in Section 5.4.3), increasing source power is believed to result in *further* bond cleavage among the initial dissociation products. Increasing source power is also understood to result in an increase in the power density at the wafer surface, which, again, is consistent

with suppression of polymer formation, both on the wafer surface and inside features. The monotonic trends in resist remaining and sidewall slope seen here stand in contrast to the effect seen with the oxide etch rate inside via hole features, where, under low polymerization conditions, increasing source power actually resulted in a lowering of the etch rate. This effect, however, was not linked to a possible shift of the process toward polymerization inside the features. Rather, it was suggested that the dominant phenomenon resulting in lower oxide etch rate may be the decrease in ion energy that is known to occur with increasing source power at fixed bias power.

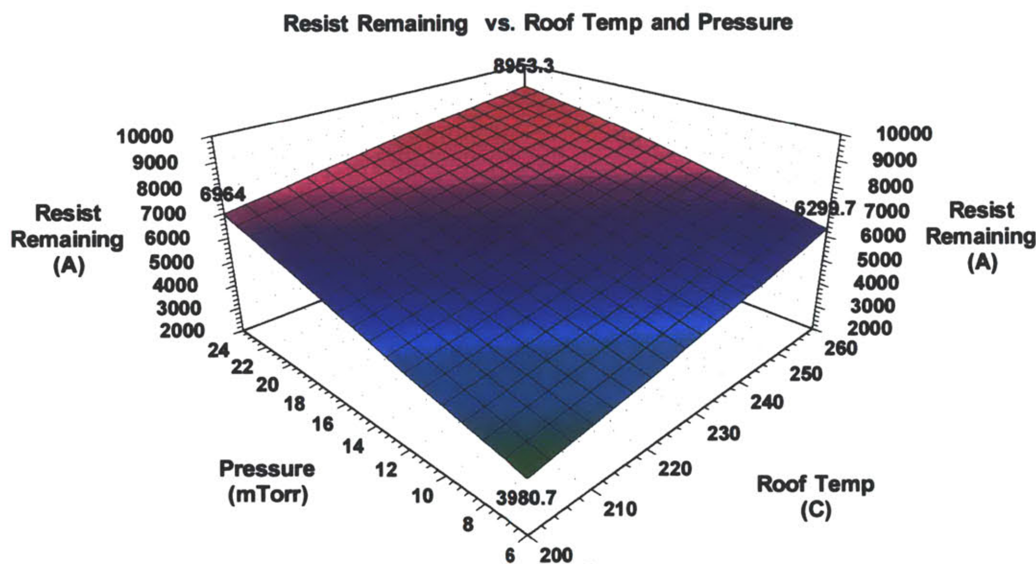

Figure 5.37: First neural network data – resist remaining vs. roof temperature and pressure. 1925 W source power, 1000 W bias power, 20.25 sccm etch gas flow, 10.5 sccm CH_3F flow.

Bias Power (*BP*). The bias power trend in resist remaining is consistent with the observations made earlier regarding oxide etch rate. The dominant effect appears to be the increase in ion energy and/or ion density resulting from increased bias power. This increases the etch rate of the resist, as was the case with the oxide etch rate. As will be discussed in Section 5.4.2, the abundance of massive iodine ions in the plasma will serve to enhance the physical sputtering component of the etch. It is therefore not surprising that increasing bias power has an unambiguous, monotonic effect on the etch rates of both the oxide and the resist. The sidewall slope trend is also monotonic with respect to

bias power. Again, the effect appears to be relatively straightforward to understand: higher bias power results in higher power density within the features being etched, suppressing polymer formation in feature corners, and thus preventing the vias from tapering inward.

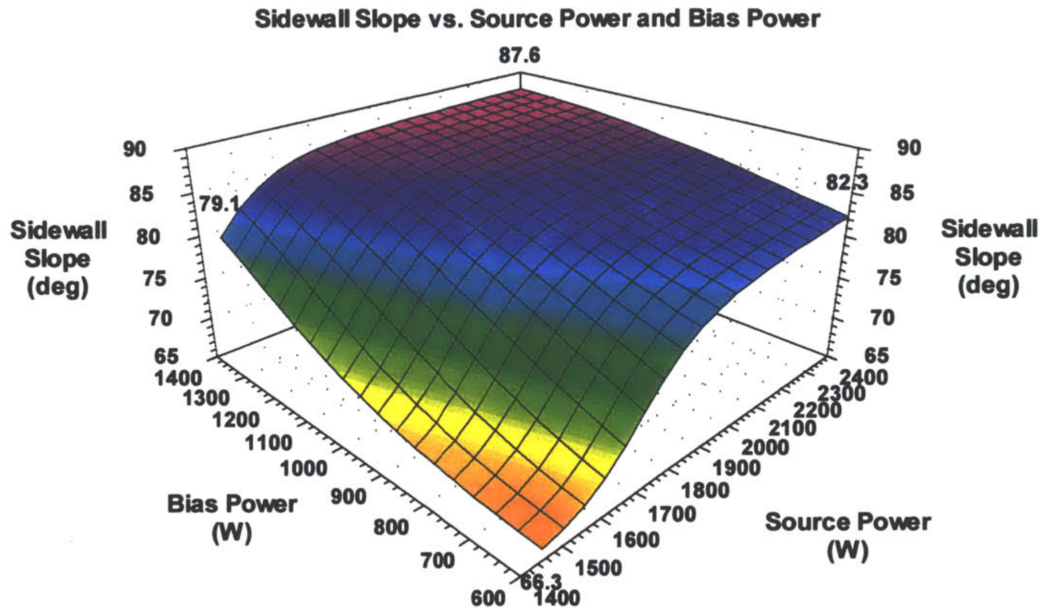

Figure 5.38: First neural network data – sidewall slope vs. source power and bias power. 20.25 sccm etch gas flow, 10.5 sccm CH_3F flow, 230 °C roof temp, 15 mTorr pressure.

Etch Gas Flow Rate (*EF*). The dominant trend here appears to be the enhancement in polymer formation with increasing fluorocarbon fluxes that result from higher etch gas flow. The monotonic trends observed with respect to resist remaining and sidewall slope can again be contrasted with the more complex effect seen in the oxide etch rate case: in low polymerization regimes, increasing etch gas flow rate is observed to increase oxide etch rate by supplying more etchant species, while, in high polymerization regimes, increasing etch gas flow rate slows down the oxide etch by promoting more polymer formation. The behavior of all three variables under high polymer formation conditions is easily explained: more polymer formation with higher etch gas flow leads to slower oxide etch rate, poorer profiles due to buildup of sidewall and bottom corner polymer films (and eventually etch stop), and less resist erosion.

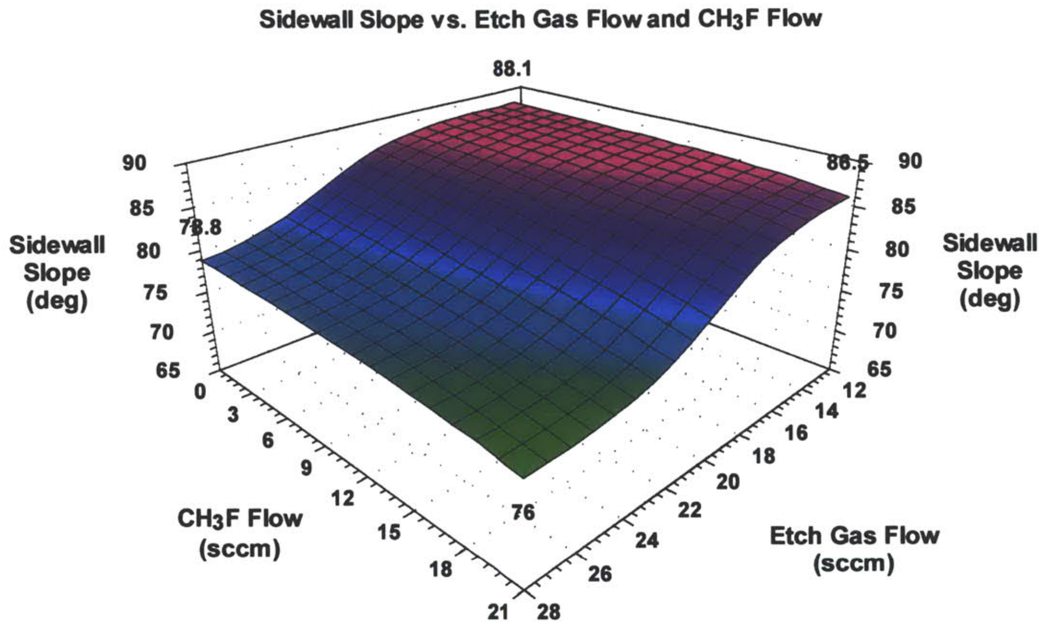

Figure 5.39: First neural network data – sidewall slope vs. etch gas flow and CH_3F flow. 1925 W source power, 1000 W bias power, 230 °C roof temp, 15 mTorr pressure.

The difference in behavior between resist etch rate and oxide etch rate in low polymerization conditions is probably at least partially explainable by the difference in etching mechanisms between the two materials under polymerizing conditions. In most regimes where oxide surfaces are etched, fluorocarbon film formation occurs more readily on resist surfaces, in large part due to the effect oxygen in SiO_x is believed to play in the removal of carbon in the CF_x film (See Section 3.3.3 and references therein). Thus, on oxide surfaces, where oxygen is available to assist with the removal of carbon from the CF_x layer being formed, higher CF_x flux to the surface can increase the oxide etch rate while, at the same time, it contributes to building polymeric film on resist.

On the other hand, the difference in behavior between the oxide etch rate trend and the sidewall slope trend in low polymerization conditions can probably be explained in terms of the difference in power density on the feature sidewalls and in corners, where higher etch gas flow causes more polymer buildup, versus the center of the feature bottom, where higher etch gas flow causes an increase in the measured etch depth. Whereas the sidewalls and corners are subjected to a less energetic flux of incident species due to

shadowing and charging effects [1, 2], the center of the feature bottom receives much higher power density. In the former case, the arrival of additional CF_x species contributes to film formation; in the latter case, where more energy is available, additional CF_x species result in an increase in the local etch rate.

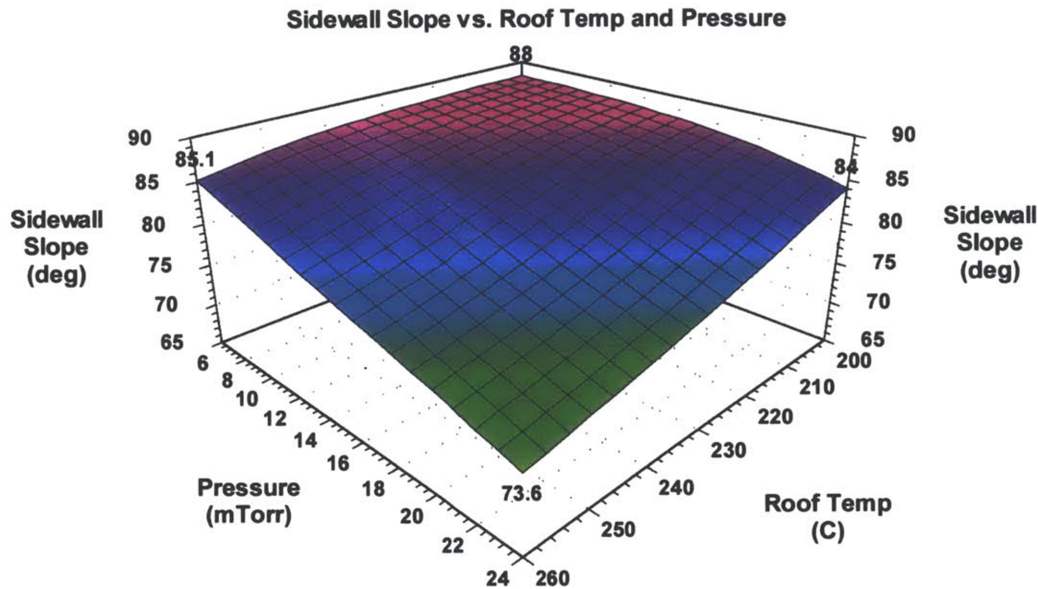

Figure 5.40: First neural network data – sidewall slope vs. roof temperature and pressure. 1925 W source power, 1000 W bias power, 20.25 sccm etch gas flow, 10.5 sccm CH_3F flow.

CH_3F Flow Rate (*CF*), Roof Temperature (*RT*), and Pressure (*PR*). The principal effect of increasing each of these variables is that of enhancing polymer formation, as had been discussed earlier. Here, once again, the observed resist remaining and sidewall slope trends are monotonic with respect to each of these variables, with no evidence of inversion in low polymerization regimes. On the other hand, under low polymerization conditions, measured in-feature oxide etch rate was observed to increase with increases in CH_3F flow rate, roof temperature, and pressure, despite evidence of increased polymer formation on the bulk of the resist and on feature sidewalls and corners. This again implies that there are differences in the polymer formation mechanisms on the oxide surfaces in the center of via holes and those on feature sidewalls and corners as well as on the bulk of the resist. The same explanations which are believed to hold for the etch gas flow rate case discussed above are likely to be at work here, given the fact that

carbonaceous deposits are more readily removed from oxide surfaces under energetic ion bombardment than from oxide surfaces which are shielded from that bombardment or from resist surfaces. In the former case, the increase in CF_x fluxes to the surface with increasing *CF*, *RT*, and *PR* results in etch rate enhancement, whereas, in the latter cases, it promotes more film growth.

2nd Neural Network

The trends for both oxide etch rate and resist remaining with respect to source power and pressure in the second (230 °C *WT*) neural network experimental set are consistent with the primary trends seen in the main (200 °C *WT*) data set. Over the range of 1500 to 1700 W, oxide etch rate is seen to increase with increasing source power while the thickness of resist remaining is observed to decrease. Over the range of 20 to 30 mTorr, oxide etch rate is seen to decrease with increasing pressure while the thickness of resist remaining is observed to increase. See Figures 5.41 and 5.42. The sidewall slope values for the nine runs that comprised this set of experiments were nearly the same (79.6°±1.3°) with no trend seen with respect to either source power or pressure. This effect is attributed to the fact that, in this high pressure regime, significant etch stop was occurring at all process conditions and this effect dominated over other feature-level mechanisms that would affect profile evolution.

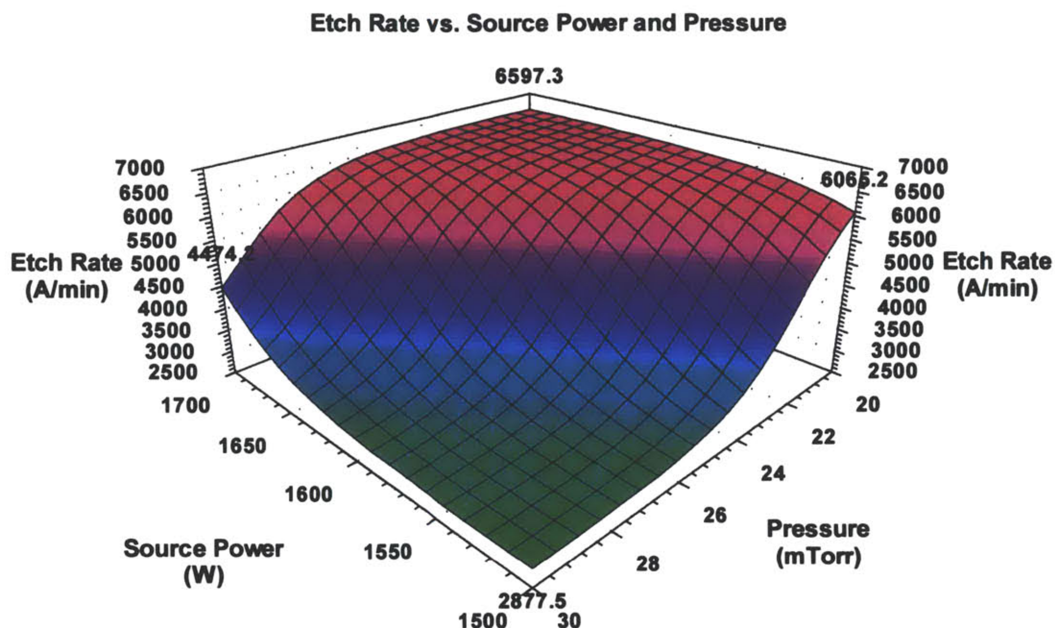

Figure 5.43: Second neural network data – TEOS oxide etch rate vs. source power and pressure. 800 W bias power, 14 sccm etch gas flow, 0 sccm CH_3F flow, 230 °C roof temp, 230 °C wall temp.

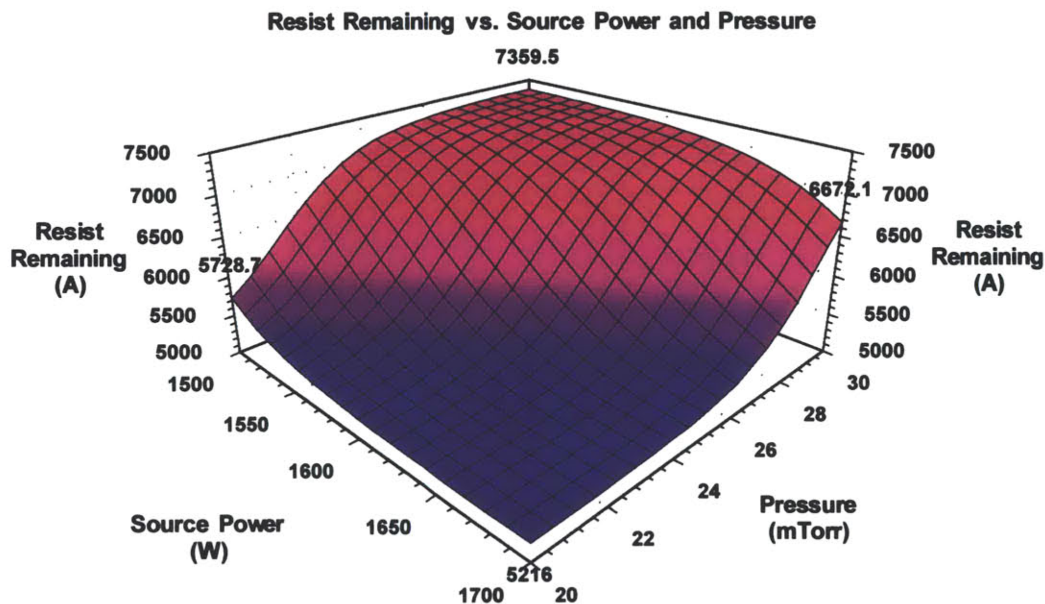

Figure 5.42: Second neural network data – resist remaining vs. source power and pressure. 800 W bias power, 14 sccm etch gas flow, 0 sccm CH_3F flow, 230 °C roof temp, 230 °C wall temp.

5.4.1.3 Results and Discussion Effects of Wall and Chiller Temperature

Varying wall temperature from 200 to 215 to 230 °C in the regime studied (at 2000 W *SP*, 800 W *BP*, 16 sccm *EF*, 15 sccm *CF*, 230 °C *RT*, 6 mTorr *PR*) appears to have had no appreciable effect on oxide etch rate or feature profile. It did, however, result in a noticeable increase in resist remaining, with an average of 5970 Å of resist remaining at the 230 °C condition versus an average of 5490 Å at the 200 °C condition, a difference of 480 Å. This is in keeping with the chamber surface heating mechanisms elaborated earlier, although it appears that the effect of varying wall temperature is not as pronounced as that of varying roof temperature. By comparison, varying roof temperature over the range of 200 °C to 230 °C in one set of experiments (at 1600 W *SP*, 800 W *BP*, 16 sccm *EF*, 0 sccm *CF*, 200 °C *WT*, 9 mTorr *PR*) resulted in a 2440 Å increase in the thickness of resist left. The greater sensitivity of the process with respect to roof temperature over wall temperature is not necessarily surprising, since the surface area of the Si roof is larger than the surface area of the quartz dome (heated portion of the chamber wall); moreover, the roof slab lies in greater proximity to the wafer surface.

Decreasing chiller temperature was found to result in an increase in the oxide etch rate over the 34 to 0 °C range in the regime examined (2400 W *SP*, 600 W *BP*, 20 sccm *EF*, 12 sccm *CF*, 230 °C *RT*, 200 °C WT, 6 mTorr *PR*). At –15 °C, however, the onset of etch stop was reached inside the via features, which resulted in a reversal in the etch rate trend and a large *decrease* in etch rate from 0 °C to –15 °C. See Figure 5.43. The via profile exhibited a monotonic trend over the entire 34 to –15 °C range, becoming progressively more tapered as chiller temperature was decreased, suggesting more polymer formation was taking place inside the features at lower wafer temperature. The amount of resist erosion, however, increased with decreasing chiller temperature. The net effect on oxide:resist selectivity was negative, with a drop in the average selectivity measured using 0.35 μm CD vias from 3.01:1 at 34 °C to 1.78:1 at –15 °C.

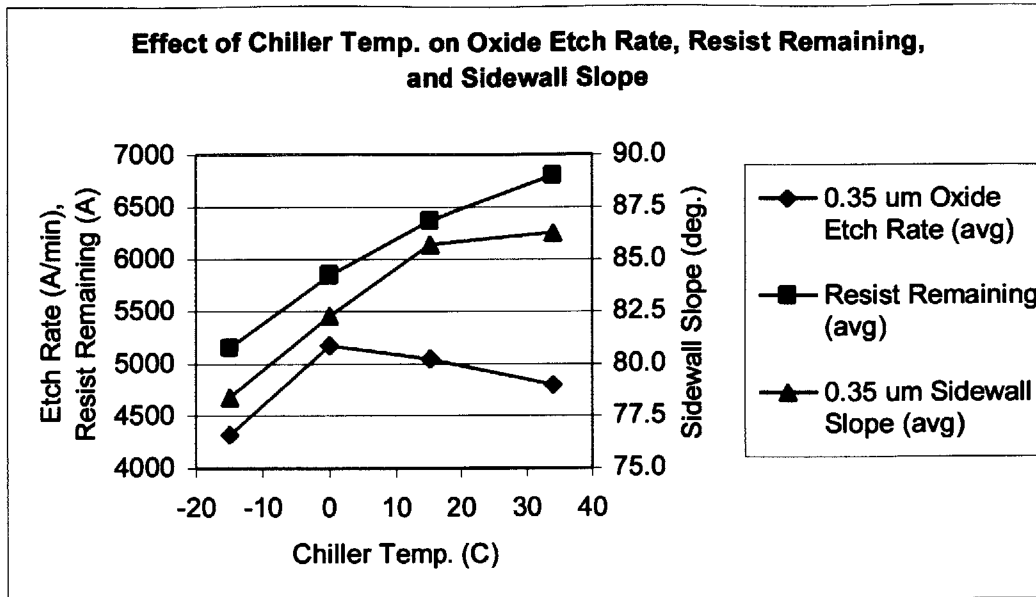

Figure 5.43 Effect of chiller temperature on oxide etch rate, thickness of resist remaining, and sidewall profile. 2400 W *SP*, 600 W *BP*, 20 sccm *EF*, 12 sccm *CF*, 230 °C *RT*, 200 °C WT, 6 mTorr *PR*.

Application of the mechanism outlined earlier with respect to condensation and chamber surface temperatures would lead one to expect that lowering wafer temperature through lowering the chiller loop temperature should lead to more polymer formation. This is, in fact, seen inside the features, where more sidewall and bottom corner deposits are seen to form with decreasing wafer temperature, leading to more via taper and eventually etch stop. However, the amount of resist eroded steadily increases while this is occurring, suggesting that *less* polymer formation is taking place on the wafer surface. Further investigation may be required before this effect is fully understood.

5.4.1.4 Results and Discussion – Cross-sectional SEM Analysis

Cross sectional SEMs were taken on all of the patterned wafers used in this work. Figure 5.44 shows cross sections of 0.35 µm nominal printed CD via hole features etched with the C_3F_8/CH_3F reference process. The standard *in-situ* O_2-based post-etch treatment (PET) that is normally run after etch processes in the tool used for this study was not run on any of the wafers used for this work (except the stop on PEN/Cu wafers, see Section 5.4.1.6 below) so that the resist could be preserved for measurement. Because the PET

was not run, residual sidewall polymer also remains; these residues, which are easily removed with the PET, can be seen in Figure 5.44 as well as other figures in this section. Table 5.9 summarizes the process conditions and process results obtained for the five SEM cross sections discussed here.

Table 5.9: Comparison of C_3F_8/CH_3F reference recipe with representative 1-iodoheptafluoropropane based processes. *WT* = 200 °C; 0.35 μm process data shown: oxide etch rate (Å/min), resist remaining (Å), oxide:resist selectivity, sidewall slope (deg.).

Fig.	SP (W)	BP (W)	EF (sccm)	CF (sccm)	RT (°C)	PR (mTorr)	0.35 μm center				0.35 μm edge			
							Etch Rate	Resist Rem.	OX:PR Sel.	Side-wall Slope	Etch Rate	Resist Rem.	OX:PR Sel.	Side-wall Slope
5.44	C_3F_8/CH_3F reference recipe						4206	9690	27.13	88.9	4546	9220	11.66	89.1
5.45	1900	800	24	3	230	6	7100	5425	3.10	84.2	7400	5488	3.28	86.2
5.46	1600	800	14	9	230	6	5910	5610	2.69	88.2	6290	5300	2.68	88.3
5.47	1580	800	14	0	230	12	4700	5046	2.49	88.6	5100	4983	2.61	88.1
5.48	1720	800	16	0	255	9	6050	5257	2.61	87.0	6300	5195	2.83	87.6

Figure 5.45 shows 0.35 μm nominal printed CD cross-sections of a representative 1-iodoheptafluoropropane/CH_3F process from some of the earlier stages of this work, before the results in Figures 5.46, 5.47, and 5.48 were obtained. The conditions used are given in Table 5.9. This figure highlights some of the key issues encountered in developing these processes. One can see from the micrograph and from Table 5.9 that high etch rate is attainable. The amount of resist eroded, however, is relatively high, with correspondingly low selectivity values. There is, moreover, a significant slope to the feature sidewalls (~4 – 6 °). Etch stop will eventually occur at the bottom of the via as the feature pinches off due to the encroachment of sidewall polymer, the formation of which is being promoted by power density loss at the corners of the feature with increasing aspect ratio as the etch proceeds. What is of key importance is that a significant amount of polymer formation inside the feature is seen – resulting in noticeable via taper, despite the fact that considerable resist erosion (~45% resist loss) has taken place. In typical fluorocarbon processes, conditions that lead to heavy sidewall polymer formation (as is the case here) generally also see slow oxide etch rate on one

hand and low resist erosion on the wafer surface on the other hand, both effects consistent with operation in a heavy polymerization regime. Here, however, one sees that the etching of both resist and oxide (in the center of the feature) proceeds at rapid rates, while large amounts of polymer deposits are formed on the sidewalls of the via.

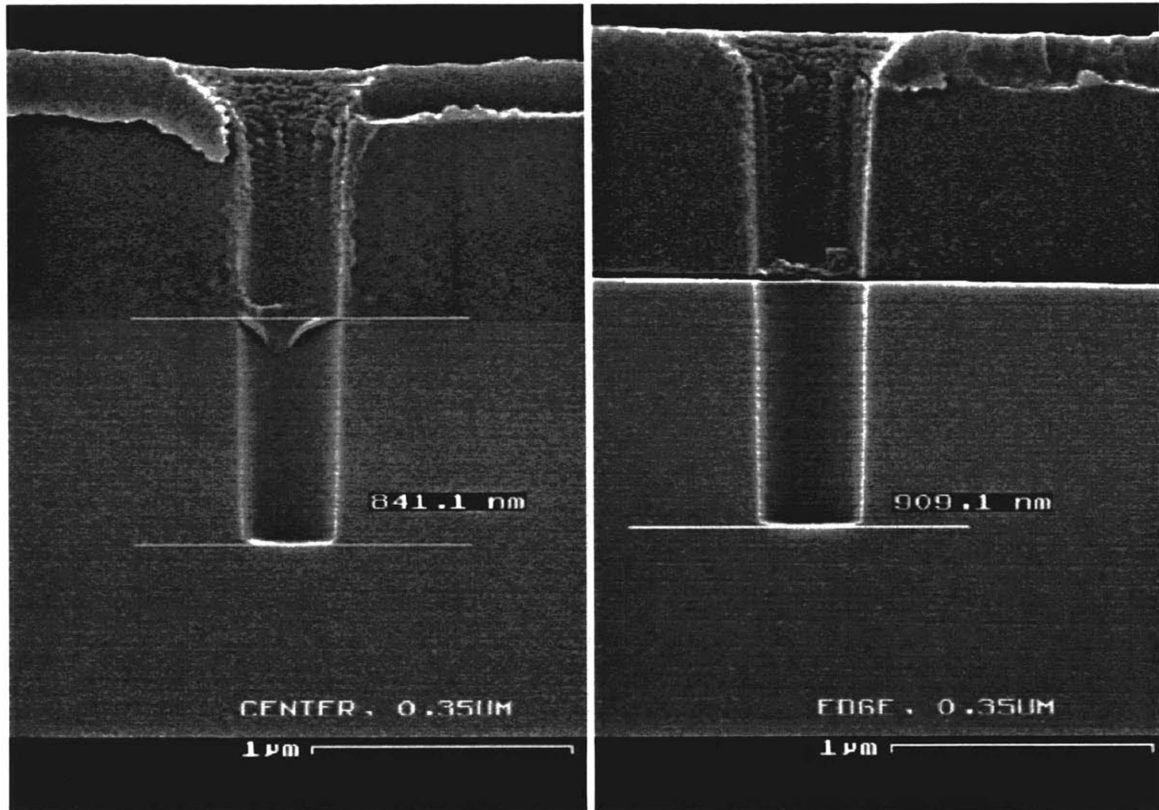

Figure 5.44: C_3F_8/CH_3F reference process, 0.35 μm nominal printed CD.

Details of the explanation which accounts for the above departures from typical fluorocarbon etch behavior are provided in Section 5.4.2. One of the salient results arrived at in the film characterization study of 1-iodoheptafluoropropane deposits is that the iodine arriving at the wafer surface is driven in much more deeply than the surface mixing layer, indicating that the physical component of the etch process, principally driven by bombardment of the wafer by massive iodine ions, plays a very significant role. The enhancement of the physical sputtering component by the presence of these massive ions is what accounts for the high etch rate and the high degree of resist loss. Despite this, however, it is also clear that the 1-iodoheptafluoropropane process shown in Figure

5.45 is a highly polymerizing one, this being evident from examining surfaces which are exposed to only glancing ion impacts, namely the feature sidewalls. In this regime, therefore, 1-iodoheptafluoropropane provides high etch rate, but also combines the disadvantages of high polymerization inside the feature with poor selectivity to the mask layer.

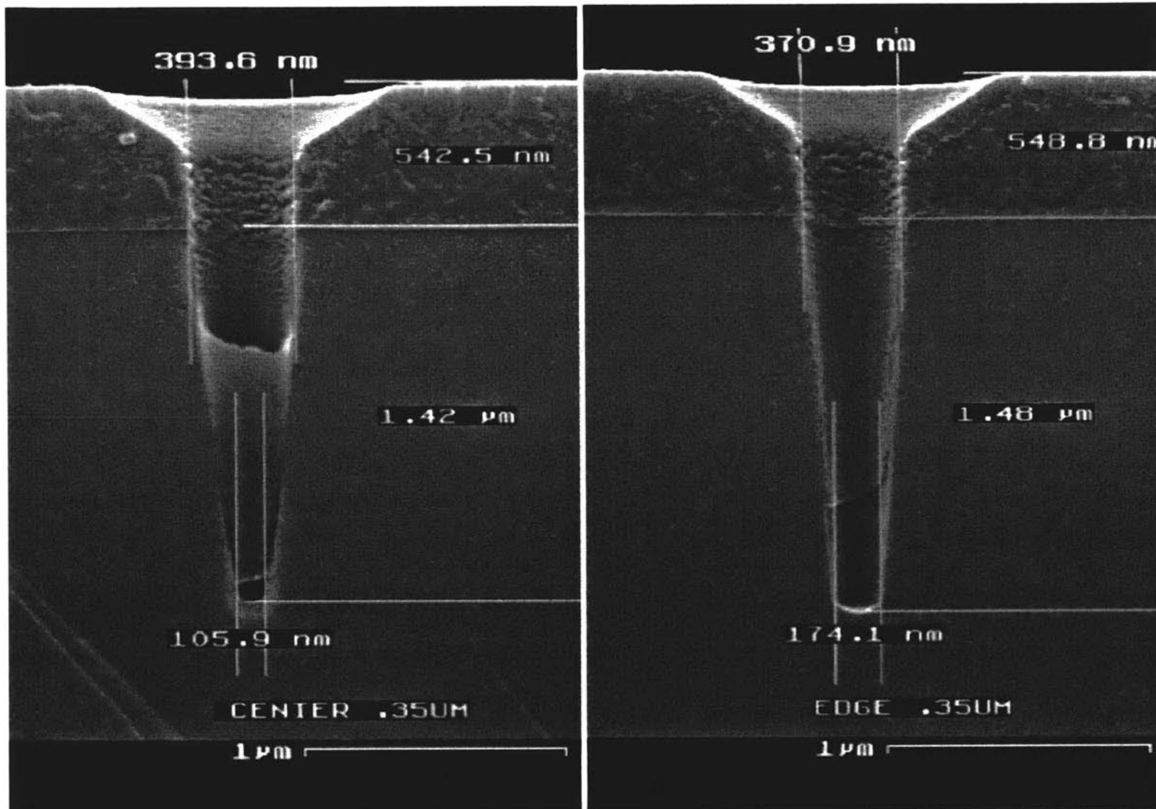

Figure 5.45: An example of an early 1-iodoheptafluoropropane process with CH_3F illustrating typical issues seen with this chemistry: resist erosion on the surface but heavy polymerization leading to via taper inside the feature; 1900 W *SP*, 800 W *BP*, 24 sccm *EF*, 3 sccm *CF*, 230 °C *RT*, 6 mTorr *PR*, 0.35 μm nominal printed CD.

The process was subsequently tuned, however, to yield much more vertical via profiles, as Figures 5.46 and 5.47 illustrate. Figure 5.46 shows cross-sections of 0.35 μm nominal printed CD via hole features etched with a 1-iodoheptafluoropropane/CH_3F process. The features shown in Figure 5.46 represent a "best process" point for the 1-iodoheptafluoropropane/CH_3F combination. The criterion for determining this was the highest oxide:resist selectivity for a profile with no more than 2° of sidewall taper.

Figure 5.47, on the other hand, shows cross-sections of the same features etched with the 1-iodoheptafluoropropane/*no* CH_3F process with the highest oxide:resist selectivity for a profile with no more than 2° of sidewall taper. This was the process selected for the stop layer selectivity experiments to be discussed below; it was also among the 1-iodoheptafluoropropane processes with the lowest global warming emissions recorded (~67 grams of carbon equivalent, which corresponded to a reduction ~79.4% relative to the C_3F_8/CH_3F reference process) - see Section 5.4.3, where this process is discussed in more detail. Finally, Figure 5.48 shows 0.35 μm nominal printed CD cross sections for the highest selectivity 1-iodoheptafluoropropane/no CH_3F process where the profile criterion is relaxed to allow for 3° of sidewall taper.

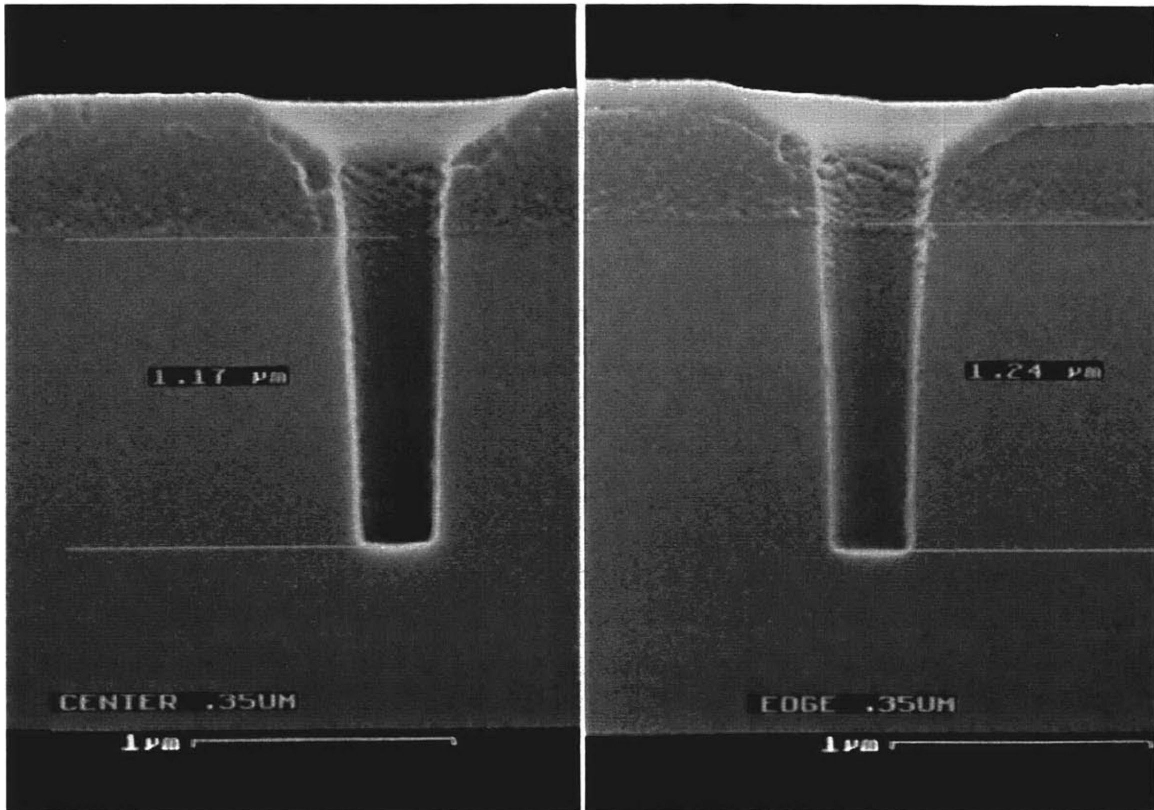

Figure 5.46: Best overall 1-iodoheptafluoropropane process with CH_3F: 1600 W *SP*, 800 W *BP*, 14 sccm *EF*, 9 sccm *CF*, 230 °C *RT*, 6 mTorr *PR*, 0.35 μm nominal printed CD.

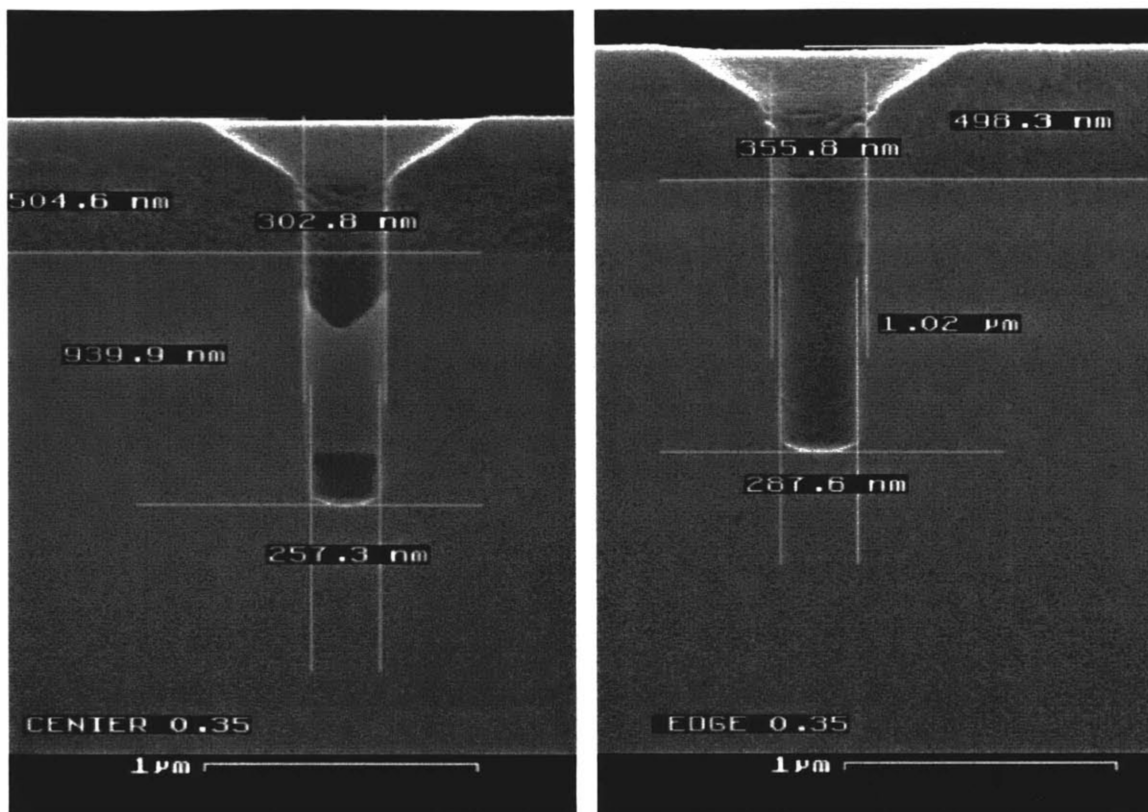

Figure 5.47: Best profile 1-iodoheptafluoropropane process without CH_3F: 1580 W *SP*, 800 W *BP*, 14 sccm *EF*, 0 sccm *CF*, 230 °C *RT*, 12 mTorr *PR*, 0.35 μm nominal printed CD.

Use of CH_3F. CH_3F was introduced early on in this study in an attempt to improve oxide:resist selectivity, which was identified as a key issue in 1-iodoheptafluoropropane process in the initial HDP work carried out with that compound (see Section 5.1). Indeed, the addition of CH_3F was found to be effective in this regard, although the improvements obtained did not approach the values seen in the C_3F_8/CH_3F reference recipe. The iodine bombardment effect was found to be so dominant that oxide:resist selectivities of ~3:1 were found to be the upper limit of what could be attained while maintaining reasonable profile control. After the results seen in Figure 5.46 were obtained, however, the process window was again moved to a CH_3F free regime. The motivation for re-optimizing the process window without CH_3F was based on FTIR effluent data (see Section 5.4.3) which indicated that the presence of CH_3F in the feed gas adversely affects global warming process emissions by contributing to the creation of significant amounts of CHF_3. Whereas CH_3F itself has a low global warming potential

(GWP), CHF_3 is a high-GWP compound. As can be seen from a comparison of Figure 5.46 with Figure 5.48, comparable etch rate, oxide:resist selectivity, and sidewall profile can be achieved with or without CH_3F. The beneficial effect on selectivity arising from the use of CH_3F was preserved by compensation with other variables, namely higher etch gas flow rate, roof temperature, and pressure.

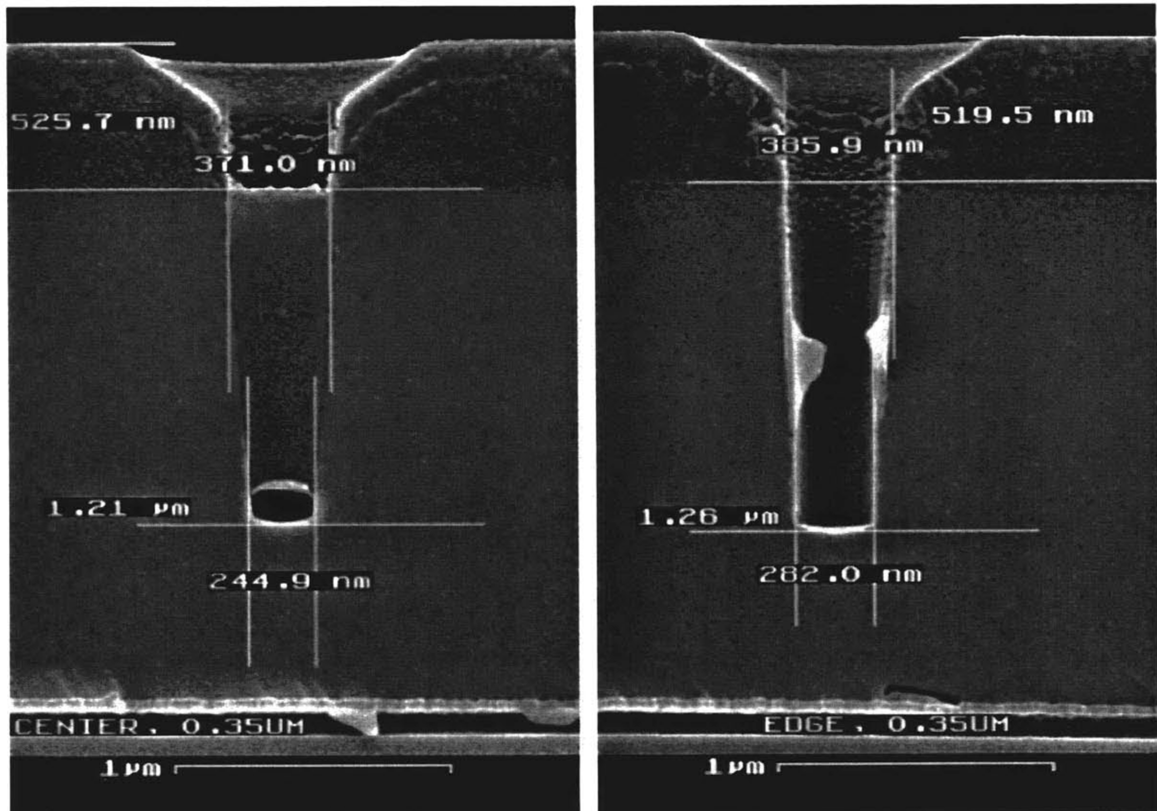

Figure 5.48: Best overall 1-iodoheptafluoropropane process without CH_3F: 1720 W *SP*, 800 W *BP*, 16 sccm *EF*, 0 sccm *CF*, 255 °C *RT*, 9 mTorr *PR*, 0.35 µm nominal printed CD.

5.4.1.5 Results and Discussion – Comparison between 1- and 2-iodoheptafluoropropane

The general characteristics of the 2-iodoheptafluoropropane processes were similar to those seen with the other isomer. Good oxide etch rates were obtained, but oxide:resist selectivity was low, and, again, under certain conditions, significant polymer deposits were seen inside the features, resulting in via taper. In the parameter space explored, the amount of resist remaining, overall selectivity ratios, and amount of sidewall taper generally fell into similar ranges for the two isomers. The thickness of resist remaining

ranged from 4014 Å to 5925 Å for 2-iodoheptafluoropropane versus 4143 Å to 5875 Å for 1-iodoheptafluoropropane. 2-iodoheptafluoropropane oxide:resist selectivities based on 0.35 μm feature measurements ranged from 1.90:1 to 3.73:1 versus a range of 2.06:1 to 3.18:1 for the other isomer, while the ranges of sidewall slope values for the same features spanned 85.7° to 89.1° for 2-iodoheptafluoropropane versus 84.7° to 88.6° for 1-iodoheptafluoropropane. 0.35 μm feature etch rates, however, did appear to differ somewhat for the two isomers, with a range of 4747 to 6300 Å/min for 2-iodoheptafluoropropane versus 5800 to 7100 Å/min for 1-iodoheptafluoropropane. In general, for any given process condition, while similar profiles and amounts of resist remaining were seen, lower etch rates were consistently measured for the 2-iodo isomer, with the difference reaching over 1000 Å/min for a number of the process conditions.

5.4.1.6 Results and Discussion – Stop Layer Selectivity Experiments

The process shown in Figure 5.47 was the one selected for the stop layer selectivity experiments with 1- and 2-ioheptafluoropropane as the etch gas. This critical series of experiments showed conclusively the disproportionate role that the physical component of the etch plays in these IFC processes. As is discussed in detail in Section 5.4.2, iodine bombardment has been found to play a critical role in iodoheptafluoropropane etching. In both the stop-on-PEN and stop-on-TiN experiments with both gases, the etch penetrated through the intended stop layer, terminating on the Ti layer beneath. More dramatic results were obtained with the stop-on-PEN/Cu wafers. Figure 5.49 shows a cross-sectional view of the trench/via structures. The resist layer and any sidewall polymer residues are not present in these micrographs because the wafers had been subjected to a PET after the main etch step. As the figure shows, the PEN layer was removed and the Cu line was reached during the etch. The irregular formations seen inside the vias for both isomers are so-called via veils – the result of sputtered and redeposited Cu within the features. These formations are again attributed to iodine bombardment. Figure 5.50 shows a top-down SEM view of similar features. Again, the via veil structure is clearly visible for both isomers. The C_3F_8-based reference process did not produce such formations.

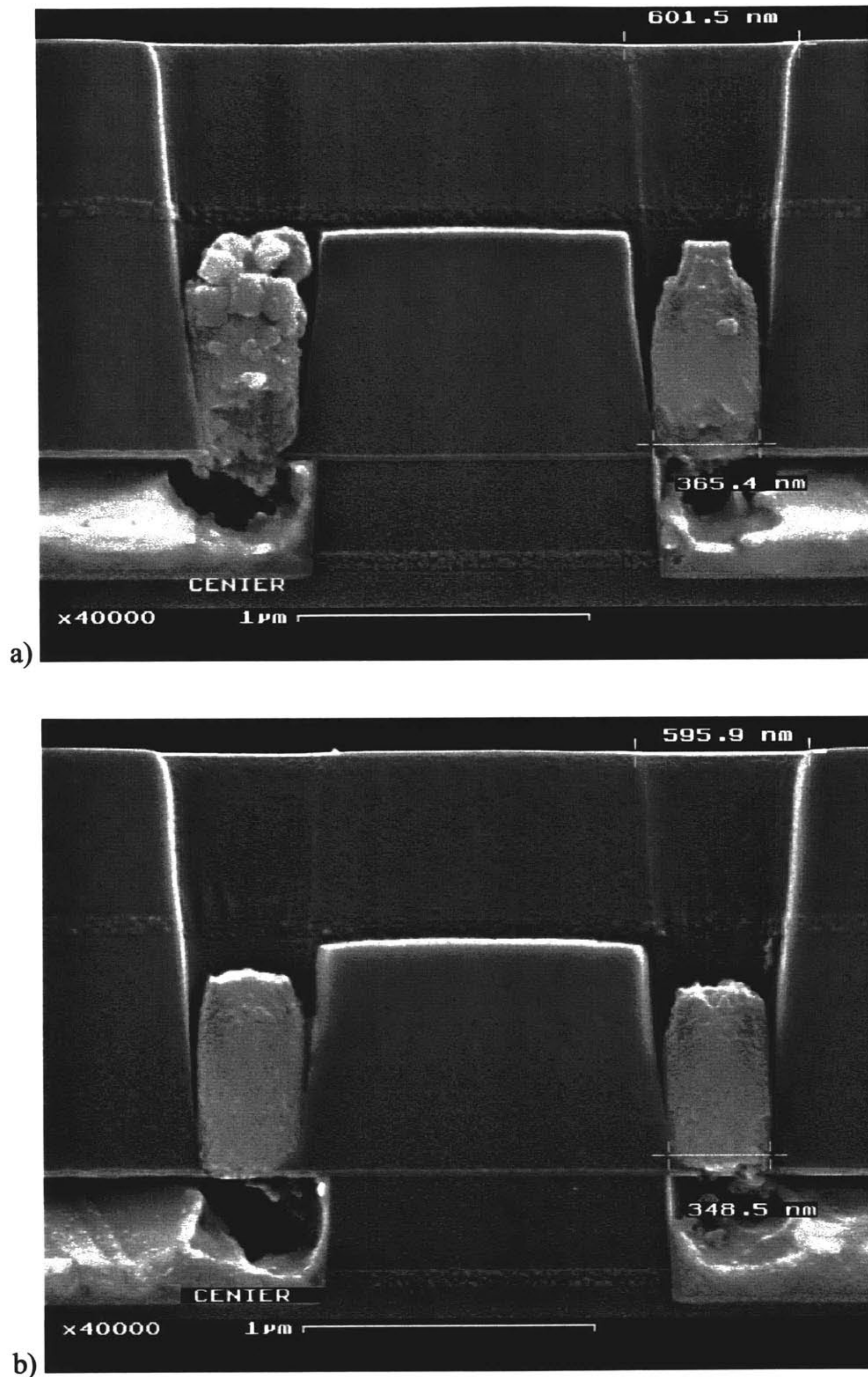

Figure 5.49: Cross-sectional micrographs of via features stopping on Cu metal lines covered with 500 Å of silicon nitride: a). 1-iodoheptafluoropropane, b) 2-iodoheptafluoropropane. 1580 W *SP*, 800 W *BP*, 14 sccm *EF*, 0 sccm *CF*, 230 °C *RT*, 12 mTorr *PR*. Note the formation of via veils upon exposure of the Cu line to the process chemistry.

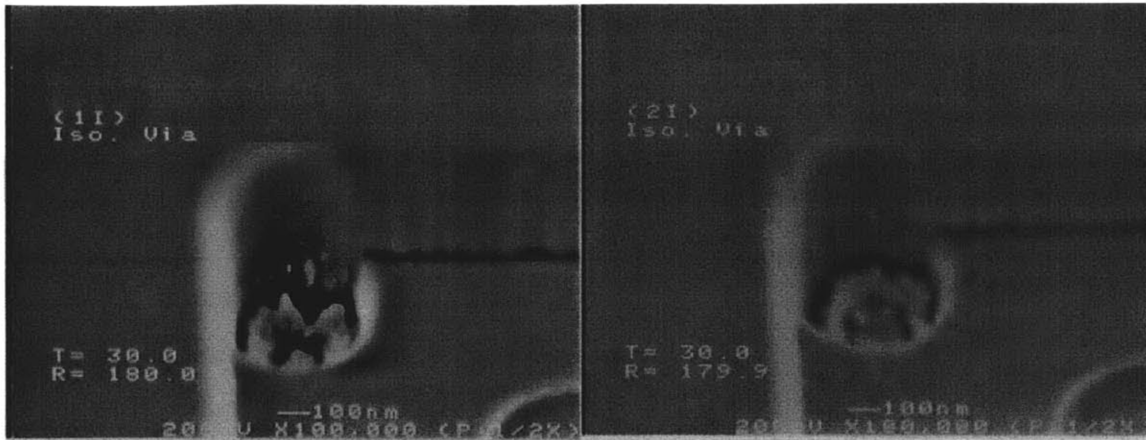

a) 1-iodoheptafluoropropane b) 2-iodoheptafluoropropane

Figure 5.50: Top-down micrographs of isolated via features from the same wafers as those shown in Figure 5.49: a) 1-iodoheptafluoropropane, b) 2-iodoheptafluoropropane. The formation of via veils inside the vias can again be clearly seen.

5.4.1.7 Conclusions

An array of experiments was carried out using 1-iodoheptafluoropropane as a process gas in a typical dielectric etch application – a high aspect ratio via etch. An inductively coupled high density plasma tool was used for the work. Process performance was characterized using TEOS oxide etch rate, resist selectivity metrics, sidewall profile, and stop layer behavior as criteria. Process variables whose impact was studied were source power, bias power, etch gas flow, additive gas (CH_3F) flow, roof, wall, and chiller temperature, and pressure. Neural network analysis was used for a large portion of the experiments.

Increasing roof and wall temperature, CH_3F flow, and pressure generally led to more polymerizing conditions where lower resist erosion but more sidewall polymer inside features was observed. Increasing source and bias power tended to have the opposite effect. In the case of TEOS oxide etch rate, as measured within the features, the observed trends were more complex, although, in most process regimes explored, increasing roof and wall temperature, CH_3F flow, and pressure generally resulted in lower etch rate, while increasing source and bias power resulted in higher etch rate.

It was found that 1-iodoheptafluoropropane, in comparison to C_3F_8, exhibits more polymer forming tendencies, which is consistent with the lower F:C ratio of the molecule. In most regimes, however, these tendencies are not enough to offset the dominant phenomenon observed with this chemistry, namely a very pronounce enhancement of the physical component of the etch due to bombardment of the wafer surface by energetic, and massive, iodine ions. This bombardment accounts for the relatively high patterned TEOS oxide etch rates observed under many process conditions, as compared to those generated by the C_3F_8/CH_3F reference process. It also accounts for the higher rate of resist erosion seen with 1-iodoheptafluoropropane. Where the polymer forming mechanisms manifested themselves most strongly was inside the via features, on surfaces that experienced power density loss due to shadowing and charging effects, namely sidewalls and feature corners, leading to noticeable feature taper under higher selectivity conditions. Oxide:resist selectivities greater than 3:1 were found to be difficult to achieve with acceptable profile. This work was supplemented by a more limited series of experiments carried out with 2-iodoheptafluoropropane, which was found to have generally similar behavior.

Via holes with good profile and etch depth were etched by 1-iodoheptafluoropropane under a range of conditions, both with and without the use of CH_3F as a polymer forming additive. Etch rates matching or exceeding those of the reference process were obtained under a variety of conditions. Nearly vertical feature sidewalls were also obtained. Resist selectivity, however, remained in the 2.5-3.0 range for these processes. Adequate performance vis a vis common stop layers (silicon nitride, TiN, Cu), moreover, was not demonstrated. Via veil formation, in fact, was observed when Cu lines were exposed to the process chemistry. The data obtained in this study suggest that 1- and 2-iodoheptafluoropropane can be employed as etchants for dielectric etch applications. Their use, however, appears to be limited to processes which do not require high oxide:resist selectivities. A via etch process may be one of these. A self-aligned contact (SAC) etch, where high silicon nitride corner selectivity is required, on the other hand, would probably be difficult to implement. More problematic, however, is the behavior of these IFCs in the presence of various stop layers. Their implementation in actual

processes would require the use of a much more selective overetch step to avoid rapid stop layer penetration, metal sputtering, redeposition, and veil formation when metal lines are exposed.

5.4.2 Deposited Film Characterization

This section forms the second part of a three-part discussion which presents a systematic characterization of 1-iodoheptafluoropropane (CF_2I-CF_2-CF_3) based oxide etch processes in the Centura 5300 HDP etch tool. Sections 5.4.1 and 5.4.3 discuss etch process behavior and effluent composition, respectively. The focus of this section is on the characterization of films deposited by 1-iodoheptafluoropropane processes using two techniques: x-ray photoelectron spectroscopy (XPS) and time-of-flight secondary ion mass spectrometry (TOF-SIMS).

One significant issue that had been observed in earlier 1-iodoheptafluoropropane etch studies was the fact that the compound appears to have a tendency to polymerize more heavily than its fully fluorinated analog, C_3F_8, as was evidenced by thicker sidewall and corner deposits inside features being etched in oxide films, which, in turn led to tapering and etch stop under certain process conditions (see Section 5.1). Despite this, however, significantly more resist erosion was observed than was the case with C_3F_8. These phenomena were also confirmed in the process characterization part of the present study, as is discussed in Section 5.4.1. The films that are the subject of the discussion that follows have been deposited on blanket photoresist and bare Si wafers under conditions similar to those used in actual 1-iodoheptafluoropropane etch processes. Wafers subjected to C_3F_8 based plasmas were also characterized. Since polymerization phenomena on the surface of the wafer are believed to play a critical role in fluorocarbon etching of dielectric films such as silicon oxides, a characterization of these polymer films was undertaken in order to improve understanding of iodoheptafluoropropane etch behavior. The discussion of Section 5.4.2 is organized as follows: Section 5.4.2.1 covers the experimental setup. Section 5.4.2.2 discusses XPS surface scan data, while Section 5.4.2.3 discusses XPS depth profiles. Section 5.4.2.4 discusses the fluorine/carbon

stoichiometry of the films under consideration. Section 5.4.2.5, in turn, presents a discussion of TOF-SIMS depth profiles that is intended to complement that provided in Section 5.4.2.3. Finally, Section 5.4.2.6 offers concluding remarks regarding this portion of the study.

Table 5.10. Process conditions used for bare Si and K2G resist wafers analyzed using XPS and TOF-SIMS. 34 °C chiller temp., 15 Torr He backside cooling, 75 sccm He flow.

Process	Source Power (W)	Bias Power (W)	Etch Gas Flow (1I) (sccm)	CH_3F Flow (sccm)	Roof Temp. (°C)	Wall Temp. (°C)	Pressure (mTorr)
1 (1I-C_3F_7I)	1500	800	16	0	230	230	15
2 (1I-C_3F_7I + CH_3F)	1500	800	16	21	230	200	9
3 (1I-C_3F_7I + CH_3F)	1900	600	22	4	210	200	6
4 (C_3F_8 + CH_3F)	C_3F_8 + CH_3F based reference process						

5.4.2.1 Experimental Setup

All of the experiments discussed in this article were run using bare Si wafers as well as blanket K2G resist wafers in the same inductively coupled high density plasma etch tool that was used in Sections 5.4.1 and 5.4.3. The wafers were subsequently analyzed using x-ray photoelectron spectroscopy (XPS) and time-of-flight secondary ion mass spectrometry (TOF-SIMS). The same samples were analyzed using both techniques. A series of eight wafers was run using four processes, with a K2G resist wafer (nominal thickness 10,000 Å) and a bare Si wafer run under each condition (see Table 5.10). 1-iodoheptafluoropropane was used as the etch gas for three conditions, while a C_3F_8/CH_3F reference recipe, the same process that was used as a reference in Section 5.4.1, was run for the fourth. As an initial procedure, survey XPS spectra of the surface at the center of each wafer were taken. The composition of the surface layer was determined using the following spectra: C 1*s*, F 1*s*, O 1*s*, Si 2*s*, and I 3*d*5. After this was completed, XPS depth profiles were taken for 7 out of the 8 samples, also at the center location. The same spectral features were used here, with the exception of Si, where the Si 2*p* spectrum was

used. To supplement the data thus obtained, TOF-SIMS, which has greater sensitivity than XPS, was also employed, with the technique being used to carry out additional depth profiles at the center location on all 8 wafers.

5.4.2.2 Results and Discussion – XPS Surface Scans

All four of the bare Si samples exposed to the various fluorocarbon processes were found to have a fluorocarbon deposit on the surface. The thickness and, to some extent, the composition of this film varied, however, depending on the process. See Table 5.11. In the case of all four of the K2G resist samples, net etching of the resist was observed to occur, with a simultaneous formation of a fluorocarbon surface layer similar to that seen on their bare Si counterparts.

Table 5.11. Fluorocarbon film thickness on bare Si samples analyzed by XPS, the corresponding sputter times required to reach the Si interface, and net amount of resist erosion on K2G samples analyzed by XPS. All thickness values are wafer averages ± std. dev. based on nine point measurements.

Process	Est. Thickness of Fluorocarbon Deposit on Bare Si (Å)	XPS Sputter Time to Reach Si Interface for Bare Si Samples (s)	Approx. XPS Sputter Rate for Deposit on Bare Si (Å/s)	Thickness of K2G Resist Removed (Å)
1 (1I-C_3F_7I)	376 ± 19.6	240 ± 40	1.6	4515 ± 179.3
2 (1I-C_3F_7I + CH_3F)	143 ± 7.1	80 ± 40	1.8	4577 ± 245.5
3 (1I-C_3F_7I + CH_3F)	504 ± 36.6	340 ± 40	1.5	5709 ± 358.6
4 (C_3F_8 + CH_3F)	864 ± 169.5	990 ± 60	0.9	2446 ± 608.8

As Figures 5.51 and 5.52 indicate, the surface of all eight samples was found to contain primarily C, F, and O, with small amounts of Si and trace amounts of I detected in some samples (the ones exposed to 1-iodoheptafluoropropane plasmas). The iodine content of the surface layer was found to be similar for the six 1-iodoheptafluoropropane samples (ranging from 0.16% to 0.25%), with no evidence of iodine present on the wafers exposed to the C_3F_8/CH_3F reference process, as was expected. While the iodine signal was small enough that no clear trend could be discerned in iodine content as a function of process conditions, it does appear that the surfaces of the K2G wafers became more iodinated than the surfaces of their bare Si counterparts.

While the bulk component of the film surface was carbon for all samples, the relative amounts of the other elements present on the surface did differ considerably, with two distinct patterns being seen. Samples Si-1, Si-2, Si-3, and K2G-2, K2G-3 were found to have the remainder of the elemental composition of the surface to be primarily F, with some O, and, in the case of Process 3, trace amounts of Si. Samples Si-4, K2G-1, and K2G-4, on the other hand, appeared to have more O present than F; moreover, these three samples also contained significant amounts of Si. The surfaces of the process kit in the etch tool used for this study that are exposed to the plasma are constructed largely out of silicon and quartz. Since no oxygen* was introduced into the chamber in any of the processes, it becomes apparent that the Si and O signals seen in the XPS spectra are evidence of incorporation of process kit materials into the deposited film on some runs but not others.

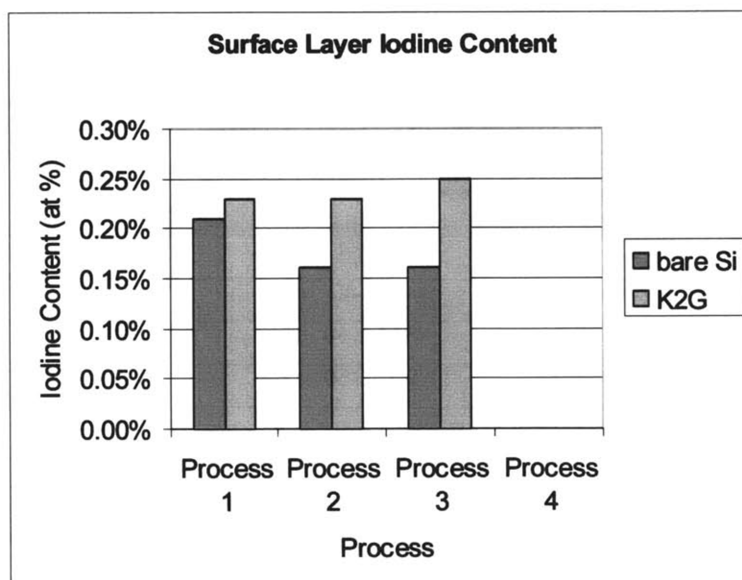

Figure 5.51: XPS data – iodine content of surface layers of films deposited by 1-iodoheptafluoropropane (process 1-3) and C_3F_8 (process 4).

* The oxygen content of the resist itself, as determined by XPS, was found to be very low (<1%).

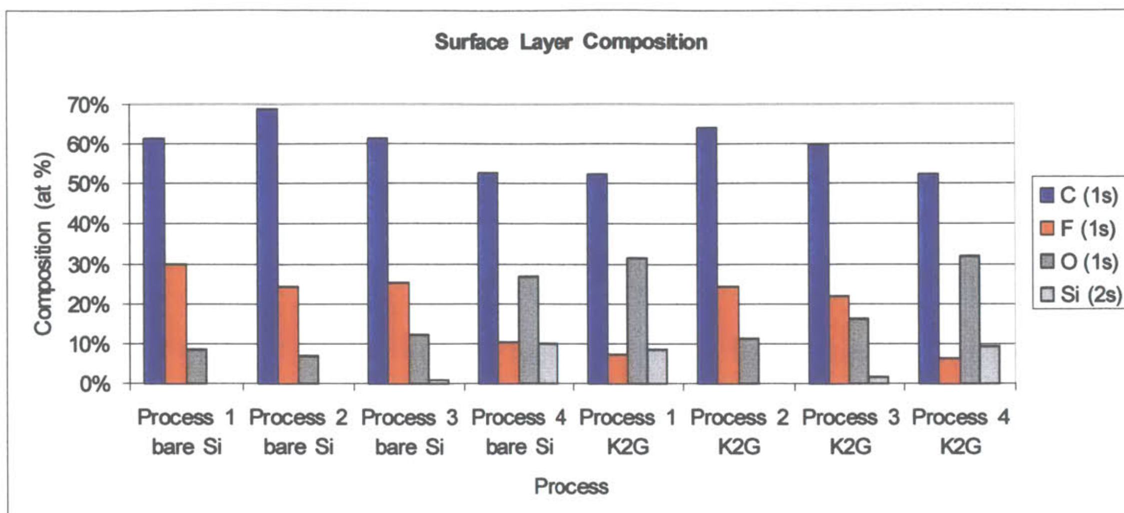

Figure 5.52: XPS data – composition of surface layers of films deposited by 1-iodoheptafluoropropane (Process 1-3) and C_3F_8 (Process 4).

5.4.2.3 Results and Discussion – XPS Depth Profiles

Bare Si Samples. Samples Si-1, Si-2, and Si-3 all exhibited similar features. The most striking of these was the pileup of I at the fluorocarbon film / Si interface seen in Figures 5.53, 5.54, and 5.55. As Figure 5.57 shows, even though the iodine levels are very low (below 1.5 at. % in these three films), the trend in the iodine concentration is clearly visible. This feature will be discussed in greater detail below. The absence of silicon from the films on these samples indicates that little, if any, etching of the process kit had occurred. The level of O in the bulk of the film was negligible for these samples. The presence of O on the surface, however, was clearly observed in all three samples. Since this was not accompanied by any appreciable levels of Si, its origin is unlikely to be quartz in the chamber process kit. Rather, the presence of this oxygen signal is consistent with surface oxidation of the carbonaceous film due to exposure to air. The increase in the O signal at the interface with the silicon wafer, seen in all three samples, is consistent with the presence of a thin native oxide on the wafer prior to processing.

All three samples also exhibit a marked change in the F:C ratio of the film at the surface relative to the bulk of the fluoropolymer film, which is more C-rich and F-poor than the surface. This will be discussed in greater detail below. Note also the change in fluorine

bonding within the film. F closer to the surface appears to be bonded to C, while F at the interface with the Si wafer appears to exhibit more Si-F bonding. This is consistent with models of fluorocarbon layers on Si presented by other workers [8, 10, 11]. Figure5.58 illustrates this chemical shift for sample Si-2. Similar trends were seen in the other two samples.

The principal difference seen in the composition of these films was in the distribution of F throughout the film bulk. In samples Si-1 and Si-2, except for the surface layer itself, F is present in the film at roughly constant levels throughout its depth. See Figures 5.53 and 5.54. In sample Si-3, however, the F:C ratio within the film changes as the Si interface is approached, with the film becoming more F-rich toward the Si surface, suggesting that the process is not quite in steady state over the course of the run. See Figures 5.55 and 5.59.

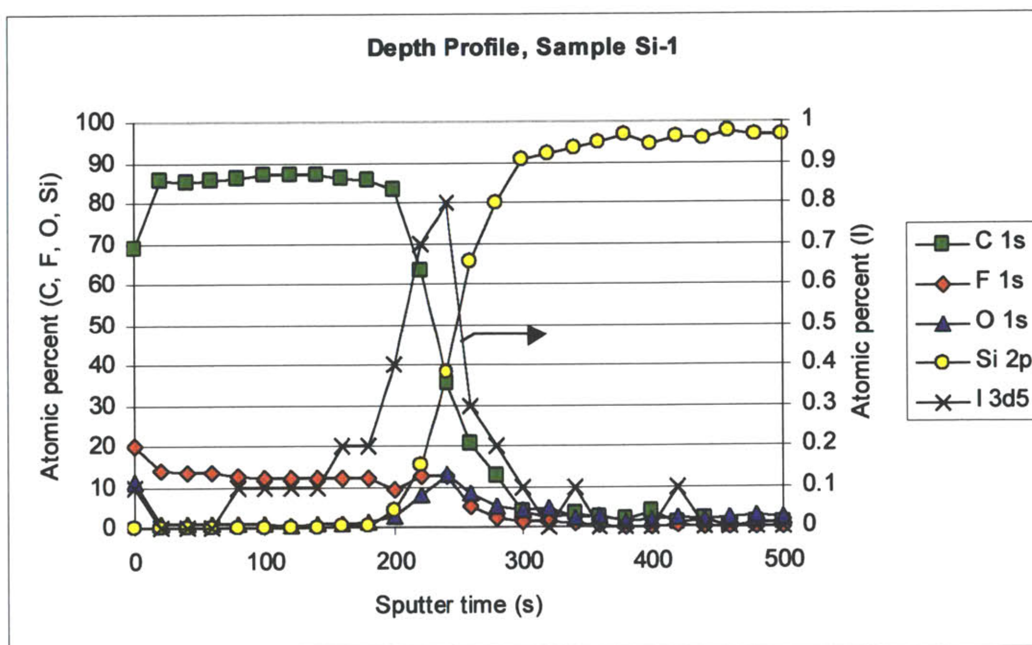

Figure 5.53: XPS depth profile for sample Si-1: film deposited on bare Si by 1-iodoheptafluoropropane process. Note that iodine at. % scale is magnified 100x.

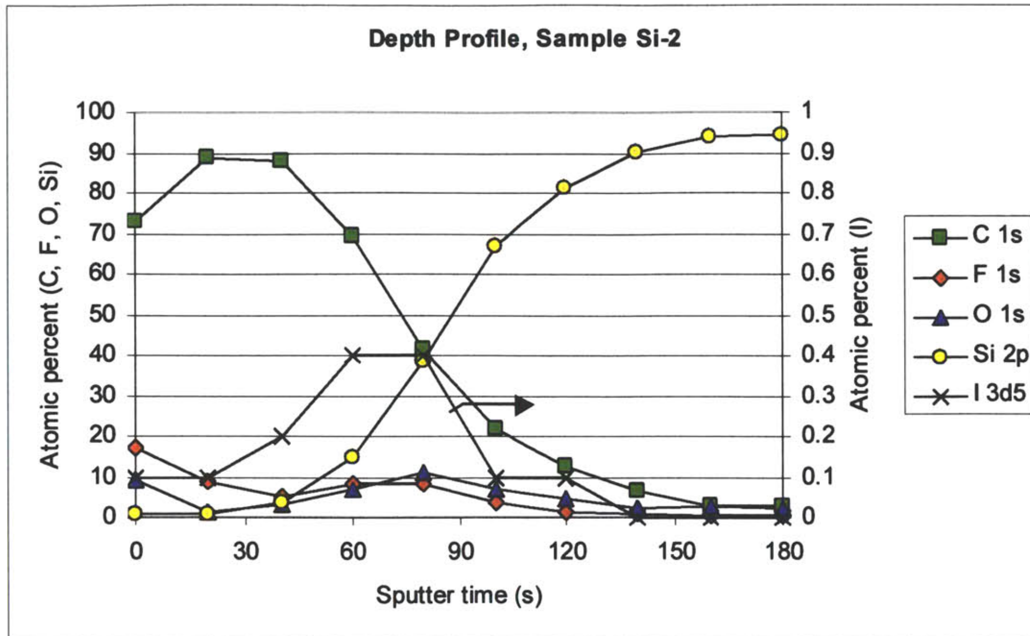

Figure 5.54: XPS depth profile for sample Si-2: film deposited on bare Si by 1-iodoheptafluoropropane/CH_3F process. Note that iodine at. % scale is magnified 100x.

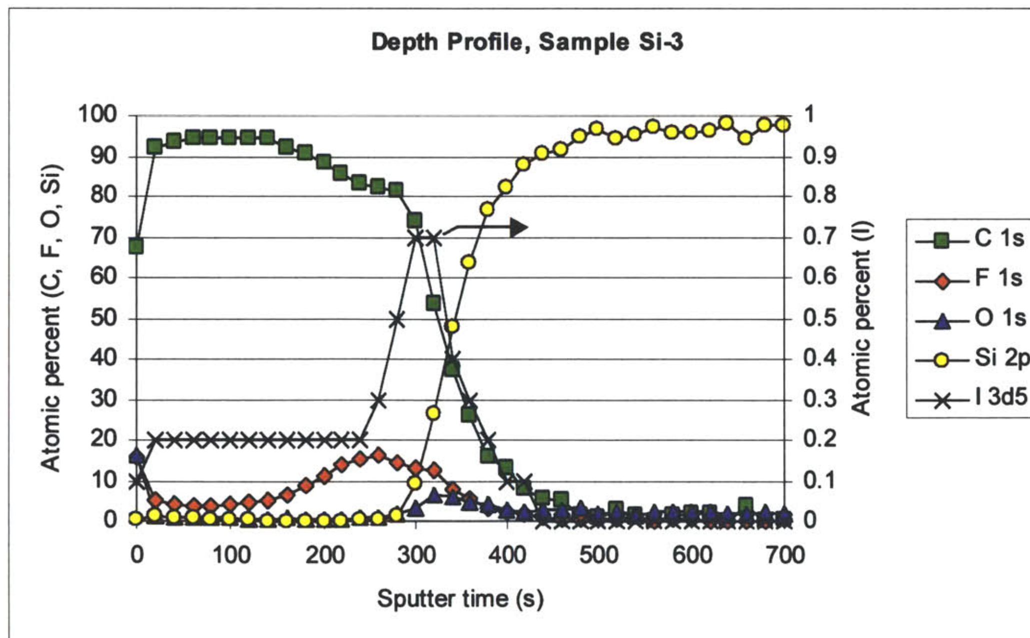

Figure 5.55: XPS depth profile for sample Si-3: film deposited on bare Si by 1-iodoheptafluoropropane/CH_3F process. Note that iodine at. % scale is magnified 100x.

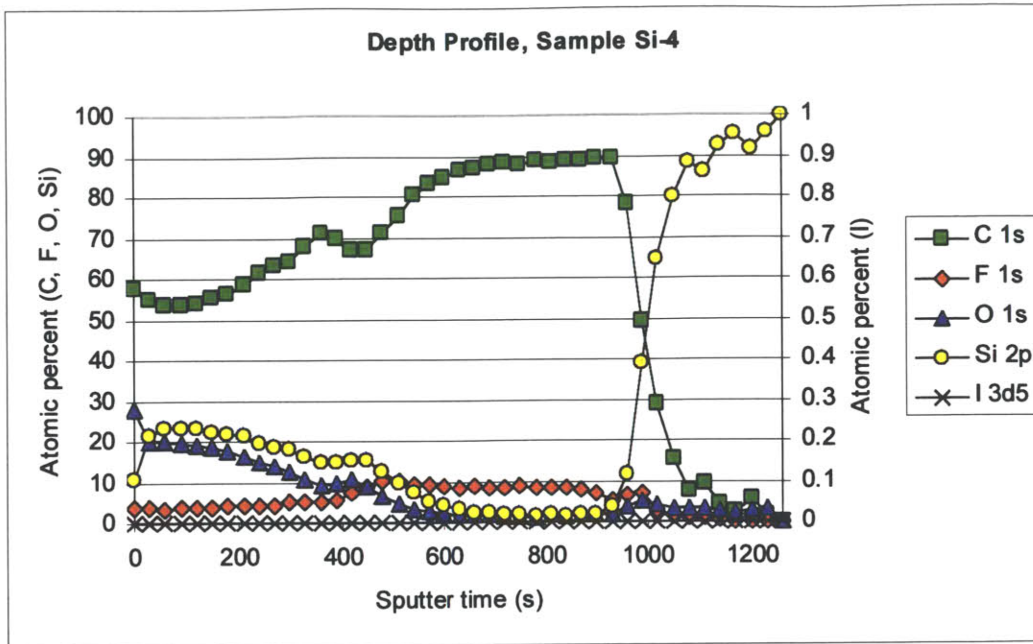

Figure 5.56: XPS depth profile for sample Si-4: film deposited on bare Si by C_3F_8/CH_3F reference process.

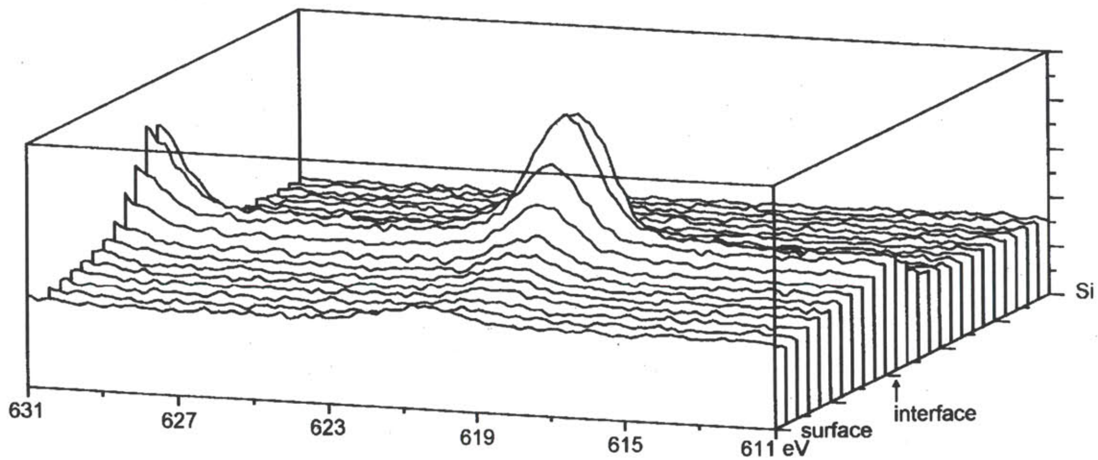

Figure 5.57: XPS depth profile data for sample Si-1: I 3*d*5 spectrum.

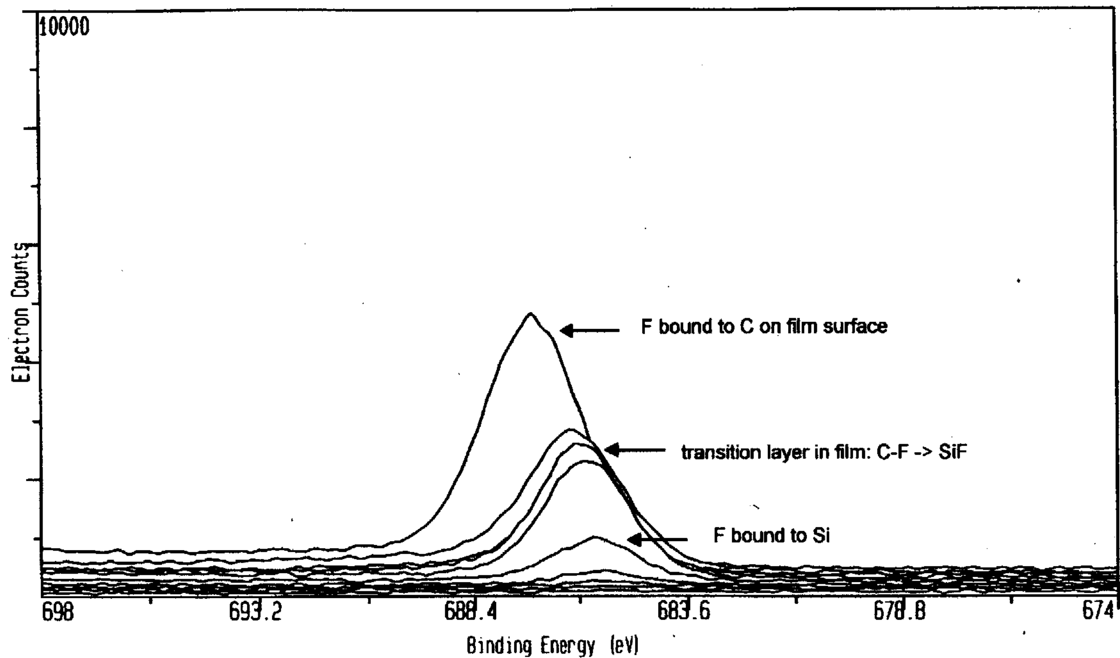

Figure 5.58: XPS depth profile data for sample Si-2: F 1*s* spectrum. Surface layers shown toward back of montage; Si interface shown toward front.

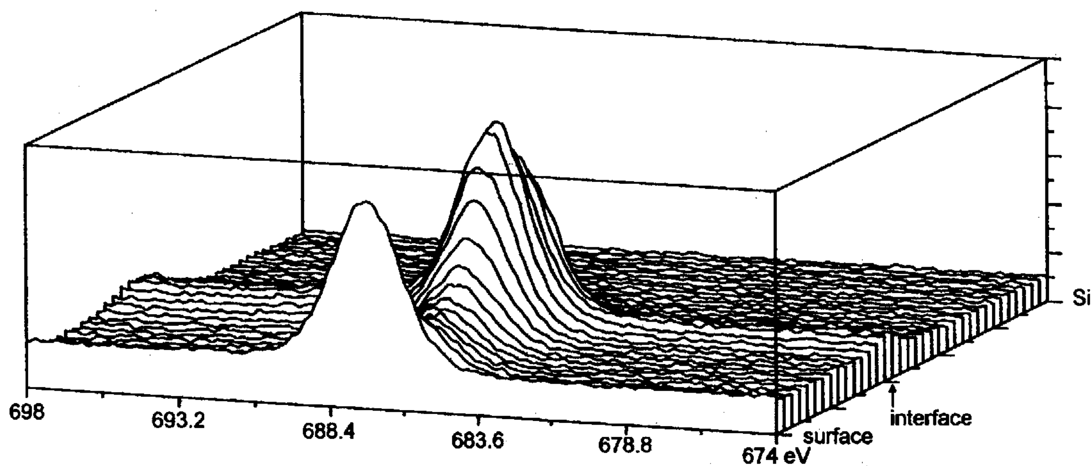

Figure 5.59: XPS depth profile data for sample Si-3: F 1*s* spectrum.

Finally, the film on sample Si-2 is quite thin, thinner than that on sample Si-1, which was deposited under otherwise similar conditions, except for the fact that Process 2 used lower pressure and wall temperature but higher CH_3F flow. As had been discussed in Section 5.4.1, higher chamber surface temperatures, higher pressure, and higher CH_3F flow all tend to result in more polymer formation on the wafer. In this case, since the

film deposited on sample Si-2 was considerably thinner than that on sample Si-1, one is led to conclude that the effects of changing wall temperature and pressure were dominant over the change in CH_3F flow.

No iodine was detected in the film deposited by the C_3F_8/CH_3F reference recipe (sample Si-4). See Figure 5.56. F is present throughout film and, as was the case with sample Si-3, there appears to exist a more heavily fluorinated sub-layer closer to the Si interface. See Figure 5.60a. The increase in oxygen content at the surface itself is still present and this is consistent with the increase seen on the other three bare Si samples that is believed to be due to air exposure. There also appears to be a slight increase in the O signal at the Si interface, consistent with the presence of a native oxide. However, there are pronounced differences between this sample and samples Si-1 through Si-3, namely, the marked increase in oxygen content in the bulk of the film near the surface and the equally dramatic increase in Si signal that tracks the oxygen signal in the film. See Figures 5.60b and c. Since the materials of construction wet by the plasma in the process chamber are mostly Si and quartz, it is clear that those materials are the source of Si and O being incorporated into the film. This suggests, therefore, that the C_3F_8/CH_3F reference recipe interacts more aggressively with the chamber surfaces than do the 1-iodoheptafluoropropane processes. The appearance of two distinct layers within the film (an SiO-rich layer near the surface and an SiO-poor layer near the Si interface) suggests perhaps that the etch process is not in steady state and that, in fact, the etching of the process kit by the C_3F_8/CH_3F chemistry intensifies as the etch proceeds.

This phenomenon may be accounted for by the fact that not all parts of the process kit are heated directly by the roof and wall heaters. In fact, substantial portions of the process kit, composed primarily of quartz, are heated only passively through contact with the chamber body and through contact with the plasma when the process is running. This suggests that, as the etch proceeds, these parts of the kit, whose temperature is otherwise unregulated, heat up, resulting in diminished polymer formation on those surfaces, in accordance with mechanisms established in Section 5.4.1. This makes those surfaces more susceptible to interaction with fluorine, which becomes consumed as it etches the

process kit more aggressively. This consumption of F is, moreover, consistent with the fact that the F content of the film appears to decrease during this stage of the process relative to its initial levels near the Si surface. Evidence of redeposition of sputtered process kit materials has, in fact, been reported by other authors working with an etch tool of the same type as the one used in this study. In their work, XPS was employed to identify SiO_2 features within the Si 2*p* spectrum on silicon and resist surfaces exposed to a C_2F_6 etch plasma. [1]

The incorporation of SiO process kit material into the film is also consistent with the difference in XPS sputter rates for the C_3F_8 film and the 1-iodoheptafluoropropane films. As Table 5.11 indicates, the sputter rate for the 1-iodoheptafluoropropane films deposited on Si was estimated to be in the range of 1.5 to 1.8 Å/s, averaged over the duration of the sputter run. On the other hand, the estimated rate for the C_3F_8 film was significantly lower: 0.9 Å/s. Since the densities of the fluorocarbon films themselves are likely to be similar and since the iodine content of the 1-iodoheptafluoropropane films was small, the difference in sputter rates is likely to be due to the silation of top portion of the film in the C_3F_8 case.

The most dramatic effect seen in the above data, however, is found in the iodine depth profiles for the 1-iodoheptafluoropropane films discussed. Namely, the iodine is seen to build up at the interface of the deposited fluoropolymer film with the underlying Si. The pileup of iodine at the Si interface constitutes evidence for much greater penetration of the surface layers of the film by iodine arriving at the wafer, with the iodine being stopped only once it impinges on the denser crystalline Si underneath. *I.e.,* the iodine is not co-deposited with the fluoropolymer in the same stoichiometric ratio as that seen in the arriving ion and neutral fluxes. Rather, it appears to *driven into* the substrate with considerably greater energy. This effect leads to the conclusion that the dominant component of I flux at the wafer is ionic, rather than neutral. This is supported by two observations: 1) that the C-I bond in 1-iodoheptafluoropropane is rather weak relative to the C-C and C-F bonds in that molecule (see discussion in Section 2.2.2); and 2) that the ionization potential of I, 10.45 eV, is also relatively low (see Table 5.12).

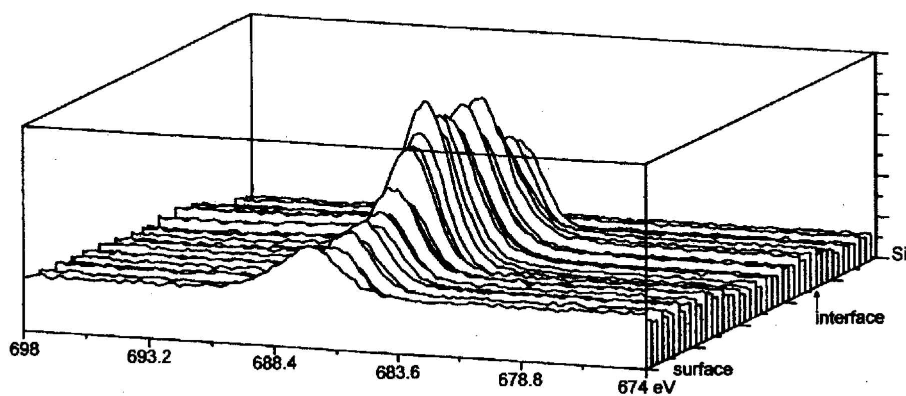

a)

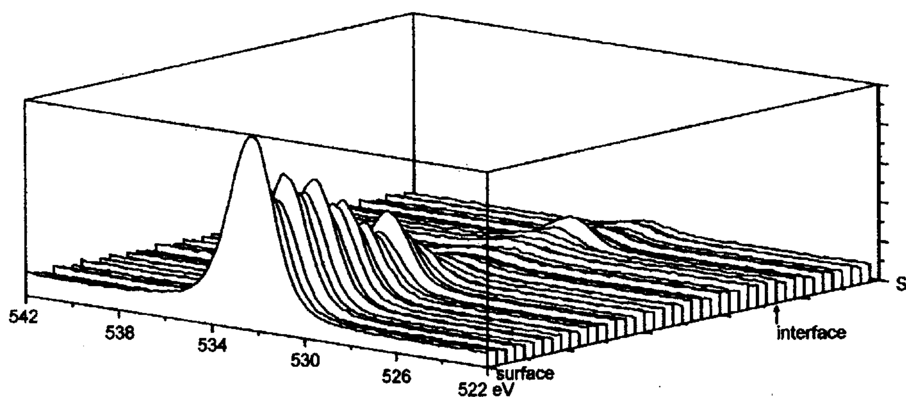

b)

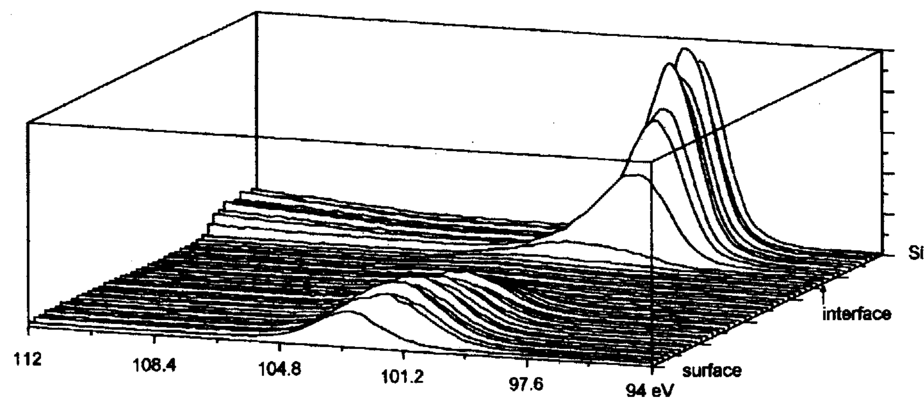

c)

Figure 5.60: XPS depth profile data for sample Si-4: a) F 1*s* spectrum, b) O 1*s* spectrum, c) Si 2*p* spectrum.

Table 5.12: Ionization potentials of selected species present in the iodofluorocarbon plasmas in this study. [12-14]

Species	Ionization Threshold (eV)	Mass (amu)
I	10.45	127
F	17.42	19
CF	9.4	31
CF_2	11.5	50
CF_3	8.9	69
He	24.59	4

These observations indicate that the iodine in 1-iodoheptafluoropropane is easily removed in electron impact collisions in the plasma and also readily ionized. At 127 amu, I^+ is also easily the most massive of the ionic species expected to be present in the fluxes arriving at the wafer surface, which accounts for the dramatic ability to penetrate so deeply into the substrate. This, combined with its relative abundance, easily explains why bulk resist selectivity above ~3:1 is difficult to achieve with 1-iodoheptafluoropropane for a process with a reasonable via profile and oxide etch rate, despite the lower F:C ratio in the molecule relative to C_3F_8 (see Section 5.4.1).

In a supporting experiment with patterned oxide wafers, straight substitution of 1-iodoheptafluoropropane into the C_3F_8/CH_3F reference recipe resulted in an average patterned oxide etch rate increase of 23.1% in the center of the wafer and 12.0% at the edge for via hole features of critical dimension (CD) ranging from 0.35 to 0.6 μm. The corresponding increase in photoresist etch rate was even more pronounced: 2388 Å/min versus 75 Å/min in the center and 2305 Å/min versus 360 Å/min at the edge – 30.8X and 5.4X increases, respectively. The increase in both resist and oxide etch rates over C_3F_8, despite the lower fluorine content in the 1-iodoheptafluoropropane molecule, is believed to be due to an appreciable increase in the physical sputtering component of the etch resulting from bombardment of the wafer surface by massive I^+ ions.

On the other hand, the fact that the 1-iodoheptafluoropropane processes exhibited no evidence of significant amounts of process kit etching suggests that the silicon and quartz surfaces of the chamber were well protected from fluorine by thicker polymer deposits in the case of 1-iodoheptafluoropropane than in the case of C_3F_8. It had been, in fact, established in Section 5.4.1 that 1-iodoheptafluoropropane tends to polymerize more heavily than its fully fluorinated counterpart, C_3F_8, which is consistent with the lower F:C ratio of the molecule. The iodine bombardment effect discussed above explains why, despite this fact, 1-iodoheptafluoropropane processes result in more resist erosion than C_3F_8. This explanation also accounts for the fact that the polymer film on sample Si-4 is significantly thicker than the films on the 1-iodoheptafluoropropane samples (see Table 5.11). Thus, on biased surfaces, *i.e.,* the wafer itself, the bombardment effect is dominant because the massive I^+ ions are accelerated across the voltage of the sheath at the wafer surface. On unbiased surfaces, on the other hand, *e.g.,* chamber walls, polymer formation rates are controlled by established phenomena such as F:C ratios in the arriving fluxes; there, the presence of the iodine appears to play little role in the polymerization mechanisms.

Resist Samples. Both the survey spectra and the depth profiles indicate that the surface layers of samples K2G-2 and K2G-3 (1-iodoheptafluoropropane/CH_3F) are similar to those of samples Si-2 and Si-3; likewise, the surface layers of sample K2G-4 (C_3F_8/CH_3F reference process) are similar to those of Si-4. Sample K2G-1, however, is an exception to this trend. Whereas, the same 1-iodoheptafluoropropane process showed no evidence of etching significant amounts of process kit materials when a bare Si substrate was used, sample K2G-1 exhibits the same features discussed above for sample Si-4: incorporation of oxygen and silicon into the film after approximately halfway through the process along with the corresponding drop in fluorine content in the upper layers of the film. See Figure 5.61. This suggests one of two explanations that can potentially account for the difference in chamber wear between the two runs: 1) the chamber condition for the two runs was significantly different, *i.e.,* the passively heated parts of the process kit were likely *colder* when wafer Si-1 was run, resulting in more polymer condensation on those surfaces and less process kit interaction with fluorine; 2) the presence of photoresist in

the chamber altered the plasma chemistry significantly enough to result in enhanced etching of the process kit. The latter explanation is unlikely, since the etching of photoresist, which is known to produce HF and CHF_3 as its principal byproducts (see, for example, Section 5.3 or 6.1), would likely result in the consumption of fluorine, rather than its increased availability to interact with process kit surfaces. The fact that wafer Si-1 was, in fact, run earlier than wafer K2G-1 also supports the former explanation and draws attention to the fact that chamber warmup and seasoning can play a significant role in process behavior. The iodine profile on sample K2G-1 shows evidence of buildup at the fluorocarbon film / resist interface, as demarcated by the extent of the fluorinated layer. Past this interface, it continues to penetrate into the resist, its concentration monotonically decreasing with sputter depth.

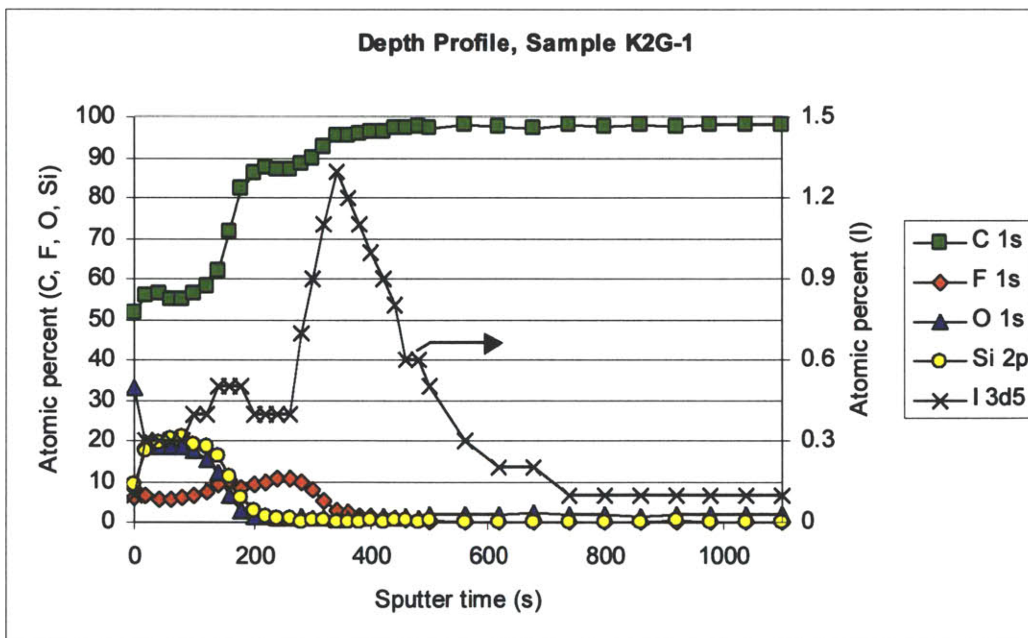

Figure 5.61: XPS depth profile for sample K2G-1: K2G resist film etched by 1-iodoheptafluoropropane process. Note that iodine at. % scale is magnified 100x.

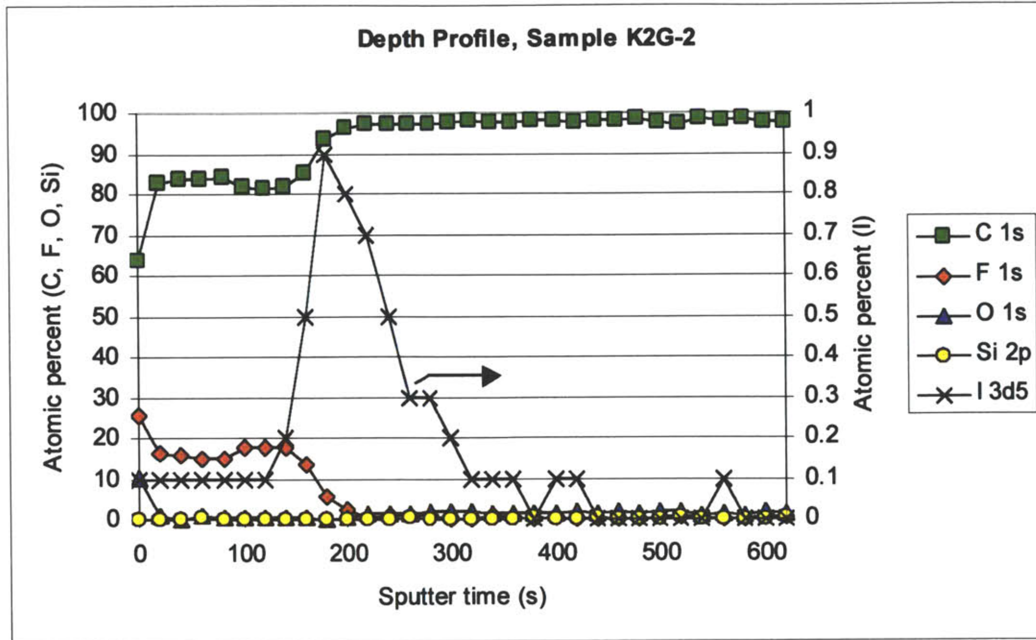

Figure 5.62: XPS depth profile for sample K2G-2: K2G resist film etched by 1-iodoheptafluoropropane/CH_3F process. Note that iodine at. % scale is magnified 100x.

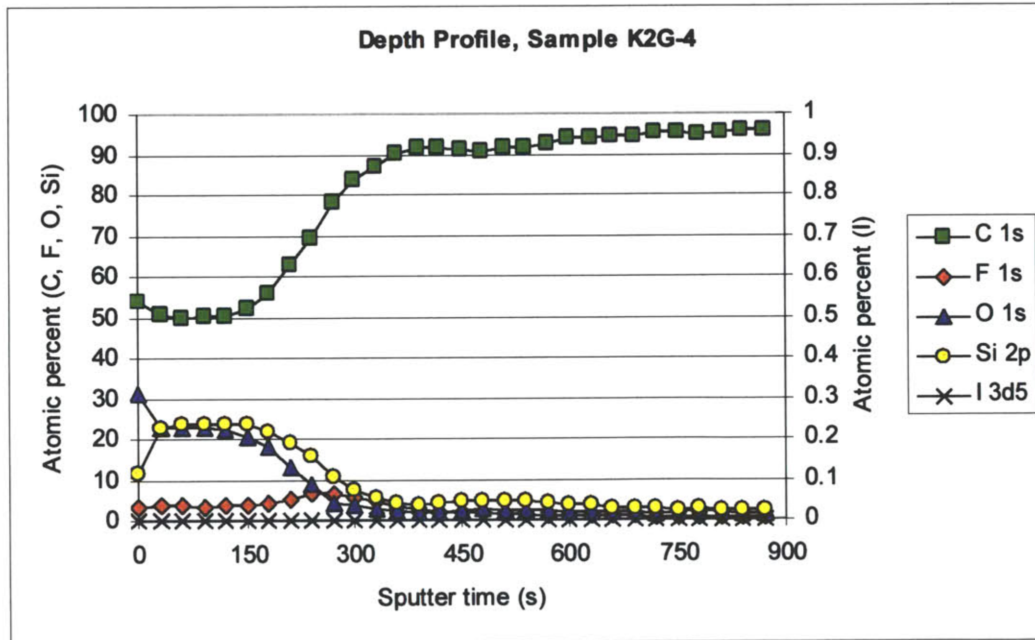

Figure 5.63: XPS depth profile for sample K2G-4: K2G resist film etched by C_3F_8/CH_3F reference process.

The depth profile for sample K2G-2 (see Figure 5.62) shows the existence of a fluorocarbon layer on top of the resist, containing virtually no silicon or oxygen (except for the surface oxidation). Once again, there is evidence of iodine buildup at the fluorocarbon film / resist interface and iodine penetration past this interface, after which its signal decreases monotonically with sputter depth.

Finally, the depth profile for sample K2G-4 possesses a number of features seen in sample Si-4. See Figure 5.63. An SiO-rich region is seen to exist in the uppers layers of the film. As the Si and O signals decrease with increasing depth, the F signal is seen to rise. However, in contrast to the trends seen on samples Si-4 and K2G-1, where the lower layers of the fluorocarbon film are dominated by CF_x stoichiometry, here the fluorine signal drops again and the Si and O signals persist at levels comparable to that of the fluorine. This suggests that different chamber surface conditions are present during the early part of the run here than was the case for samples Si-4 and K2G-1. Specifically, some etching of process kit surfaces is see to occur throughout the duration of the process, not only towards its end. The reason for the peak in fluorine content at the transition point between the two regimes, however, is not readily apparent.

The above data lead one to draw several conclusions. The first of these is that differences between various processes in terms of interaction with process kit surfaces can be quite significant. Specifically, there is evidence that the C_3F_8/CH_3F reference process interacts more aggressively with the Si/quartz process kit than do the iodofluorocarbon based recipes, whether those recipes are characterized by low polymer formation on the wafer (*e.g.,* Process 2) or high polymer formation on the wafer (*e.g.,* Process 1 or 3). The second conclusion to be drawn is that the same process can have different film formation behavior depending on the condition of the chamber, as is evidenced by the absence of any incorporation of Si or O from the process kit in run Si-1 and the presence of significant amounts of these elements in the film formed in run K2G-1. Finally, the K2G resist depth profile data support the evidence provided by the bare Si wafers for deep penetration of iodine ions into the film on the wafer. In the resist substrate cases, the thickness of the resist is too great to allow the iodine to penetrate all the way to the Si

underneath; however, the iodine is seen to penetrate the surface layers to a greater depth than the fluorine, with the fluoropolymer / resist boundary providing a stopping interface. The presence of this pileup at the interface with the resist is, in all likelihood, due to greater density of the underlying film.

Table 5.13: F:C ratios for deposited films. Surface ratios calculated from XPS survey scans. Bulk ratios averaged over depth of film in bare Si wafer case, averaged over depth of fluorinated part of film in K2G wafer case.

Process	Bare Si Samples		K2G Samples	
	F:C ratio (surface)	F:C ratio (bulk)	F:C ratio (surface)	F:C ratio (bulk)
1 (1I-C_3F_7I)	0.49	0.15	0.14	0.11
2 (1I-C_3F_7I + CH_3F)	0.35	0.12	0.38	0.22
3 (1I-C_3F_7I + CH_3F)	0.41	0.10	0.37	
4 (C_3F_8 + CH_3F)	0.20	0.09	0.12	0.06

5.4.2.4 Results and Discussion – XPS F:C Ratios and C 1*s* Spectrum Analysis

Table 5.13 lists the F:C ratios obtained for the surface and bulk layers of the fluorocarbon films on each sample. The bulk numbers were calculated by averaging the F:C ratio throughout the depth of the film, down to the beginning of the interface with the Si or resist. Since no depth profile was available for sample K2G-3, no bulk F:C value is given; it is, however, expected to be similar to that obtained for sample K2G-2. Several trends are apparent in the data. First of all, it is noteworthy that the F:C ratio of the surface layer followed two patterns: samples Si-1, Si-2, Si-3, and K2G-2, K2G-3 were calculated to have surface F:C ratios in the 0.35 to 0.49 range, whereas samples Si-4, K2G-1, and K2G-4 had ratios in the 0.12 to 0.20 range. A comparison with the surface scan data presented above suggests a correlation between the surface F:C ratio and whether or not SiO from the process kit is incorporated into the film. The surface F:C ratio is markedly lower for those samples which show significant evidence of process kit etching (Si-4, K2G-1, and K2G-4), suggesting that lower fluorine content in the surface layer may be due to higher consumption of fluorine in etching process kit surfaces. The bulk data is more ambiguous, with F:C ratios for the three films with significant SiO

incorporation ranging from 0.06 to 0.11, whereas the corresponding range is 0.10 to 0.22 for the other samples.

Table 5.14: XPS C 1*s* spectrum peak assignments (eV).

Bond	Binding Energy (values used)		Binding Energy (lit. values) [15]	Binding Energy (lit. values, other workers) [1, 6, 16-18]
	Sample Si-1	Sample Si-4		
C-C/C-H	284.13	284.35	284.2	284.5 - 287.5
C-CF_x/C=O	285.52	285.41	285.2	286.5 - 289
CF	287.00	286.66	287.0	288.8 - 290.75
CF_2	288.69	287.92	288.7	290.1 - 292.5
CF_3	290.76	289.23	290.6	293 - 295

Comparing the surface ratios against those seen in the bulk for all seven films shows that the bulk ratio is lower in all cases. Figures 5.53, 5.54, 5.55, 5.61, and 5.62 suggest that this difference may be due to the oxidation of the film surface. In all of these samples, the surface layer shows much higher oxygen content than does the bulk; moreover, it has correspondingly lower carbon content. This therefore suggests that outgassing of CO and/or CO_2 from the surface layer may have occurred. The C_3F_8 samples, Si-4 and K2G-4, also show elevated O content in the surface layer in the depth profile (see Figures 5.56 and 5.63). In these two samples, however, there is no evidence of a significant change in the F or C content from the surface layer to the layers immediately below it. Likewise, even though the depth profile for sample K2G-1 has evidence of lower C content at the surface than in the bulk, the difference is not as pronounced as with the remaining samples. A comparison of Figures 5.53-5.56 and 5.61-5.63 with Figure 5.52, moreover, shows that the composition of the surfaces of the three silated samples as seen in the depth profiles is closer to that of the bulk rather than to that indicated by the initial surface scans. Samples Si-4, K2G-1, and K2G-4 differ significantly from samples Si-1 through Si-3 and K2G-2 in that the upper portion of their bulk, including the surface itself, has significant SiO content. In all cases, the depth profiles were taken several months after the initial surface scans. The above results suggest, therefore, that the

surface layers of the silated films are perhaps less stable than those of the more purely fluorocarbon films.

The carbon bonding in the films deposited on samples Si-1 and Si-4 was examined in some detail. Figures 5.64 and 5.65 show the C 1s carbon peak around 284 eV. Table 5.14 lists the bonding energy assignments used for the features in the C 1*s* spectrum. The spectrum shown for sample Si-1 was taken from the middle layers of the deposited film; hence it is representative of the carbon bonding seen in the bulk. For this sample, since no hydrogen was introduced with the feed gas, little, if any, C-H bonding is believed to be present; hence the peak at 284.13 eV was assigned strictly to quarternary carbon (with no fluorine in the beta position) rather than a combination of C-C and C-H bonding. Likewise, since the depth profile revealed negligible oxygen content, the fitted peak at 285.52 eV was assigned strictly to C-CF (quarternary carbon with beta fluorine). As Figure 5.64 indicates, the film deposited by pure 1-iodoheptafluoropropane appears to contain mostly C-C bonding (56.7%) with smaller amounts of C-CF (20.6%) and fluorinated carbon groups (10.6% CF, 5.5% CF_2, 6.6% CF_3).

Figure 5.65 shows the C1*s* carbon spectrum for sample Si-4, also taken in the bulk of the film, in the non-silated portion. In this portion of the film, C=O bonding is also expected to be negligible (see Figure 5.56), although some C-H bonding may be present, due to the presence of CH_3F in the feed gas chemistry. (The chemical shift due to the presence of H, however, is generally too small to be resolved using XPS; moreover, H in the film is often sputtered away by Ar beam bombardment used in depth profiling.) Overall, the carbon bonding in this film appears to be very similar to that of sample Si-1, with 56.0% of the film being assigned to C-C, 21.4% to C-CF, 10.5% to CF, 5.7% to CF_2, and 6.4% to CF_3. These data therefore suggest that the stoichiometry of films deposited by 1-iodoheptafluoropropane is essentially similar to those deposited by C_3F_8/CH_3F, with both types of films being carbon-rich and composed mostly of carbon to carbon bonds with relatively few CF_x groups.

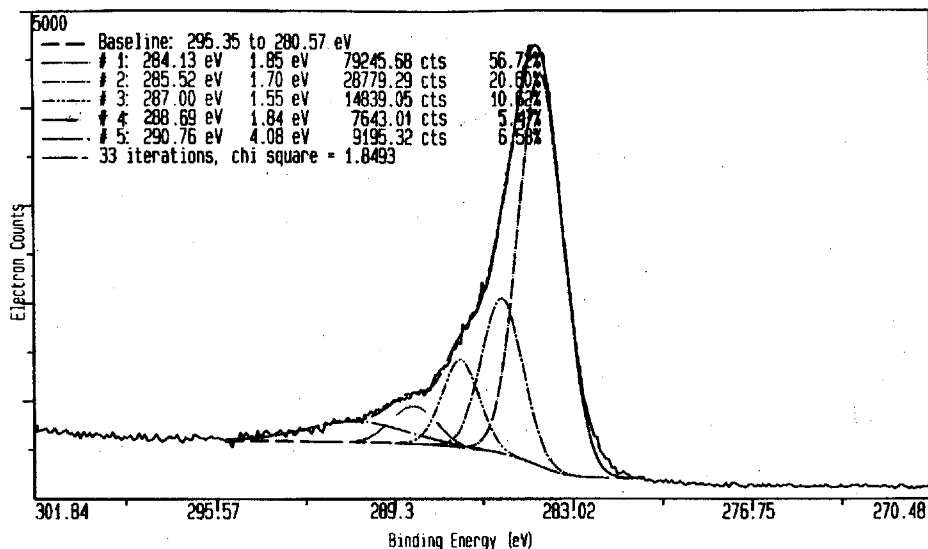

Figure 5.64: C 1*s* spectrum for bulk of fluorocarbon film deposited by 1-iodoheptafluoropropane (sample Si-1).

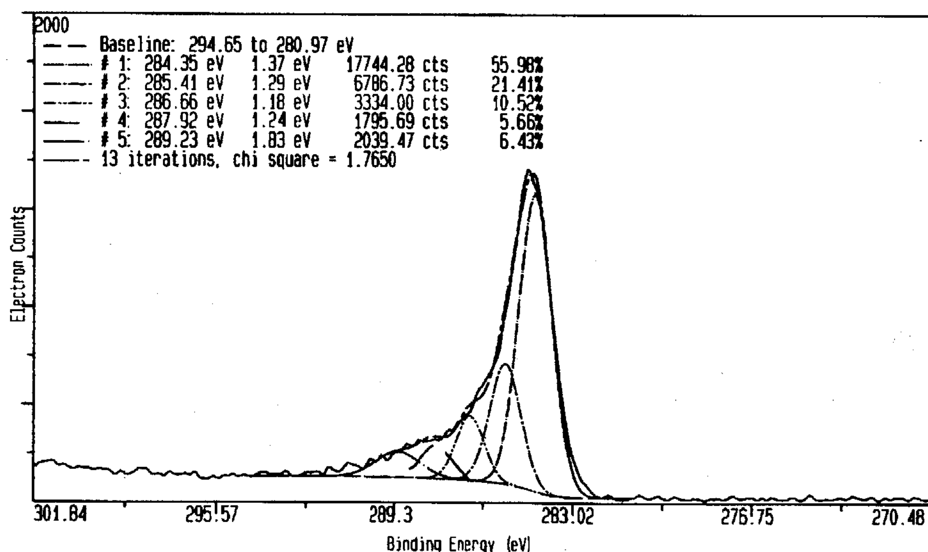

Figure 5.65: C 1*s* spectrum for bulk of fluorocarbon film deposited by the C_3F_8/CH_3F reference process (non-silated portion of sample Si-4).

5.4.2.5 Results and Discussion – TOF-SIMS Analysis (Depth Profiles)

The features seen in the XPS depth profiles are confirmed by complementary characterization using TOF-SIMS. While no assignment of relative contributions to film composition by at. % is possible on the basis of the TOF-SIMS profiles, many of the

same trends with respect to the depth profiles of individual elements are evident in both sets of spectra.

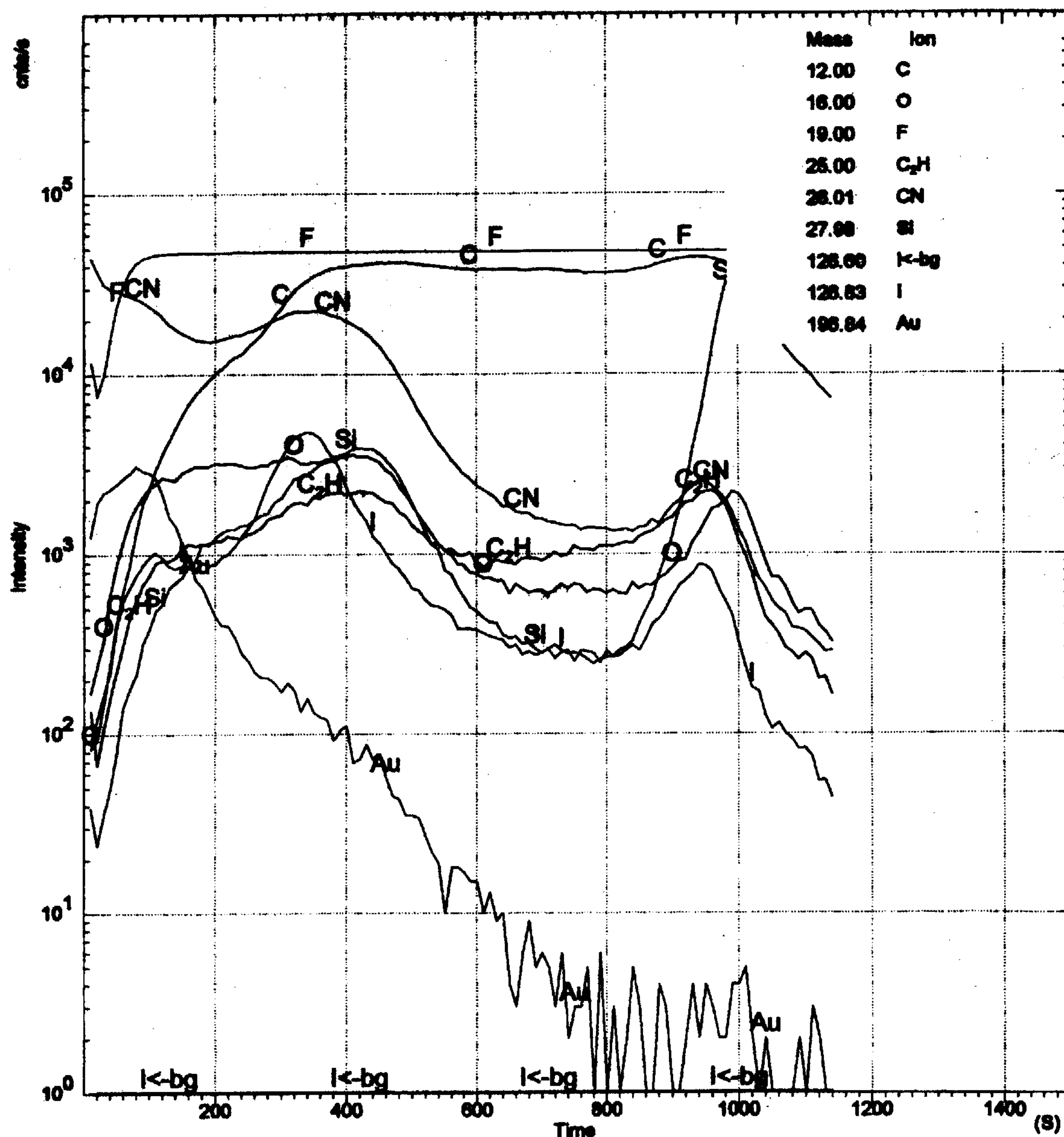

Figure 5.66: TOF-SIMS depth profile for sample Si-4: film deposited on bare Si by C_3F_8/CH_3F reference process. Film was coated with Au prior to data acquisition.

Bare Si Samples. The TOF-SIMS profiles for samples Si-1, Si-2, and Si-3 confirm the presence of a clearly defined fluorocarbon layer on top of the Si. Masses having high signal intensities in this region include 19 (F), 12 (C), 31 (CF), and 38 (F_2). Both mass

16 (O) and 127 (I) also appear to present above background levels, with a sharp peak in intensity at the fluorocarbon film / Si interface, corresponding to native oxide and the iodine pileup effect, respectively. The principal difference between these three samples lies in the differences in sputter times before the Si is reached, which are 1000 s, 350 s, and 1250 s for Si-1, Si-2, and Si-3, respectively, at a sputter energy of 1 keV and a current of 5.6 nA. The relative rates are roughly consistent with the estimates of fluorocarbon film thickness and the XPS sputter times given in Table 5.11.

The profile for sample Si-4 also indicates the presence of a thick fluorocarbon film on top of the underlying Si, with an approximate sputter time of 1000 s before the Si was reached (at a higher sputter energy, 3 keV, than that used for the 1-iodoheptafluoropropane samples). As was observed from the XPS depth profile, the film consists of two distinct regions: an SiO-rich layer near the surface and a more purely fluorocarbon based layer near the Si interface. See Figure 5.66. The increase in the O signal intensity at the Si interface was also observed. One significant feature detected using the TOF-SIMS technique, which possesses a sensitivity advantage over XPS, is the presence of trace amounts of I in the film with evidence of accumulation in the SiO-rich sub-layer with an accompanying pileup at the interface of the SiO-rich and SiO-poor sub-layers, as well as the previously seen pileup at the Si interface. An iodine signal was not identified in the XPS survey spectra and was not included in the XPS depth profile. This apparent discrepancy is not necessarily surprising, however, given the fact that the intensity of the TOF-SIMS iodine signal at the Si interface is about an order of magnitude lower for this sample than the intensities seen for Si-1 through Si-3. This suggests that the amounts of iodine present in this film are much smaller than in those deposited by the 1-iodoheptafluoropropane plasmas. What is significant about the mere detection of trace amounts of I on sample Si-4 is that its presence must be caused by cross-contamination from earlier 1-iodoheptafluoropropane runs. This view is supported by the order of magnitude difference in I signal intensity between the maximum seen in the SiO-rich sub-layer and the low-level signal seen in the SiO-poor sub-layer. The fact that the I signal intensity tracks the O and Si signals in the film implies that the source of the I is its removal from the Si/quartz surfaces of the process kit.

Resist Samples. The TOF-SIMS profiles for samples K2G-1, K2G-2, and K2G-3 show a pronounced buildup of iodine at the fluorocarbon film / resist interface along with evidence of significant levels of silicon and oxygen in the film in the case of sample K2G-1, but not K2G-2 and -3, which is consistent with the data obtained by XPS. For sample K2G-4, as was the case with the XPS depth profile, there is evidence here that Si and O are present in the fluoropolymer film in some quantity. Whereas the XPS survey scan was unable to resolve an iodine signal from the background noise for this sample, I at mass 127 is seen to be present in the fluorocarbon film at signal intensities about an order of magnitude lower than those seen for samples K2G-1 through -3, suggesting, as was the case for sample Si-4, that the source of the iodine was process kit surfaces. Again, the peak of the iodine distribution in the film appears to lie near the interface with the underlying resist layer.

In short, the time-of-flight SIMS data generally confirm, in a qualitative manner, the information that was obtained through XPS analysis. They moreover add the information that some iodine incorporation into deposited fluorocarbon film occurs even during a C_3F_8 process, indicating carryover from previous runs via redeposition of chamber residues. The iodine content in the C_3F_8 films is estimated at ~0.01 – 0.05 at. %, on the basis of comparison between the I signal in those samples and in the 1-iodoheptafluoropropane deposited films. It should be pointed out, however, that the at. % assignments used in the XPS data (and hence the above estimates as well) should be treated as tentative, as they are based on instrumental sensitivity factors, rather than calibration using a known film sample.

5.4.2.6 Conclusions

Films deposited by 1-iodoheptafluoropropane and 1-iodoheptafluoropropane/CH_3F plasmas were analyzed using x-ray photoelectron spectroscopy and time-of-flight secondary ion mass spectrometry. Both surface scans and depth profiles were taken. These data were compared to results obtained from films deposited by a C_3F_8/CH_3F reference process. The most significant finding was that, in the iodofluorocarbon films,

iodine from the plasma was found to be implanted into the fluorocarbon layer, stopping only at the interface of this film with the underlying resist or Si. This was taken as evidence that energetic bombardment of the wafer by massive iodine ions is a significant mechanism in iodoheptafluoropropane etch processes. On a biased wafer, the C_3F_8/CH_3F reference process was found to deposit a thicker film than any of the 1-iodoheptafluoropropane processes, due to absence of the iodine bombardment effect. However, the C_3F_8 process was found to interact more aggressively with Si and SiO_x process kit surfaces, implying that, on unbiased chamber surfaces, 1-iodoheptafluoropropane polymerizes more heavily than C_3F_8, as one would expect from the lower F:C ratio in the iodofluorocarbon molecule.

These results correlate with findings presented in Section 5.4.1, where it is noted that, in the absence of the iodine bombardment effect (on feature sidewalls and in feature corners), 1-iodoheptafluoropropane polymerizes more heavily that does C_3F_8. On surfaces subjected to ion bombardment, on the other hand, this effect is overwhelmed by an increase in the physical component of the etch, resulting in higher oxide etch rates inside patterned features, but also higher stop layer and bulk resist etch rates, leading to lower selectivity values than those obtained with C_3F_8.

5.4.3 Effluent Characterization

The work presented represents the effluent characterization portion of a systematic evaluation of 1-iodoheptafluoropropane (CF_2I-CF_2-CF_3) as a potential replacement for perfluorocompound (PFC) chemistries in dielectric etch applications in an inductively coupled plasma etch tool (Centura 5300 HDP).. Sections 5.4.1 and 5.4.2 discuss etch process behavior and deposited fluoropolymer films, respectively. Section 5.4.1 also examined the other isomer of the compound, 2-iodoheptafluoropropane. The present section will focus on the composition of the process effluent stream, as characterized by Fourier transform infrared (FTIR) spectroscopy. Data generated by both isomers of the compound will be presented.

Section 5.4.3 is organized as follows: Section 5.4.3.1 covers the experimental setup. Section 5.4.3.2 provides a discussion of the FTIR data obtained, along with some relevant process data. Section 5.4.3.3 provides concluding remarks regarding the effluent characterization portion of the study presented in Section 5.4.

5.4.3.1 Experimental Setup

The FTIR sampling and calibration methodology was identical to that described in Section 5.3. In brief, an extractive technique was employed downstream of the mechanical roughing pump backing the chamber turbopump. A heated Teflon line, 25 ft. in length, was used to introduce a sample of the process effluent into the FTIR cell, which was actively pumped by a diaphragm pump. Both the cell, a 10 cm cell with zinc selenide windows, and the extraction line were heated to 121 °C. The pressure in the cell was controlled at 600 Torr. 45 slm (standard liters per minute) of ballast nitrogen were delivered to the roughing pump; the flow was controlled by MFC (mass flow controller). In the present study, the following compounds were identified in the effluent from 1-iodoheptafluoropropane based processes: CF_4, CHF_3, C_2F_6, C_3F_8, C_2F_4, CO, CO_2, COF_2, HF, SiF_4, CF_3I, and 1-iodoheptafluoropropane itself. Effluent from 2-iodoheptafluoropropane processes was found to contain the same components, with 2-iodoheptafluoropropane being present instead of the 1-iodo isomer. Effluent from a C_3F_8-based process that was run as a reference was found to contain all of the above, except the iodofluorocarbon species. The C_3F_8 based process as well as some of the 1-iodoheptafluoropropane processes also employed the addition of fluoromethane (CH_3F) as part of the feed gas chemistry. The utilization of this compound in the plasma, however, was very complete: no evidence of unreacted CH_3F was found in the data from any of the runs discussed here.

In addition to quantifying individual species present in the effluent, the overall global warming impact of each process was also calculated using the kgCE metric defined in Section 5.1. In the discussion that follows, the emissions have been expressed in grams, rather than kilograms of CE, for convenience. 1998 GWP_{100} values [19] for the global warming gases identified in the effluent (CF_4, CHF_3, C_2F_6, and C_3F_8) were used. In the

analysis below, these four fluorocarbon species are believed to account for the entirety of the carbon equivalent (CE) value for all processes (with the exception of CO_2, whose contribution to the CE is less than 0.0003% in all cases). No global warming potential numbers have been assigned to the remaining fluorocarbon species identified (C_2F_4, CF_3I, 1- and 2-iodoheptafluoropropane). See Tables 1.1 and 2.2. Figure 5.67 provides FTIR spectra of 1-iodoheptafluoropropane, 2-iodoheptafluoropropane, and iodotrifluoromethane.

Three sets of experiments with 1-iodoheptafluoropropane and one involving both 1- and 2-iodoheptafluoropropane were carried out as part of this study. The first experimental series involved 1-iodoheptafluoropropane/CH_3F processes run with blanket deep UV photoresist wafers. CH_3F was initially added because earlier work with these compounds in the same process tool (Section 5.1) showed that bulk photoresist selectivity was an area in which improvement was necessary. The addition of a hydrofluorocarbon additive such as CH_3F was intended to enhance polymer formation mechanisms with the intent of lowering the amount of bulk resist loss. The resist used in these blanket film runs was K2G type deep UV resist. The aim of this first series of experiments was to establish a baseline for the overall global warming emissions from 1-iodoheptafluoropropane based processes, relative to those produced by the C_3F_8/CH_3F based process that was used as a reference. Process data from the same C_3F_8/CH_3F based process were employed as a reference in Section 5.4.1 as well. The parameter space covered by this set of experiments was: 1700 – 1900 W source power (*SP*), 22 – 26 sccm etch gas flow (*EF*), and 200 to 220 °C roof temperature (*RT*). A simple three level axial matrix was run. The remaining parameters were as follows: 600 W bias power, 4 sccm CH_3F flow, 75 sccm He flow, 6 mTorr pressure, 34 °C chiller temperature, 200 °C wall temperature, and 15 Torr backside He cooling pressure.

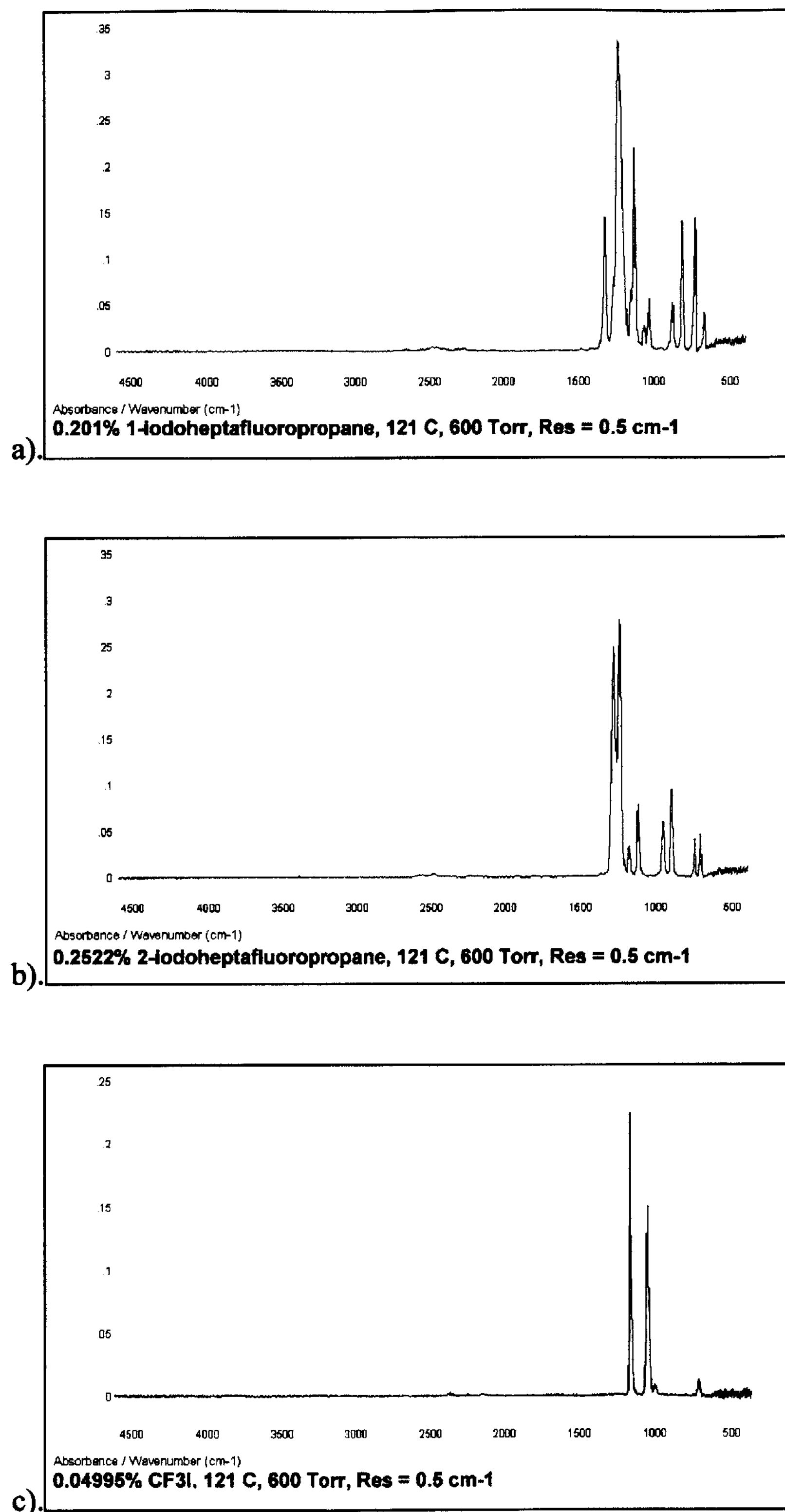

Figure 5.67: FTIR spectra of a) 1-iodoheptafluoropropane (CF_2I-CF_2-CF_3), 2010 ppm; b) 2-iodoheptafluoropropane (CF_3-CF_2I-CF_3), 2522 ppm; c) iodotrifluoromethane (CF_3I), 499.5 ppm; spectra collected at using 10 cm ZnSe cell.

The second set of experiments involved a comparison of 1-iodoheptafluoropropane based processes with and without CH_3F against the C_3F_8/CH_3F reference process, as well as against a C_2F_6 based process. Patterned oxide wafers with arrays of via hole features (0.35 μm minimum critical dimension) were employed. Two types of compositionally similar deep UV resist were used: K2G and APEX. The same C_2F_6 based process has been used as a reference for alternative chemistry experiments discussed in Sections 5.3 and 6.1. The processes run as part of this experimental series are listed in Table 5.15. In this set of experiments, the C_3F_8/CH_3F reference process and one of the 1-iodoheptafluoropropane processes were run with both K2G and APEX resist for comparison. The open area on these and all other patterned wafers used in this work was approximately 0.5%; hence, for all practical purposes, emissions from the patterned wafers were treated as equivalent to emissions from blanket resist wafers run under the same conditions.

The third experimental series used patterned oxide wafers with APEX resist run with 1-iodoheptafluoropropane processes. No CH_3F was used. The parameter space covered by this set of experiments was: 1450 – 1750 W source power (*SP*), 13 – 19 sccm etch gas flow (*EF*), and 200 to 260 °C roof temperature (*RT*). A five level, three variable central composite (CCD) matrix was run with two runs taken at the center point condition. The remaining parameters were as follows: 800 W bias power, 0 sccm CH_3F flow, 75 sccm He flow, 9 mTorr pressure, 34 °C chiller temperature, 200 °C wall temperature, and 15 Torr backside He cooling pressure. Process data from the patterned wafer runs in this series of experiments as well as the 1-iodoheptafluoropropane process data from the second set of experiments were incorporated into the large matrix of 146 experimental points that was used to generate much of the neural network data discussed in Section 5.4.1.

Additionally, a fourth experimental series was also run. A single 1-iodoheptafluoropropane process was run with three substrates: a patterned oxide wafer with APEX resist, a patterned oxide wafer with K2G resist, and a bare Si wafer. The

same three substrates were also run with the C_3F_8/CH_3F reference process. Finally the APEX and K2G resist wafers were run with the 2-iodo isomer as well. The conditions for the iodoheptafluoropropane processes were as follows: 1580 W source power, 800 W bias power, 14 sccm etch gas flow, no CH_3F, 75 sccm He, 12 mTorr pressure, 230 °C roof temperature, 200 °C wall temperature, 34 °C chiller temperature, 15 Torr backside He pressure. See Table 5.16.

All runs discussed below were of 120 s duration. An O_2/Ar preprocess was run before each wafer to restore the chamber to a clean condition for the upcoming run.

Table 5.15: Experimental conditions used in second set of experiments. 75 sccm He flow, exc. C_2F_6 process (100 sccm), 15 Torr backside He pressure.

Run	Etch Gas	Source Power (W)	Bias Power (W)	Etch Gas Flow (sccm)	CH_3F Flow (sccm)	Roof Temp (°C)	Wall Temp (°C)	Chiller Temp (°C)	Pressure (mTorr)	Resist type	CE (grams)	% Reduction vs. C_3F_8 ref. (APEX)	Utilization efficiency
A	C_2F_6	1600	1400	25	0	240	220	-10	7.1	K2G	339.6	-4.3%	78.4%
B	1I	1600	800	14	0	230	200	34	6	K2G	130.4	59.9%	95.7%
C	1I+CH_3F	1600	800	14	15	230	200	34	6	K2G	204.9	37.1%	95.8%
D	1I+CH_3F	1600	800	14	15	230	200	34	6	APEX	179.2	44.9%	97.2%
E	C_3F_8+CH_3F	C_3F_8/CH_3F reference process								K2G	336.9	-3.5%	79.1%
F	C_3F_8+CH_3F	C_3F_8/CH_3F reference process								APEX	325.5	0.0%	79.4%

Table 5.16: Experimental conditions used in fourth set of experiments. 75 sccm He flow, 15 Torr backside He pressure. The % reduction column references the C_3F_8/CH_3F reference process run in the second set of experiments (see Table 5.15).

Run	Etch Gas	Source Power (W)	Bias Power (W)	Etch Gas Flow (sccm)	CH_3F Flow (sccm)	Roof Temp (°C)	Wall Temp (°C)	Chiller Temp (°C)	Pressure (mTorr)	Substrate / resist type	CE (grams)	% Reduction vs. C_3F_8 ref. (APEX)	Utilization efficiency
A	1I	1580	800	14	0	230	200	34	12	Bare Si	9.0	97.2%	96.0%
B	1I	1580	800	14	0	230	200	34	12	APEX	67.9	79.1%	96.4%
C	1I	1580	800	14	0	230	200	34	12	K2G	66.1	79.7%	96.3%
D	2I	1580	800	14	0	230	200	34	12	APEX	53.1	83.7%	96.8%
E	2I	1580	800	14	0	230	200	34	12	K2G	48.3	85.2%	96.2%
F	C_3F_8+CH_3F	C_3F_8/CH_3F reference process								Bare Si	281.7	13.5%	81.7%
G	C_3F_8+CH_3F	C_3F_8/CH_3F reference process								APEX	268.3	17.6%	82.2%
H	C_3F_8+CH_3F	C_3F_8/CH_3F reference process								K2G	252.8	22.3%	81.9%

5.4.3.2 Results and Discussion

1st Set of Experiments. In the initial axial matrix of experiments run with CH_3F, the average carbon equivalent (CE) value was 163.8 grams, corresponding to an emissions reduction of 49.7% against the C_3F_8/CH_3F reference process, whose CE value was established at 325.5 grams (see below). For the center point process in this matrix (170.1 CE, 47.7% reduction), the breakdown of the CE value by individual component was as follows: 63.7% CHF_3, 17.2% C_2F_6, 13.8% CF_4, and 5.3% C_3F_8. On a molar basis, however, the most abundant fluorocarbon species was C_2F_4, with 40.1 x 10^{-5} moles emitted by the process. The other fluorocarbon species found to be present were (in order of abundance): CHF_3 (38.4 x 10^{-5} moles), CF_3I (33.5 x 10^{-5}), CF_4 (17.2 x 10^{-5}), 1-iodoheptafluoropropane (9.7 x 10^{-5}), C_2F_6 (6.8 x 10^{-5}), and C_3F_8 (2.1 x 10^{-5}). The most abundant species, however, were HF (303.1 x 10^{-5}) and CO (117.2 x 10^{-5}) with SiF_4 (48.1 x 10^{-5}), COF_2 (13.6 x 10^{-5}), and CO_2 (3.0 x 10^{-5}) also being detected. The utilization efficiency of 1-iodoheptafluoropropane in these experiments was calculated to be 95.7% for the center point and 96.0% on average.

2nd Set of Experiments. Table 5.15 lists the CE values and utilization efficiencies for the runs that comprised the second set of experiments. As the table indicates, the three PFC-based processes run for comparison all showed similar levels of overall global warming impact (~330 grams of CE) and similar utilization efficiencies (~80%). The CE value obtained for the C_3F_8/CH_3F reference process run with APEX resist was taken as the reference value for these studies. The C_2F_6 process run here was the same process used as the PFC reference in Sections 5.3 and 6.1, where its CE value was reported as 289.0 grams. This discrepancy arises from the use of 1995 GWP_{100} values in the other studies, whose data were analyzed earlier. (1995 GWP_{100} estimates for CHF_3 and C_2F_6, the two principal contributors to the CE figure for this process, were lower than the corresponding 1998 values (11,700 vs. 14,800 and 9,200 vs. 11,400, respectively), which were the ones used in this study.)

Two 1-iodoheptafluoropropane based processes were compared against the PFC processes: one with 15 sccm CH_3F and one without CH_3F, with otherwise identical

process parameters. As Table 5.15 shows, the process with the hydrofluorocarbon additive had significantly higher global warming impact than the one without. A breakdown of the global warming effluent (see Table 5.17) shows that, from a global warming standpoint, the principal difference between these two runs lies in the amount of CHF_3 produced. A direct consequence of these results was the decision to remove CH_3F from the process recipe for further process development studies. A comparison of the 1-iodoheptafluoropropane runs in Table 5.17 with the PFC based ones shows that, in the latter case, the largest share of the global warming emissions was due to unreacted feed gas, whether it was C_2F_6 or C_3F_8. In the former case, feed gas utilization was much higher: All 1-iodoheptafluoropropane based processes run in this experimental stage had utilization efficiencies on the order of 96%, which is consistent with the results from the first set of experiments. For the 1-iodoheptafluoropropane based processes, the largest share of the CE value was contributed by CHF_3. The amount of CHF_3 emitted, on a molar basis, was significantly smaller for the run without CH_3F in the feed gas, suggesting that CH_3F supplies a significant fraction of the hydrogen necessary to form CHF_3. However, even when no hydrogen bearing species were introduced in the feed gas mixture, CHF_3 was still the leading component of the global warming fluorocarbon effluent, indicating that the etching of the photoresist by 1-iodoheptafluoropropane created significant amounts of CHF_3 as well. The amounts of resist eroded by each process are also given in Table 5.17. The runs with the lowest amounts of resist erosion (C_3F_8 runs) are also the ones with the lowest CHF_3 emissions.

Table 5.17: Breakdown of global warming emissions by moles of individual species (x 10^{-5}), percent contribution to CE (adjusted for GWP), and average thickness of photoresist eroded for the second set of experiments.

Run	Etch Gas	Resist type	Moles emitted (x 10^{-5})				% Contribution to CE				Resist eroded (Å)
			C_2F_6	C_3F_8	CF_4	CHF_3	C_2F_6	C_3F_8	CF_4	CHF_3	
A	C_2F_6	K2G	48.1	2.4	34.5	26.7	60.8%	3.1%	13.9%	22.2%	4260
B	1I	K2G	5.2	1.9	12.5	29.2	17.1%	6.6%	13.1%	63.2%	4821
C	1I+CH_3F	K2G	5.1	1.1	15.3	55.6	10.8%	2.4%	10.2%	76.6%	4109
D	1I+CH_3F	APEX	3.8	0.7	19.4	47.3	9.1%	1.6%	14.8%	74.5%	3932
E	C_3F_8+CH_3F	K2G	9.1	40.3	49.4	18.6	11.6%	52.8%	20.1%	15.6%	1102
F	C_3F_8+CH_3F	APEX	8.9	40.4	50.7	14.2	11.7%	54.7%	21.3%	12.3%	1280

Finally, both the 1-iodoheptafluoropropane/CH_3F process and the C_3F_8/CH_3F reference process were run with patterned oxide wafers with *both* APEX and K2G resist. In both cases, the global warming emissions from the K2G wafers were somewhat higher. However, as will be discussed below, these differences were later determined not to be statistically significant.

3rd Set of Experiments. In the CCD matrix of experiments run without CH_3F (the third set of experiments), the average CE value was 83.9 grams, corresponding to an emissions reduction of 74.2% against the reference process. For the center point process in this matrix (88.8 grams CE, 72.7% reduction), the breakdown of the CE value by individual component was as follows: 57.5% CHF_3, 21.4% C_2F_6, 16.6% CF_4, and 4.5% C_3F_8. On a molar basis, the most abundant fluorocarbon species was no longer C_2F_4 (13.0×10^{-5} moles). CF_3I (20.4×10^{-5} moles) and CHF_3 (18.1×10^{-5} moles) were now the fluorocarbons emitted in greatest abundance. The other fluorocarbon species found to be present were (in order of abundance): CF_4 (10.8×10^{-5}), C_2F_6 (4.4×10^{-5}), and C_3F_8 (0.9×10^{-5}). The most abundant species again were HF (150.3×10^{-5}) and CO (100.6×10^{-5}) with SiF_4 (33.2×10^{-5}), COF_2 (11.7×10^{-5}), and CO_2 (3.3×10^{-5}) also being detected. 1-iodoheptafluoropropane was detected but, in this particular set of runs, it could not be quantified accurately because of an instrumental baseline artifact in the part of the IR spectrum where 1-iodoheptafluoropropane is known to absorb that caused 1-iodoheptafluoropropane concentrations to be overstated. Because of large uncertainty associated with the concentration values obtained for this compound, a utilization efficiency for 1-iodoheptafluoropropane was not calculated. It is estimated, however, that the utilization efficiency in the runs that comprised this matrix was in line with earlier and later experiments, which consistently indicated a value of 95-96%. Table 5.18 provides a comparison of the center point from this matrix with the center point from the first set of experiments.

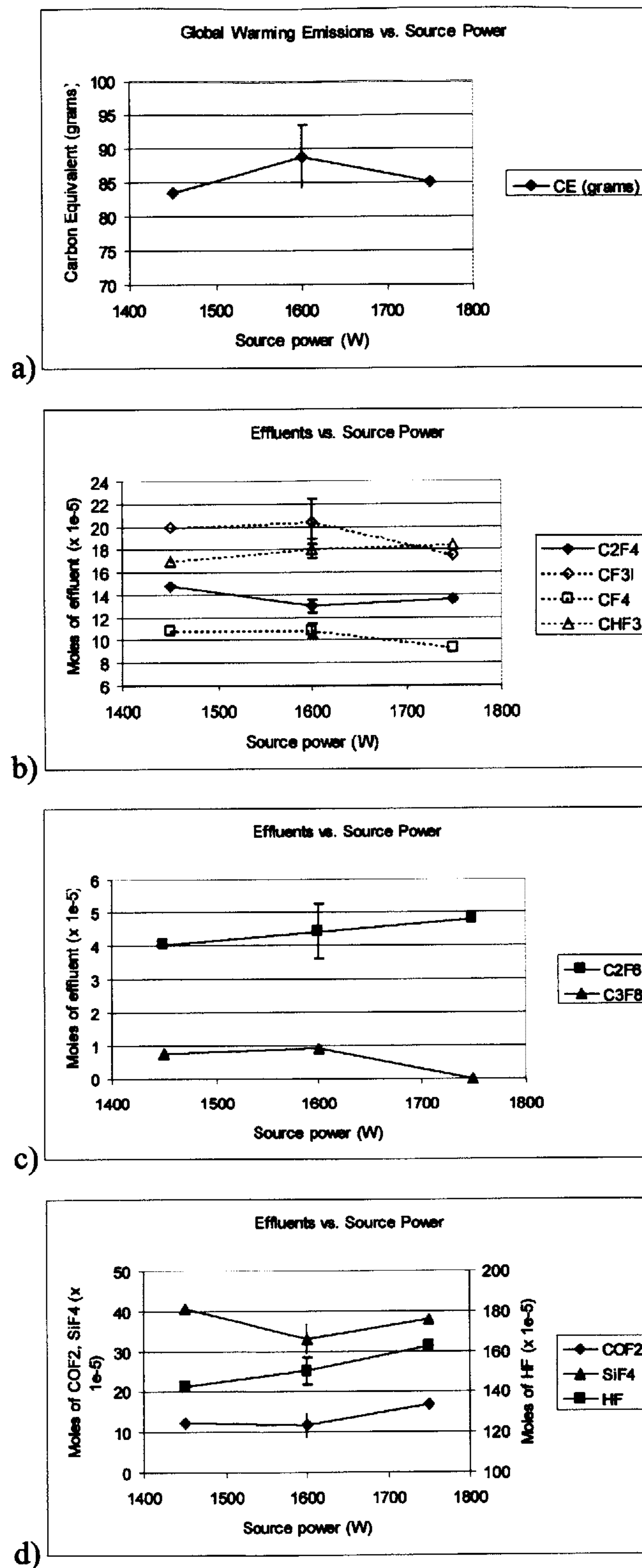

Figure 5.68: Effect of source power on a) overall CE and b), c), d) on individual species detected in the effluent. 16 sccm etch gas flow, 230 °C roof temperature.

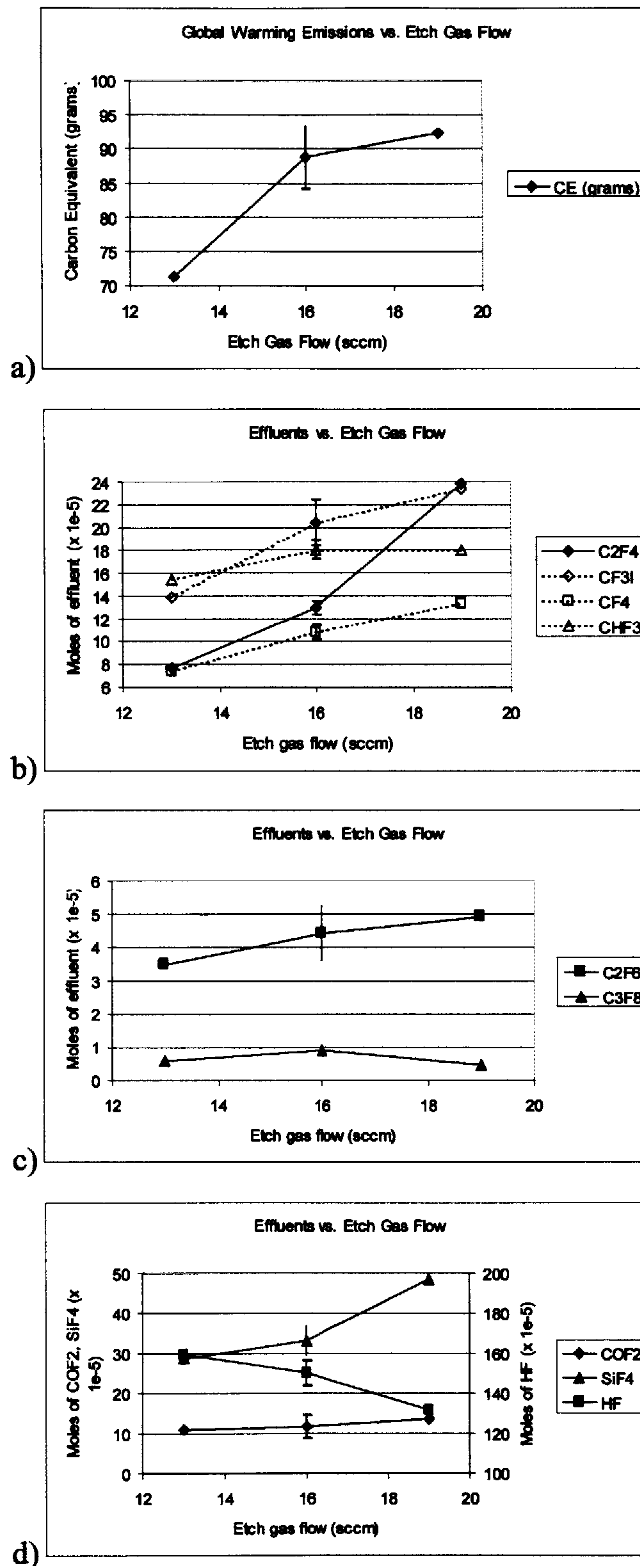

Figure 5.69: Effect of etch gas flow rate on a) overall CE and b), c), d) on individual species detected in the effluent. 1600 W source power, 230 °C roof temperature.

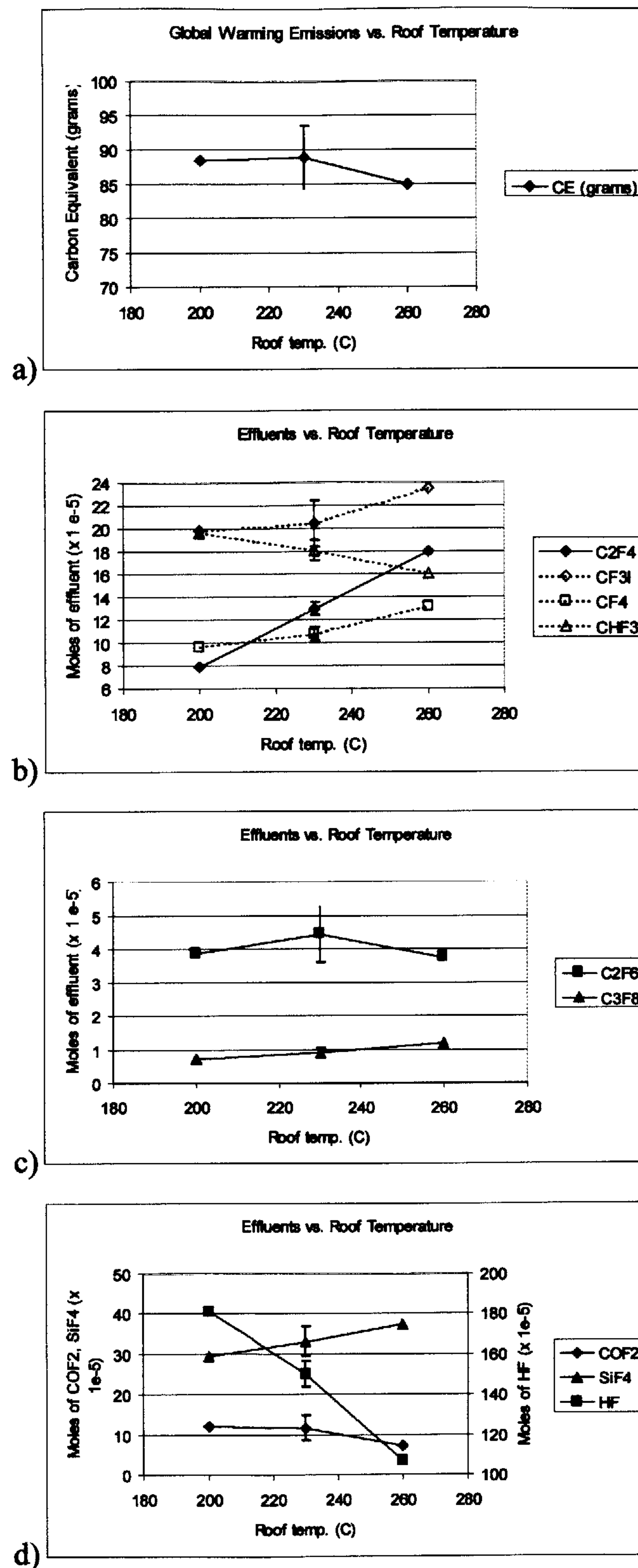

Figure 5.70: Effect of roof temperature on a) overall CE and b), c), d) on individual species detected in the effluent. 1600 W source power, 16 sccm etch gas flow.

Table 5.18: Comparison between center point processes from first and third set of experiments. (% reduction vs. APEX C_3F_8 reference).

	Process Conditions						CE	% red.	Moles emitted (x 10^{-9})											
	SP	BP	EF	CF	RT	PR	(grams)		1I	C_2F_4	C_2F_6	C_3F_8	CF_3I	CF_4	CHF_3	CO	CO_2	COF_2	HF	SiF_4
Ctr Pt. I	1800	600	24	4	210	6	170.1	47.7%	9.7	40.1	6.8	2.0	33.5	17.2	38.3	117.2	3.0	13.5	303.1	48.1
Ctr Pt III	1600	800	16	0	230	9	88.8	72.7%	N/A	13.0	4.4	0.9	20.4	10.8	18.1	100.6	3.3	11.7	150.3	33.2
Delta (%)			-33.3				-47.8			-67.6	-35.0	-55.5	-39.0	-37.2	-52.9	-14.2	12.1	-13.6	-50.4	-31.0

Given fact that the etch gas flow rate was 1/3 lower in the center point of this matrix than in the center point of the first set of experiments, it is not necessarily surprising that the CF_4, C_2F_6, SiF_4 and CF_3I emissions were approximately 1/3 lower (see Table 5.18). A more significant change in the effluent profile for this process versus that of the earlier one, however, was the marked reduction in CHF_3 (~53%), which accounted for 63.7% of the global warming emissions in the case of the first matrix center point and 57.5% in the case of the CCD matrix center point. Similarly, HF emissions were also reduced by approximately 50%, indicating that the elimination of CH_3F from the feed gas chemistry had a significant impact on the emission of hydrogen containing species. Whereas, in the first set of experiments, the hydrogen required for the formation of HF and CHF_3 was supplied by both the etch chemistry itself and by the interaction of fluorine and CF_x species with the resist, in the latter set of experiments, this first pathway was eliminated. Given the fact that, in all iodoheptafluoropropane processes examined in this study, CHF_3 was the largest contributor to the CE value, reducing the amount of hydrogen available for its formation had a very significant effect on the global warming impact of the process.

It is also interesting to note that the species whose aggregate quantity emitted changed the most between the two processes was C_2F_4. Among the differences in process conditions between the two runs are the following: somewhat higher source power in the earlier run, lower roof temperature in the earlier run, and 50% higher etch gas flow in the earlier run. As will be seen in the trend discussion below, C_2F_4 output appears to be largely insensitive to source power, tends to increase with increasing roof temperature, and tends

to increase very strongly with increasing etch gas flow rate. Even though the emissions of all fluorocarbon species were found to increase pronouncedly with etch gas flow rate, the increase in C_2F_4 is most dramatic, with C_2F_4 output found to triple with a ~50% increase in etch gas flow. The same effect is seen here, with C_2F_4 emissions being roughly 3 times higher for the 24 sccm process versus the 16 sccm process (see again Table 5.18). This very pronounced effect appears to dominate over any countervailing trend (see discussion below) that may also be present due to the increase in roof temperature in the 16 sccm process versus the 24 sccm process. As will be discussed in greater detail below, the formation of C_2F_4, in contrast to the formation of other fluorocarbon species detected, is believed to be more heavily influenced by gas phase mechanisms than is the formation of other fluorocarbon species.

The C_3F_8 quantity also appeared to be reduced by an amount larger than the 1/3 expected from the ratio of the gas flows between the two runs. However, because the detected quantities of C_3F_8 were much lower than those of the other fluorocarbon species and approaching the detection limit of the instrument, few conclusions can be drawn from these data. Similarly, in the discussion below, while C_3F_8 emissions are plotted in Figures 5.68 through 5.70, the concentrations of this compound were so close to the detection limit that few conclusions can be drawn regarding trends with respect to any of the process variables discussed.

Figures 5.68 through 5.70 plot aggregate global warming emissions and emissions of individual species on a molar basis as a function of the three process parameters explored in the third experimental series: source power, etch gas flow, and roof temperature. Only the axial points are plotted. Source power does not appear to have a pronounced impact on the overall CE metric. A breakdown of the emissions shows that almost all the fluorocarbon species exhibit essentially flat responses with respect to this parameter. This is perhaps not necessarily surprising, given the fact that 1-iodoheptafluoropropane is utilized almost completely at all process conditions. Whereas supplying additional source power in PFC based processes tends to result in greater utilization of the gas, it appears that, in the case of 1-iodoheptafluoropropane, source power does not

significantly affect the composition of the fluorocarbon portion of the emissions. While this is true overall, C_2F_6 does show a modest upward trend, as does CHF_3. See Figure 5.68. The latter is readily accounted for by the fact that more resist erosion is known to occur with higher source power (see Section 5.4.1), supplying more hydrogen for the formation of CHF_3. This trend is also seen in the HF data shown in Figure 5.68. It is not unusual for HF and CHF_3 trends to track each other in fluorocarbon etch processes because both are dependent on a supply of hydrogen for their formation. As Figure 5.68 also shows, COF_2 is also seen to increase with source power as does SiF_4, with the exception of the low source power point. The increase in the emissions of these two species is readily explained by the fact that the Si/quartz process kit is known to be etched more aggressively at higher source power (see again Section 5.4.1) Except for the open area on the wafer, which is small relative to the surface area of the process kit, the process kit is essentially the only source of silicon and oxygen in the system. Hence an increase in Si and O containing species can generally be taken as an unambiguous indication of greater interaction with the chamber hardware. The reversal of this trend at 1450 W for SiF_4, which has been confirmed by manual inspection of the FTIR spectra that were acquired, has not yet been accounted for.

Increasing etch gas flow has a predictable and unambiguous effect on most quantities involved. See Figure 5.69. Aggregate CE values tend to increase with higher etch gas flow, which stems from the increase in quantities of all fluorocarbon species (C_3F_8, once again, excluded). What is significant about the data plotted in Figure 5.69, however, is the rate at which C_2F_4 emissions increase with etch gas flow relative to the emissions of other fluorocarbon species. As had been pointed out above, a ~50% increase in 1-iodoheptafluoropropane flow rate causes the amount of C_2F_4 produced to increase threefold from approximately 8×10^{-5} moles to approximately 24×10^{-5} moles.

The only exception, other than C_3F_8, to the monotonic increase with respect to etch gas flow rate is seen for CHF_3, which exhibits a flat trend from 16 to 19 sccm. This phenomenon is very likely due to the fact that one of the first order effects of increasing etch gas flow, particularly in higher flow regimes, is an increase in polymer formation on

the wafer surface (see Section 5.4.1). This results in lower resist erosion, which would be consistent with the leveling off seen in the CHF_3 trend. The HF trend confirms this hypothesis, with HF being the only major effluent observed to decrease with increasing flow rate. This decrease is attributed to lower resist erosion arising from more polymer formation on the resist surface with higher etch gas flow. The quantities of SiF_4 and COF_2 emitted, on the other hand, are seen to increase with higher 1-iodoheptafluoropropane flow rate, indicating that the etching of process kit surfaces must be a supply limited process.

Finally, roof temperature, like source power, is observed not to have a significant effect on overall CE. See Figure 5.70. In this case, however, the fluorocarbon trends are mixed. Moles of CF_4, CF_3I, and, especially, C_2F_4 are observed to rise with higher roof temperature, whereas CHF_3 production exhibits the opposite trend. No trend is discerned in the C_2F_6 data. As is discussed in Section 5.4.1, increasing roof temperature is generally known to result in lower resist erosion by lowering the rates at which polymeric film forms on the heated chamber surfaces and thus causing more polymer precursors to be available for condensing on the wafer, which is approximately 200 °C cooler than the process kit. The increases in CF_4 and CF_3I at higher roof temperature are thus explainable in terms of CF_3 groups that are now desorbed from the roof surface as volatile products. Similarly, the increase in C_2F_4 production is likely to be caused by an increase in the desorption of CF_2 groups from the heated roof surface as volatile C_2F_4.

The decrease in CHF_3, on the other hand, relates principally to surface phenomena taking place on the wafer. With more polymer deposition on the wafer surface at higher roof temperatures, the resist erosion rate becomes slower and less CHF_3 is produced. The HF trend again confirms this, showing a pronounced decrease in HF emissions as roof temperature is increased. With less polymer deposition on the roof surface, the roof slab receives less protection from attack by fluorine, resulting in an increase in SiF_4 emissions. The COF_2 trend, however, does not track the SiF_4 trend in this case, remaining essentially flat, even decreasing at higher roof temperature. This, however, is not inconsistent with the mechanisms being discussed here, because the roof slab is made

entire of silicon, not quartz. In the preceding discussion, the process kit, which contains both quartz and Si surfaces, was treated collectively. In the present case, however, a distinction is made between the roof slab itself, which is composed entirely of silicon, and the remaining parts of the process kit, which are composed primarily of quartz, with only a small area of Si (a silicon ring surrounding the perimeter of the chuck) being exposed to the plasma: While all parts of the process kit are at a higher temperature than the chuck, with the wall temperature set at 200 °C and other parts of the process kit only passively heated by the plasma and by proximity to actively heated surfaces, the roof slab is the hottest surface in the system. Thus, at the 260 °C condition, with the roof 60 °C or more hotter than the quartz parts of the process kit, it is not surprising that the COF_2 emissions are actually lower, since less polymer formation on the roof implies more polymer formation on all cooler surfaces.

Table 5.19: Breakdown of global warming emissions by moles of individual species (x 10^{-5}), percent contribution to CE (adjusted for GWP), and thickness of photoresist eroded (center of wafer) for the fourth set of experiments.

Run	Etch Gas	Substrate / resist type	Moles emitted (x 10^{-5})				% Contribution to CE				Resist eroded (A)
			C_2F_6	C_3F_8	CF_4	CHF_3	C_2F_6	C_3F_8	CF_4	CHF_3	
A	1I	Bare Si	0.3	0.7	1.5	0.8	15.7%	35.9%	22.8%	25.6%	
B	1I	APEX	2.2	1.7	9.7	13.3	14.1%	10.9%	19.6%	55.4%	3757
C	1I	K2G	2.2	1.0	9.9	13.8	14.0%	6.5%	20.5%	59.0%	4201
D	2I	APEX	2.4	0.0	9.5	10.5	19.5%	0.4%	24.4%	55.7%	4324
E	2I	K2G	1.8	0.3	9.1	9.5	15.8%	2.9%	25.7%	55.6%	4215
F	C_3F_8+CH_3F	Bare Si	6.4	35.3	40.4	15.3	9.7%	55.3%	19.6%	15.4%	
G	C_3F_8+CH_3F	APEX	4.9	34.7	36.4	15.6	7.9%	57.1%	18.6%	16.5%	112
H	C_3F_8+CH_3F	K2G	3.8	35.3	35.2	11.5	6.5%	61.7%	19.0%	12.8%	25

4th Set of Experiments. Table 5.16 lists the CE values and utilization efficiencies for the runs that comprised the fourth and final set of experiments. Once again, utilization efficiency values were consistent with those obtained in earlier datasets: on the order of 95% for 1-iodoheptafluoropropane (and its isomer) and on the order of 80% for C_3F_8. The CE reduction for the two 1-iodoheptafluoropropane runs with resist substrates is on the order of 80% relative to the reference process (Run F from the second set of experiments). The two 2-iodoheptafluoropropane runs exhibit somewhat higher

reductions (on the order of 84%). As Tables 5.19 and 5.20 indicate, however, the emissions breakdown for the two isomers is quite similar.

Table 5.20: Breakdown of process emissions by moles of individual species (x 10^{-5}) for the fourth set of experiments (non-global warming species).

Run	Etch Gas	Substrate / resist type	1I / 2I	C_2F_4	CF_3I	CO	CO_2	COF_2	HF	SiF_4
A	1I	Bare Si	5.5	5.1	4.7	10.4	1.5	0.9	1.1	100.1
B	1I	APEX	5.0	8.5	14.6	92.9	3.4	7.5	127.0	35.3
C	1I	K2G	5.5	9.4	15.9	98.5	2.6	8.3	130.0	35.2
D	2I	APEX	4.1	6.7	15.8	98.1	2.6	12.7	136.2	36.6
E	2I	K2G	5.0	8.3	15.6	95.8	2.3	9.5	140.4	35.7
F	C_3F_8+CH_3F	Bare Si		48.6		212.3	3.1	19.0	168.8	101.1
G	C_3F_8+CH_3F	APEX		55.1		217.0	3.4	18.2	222.1	93.8
H	C_3F_8+CH_3F	K2G		59.4		232.7	3.7	16.7	230.0	97.6

A comparison between the APEX and K2G wafers for all three gases indicated that essentially similar CE values are obtained with the two resists for a given process chemistry. Nevertheless, in these experiments, the CE values for the APEX wafers were consistently lower than those for their K2G counterparts, whereas in the second set of experiments, the reverse was true (see Table 5.15). The differences between APEX and K2G wafers, however, were significantly smaller than the discrepancy between the C_3F_8/CH_3F runs in this experimental set and the same processes with the same substrates in the second experimental set (compare Table 5.15 and Table 5.16). The standard deviation of the CE values obtained for the four C_3F_8/CH_3F runs with resist wafers was 41.5 grams or 12.8%. The most likely explanation for this discrepancy is difference in chamber condition (*i.e.*, amount of polymer residue in the chamber), both from one set of runs to the other as well as within a given set of runs. Even though an O_2/Ar preprocess (typically of 120 s duration) was run between all wafers for all experiments that were carried out, the present data suggest that this clean may have been insufficient to restore the chamber to the same condition for every run. What this implies is that even subtle differences in chamber condition can have a significant effect on the quantities of global warming fluorocarbon species that are emitted by the process.

The fact that the differences between APEX and K2G resist wafers were in all cases smaller than the overall 12.8% error assigned to the C_3F_8/CH_3F reference process suggests that these differences are unlikely to be statistically significant and that, for global warming impact calculations, the two types of deep UV resist are essentially the same. More interesting conclusions, however, may be drawn from the comparison of the resist wafers to the bare Si wafers. In the case of the C_3F_8 process, where FTIR analysis reveals that the largest portion of the global warming emissions is attributed to unreacted C_3F_8 itself, the change in substrate material does not significantly impact the global warming emissions. On the other hand, in the case of 1-iodoheptafluoropropane, the source gas, which itself has negligible global warming potential, is almost completely reacted. Here, removing the resist all but eliminates the production of fluorocarbon by-products in quantities comparable to those generated in its presence.

The fluorinated by-product whose emissions appear to be least affected by the change of substrate is C_2F_4. A possible explanation for this may be that C_2F_4 may be partially the product of gas phase processes, whereas other fluorocarbon species are more likely to be formed largely through surface reactions. This is reasonable to suggest given the fact that, in both C_3F_8 and iodoheptafluoropropane plasmas, CF_3I, CF_4, CHF_3, and C_2F_6 cannot be formed through mere scission of bonds in the parent three carbon molecule. Rather, their formation can only proceed through the recombination of a CF_x fragment with F, H, or another CF_x species:

$$CF_n + X \rightarrow CF_nX, \qquad (5.9)$$

$$\text{and/or } CF_nX + F \rightarrow CF_{n+1}X, \qquad (5.10)$$

where $X = F, H, I$, or CF_m.

The above reactions are not intended to be all inclusive, but merely to suggest plausible reaction pathways. In the pressure regime of interest, where the mean free path is on the order of centimeters, it is likely that these reactions would proceed much more efficiently in the presence of a third body, such as a surface, than in the gas phase. On the other hand, while C_2F_4 can be formed through the surface phase dimerization of CF_2 radicals:

$$CF_2 + CF_2 \rightarrow C_2F_4, \qquad (5.11)$$

it is also possible for it to be formed in the gas phase only through electron impact collisions, *e.g.*:

$$CF_2I\text{-}CF_2\text{-}CF_3 + e \rightarrow I + CF_2\text{-}CF_2\text{-}CF_3 + e, \quad (5.12a)$$

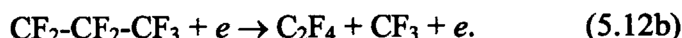

$$CF_2\text{-}CF_2\text{-}CF_3 + e \rightarrow C_2F_4 + CF_3 + e. \quad (5.12b)$$

The fact that the production of fluorocarbon by-products (with the exception of C_2F_4) appears to be a surface dominated process suggests that the global warming impact of the process can, to an extent, be influenced by control over reactions on the wafer surface. A comparison between the 1-iodoheptafluoropropane / no CH_3F process in the second dataset (Run B) and the 1-iodoheptafluoropropane / no CH_3F process in the fourth dataset (Run C), for instance, shows that, despite considerable similarities in the process recipes (see Tables 5.15 and 5.16), the latter process (at 12 mTorr) had significantly lower global warming impact than the former (at 6 mTorr): 66.1 grams of CE vs. 130.4 grams of CE. The principal difference between the two processes was the amount of CHF_3 produced: 13.8×10^{-5} moles for Run C in the fourth dataset versus 29.2×10^{-5} moles for Run B in the second dataset (see Tables 5.17 and 5.19). Since, other than residual deposits on chamber surfaces, the only source of hydrogen in these 1-iodoheptafluoropropane processes is the photoresist itself, the reduction in CHF_3 formation must have been the direct consequence of lower resist erosion rates. Indeed, process data for the two wafers confirms this, with measured thicknesses of K2G resist eroded being higher for the 6 mTorr run than for the 12 mTorr run. As had been discussed in Section 5.4.1, higher pressure generally favors higher rates of polymer formation on the wafer surface, which tends to protect the photoresist from being etched. Polymer formed on wafer surfaces is normally removed using an oxygen-based post-etch treatment (PET), essentially an *in-situ* ash. FTIR data shows that the principal carbon sinks in this process step are CO, CO_2, and COF_2, whereas COF_2, HF, and, to a lesser extent, SiF_4 are the main fluorine bearing species. In such oxygen rich plasma environments, fluorocarbon formation is negligible. Hence, from a global warming emissions standpoint, formation of polymer in the chamber and on the wafer, to be removed later by an oxygen based step, may be desirable.

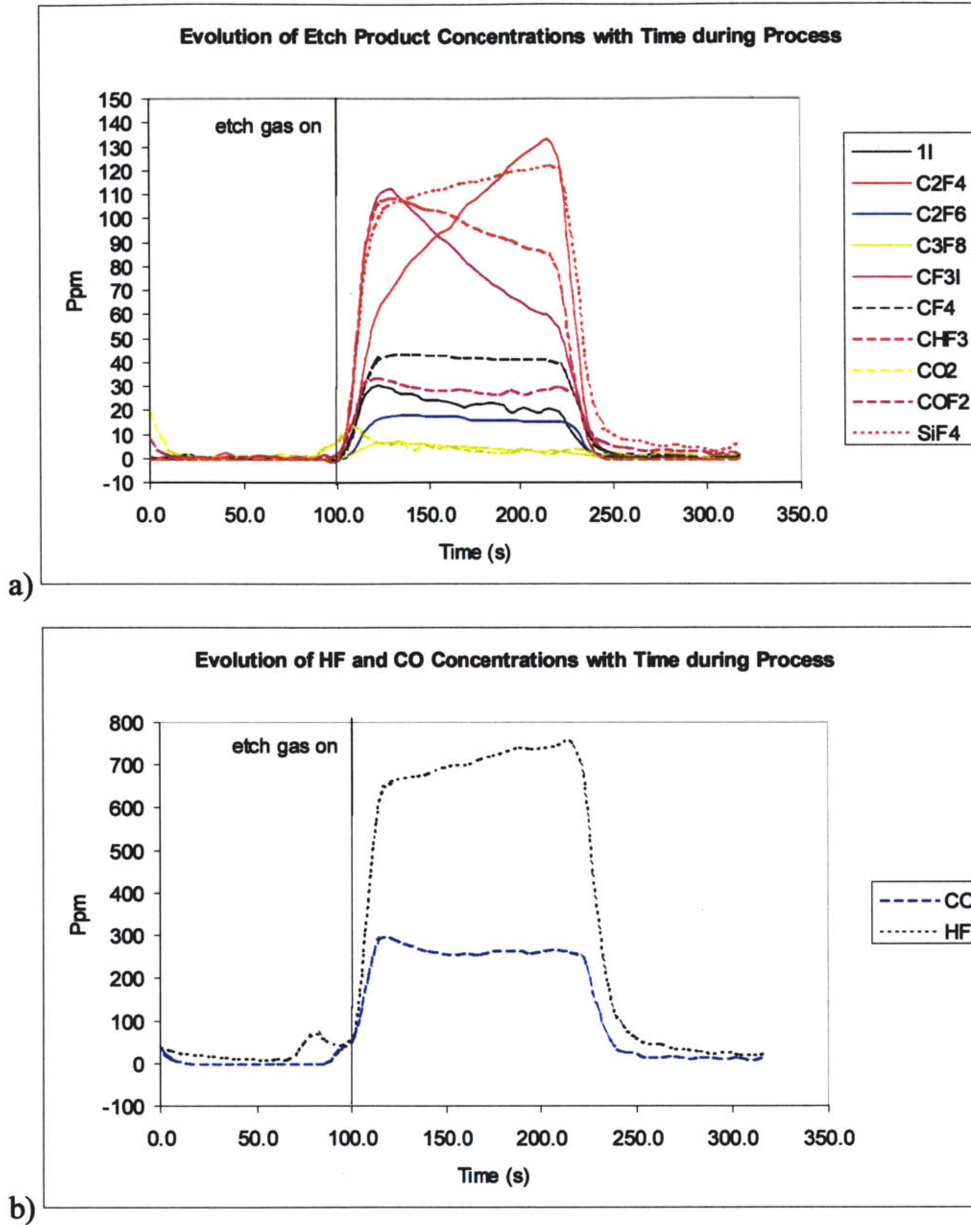

Figure 5.71: Concentrations of plasma by-products in effluent stream as measured by FTIR (center point of first experimental series).

It is worth noting that, in the case of the C_3F_8/CH_3F reference process, not only are the aggregate CE values similar for Si and resist covered wafers, but the emissions of individual species are similar as well. The only noticeable difference between the Si case and the APEX/K2G cases lies in the emissions of HF, which are 168.8×10^{-5} moles for bare Si and 222.1×10^{-5} (230.0×10^{-5}) for APEX (K2G). Otherwise, the amounts of the individual gases emitted are very close. The fact that, in contrast to what is seen with 1-

iodoheptafluoropropane, the change in substrate does not significantly impact emissions in the case of C_3F_8/CH_3F is understood in terms of the relative propensities of the processes under consideration to polymerize on Si and resist. In Section 5.4.2, data were presented that indicated that 1) 1-iodoheptafluoropropane processes tend to leave smaller amounts of polymer deposit on the wafer surface than does the C_3F_8/CH_3F reference process (due to the iodine bombardment effect) and 2) while the C_3F_8/CH_3F reference process did not produce a net buildup of polymer on resist surfaces, its interaction with the resist was much less aggressive than that seen in the case of 1-iodoheptafluoropropane. Hence, in effect, the author posits that the steady state surfaces of both Si and resist wafers present similar fluoropolymer layers to the plasma during their exposure to the C_3F_8/CH_3F reference process. Some etching of resist does occur, accounting for the difference in HF emissions, but the similarity between the wafer surfaces in the two cases is much greater than is the case for the 1-iodoheptafluoropropane process under consideration, which interacts more aggressively with the resist layer.

Table 5.20 reveals several other noteworthy differences between the C_3F_8/CH_3F reference process and the iodoheptafluoropropane processes. The CO, COF_2, and SiF_4 emissions are significantly higher in the case of the C_3F_8 process. This suggests that the reference process may be etching the process kit more aggressively than the iodoheptafluoropropane recipes. This conclusion is consistent with x-ray photoelectron spectroscopy (XPS) data presented in Section 5.4.2, which showed that significantly higher amounts of Si and O are incorporated into the top layers of films formed on the wafer by the C_3F_8/CH_3F reference process than by 1-iodoheptafluoropropane processes. It had also been established in Sections 5.4.1 and 5.4.2 that, on surfaces not exposed to ion bombardment, *e.g.*, feature sidewalls and corners, 1-iodoheptafluoropropane polymerizes *more* heavily than the C_3F_8/CH_3F reference process. It was postulated that the reversal in behavior stems from the role of iodine ions in the iodoheptafluoropropane plasma. Since the wafer is biased, the augmentation of the physical sputtering effect due to the presence of the iodine ion is a dominant aspect of the interaction of the plasma with the wafer surface. On unbiased surfaces, on the other hand, the role of the physical

component is greatly reduced and polymer formation becomes more dependent on F:C ratios of the incoming fluxes. Hence the C_3F_8/CH_3F reference process polymerizes more heavily on the wafer but less heavily on process kit surfaces, in comparison to iodoheptafluoropropane processes.

Finally, FTIR data also indicated that the concentrations of several species changed significantly over the course of the etch. An example of this is seen in Figure 5.71, which shows the concentrations of the various species detected by FTIR as a function of time during the etch for the center point of the first set of experiments (1800 W source power, 600 W bias power, 24 sccm etch gas flow, 4 sccm CH_3F flow, 75 sccm He flow, 15 Torr backside He pressure, 210 °C roof temperature, 200 °C wall temperature, 34 °C chiller temperature, and 6 mTorr chamber pressure). It should be pointed out that, while the etch process itself had a duration of 120 s, the window during which these signals persist in the FTIR cell is somewhat longer, due to the effect of a finite residence time for the process effluent in the roughing pump. One can see that C_2F_4 and HF concentrations exhibit a noticeable increase as the etch progresses, while CHF_3 and CF_3I concentrations have the opposite trend. The trends seen in Figure 5.71 were typical of most runs, including, in the case of C_2F_4, HF, and CHF_3, the PFC based references. In fact, the only case in which these trends were absent entirely had been the 1-iodoheptafluoropropane run with a bare Si substrate (Run A in the fourth experimental series), suggesting that the trends seen in Figure 5.71 are driven principally by the interaction of the plasma with the resist, rather than interaction with process kit surfaces or gas phase mechanisms. The present data are insufficient to fully account for the shift that is observed. In future studies on these or other fluorocarbon compounds, however, it may be possible to gain further insight into the details of the by-product formation mechanisms using time-resolved plasma and surface analysis techniques.

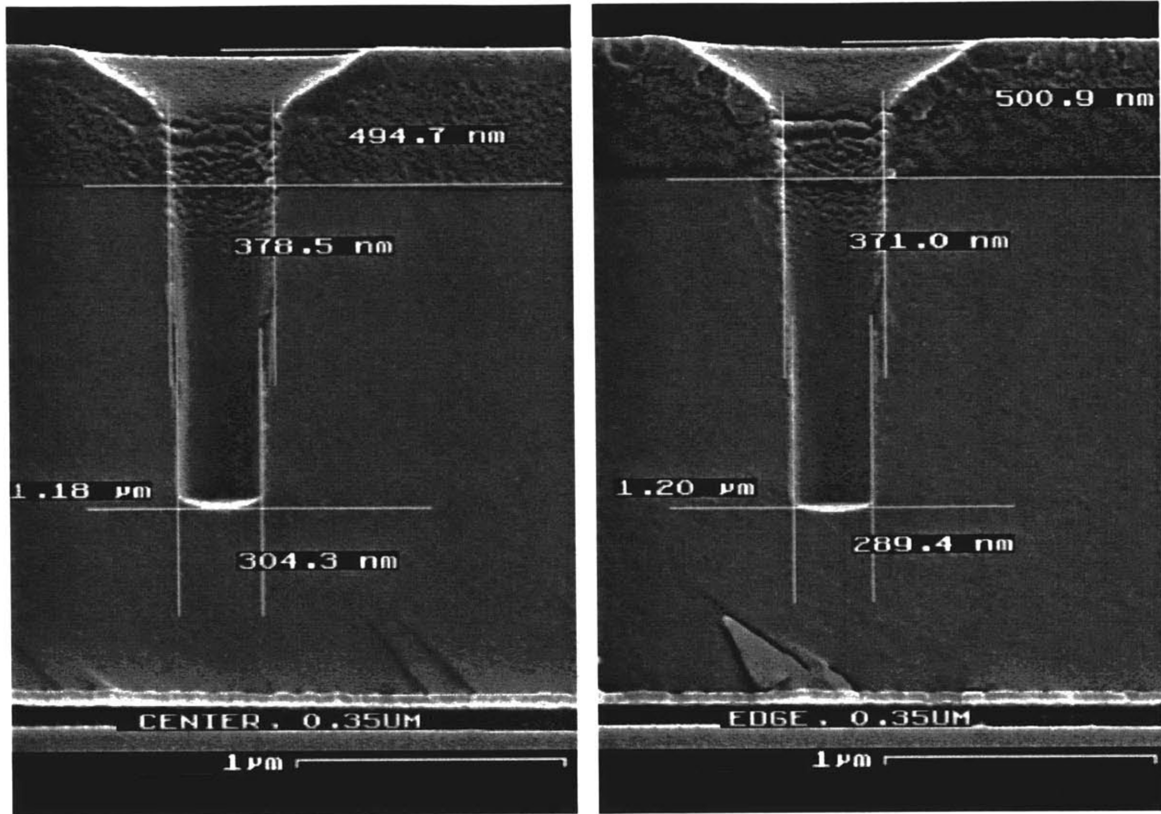

Figure 5.72: Best 1-iodoheptafluoropropane process and emissions point from third set of experminets: 1675 W *SP*, 800 W *BP*, 14.5 sccm *EF*, 0 sccm *CF*, 245 °C *RT*, 9 mTorr *PR*, 0.35 μm nominal printed CD.

Process Data. The 1-iodoheptafluoropropane runs with the best overall emissions results (>79% reduction) were also among the those that yielded the best process results in this study. The best process results obtained in the third set of experiments, for instance, corresponded to the point which yielded the largest % reduction versus C_3F_8 in that set of experiments. Figure 5.72 shows a cross-sectional scanning electron micrograph (SEM) of 0.35 μm via holes etched at 1675 W source power, 800 W bias power, 14.5 sccm etch gas flow, 0 sccm CH_3F flow, 75 sccm He flow, 15 Torr backside He pressure, 245 °C roof temperature, 200 °C wall temperature, 34 °C chiller temperature, and 9 mTorr chamber pressure. The oxide etch rate in the center of the wafer was 5900 Å/min, with 4950 Å of APEX resist eroded (out of a nominal starting thickness of slightly less than 1 μm), which corresponded to a selectivity value of 2.38:1. The sidewall slope obtained was 88.2°. The corresponding values at the edge of the wafer were: 6000 Å/min oxide

etch rate, 4770 Å of resist eroded, giving a selectivity of 2.52, and a sidewall slope of 88.1°. The average carbon equivalent (CE) value was 66.8 grams, corresponding to an emissions reduction of 79.5% against the C_3F_8/CH_3F reference process. The breakdown of the CE value by individual component was as follows: 55.3% CHF_3, 19.7% C_2F_6, 18.9% CF_4, and 6.0% C_3F_8. On a molar basis, the fluorocarbon species found to be present were (in order of abundance): CF_3I (15.5 x 10^{-5} moles), C_2F_4 (14.2 x 10^{-5}), CHF_3 (13.1 x 10^{-5} moles), CF_4 (9.2 x 10^{-5}), 1-iodoheptafluoropropane (5.1 x 10^{-5}), C_2F_6 (3.1 x 10^{-5}), and C_3F_8 (0.9 x 10^{-5}). The most abundant species were again HF (159.1 x 10^{-5}) and CO (93.6 x 10^{-5}) and SiF_4 (32.4 x 10^{-5}), with COF_2 (10.1 x 10^{-5}), and CO_2 (2.7 x 10^{-5}) also being detected. The utilization efficiency of 1-iodoheptafluoropropane in these experiments was calculated to be 97.1%.

The 1-iodoheptafluoropropane process which was chosen for the fourth series of experiments in this study (Runs B-C in the fourth series, which also yielded reductions in excess of 79%) had earlier been characterized in terms of process performance (see Section 5.4.1) and determined to be the overall best process in terms of resist selectivity and sidewall slope. Those results are shown in Figure 5.47 and Table 5.9 in Section 5.4.1.

5.4.3.3 Conclusions

1- and 2-iodoheptafluoropropane have been evaluated as etchants in an oxide via etch application. The process effluent from processes run with these two compounds has been characterized using Fourier transform infrared spectroscopy. The salient findings were: 1) introducing hydrogen containing species such as CH_3F has a pronounced negative impact on global warming emissions because it promotes the formation of CHF_3; 2) without the use of hydrogen containing additives, 1- and 2-iodoheptafluoropropane etch processes have demonstrated reductions in overall global warming emissions up to ~80% and ~85%, respectively, versus a C_3F_8/CH_3F reference process; 3) C_2F_6 and C_3F_8 based reference processes had comparable global warming impact as well as very similar utilization efficiencies; 4) the choice of photoresist did not have an impact on process emissions; however, the substitution of a bare Si substrate for a resist covered wafer led

to the near elimination of fluorocarbon emissions with a 1-iodoheptafluoropropane process, but not a C_3F_8 process, where most of the global warming effluent is unreacted source gas and which has different polymer forming behavior on the wafer surface than does iodoheptafluoropropane (due to the bombardment of the wafer surface by iodine ions in the latter case); 5) the comparison between bare Si and resist wafers exposed to the same 1-iodoheptafluoropropane process suggests that the bulk of the fluorocarbon by-products generated by the process may be formed by surface, rather than gas phase, processes; 6) on the wafer surface, iodoheptafluoropropane interacts more aggressively with the resist than does the C_3F_8/CH_3F reference process used in this study (again due to the iodine bombardment effect on biased surfaces); it is found to interact less aggressively with process kit surfaces, however, which is likely due to its lower F:C ratio and hence its tendency to polymerize more heavily on unbiased surfaces.

It has been demonstrated that iodoheptafluoropropane can be used in dielectric etch processes where it can provide a significant reduction in global warming emissions relative to PFC based processes. Sections 5.4.1 and 5.4.2 explore the process performance and surface phenomena that affect process performance in greater detail. Those sections discuss the limitations of iodoheptafluoropropane from a process standpoint. Its poor selectivity to mask and stop layers presents a challenge for the successful implementation of this material in actual etch applications, despite the significant global warming reductions than can be attained through its use.

References

1. O. Joubert, P. Czuprynski, F. H. Bell, P. Berruyer, and R. Blanc, *Analyses of the chemical topography of silicon dioxide contact holes etched in a high density plasma source*, J. Vac. Sci. Technol. B, **15**(3), p. 629-639 (1997).
2. P. Czuprynski and O. Joubert, *X-ray photoelectron spectroscopy analyses of silicon dioxide contact holes etched in a magnetically enhanced reactive ion etching reactor*, J. Vac. Sci. Technol. B, **16**(3), p. 1051-1058 (1998).
3. S. K. Baldwin, R. Patrick, and N. Williams, *RF Peak Voltage Control at the Bias Electrode of Inductively Coupled Plasma Etchers for Improved Process Stability*, in Proceedings of *Plasma Etching Processes for Sub-Quarter Micron Devices*, Honolulu, HI, G. S. Mathad, Editor, Electrochemical Society Meeting Abstracts, **PV 99-30**, p. 55-63, Electrochemical Society, Pennington, NJ (1999).

4. H.-J. Lee, J. K. Kim, J. H. Kim, K.-W. Whang, J. H. Kim, and J. H. Joo, *Selective SiO_2/Si_3N_4 etching in magnetized inductively coupled C_4F_8 plasma*, J. Vac. Sci. Technol. B, **16**(2), p. 500-506 (1998).
5. D. C. Marra and E. S. Aydil, *Effect of H_2 addition on surface reactions during CF_4/H_2 plasma etching of silicon and silicon dioxide films*, J. Vac. Sci. Technol. A, **15**(5), p. 2508-2517 (1997).
6. C. B. Labelle and K. K. Gleason, *Pulsed plasma-enhanced chemical vapor deposition from CH_2F_2, $C_2H_2F_4$, and $CHClF_2$*, J. Vac. Sci. Technol. A, **17**(2), p. 445-452 (1999).
7. S. Den, T. Kuno, M. Ito, M. Hori, T. Goto, P. O'Keeffe, Y. Hayashi, and Y. Sakamoto, *Influence on selective SiO_2/Si etching of carbon atoms produced by CH_4 addition to a C_4F_8 permanent magnet electron cyclotron resonance etching plasma*, J. Vac. Sci. Technol. A, **15**(6), p. 2880-2884 (1997).
8. T. E. F. M. Standaert, M. Schaepkens, N. R. Rueger, P. G. M. Sebel, and G. S. Oehrlein, *High density fluorocarbon etching of silicon in an inductively coupled plasma: Mechanism of etching through a thick steady state fluorocarbon layer*, J. Vac. Sci. Technol. A, **16**(1), p. 239 (1998).
9. M. Schaepkens, R. C. M. Bosch, T. E. F. M. Standaert, G. S. Oehrlein, and J. M. Cook, *Influence of reactor wall conditions on etch processes in inductively coupled fluorocarbon plasmas*, J. Vac. Sci. Technol. A, **16**(4), p. 2099-2107 (1998).
10. N. R. Rueger, M. F. Doemling, M. Schaepkens, J. J. Beulens, T. E. F. M. Standaert, and G. S. Oehrlein, *Selective etching of SiO_2 over polycrystalline silicon using CHF_3 in an inductively coupled plasma reactor*, J. Vac. Sci. Technol. A, **17**(5), p. 2492-2502 (1999).
11. N. R. Rueger, J. J. Beulens, M. Schaepkens, M. F. Doemling, J. M. Mirza, T. E. F. M. Standaert, and G. S. Oehrlein, *Role of steady state fluorocarbon films in the etching of silicon dioxide using CHF_3 in an inductively coupled plasma reactor*, J. Vac. Sci. Technol. A, **15**(4), p. 1881 (1997).
12. National Institute of Standards and Technology, http://physics.nist.gov/PhysRefData/IonEnergy/tblNew.html (2000).
13. V. Tarnovsky and K. Becker, J. Chem. Phys., **98**, p. 7868 (1993).
14. S. G. Lias, J. E. Bartmess, J. F. Liebman, J. L. Holmes, R. D. Levine, and W. G. Mallard, J. Phys. Chem. Ref. Data, **17**(Suppl 1) (1988).
15. G. Nanse, E. Papirer, P. Siux, F. Mogeuet, and A. Tressaud, Carbon, **35**, p. 175 (1997).
16. S. J. Limb, K. K. Gleason, D. J. Edell, and E. F. Gleason, *Flexible fluorocarbon wire coatings by pulsed plasma enhanced chemical vapor deposition*, J. Vac. Sci. Technol. A, **15**(4), p. 1814-1818 (1997).
17. I. Banerjee, M. Harker, L. Wong, P. A. Coon, and K. K. Gleason, *Characterization of Chemical Vapor Deposited Amorphous Fluorocarbons for Low Dielectric Constant Interlayer Dielectrics*, J. Electrochem. Soc., **146**(6), p. 2219-2224 (1999).

18. T. Hara, M. Sato, and K. Sakiyama, *Fluorocarbon Polymer Deposited by Inductively Coupled Plasma Oxide Etching*, J. Electrochem Soc., **145**(4), p. L67-L70 (1998).
19. *Scientific Assessment of Ozone Depletion: 1998, Volume 2,* World Meteorological Organization, Global Ozone Research and Monitoring Project, Report No. 44 (1998).

6. Wafer Patterning Studies: Unsaturated Fluorocarbons and Other Compounds

Whereas the focus of Chapter 5 was the hydrofluorocarbon and iodofluorocarbon families of compounds, Chapter 6 will discuss studies carried out with other chemistries. The same testbed as in Chapter 5 (oxide via etch process in the Applied Materials Centura 5300 HDP etch tool) was employed in these studies, along with the same principal characterization methodologies: cross-sectional SEM for process evaluation and Fourier transform infrared (FTIR) spectroscopy for effluent analysis.

The present chapter is organized as follows: Section 6.1 will provide a discussion of a study carried out with oxalyl fluoride. Section 6.2 will cover the most recent – and, arguably, most successful – activity carried out as part of the author's thesis research, the unsaturated fluorocarbon concept-and-feasibility study. This study was focused on the initial evaluation of a number of unsaturated fluorocarbon compounds – C_3F_6, three isomers of C_4F_6, c-C_5F_8, and a linear isomer of C_4F_8 (octafluoro-2-butene); it also included the characterization of several additional perfluorinated compounds as additional comparison points (n-C_4F_{10}, c-C_4F_8), along with the evaluation of c-C_4F_8O (octafluorotetrahydrofuran).

Whereas the oxalyl fluoride study provided the author and his coworkers with valuable insights into some of the mechanisms that affect the re-formation of high global warming byproducts, it was not expected to yield a viable candidate chemistry for further evaluation for dielectric etch applications. The UFC study, on the other hand, proved to be the largest step forward so far in the attempt to combine viable process performance with significant global warming emissions reductions. The results presented in Section 6.2 are only preliminary – the detailed characterization studies that had been conducted for some of the HFC and IFC chemistries (see sections 5.3 and 5.4) have yet to be carried out as of this writing. Nevertheless, the existing data are sufficiently encouraging, in the author's view, to warrant the belief that unsaturated fluorocarbons in general and, as the

data will show, C_4F_6 in particular hold considerable promise as new etchants that can satisfy performance demands while proving a long-term environmental benefit.

In Sections 6.1, all carbon equivalent calculations are carried out using 1995 GWP_{100} values taken from Ref. [1]. In Section 6.2, all carbon equivalent calculations are carried out using 1998 GWP_{100} values taken from Ref. [2].

6.1 Oxalyl Fluoride Concept-and-Feasibility Study

The goal of the work presented in this section was to provide a preliminary screening for a novel fluorinated compound, oxalyl fluoride, $C_2O_2F_2$, (F-(C=O)-(C=O)-F) as a potential replacement for perfluorocompounds in dielectric etch applications. Both process and emissions data were collected and the results were compared to those provided by a process utilizing a standard perfluorinated etch chemistry (C_2F_6). In this evaluation, oxalyl fluoride was found to produce very low quantities of global warming compounds, under the conditions in which it was tested, as compared to the C_2F_6 process. A preliminary evaluation of the compound's process performance was also carried out. Patterned TEOS (tetraethoxysilane)-deposited silicon oxide masked with deep UV photoresist having 0.6, 0.45, and 0.35 μm via hole features was used as the test vehicle. Although $C_2O_2F_2$ was found to be capable of etching silicon dioxide, low oxide etch rate and poor selectivity to the mask layer were observed.

The molecules that had been evaluated in previous chapters have all been modified fluorocarbons. In a number of cases, they have been found to provide significant emissions reductions relative to PFC based processes. However, the HFC and IFC molecules examined still possess CF_x moieties that are recognized as precursors in the plasma formation of species such as CF_4, CHF_3, and C_2F_6. The primary motivation for the evaluation of oxalyl fluoride as an etchant is the absence of CF_x groups in its molecular structure, which was expected to minimize the formation of CF_x-based plasma by-products. Moreover, oxalyl fluoride itself is hygroscopic and its atmospheric stability

is therefore expected to be low. The global warming impact of unutilized oxalyl fluoride in process emissions is predicted to be negligible.

The discussion of this study is organized as follows: Section 6.1.1 discusses the experimental setup used. Section 6.1.2 provides a discussion of the experimental data. Finally Section 6.1.3 offers conclusions regarding this study. The material in Section 6.1 is based on work submitted for publication by the author and his coworkers in Ref. [3].

6.1.1 Experimental Setup

Two sets of experiments were carried out using oxalyl fluoride as a source gas for a dielectric etch process in the Centura 5300 HDP inductively coupled, high density plasma etch tool. The first was a screening experiment which used patterned oxide wafers: TEOS (tetraethoxysilane)-deposited silicon oxide masked with a deep UV photoresist (~7650 Å thick, on average). The test features used were via arrays of 0.6, 0.45, and 0.35 μm nominal printed critical dimension (CD). The second set of experiments involved a 2-variable, 3-level factorial matrix in which blanket deep UV photoresist (~9900 Å thick, on average) wafers were etched with oxalyl fluoride to obtain process effluent data. The open area on the patterned wafers used in the screening experiments was approximately 0.5%; in addition, the resist films used in both sets of experiments were compositionally very similar (K2G resist in the former case, APEX resist in the latter). Hence, from an emissions standpoint, the patterned and blanket photoresist substrates were for all practical purposes indistinguishable. Cross-sectional scanning electron microscopy (SEM) was used to characterize the features etched in the first experiment. Fourier transform infrared (FTIR) spectroscopy was used to quantify tool exhaust emissions in the second experiment. A standard C_2F_6 via etch recipe was used as a reference for both process and emissions data. The process tool and the emissions diagnostics used for this work have been described in detail in earlier sections (Section 3.4.2 and 5.3.1).

The initial experimental parameters for both sets of oxalyl fluoride experiments were based on the reference C_2F_6 recipe, with an equivalent flow of oxalyl fluoride substituted

for C_2F_6. In the blanket resist experiments, this recipe formed the center point of the factorial matrix. The conditions for this experimental point were as follows: 1600 W source power, 1400 W bias power, 25 sccm etch gas (C_2F_6 or oxalyl fluoride), 100 sccm He, throttle valve at 50%, 240 °C roof temperature, 220 °C wall temperature, -10 °C chiller temperature, and 15 Torr backside He pressure.* In the patterned wafer experiments, two hydrofluorocarbon additives (fluoromethane, CH_3F, and trifluoromethane, CHF_3) were also added in varying ratios to the oxalyl fluoride/He chemistry with the intent of enhancing polymerization. In these experiments, three parameters were varied: total etch gas flow rate, amount of additive gas as fraction of total etch gas flow rate, and identity of the additive gas. With total etch gas flow rate held constant at 25 sccm, CH_3F was added in fractions of 0, 10%, and 20% of the total etch gas flow. A similar procedure was carried out with CHF_3. Finally, using CH_3F as the additive and the CH_3F fraction of the total etch gas flow held constant at 10%, the total etch gas flow rate was varied. Total flows of 22, 25, and 28 sccm were run.

In the blanket resist experiments used to obtain emissions data, no hydrofluorocarbon additive was used. Source power (1400, 1600, 1800 W) and etch gas flow rate (21, 25, 29 sccm) were varied, with all other parameters held constant at the same values as those in the reference C_2F_6 recipe. All processes used in both experimental stages had an etch time of 120 s. All runs were preceded by a standard Ar/O_2 preprocess which is intended to restore the chamber condition for the run to follow. The process conditions used for the two sets of experiments are listed in Tables 6.1 and 6.2.

* The 50% throttle valve setting corresponded to pressures of 7-8 mTorr for these and all other oxalyl fluoride processes. "Source power" refers to the power applied to the source antenna in the chamber, whereas "bias power" refers to the power applied independently to the electrostatic chuck. "Roof temperature" refers to the temperature of the silicon slab which forms the top portion of the etch chamber.

Table 6.1: Process conditions used in first stage of experiments (patterned wafers). Bias power 1400 W, throttle valve setting 50%, roof temp. 240 °C, wall temp. 220 °C, chiller temp. –10 °C, He flow 100 sccm, backside He pressure 15 Torr, etch time 120 s.

Exp. Point #	Point type	Etch Gas	Source Power (W)	Total Flow (sccm)	% CH_3F <CHF_3>	Oxalyl Fluoride <C_2F_6> Flow (sccm)	CH_3F <CHF_3> Flow (sccm)
1	25 sccm total, 0% additive	Oxalyl Fluoride	1600	25	0	25	0
2	25 sccm total, 10% CH_3F	Oxalyl Fluoride+CH_3F	1600	25	10	22.5	2.5
3	25 sccm total, 20% CH_3F	Oxalyl Fluoride+CH_3F	1600	25	20	20	5
4	25 sccm total, 10% CHF_3	Oxalyl Fluoride+CHF_3	1600	25	<10>	22.5	<2.5>
5	25 sccm total, 20% CHF_3	Oxalyl Fluoride+CHF_3	1600	25	<20>	20	<5>
6	22 sccm total, 10% CH_3F	Oxalyl Fluoride+CH_3F	1600	22	10	19.8	2.2
7	28 sccm total, 10% CH_3F	Oxalyl Fluoride+CH_3F	1600	28	10	25.2	2.8
*	C_2F_6 ref	C_2F_6	1600	25	0	<25>	0

Table 6.2: Process conditions used in second stage of experiments (blanket photoresist wafers). Bias power 1400 W, throttle valve setting 50%, roof temp. 240 °C, wall temp. 220 °C, chiller temp. –10 °C, He flow 100 sccm, backside He pressure 15 Torr, etch time 120 s.

Exp. Point #	Point type	Source Power (W)	Oxalyl Fluoride Flow (sccm)
1	-1, -1	1400 W	21
2	-1, 0	1400 W	25
3	-1, +1	1400 W	29
4	0, -1	1600 W	21
5	0, 0	1600 W	25
6	0, +1	1600 W	29
7	+1, -1	1800 W	21
8	+1, 0	1800 W	25
9	+1, +1	1800 W	29

The emissions data were collected using an FTIR optical bench equipped with a heated 10 cm stainless steel absorption cell with zinc selenide windows. The sampling setup and calibration procedures have been described in detail in Section 5.3.1. The compounds identified in the effluent and quantified in this study were CF_4, C_2F_6, CO, CO_2, COF_2, CHF_3, HF, SiF_4, as well as $C_2O_2F_2$. The global warming impact of each process was characterized by calculating the mass of carbon equivalent emitted by the process, using the kgCE (kilograms of carbon equivalent) metric, which had been defined earlier (Section 5.1.1). In the discussion that follows, the emissions have been expressed in grams, rather than kilograms of CE, for convenience. GWP_{100} values for the global warming gases identified in the effluent (CHF_3, CF_4, and C_2F_6) were obtained from Ref. [1]. No published value exists for $C_2O_2F_2$; for the purposes of the calculations in this study, it was not assigned a GWP value because, due to its hygroscopic properties, it is believed to decompose rapidly in the atmosphere. Figure 6.1 provides an FTIR spectrum of oxalyl fluoride. The oxalyl fluoride material used in this study was supplied by AlliedSignal, Inc, Buffalo, NY, and was assayed at a purity of 99.89%.

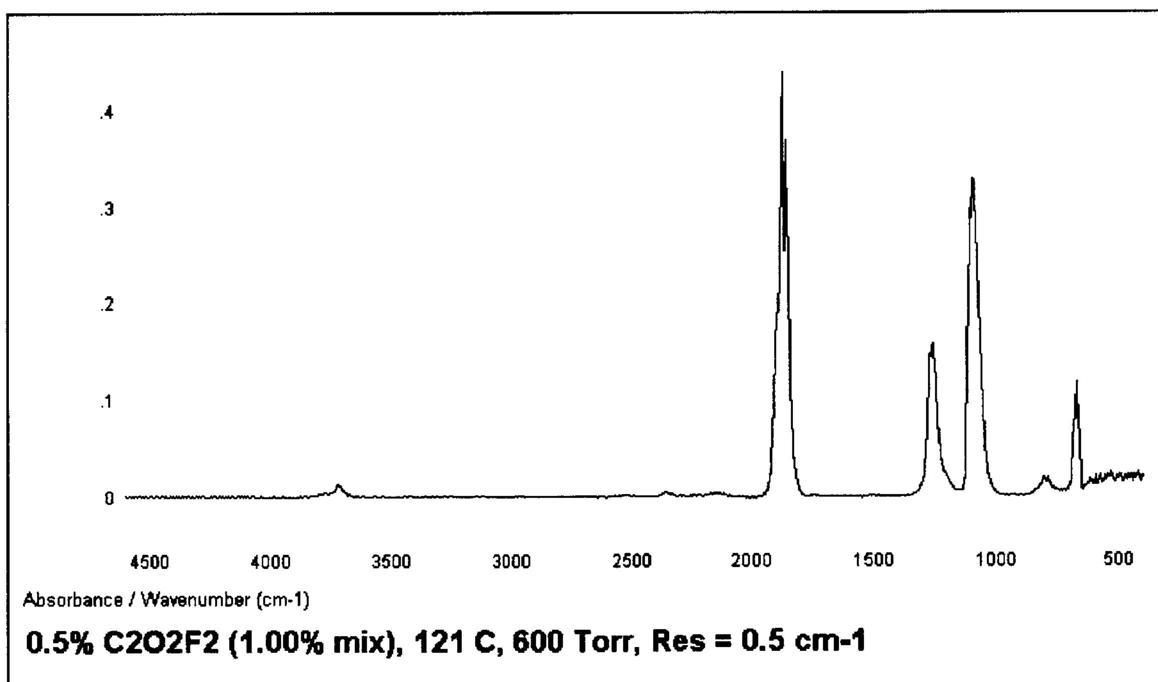

Figure 6.1. FTIR spectrum of oxalyl fluoride, $C_2O_2F_2$, collected at 5000 ppm using 10 cm cell (500 ppm-m nominal optical depth).

6.1.2 Results and Discussion

Patterned Wafer Experiments. During the 120 s etch time in all of the runs in the patterned wafer stage of experiments, all photoresist was removed from the surface of the patterned wafer, indicating a photoresist etch rate of at least 3825 Å/min, based on an average resist thickness of 7650 Å for the wafers used in this set of experiments. However, because in all cases the photoresist was completely removed before the end of the etch, this etch rate should be taken as a lower limit. Figure 6.2 shows 0.6 μm nominal printed CD via features typical of the results obtained. All data presented below were obtained from SEM measurements of the 0.6 μm features.

In the discussion that follows, the *feature depth* is the measured step height difference between the bottom of the feature and the oxide layer surface at the conclusion of the etch. This depth is an estimate of the amount of oxide etched until the photoresist was removed. However, because of the complete photoresist and partial bulk oxide erosion in these experiments, it is difficult to provide accurate etch rates and selectivities. An attempt was made to estimate the *total etch depth* (and hence an average etch rate over the 120 s etch) by adding the amount of bulk oxide eroded (as measured by the change in bulk oxide thickness) to the feature depth. This calculation was made under the following assumptions: 1) the etch rate of the oxide film within the feature was the same before and after the photoresist cleared (no loading effect, *i.e.,* the etch rate was unaffected by amount of oxide surface area exposed to plasma); 2) the etch rate of the oxide bulk was the same as the etch rate within the feature after the photoresist was removed (no lag effect for features versus open area). However, the trends in total etch depth calculated in this way did not correlate well with the trends in feature depth, suggesting that these assumptions may not hold. The following discussion of trends with respect to various process variables is therefore based solely on the measured feature depth. An estimate of photoresist selectivity was also made and is given by the ratio of the feature depth divided by the initial thickness of the photoresist layer, measured at center and edge locations for each wafer prior to the etch (0.765 μm, on average).

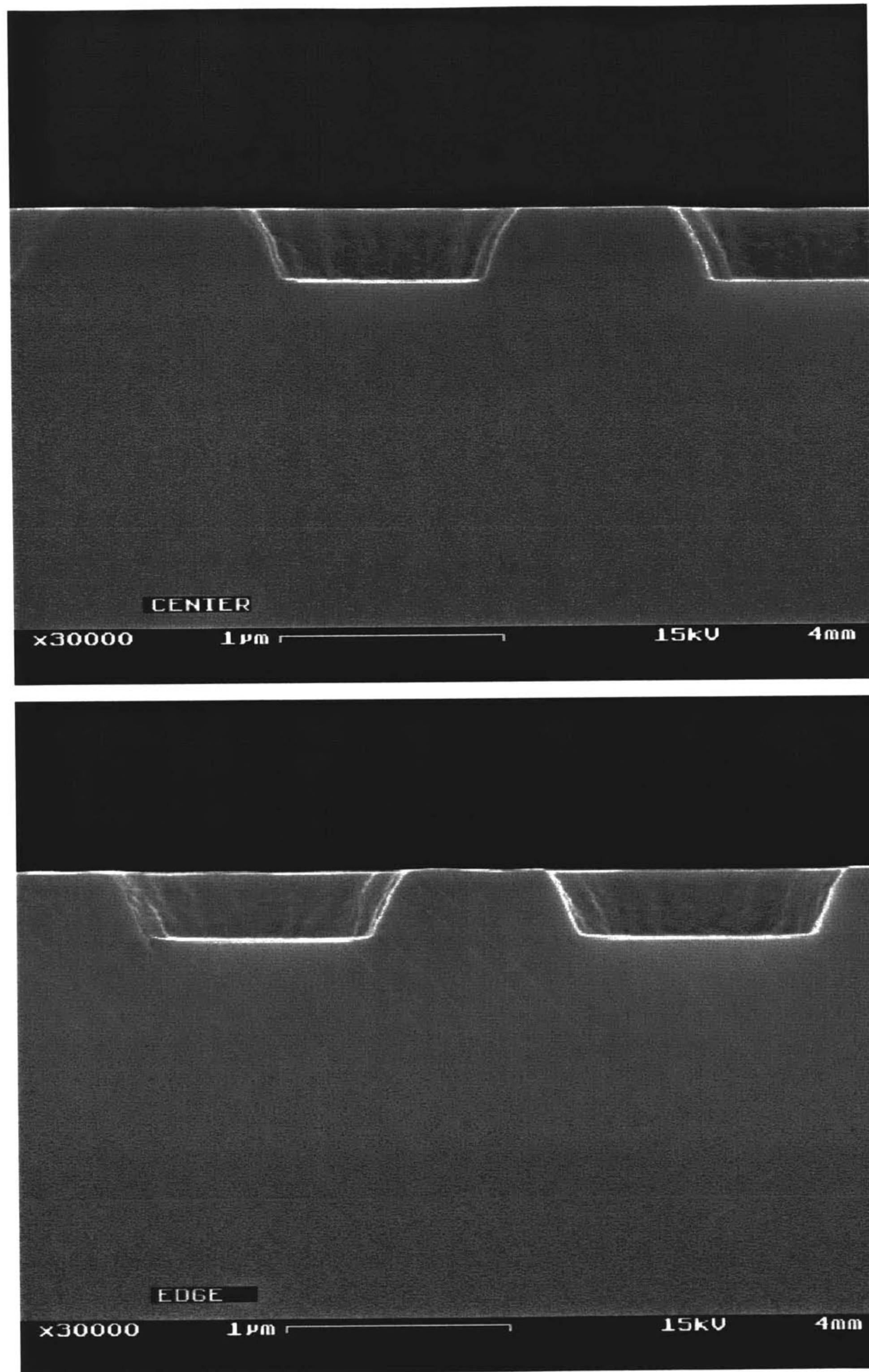

Figure 6.2: Patterned wafer experiments: experimental point 1, 0.6 µm nominal printed CD.

The estimated TEOS oxide etch rate (based on the feature depth measurement) ranged from 1520 Å/min to 2010 Å/min for the 0.6 μm nominal printed CD features in these experimental points. (Based on the total etch depth estimate, the corresponding range was 1870 Å/min to 2560 Å/min.) Both sets of numbers are averages of center and edge measurements on the wafer. The minimum measured oxide:photoresist selectivity ranged from 0.39:1 to 0.52:1. The shallow features etched by oxalyl fluoride exhibited considerable taper as well: sidewall slope ranged from 63 to 68 degrees (average of center and edge measurements). SEM measurements indicate that, in addition to significant bulk photoresist erosion, there was also considerable CD blowout at all experimental conditions. For all experimental points in Table 6.1, the measured top CD of the nominally 0.6 μm feature exceeded 1 μm after the 120 s etch.

By comparison, the minimum measured photoresist selectivity for the C_2F_6 process was 3.52:1 for the 0.6 μm features. Oxide etch rate, sidewall slope, and top CD were 8600 Å/min, 87 degrees, and 0.68 μm, respectively (average of center and edge measurements at 0.6 μm for all three metrics).

The introduction of a hydrofluorocarbon additive appears to have had a beneficial effect on photoresist selectivity. As Figures 6.3a and b indicate, adding CH_3F or CHF_3 appears to result in greater etched feature depth, which, in turn, translates to greater photoresist selectivity by the metric used above. As a first order effect, it would be expected that the addition of these carbon and hydrogen containing species would decrease the photoresist etch rate due to the tendency of these gases to polymerize, which is consistent with the effect seen in Figure 6.3b. It is also not necessarily surprising that increasing the fraction of CHF_3 in a fixed total flow of etch gas would increase the oxide etch rate, since CHF_3 contains more fluorine atoms than oxalyl fluoride itself. It is more interesting, however, that the addition of CH_3F, which bears only one fluorine atom versus two in oxalyl fluoride, appears to have a similar, though smaller, effect, as the relatively high amount of hydrogen would be expected to scavenge atomic fluorine.

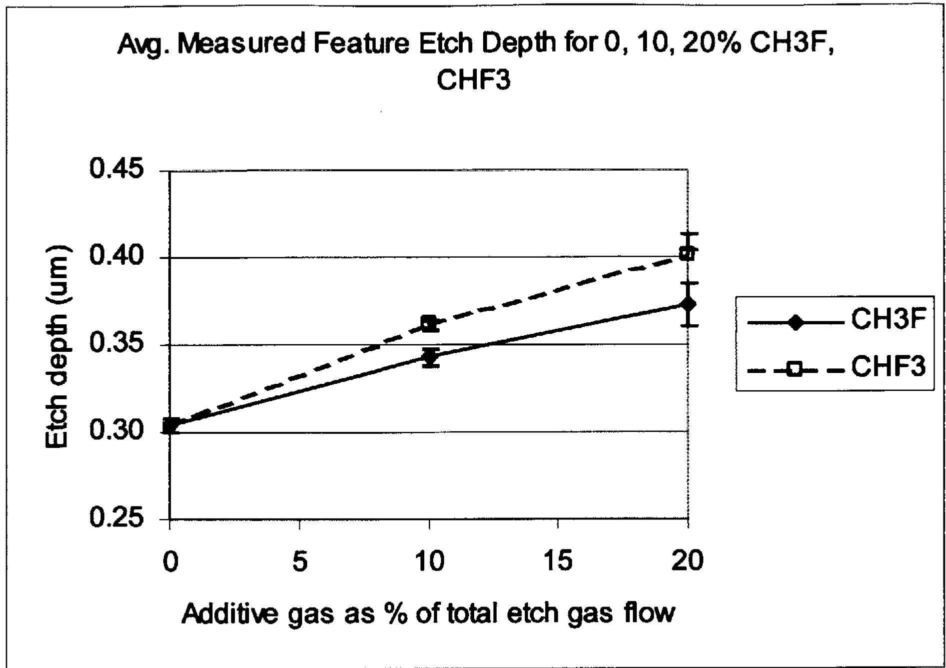

a)

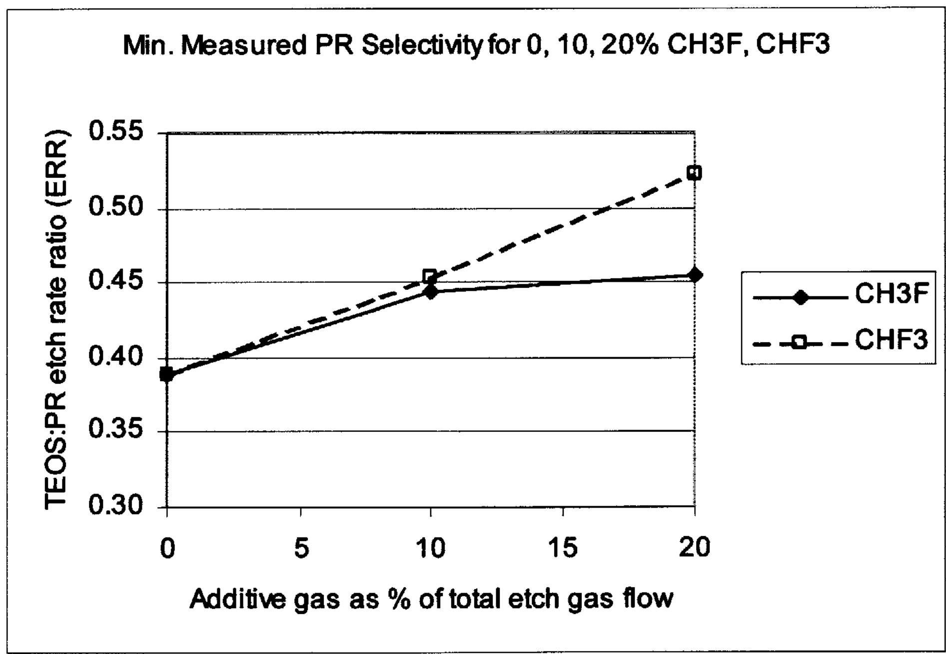

b)

Figure 6.3: Patterned wafer experiments: effect of CH_3F and CHF_3 addition, 0.6 μm nominal printed CD: a) feature depth, b) minimum photoresist selectivity. Etch rate values are averages of center and edge measurements.

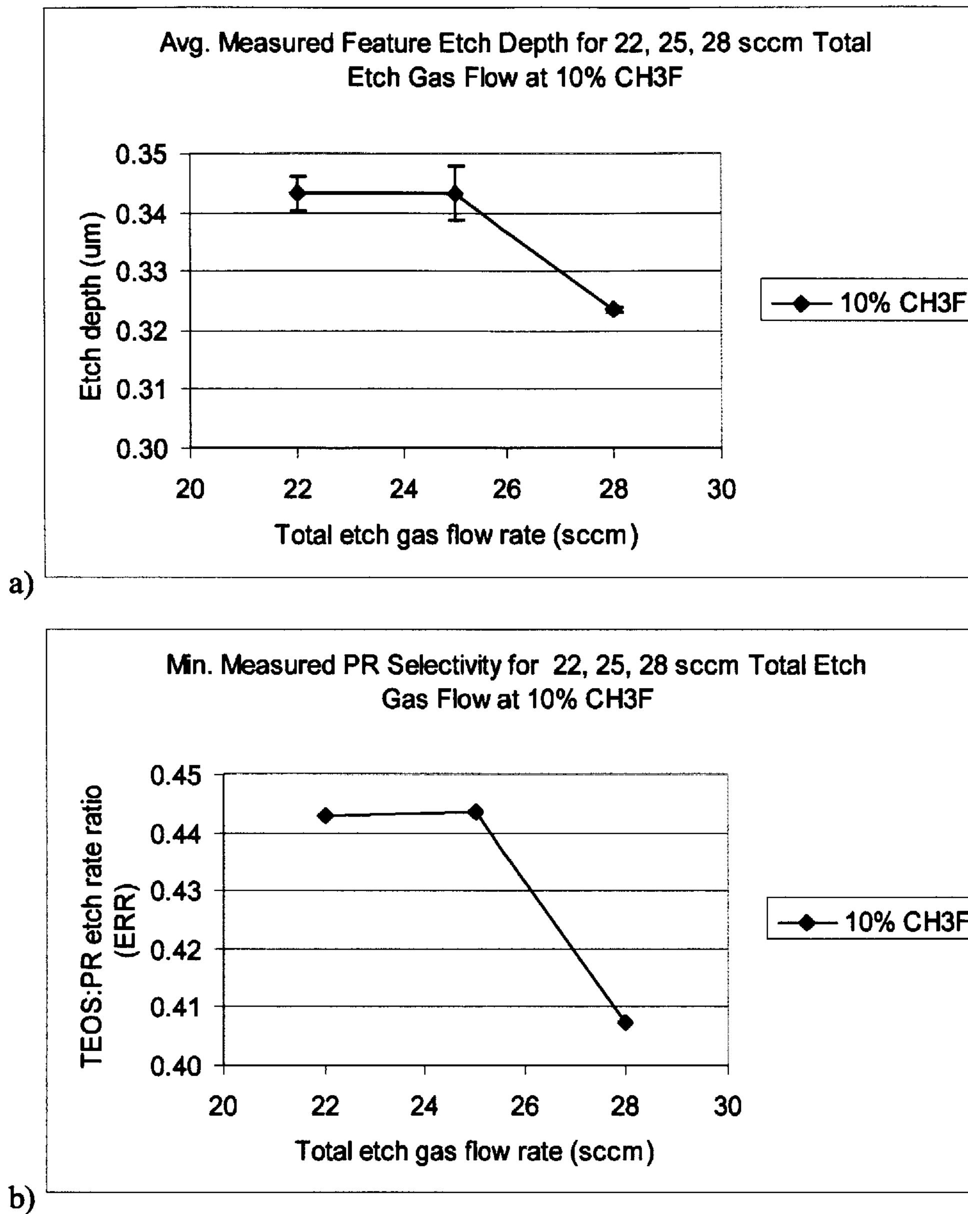

Figure 6.4: Patterned wafer experiments: effect of varying total etch gas flow, 0.6 μm nominal printed CD: a) feature depth, b) minimum photoresist selectivity. Etch rate values are averages of center and edge measurements.

With the CH_3F fraction held constant at 10% of the total etch gas flow, the measured feature depth does not appear to be affected by total etch gas flow rate up to 25 sccm; however, it does decrease markedly from 25 sccm to 28 sccm, which corresponds to a decrease in the photoresist selectivity metric used here (see Figures 6.4a and b). In the case of polymerizing fluorocarbon etchants, the appearance of this trend at higher flows is normally indicative of polymerization mechanisms proceeding at a faster rate than etch mechanisms. In the case of oxalyl fluoride, however, there is no evidence of net polymerization occurring on the wafer, as indicated by the SEMs in Figure 6.2. Moreover, the decrease in oxide etch rate at higher etch gas flow cannot be attributed to a reduction in residence time because at all conditions the overall flow is dominated by 100 sccm of He diluent.

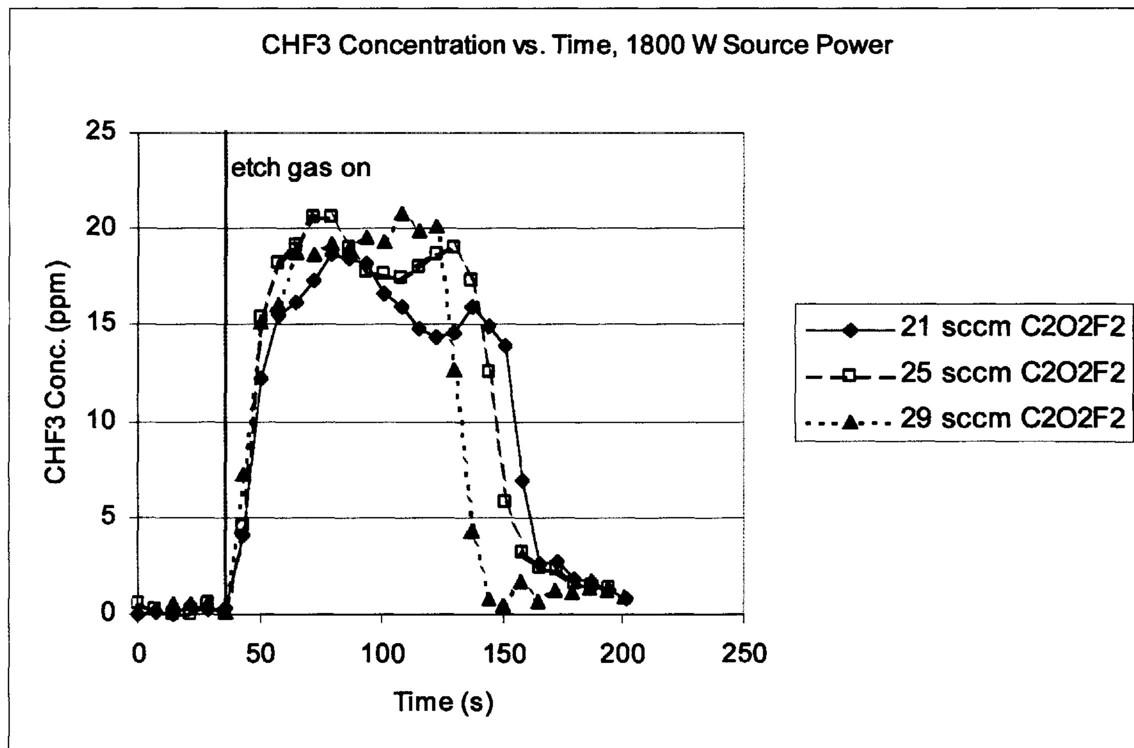

Figure 6.5. Blanket resist experiments - CHF_3 concentration in effluent stream as measured by FTIR (no fluorocarbon additive, 1800 W source power)

A conclusive explanation for this effect has not been established. However, if the measured feature depth is to be taken as an estimate of the thickness of oxide etched before the resist is completely removed, then the above results suggest that either the

instantaneous oxide etch rate during that period in the process was lower at the highest etch gas flow or that the resist was completely removed earlier. FTIR emissions data (to be discussed in greater detail in a later section) are consistent with the latter statement, although they do not necessarily exclude the former.

While no emissions data were taken during the first series of experiments, effluent measurements from the second series provide evidence that photoresist etch rate increases with higher $C_2O_2F_2$ flow. The data indicate that exposure of photoresist to the $C_2O_2F_2$/He plasma results in the formation of CHF_3. Figure 6.5 shows emissions data obtained for an experimental point in the blanket wafer stage of experiments: concentration of CHF_3 in the effluent versus time during etch at three different etch gas flows at 1800 W source power. As the plot indicates, the concentration of CHF_3 in the effluent stream decreases sharply before the end of the process at a point corresponding to the complete removal of the resist layer. This point occurs earlier in the process as the oxalyl fluoride flow rate is increased, suggesting that, with increased $C_2O_2F_2$ flow, the photoresist etch rate increases measurably, resulting in the accelerated removal of the resist.

The second stage experiments, in which the emissions data were collected, involved no addition of a hydrofluorocarbon additive. Since the source gas in these experiments consisted only of $C_2O_2F_2$ and He and since the photoresist is the only source of hydrogen, the only source of CHF_3 in this system can be the interaction of either fluorine or carbon-fluorine fragments with the photoresist. It can therefore readily be seen that the photoresist is removed earlier at higher oxalyl fluoride flow in these experiments. The same effect is believed to be present in the patterned wafer experiments. In the blanket resist experiments, this effect was seen most clearly at high source power, where resist etch rate is believed to be highest. For the 21, 25, and 29 sccm data points used in Figure 6.5, the approximate times at which the CHF_3 signal is seen to decrease below 25% of its peak value are 136, 129, and 108 s relative to the start of the etch, respectively. (Note that the reason for the persistence of the CHF_3 signal for a period longer than the 120 s etch time in some cases results from the fact that the FTIR sampling loop is located

downstream of the mechanical backing pump; hence there exists a delay period during which residual process effluent continues to be purged from the pump.)

It is also possible, however, that the instantaneous oxide etch rate may actually be enhanced in the presence of photoresist on the wafer and that it slows down once the resist is removed. CHF_3 is itself known to be an effective oxide etchant under non-polymerizing conditions. Under the proposed mechanism, at higher $C_2O_2F_2$ flow, the earlier removal of the resist could effect a reduction in the measured feature depth due to earlier termination of CHF_3 production, compared to lower $C_2O_2F_2$ flows.

It is impossible to establish conclusively whether the instantaneous oxide etch rate within the via features does actually decrease after the resist is completely removed. However, regardless of whether this actually occurs, it is clear that, if the resist is removed earlier, the feature depth remaining is likely to be smaller, since, after the resist is removed, both the bottom of the feature and the surface bulk against which the depth is referenced will now be etched. The relative etch rates of these surfaces may also be different, though that information, again, cannot be extracted out of the present set of data.

Table 6.3: Emissions data from second set of experiments.

Exp Point #	CE (grams)	CE normalized to C_2F_6	% CE reduction	Utilization efficiency (%)
1	17.586	0.061	93.91%	98.31%
2	19.656	0.068	93.20%	96.09%
3	22.116	0.077	92.35%	94.85%
4	15.003	0.052	94.81%	98.67%
5	15.629	0.054	94.59%	96.79%
6	21.014	0.073	92.73%	95.90%
7	15.037	0.052	94.80%	98.57%
8	17.256	0.060	94.03%	97.41%
9	17.997	0.062	93.77%	96.61%
C_2F_6 ref	288.98	1.000	-	78.30%

Blanket Resist Experiments. In contrast to its process behavior, in which both oxide etch rate and resist selectivity are poor, oxalyl fluoride does exhibit desirable properties from an emissions standpoint. Table 6.3 lists the emissions results from the nine experimental points that formed the factorial matrix carried out during the second stage of the study. This data was analyzed using a neural network software package [4] and the resulting response surfaces for overall global warming emissions and oxalyl fluoride utilization efficiency have been plotted in Figures 6.6 and 6.7, respectively. The emissions for the oxalyl fluoride processes evaluated ranged from approximately 15.0 to 22.1 grams of carbon equivalent (CE). The utilization efficiency (averaged over the duration of the etch process) for oxalyl fluoride in these experiments ranged from 94.9 to 98.7%. For comparison, the CE value measured for the C_2F_6 reference process was 289.0 grams; hence the values obtained for oxalyl fluoride represent emissions savings ranging from 92.3 to 94.8% relative to the reference process. The average utilization efficiency obtained for the C_2F_6 process was 78.3%.

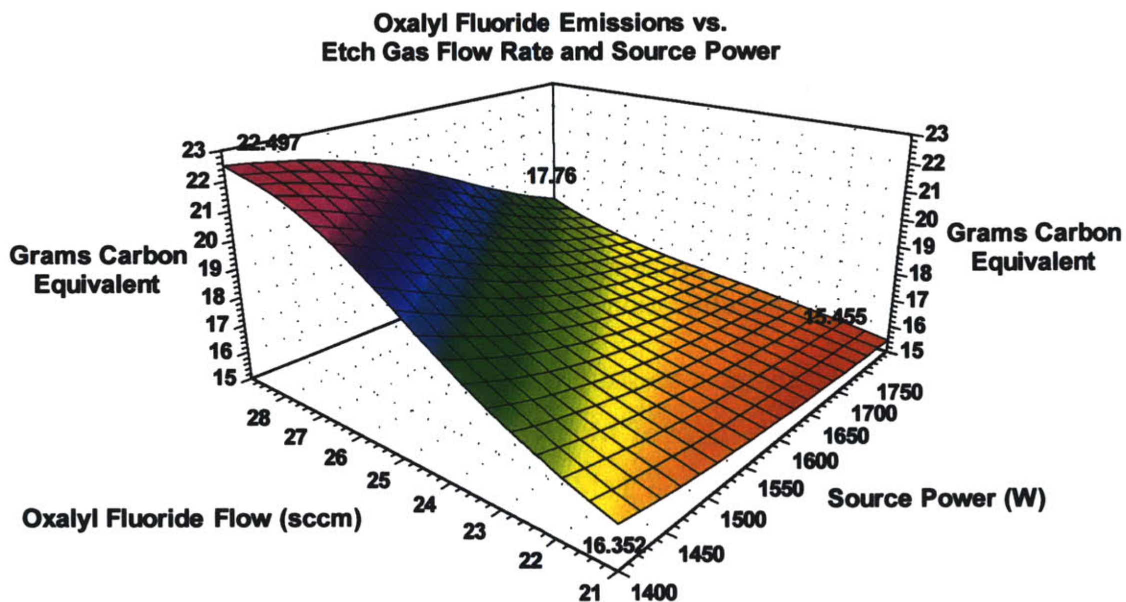

Figure 6.6: Blanket resist experiments - neural network model of oxalyl fluoride emissions data.

As Figures 6.6 and 6.7 indicate, the largest emissions savings as well as the highest utilization efficiencies were obtained at high source power and low gas flow settings. In

general, an increase in source power tends to decrease overall global warming emissions as well as increase oxalyl fluoride utilization efficiency, whereas an increase in oxalyl fluoride flow tends to increase emissions and decrease utilization efficiency. At low etch gas flow conditions (21 sccm oxalyl fluoride), however, almost complete utilization of oxalyl fluoride was observed; hence, in this regime, the utilization efficiency exhibited little sensitivity to changes in source power.

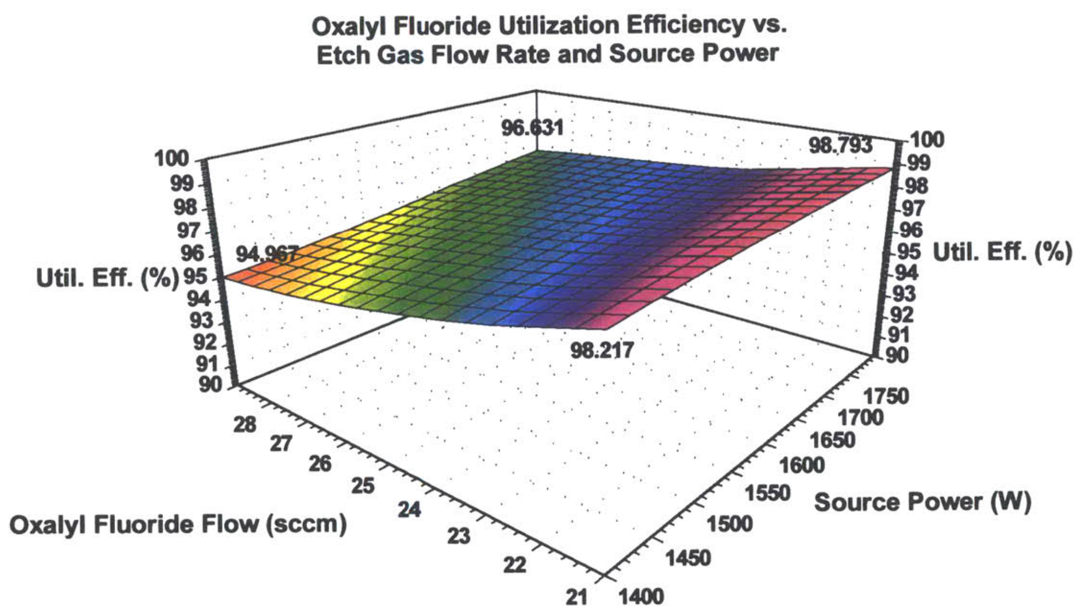

Figure 6.7: Blanket resist experiments - neural network model of oxalyl fluoride utilization efficiency data.

During these experiments, chamber pressure was also monitored (the throttle valve was fixed at 50%). Pressures in the range of 7-8 mTorr were recorded. In all runs, with the exception of experimental points 1 and 2 (1400 W source power at 21 and 25 sccm oxalyl fluoride flow, respectively), the photoresist was removed completely before the end of the 120 s etch. As the photoresist began to clear, a decrease in pressure from its steady state value of 7-8 mTorr was observed, which also correlated with a change in the composition of the effluent measured by FTIR, to be discussed below. In all runs in this set of experiments, the species present in the effluent in the highest concentrations were HF and CO, with measured concentrations ranging from approximately 500 ppm to approximately 1000 ppm; the nitrogen purge flow to the mechanical backing pump was

set by mass flow controller (MFC) at 45 slm. The concentrations of all other species measured by FTIR were generally below 100 ppm. Other gases observed in the effluent were CO_2, SiF_4[†], CHF_3, COF_2, and unreacted oxalyl fluoride; typical concentrations seen were in the 20 to 40 ppm range, with the exception of CO_2, which was in the 60 to 100 ppm range. Very low amounts of C_2F_6 were also detected (C_2F_6 concentrations were lower than the error associated with C_2F_6 in the FTIR software analysis method: 0.24 – 0.30 ppm). Low concentrations of CF_4 were recorded during the photoresist etch phase (typically 2 ppm or less, with the exception of experimental points 2, 3, and 6, where concentrations on the order of several ppm were briefly recorded).

As the photoresist was removed completely, the drop in chamber pressure correlated with a sharp decrease in the CHF_3 and HF concentrations and a smaller decrease in the CO concentration. This also corresponded to an increase in the concentrations of CF_4, SiF_4, COF_2, and, less noticeably, CO_2 and C_2F_6 as well. See Figure 6.8. For all experimental points, the largest fraction of the CE value (72.3 to 94.7%) was contributed by CHF_3, which is formed only when photoresist is still present. The CF_4 contribution ranged from 4.4% to 25.1%, whereas the calculated contribution due to C_2F_6 ranged from 0.7% to 2.6%. In all runs, these three compounds were calculated to account for 99.97% or more of the total CE value (with CO_2 making up the balance).

Generally, the CF_4 and C_2F_6 fractions of the CE value were found in increase with oxalyl fluoride flow at the expense of the CHF_3 contribution. This effect appeared to be most pronounced at higher source power, where the resist was observed to clear earliest. An analysis of effluent concentration versus time during etch indicates that, in most runs, the CHF_3 concentration drops off precipitously before the end of the etch process, which is an indication of the removal of all resist on the wafer surface. As this occurs, the CF_4 and, in some runs, C_2F_6 concentrations are observed to increase. Thus, higher oxalyl fluoride flow, which causes an increase in resist etch rate, results in earlier removal of

---

[†] The process chamber contains quartz and silicon surfaces that are exposed to the process plasma and these account for the SiF_4 emissions from etch processes in the chamber even when no silicon-based materials on the wafer are exposed to the plasma.

resist on the wafer; this, in turn results in an earlier dropoff in CHF_3 emissions, as the source of H for CHF_3 formation is removed. This causes an earlier transition to a regime where fluorocarbon emissions are dominated by CF_4 (with trace amounts of C_2F_6). See Figure 6.8. This mechanism is consistent with the decrease in the CHF_3 fraction of the CE value that is seen to take place with increasing etch gas flow. (The CE metric is integrated over the entire time of the process, so the CHF_3 fraction is reduced as the fraction of time CHF_3 is present is reduced.) This trend, which becomes more pronounced at higher source power, can be seen in Figure 6.9a for the 1400 W and 1800 W source power conditions. Analogous data for the 1600 W condition indicates a similar trend but is not shown for brevity.

On a molar basis, the amounts of all fluorinated by-products which were detected in the effluent and quantified (CHF_3, CF_4, C_2F_6, COF_2, HF, and SiF_4) generally appear to increase with higher oxalyl fluoride flow, as is expected. Figure 6.9b is a plot of the moles of fluorinated by-products emitted for 1400 W and 1800 W source power. The 1600 W condition, which exhibited the same general trends as those seen at 1400 W, is not shown for brevity. What is more interesting, however, is how the relative quantities of these compounds change as the process transitions between the resist covered surface and the exposed silicon surface. The change in relative fluorocarbon emissions has already been discussed. HF, COF_2, and SiF_4 concentrations are also affected by the transition. As Figure 6.8 indicates, SiF_4 production increases markedly once the resist is removed completely and more silicon area is exposed, which is seen to happen earlier as etch gas flow is increased. This increase in SiF_4 emissions is most easily seen at high etch gas flow and high source power, conditions under which the resist clears earliest.

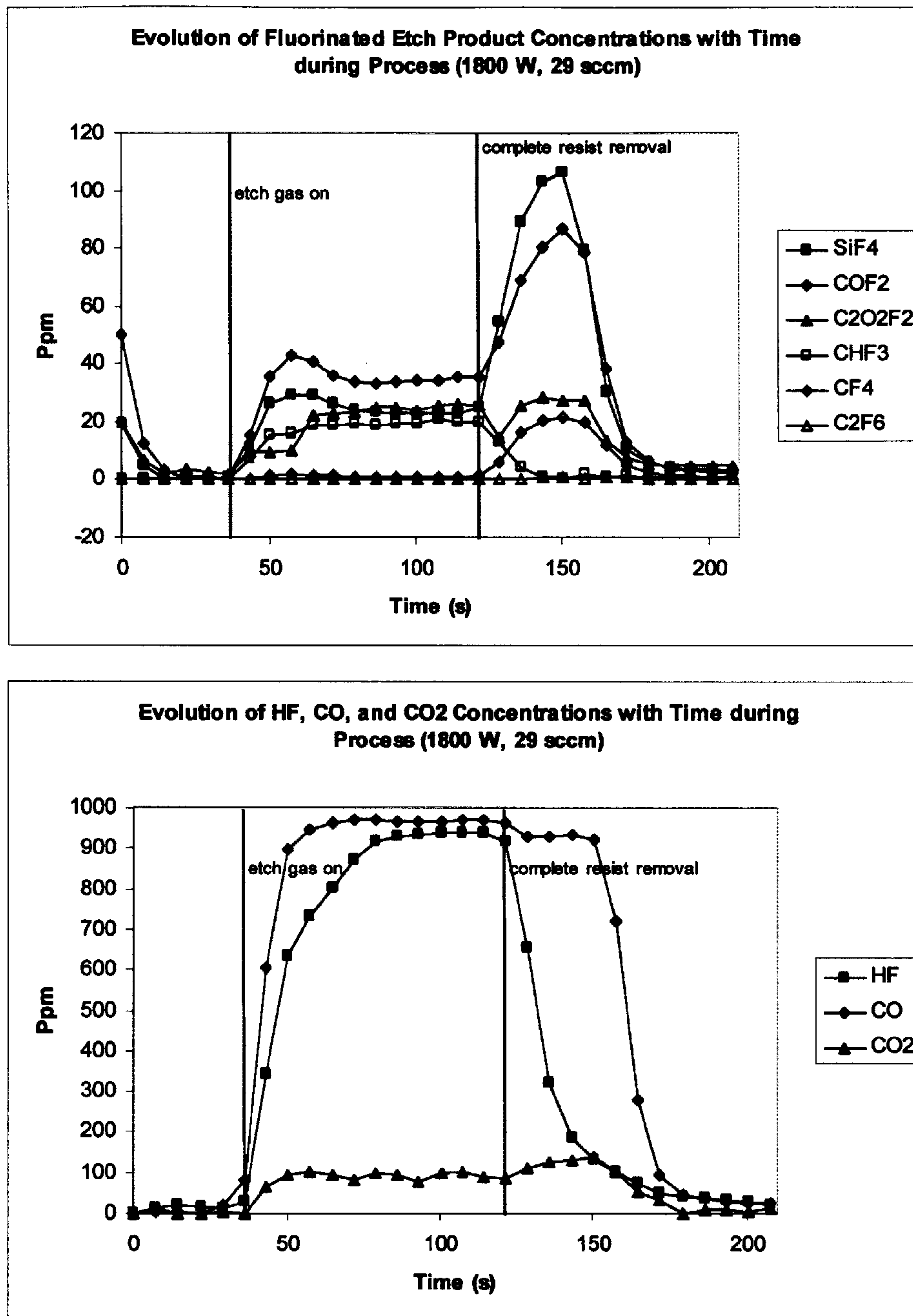

Figure 6.8: Blanket resist experiments – concentrations of plasma by-products in effluent stream as measured by FTIR (no fluorocarbon additive, 1800 W source power, 29 sccm oxalyl fluoride flow).

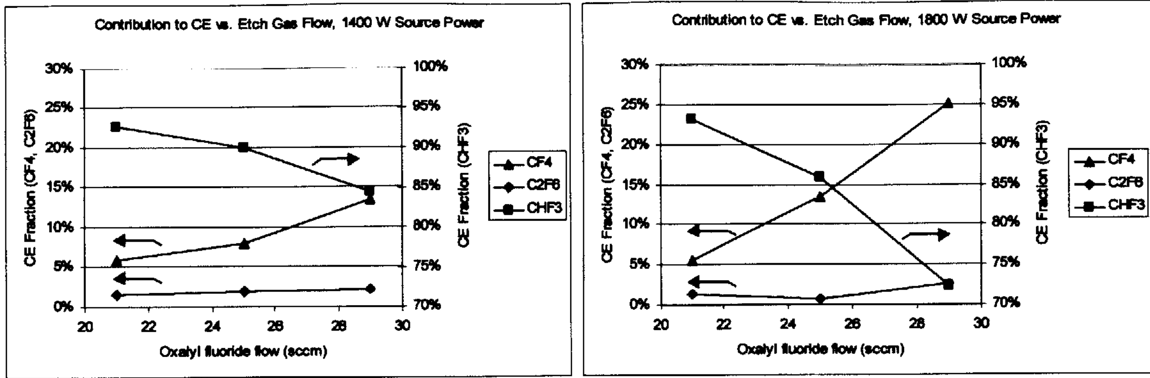

Figure 6.9a: Blanket resist experiments - relative carbon equivalent (CE) contribution vs. etch gas flow at 1400 W (left) and 1800 W (right) source power.

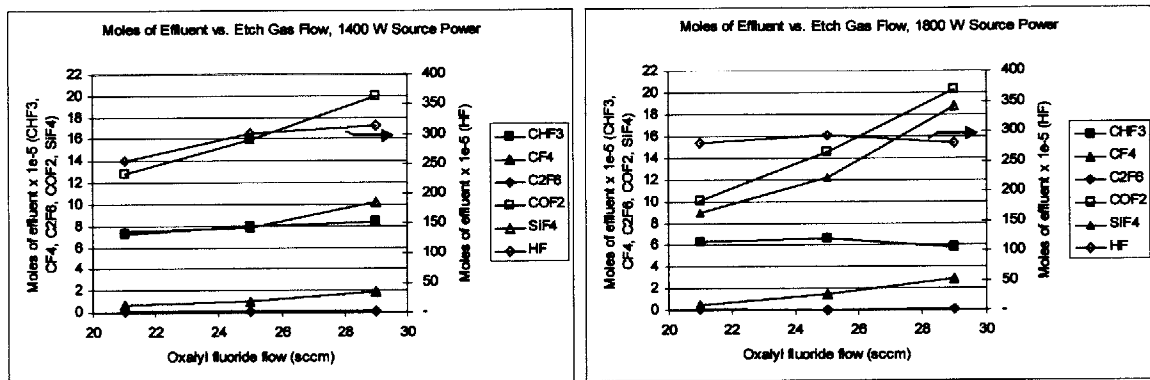

Figure 6.9b: Blanket resist experiments - moles of effluent vs. etch gas flow at 1400 W (left) and 1800 W (right) source power.

COF_2 emissions, which also tend to increase with etch gas flow at all power conditions, roughly track the SiF_4 trend within the process as well. As was seen to be the case with SiF_4, the COF_2 signal is observed to rise sharply as the resist is removed, which is consistent with the fact that more COF_2 is seen in the process effluent as oxalyl fluoride flow rate is increased since higher etch gas flow has been found to result in earlier removal of the resist. As the resist is removed completely, the CO_2 signal also rises, while the CO signal falls. The CO, CO_2, and COF_2 trends are consistent across all conditions where the resist is completely removed before the end of the run. The increase in CO_2 production in the absence of resist is likely due to the increased availability of free O that would otherwise be consumed as CO, the principal etch product in the interaction of the etch gas with the resist. Similarly, the increase in COF_2 formation is likely to be

due to the increased availability of free F in the absence of resist. If one accepts that a possible mechanism of COF_2 formation is the attachment of free F to CO,

$$CO + 2F \rightarrow COF_2, \qquad (6.1)$$

then one can expect COF_2 production to increase in the presence of excess CO (see Figure 6.8) if the etch enters a phase where less fluorine is being consumed. It is likely that this is the case here, since the etch rate of silicon in oxalyl fluoride is expected to be slower than that of resist. (It was observed in the patterned wafer stage that oxalyl fluoride etches resist faster than it does oxide by a factor of ~2 or more.)

One notable exception to the trend that the emissions of all fluorinated by-products increase with higher oxalyl fluoride flow occurs at high power (1800 W) and high flow (from 25 to 28 sccm), where total moles of HF and CHF_3 actually decrease from 25 sccm to 28 sccm. At these conditions, complete removal of the resist from the wafer occurs so much earlier than the end of the etch step (see Figure 6.5) that this phenomenon actually dominates over the general increase in CHF_3 and HF emissions that otherwise occurs with increasing etch gas flow. The integrated amount of CHF_3 and HF produced per run thus decreases because the supply of H needed to form these species becomes unavailable early enough to have a significant impact. This effect can be seen clearly in Figure 6.8: note the decrease in HF and CHF_3 emissions that occurs after the resist is removed.

This proposed mechanism raises the dilemma that, if the resist is the only source of hydrogen, and all of the resist is removed under different process conditions, the molar balance of hydrogen containing species over the duration of the etch should be the same for those conditions. This is clearly not the case, which suggests that CHF_3 and HF, the only hydrogen containing species detected with FTIR, do not fully account for all hydrogen leaving the chamber. One limitation of infrared spectroscopy is its inability to detect homonuclear diatomic species, which have no induced dipole, such as F_2 or H_2. It is therefore possible that hydrogen is leaving the chamber in the form of H_2, undetected by FTIR. Under this assumption, the data presented above suggest that, since the CHF_3 and HF amounts emitted by the process appear to vary with process conditions, the relative rates of formation for these compounds versus that of H_2 may vary as well.

The dependence of the relative CE fractions of CHF_3, CF_4, and C_2F_6 on source power is shown in Figure 6.10a. At high oxalyl fluoride flow rate (29 sccm), the CHF_3 contribution decreases with increasing power, while the CF_4 contribution increases. There is no discernable trend in the C_2F_6 fraction; however, C_2F_6 concentrations are very low under all conditions, hence it is not surprising that any trend that might be present could be obfuscated by the noise in the data.

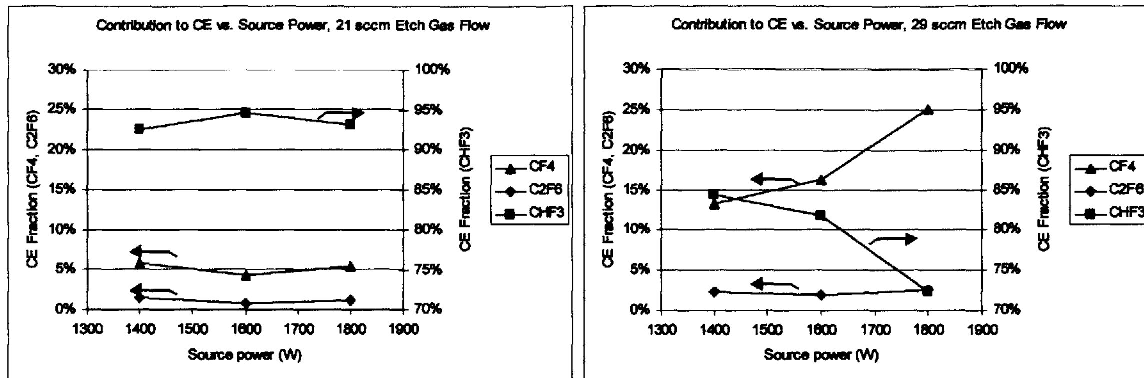

Figure 6.10a: Blanket resist experiments - relative carbon equivalent (CE) contribution vs. source power at 21 sccm (left) and 29 sccm (right) etch gas flow.

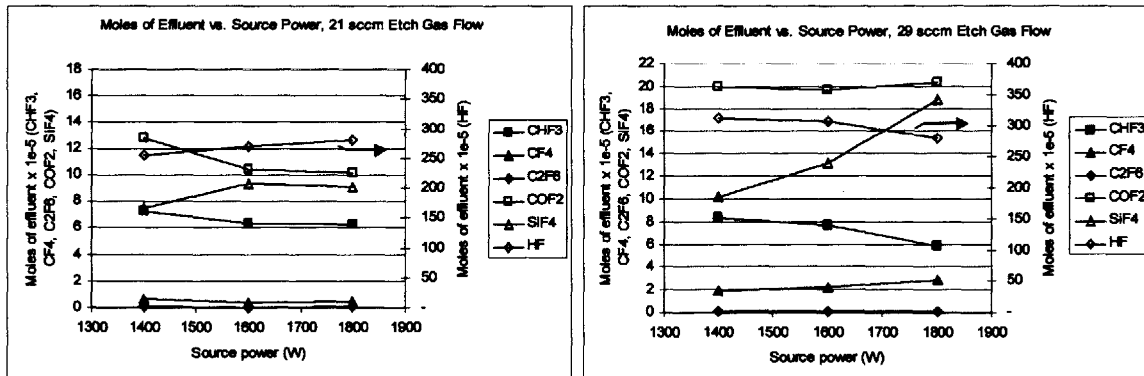

Figure 6.10b: Blanket resist experiments - moles of effluent vs. source power at 21 sccm (left) and 29 sccm (right) etch gas flow.

As was the case with increasing etch gas flow for all power conditions, increasing source power at the high etch gas flow (29 sccm) condition results in higher resist etch rate, leading to earlier removal of the resist layer. As a result, earlier transition from fluorocarbon emissions dominated by the production of CHF_3 in the presence of

hydrogen to fluorocarbon emissions dominated by the production of CF_4 when no H is available is observed. At lower oxalyl fluoride flows (21, 25 sccm), however, this effect is less pronounced; in fact, at 21 sccm, no trend in the relative CE fractions can be discerned (see Figure 6.10a). This suggests that source power alone may not significantly alter the relative distribution of the principal fluorocarbon etch products. The principal effect of source power on relative CE contributions seems to be through its effect on resist etch rate, *i.e.,* increased source power causes more rapid resist removal due to increased dissociation of the etch gas into radical species that react with the resist layer. The data for the 25 sccm condition, not shown graphically for brevity, exhibits the same general trends as those seen at 29 sccm.

Figure 6.10b plots the moles of each fluorinated by-product emitted against source power at 21 and 29 sccm etch gas flow. At the high flow condition, there is a general decrease in the moles of CHF_3 emitted as source power is increased which corresponds to a general increase in the CF_4 emissions. At the low flow condition, this effect is not readily discernable, with some decrease seen in the CHF_3 emissions, but no net trend in CF_4. This, however, is consistent with the trends with respect to CHF_3 and CF_4 fractional contribution to emissions seen at 21 sccm in Figure 6.10a. The fluorocarbon trends seen at 29 sccm are again attributed to higher source power resulting in an earlier transition from fluorocarbon emissions dominated by CHF_3 in the presence of hydrogen to fluorocarbon emissions dominated by the production of CF_4 once the resist has been removed. Although an upward trend in C_2F_6 emissions is expected to accompany that in CF_4 emissions, the C_2F_6 concentrations are so low that no trend can be discerned. The 25 sccm data is in general agreement with the CHF_3 and CF_4 trends seen at 29 sccm.

Figure 6.10b also shows the SiF_4, COF_2, and HF emissions as a function of source power. As was the case with the etch gas flow dependence, SiF_4 emissions generally increase with source power, quite sharply at the 29 sccm condition. The mechanism is believed to be essentially the same as the process outlined above in the etch gas flow discussion. Since SiF_4 and COF_2 exhibit the same behavior with regard to an observed increase in emissions after the resist is removed, one would expect COF_2 emissions as a function of

source power to behave similarly to SiF_4. However, this is not the case, for COF_2 is observed to be rather insensitive to source power at high etch gas flow and is actually seen to *decrease* with increasing source power at low etch gas flow (see Figure 6.10b). This trend suggests that another mechanism dominates over the increase in COF_2 emissions caused by earlier resist removal with higher source power. The decrease with respect to source power may be explained via a consideration of the order of bond strengths in the oxalyl fluoride molecule. The weakest bond in oxalyl fluoride is the C-C bond, which suggests that the most probable dissociation reaction upon electron impact is likely to be:

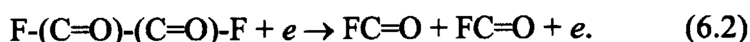

$$\text{F-(C=O)-(C=O)-F} + e \rightarrow \text{FC=O} + \text{FC=O} + e. \qquad (6.2)$$

A likely pathway for the subsequent formation of COF_2 may then be:

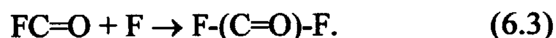

$$\text{FC=O} + \text{F} \rightarrow \text{F-(C=O)-F}. \qquad (6.3)$$

However, as source power is increased, the degree to which the feed gas molecule is dissociated also increases; hence it is likely that a greater number of the C=O and C-F bonds in oxalyl fluoride and/or FC=O will be broken, decreasing the concentration of FC=O radicals available for reaction with F to form COF_2.

Finally, HF emissions appear to decrease with source power at 29 sccm but increase with source power at 21 sccm, with a mixed trend seen at 25 sccm. It is likely that the decrease seen at the high flow condition is caused by the same effect that causes the decrease in CHF_3 emissions, namely the early removal of the hydrogen source required for HF and CHF_3 formation. The increase in HF with source power at low flow (21 sccm), on the other hand, suggests that another, competing mechanism dominates in that regime. Namely, as power is increased, the concentration of atomic fluorine in the plasma is increases due to more complete dissociation of the etchant. More fluorine is available for etching the photoresist layer and resulting HF formation. The difference between this regime and the one at the high flow (29 sccm) condition is that the photoresist is removed later at 21 sccm compared to 29 sccm for the same source power. (In fact, at 21 sccm and 1400 W source power, it is not completely removed at all.) Hence, the effect of hydrogen source elimination on HF formation is reduced at 21 sccm, in contrast to what is seen at 29 sccm. This hypothesis is supported by the fact that, while

CHF_3 emissions still decrease with source power at 21 sccm, the decrease is much less pronounced at 21 sccm than at 29 sccm (see Figure 6.10b). Again, since the HF and CHF_3 emissions vary under different process conditions, even for cases where all of the photoresist is removed, it is reasonable to posit that the remainder of the hydrogen balance leaving the chamber must be made up by a species not detected by FTIR, namely H_2.

It is believed that a principal reason for the low global warming emissions from oxalyl fluoride plasmas is the absence of trifluoromethyl (CF_3) groups in the oxalyl fluoride molecule. The CF_3 radical is believed to play a key role in the formation of CF_4, CHF_3, and C_2F_6 through mechanisms such as:

$$CF_3 + F \rightarrow CF_4, \quad (6.4)$$

$$CF_3 + H \rightarrow CHF_3, \quad (6.5)$$

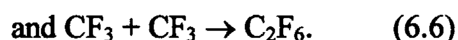

$$\text{and } CF_3 + CF_3 \rightarrow C_2F_6. \quad (6.6)$$

Hence the elimination of the CF_3 moiety in the parent molecule reduces the probability of formation of these species. On the other hand, the plasmas formed by oxalyl fluoride, despite nearly complete utilization of the etchant, are fluorine poor, given that each molecule of oxalyl fluoride contributes only two F atoms versus six or eight in C_2F_6 or C_3F_8. This is supported by the low oxide etch rates measured in the patterned wafer experiments. The presence of two O atoms in the molecule, moreover, is believed to be responsible for the rapid photoresist etch rates, as oxygen is known to be a very efficient etchant for organic films. The rapid erosion of the mask layer is also a likely cause of the blowout of feature critical dimension, with an increase over nominal printed CD on the order of 75 to 125% being observed in these experiments. Thus, while, structurally, oxalyl fluoride appears to be desirable from an emissions standpoint, the fact that it yields a fluorine poor and oxygen rich plasma environment is less satisfactory from a process standpoint for the types of applications considered in these experiments.

6.1.3 Conclusions

Use of oxalyl fluoride as a dielectric etchant has been investigated in an inductively coupled, high density plasma etch tool. Comparison with a C_2F_6-based process indicated

that substantial emissions reductions (up to 95%) are possible with this chemistry under the conditions tested. Oxalyl fluoride also appears to be efficiently utilized in the plasma, with utilization efficiencies as high 98.7% observed. With photoresist wafers, the principal process by-products are HF and CO with low levels of global warming species emitted. From a process standpoint, however, several critical issues are evident, specifically, poor photoresist selectivity and low oxide etch rate. It therefore appears that, at least in the process regime explored here, the implementation of this compound in a conventional dielectric etch application in a high density etch tool such as the one used for this study would be challenging. Nevertheless, the low global warming emissions produced by oxalyl fluoride indicate that it may have the potential to be used for global warming emissions reduction in other applications. Examples may include dielectric film removal applications where selectivity is not critical, such as chamber clean applications, or etch applications where the presence of both fluorine and significant quantities of oxygen is desirable, such as de-veil etch or *in-situ* strip of silated resist. The results of this study also suggest that attention be given to intramolecular bond strengths and structural characteristics of the molecule for improved etch rate and resist selectivity with low global warming emissions.

References

1. *Radiative Forcing of Climate Change: The 1995 Working Report of the Scientific Assessment Working Group of IPCC,* Intergovernmental Panel on Climate Change (IPCC) (1995).
2. *Scientific Assessment of Ozone Depletion: 1998, Volume 2,* World Meteorological Organization, Global Ozone Research and Monitoring Project, Report No. 44 (1998).
3. S. Karecki, R. Chatterjee, L. Pruette, R. Reif, T. Sparks, L. Beu, and V. Vartanian, *Evaluation of Oxalyl Fluoride for a Dielectric Etch Application in an Inductively Coupled Plasma Etch Tool,* J. Electrochem. Soc., submitted (2000).
4. Neural Network Analyzer of Process Evaluation Responses, developed by E. I. du Pont Nemours and Company.

6.2 Unsaturated Fluorocarbon Concept-and-Feasibility Study

This section presents the results of a concept-and-feasibility study conducted with six unsaturated fluorocarbon (UFC) gases as well as a fluorinated ether. These were evaluated in the same dielectric etch application in the same Centura 5300 HDP process tool that was employed in the other studies presented in Chapters 5 and 6. Process and global warming emissions performance was characterized and compared to three perfluorocompound (PFC) gases. It was found that all of the UFC gases were capable of etch performance comparable to that of the C_3F_8/CH_3F reference process used in Section 5.4, while exhibiting global warming emissions reductions compared to the PFCs. A low flow hexafluoro-2-butyne process was found to have significant emissions benefit, showing an emissions reduction of 86.2% compared to the C_3F_8 process. Two other C_4F_6 isomers (hexafluoro-1,3-butadiene and hexafluorocyclobutene) also exhibited reductions greater than 80%, while hexafluoropropene and octafluorocyclopentene exhibited emissions reductions greater than 70% versus the C_3F_8 based process. An extended 4 minute etch with hexafluoro-1,3-butadiene resulted in a deep via with an aspect ratio of 5:1, high selectivity to photoresist, and no evidence of etch stopping.

Section 6.2.1 discusses the experimental setup used. Section 6.2.2 provides a discussion of the experimental data. Finally Section 6.2.3 offers conclusions regarding this study. The present study was intended as an initial exploration of this family of compounds in the Centura 5300 HDP tool, rather than an in depth characterization of the same nature as that presented in Section 5.4. In many respects, this study generated as many questions as it did answers. It did, however, establish the viability of using UFC etchants for dielectric etch processes in an ICP tool such as the Centura 5300 HDP. Among the numerous compounds studied in this tool that are discussed in this document, the UFC family appears to offer the greatest promise in terms of successfully meeting process performance targets *and* offering substantial emissions reductions. The material in Section 6.2 is based on work published by the author and his coworkers in Ref. [1].

6.2.1 Experimental Setup

The following six UFC compounds have been examined in this study: hexafluorocyclobutene (c-C_4F_6), hexafluoro-1,3-butadiene (C_4F_6, CF_2=CF-CF=CF_2), hexafluoro-2-butyne (C_4F_6, CF_3-C≡C-CF_3), hexafluoropropene (C_3F_6, CF_2=CF-CF_3), octafluoro-2-butene (C_4F_8, CF_3-CF=CF-CF_3), and octafluorocyclopentene (c-C_5F_8). In this study, processes based on these UFCs have been compared with processes based on one fluorinated ether: octafluorotetrahydrofuran (c-C_4F_8O), and three PFCs: n-decafluorobutane (C_4F_{10}, CF_3-CF_2-CF_2-CF_3), octafluoropropane (C_3F_8), and octafluorocyclobutane (c-C_4F_8). For conciseness, in the tables and figures in this paper, octafluoro-2-butene is abbreviated as OF2B, hexafluoro-1,3-butadiene as HF13B, and hexafluoro-2-butyne as HF2B. Octafluorotetrahydrofuran, though itself a global warming compound, had been successfully employed as an etch gas in a chamber clean application (see Section 1.2.2.2), with good process performance and substantial global warming emissions reductions [2, 3].

The process tool used for this study was the same Centura 5300 HDP tool that had been employed for the work discussed in Sections 5.1 through 6.1. In the present study, both process and emissions performance are reported. Post etch via cross sections were examined using cross-sectional scanning electron microscopy (SEM). The effluents during the etch processes were monitored with a Fourier transform infrared (FTIR) spectrograph with a 10 cm zinc selenide cell sampling downstream of the dry backing pump. The species monitored using FTIR were: CF_4, C_2F_6, C_3F_8, CHF_3, CO, CO_2, SiF_4, COF_2, HF, C_2F_4 and the etch gas being used. The methodology employed was consistent with that used for the work described in Sections 5.3 through 6.1. The metric used for reporting the emissions was again kilograms of carbon equivalent (kgCE), defined as:

$$kgCE = \sum_i Q_i \times \frac{12}{44} \times GWP_{100i},$$

where i indexes the gases monitored, Q_i is the quantity in kilograms of each gas, and GWP_{100i} is the 100 year integrated global warming potential of the gas. The reference process for comparison was the same 120 s C_3F_8/CH_3F based process that was used for the work in Section 5.4. In the present study, because a slightly different FTIR analysis

method was used, the global warming emissions value that was employed in all emissions reductions calculations was 0.316 kgCE. In this section, 1998 revised GWP_{100} values are used for all emissions reporting: CF_4 5700, C_2F_6 11400, C_3F_8 8600, c-C_4F_8 11200, C_4F_{10} 8600, CHF_3 14800 [4]. The present study introduces a new metric, that of normalized global warming emissions, which are simply the emissions in kgCE scaled for a 1 μm etch (as determined by the etch rate at the center of wafer location) and reported in units of kgCE/μm. The normalized emissions value for the C_3F_8/CH_3F reference process was 0.376 kgCE/μm, based on the 0.35 μm nominal CD via etch depth value of 0.8411 μm (center of the wafer). See Figure 5.44.

It is important to note that that the GWP_{100} values of all of the UFCs except c-C_5F_8 (GWP_{100} = 90, [4-7]) have not yet been determined. The GWP_{100} values of these UFC gases, however, are expected to be very small; furthermore, the destruction efficiency of all the UFCs in all of the process settings examined in this experiment was very high (greater than 98% in every case). This implies that inclusion of the effects of the unreacted UFC source gases would have a negligible impact on the reported global warming emissions values. Hence, except for c-C_5F_8, the UFC source gases were not included in the calculation of the global warming emissions. The GWP_{100} value for c-C_4F_8O (8700) used in these calculations is an estimated value based on earlier work [2, 3]; see Section 1.2.2.2.

The experiment was divided into three stages. In the first stage, all of the gases were run at a common process point (A in Table 6.4) on blanket photoresist or patterned wafers. In addition, all of the gases except C_3F_8 were run at process conditions B and C as shown in Table 6.4. the blanket resist wafers used K2G deep UV resist. The film stack on the patterned substrates consisted of TEOS (tetraethoxysilane)-deposited silicon oxide masked with APEX deep UV photoresist. The test structures used on the patterned substrates were via holes with nominal printed critical dimensions (CDs) ranging from 0.6 μm to 0.35 μm. All via cross sections shown in this section are 0.35 μm features. The initial resist thickness on all patterned substrates used was 1.00 μm. This stage provided information on the performance of all process gases at the same process

condition and preliminary information on the performance of the various gases as a function of source power. In terms of emissions, the photoresist and patterned substrates were, once again, treated as being, for all practical purposes, identical, as the patterned wafer surfaces are mainly photoresist with very little open area (approximately 0.5%) and the resist used for both types of wafers was compositionally very similar.

Table 6.4: Stage 1: Process conditions A, B, and C. Chamber pressure 6 mTorr, etch time 120s, O_2 additive flow 0 sccm, 100 sccm He flow, roof/wall/chiller temperature 210/200/34 °C, 15 Torr backside He.

Process Condition	Etch Gas Flow (sccm)	Bias Power (Watts)	Source Power (Watts)	Gases and substrates
A	16	800	1900	All gases; PR and patterned wafers
B	16	800	1750	All gases, except C_3F_8; Patterned: c-C_4F_8, OF2B, and HF13B, PR wafers for rest.
C	16	800	2050	All gases, except C_3F_8; Patterned: c-C_4F_8, OF2B, and HF13B, PR wafers for rest.

After the experiments described in Table 6.4 were run, a second stage of experiments was carried out, with additional development work performed with hexafluoro-1,3-butadiene, hexafluorocyclobutene, hexafluoropropene, octafluorotetrahydrofuran, octafluorocyclopentene, and hexafluoro-2-butyne. Patterned wafers were used for all experiments in this stage. Cross-sectional SEM data and FTIR effluent data were collected from all wafers. These processes are shown in Table 6.5.

The third stage of the experiments involved longer etch processes using the hexafluoro-1,3-butadiene, hexafluorocyclobutene, and hexafluoropropene chemistries. Emissions data were not collected for these longer etch times. Etch times of 180 s and 240 s were employed. Patterned substrates of the same type as the ones used earlier were evaluated using cross-sectional SEM.

Table 6.5: Follow-up process conditions for hexafluoro-1,3-butadiene, hexafluorocyclobutene, hexafluoro-2-butene, hexafluoropropene, octafluorocyclopentene, and octafluorotetrahydrofuran experiments. Chamber pressure 6 mTorr, etch time 120s, 100 sccm He flow, roof/wall/chiller temperature 210/200/34 °C, 15 Torr backside He.

Process Condition	Etch Gas Flow (sccm)	Bias Power (Watts)	Source Power (Watts)	Additive O_2 Flow (sccm)	Gases
D	14	1400	1150	4	HF13B, c-C_4F_6
E	15	1400	1100	4.3	HF13B, c-C_4F_6
F	13	1400	1100	3.7	HF13B, c-C_4F_6, HF2B
G	12	1400	1100	3.4	HF13B, c-C_4F_6, HF2B
H	12	1500	1100	3.4	HF13B, c-C_4F_6
I	15	1500	1050	4.3	c-C_4F_6
J	13	1500	1050	3.7	c-C_4F_6
K	14	1400	1000	4	c-C_4F_6
L	14	1400	1000	2	c-C_4F_6
M	14	1400	1000	0	c-C_4F_6
N	15	1400	1100	0	C_3F_6
O	13	1400	1100	0	C_3F_6
P	12	1400	1100	0	C_3F_6
Q	12	1500	1100	0	C_3F_6
R	11	1000	1750	4	c-C_5F_8
S	11	1000	1450	4	c-C_5F_8
T	11	1000	1150	4	c-C_5F_8
U	14	1000	1150	0	c-C_4F_8O
V	14	1000	1000	0	c-C_4F_8O

The unsaturated fluorocarbon gases used in this study were provided by Oakwood Products, Inc., W. Columbia, SC and Lancaster Synthesis, Inc., Windham, NH. c-C_4F_8O and C_4F_{10} were provided by the 3M Company, St. Paul, MN.

6.2.2 Results and Discussion

Given the exploratory nature of this study, a number of observed effects have not yet been fully understood. Hence, the treatment presented below is not intended to be a systematic characterization. Nevertheless, some key effects have been identified and will be discussed below, with the hope that further insight will be gained in subsequent studies. The discussion that follows will be a departure from the style of analysis that was presented in Sections 5.3 through 6.1, focusing on comparative observations, rather than plasma mechanisms or process variable trends. It hoped that, in future studies, many of the effects noted herein will become more fully understood and that a systematic study of the subtle, yet readily discernable differences between similar compounds in this family will contribute to a better understanding of fluorocarbon plasma chemistry in high density tools.

6.2.2.1 Comparison of all Gases at Same Process Condition

The global warming emissions resulting from process condition A run with all the gases are shown in Figure 6.11. The four high GWP gases exhibit the highest emissions while the three C_4F_6 isomers exhibit the lowest emissions, which, at this particular condition, is likely due to the fact that the C_4F_6 isomers did not etch and only polymerized. As had been noted in Section 5.4.3, highly polymerizing behavior appears to result in lower global warming emissions, since a significant portion of the CF_x species that would otherwise recombine into fluorocarbon effluent remain in the chamber as a fluoropolymer film. This film is later removed during standard oxygen based chamber clean processes – either an *in-situ* resist ash (post etch treatment, PET) or a preprocess run before each wafer; the principal carbon-bearing products of these processes are CO, CO_2, and COF_2, with negligible fluorocarbon formation being observed.

The breakdown of the emissions is shown in Figure 6.12. It is seen that CF_4, CHF_3, and C_2F_6 account for nearly all of the global warming emissions for all of these processes, regardless of the source gas, except where the source gas itself is a long chain high GWP compound. The PFCs exhibit the highest etch rates at this process condition, as is shown

in Figure 6.13, whereas some of the gases (C_4F_6 isomers) are in a net polymerization regime. The resist erosion at this condition is shown in Figure 6.14. It is seen that, with most of the chemistries, net deposition occurs on resist, as is shown by the negative resist erosion numbers. The C_3F_8 process shows slight erosion; the etchant that resulted in the greatest degree of resist erosion, however, was c-C_4F_8O, which was likely due to the oxygen in the molecule attacking the photoresist.

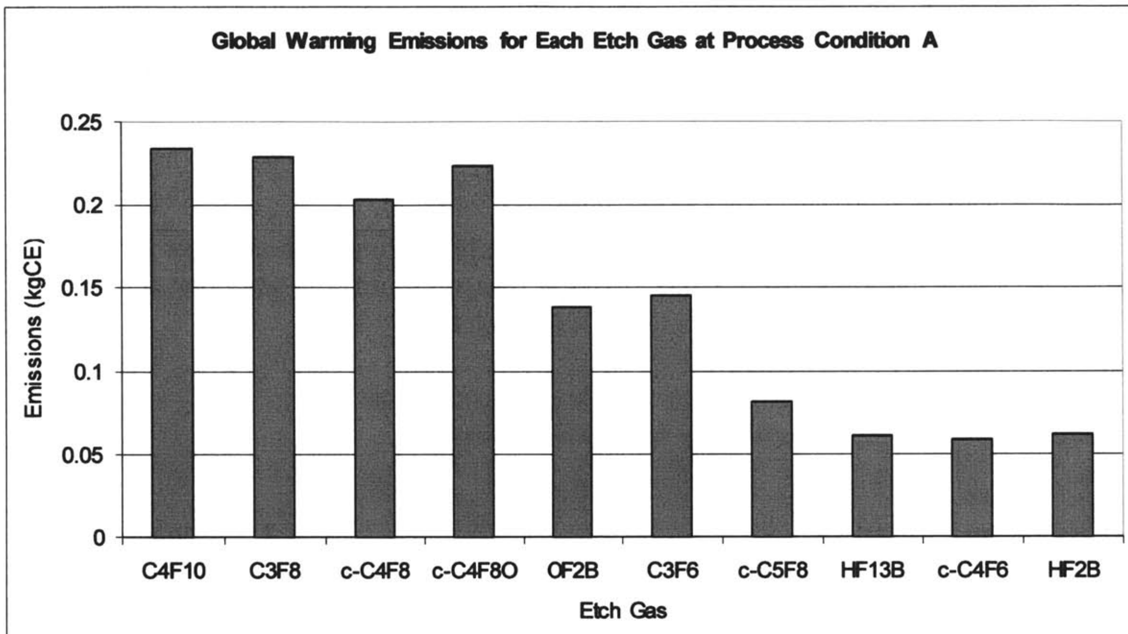

Figure 6.11: Global warming emissions from each etch gas for the conditions of process A: 1900 W source, 800 W bias, 16 sccm etch gas flow, 0 sccm O_2 additive flow, 120 s etch time.

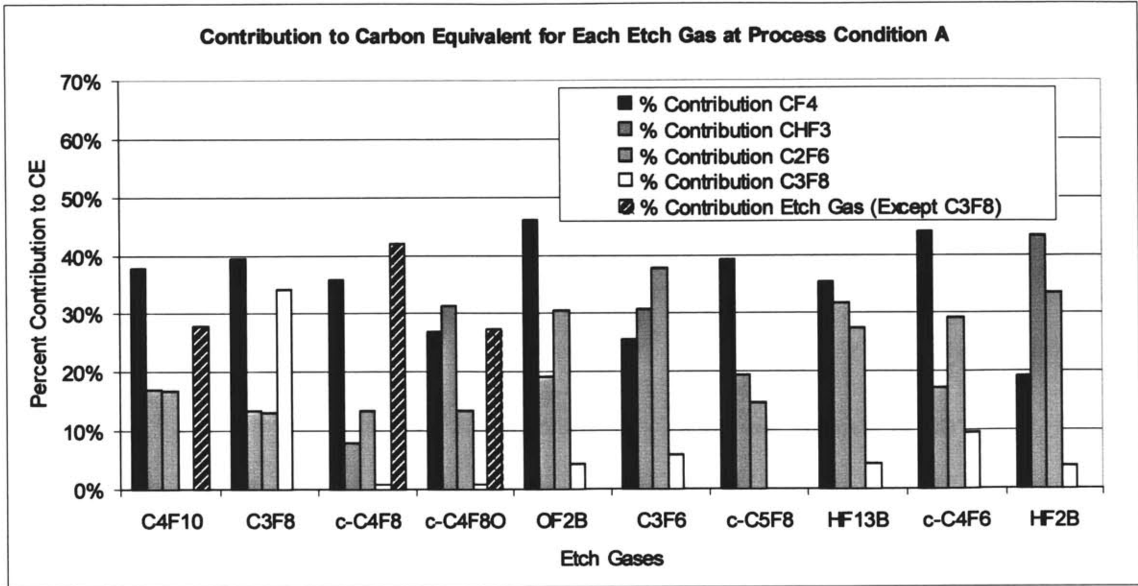

Figure 6.12: Breakdown of global warming emissions from each etch gas for the conditions of process A: 1900 W source, 800 W bias, 16 sccm etch gas flow, 0 sccm O_2 additive flow, 120 s etch time.

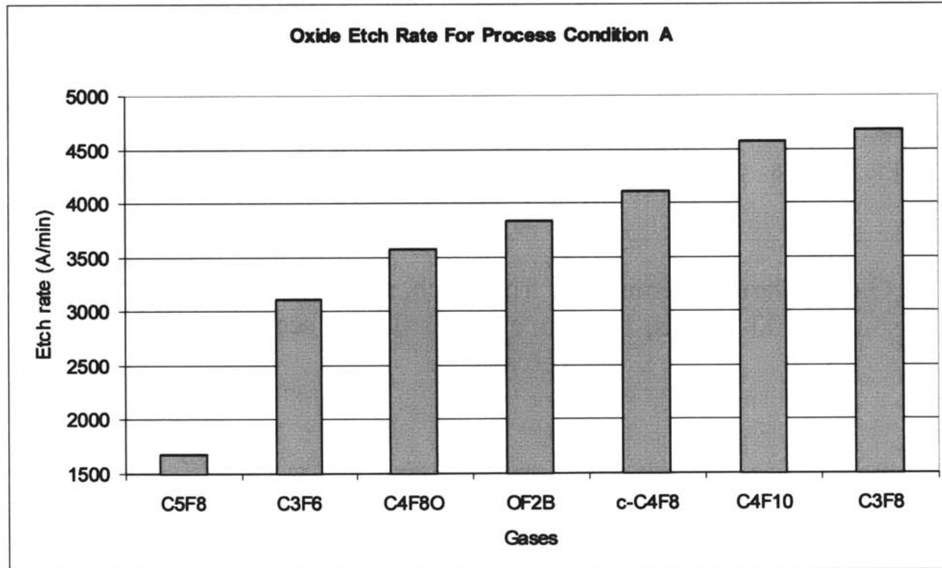

Figure 6.13: Oxide etch rate for each etch gas for the conditions of process A: 1900 W source, 800 W bias, 16 sccm etch gas flow, 0 sccm O2 additive flow, 120 s etch time, 0.35 μm nominal CD via in center of wafer.

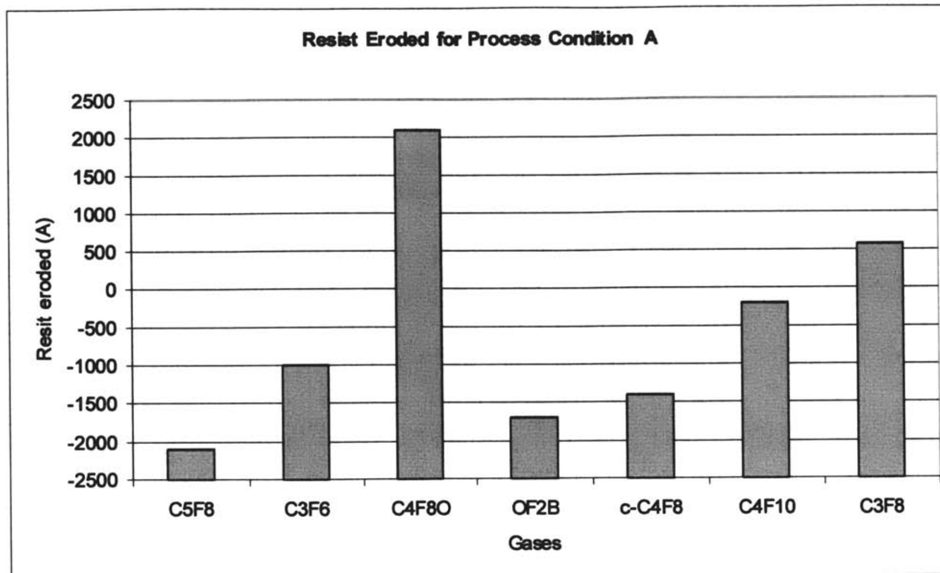

Figure 6.14: Resist eroded for each etch gas for the conditions of process A: 1900 W source, 800 W bias, 16 sccm etch gas flow, 0 sccm O_2 additive flow, 120 s etch time, measurement taken at 0.35 μm nominal CD via in center of wafer.

The via cross sections for the C_3F_8, c-C_4F_8, C_4F_{10}, and octafluoro-2-butene processes, which exhibited the best etch results at process condition A, are shown in Figure 6.15. It can be seen that all of the PFCs as well as octafluoro-2-butene etch with good etch rates, highly anisotropic sidewall profiles, and high selectivity to photoresist. The normalized emissions reduction obtained with octafluoro-2-butene at this condition was 52.2% compared to the C_3F_8 reference process. All the other gases showed poor etch performance at this process condition.

Process conditions A, B, and C varied the source power from 1750 W to 2050 W for each of the gases. Overall global warming emissions were found to be insensitive to source power in this range. As was the case at 1900 W, at 1750 W and 2050 W, the three isomers of C_4F_6 polymerized, resulting in net deposition and did not etch, while the PFCs again exhibited the best process performance.

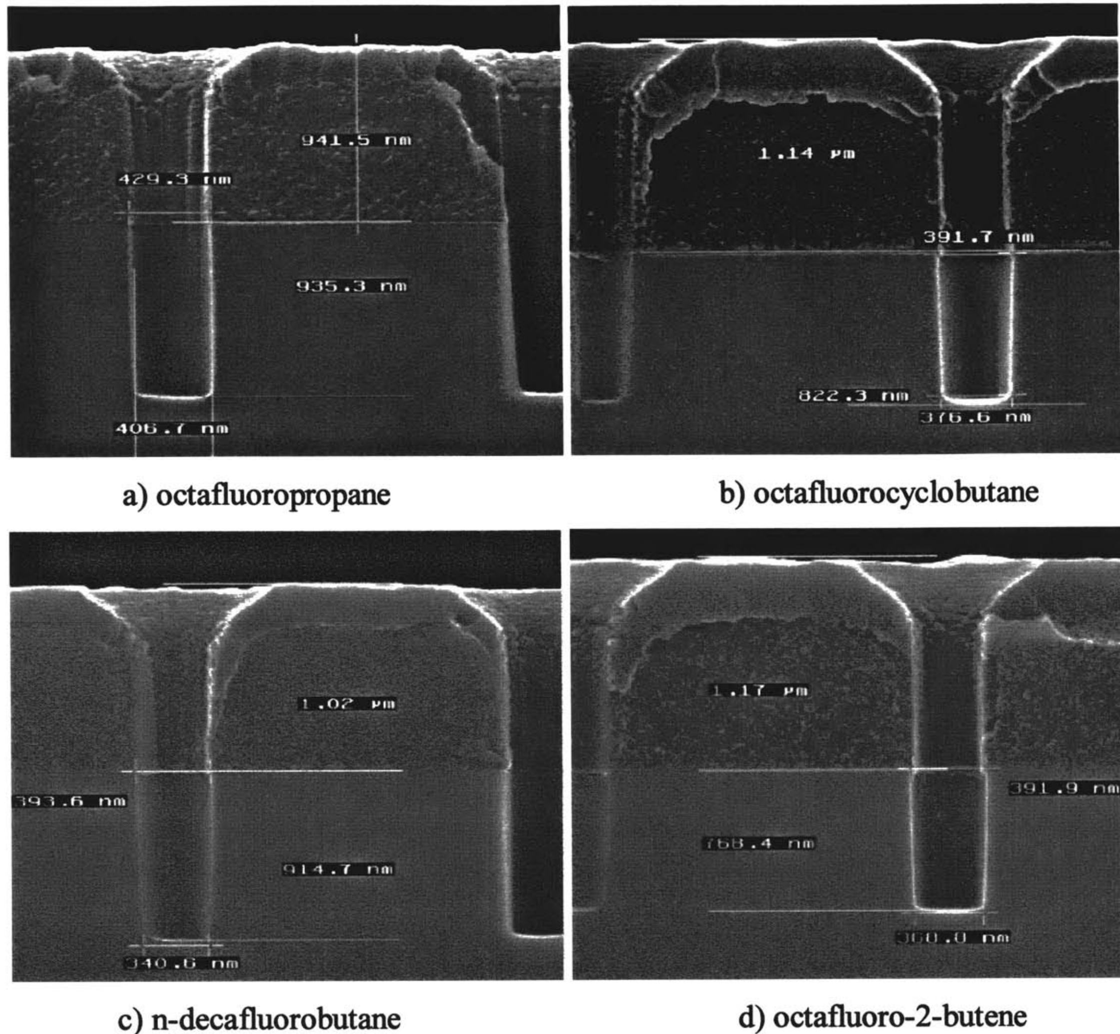

a) octafluoropropane

b) octafluorocyclobutane

c) n-decafluorobutane

d) octafluoro-2-butene

Figure 6.15: Via cross sections at process condition A: 1900 W source, 800 W bias, 16 sccm etch gas flow, 0 sccm O_2 additive flow, 120 s etch time, 0.35 μm nominal CD via in center of wafer.

6.2.2.2 Comparison of C_4F_8 Isomers

Figures 6.16 and 6.17 show the oxide etch rate as a function of source power with c-C_4F_8 and octafluoro-2-butene as the etch gas, respectively. For the same feature sizes and source powers, the center etch rates are lower than the edge etch rates, an effect that has been observed in the other studies carried out in the same process tool (see Sections 5.3 and 5.4) and is understood to be caused by the greater proximity of the edge of the wafer to the source antenna. In the case of octafluoro-2-butene, a clearly identifiable but weak decrease in oxide etch rate is observed with increasing source power for all feature sizes

and locations. In the case of its cyclic isomer, this decrease is seen for the 0.6 μm features and the 0.45 μm edge feature. For the 0.45 μm center feature and the 0.35 μm features, no clear trend is observed.

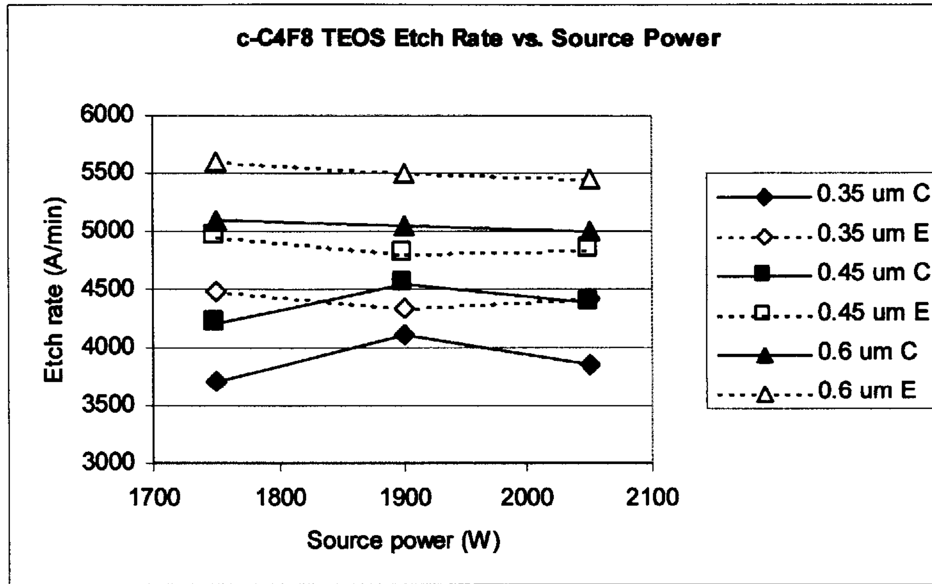

Figure 6.16: c-C_4F_8 oxide etch rate vs. source power (process conditions A, B, and C).

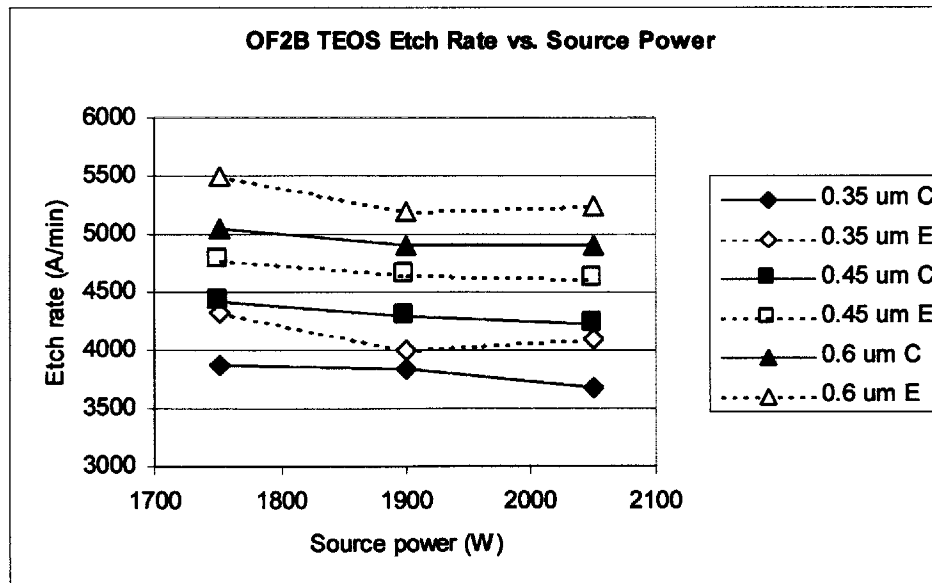

Figure 6.17: Octafluoro-2-butene oxide etch rate vs. source power (process conditions A, B, and C).

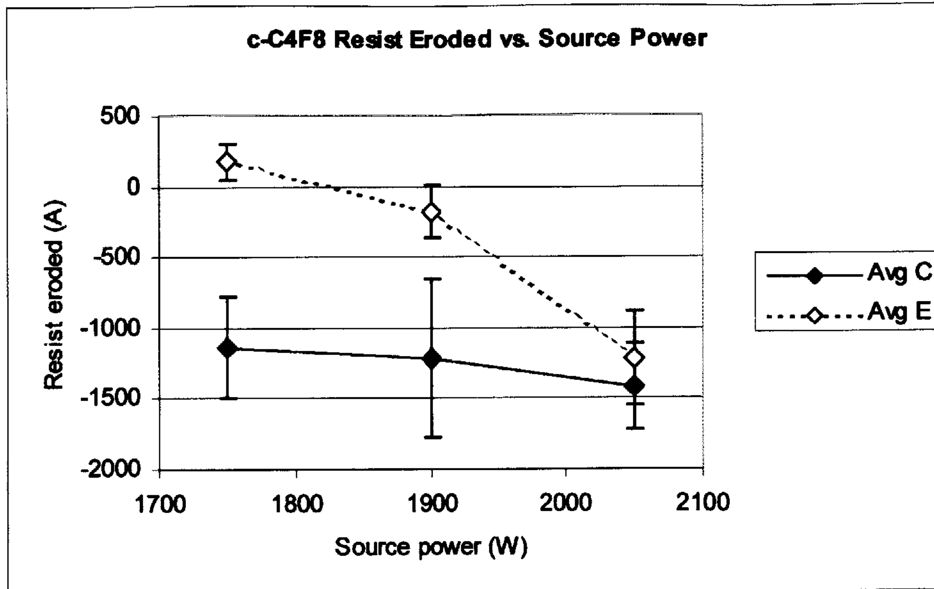

Figure 6.18: Resist erosion vs. source power for c-C_4F_8 (process conditions A, B, and C).

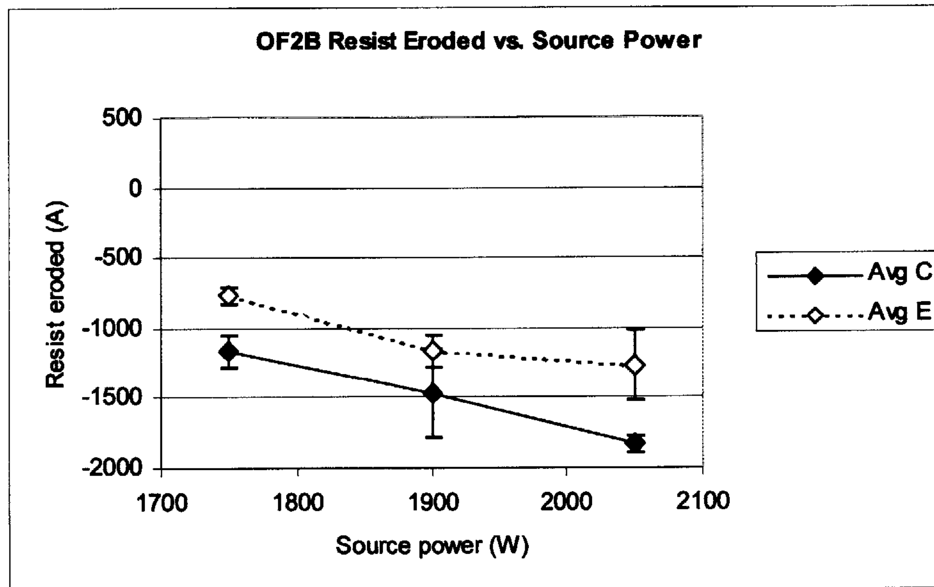

Figure 6.19: Resist erosion vs. source power for octafluoro-2-butene (process conditions A, B and C).

Figures 6.18 and 6.19 show the amount of resist eroded (average of three measurements at each of the two locations on the wafer) as a function of source power for c-C_4F_8 and octafluoro-2-butene, respectively. A monotonic decrease in the amount of resist erosion (*i.e.*, an increase in the amount of net polymer deposition, as indicated by the negative values for many of the data points) is seen at both the center and edge locations. The

amount of erosion at the edge is consistently greater than in the center for both isomers, again, an effect observed in the other studies in the same etch tool (Sections 5.3 and 5.4) and also pointed out by other authors [8].

With the exception of the smaller features in the case of oxide etch rate for c-C_4F_8, all trends seen in Figures 6.16 through 6.19 suggest that the process tends to shift closer to a net polymerization regime with increasing source power. These trends stand in contrast to observations made earlier (Sections 5.3 and 5.4) that resist erosion generally increases with increasing source power because increasing source power generally results in suppression of polymer formation on the wafer surface, which is the principal mechanism that competes with the etching of the resist. Reduced polymer formation on the wafer is believed to result from more complete breakup of the feed gas molecule and/or an increase in the power density at the wafer surface, both of which tend to shift the process away from the polymer deposition regime. However, it has also been noted (Section 5.4) that, in certain regimes, in-feature oxide etch rates do decrease with increasing source power and this effect has been attributed to a decrease in bias voltage at the wafer surface dominating over the more intuitively understood trends described above.

Indeed, other workers have shown that, in inductively coupled systems where source coil power is varied while bias power is fixed, the bias *voltage* decreases with higher source power. This has been attributed to an increase in plasma density which reduces the thickness of the sheath at the wafer resulting in lower voltage [9]. Put another way, as source power increases, so does the ion flux (hence current) to the wafer surface. For a fixed bias power, this must necessarily result in a decrease in the bias voltage. Applying this observation to the above data suggests that, despite the higher ion flux to the surface, the net effect may be dominated by the lowering of the bias voltage. It is also possible that, for these processes, the increase in plasma density arising from higher source power may not necessarily produce more etchant species. In fact, it is plausible to suggest that what is observed is the result of larger ion and neutral fluxes of CF_x species that result in more polymer formation.

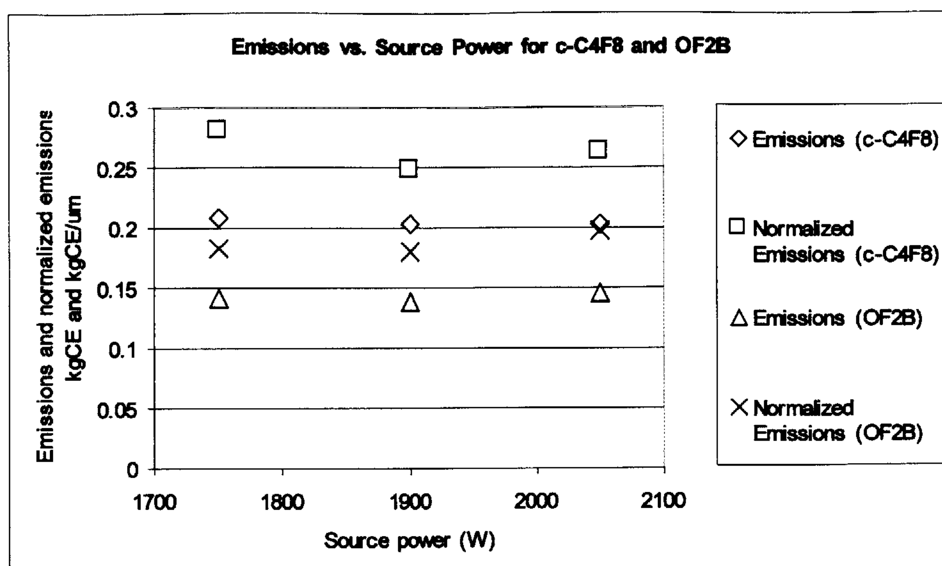

Figure 6.20: Emissions and normalized emissions vs. source power for c-C_4F_8 and octafluoro-2-butene (process conditions A, B, and C).

The emissions and normalized emissions for octafluorocyclobutane and octafluoro-2-butene are plotted in Figure 6.20. It is seen that both these metrics do not show much variation with respect to source power for either isomer in this regime. Octafluorocyclobutane, however, does exhibit higher emissions. The reason for this stems primarily from the fact that unreacted source gas in the case of octafluorocyclobutane is a high-GWP effluent, whereas for octafluoro-2-butene, which is almost completely utilized to begin with, it is not. In fact, unreacted source gas accounts for approximately 40% of the carbon equivalent value from the octafluorocyclobutane processes. Whereas the utilization efficiency octafluoro-2-butene is greater than 99% for all three conditions, it ranges from 90.3% at 1750 W to 91.8% at 2050 W for c-C_4F_8.

a)

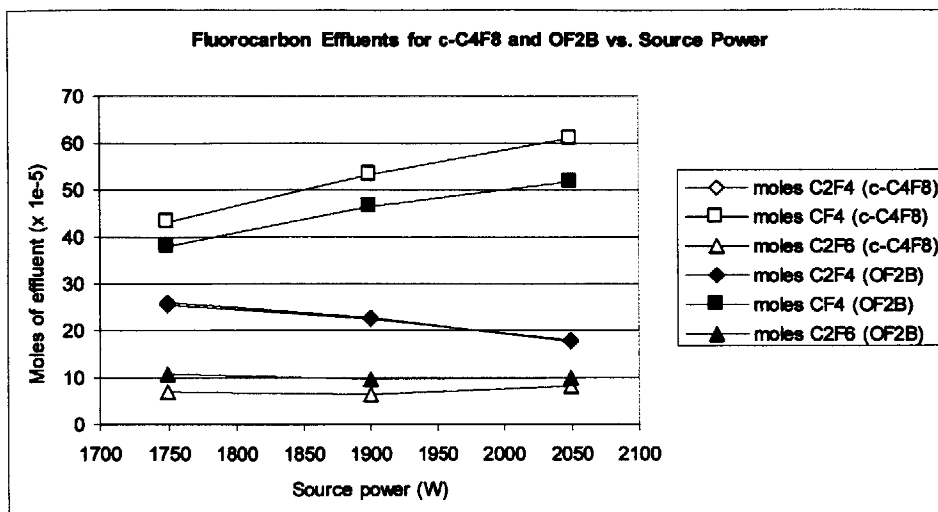

b)

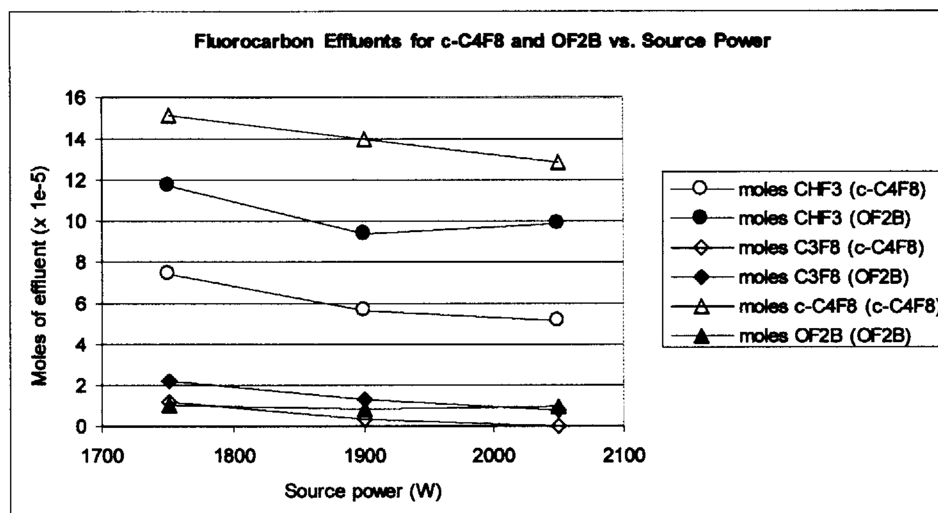

Figure 6.21: Fluorocarbon effluents from c-C_4F_8 and octafluoro-2-butene vs. source power: a) C_2F_4, CF_4, C_2F_6; b) CHF_3, C_3F_8, and source gas (c-C_4F_8 or OF2B), (process conditions A, B, and C).

Figure 6.21 shows the emissions of fluorocarbon effluents for the two chemistries at the three process conditions (A, B, and C) being considered. It is seen that the emissions of CF_4 are higher, on a molar basis, for octafluorocyclobutane at all three power levels. Emissions of C_3F_8, C_2F_6, and CHF_3, however, are higher for octafluoro-2-butene, although these amounts are considerably smaller than the CF_4 emissions, while C_2F_4 emissions (which are not included in the carbon equivalent calculation because of the low global warming impact of this compound), are almost identically the same for the two

isomers. The lack of *net* change in global warming emissions with respect to source power can be explained, in the case of both gases, by the fact that the increase in CF_4 emissions with respect to source power appears to be counterbalanced by decreasing CHF_3 and C_3F_8 emissions. Moreover, in the case of c-C_4F_8, the utilization efficiency of the source gas is also observed to increase with higher source power, resulting in a smaller c-C_4F_8 contribution. The decrease in CHF_3 emissions observed for both isomers is, moreover, consistent with a decrease in resist erosion. Interestingly, C_2F_6 emissions do not appear to be significantly affected by variation in source power for either gas. It is counterintuitive that octafluorocyclobutane produces more CF_4 for the same process condition as its structure consists entirely of CF_2 moieties, whereas octafluoro-2-butene has terminal CF_3 groups.

6.2.2.3 Comparison of C_4F_6 Isomers

Further process development was done with some of the more promising gases for improved global warming emissions reduction and process performance. Of particular interest were the three isomers of C_4F_6. The 0.35 μm via etch depth and amount of resist eroded (center of wafer values) at two low flow process conditions (F and G) are shown for each of these chemistries in Figure 6.22. The etch depth for each of these processes was comparable to the C_3F_8/CH_3F reference process. The etch rate at the 13 sccm etch gas flow condition (process condition F) yields similar etch rate and resist erosion for all of the three isomers. For the 12 sccm etch gas flow condition (process condition G), one observes that there is a decrease in the etch rate for each of the isomers compared to the 13 sccm flow condition as well as a marked increase in the resist erosion for hexafluoro-1,3-butadiene.

The global warming emissions and moles of fluorocarbon effluents produced from these gases (other than the source gases themselves, whose utilization efficiencies were greater than 99.5% at both process conditions) are shown in Figures 6.23 and 6.24, respectively. Interestingly, for both hexafluoro-1,3-butadiene and hexafluoro-2-butyne, the global warming emissions appear to be higher at 12 than at 13 sccm etch gas flow while the trend is opposite (but much less pronounced) for the hexafluorocyclobutene in this regime.

At first, this trend seems counterintuitive, but can be explained by close examination of the moles of effluents emitted (see Figure 6.24). For hexafluoro-1,3-butadiene, the most pronounced difference between these two process conditions lies in the amounts of C_2F_4 and CHF_3 emitted. At the lower gas flow condition, the quantity of C_2F_4 emitted is significantly lower, whereas the emissions of CHF_3 are significantly higher. Since C_2F_4 is not a high-GWP gas and CHF_3 is, this phenomenon leads to higher global warming emissions for hexafluoro-1,3-butadiene at lower gas flow conditions. This effect dominates despite a small decrease in the emissions of CF_4 at the lower flow condition. The higher CHF_3 is accompanied by an increase in resist erosion as would be expected, since the resist is the sole source of hydrogen in the system. In fact a correlation between CHF_3 emissions and resist erosion applies across all C_4F_6 processes and is shown in Figure 6.25 for hexafluoro-1,3-butadiene.

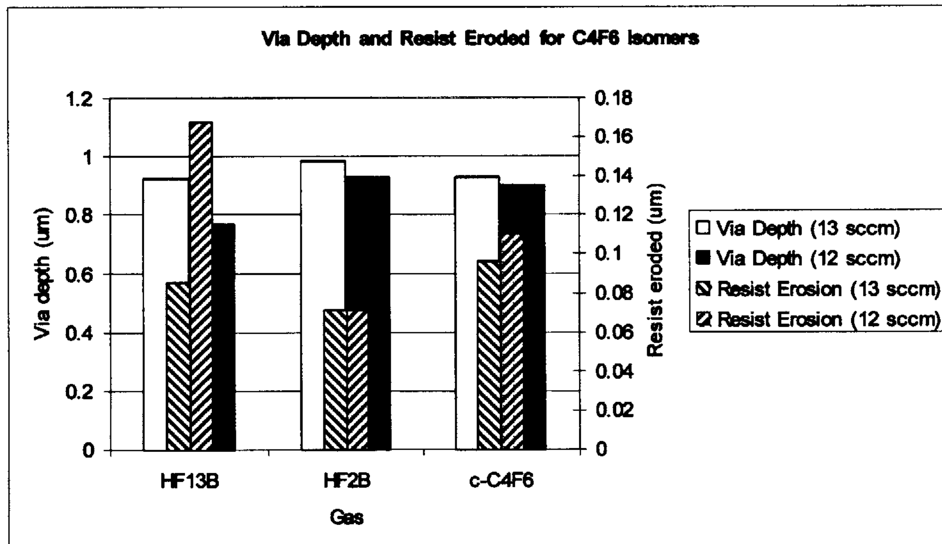

Figure 6.22: 0.35 μm via depth and amount of resist eroded for C_4F_6 isomers at flows of 12 and 13 sccm: 1100 W source, 1400 W bias, 3.4 and 3.7 sccm O_2 additive flow, respectively, 120 s etch time (process conditions F and G); center of wafer data.

The explanation in the case of hexafluoro-2-butyne is somewhat different: at the lower gas flow condition, there appears to be somewhat higher C_2F_6 and C_3F_8 formation, which is enough to account for the higher global warming emissions at process condition G (12

sccm) as compared to F (13 sccm). In the case of hexafluorocyclobutene, the effluents emitted for both of these process conditions do not change significantly, resulting in little difference in the global warming emissions from these two processes.

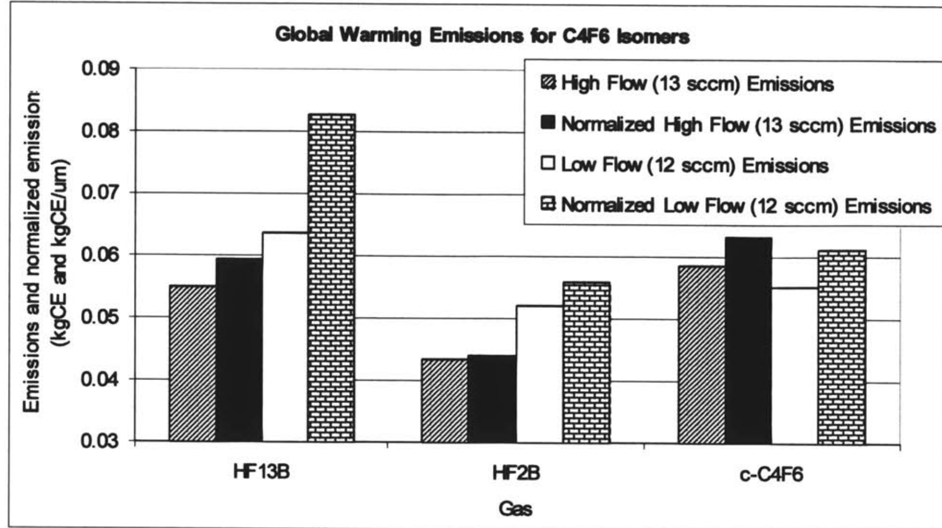

Figure 6.23: Emissions performance of C_4F_6 isomers at flows of 12 and 13 sccm: 1100 W source, 1400 W bias, 16 sccm etch gas flow, 3.4 and 3.7 sccm O_2 additive flow, respectively, 120 s etch time. (process conditions F and G).

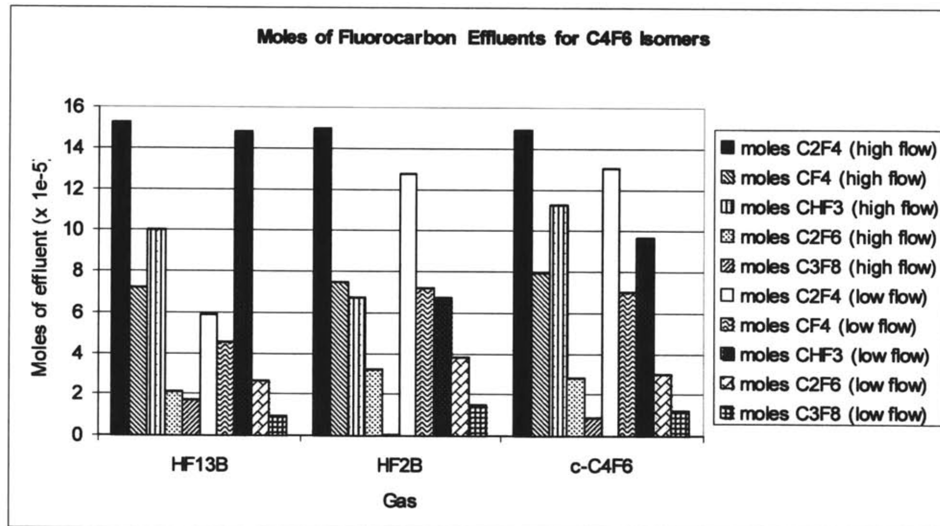

Figure 6.24: Moles of fluorocarbon effluents emitted for C_4F_6 isomers at flows of 12 and 13 sccm: 1100 W source, 1400 W bias, 3.4 and 3.7 sccm O_2 additive flow, respectively, 120 s etch time (process conditions F and G).

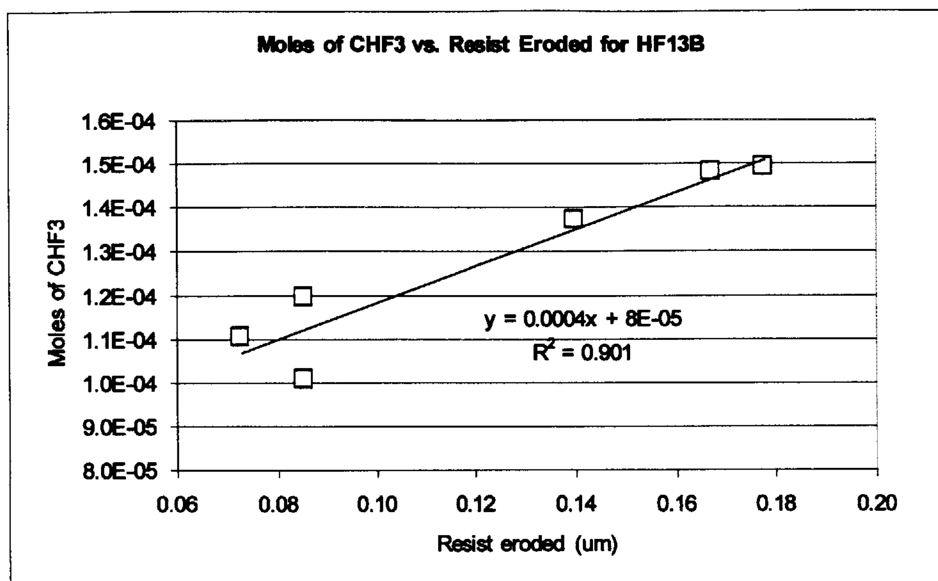

Figure 6.25: Moles of CHF_3 emitted vs. resist eroded for hexafluoro-1,3-butadiene processes.

Center of wafer SEM cross sections of via hole features etched by each of these gases at process conditions F and G are shown in Figures 6.26 through 6.28. At these conditions, hexafluoro-2-butyne had the best global warming emissions performance out of the three isomers, with a carbon equivalent value of 0.043 kg at process condition F (13 sccm, 1400 W bias power), which was also the lowest emissions value achieved for any gas at any condition in this study. The corresponding emissions reduction of 86.2% relative to the C_3F_8/CH_3F reference process (with both the emissions for both the hexafluoro-2-butyne process and the reference process scaled to a 1 μm etch depth, the normalized emissions reduction was 88.2%). Hexafluoro-2-butyne, however, also exhibited the most evidence of etch stopping (see Figure 6.28). The other isomers also exhibited significant reductions in global warming emissions with good etch rates, low mask layer erosion, and anisotropic profiles. The best emissions value for any hexafluoro-1,3-butadiene process was also achieved at process condition F: 0.055 kgCE, representing a reduction of 82.6% (normalized reduction of 84.2%). The best emissions value for c-C_4F_6, on the other hand, was obtained at condition H (12 sccm, 1500 W bias power): 0.051 kgCE, representing a reduction of 83.9% (normalized reduction of 85.2%).

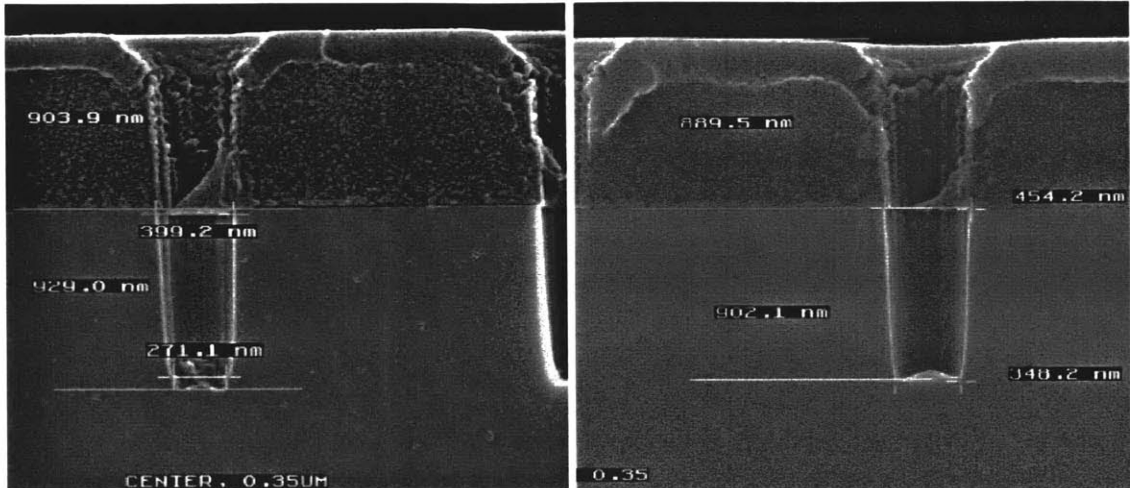

Figure 6.26: Hexafluorocyclobutene process condition F (left): 13 sccm etch gas flow/3.7 sccm O_2 flow, and G (right): 12 sccm etch gas flow/3.4 sccm O_2 flow; 0.35 μm nominal CD vias in center of wafer.

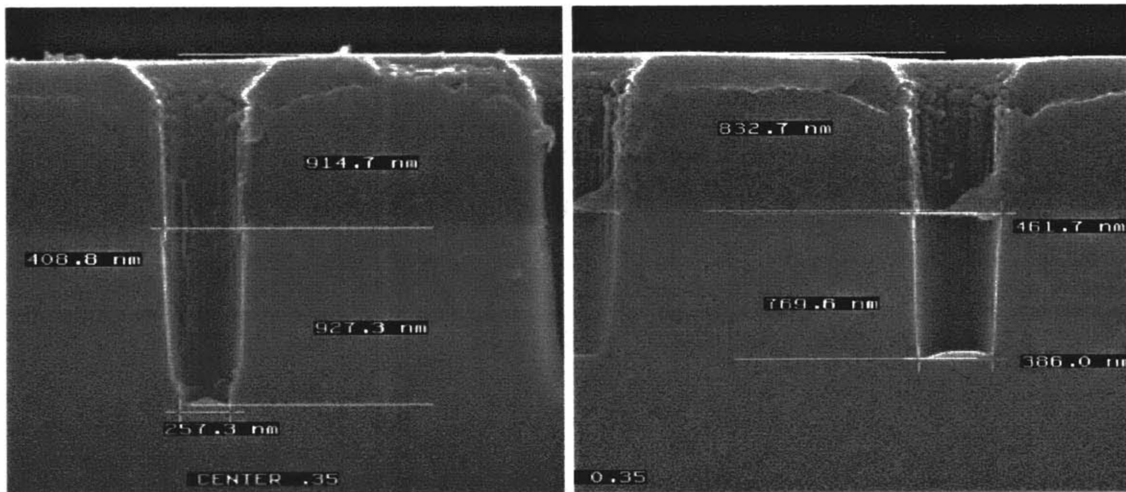

Figure 6.27: Hexafluoro-1,3-butadiene process condition F (left): 13 sccm etch gas flow/3.7 sccm O_2 flow, and G (right): 12 sccm etch gas flow/3.4 sccm O_2 flow; 0.35 μm nominal CD vias in center of wafer.

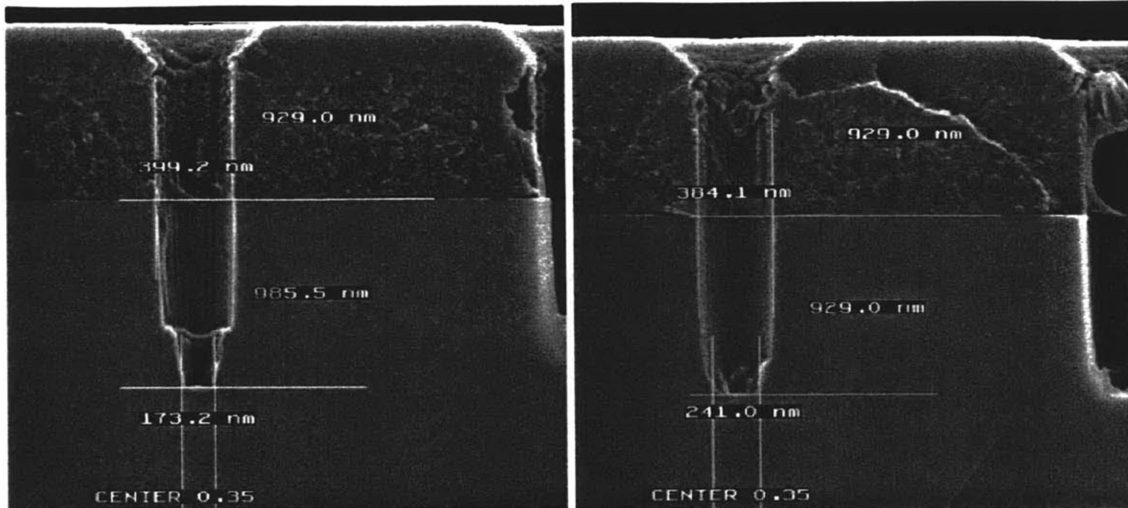

Figure 6.28: Hexafluoro-2-butyne process condition F (left): 13 sccm etch gas flow/3.7 sccm O_2 flow, and G (right): 12 sccm etch gas flow/3.4 sccm O_2 flow; 0.35 μm nominal CD vias in center of wafer.

6.2.2.4 c-C_5F_8, C_3F_6, and c-C_4F_8O Processes

The best c-C_5F_8 data point, as determined by overall process performance, is shown in Figure 6.29. This process condition (T) also had the best normalized emissions performance, generating 0.088 kgCE, a reduction of 72.3% compared to the C_3F_8 reference process. The corresponding normalized reduction, based on the center location via depth of 0.8976 μm, was 74.0% (0.098 kgCE/μm). The best C_3F_6 process, as determined by overall process performance, is shown in Figure 6.30. This process condition (P) resulted in emissions of 0.095 kgCE, a reduction of 69.9% versus the C_3F_8 reference process (corresponding to a normalized reduction of 72.4%, based on an center location etch depth of 0.9164 μm). The best C_3F_6 process, as determined by normalized emissions was process Q, which had higher etch rate (0.9980 μm center location etch depth) as well as lower emissions (0.087 kgCE, 72.4% reduction; 0.087 kgCE/μm, 76.7% normalized reduction). This process point, however exhibited a somewhat poorer profile than process P at the 0.35 μm center location.

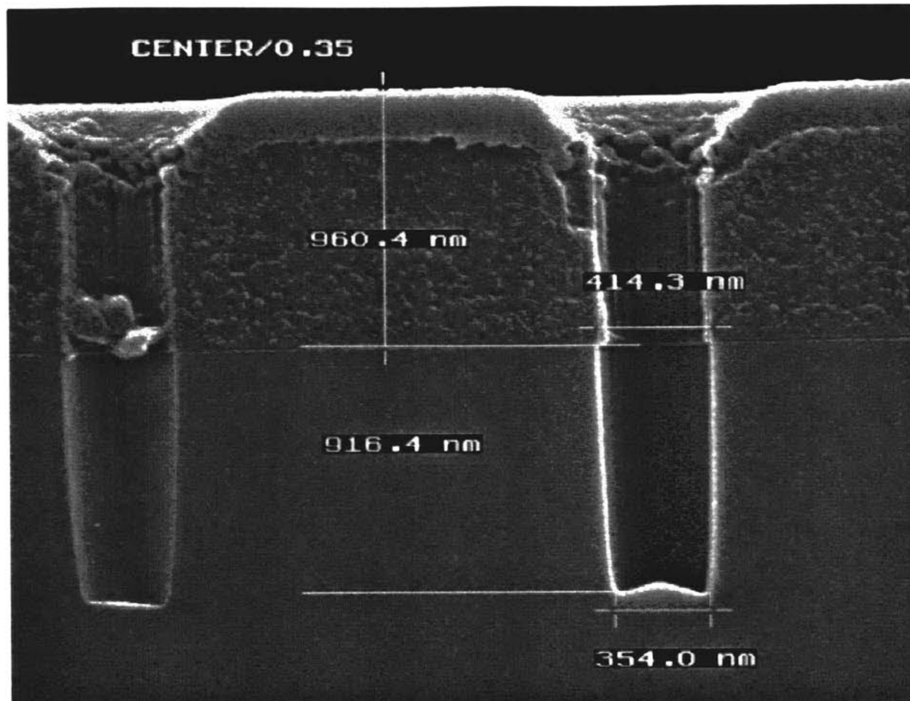

Figure 6.30: Best C_3F_6 process (process condition P): 12 sccm etch gas flow, 1100 W source power, 1400 W bias power, 0 sccm O_2, 120 s etch time, 0.35 μm nominal CD via in center of wafer.

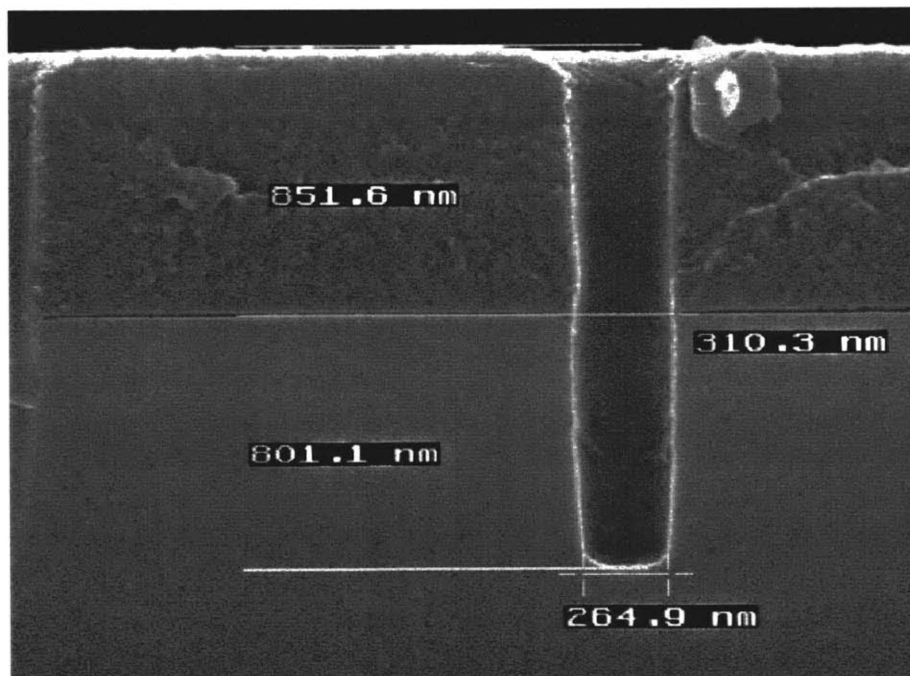

Figure 6.31: Best c-C_4F_8O process (process condition V): 14 sccm etch gas flow, 1000 W source power, 1000 W bias power, 0 sccm O_2, 120 s etch time, 0.35 μm nominal CD via in center of wafer.

6.2.2.5 Extended Etch Time Experiments

In the third stage of experiments, extended time (3 and 4 minute) etches were conducted with hexafluorocyclobutene (at process condition G), hexafluoropropene (at process condition P) and hexafluoro-1,3-butadiene (at process condition F and an F variant). The best performing extended etch was at the F variant condition (11.4 sccm etch gas flow, 1400 W source power, 1100 W bias power, 3.7 sccm O_2, 240 seconds etch time) with hexafluoro-1,3-butadiene. The via cross section for this is shown in Figure 6.32. This etch exhibits high selectivity with over 70% of the photoresist remaining after a 4 minute etch and a nominal aspect ratio of 5:1, based on a CD of 0.35 μm. Despite some bowing, which is likely due to charging/shadowing effects, and significant amounts of sidewall polymer, the corners of the via show no evidence of etch stopping, indicating that the etch may be extended to even longer periods of time. There is however some evidence of CD blowout. The other gases and conditions exhibited significant etch stopping at 4 minutes.

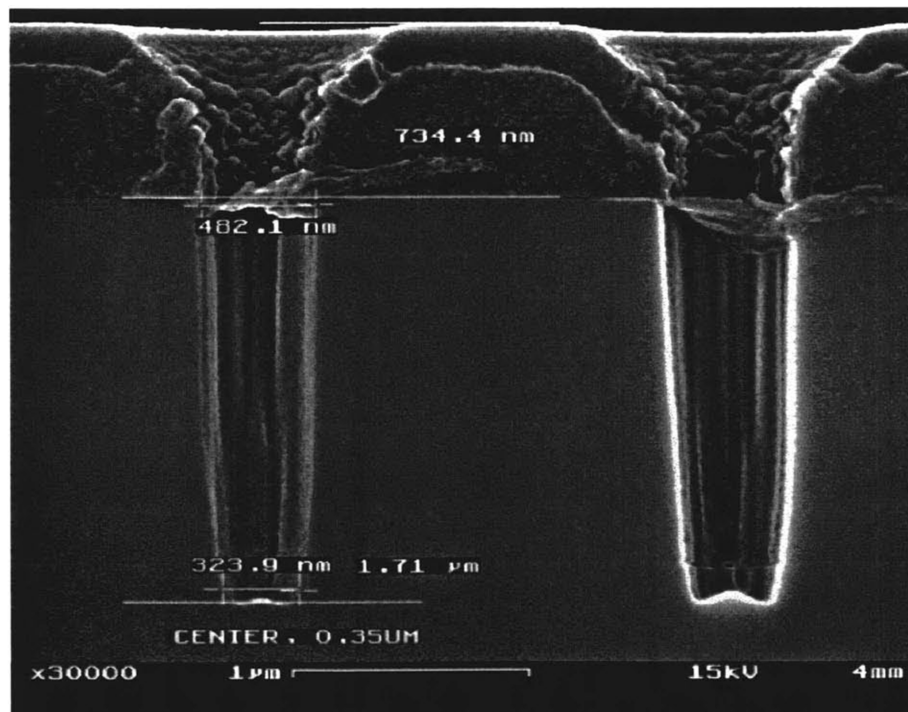

Figure 6.32: Best hexafluoro-1,3-butadiene extended etch process: 11.4 sccm etch gas flow, 1100 W source power, 1400 W bias power, 3.7 sccm O_2, 240 s etch time, 0.35 μm nominal CD via in center of wafer.

6.2.2.5 Extended Etch Time Experiments

In the third stage of experiments, extended time (3 and 4 minute) etches were conducted with hexafluorocyclobutene (at process condition G), hexafluoropropene (at process condition P) and hexafluoro-1,3-butadiene (at process condition F and an F variant). The best performing extended etch was at the F variant condition (11.4 sccm etch gas flow, 1400 W source power, 1100 W bias power, 3.7 sccm O_2, 240 seconds etch time) with hexafluoro-1,3-butadiene. The via cross section for this is shown in Figure 6.32. This etch exhibits high selectivity with over 70% of the photoresist remaining after a 4 minute etch and a nominal aspect ratio of 5:1, based on a CD of 0.35 μm. Despite some bowing, which is likely due to charging/shadowing effects, and significant amounts of sidewall polymer, the corners of the via show no evidence of etch stopping, indicating that the etch may be extended to even longer periods of time. There is however some evidence of CD blowout. The other gases and conditions exhibited significant etch stopping at 4 minutes.

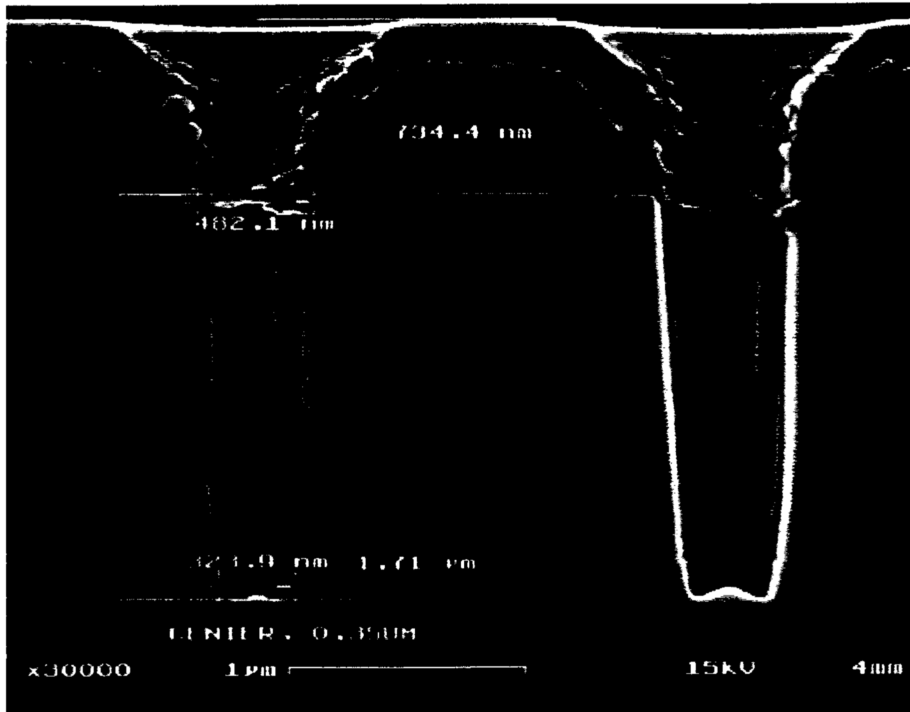

Figure 6.32: Best hexafluoro-1,3-butadiene extended etch process: 11.4 sccm etch gas flow, 1100 W source power, 1400 W bias power, 3.7 sccm O_2, 240 s etch time, 0.35 μm nominal CD via in center of wafer.

6.2.3 Conclusions

Several UFC gases as well as a fluorinated ether were examined for dielectric etch and global warming emissions performance. It was found that all of the gases are capable of etch performance comparable to that of a typical C_3F_8 process, while providing global warming emissions reductions. There is evidence that a large portion of the emissions from the C_4F_6 isomers is due to the formation of CHF_3, with the source of the hydrogen being the photoresist. Processes tuned to protection of the photoresist also achieve low emissions for these chemistries. One of the isomers of C_4F_6, hexafluoro-2-butyne, was found to have the best normalized emissions performance of all the gases examined, showing a reduction of 88.2% compared to a typical C_3F_8 process. The other C_4F_6 isomers (hexafluoro-1,3-butadiene and hexafluorocyclobutene) were also capable of global warming reductions in excess of 80%, while hexafluoropropene and octafluorocyclopentene exhibited emissions reductions greater than 70%. Processes based on octafluorotetrahydrofuran and octafluoro-2-butene also demonstrated some emissions reductions. An extended 240 second etch with hexafluoro-1,3-butadiene resulted in a 1.71 μm deep via with an aspect ratio of 5:1, very high selectivity to photoresist and no evidence of etch stopping.

The work described in this section was exploratory in nature, generating, in many cases, more questions than answers. Among the salient observations that were made – and which do not yet have conclusive explanations – is the fact that, from a process standpoint, the three isomers appear to offer very similar performance, while from an emissions standpoint, there appear to be some noticeable differences in the composition of the effluent.

Nevertheless, the unsaturated fluorocarbon concept-and feasibility study described in this section was considered to be among the most successful efforts within the framework of the alternative chemistries project. It demonstrated that good process performance and large emissions reductions were possible and that one was not necessarily a tradeoff for

the other. Future developmental work is planned for compounds belonging to the UFC family, including examining the selectivity of these chemistries to various common stop layers. Additionally, the opportunity to study isomeric molecules in this context will hopefully provide a means toward gaining greater understanding of how the structure of the fluorocarbon molecule affects both process performance and effluent composition.

References

1. R. Chatterjee, S. Karecki, L. Pruette, R. Reif, V. Vartanian, and T. Sparks, *Evaluation of Unsaturated Fluorocarbons for Dielectric Etch Applications*, in Proceedings of *Plasma Etching Processes for Sub-Quarter Micron Devices*, Honolulu, HI, G. S. Mathad, Editor, The Electrochemical Society Proceedings Series, **PV 99-30**, p. 251-262, Electrochemical Society, Pennington, NJ (1999).
2. L. Pruette, S. Karecki, R. Reif, L. Tousignant, W. Reagan, S. Kesari, and L. Zazzera, *Evaluation of C_4F_8O as an Alternative Plasma Enhanced Chemical Vapor Deposition Chamber Clean Chemistry*, in Proceedings of *Environmental Issues in the Electronics and Semiconductor Industries (Second International Symposium)*, Seattle, WA, L. Mendicino, Editor, The Electrochemical Society Proceedings Series, **PV 99-8**, p. 20-29, Electrochemical Society, Pennington, NJ (1999).
3. L. Pruette, S. Karecki, R. Reif, L. Tousignant, W. Reagan, S. Kesari, and L. Zazzera, *Evaluation of C_4F_8O as an Alternative Plasma Enhanced Chemical Vapor Deposition Chamber Clean Chemistry*, J. Electrochem. Soc., **147**(3), p. 1149-1153 (2000).
4. *Scientific Assessment of Ozone Depletion: 1998, Volume 2,* World Meteorological Organization, Global Ozone Research and Monitoring Project, Report No. 44 (1998).
5. S. Ibuka, *PFC Reduction Approach for Oxide Etchers*, in Proceedings of *U.S. EPA Global Semiconductor Industry Conference on Perfluorocompound Emissions Control*, Monterey, CA, Section 3 (1998).
6. S. Jimbo, M. Muto, K. Ito, and K. Goto, *C_5F_8 evaluation as an alternative gas to CF_4 using Chemical Dry Etch*, in Proceedings of *6th Annual International Semiconductor Environmental, Safety, and Health Conference*, Williamsburg, VA (1999).
7. Y. Matsushita, *EIAJ Presentation*, in Proceedings of *6th Annual International Semiconductor Environmental, Safety, and Health Conference*, Williamsburg, VA (1999).
8. O. Joubert, P. Czuprynski, F. H. Bell, P. Berruyer, and R. Blanc, *Analyses of the chemical topography of silicon dioxide contact holes etched in a high density plasma source*, J. Vac. Sci. Technol. B, **15**(3), p. 629-639 (1997).
9. S. K. Baldwin, R. Patrick, and N. Williams, *RF Peak Voltage Control at the Bias Electrode of Inductively Coupled Plasma Etchers for Improved Process Stability*,

in Proceedings of *Plasma Etching Processes for Sub-Quarter Micron Devices*, Honolulu, HI, G. S. Mathad, Editor, Electrochemical Society Meeting Abstracts, **PV 99-30**, p. 55-63, Electrochemical Society, Pennington, NJ (1999).

7. Summary and Recommendations for Future Studies

In the course of the work that had been described in the previous three chapters, a number of novel fluorinated chemistries had been evaluated as potential replacements for PFCs in dielectric etch applications. Both medium and high density plasma tools were employed as part of this work, with the bulk of the research effort being focused on high density tools. Throughout the course of these efforts, twin goals were pursued: substantial reductions in global warming emissions as well as viable process performance. PFC based reference processes were employed throughout this work as benchmarks for comparison with regard to both process and emissions data. Not all of the potential solutions that were examined bore fruit as credible replacement candidates. Some were found to provide good process performance, with only incremental emissions reductions. Others were found capable of substantial emissions reductions, but with significant difficulties being encountered from a process standpoint. However, as the project matured and greater understanding of plasma chemistry affecting both process and emissions performance was attained, the pathways leading toward solutions that could be potentially successful on both fronts began to manifest themselves. At the time of this writing, it is the author's opinion that successful alternative chemistry solutions for dielectric etch are within reach and that they can be implemented in manufacturing environments provided that process performance objectives continue to be congruent with emissions reductions, as had been shown to be possible in Section 6.2.

The present chapter will attempt to bring together some key lessons acquired through the studies discussed in Chapters 4 through 6. Section 7.1 will provide a summary of the experimental results. Section 7.2 will extract some general conclusions from this body of work and discuss their implications for future efforts in the area of new etch chemistry development. Finally, Section 7.3 will provide some comments on the state of alternative chemistry development today, along with some thoughts on recommendations for future work.

7.1 Summary of Results

A number of novel fluorinated compounds were examined as part of this work. These molecules belonged principally to three families of modified fluorocarbons: hydrofluorocarbons (HFCs), iodofluorocarbons (IFCs), and unsaturated fluorocarbons (UFCs). The project strategy began with the examination of the most conservative of these options (from a handling properties standpoint) – HFCs such as 2H-heptafluoropropane and pentafluoroethane, which, generally speaking, have low toxicity concerns, no corrosive properties, and, provided the number of hydrogens in the molecule is low relative to the number of fluorines, no flammability concerns. From an atmospheric properties standpoint, HFCs have significantly lower lifetimes than their fully fluorinated analogs and lower, but still sizeable, global warming potentials. Screening studies using HFCs in a medium density plasma etch tool had been carried out as part of the author's M.S. thesis research and have been discussed briefly in Section 1.2.2.1. In the present document, HFC studies in a high density plasma tool had been based on 2H-heptafluoropropane, whose selection for these tests had been based in large part on the earlier screening work, as well as the mixture of pentafluoroethane / 1,1-difluoroethane.

Good process performance, as measured by its behavior in a high aspect ratio oxide via etch process, was very readily attained with 2H-heptafluoropropane, with global warming emissions reductions on the order of 40-60% versus a PFC based reference process being reported (Sections 5.1, 5.2). These numbers, while encouraging for an initial effort to develop etch processes based on non-PFC chemistry, were deemed as an incremental improvement, well short of the 90% emissions reduction goal set for this project. The pentafluoroethane / 1,1-difluoroethane processes evaluated later in the same high density etch tool as part of a collaboration with DuPont Fluoroproducts proved capable of higher emissions reductions – up to ~75% – though not at the same level of process performance as those developed with 2H-heptafluoropropane, with etch stopping tendencies being seen across much of the process space examined (Section 5.3).

It had also been established fairly early on in the project that it is difficult to identify atmospherically reactive compounds for which that atmospheric instability is not accompanied by increased handling risks, *e.g.*, toxicity, flammability, or corrosivity. One of the few families of compounds which appeared to be a possible exception to the stability-reactivity tradeoff discussed in Section 2.1, was the IFC family, where a weak C-I bond made these substituted fluorocarbons readily photolyzed in the lower atmosphere. Thus, they were atmospherically quite reactive and possessed minimal long-term environmental impact. Yet, from a handling standpoint, IFCs were still relatively benign: non-flammable, non-corrosive, having higher toxicities than HFCs but still relatively low when compared to other compounds already being used in wafer fab operations. Indeed, from an emissions reduction standpoint, IFCs did perform better than HFCs, with reductions on the order of 80-90% being reported for both isomers of iodoheptafluoropropane in the initial HDP concept-and-feasibility study (Section 5.1) and results on the order of 80-85% being reported for the same compounds in the subsequent process development activity (Section 5.4). From a process standpoint, the initial medium density plasma tool screening study (Chapter 4) provided the first information that IFCs could be made to etch dielectric films at reasonable rates. In the HDP studies, however, while good etch rate and profile control could be achieved, one critical problem that emerged was poor selectivity to mask and stop layers. A detailed study of iodoheptafluoropropane HDP etch processes indicated that bombardment of the surface by energetic iodine ions was chiefly responsible.

The most promising results were obtained with the UFC family. As of this writing, only the pilot HDP study had been conducted. Yet, even in this study, data were obtained that indicated that good process performance could be *combined* with substantial emissions reductions. The most promising UFC compounds out of the set examined were the three isomers of C_4F_6. With these compounds, etch performance essentially matching that of the reference process was obtained, accompanied by emissions reductions around 85%. UFCs are more reactive than HFCs or IFCs. A number are flammable. Moreover, they tend to be more toxic than either of the previously explored families. The UFC study was significant because it was the first alternative chemistries study conducted within the

scope of the activities discussed in this document where process performance essentially matching that of the reference process was obtained on every metric tested thus far, *while* achieving significant reductions in global warming emissions. Presently, UFCs appear to be a very promising avenue for exploration. Because of their low F:C ratio, gases such as C_4F_6, moreover, appear to be well suited for applications where thinner resist layers make high mask layer selectivity a critical parameter.

In addition to the various modified fluorocarbons that have been discussed above, three other compounds have been evaluated in the various studies included in this document. The first of these was trifluoroacetic acid anhydride (TFAA), which was evaluated in the medium density screening experiments, but not in any of the later high density studies. TFAA was proposed as a potential etch and PECVD chamber clean solution by Schumacher, a division of Air Products and Chemicals, Inc. The etch behavior of TFAA looked promising enough in these early studies. However, concerns about its hygroscopic and hence potentially corrosive nature, particularly as it related to the potential for formation of trifluoroacetic acid in fab exhaust, came to weigh against the continuation of development activities with this compound.

Another hygroscopic gas that was proposed for evaluation in etch applications was oxalyl fluoride ($C_2O_2F_2$), manufactured by AlliedSignal, Inc. This compound was evaluated as part of the series of high density plasma studies that make up the bulk of this document. Because of its high oxygen and low fluorine content, it was not expected to be an effective etch gas for dielectric films masked with organic resists. Indeed, its oxide etch rate was slow, whereas its resist etch rate was unacceptably rapid, resulting in complete removal of 1 μm thick resist layers under almost all process conditions explored. However, this study proved of value in that it showed that the elimination of saturated CF_x grouping in a carbon and fluorine containing molecule can result in almost complete elimination of global warming emissions. Emissions reductions up to 95% were recorded under a range of conditions.

The third compound that was evaluated was octafluorotetrahydrofuran (c-C_4F_8O), a gas proposed by the 3M company as a potential new etchant for dielectric applications. c-C_4F_8O itself is quite stable atmospherically, believed to have atmospheric properties similar to those of c-C_4F_8. In a chamber cleaning study conducted by the author and his coworkers in collaboration with 3M, however, it was found that very high utilization efficiencies could be obtained with this compound, resulting in a significant reduction in global warming emissions relative to a PFC based chamber clean process (see Section 1.2.2.2). In the HDP etch tool where it was employed in an etch application, however, its utilization was only on the order of 87%, with emissions reductions relative to a PFC based reference on the order of 40%. Moreover, the presence of oxygen in a 1:4 ratio to carbon in the molecule proved to be excessive for maintaining the same high levels of resist selectivity that were readily achievable with UFC chemistries.

7.2 Conclusions Regarding Fluorocarbon Plasmas and Global Warming Emissions

Among the most significant strategy shifts that occurred in the course of the project was the decision to focus on fluorinated byproduct re-formation processes in the plasma as the area which needed the most understanding to achieve order-of-magnitude emissions reductions. Initial efforts focused heavily on the properties of the source gas molecule. This was not without reason, since, even in high density plasma tools, a substantial portion of the source gas is exhausted without being reacted (~20% in the Centura 5300 HDP, more in low density tools); not surprisingly, the use of a source gas with better atmospheric properties was found to make a significant impact on overall emissions. In the early studies, however, this impact was short of the desired order-of-magnitude reduction. For instance, the studies with H-substituted fluoroalkanes indicated that this impact was in the 40-70% range, generally speaking. Thus replacing a global warming fluorocarbon chemistry with one that was either less global warming or more completely utilized, while a useful first step, was only a partial solution to the problem.

In the course of the HFC and IFC high density plasma studies, it became apparent that, even with no contribution to global warming emissions from the source gas itself, high-GWP fluorocarbons (principally CF_4, CHF_3, and C_2F_6) were being emitted in still significant quantities. It was posited that saturated CF_x moieties within the parent molecule, *e.g.,* the trifluoromethyl radical (CF_3), played a key role in the formation of these species, through reactions such as the ones suggested by equations 5.2 through 5.4. The hypothesis was put forward that the elimination of these groups in the feed gas may lead to lower amounts of high-GWP fluorocarbons formed in the process.

Given that some of the best emissions reductions from realistic processes have been obtained with unsaturated fluorocarbons, specifically C_4F_6, it appears that the above hypothesis may have some validity. It is not clear at this stage, however, based on the limited data available from the UFC high density plasma study (Section 6.2), to what *extent* this hypothesis bears itself out. For example, in comparing emissions from the three C_4F_6 isomers at the same process conditions, one finds that similar overall levels of global warming emissions were found to be generated by hexafluoro-1,3-butadiene (CF_2=CF-CF=CF_2), hexafluorocyclobutene (c-C_4F_6), and, most interestingly, hexafluoro-2- butyne (CF_3-C≡C-CF_3), with the latter compound possessing terminal trifluoromethyl groups. If the re-formation process were dominated by gas phase reactions, the idea that the presence of terminal CF_3 groups leads to the formation of CF_4, CHF_3, and C_2F_6, would be intuitive. However, as will be discussed shortly, it appears to be the case that surface phenomena, in particular, surface reactions on the wafer, rather than on the process kit surfaces appear to dominate the re-formation mechanisms. In the C_4F_6 experiments presented in Section 6.2, there do exist noticeable differences between the emissions recorded from the three isomers (see Figure 6.24). Hexafluoro-2-butyne, in fact, does appear to produce larger amounts of C_2F_6 than the other two isomers under both flow conditions presented in Figure 6.24. However, it is by no means apparent that this also translates to higher levels of CF_4 and CHF_3 production; in fact, at the 12 sccm condition shown, the most dramatic difference between the three isomers is seen in the hexafluoro-1,3-butadiene data, where one observes a large increase in CHF_3 production (correlated with more resist erosion) at the expense of C_2F_4. Clearly, further work will

need to be carried out before these effects are fully understood. Moreover, if it is indeed the case that surface reactions dominate over gas phase phenomena in the formation mechanisms for CF_4, CHF_3, and C_2F_6, one may find that parameters such as the stoichiometry of the deposited fluoropolymer film, rather than the structure of the source gas molecule, may play the dominant role in general. One can argue that there is evidence of this in the C_4F_6 isomer process performance comparison, with process behavior for all three isomers being fairly similar at the same process conditions, despite some differences in effluent composition, suggesting that the process behavior may, in fact, be dominated by deposited film stoichiometry.

As had been pointed out in Section 5.4.3, there already exists some evidence that the wafer surface may play a disproportionately large role in influencing the composition and quantity of fluorocarbon emissions from the process. The 1-iodoheptafluoropropane and C_3F_8 experiments discussed therein indicated that the presence of resist or thick polymer deposits can significantly affect the process emissions versus the case when a bare Si surface is exposed to the plasma. A 1-iodoheptafluoropropane process run with a resist wafer produced measurable quantities of fluorocarbon byproducts. However, when the same process was run with a bare Si wafer, the levels of fluorocarbon byproducts emitted were dramatically reduced. However, in the C_3F_8 case, the emissions from the two types of runs (resist versus bare Si) were much more similar. This was attributed in part to the fact that, with the C_3F_8 process, a much thicker fluoropolymer layer was found to form *on the wafer* than was the case with the 1-iodoheptafluoropropane process under consideration. This, in turn, was posited to make the wafer surface appear similar to the plasma regardless of the type of substrate that was used in the C_3F_8 case.

Finally, it has also been observed that fluoropolymer deposits in the chamber, when cleaned by an O_2/Ar plasma during a post etch treatment (*in-situ* ash) or a preprocess step for the next wafer, tend to be removed primarily as CO, CO_2, COF_2, and HF with some SiF_4 also present. Since CO is non-global warming, CO_2 has negligible impact relative to perfluorocarbon species, and COF_2, HF, and SiF_4 are readily treated by existing acid gas scrubbers in the quantities in which they are emitted by etch processes, from an emissions

standpoint, the deposition of fluoropolymer layers within the chamber may actually be advantageous relative to their emission as fluorocarbon species during the etch itself. This statement, however, needs to be heavily qualified by the fact that excessive polymer formation in tools such as the Centura 5300 HDP is likely to be undesirable from a chamber stability standpoint, even if it was accompanied by good process performance.

7.3 Future Directions for New Dielectric Etchants

In this final section, a few concluding remarks regarding the future of alternative chemistry development will be made. Firstly, it is abundantly clear at this point in the MIT alternative chemistries project that certain tradeoffs regarding the reactivity of the molecule will need to be accepted if an attempt is made to employ fluorinated etchants that have desirable long-term environmental impact. Fluorinated molecules which have short atmospheric lifetimes and low or negligible global warming potentials will also tend to be more reactive. The unsaturated fluorocarbon family typifies this. This tradeoff is also evident in combinations such as the NF_3/hydrocarbon approach, which is being pursued concurrently with the UFC effort and which is beyond the scope of the present document. NF_3, despite its global warming properties, is not an inert compound, being a potent oxidizer and possessing some toxicity concerns. Hydrocarbons are, of course, flammable.

Secondly, it is an obvious point that nevertheless bear repetition that emissions improvements in an etch process are largely meaningless without the ability to meet process performance targets. The idea of developing new etch chemistries as drop-in replacements into existing etch processes is unlikely to be successful given the expense, in terms of both time and dollar cost, of requalifying production steps as complex as dielectric etch processes. Rather, it seems logical and, in fact, appropriate to attempt to introduce new etch chemistries with new process tools or, at least, into existing tools as new processes for upcoming technology generations as they enter development. This strategy, however, places even more emphasis on the importance of being able to meet already difficult performance targets. Fortunately, it appears to be the case that emissions

reductions and process requirements may be moving in convergent direction. There appears to be a trend within the dielectric etch process community to employ processes with increasingly lower F:C ratios in order to meet increasingly more stringent selectivity requirements. Compounds such as the various isomers of C_4F_6 may thus find themselves being desirable from a process standpoint, not only an emissions standpoint. If significant process advantage can be extracted from the use of novel chemistries, then alternative chemistries will be more likely to become a solution of choice for addressing the PFC emissions issue and may, in fact, come to coexist in fabs alongside end-of-pipe PFC abatement technologies which, in such a scenario, are likely to find greater applicability to addressing emissions from older tools / etch technologies.

Thirdly, it appears that a key focus in new chemistry development must be the generation of a better understanding of the processes that result in high-GWP byproduct formation. The same path is likely to also provide insight into mechanisms that affect process performance, the latter, of course, being likely to be relevant to the former and vice versa, especially if surface processes do, in fact, turn out to play a dominant role. In light of this, a greater emphasis on diagnostics is likely to emerge as a requirement. Plasma diagnostics such as optical emissions spectroscopy, appearance mass spectrometry, infrared laser absorption spectroscopy, etc. may need to be employed. Surface analysis techniques such as x-ray photoelectron spectroscopy are likely to play an even larger role than the one they played in the present studies. The use of extractive mass spectrometry in tandem with FTIR spectroscopy may also prove of value for purposes of closing materials balances in emissions calculations, particularly in the case of F_2, which is not detectable in the infrared. Additionally, the need for high process performance alongside large emissions reductions will probably become even more prominent than it has been to date, given the recognition that, to be successful, alternative chemistry processes will need to be high performance processes meeting next generation etch requirements.

Finally, the focus of the body of work being presented herein has been largely limited to silicon oxides as the principal dielectric material of interest. As of this writing, a number of new low-k dielectric technologies are fast approaching implementation in

manufacturing environments. Etch technologies for these new materials are presently being developed. Some being entirely organic in composition, will require oxygen based etch chemistries that are likely to have minimal impact in terms of global warming emissions. It is a fallacy to think, however, that, in the near future, all dielectric etch processes will rely on oxygen, rather than fluorine, based chemistries and that the issue of global warming emissions from etch applications will no longer be relevant. For many new dielectric materials are, in fact, silicon-carbon blends that will still require fluorinated etchants. Moreover, many of the more advanced porous dielectrics will, in fact, be silicon based again. Since the masking layers are likely to remain organic, the same central issue that has emerged out of the studies presented in this document will continue figure prominently in the future – namely, that the interaction between fluorine based etch chemistry and organic resist layers is of central importance in high-GWP byproduct formation. Even in high pressure regimes where gas phase phenomena play a more important role than they do in low pressure, high density plasma tools, the issue of high-GWP fluorocarbon formation in plasmas that contain carbon and fluorine will continue to be of importance.

In conclusion, the body of work presented in this document should perhaps best be viewed as attempt to bridge two fields – that of etch process development and that of effluent characterization. In the more advanced studies presented herein, an effort was made to provide as complete a picture of the etch process as possible, linking the feature-scale world of the wafer with the effluent characterization component whenever possible. Successful future efforts in the area of new chemistry development will need to expand the scope of their activities even further – through the use of more diagnostics and instrumentation – in order to meet the need for greater understanding of the plasma chemistry involved.

Appendix A FTIR Methodology

The use of Fourier transform infrared (FTIR) spectroscopy for effluent characterization has played a critical role within the context of the alternative chemistries project. This section will provide some practical notes on the implementation of this technique in characterizing the effluent from etch processes.

A.1 FTIR Instrument

Optics. The FTIR instrument used for most of the work discussed in this document was a Midac I-series optical bench. The setup discussed below, or a close derivative thereof, was used for all of the FTIR spectroscopy work, except that described in Sections 5.1 and 5.2. The bench was equipped with a glower element, whose output was collimated before being passed through the instrument's optics. A KBr beamsplitter was used. In order to protect it from moisture and to remove all H_2O and CO_2 content from the optical bench, the bench was purged with N_2, even when idle. The ability to purge the optical path of the beam is critical because the presence of ambient H_2O and CO_2 will result in interferences in parts of the mid-IR spectrum that contain features of many compounds of interest, including fluorocarbons.

1 cm and 10 cm FTIR cells were used, with the 1 cm cell being appropriate to the effluent concentrations seen in PECVD processes, whereas the 10 cm cell was employed in most of the etch experiments.* The cell windows were made of ZnSe, which offers superior resistance to chemical attack in corrosive environments compared to KBr – at a considerable premium in cost. Thus, in the configuration described here, ZnSe optics were used for the cell itself, which was routinely exposed to corrosive effluent streams and/or calibration mixtures, while KBr optics were employed for the beamsplitter, which was not exposed to corrosive environments. One advantage that KBr optics possess over ZnSe is a lower cutoff (400 cm^{-1} versus 650 cm^{-1}) in the IR spectrum. However, the 650-

* The 1.3 cm cell used with the Nicolet bench described in Section 5.1.1 was found to provide inadequate sensitivity for the concentrations seen in that study.

400 cm^{-1} region is, for the most part, of little interest in the type of spectroscopy work that was carried out, whereas resistance to corrosion is a critical need, necessitating the use of ZnSe optics for the cell windows.

The detector used in this configuration was a liquid nitrogen cooled MCT (mercury cadmium telluride) detector. It is recommended that, after several years of use, the detector be serviced, namely that its seals be replaced and that it be pumped down to restore its vacuum integrity. The resolution used for all references and all data collected was 0.5 cm^{-1}.

The spectral range used for data collection was generally 4600 cm^{-1} to 400 cm^{-1}. This was done for consistency with library reference files that were occasionally employed in the earlier work and which were at times collected on instruments with KBr optics. However, in general, the use of library references for quantitative work and, in fact, the use of *any* reference spectra generated on instruments other than the one being used for data collection is *strongly* discouraged, due to significant variation between instruments. In one exercise, CF_4 spectra collected on a 10 cm cell in two nearly identical Midac I-series instruments were compared. See Figure A.1. Within the linear concentration range for CF_4 (approximately 0.02% and below, see Figure A.1b) differences of up to 11.4% in feature area and 17.3% in feature height were recorded for the spectral region defined by 1350-1200 cm^{-1}. Equally important is the need for generating new reference spectra for all compounds of interest if any major adjustments are made to the instrument's optics or detector. Indicative of this was another exercise, in which CF_4 spectra collected on the same I-series optical bench before and after an overhaul of the optics and detector assembly were compared. See again Figure A.1. Differences of up to 2.5% in feature area and up to 21.7% in feature height for the region defined by 1350-1200 cm^{-1} were recorded. These differences translated to a discrepancy of approximately 27% in calculated concentrations of CF_4 when the reference spectra in question were employed within an actual FTIR analysis method.

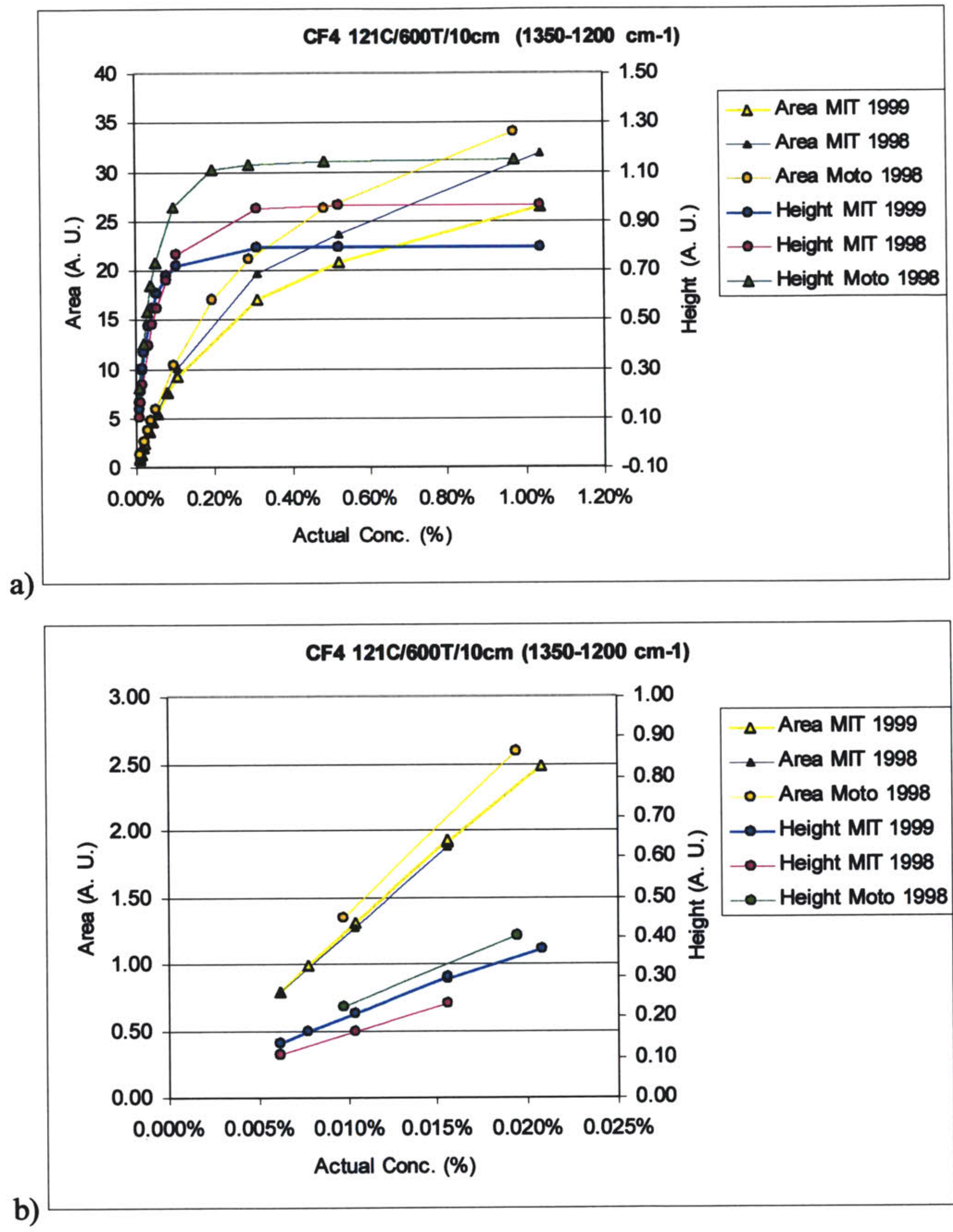

Figure A.1: Comparison of CF_4 peak areas and heights taken on two Midac I-series instruments and on the same Midac I-series instrument at different times – a) entire concentration range up to 1% (including saturation range), b) linear concentration range only.

Sampling. Except as noted in the text, all data in these studies were collected at 121 °C (250 °F) and 600 Torr. It is important to sample at elevated temperature when gases such as HF are involved due to unacceptably high line losses often encountered with HF in particular at ambient temperatures. The value 121 °C was chosen because it is a standard

value used for elevated temperature references in spectral collections. Even though most spectral libraries choose to present their references at 760 Torr (1 atm), 600 Torr was chosen as the sampling pressure for work in this project. Some FTIR sampling methodologies advocate attempting to sample from tool exhaust at ambient pressure, which tends to be slightly sub-atmospheric. In these cases, the assumption is made that the sampling cell is at ~1 atm and no attempt is made to regulate the cell pressure. The author and his coworkers, however, decided, however, that this methodology was problematic because it was susceptible to being influenced by variations in tool exhaust pressure, which is not regulated in any way. 600 Torr was chosen because it allowed for accurate control of cell pressure at a value that was well below any range of variation encountered in process tool exhaust.

In the configuration being described presently, the cell pressure was regulated with two metering valves placed in parallel, just downstream of the cell itself (one for coarse and one for fine adjustment). Given well chosen valve combinations, pressure can be maintained at 600 Torr ± 0.5 Torr with little difficulty during a typical data collection run lasting several minutes. An additional (coarse) metering valve was placed just upstream of the cell for the purpose of regulating flow through the sampling loop, if necessary. Typical flows were on the order of several slm (standard liters per minute). It should be pointed out that the flow rate through the sampling loop does not affect the concentrations measured by the instrument, whereas cell pressure and cell temperature control is critical. It is, however, generally preferable to use higher flows through the sampling line, if possible. This is because using higher flows makes it easier to stabilize the pressure in the cell (because of the higher turnover rate and hence quicker response time). Too high a flow, however, can also be problematic in that it will tend to cool the heated line and cell, in which case, the heating elements may not be able to maintain the target temperature. Typically, sampling line flows between ~3 and ~15 slm have been found to be acceptable.

A baratron or convectron gauge capable of operating at elevated temperature was placed either directly on a port on the cell or on a tee nearby. The cell, the sampling line (3/8" or

1/4" Teflon), as well as the pressure transducer were all heated to 121 °C. The pressure transducer was heated to order to maintain accuracy in the pressure measurement. The sample line was heated in order to prevent line losses in the case of reactive compounds as well as to ensure that the sample entering the cell was already at the desired temperature. Teflon sampling lines ranging from 6 ft to 25 ft in length were employed at various times in the project. The remaining portions of the sampling loop were constructed of stainless steel.

A typical pump purge through the process tool roughing pump was 45 slm. Some methodologies advocate calculating this purge rate by flowing a known quantity of gas through the system and measuring its concentration. This was, in fact done as part of the work discussed in Section 5.1. Later studies, however, used a 100 slm MFC (mass flow controller) on the nitrogen supply to the pump to regulate this flow, which *significantly* improved overall data accuracy.

Software. In most cases, Galactic Grams/32 v. 4.11 was used for spectral analysis and reference spectrum collection, whereas Midac AutoQuant v. 3.0 or 3.1 was used for process data collection and building of analysis methods / quantitation.

A.2 Calibration

Proper calibration procedures, *i.e.* the generation of reference spectra for each compound to be included in a data collection method, were critical for the methodology to yield accurate results. Dynamic, rather than static, calibration was employed. The advantages of using dynamic dilution versus relying on a partial pressure based static setup are that dynamic reference generation resembles the actual sampling environment and that, because the references are being generated at the pressure at which the sampling will occur, one does not need to concern oneself with effects such as pressure broadening, etc.

1% (nominal) certified mixtures of the analyte of interest in ultrapure nitrogen were used for all reference standards. (Nitrogen, being a homonuclear diatomic molecule, does not

absorb in the mid-IR region.) The same pressure and temperature conditions as those to be used for the data collection were employed. A calibration manifold consisting of two MFCs and one MFM (mass flow meter) downstream of the two MFCs was used. The sizes of the MFCs were 500 sccm for the 1% mix and 5000 sccm for the dilution N_2. (typically Grade 5.0 (99.999%) N_2 from a cylinder source). The MFM was employed in order to provide a check on the accuracy of the MFC flow readings. The MFCs and MFM had metal, rather than elastomer, seals for compatibility with corrosive materials. All three mass flow instruments used a default conversion factor of 1, *i.e.,* were calibrated for nitrogen. The reason for using 1% mixtures is that, at such a level of dilution, one need not be concerned about the accuracy of the MFC conversion factor used for the gas, which would be an issue if pure material (with a potentially unknown MFC factor were to be used). This is particularly important when working with gases for which the MFC conversion factor relative to nitrogen has not been published or when working with materials with high boiling points (which, if supplied undiluted, might cause flow problems in large MFCs). Another reason is that, as a practical matter, in a 10 cm cell, concentrations greater than ~1% or a fraction thereof tend to result in nonlinear behavior *i.e.,* saturation (producing deviation from Beer's law). In general, the point at which one enters into a nonlinear regime in the signal versus concentration relation varies. It depends on the length of the cell, on the absolute intensity of the glower being used at the wavelength of interest, on the absorbance factor of the compound of interest at that wavelength, and (in practice) on the setup of the particular optical bench being used.

A typical multipoint calibration procedure may involve 12 or 15 settings, ranging from 1% (10000 ppm: 500 sccm mix, no dilution N_2 flow) down to 0.006% (60 ppm: 30 sccm mix, 4970 sccm dilution N_2 flow). Typically, 2 or 3 samples are collected at each setting to verify the stability of the concentrations being measured. In the case of gases that are known to exhibit significant line losses (*e.g.,* HF)[†], line passivation is carried out prior to

---

[†] Corrosive gas mixtures, *e.g.,* COF_2, SiF_4, and (especially) HF, need to be supplied in nickel-lined cylinders to minimize sample loss due to wall reactions. Ordinary carbon steel cylinders are entirely inadequate in this role. Even when packaged properly, standards of COF_2 and SiF_4 should be recertified prior to each usage if it is more than several months after the initial assay. As an indication of the amount of sample loss that can be expected, a COF_2 standard (packaged in a nickel lined cylinder) that was initially

reference generation. Additionally, more samples are taken at each setting; the height and area of a large feature in the compound's spectrum are monitored. Typically, stability to within ±1% in both feature height and area is sought before changing flows and moving to the next setting.

A.3 Beer's Law and Pressure / Temperature Scaling

In a *linear* concentration regime, the absorbance signal (Y), that is to say the height or area of a given peak, is directly proportional to the *number of molecules of the compound of interest in the optical path* (N). N is proportional to the concentration of the compound in the flow stream (c) and the pressure of the sample (P). At a given pressure, N, hence Y, is also inversely proportional to the temperature of the sample in kelvin (T) (because PV = nRT, and N, the number of molecules of the analyte of interest in the optical path, is just a fixed fraction of n, the total number of molecules in the cell). *I.e.*, the same static gas sample, starting at 1 atm, heated, for example, from 25 °C (298 K) to 121 °C (394 K) will provide the same peak areas (even though it will be at a much higher pressure: 760 Torr × (394/298) = 1004 Torr) because the number of molecules in the cell is the same.

Scaling of reference spectra. To correct for small differences in sampling temperature and/or pressure, one may scale raw spectral data (peak height or area). Consider a reference spectrum generated from a flow containing a fixed percentage of some gas in nitrogen at an actual pressure other than the desired nominal pressure (600 Torr) and some temperature T, which results in some N_{actual}, which is proportional to some signal Y_{actual}. In defining an analysis method that is to make use of this reference spectrum, one needs to scale the concentration value appropriately. To do this, one must calculate how much of the gas (in ppm) this signal would represent *had it been taken at 600 T:*

$$Y_{actual} = Y_{nominal} \text{ (by definition),}$$

assayed at 0.999% was found to degrade to 0.92% after approximately 2.5 years. HF standards, on the other hand, even when packaged properly in nickel lined cylinders, must be used within weeks of the initial assay.

$$\text{hence, } N_{actual} = N_{nominal}$$

Since N is proportional to $c \times P \times 1/T$, for the same T:

$$c_{actual} \times P_{actual} = c_{nominal} \times P_{nominal},$$

$$c_{nominal} = c_{actual} \times (P_{actual}/P_{nominal}),$$

where c is the concentration (in ppm). If the temperatures are different, this becomes:

$$c_{nominal} = c_{actual} \times (P_{actual}/P_{nominal}) \times (T_{nominal}/T_{actual}), \qquad \text{(A.1)}$$

where $T_{nominal}$ is the desired sampling temperature in kelvin (*e.g.,* 121 °C = 394 K). Thus a signal referenced as "100 ppm-m at 760 Torr" represents the same number of molecules in the path as 126.7 ppm-m at 600 Torr ("ppm-m" being the "optical depth" or the pathlength-concentration product, where the pathlength is simply the length of the cell, in meters).

Scaling of concentration data. Suppose one has obtained some ppm value measured at some pressure P_{actual}. What is needed for further calculations is not this value but the actual percentage of the total flow (which is known and which to first order is defined to be the purge flow) that can be assigned to the compound of interest, so that one can then express the amount of that compound being emitted in sccm, moles, grams, etc. In the configuration being discussed, the software was not provided with actual pressure or temperature data, hence all recorded concentrations were calculated *as if the data had been taken at 600 T*. That is, the signal intensity was related to ppm using the 600 Torr reference spectrum for that compound with no additional adjustment. Thus the concentration value provided was $c_{nominal}$ ($c_{600\ Torr}$), not c_{actual}. To obtain c_{actual}, one writes:

$$c_{actual} = c_{nominal} \times (P_{nominal}/P_{actual}).$$

For different temperatures, this becomes:

$$c_{actual} = c_{nominal} \times (P_{nominal}/P_{actual}) \times (T_{actual}/T_{nominal}). \qquad \text{(A.2)}$$

Thus a signal recorded by software set up for sampling at 600 Torr which is calculated to correspond to 1000 ppm, represents the same number of molecules in the path as 1034.5 ppm of the compound at 580 Torr.

A.4 Analysis Methods

A number of points are useful to keep in mind when creating analysis methods, whether in AutoQuant or in other software. The following procedure is a step-by-step protocol developed for method generation using Midac AutoQuant 3.x software. Many of the items below are specific to this software. However, many concepts (ghost checking, linearity determination) are applicable generally.

1). Verify actual concentrations for the calibrated standards used from Certificates of Analysis.

2). Create spreadsheet plotting area and height of major features against actual concentration and determine the linear range for each compound; select file to use as primary reference (typically the highest concentration that is still linear, for best signal-to-noise).

3). Pull up spectra for each compound at all concentrations taken in Grams, determine regions in which features appear. It is important to locate all features, even small ones that are not going to be used for quantitation, because those features need to be flagged as interferents for other compounds in the same region.

Issues at high concentrations:

If there is any question as to the extent of the linear regime, the 0.35-or-less height rule is usually reliable for spectra collected on Midac instruments.

Additionally, an easy linearity verification can be made by overlaying a feature at all the concentrations used and matching the shape; if the shapes do not match, do not use that feature at that high a concentration for a single-spectrum reference.

Issues at low concentrations:

Ensure that a feature intended to be used for quantitation as part of a multi-spectrum reference is visible at all concentrations to be used.

ZnSe transmission cutoff:

Avoid using very sharp apparent features whose centroids fall below 700 cm^{-1}. For small features, verify whether a given apparent feature is in fact a peak or merely an instrumental artifact, by comparing with another reference, preferably one taken on a different instrument or a library reference.

4). Pull up representative data spectra in Grams and check for presence of compounds other than those for which references are available.

5). Create method; Ppm-m product = cell length (m) × concentration (ppm) at $T_{nominal}$ and $P_{nominal}$ (see "Scaling of reference spectra" above). An AutoQuant limitation: filenames must be unique, because they are eventually saved in the same method directory. (Create a separate directory in which to store appropriately renamed copies of the files to be used. Preserve 8.3 filename format.)

1 - enter all compounds into method;

2 - specify all spectrum files for each compound; for compounds with multiple spectra, start with upper end of linear range and add higher concentration spectra as necessary to cover desired range; set lowest concentration (upper end of linear range) as "Primary";

3 - specify ppm-m product for each spectrum file;

N.B.: if a given reference spectrum is not at 121 °C, 600 Torr (in this case) *and* these default values for Pressure and Temperature will be entered for each compound (see item 6 below), the ppm-m product should be scaled accordingly: *i.e.,* if the pressure at which the sample was taken was different than 600 Torr, then the signal intensity in the given spectrum would correspond to (P_actual/600)*nominal_ppm-m; the inverse holds true for temperature (in kelvin). However, as a rule of thumb, spectra that have been taken within ± 2 T of 600 Torr do not require scaling because the associated error is very small (0.33%).

A preferable scaling method (and, in theory, one equivalent to scaling the ppm-m product) is the use of actual temperature and pressure readings under which the references were taken for item 6 below. However, a limitation which affects methods using multiple spectra for a single compound is that AutoQuant only allows a single pressure/temperature value for all spectra for a given compound. (*I.e.*, if one is using three CF_4 spectra taken at 599, 598, and 601 T, one cannot specify all those values.)[‡]

4 - define regions for each compound; use all regions identified, except those that are so small that they are difficult to distinguish from baseline noise;

5 - define parameters for method (*e.g.,* cell path = 0.1 m, range = 600-4600 cm^{-1}, zoom window = 600-1400 cm^{-1});

6 - for each compound, under "Edit…", enter the pressure and temperature at which the spectrum was collected; if all spectra for a given compound have been taken at the same pressure and temperature or if the method uses only single spectrum references for each compound, one can specify the actual pressure/temperature at which a given compound was collected instead of using the global default values (which were 121 °C and 0.7894737 atm (= 600 Torr) in these studies);

6). In "Setup", enable "Store Temperature and Pressure". Under the setup for that feature, select "Use Default Value" for both. (*e.g.,* 121 °C and 0.7894737 atm (= 600 Torr))

7). Enable temperature and pressure adjustments in the Method Editor if one anticipates specifying a different pressure/temperature for the data than the pressure/temperature under which the references were collected.

8). Calibrate method.

9). When analyzing data, if one desires to adjust the data for pressure/temperature, select "Create Temp. & Pres. Adjusted Conc. Set" It is possible to specify different default values for each dataset from those entered under 6). above.

10). If one wants to use pressure/temperature adjustment, after AutoQuant is done displaying the concentrations, select "Temp. & Pres. Adjusted Conc. Set" under "Result Set"

N.B.: If all pressure/temperature values used are defaults, results will be numerically identical with and without pressure/temperature adjustment, except for trivially small rounding errors.

11). Run method on spectra with known compounds to check for "ghosts"; an easy way to do this is to simply open the method files directory created above and check the reference files themselves. Ignore ghosts in files that have higher concentrations than what is covered by the method. However, identifying which compounds can appear as ghosts, even in this case, is useful for troubleshooting later.

12). Run method on data files; verify that all concentrations reported for a given compound fall below the maximum concentrations used for that compound in the method. If not, the method will need to be revised so that it brackets the range of interest.

Important point: the number of submethods is the product of the number of files used for each compound. *I.e.,* there will be a separate submethod corresponding to *each* linear combination of reference files. *E.g.,* a method with 1 C_3F_8 file, 1 CHF_3 file, 4 CF_4 files, and 5 HF files will have 20 submethods. On a 166 MHz Pentium MMX system with 80 MB RAM, 32 submethods work reasonably well (method compilation takes about a minute), but 64 submethods result in unacceptable performance. On a 266 MHz Pentium II system with 128 MB RAM, 384 submethods work reasonably well (method compilation takes several minutes).

---

‡ In light of this limitation, and since all spectra were usually taken within 2 Torr of 600 Torr, default values of 121 °C and 600 Torr were typically used everywhere in the methods used in these studies.

Appendix B FTIR Spectra and Calibration Data

Appendix B provides representative spectra for numerous compounds of interest in this document. All spectra were collected at 600 Torr, 121 °C, using a ZnSe cell on a Midac I-series optical bench. The resolution of all references provided is 0.5 cm^{-1}.

The following families of compounds are represented in this appendix: perfluorocarbons (Section B.1), hydrofluorocarbons (Section B.2), iodofluorocarbons (Section B.3), unsaturated fluorocarbons (Section B.4), hygroscopic gases (Section B.5), hydrocarbons (Section B.6), and several other compounds (Section B.7). Except in the case of pentafluoroethane (C_2F_5H) and 2H-heptafluoropropane (2H-C_3F_7H), the spectrum selected for each compound is the spectrum for the highest concentration that is still in the linear region.

B.1 Perfluorocarbons

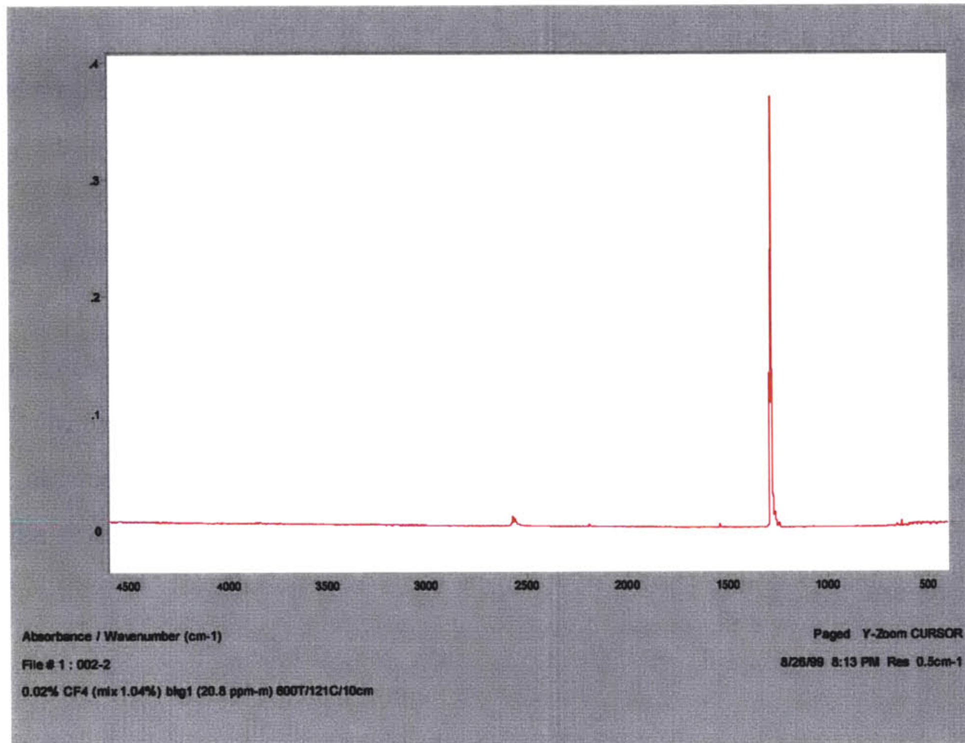

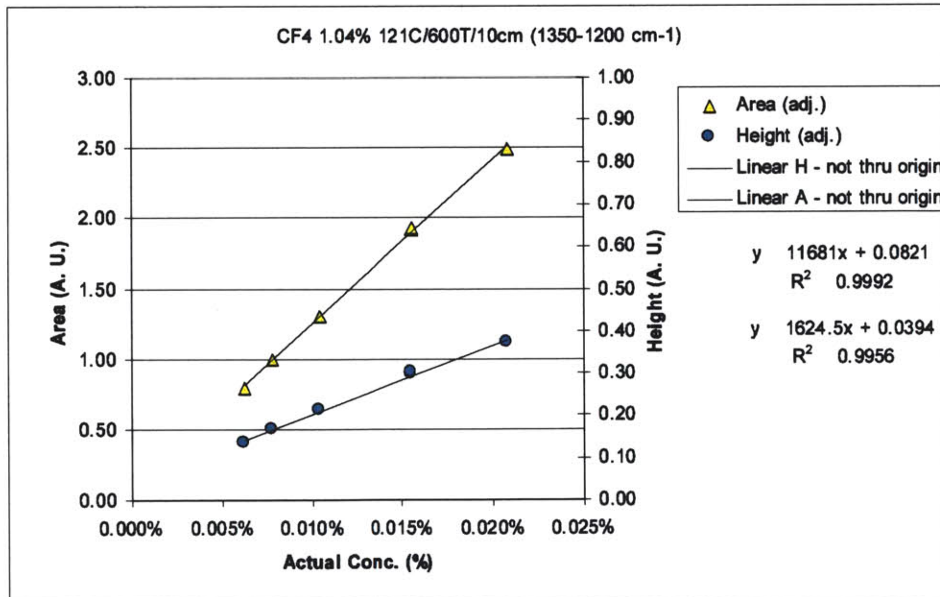

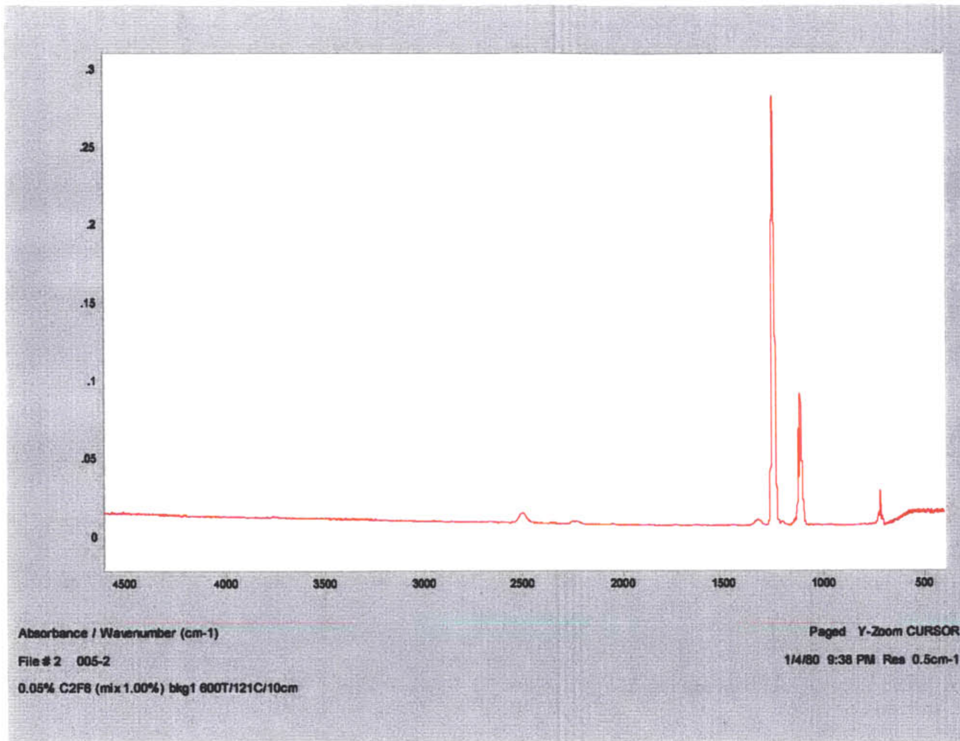
.3
.25
.2
.15
.1
.05
0
4500
4000
3500
3000
2500
2000
1500
1000
500
Absorbance / Wavenumber (cm-1)
Paged Y-Zoom CURSOR
File # 2 005-2
1/4/80 9:38 PM Res 0.5cm-1
0.05% C2F6 (mix 1.00%) bkg1 600T/121C/10cm

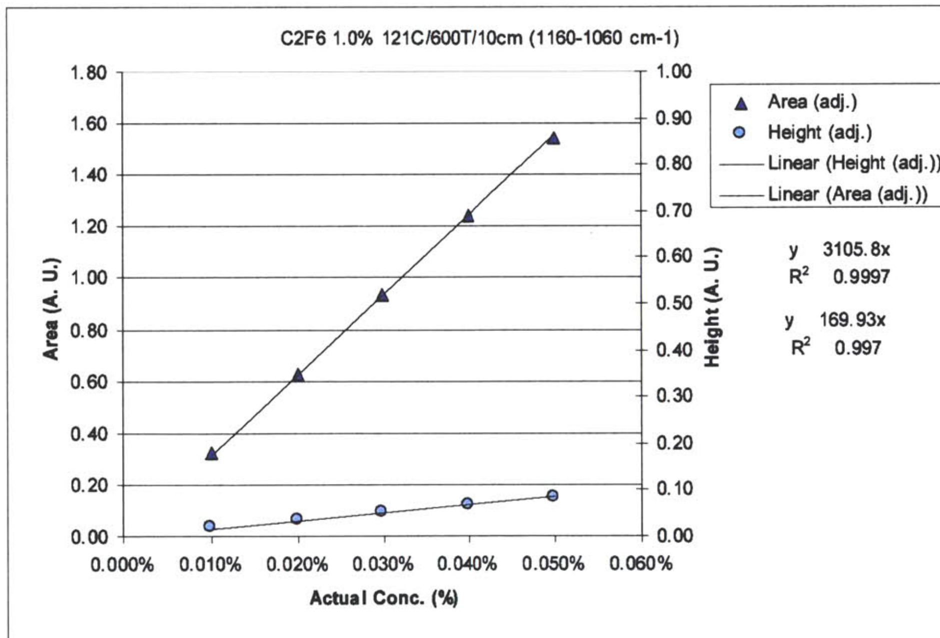
C2F6 1.0% 121C/600T/10cm (1160-1060 cm-1)
Area (A. U.)
1.80
1.60
1.40
1.20
1.00
0.80
0.60
0.40
0.20
0.00
Height (A. U.)
1.00
0.90
0.80
0.70
0.60
0.50
0.40
0.30
0.20
0.10
0.00
0.000%
0.010%
0.020%
0.030%
0.040%
0.050%
0.060%
Actual Conc. (%)
Area (adj.)
Height (adj.)
Linear (Height (adj.))
Linear (Area (adj.))
y 3105.8x
R2 0.9997
y 169.93x
R2 0.997

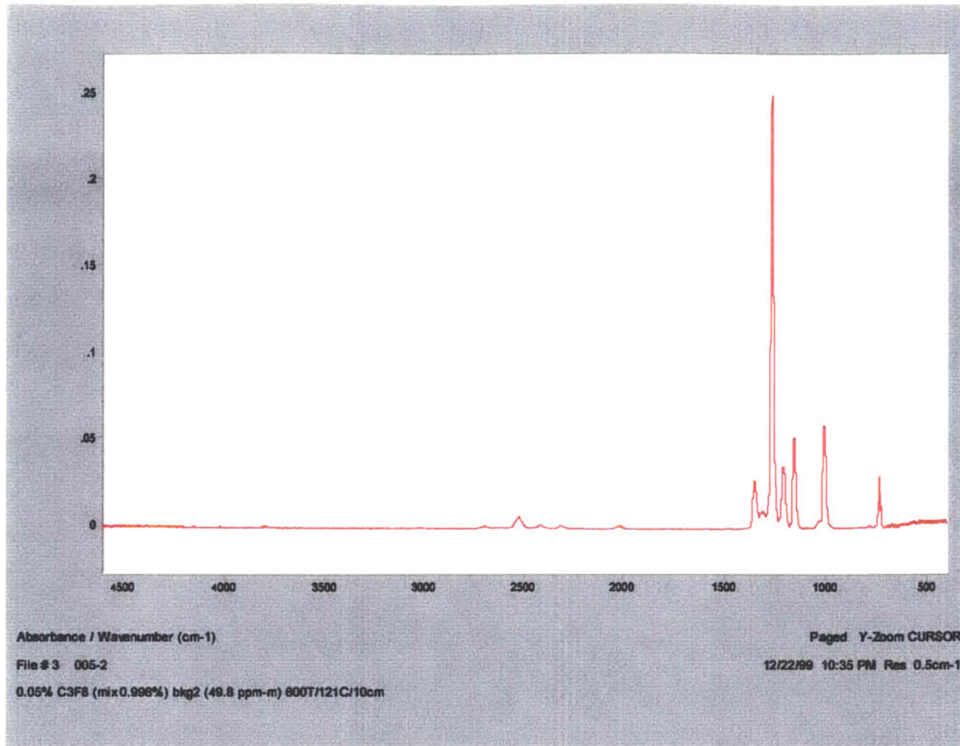
.25
.2
.15
.1
.05
0
4500
4000
3500
3000
2500
2000
1500
1000
500
Absorbance / Wavenumber (cm-1)
Paged Y-Zoom CURSOR
File # 3 005-2
12/22/99 10:35 PM Res 0.5cm-1
0.05% C3F8 (mix0.996%) bkg2 (49.8 ppm-m) 600T/121C/10cm

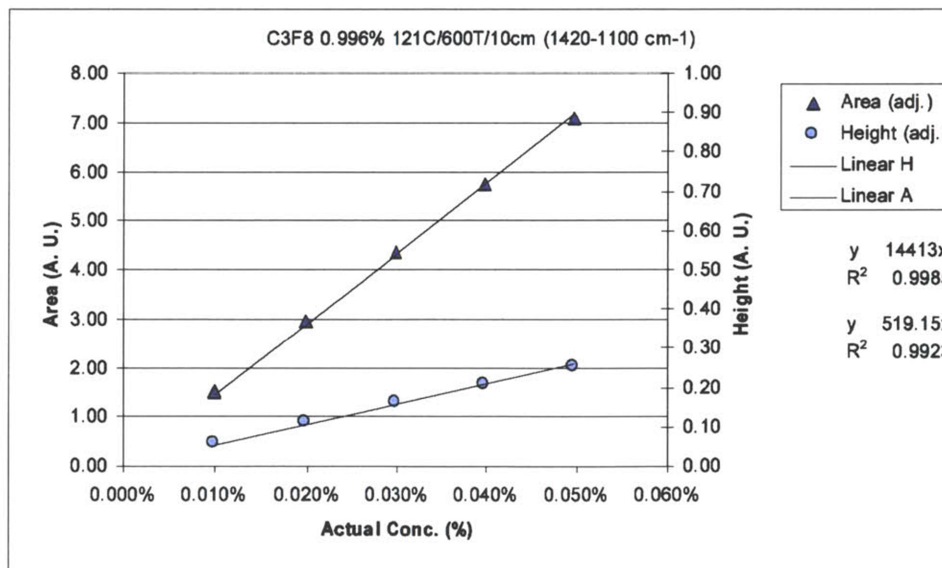
C3F8 0.996% 121C/600T/10cm (1420-1100 cm-1)
Area (A. U.)
8.00
7.00
6.00
5.00
4.00
3.00
2.00
1.00
0.00
Height (A. U.)
1.00
0.90
0.80
0.70
0.60
0.50
0.40
0.30
0.20
0.10
0.00
0.000%
0.010%
0.020%
0.030%
0.040%
0.050%
0.060%
Actual Conc. (%)
Area (adj.)
Height (adj.)
Linear H
Linear A
y 14413x
R² 0.9985
y 519.15x
R² 0.9923

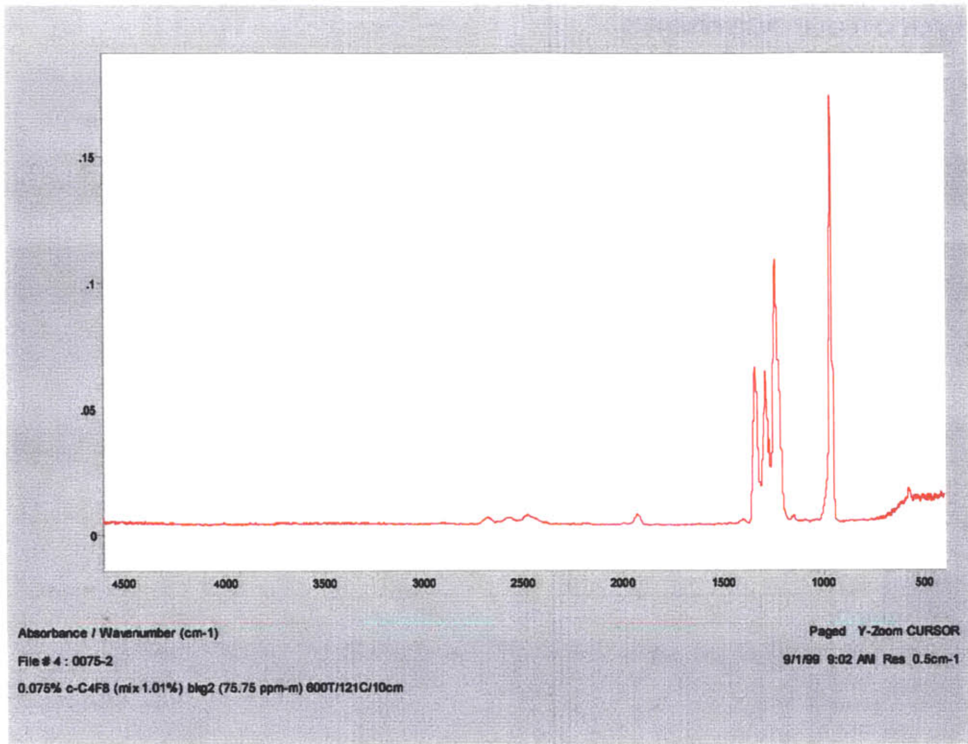
.15
.1
.05
0
4500
4000
3500
3000
2500
2000
1500
1000
500
Absorbance / Wavenumber (cm-1)
File # 4 : 0075-2
0.075% c-C4F8 (mix 1.01%) bkg2 (75.75 ppm-m) 600T/121C/10cm
Paged Y-Zoom CURSOR
9/1/99 9:02 AM Res 0.5cm-1

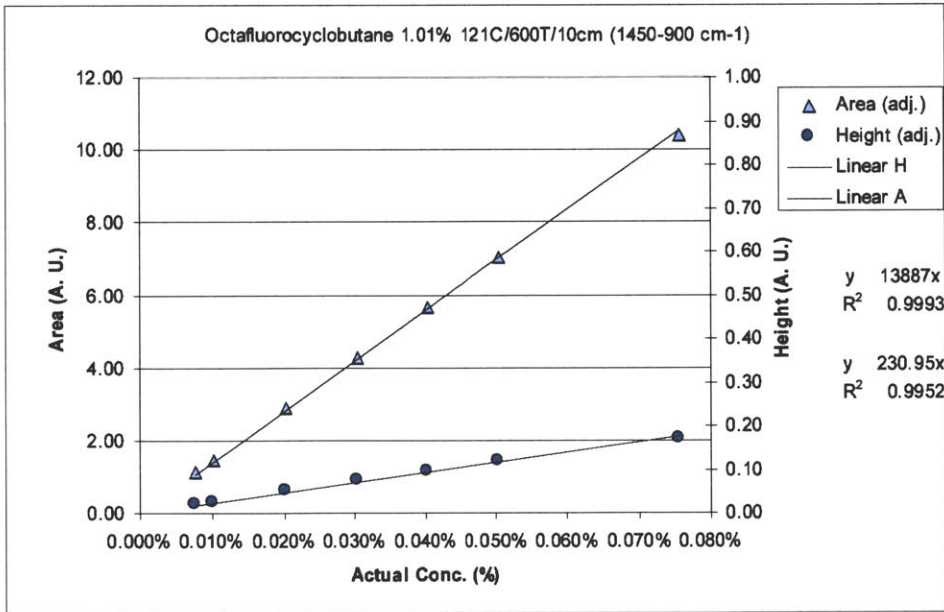
Octafluorocyclobutane 1.01% 121C/600T/10cm (1450-900 cm-1)
Area (A. U.)
12.00
10.00
8.00
6.00
4.00
2.00
0.00
Height (A. U.)
1.00
0.90
0.80
0.70
0.60
0.50
0.40
0.30
0.20
0.10
0.00
0.000% 0.010% 0.020% 0.030% 0.040% 0.050% 0.060% 0.070% 0.080%
Actual Conc. (%)
Area (adj.)
Height (adj.)
Linear H
Linear A
y 13887x
R^2 0.9993
y 230.95x
R^2 0.9952

B.2 Hydrofluorocarbons

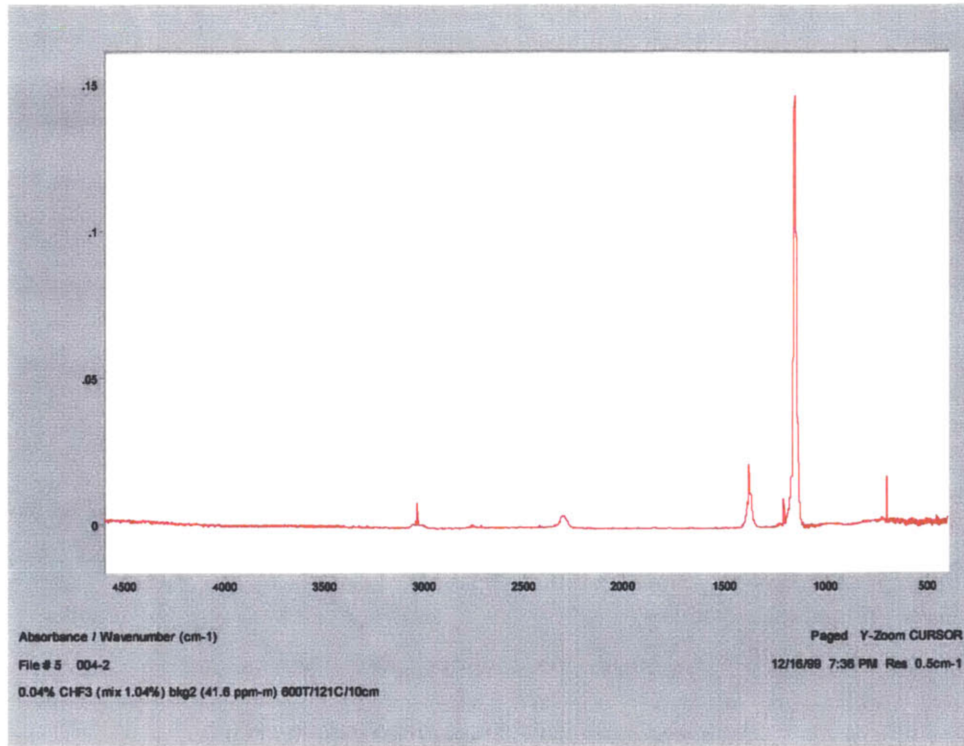

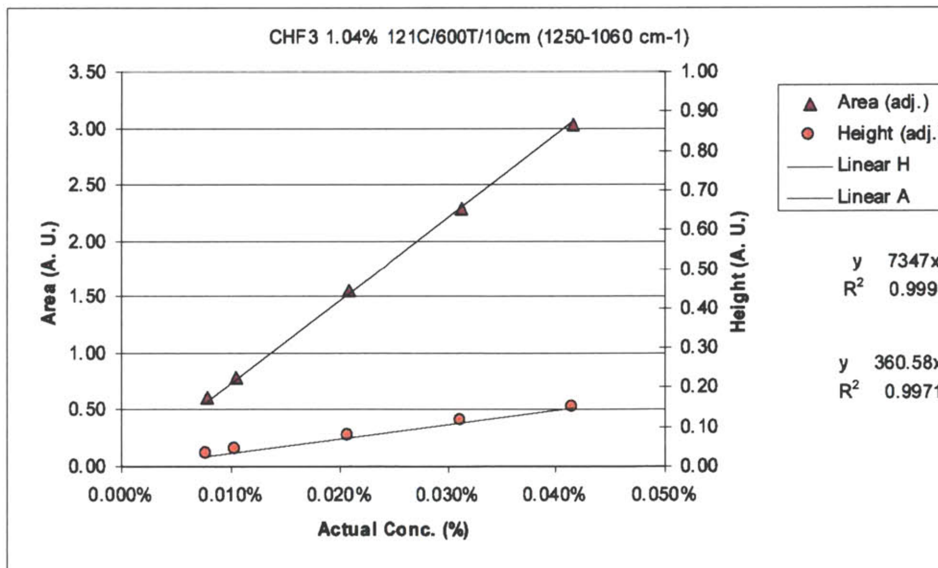

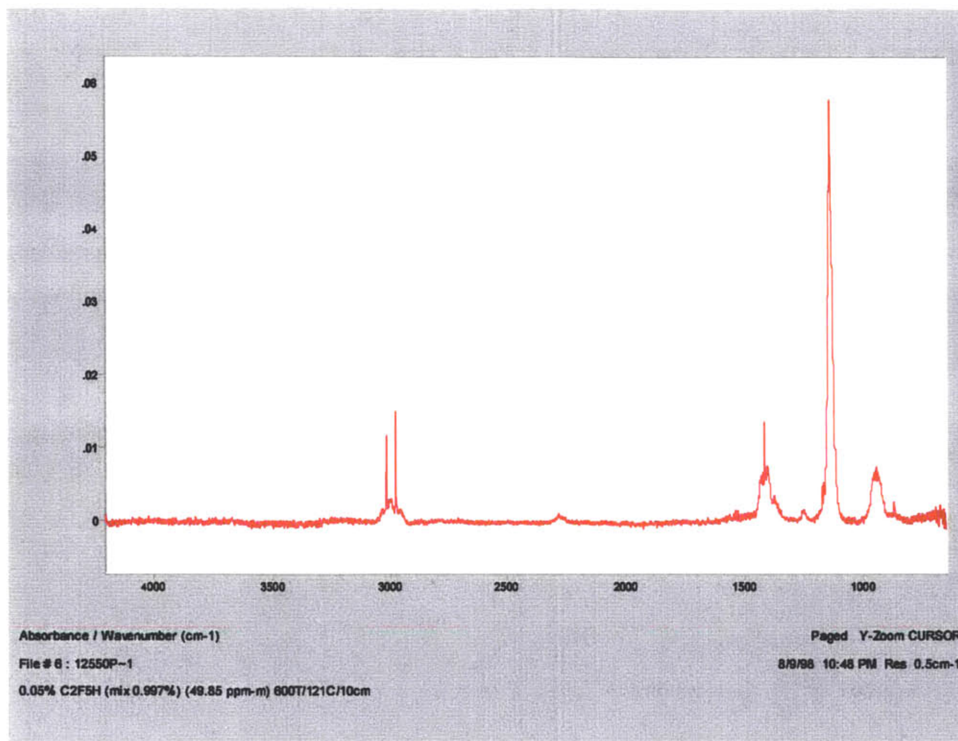
.06
.05
.04
.03
.02
.01
0
4000
3500
3000
2500
2000
1500
1000
Absorbance / Wavenumber (cm-1)
Paged Y-Zoom CURSOR
File # 6 : 12550P~1
8/9/98 10:46 PM Res 0.5cm-1
0.05% C2F5H (mix 0.997%) (49.85 ppm-m) 600T/121C/10cm

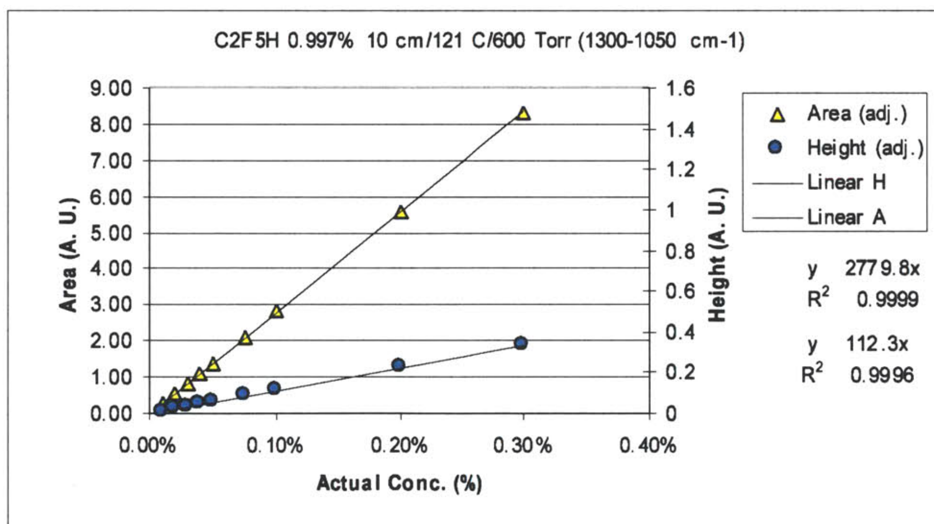
C2F5H 0.997% 10 cm/121 C/600 Torr (1300-1050 cm-1)
9.00
8.00
7.00
6.00
5.00
4.00
3.00
2.00
1.00
0.00
Area (A. U.)
1.6
1.4
1.2
1
0.8
0.6
0.4
0.2
0
Height (A. U.)
0.00%
0.10%
0.20%
0.30%
0.40%
Actual Conc. (%)
Area (adj.)
Height (adj.)
Linear H
Linear A
y 2779.8x
R2 0.9999
y 112.3x
R2 0.9996

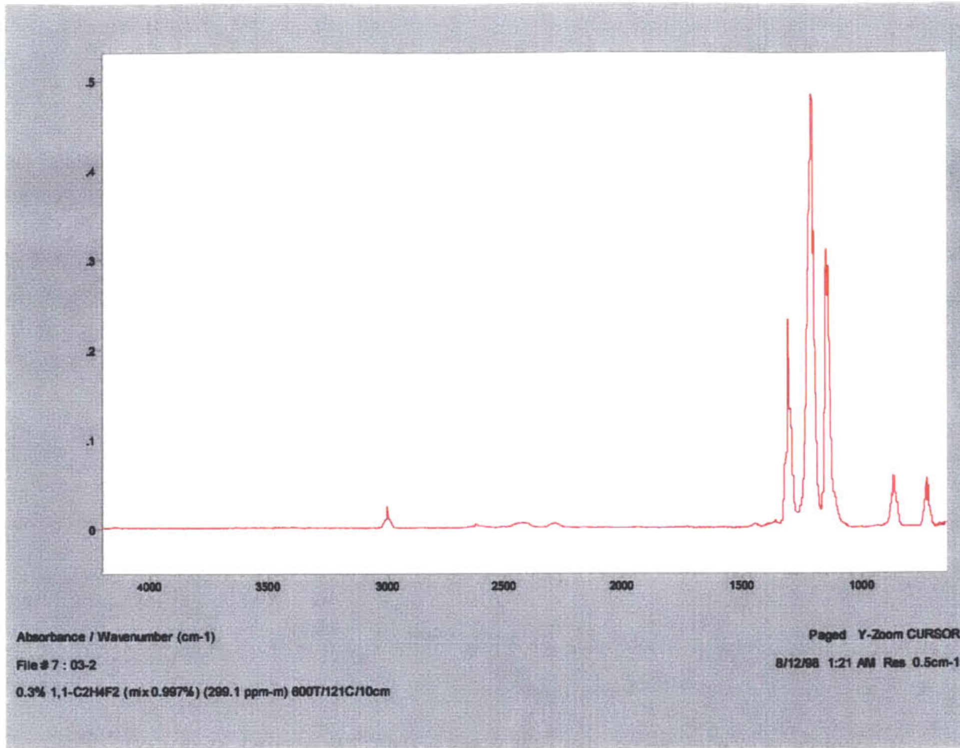
.5
.4
.3
.2
.1
0
4000
3500
3000
2500
2000
1500
1000
Absorbance / Wavenumber (cm-1)
File # 7 : 03-2
0.3% 1,1-C2H4F2 (mix 0.997%) (299.1 ppm-m) 600T/121C/10cm
Paged Y-Zoom CURSOR
8/12/98 1:21 AM Res 0.5cm-1

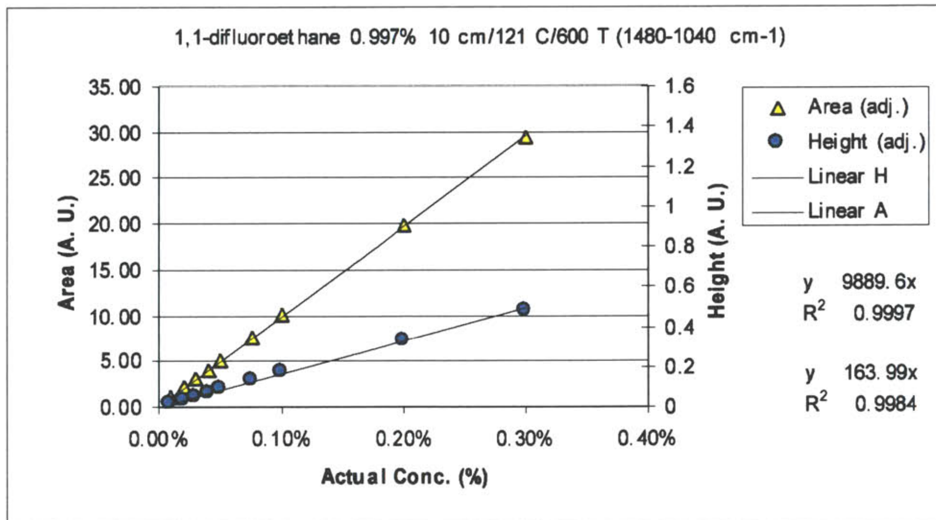
1,1-difluoroethane 0.997% 10 cm/121 C/600 T (1480-1040 cm-1)
35.00
30.00
25.00
20.00
15.00
10.00
5.00
0.00
Area (A. U.)
1.6
1.4
1.2
1
0.8
0.6
0.4
0.2
0
Height (A. U.)
0.00%
0.10%
0.20%
0.30%
0.40%
Actual Conc. (%)
Area (adj.)
Height (adj.)
Linear H
Linear A
y 9889.6x
R2 0.9997
y 163.99x
R2 0.9984

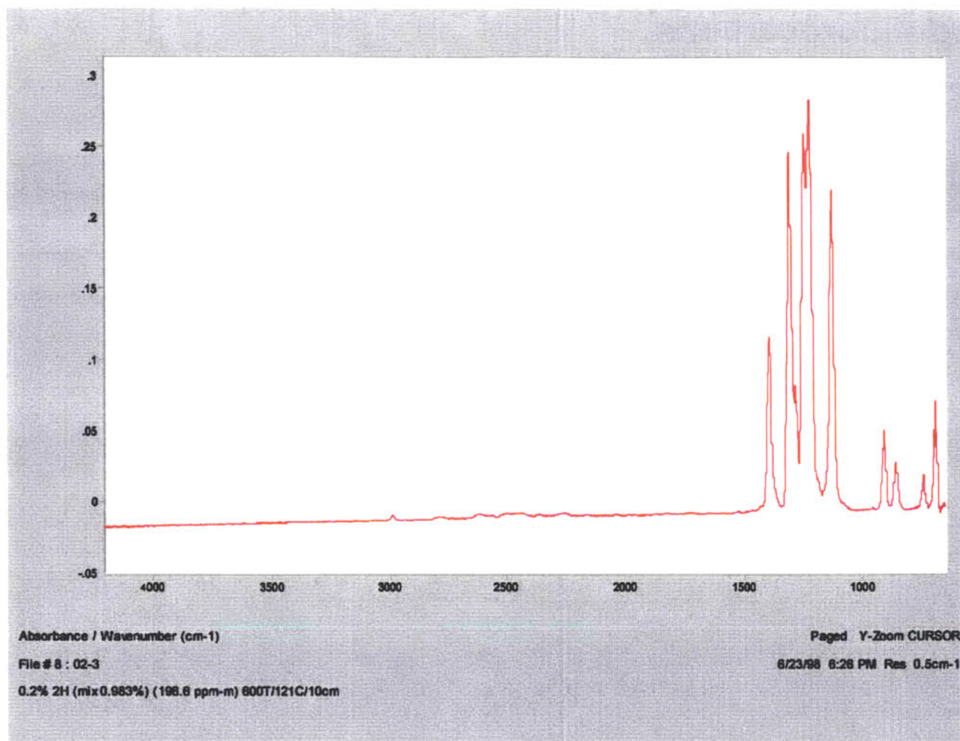
.3
.25
.2
.15
.1
.05
0
-.05
4000
3500
3000
2500
2000
1500
1000
Absorbance / Wavenumber (cm-1)
Paged Y-Zoom CURSOR
File # 8 : 02-3
6/23/98 6:26 PM Res 0.5cm-1
0.2% 2H (mix 0.983%) (198.6 ppm-m) 600T/121C/10cm

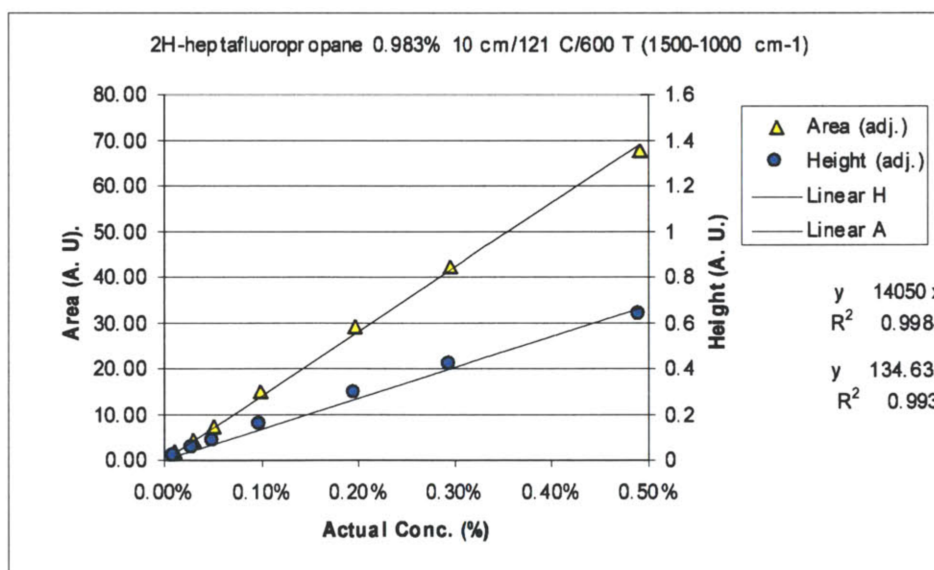
2H-heptafluoropropane 0.983% 10 cm/121 C/600 T (1500-1000 cm-1)
Area (A. U).
Height (A. U.)
Actual Conc. (%)
80.00
70.00
60.00
50.00
40.00
30.00
20.00
10.00
0.00
1.6
1.4
1.2
1
0.8
0.6
0.4
0.2
0
0.00%
0.10%
0.20%
0.30%
0.40%
0.50%
Area (adj.)
Height (adj.)
Linear H
Linear A
y 14050 x
R2 0.9984
y 134.63x
R2 0.993

B.3 Iodofluorocarbons

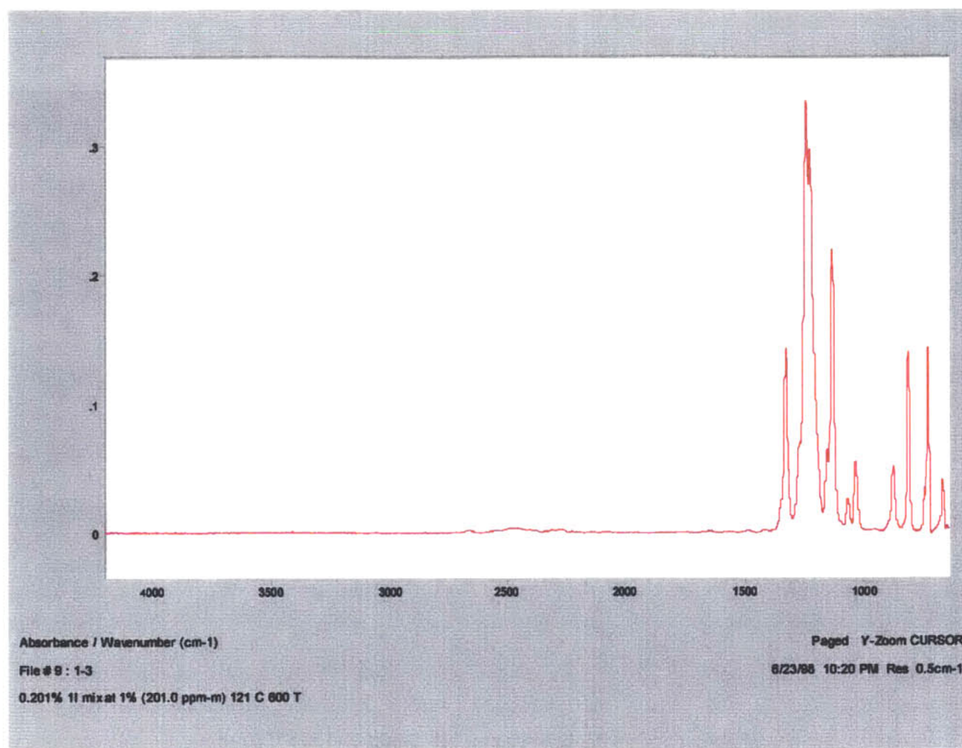

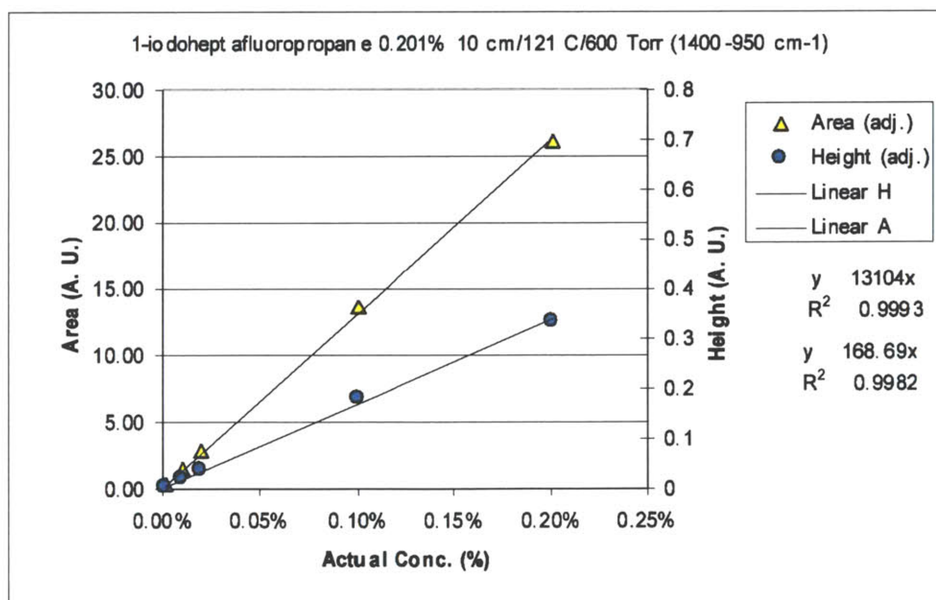

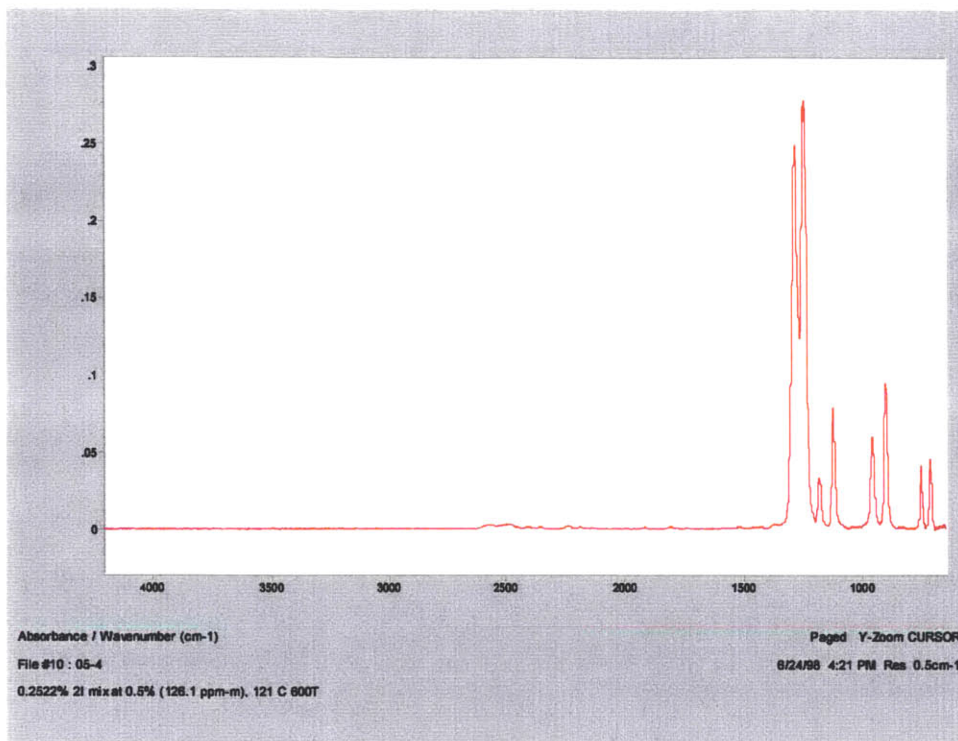
.3
.25
.2
.15
.1
.05
0
4000
3500
3000
2500
2000
1500
1000
Absorbance / Wavenumber (cm-1)
File #10 : 05-4
0.2522% 2I mix at 0.5% (126.1 ppm-m). 121 C 600T
Paged Y-Zoom CURSOR
6/24/98 4:21 PM Res 0.5cm-1

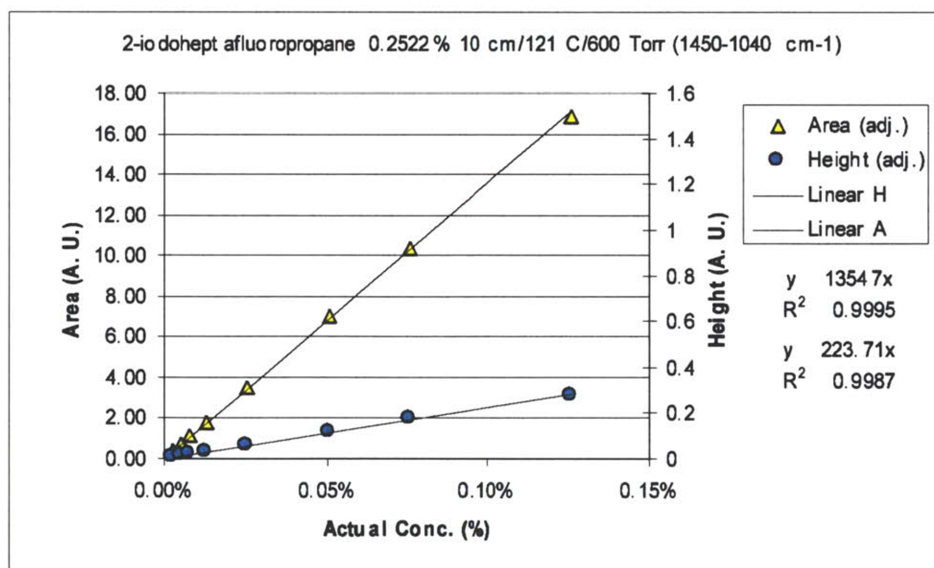
2-iodoheptafluoropropane 0.2522% 10 cm/121 C/600 Torr (1450-1040 cm-1)
18.00
16.00
14.00
12.00
10.00
8.00
6.00
4.00
2.00
0.00
Area (A. U.)
1.6
1.4
1.2
1
0.8
0.6
0.4
0.2
0
Height (A. U.)
0.00%
0.05%
0.10%
0.15%
Actual Conc. (%)
Area (adj.)
Height (adj.)
Linear H
Linear A
y 1354.7x
R² 0.9995
y 223.71x
R² 0.9987

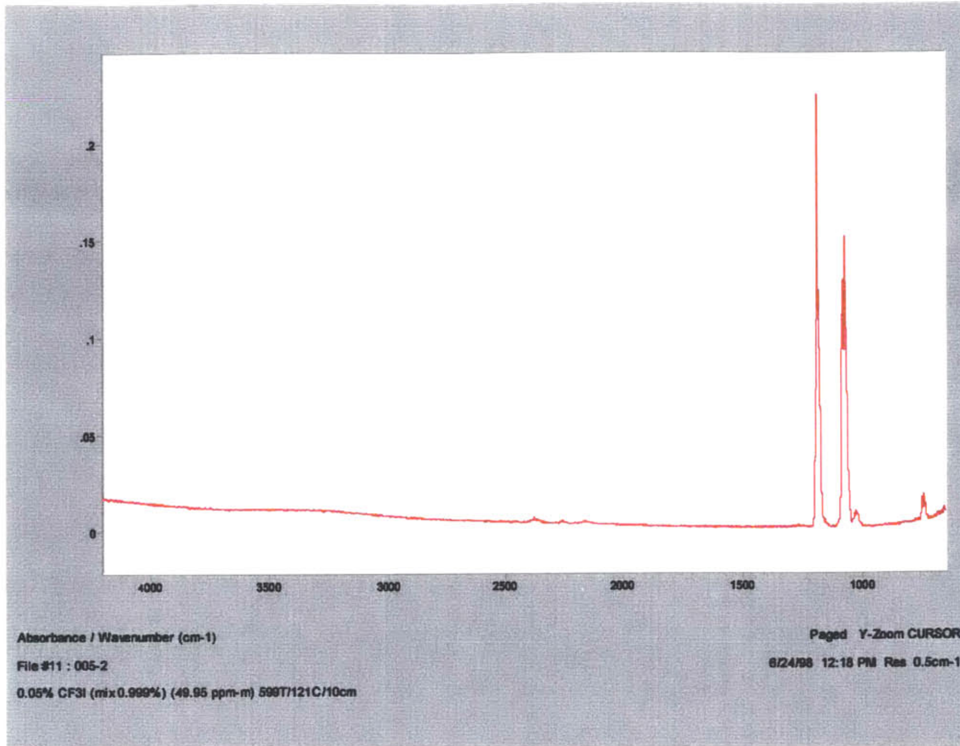
.2
.15
.1
.05
0
4000
3500
3000
2500
2000
1500
1000
Absorbance / Wavenumber (cm-1)
File #11 : 005-2
0.05% CF3I (mix 0.999%) (49.95 ppm-m) 599T/121C/10cm
Paged Y-Zoom CURSOR
6/24/98 12:18 PM Res 0.5cm-1

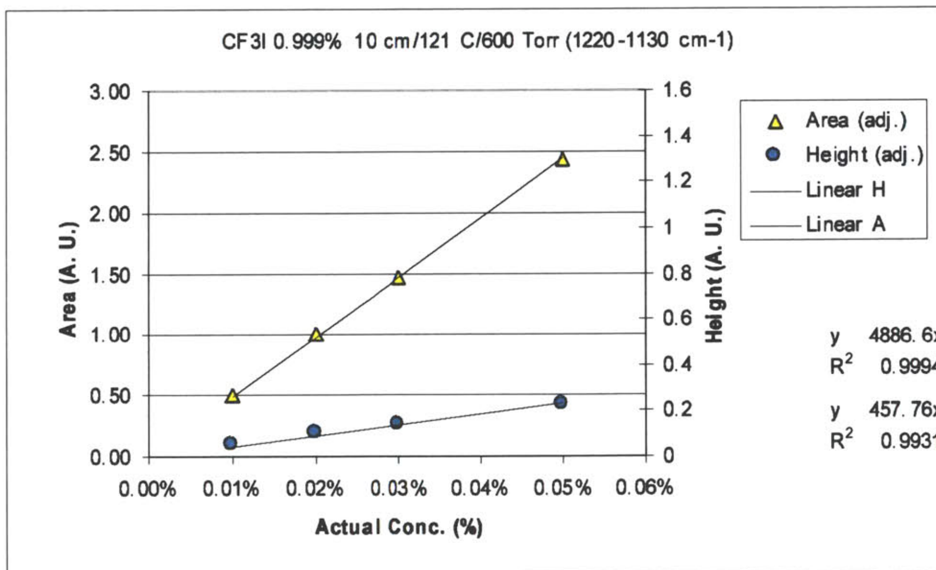
CF3I 0.999% 10 cm/121 C/600 Torr (1220-1130 cm-1)
Area (A. U.)
Height (A. U.)
Actual Conc. (%)
Area (adj.)
Height (adj.)
Linear H
Linear A
y 4886.6x
R2 0.9994
y 457.76x
R2 0.9931
3.00
2.50
2.00
1.50
1.00
0.50
0.00
1.6
1.4
1.2
1
0.8
0.6
0.4
0.2
0
0.00%
0.01%
0.02%
0.03%
0.04%
0.05%
0.06%

B.4 Unsaturated Fluorocarbons

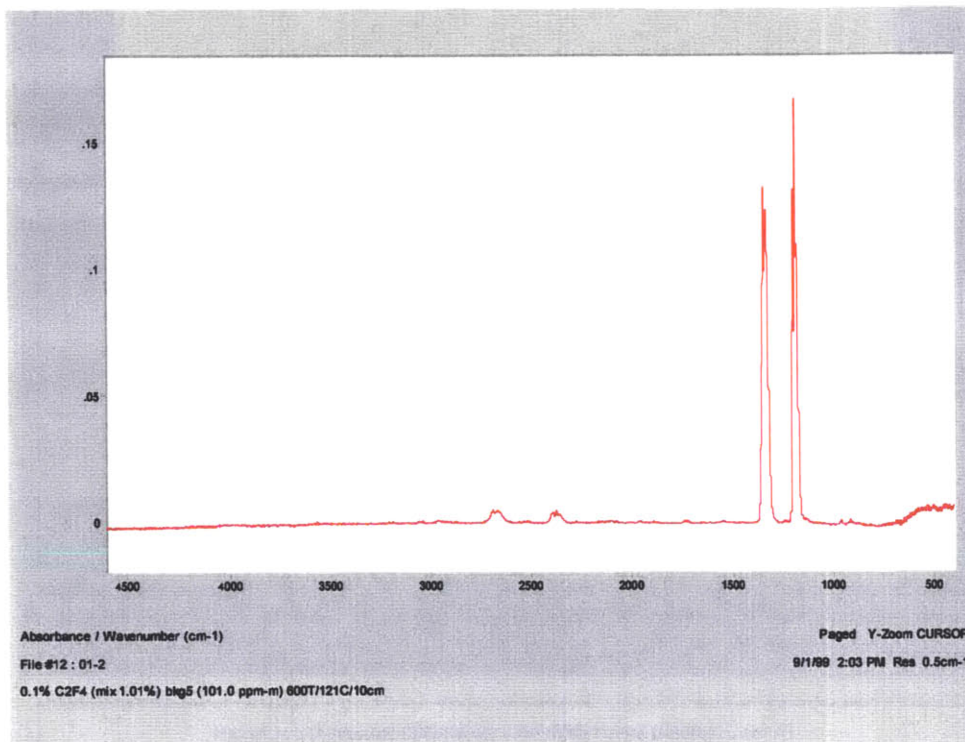

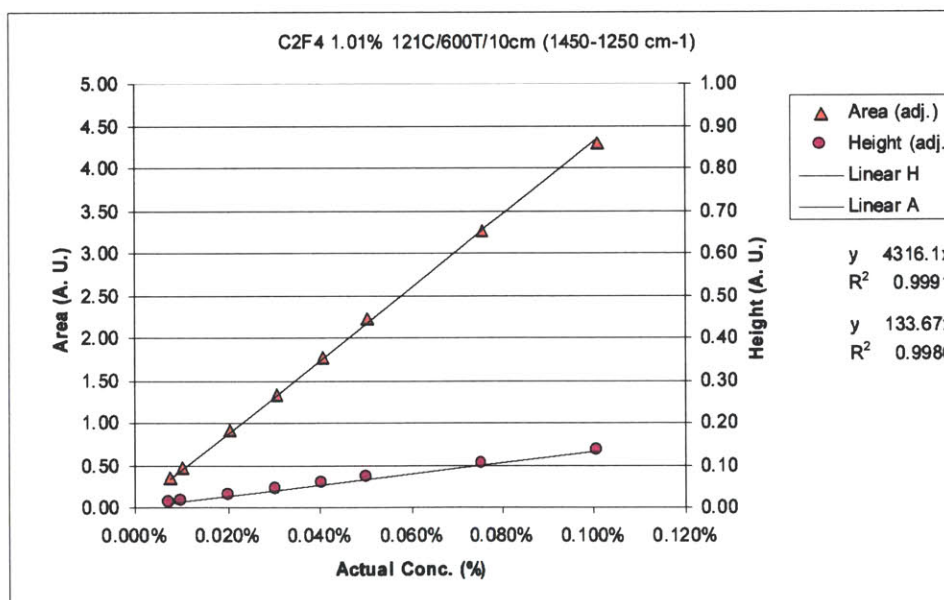

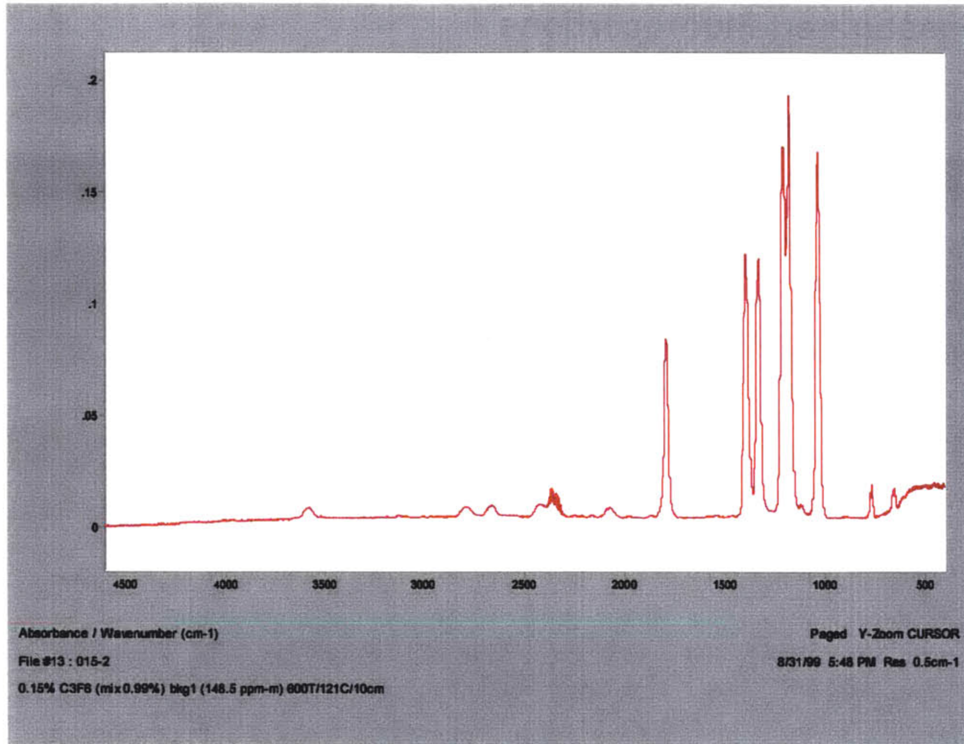
.2
.15
.1
.05
0
4500
4000
3500
3000
2500
2000
1500
1000
500
Absorbance / Wavenumber (cm-1)
Paged Y-Zoom CURSOR
File #13 : 015-2
8/31/99 5:48 PM Res 0.5cm-1
0.15% C3F6 (mix 0.99%) bkg1 (148.5 ppm-m) 600T/121C/10cm

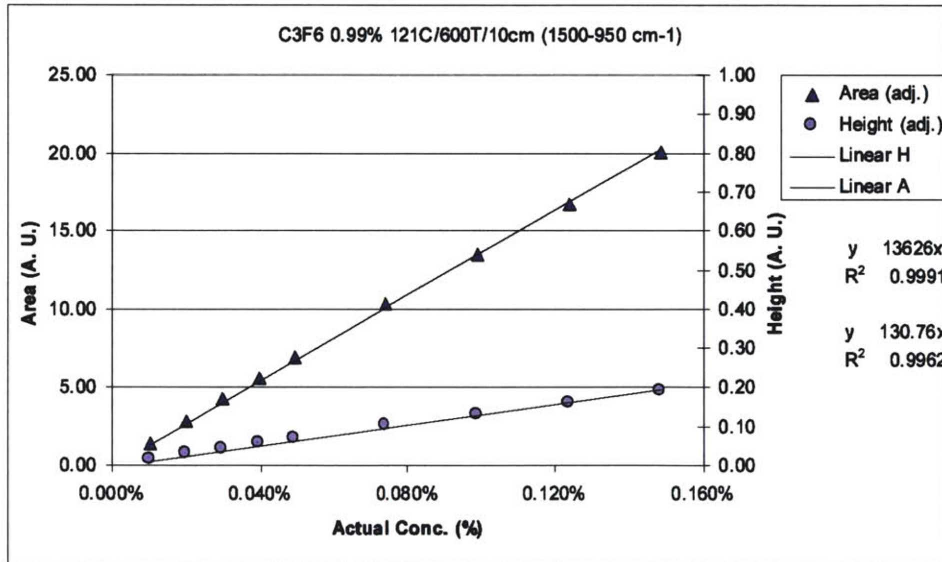
C3F6 0.99% 121C/600T/10cm (1500-950 cm-1)
Area (A. U.)
Height (A. U.)
Actual Conc. (%)
25.00
20.00
15.00
10.00
5.00
0.00
1.00
0.90
0.80
0.70
0.60
0.50
0.40
0.30
0.20
0.10
0.00
0.000%
0.040%
0.080%
0.120%
0.160%
Area (adj.)
Height (adj.)
Linear H
Linear A
y 13626x
R² 0.9991
y 130.76x
R² 0.9962

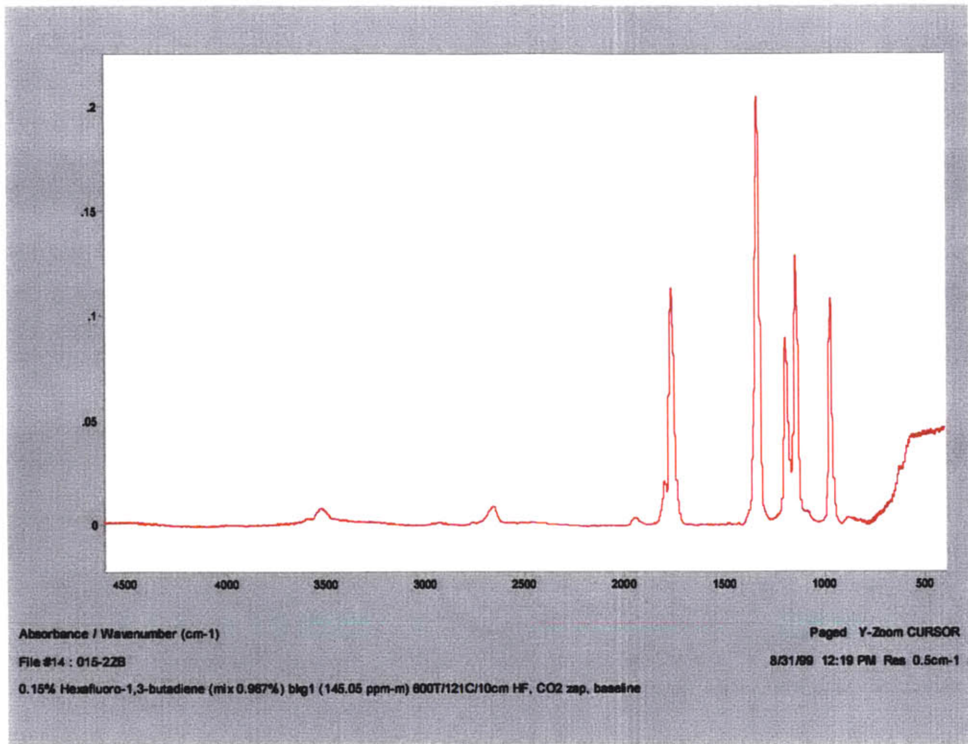
.2
.15
.1
.05
0
4500
4000
3500
3000
2500
2000
1500
1000
500
Absorbance / Wavenumber (cm-1)
Paged Y-Zoom CURSOR
File #14 : 015-22B
8/31/99 12:19 PM Res 0.5cm-1
0.15% Hexafluoro-1,3-butadiene (mix 0.967%) bkg1 (145.05 ppm-m) 600T/121C/10cm HF, CO2 zap, baseline

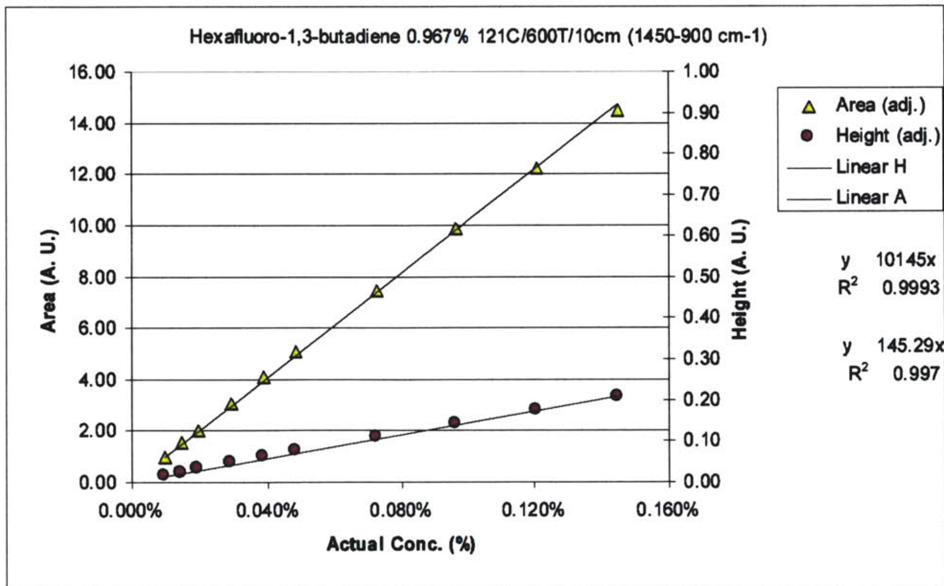
Hexafluoro-1,3-butadiene 0.967% 121C/600T/10cm (1450-900 cm-1)
16.00
14.00
12.00
10.00
8.00
6.00
4.00
2.00
0.00
Area (A. U.)
1.00
0.90
0.80
0.70
0.60
0.50
0.40
0.30
0.20
0.10
0.00
Height (A. U.)
0.000%
0.040%
0.080%
0.120%
0.160%
Actual Conc. (%)
Area (adj.)
Height (adj.)
Linear H
Linear A
y 10145x
R2 0.9993
y 145.29x
R2 0.997

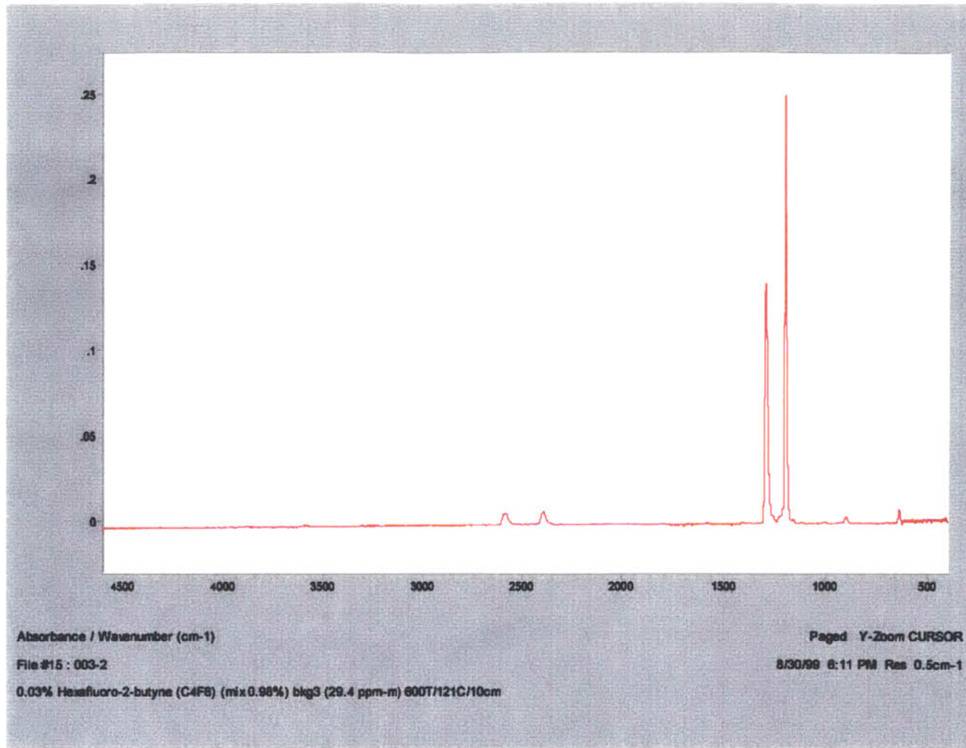
.25
.2
.15
.1
.05
0
4500
4000
3500
3000
2500
2000
1500
1000
500
Absorbance / Wavenumber (cm-1)
Paged Y-Zoom CURSOR
File #15 : 003-2
8/30/99 6:11 PM Res 0.5cm-1
0.03% Hexafluoro-2-butyne (C4F6) (mix 0.98%) bkg3 (29.4 ppm-m) 600T/121C/10cm

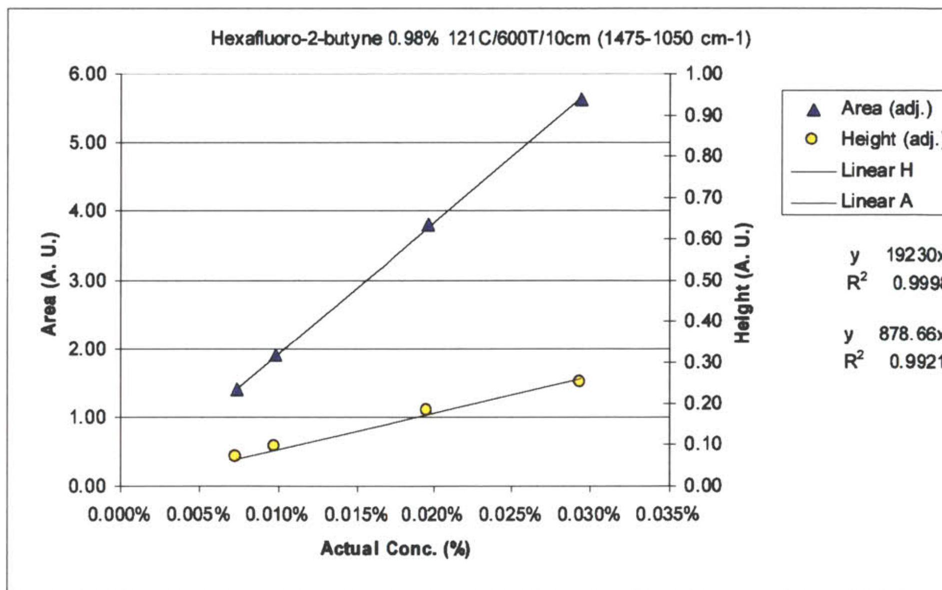
Hexafluoro-2-butyne 0.98% 121C/600T/10cm (1475-1050 cm-1)
6.00
5.00
4.00
3.00
2.00
1.00
0.00
Area (A. U.)
1.00
0.90
0.80
0.70
0.60
0.50
0.40
0.30
0.20
0.10
0.00
Height (A. U.)
0.000%
0.005%
0.010%
0.015%
0.020%
0.025%
0.030%
0.035%
Actual Conc. (%)
Area (adj.)
Height (adj.)
Linear H
Linear A
y 19230x
R2 0.9998
y 878.66x
R2 0.9921

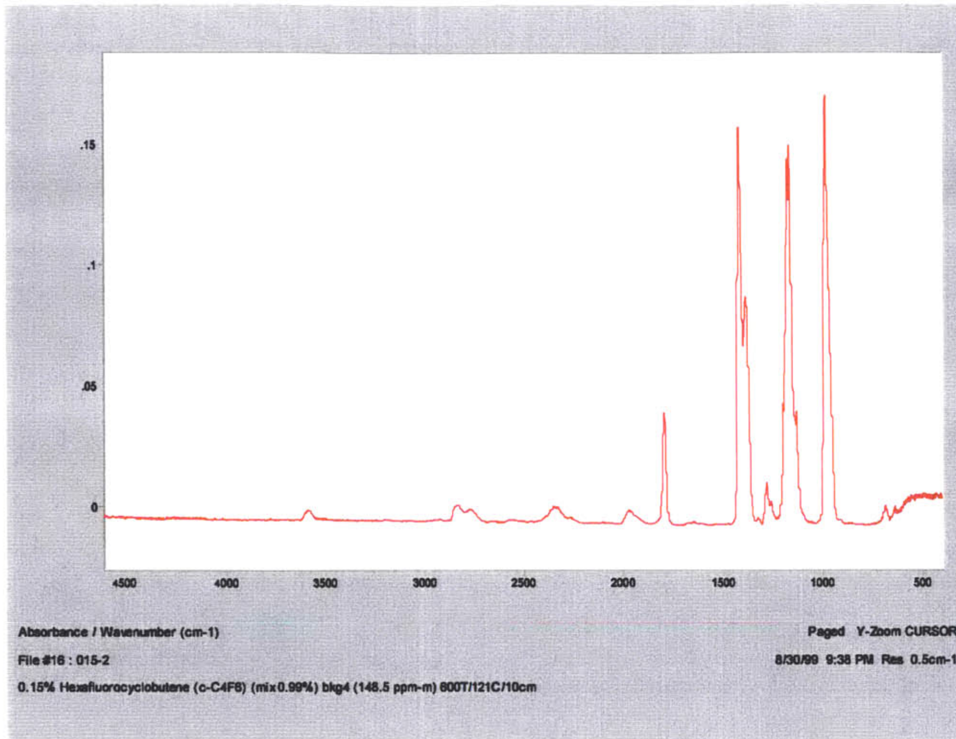
.15
.1
.05
0
4500
4000
3500
3000
2500
2000
1500
1000
500
Absorbance / Wavenumber (cm-1)
Paged Y-Zoom CURSOR
File #16 : 015-2
8/30/99 9:38 PM Res 0.5cm-1
0.15% Hexafluorocyclobutene (c-C4F6) (mix 0.99%) bkg4 (148.5 ppm-m) 600T/121C/10cm

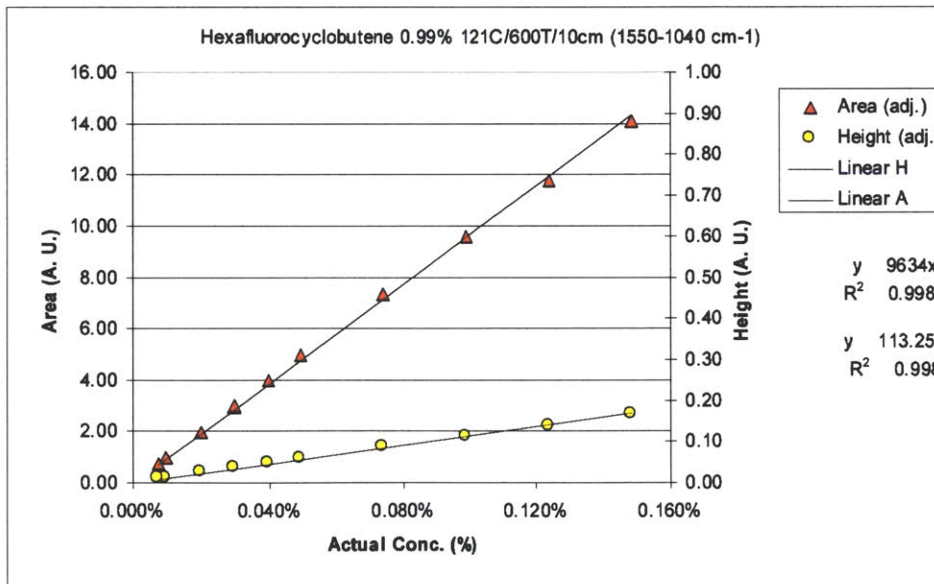
Hexafluorocyclobutene 0.99% 121C/600T/10cm (1550-1040 cm-1)
Area (A. U.)
Height (A. U.)
Actual Conc. (%)
16.00
14.00
12.00
10.00
8.00
6.00
4.00
2.00
0.00
1.00
0.90
0.80
0.70
0.60
0.50
0.40
0.30
0.20
0.10
0.00
0.000%
0.040%
0.080%
0.120%
0.160%
Area (adj.)
Height (adj.)
Linear H
Linear A
y 9634x
R2 0.9989
y 113.25x
R2 0.998

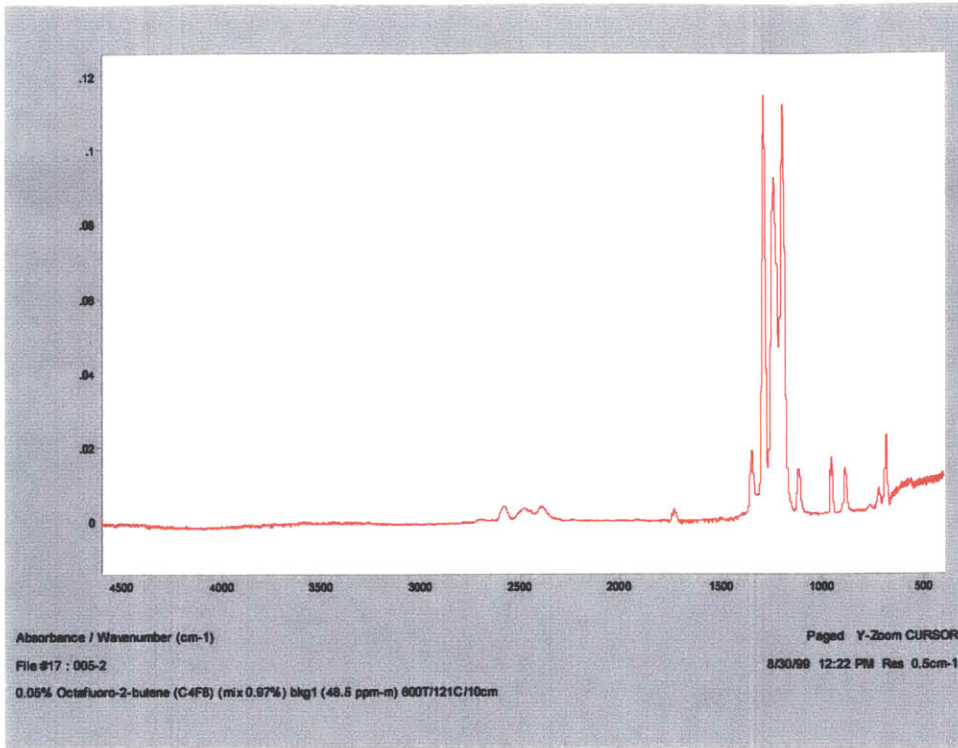
.12
.1
.08
.06
.04
.02
0
4500
4000
3500
3000
2500
2000
1500
1000
500
Absorbance / Wavenumber (cm-1)
File #17 : 005-2
0.05% Octafluoro-2-butene (C4F8) (mix 0.97%) bkg1 (48.5 ppm-m) 600T/121C/10cm
Paged Y-Zoom CURSOR
8/30/99 12:22 PM Res 0.5cm-1

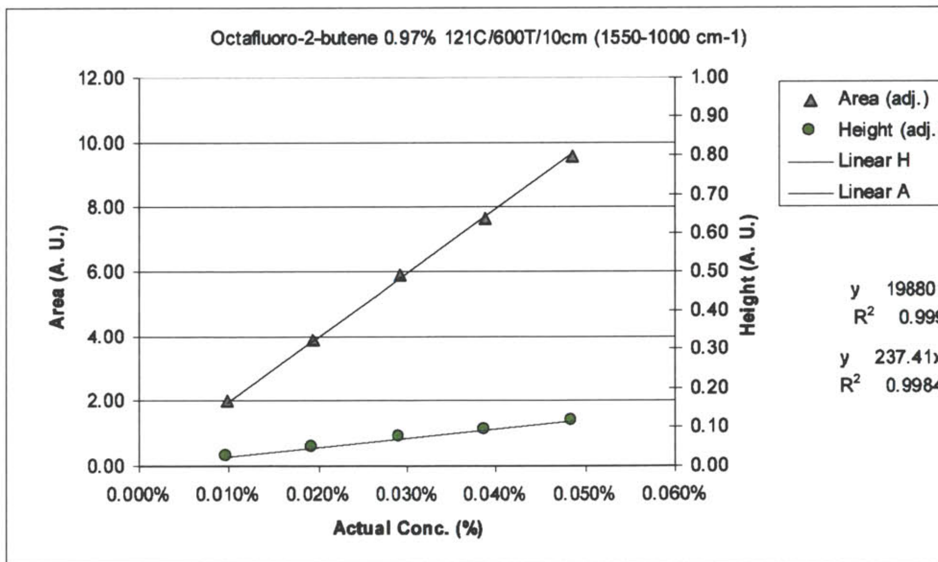
Octafluoro-2-butene 0.97% 121C/600T/10cm (1550-1000 cm-1)
12.00
10.00
8.00
6.00
4.00
2.00
0.00
Area (A. U.)
1.00
0.90
0.80
0.70
0.60
0.50
0.40
0.30
0.20
0.10
0.00
Height (A. U.)
0.000%
0.010%
0.020%
0.030%
0.040%
0.050%
0.060%
Actual Conc. (%)
Area (adj.)
Height (adj.)
Linear H
Linear A
y 19880x
R² 0.999
y 237.41x
R² 0.9984

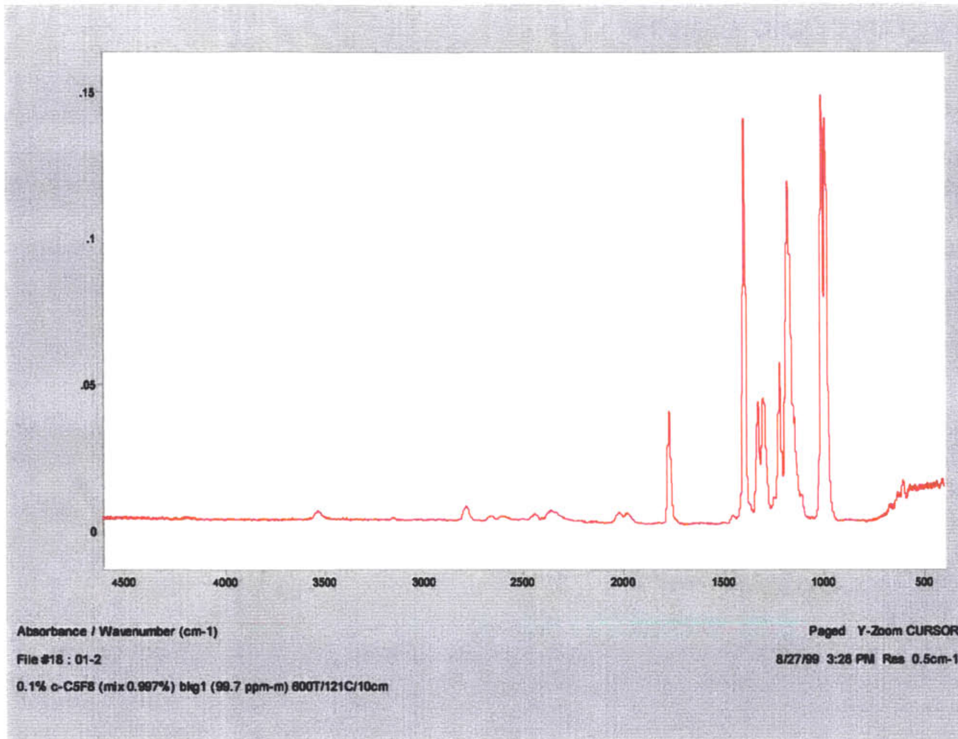
.15
.1
.05
0
4500
4000
3500
3000
2500
2000
1500
1000
500
Absorbance / Wavenumber (cm-1)
Paged Y-Zoom CURSOR
File #18 : 01-2
8/27/99 3:28 PM Res 0.5cm-1
0.1% c-C5F8 (mix 0.997%) bkg1 (99.7 ppm-m) 600T/121C/10cm

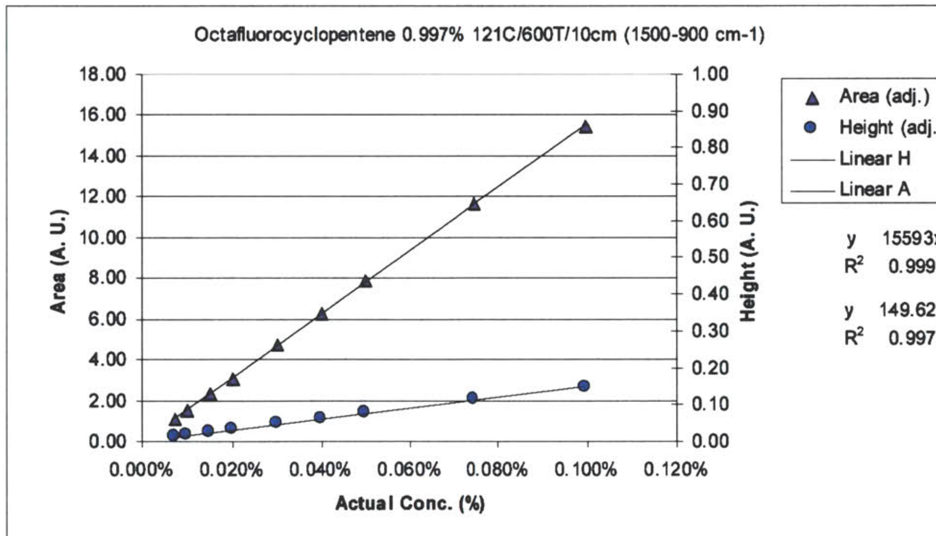
Octafluorocyclopentene 0.997% 121C/600T/10cm (1500-900 cm-1)
Area (A. U.)
18.00
16.00
14.00
12.00
10.00
8.00
6.00
4.00
2.00
0.00
Height (A. U.)
1.00
0.90
0.80
0.70
0.60
0.50
0.40
0.30
0.20
0.10
0.00
0.000%
0.020%
0.040%
0.060%
0.080%
0.100%
0.120%
Actual Conc. (%)
Area (adj.)
Height (adj.)
Linear H
Linear A
y 15593x
R² 0.9999
y 149.62x
R² 0.9979

B.5 Hygroscopic Gases

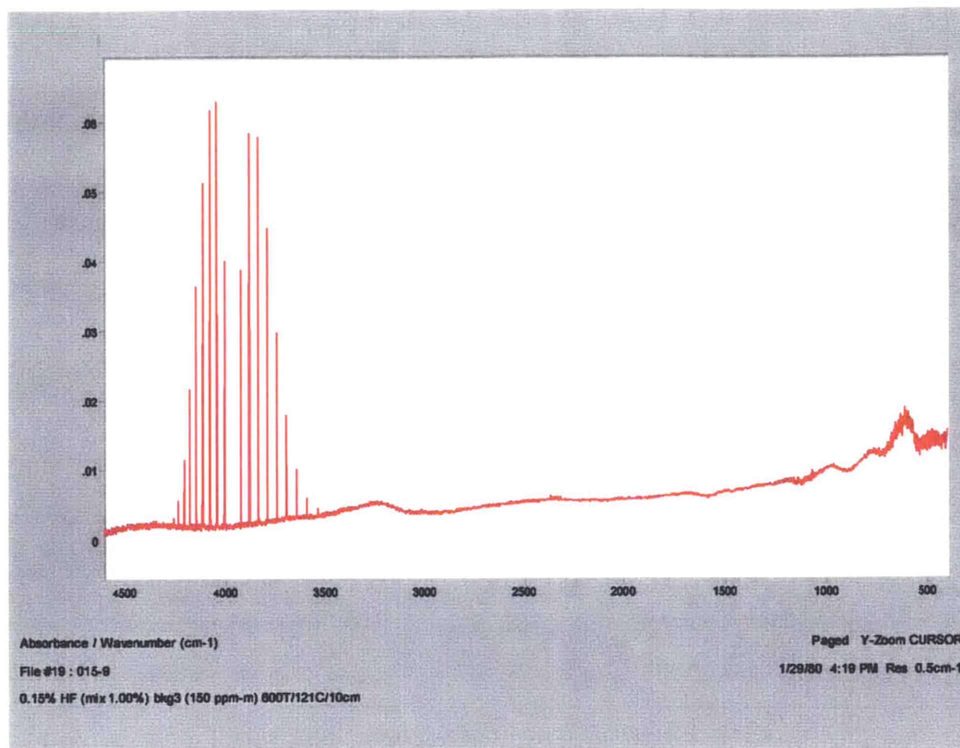

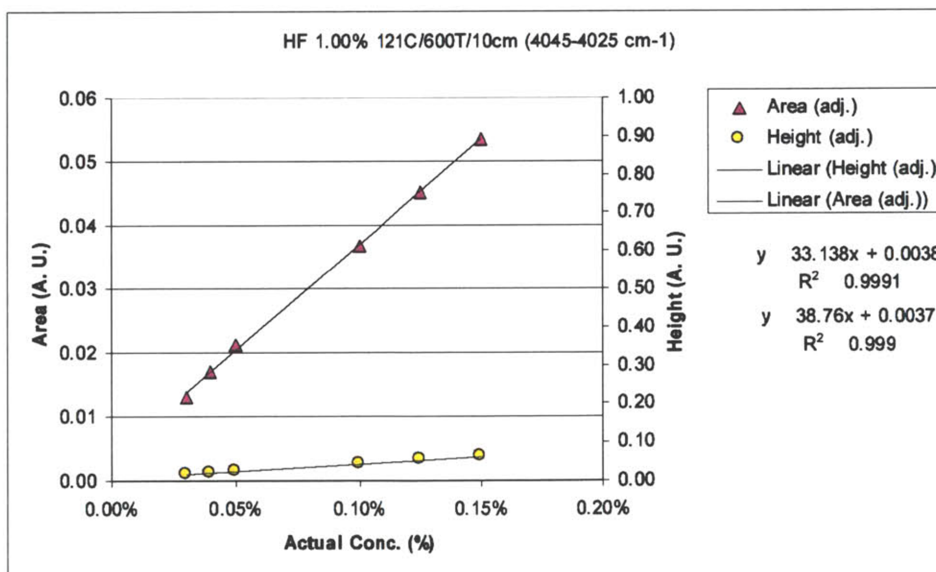

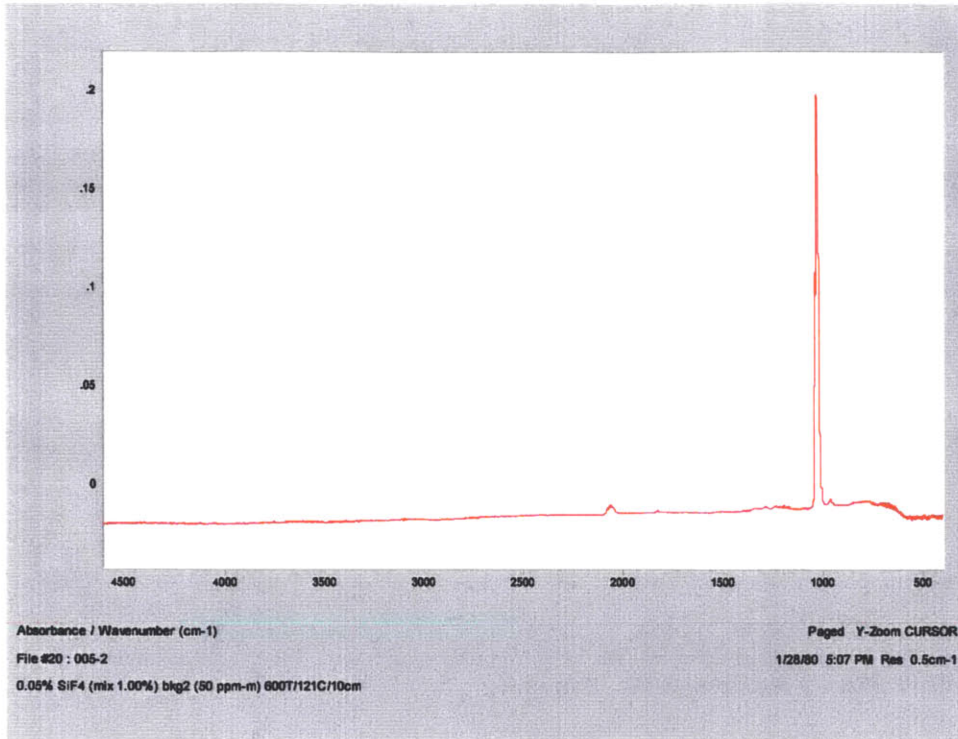
.2
.15
.1
.05
0
4500
4000
3500
3000
2500
2000
1500
1000
500
Absorbance / Wavenumber (cm-1)
File #20 : 005-2
0.05% SiF4 (mix 1.00%) bkg2 (50 ppm-m) 600T/121C/10cm
Paged Y-Zoom CURSOR
1/28/80 5:07 PM Res 0.5cm-1

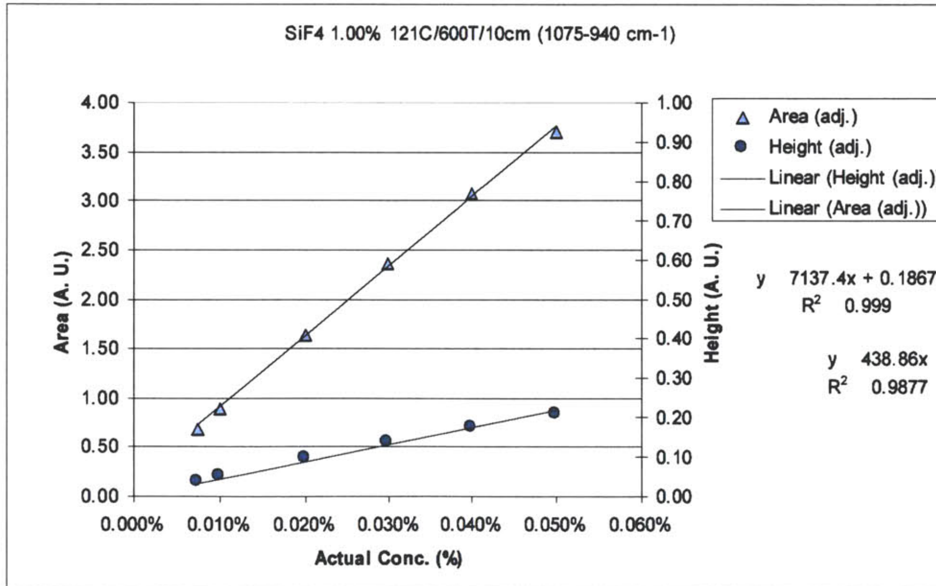
SiF4 1.00% 121C/600T/10cm (1075-940 cm-1)
Area (adj.)
Height (adj.)
Linear (Height (adj.))
Linear (Area (adj.))
y 7137.4x + 0.1867
R² 0.999
y 438.86x
R² 0.9877
Area (A. U.)
Height (A. U.)
Actual Conc. (%)
4.00
3.50
3.00
2.50
2.00
1.50
1.00
0.50
0.00
1.00
0.90
0.80
0.70
0.60
0.50
0.40
0.30
0.20
0.10
0.00
0.000%
0.010%
0.020%
0.030%
0.040%
0.050%
0.060%

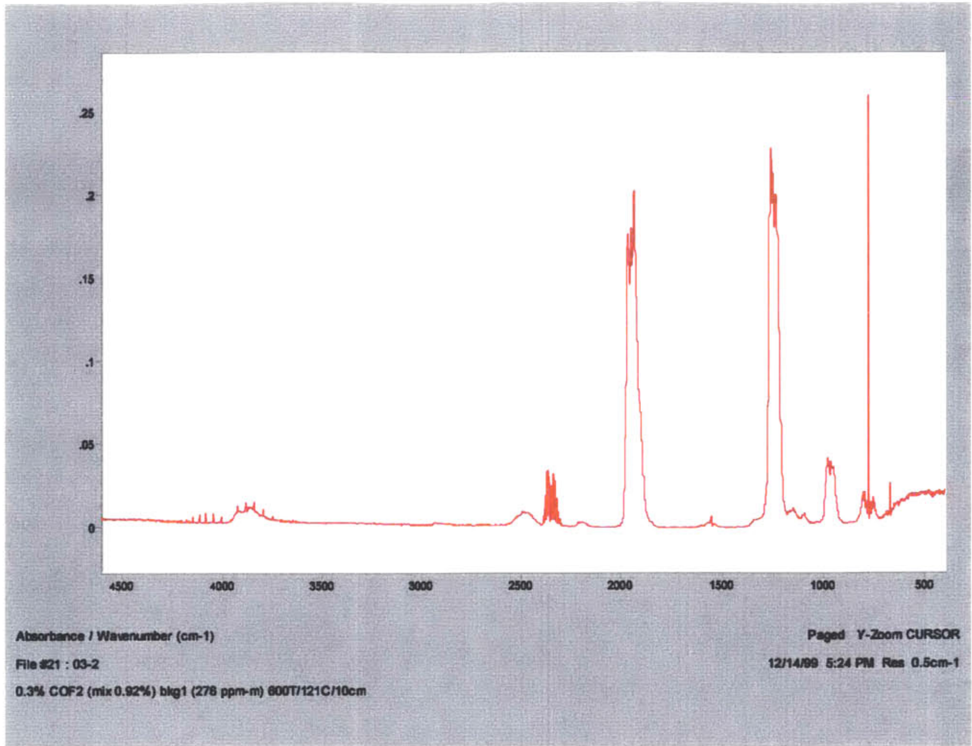
.25
.2
.15
.1
.05
0
4500
4000
3500
3000
2500
2000
1500
1000
500
Absorbance / Wavenumber (cm-1)
File #21 : 03-2
0.3% COF2 (mix 0.92%) bkg1 (276 ppm-m) 600T/121C/10cm
Paged Y-Zoom CURSOR
12/14/99 5:24 PM Res 0.5cm-1

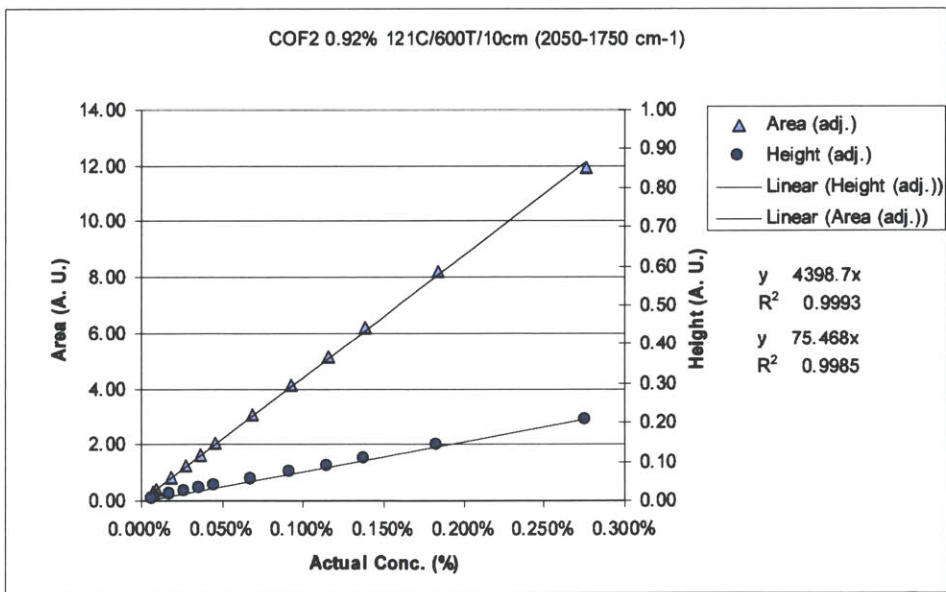
COF2 0.92% 121C/600T/10cm (2050-1750 cm-1)
Area (A. U.)
Height (A. U.)
Actual Conc. (%)
14.00
12.00
10.00
8.00
6.00
4.00
2.00
0.00
1.00
0.90
0.80
0.70
0.60
0.50
0.40
0.30
0.20
0.10
0.00
0.000%
0.050%
0.100%
0.150%
0.200%
0.250%
0.300%
Area (adj.)
Height (adj.)
Linear (Height (adj.))
Linear (Area (adj.))
y 4398.7x
R² 0.9993
y 75.468x
R² 0.9985

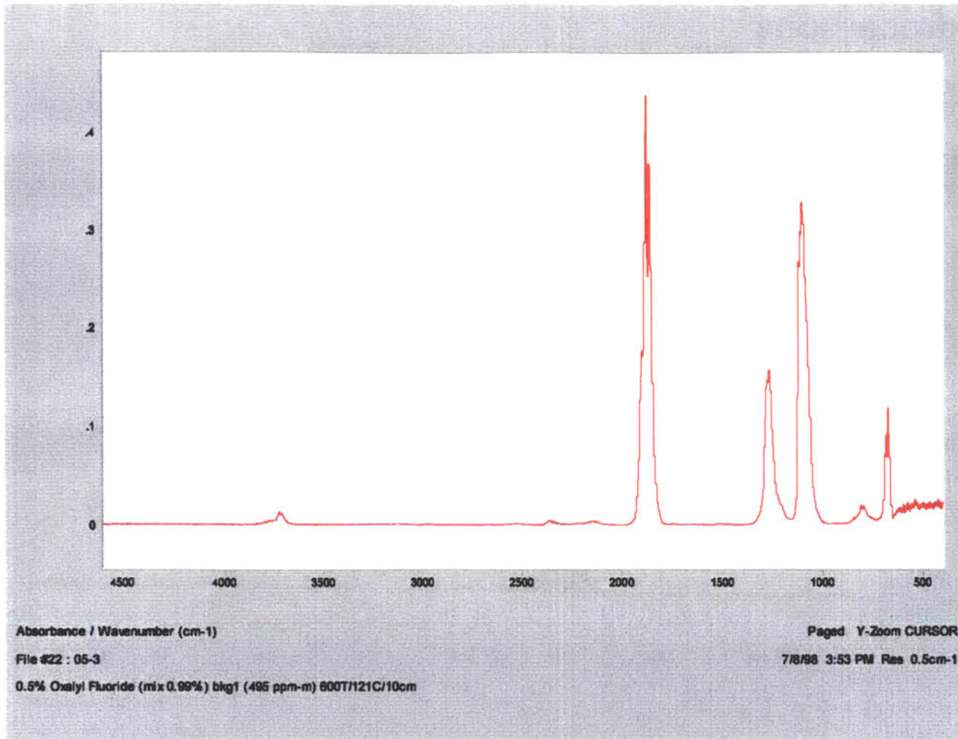
.4
.3
.2
.1
0
4500
4000
3500
3000
2500
2000
1500
1000
500
Absorbance / Wavenumber (cm-1)
Paged Y-Zoom CURSOR
File #22 : 05-3
7/8/98 3:53 PM Res 0.5cm-1
0.5% Oxalyl Fluoride (mix 0.99%) bkg1 (495 ppm-m) 600T/121C/10cm

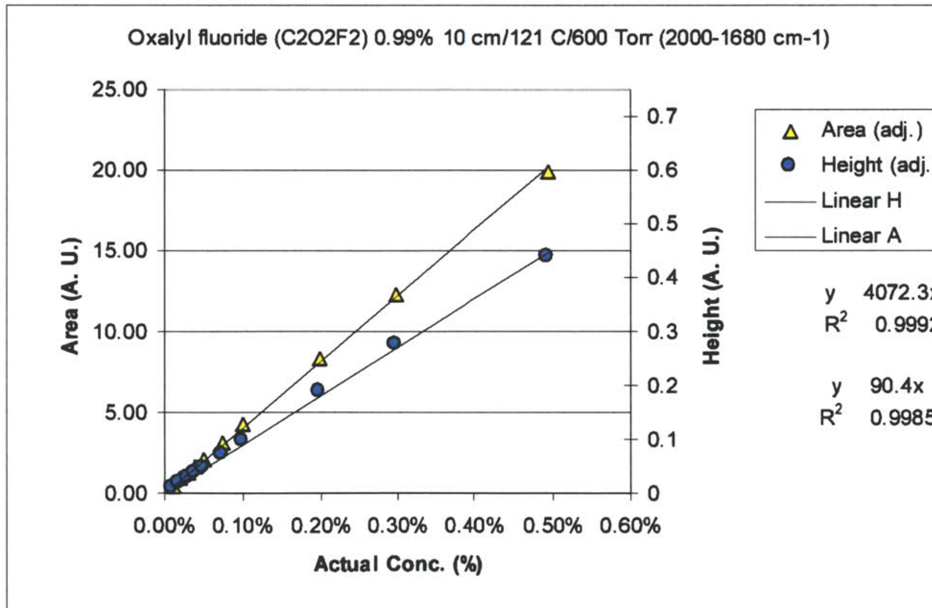
Oxalyl fluoride (C2O2F2) 0.99% 10 cm/121 C/600 Torr (2000-1680 cm-1)
25.00
20.00
15.00
10.00
5.00
0.00
Area (A. U.)
0.7
0.6
0.5
0.4
0.3
0.2
0.1
0
Height (A. U.)
0.00%
0.10%
0.20%
0.30%
0.40%
0.50%
0.60%
Actual Conc. (%)
Area (adj.)
Height (adj.)
Linear H
Linear A
y 4072.3x
R2 0.9992
y 90.4x
R2 0.9985

B.6 Hydrocarbons

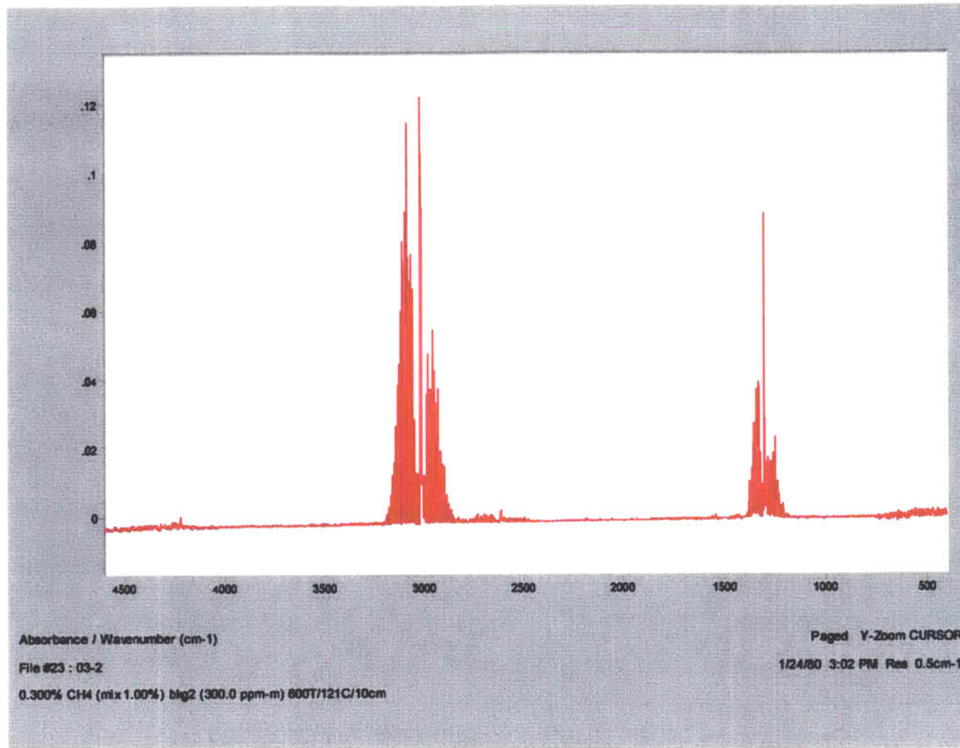

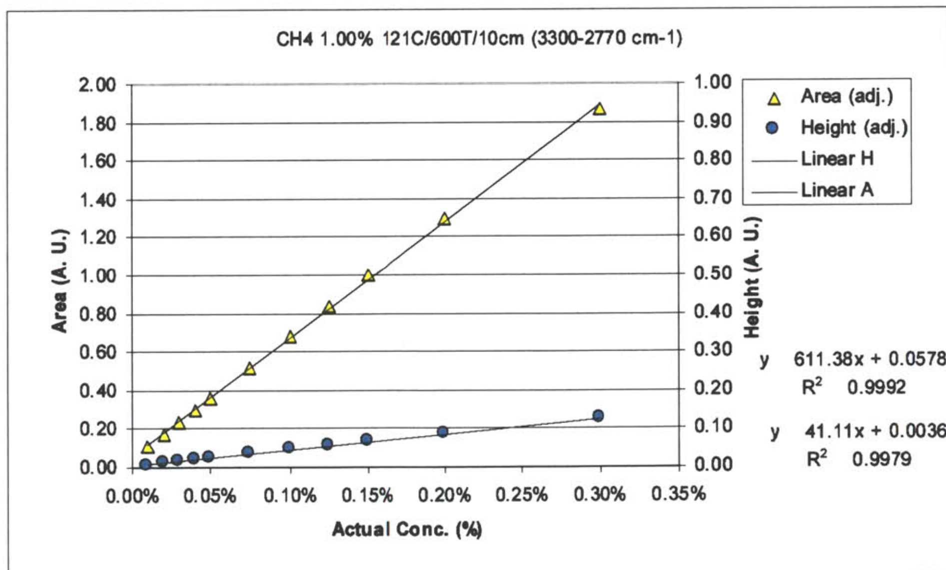

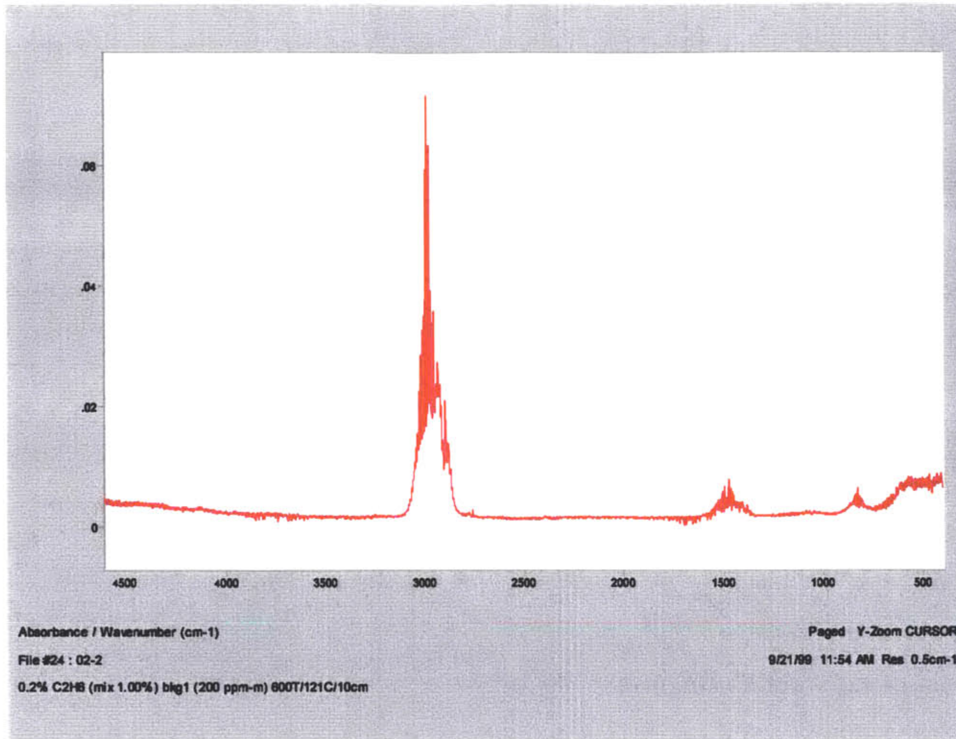
.06
.04
.02
0
4500
4000
3500
3000
2500
2000
1500
1000
500
Absorbance / Wavenumber (cm-1)
Paged Y-Zoom CURSOR
File #24 : 02-2
9/21/99 11:54 AM Res 0.5cm-1
0.2% C2H6 (mix 1.00%) bkg1 (200 ppm-m) 600T/121C/10cm

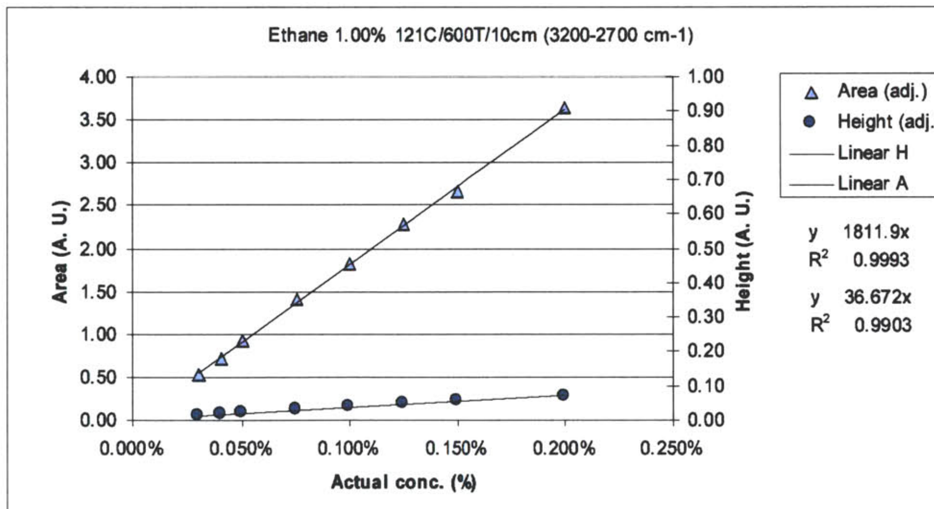
Ethane 1.00% 121C/600T/10cm (3200-2700 cm-1)
Area (A. U.)
4.00
3.50
3.00
2.50
2.00
1.50
1.00
0.50
0.00
Height (A. U.)
1.00
0.90
0.80
0.70
0.60
0.50
0.40
0.30
0.20
0.10
0.00
0.000%
0.050%
0.100%
0.150%
0.200%
0.250%
Actual conc. (%)
Area (adj.)
Height (adj.)
Linear H
Linear A
y 1811.9x
R2 0.9993
y 36.672x
R2 0.9903

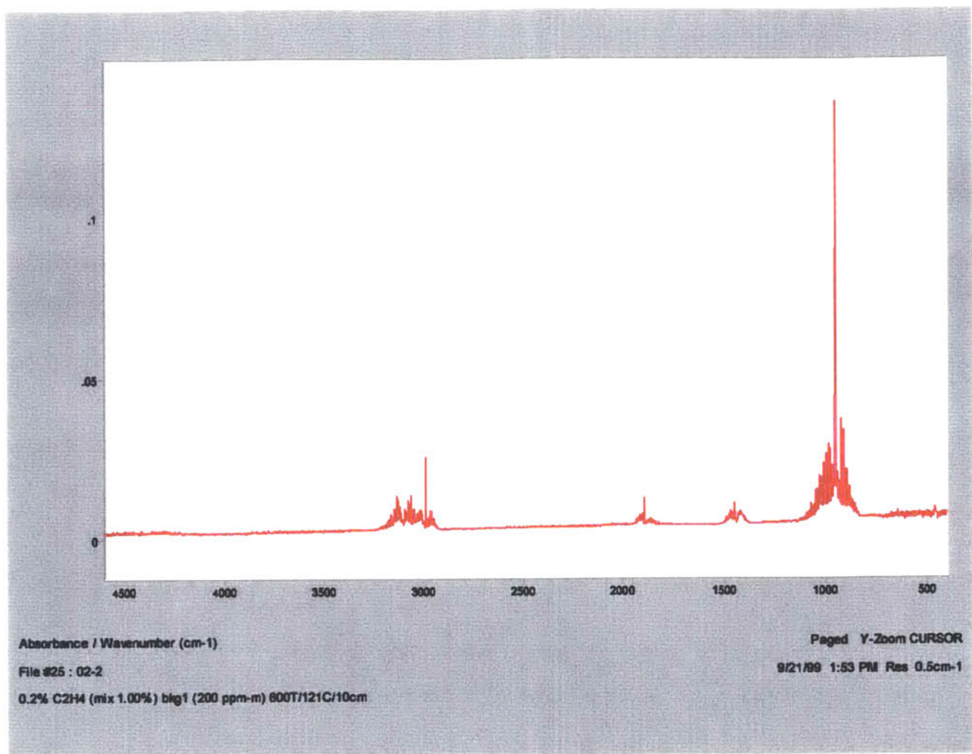
.1
.05
0
4500
4000
3500
3000
2500
2000
1500
1000
500
Absorbance / Wavenumber (cm-1)
File #25 : 02-2
0.2% C2H4 (mix 1.00%) bkg1 (200 ppm-m) 600T/121C/10cm
Paged Y-Zoom CURSOR
9/21/99 1:53 PM Res 0.5cm-1

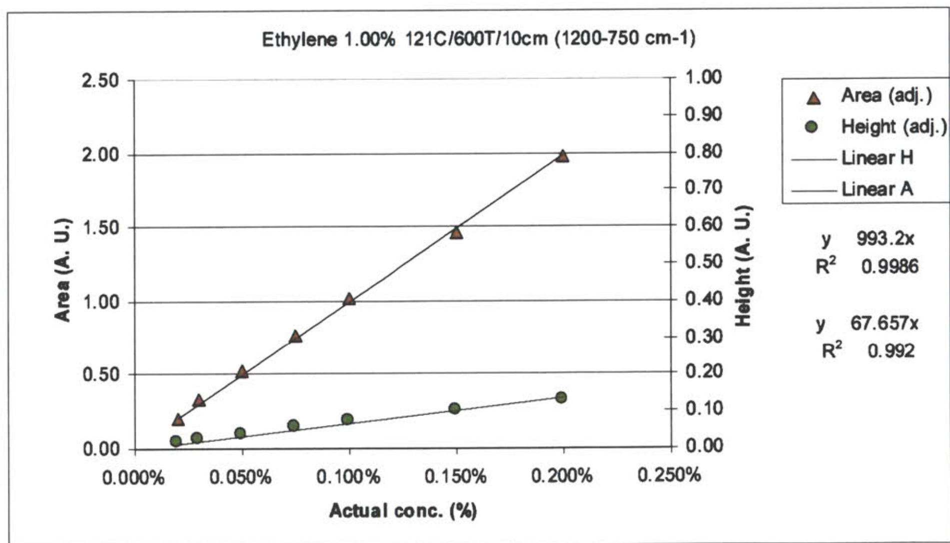
Ethylene 1.00% 121C/600T/10cm (1200-750 cm-1)
Area (A. U.)
2.50
2.00
1.50
1.00
0.50
0.00
Height (A. U.)
1.00
0.90
0.80
0.70
0.60
0.50
0.40
0.30
0.20
0.10
0.00
0.000%
0.050%
0.100%
0.150%
0.200%
0.250%
Actual conc. (%)
Area (adj.)
Height (adj.)
Linear H
Linear A
y 993.2x
R2 0.9986
y 67.657x
R2 0.992

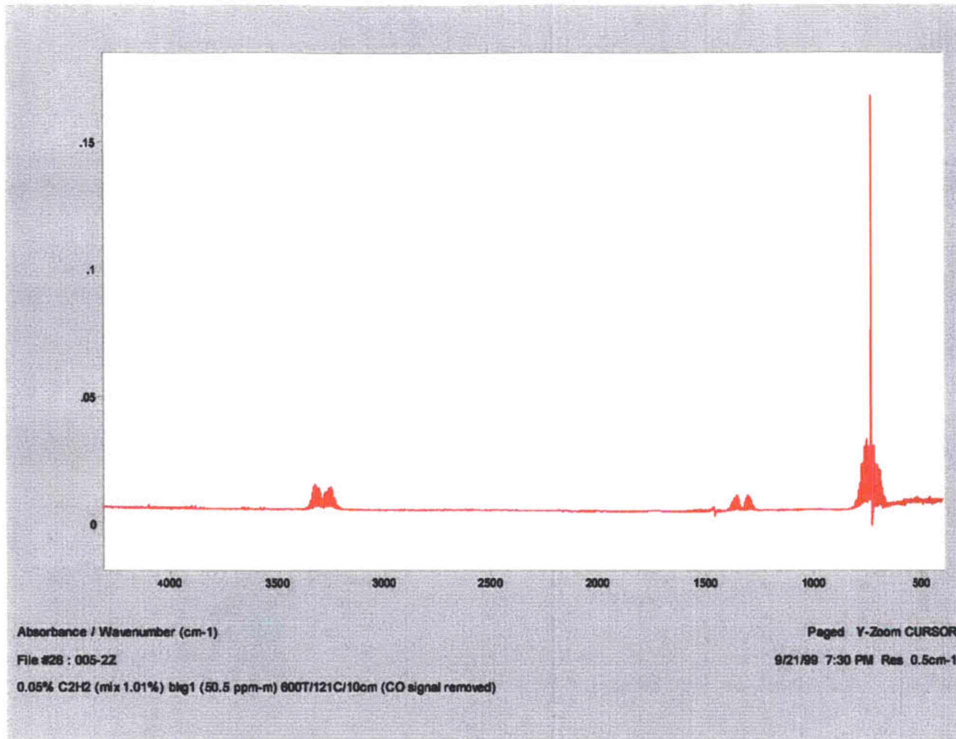
.15
.1
.05
0
4000
3500
3000
2500
2000
1500
1000
500
Absorbance / Wavenumber (cm-1)
Paged Y-Zoom CURSOR
File #28 : 005-2Z
9/21/99 7:30 PM Res 0.5cm-1
0.05% C2H2 (mix 1.01%) bkg1 (50.5 ppm-m) 600T/121C/10cm (CO signal removed)

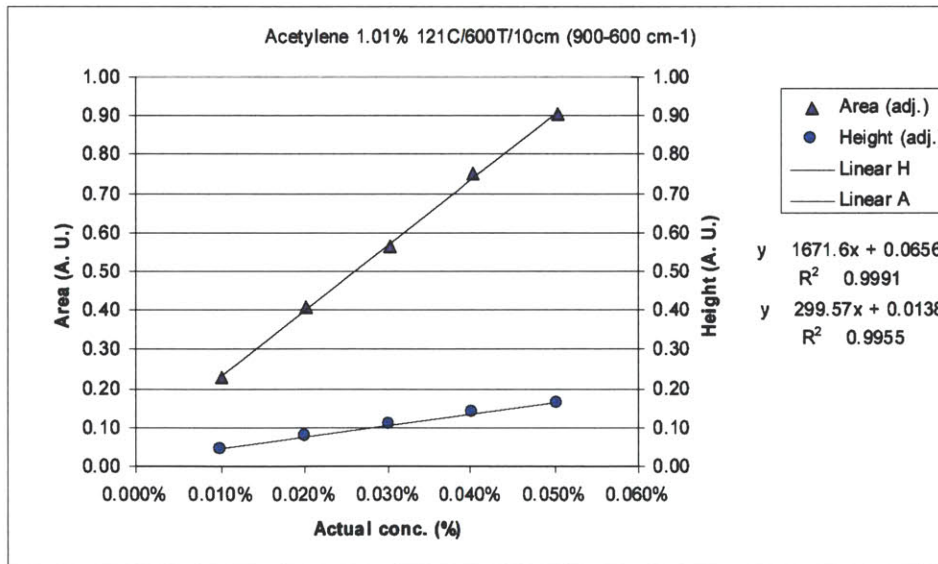
Acetylene 1.01% 121C/600T/10cm (900-600 cm-1)
Area (A. U.)
Height (A. U.)
1.00
0.90
0.80
0.70
0.60
0.50
0.40
0.30
0.20
0.10
0.00
0.000%
0.010%
0.020%
0.030%
0.040%
0.050%
0.060%
Actual conc. (%)
Area (adj.)
Height (adj.)
Linear H
Linear A
y 1671.6x + 0.0656
R2 0.9991
y 299.57x + 0.0138
R2 0.9955

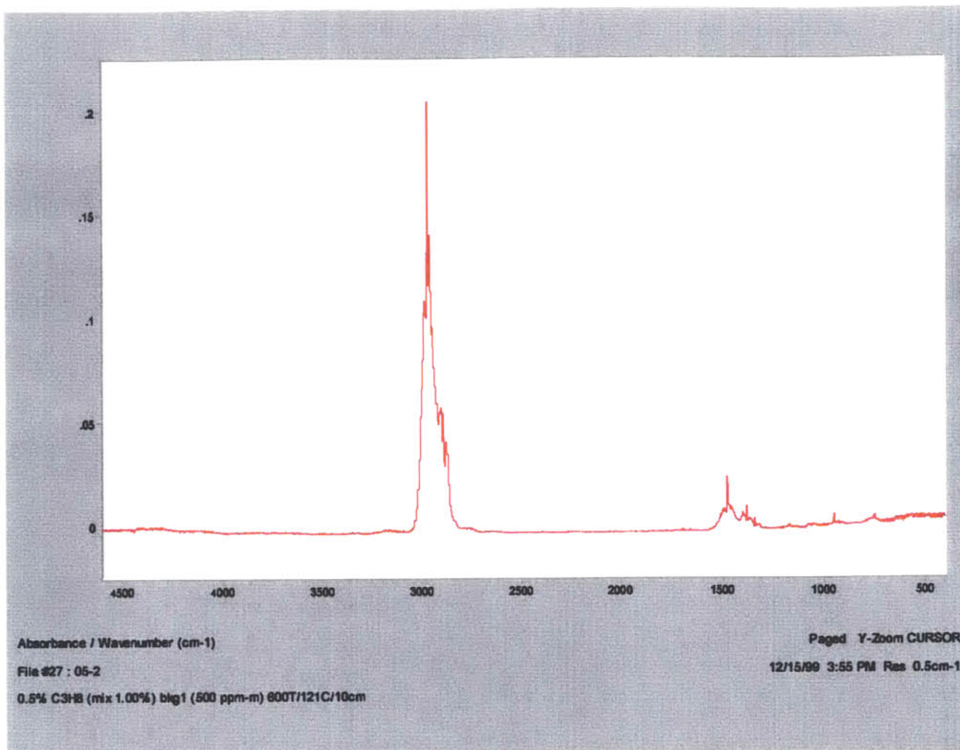
.2
.15
.1
.05
0
4500
4000
3500
3000
2500
2000
1500
1000
500
Absorbance / Wavenumber (cm-1)
File #27 : 05-2
0.5% C3H8 (mix 1.00%) bkg1 (500 ppm-m) 600T/121C/10cm
Paged Y-Zoom CURSOR
12/15/99 3:55 PM Res 0.5cm-1

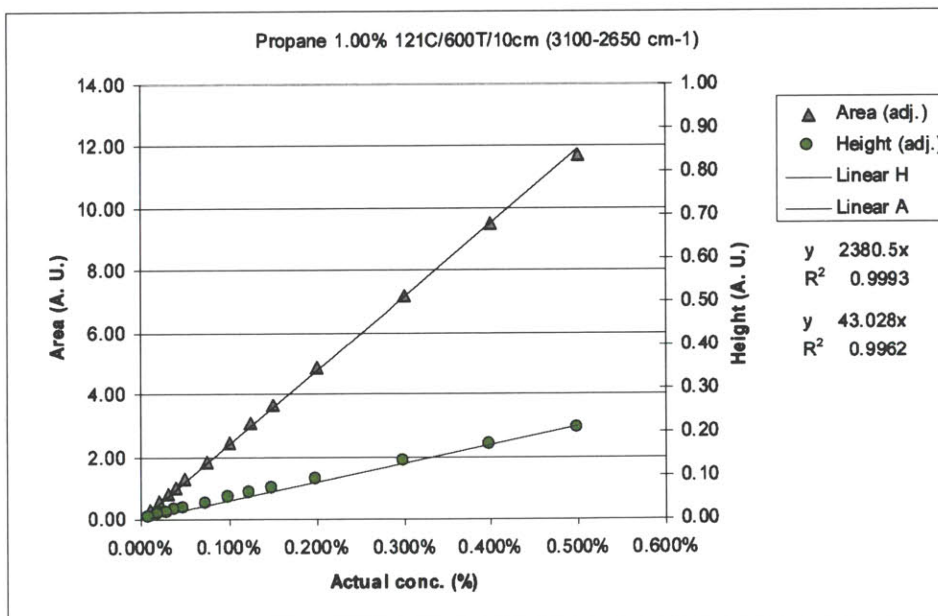
Propane 1.00% 121C/600T/10cm (3100-2650 cm-1)
Area (A. U.)
Height (A. U.)
Actual conc. (%)
14.00
12.00
10.00
8.00
6.00
4.00
2.00
0.00
1.00
0.90
0.80
0.70
0.60
0.50
0.40
0.30
0.20
0.10
0.00
0.000%
0.100%
0.200%
0.300%
0.400%
0.500%
0.600%
Area (adj.)
Height (adj.)
Linear H
Linear A
y 2380.5x
R2 0.9993
y 43.028x
R2 0.9962

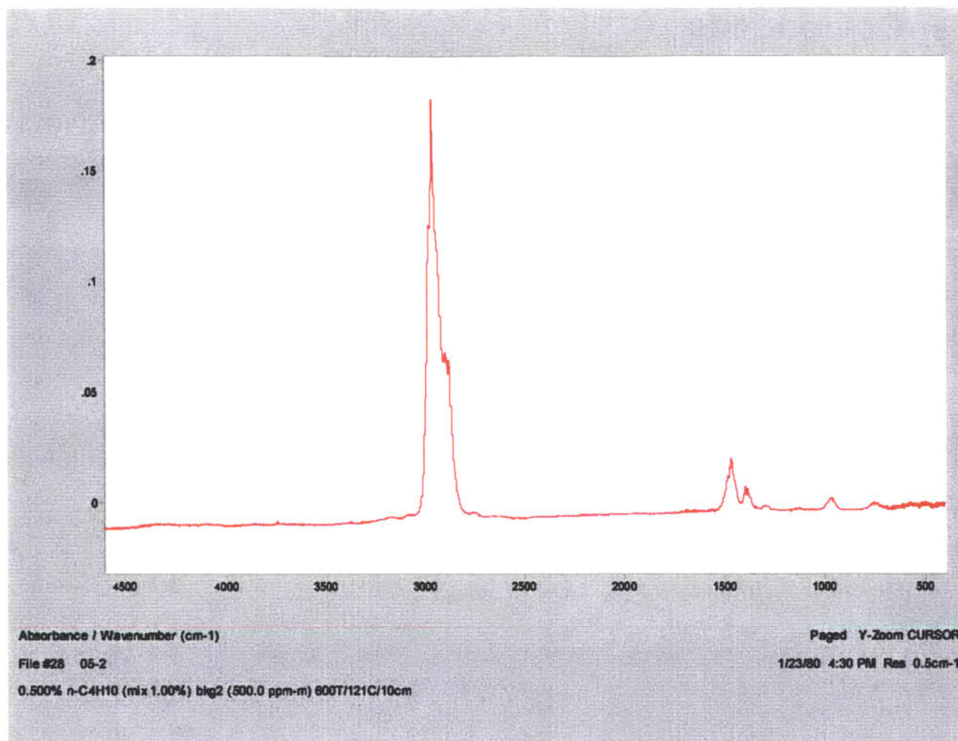

.2
.15
.1
.05
0
4500
4000
3500
3000
2500
2000
1500
1000
500
Absorbance / Wavenumber (cm-1)
Paged Y-Zoom CURSOR
File #28 05-2
1/23/80 4:30 PM Res 0.5cm-1
0.500% n-C4H10 (mix 1.00%) bkg2 (500.0 ppm-m) 600T/121C/10cm

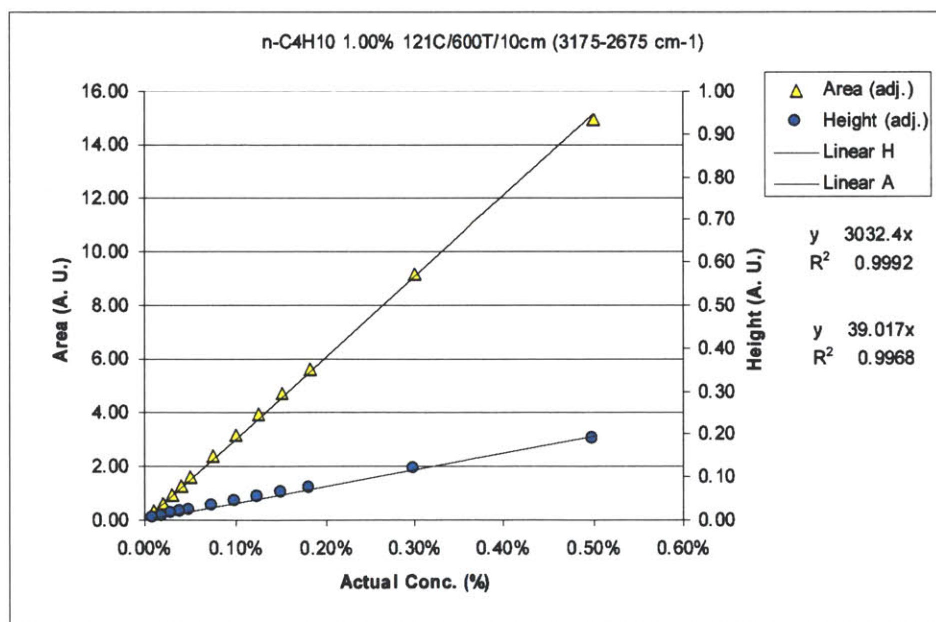

n-C4H10 1.00% 121C/600T/10cm (3175-2675 cm-1)
Area (A. U.)
Height (A. U.)
Actual Conc. (%)
16.00
14.00
12.00
10.00
8.00
6.00
4.00
2.00
0.00
1.00
0.90
0.80
0.70
0.60
0.50
0.40
0.30
0.20
0.10
0.00
0.00%
0.10%
0.20%
0.30%
0.40%
0.50%
0.60%
Area (adj.)
Height (adj.)
Linear H
Linear A
y 3032.4x
R² 0.9992
y 39.017x
R² 0.9968

B.7 Other Compounds

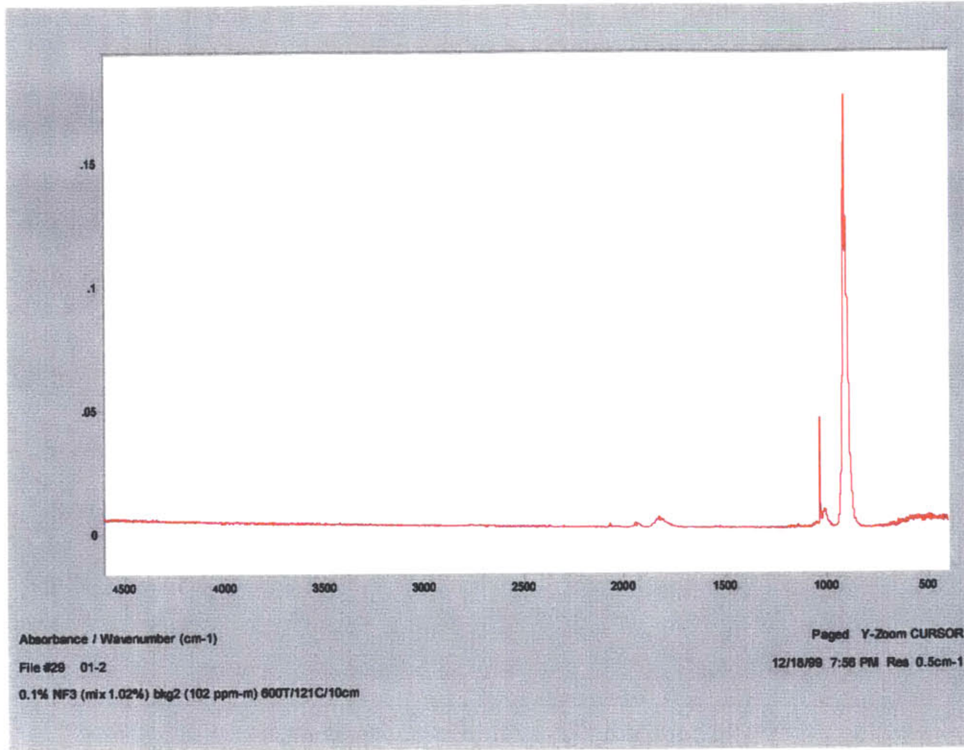

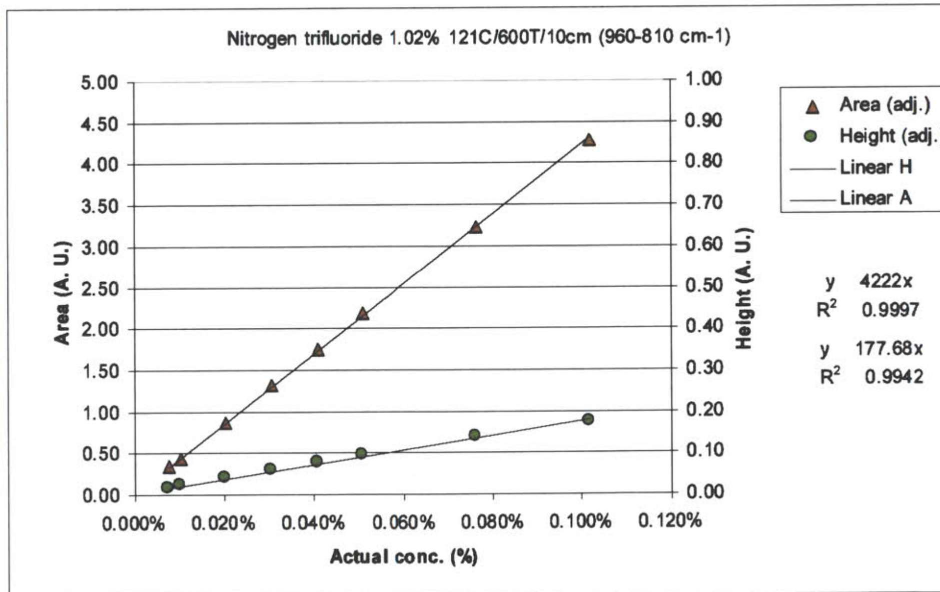

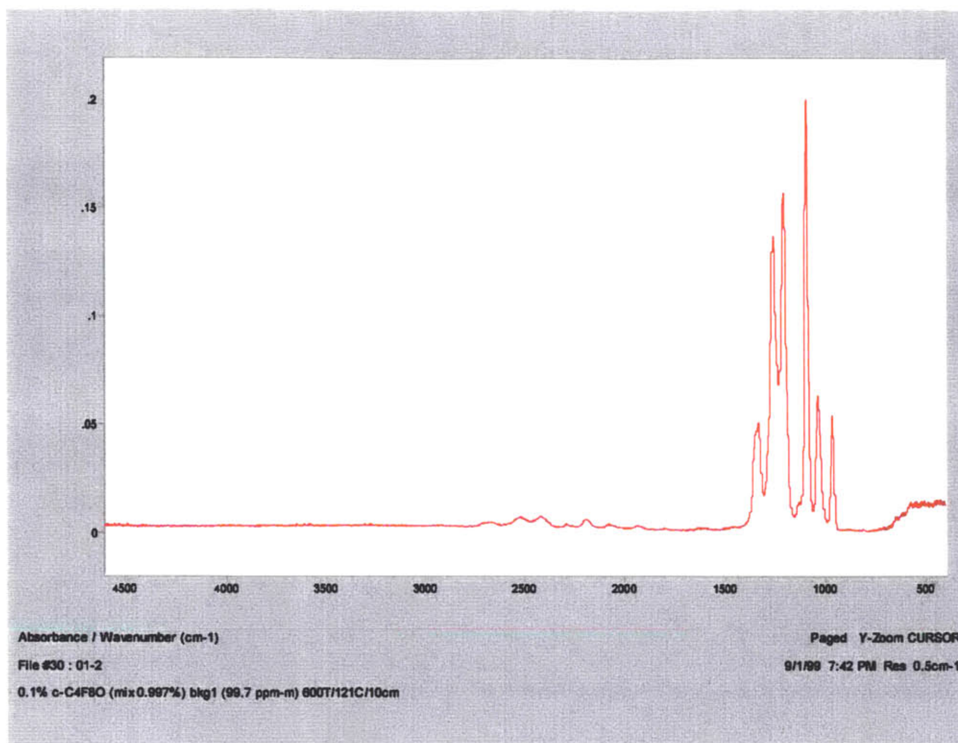
.2
.15
.1
.05
0
4500
4000
3500
3000
2500
2000
1500
1000
500
Absorbance / Wavenumber (cm-1)
File #30 : 01-2
0.1% c-C4F8O (mix 0.997%) bkg1 (99.7 ppm-m) 600T/121C/10cm
Paged Y-Zoom CURSOR
9/1/99 7:42 PM Res 0.5cm-1

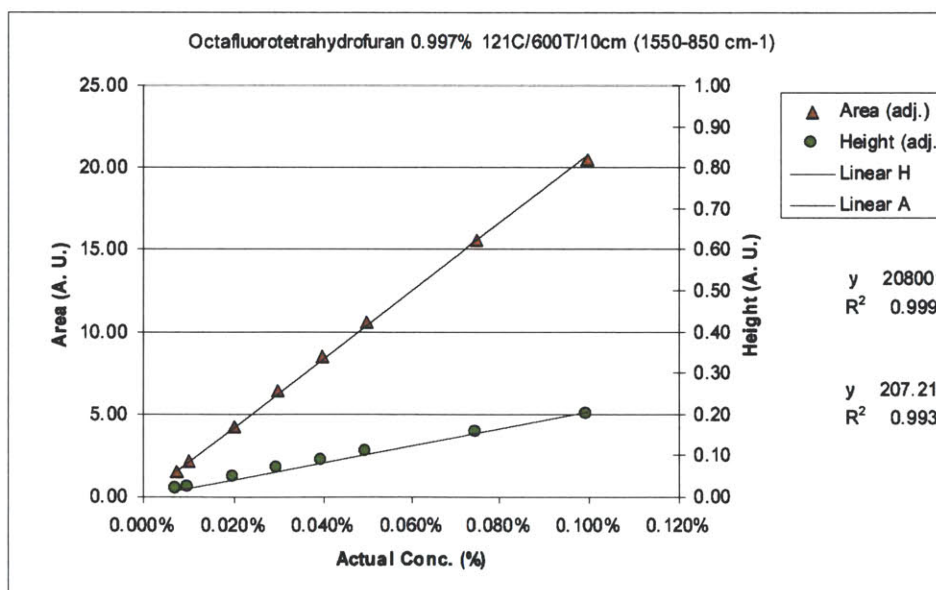
Octafluorotetrahydrofuran 0.997% 121C/600T/10cm (1550-850 cm-1)
Area (A. U.)
25.00
20.00
15.00
10.00
5.00
0.00
Height (A. U.)
1.00
0.90
0.80
0.70
0.60
0.50
0.40
0.30
0.20
0.10
0.00
0.000%
0.020%
0.040%
0.060%
0.080%
0.100%
0.120%
Actual Conc. (%)
Area (adj.)
Height (adj.)
Linear H
Linear A
y 20800x
R² 0.9992
y 207.21x
R² 0.9933

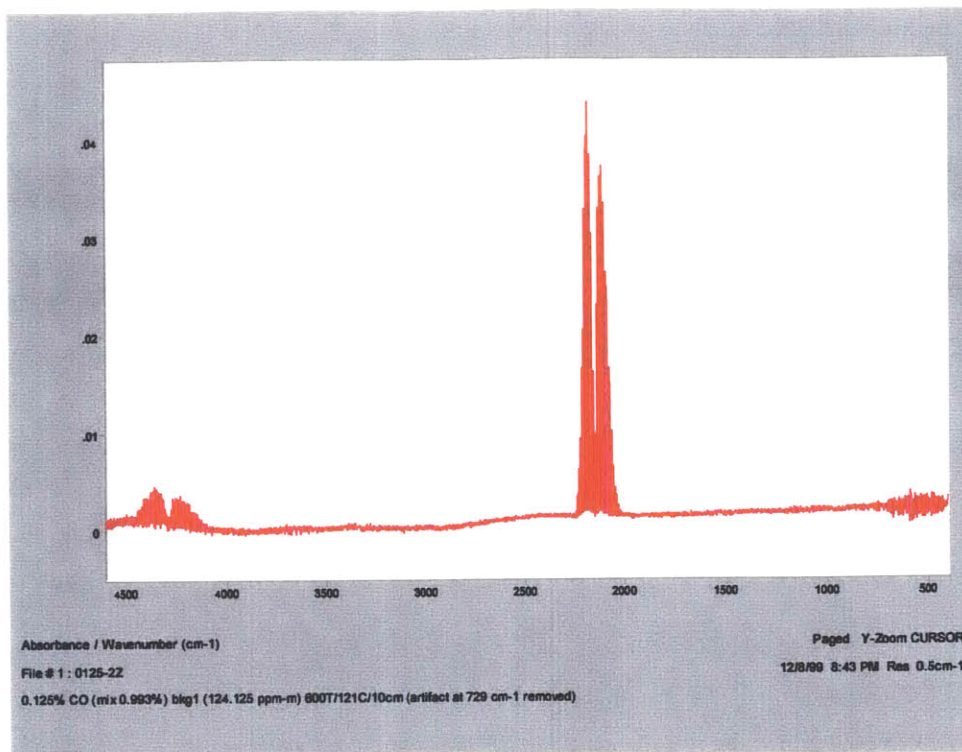
.04
.03
.02
.01
0
4500
4000
3500
3000
2500
2000
1500
1000
500
Absorbance / Wavenumber (cm-1)
File # 1 : 0125-2Z
0.125% CO (mix 0.993%) bkg1 (124.125 ppm-m) 600T/121C/10cm (artifact at 729 cm-1 removed)
Paged Y-Zoom CURSOR
12/8/99 8:43 PM Res 0.5cm-1

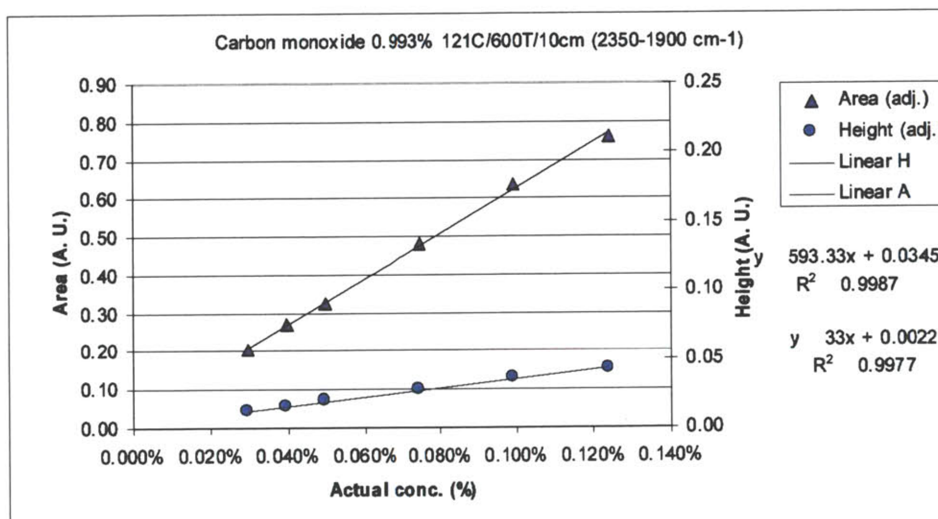
Carbon monoxide 0.993% 121C/600T/10cm (2350-1900 cm-1)
0.90
0.80
0.70
0.60
0.50
0.40
0.30
0.20
0.10
0.00
Area (A. U.)
0.25
0.20
0.15
0.10
0.05
0.00
Height (A. U.)
0.000% 0.020% 0.040% 0.060% 0.080% 0.100% 0.120% 0.140%
Actual conc. (%)
Area (adj.)
Height (adj.)
Linear H
Linear A
y 593.33x + 0.0345
R² 0.9987
y 33x + 0.0022
R² 0.9977

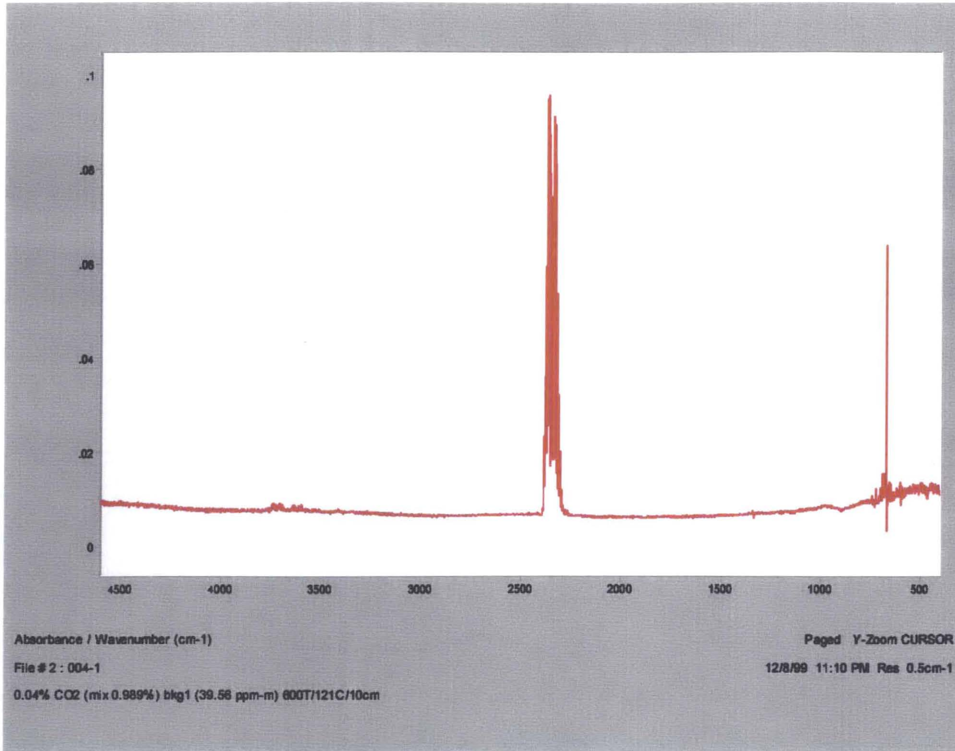
.1
.08
.06
.04
.02
0
4500
4000
3500
3000
2500
2000
1500
1000
500
Absorbance / Wavenumber (cm-1)
Paged Y-Zoom CURSOR
File # 2 : 004-1
12/8/99 11:10 PM Res 0.5cm-1
0.04% CO2 (mix 0.989%) bkg1 (39.56 ppm-m) 600T/121C/10cm

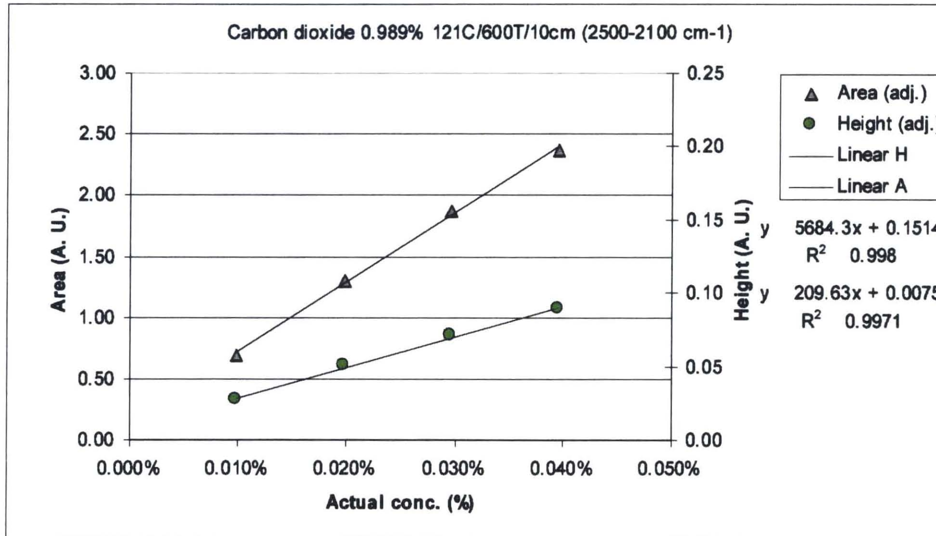
Carbon dioxide 0.989% 121C/600T/10cm (2500-2100 cm-1)
Area (A. U.)
3.00
2.50
2.00
1.50
1.00
0.50
0.00
Height (A. U.)
0.25
0.20
0.15
0.10
0.05
0.00
0.000%
0.010%
0.020%
0.030%
0.040%
0.050%
Actual conc. (%)
Area (adj.)
Height (adj.)
Linear H
Linear A
y 5684.3x + 0.1514
R^2 0.998
y 209.63x + 0.0075
R^2 0.9971